

Development and application of the Re-Os isotope system to sediment-hosted Zn-Pb ores and sedimentary pore waters

by

Danny Hnatyshin

A thesis submitted in partial fulfillment of the requirements for the degree of

Doctor of Philosophy

Department of Earth and Atmospheric Sciences
University of Alberta

© Danny Hnatyshin, 2018

Abstract

The rhenium-osmium (Re-Os) isotopic system is used to determine the age of, and trace the origins of, minerals and fluids found within the Earth's crust. This thesis focuses on application of Re-Os geochronology and isotope systematics to sulphide minerals from carbonate-hosted Zn-Pb ore deposits, surface waters, and shallow to deep pore waters from the Western Canada Sedimentary Basin.

Re-Os geochronology for the Silvermines deposit in Ireland produced a similar age (334.0 ± 6.1 Ma) to a previously published date from the nearby Lisheen deposit (346.6 ± 3.0 Ma). These ages require that mineralization in the Irish orefield occurred in the shallow subsurface, but over a protracted, likely episodic, period in early Carboniferous time. This result refutes models of ore formation based on paleomagnetic ages, and may link ore formation to periods of volcanism in the orefield.

Following the success of Re-Os geochronology in the Irish orefield, the Re-Os system was applied to a suite of Zn-Pb carbonate-hosted ore deposits from the Canadian Cordillera. These include metamorphosed deposits from the southern Canadian Cordillera (Salmo District), tectonically complex deposits in northern British Columbia (Robb Lake) and the southern Northwest Territories (Prairie Creek) of the northern Canadian Cordillera. Pyrite Re-Os ages of >300 Ma for all these deposits suggest that mineralization was associated with an extensional tectonic regime that developed behind an active subduction zone west of these deposits during the Paleozoic. These results agree with previous sphalerite Rb-Sr dating and invalidate the much younger paleomagnetic ages for Zn-Pb ores in the Canadian Cordillera. Therefore, other deposits that have paleomagnetic age constraints (e.g. Pine Point, Monarch-Kickinghorse) are also now considered suspect.

This thesis investigated Re at the ppb-level on a micro-scale in sulphide minerals, which permits a unique perspective of the Re-Os systematics of minerals widely used for geochronology. Laser ablation ICP-MS compositional mapping of the precisely-dated sample (8S08FW) from Lisheen, is characterized by a relatively homogenous Re distribution (~1-25 ppb) and contains negligible alteration or impurity phases. All other samples that were analyzed contain Re abundances that could vary by several orders of magnitude. Clean ore-stage pyrite typically has the lowest concentration of Re, whereas areas associated with alteration, identified by oxidation or Al enrichment, may contain several orders of magnitude higher concentrations of Re. The unexpected discovery of putative micron-scale molybdenite crystals that postdate mineralization in many samples influences the Re-Os age of some samples. From the Nanisivik area of Arctic Canada, unusual Re-Os systematics of one sample from Hawker Creek, are readily explained by the findings of two generations of Re-poor and Re-rich pyrite, identified only by LA-ICPMS. In light of these results it is recommended that samples are characterized at the micron-scale to ensure that only paragenetically simple, unaltered material is selected for Re-Os geochronology.

On a broader scale, the Re-Os systematics of pore fluids were characterized from the Williston Basin in southern Saskatchewan to help discern possible sources, sinks, and transport mechanisms of Re and Os within sedimentary basins. Pore fluids in near surface aquifers appear to mimic surface water Os isotopic compositions ($^{187}\text{Os}/^{188}\text{Os} > 1$), although at higher concentrations (15-95 ppq). However, deeper confined aquifers typically contain undetectable levels of Re and Os (< 300 ppq and < 5 ppq, respectively). This necessitates that removal processes dominate any leaching of Re and/or Os from the aquifer skeleton, even in highly saline brines. Interaction between water and oil may explain the observed depletion in some cases, however the cause of Re and Os

depletion in petroleum-barren aquifers remains enigmatic. It is speculated that Re and/or Os are adsorbed into organic matter or clay minerals along the fluid migration pathways.

Preface

Some of the material within this thesis was part of collaborative research and includes datasets that were published in my previous MSc thesis as elaborated below.

Chapter 3 of this thesis has been published as "Hnatyshin, D., Creaser, R. A., Wilkinson, J. J., & Gleeson, S. A. (2015). Re-Os dating of pyrite confirms an early diagenetic onset and extended duration of mineralization in the Irish Zn-Pb ore field. *Geology*, 43(2), 143-146". The data present within this chapter is a mix of original PhD research (Silvermines deposit) and that of material analysed during my MSc thesis (Lisheen deposit). For this publication I was in charge of data acquisition and wrote the majority of the text. However, many important edits and comments from my collaborators made this publication possible. Chapter 3 may be referenced in other chapters as Hnatyshin et al. (2015) as opposed to Chapter 3.

Chapter 4 is split into two sections (Chapter 4A and Chapter 4B) to ensure better organization between two projects that use the same datasets. These chapters used datasets from my previous MSc research with additional follow up work applied to them. Chapter 4 also contain a large amount of new data to complement the basic data provide in my MSc thesis. The MSc datasets are referenced within Chapter 4 either as Hnatyshin (2012) or Hnatyshin et al. (2015). Some of the statistical analyses (i.e. correlograms) were constructed with the help of Kenny Kocon from Statistics Canada.

Chapter 4, 5, and 6 represent original work unique to this thesis project and are planned to be incorporated into future publications.

Acknowledgements

This thesis was completed under the supervision of Dr. Robert A. Creaser. Without his expertise and willingness to openly discuss the complexities of this research, this thesis would not have been possible. Additional thanks go out to Dr. Jamie Wilkinson, Dr. Elizabeth Turner, Dr. Suzanne Paradis, and Dr. Ben Rostron, who provided the numerous samples required for this thesis. Furthermore, discussions with Dr. Jamie Wilkinson, Dr. Suzanne Paradis, Dr. Sarah Gleeson and Dr. Ben Rostron were engaging and productive, allowing me to have a more comprehensive understanding of the results gathered for this thesis. The data acquisition for this thesis required the assistance of numerous individuals with technical expertise. For work produced from the Crustal Re-Os Geochronology Laboratory at the University of Alberta I would like to express thanks to Krystle Moore, Barbara Ziger, and Mark Simms for assisting me with sample preparation and data acquisition. The micro-analytical techniques used in this thesis project would not have been possible without the help of Dr. Richard Stern (SIMS, University of Alberta), Dr. Sebastien Meffre (LA-ICPMS, University of Tasmania), Dr. Andy DuFrane (LA-ICPMS, University of Alberta), Dr. Andrew Locock (EMPA, University of Alberta). Field work associated with the collection of well water samples (Chapter 6) would have been impossible without the support of the Saskatchewan Government, and in particular Gavin Jensen, who put in tremendous work in organizing the field work sessions. I would finally like to thank my fellow graduate students (Naomi Miles, Lin Chen, Merilie Reynolds, Jon Toma, and Sam Bowman) for a number of very helpful discussions about my research topics. Additional funding for this thesis was generously provided by Queen Elizabeth II Graduate Scholarship.

Table of Contents

| | |
|--|-----------|
| 1.0 - INTRODUCTION: | 1 |
| 1.1 - Background | 1 |
| 1.2 - The Re-Os system | 2 |
| 1.3- Applications of Re-Os geochronology in ore deposits | 3 |
| 1.4 - Dating of carbonate-hosted Zn-Pb ore deposits | 4 |
| 1.5 - Objectives and structure of this PhD Thesis | 6 |
| 1.6 - References | 7 |
| 2.0 - THEORETICAL AND EMPIRICAL BACKGROUND | 15 |
| 2.1 - Fundamentals of Re-Os geochronology | 15 |
| 2.2 - Assumptions | 16 |
| 2.2.1 - (1) Samples are formed synchronously | 16 |
| 2.2.2 - (2) Single osmium reservoir | 17 |
| 2.2.3 - (3) No alteration | 18 |
| 2.2.4 - (4) No contamination | 19 |
| 2.3 - Current constraints on Re-Os isotopic reservoirs | 19 |
| 2.4 - References | 21 |
| 3.0 - RE-OS DATING OF PYRITE CONFIRMS AN EARLY DIAGENETIC ONSET AND EXTENDED DURATION OF MINERALIZATION IN THE IRISH ZN-PB OREFIELD | 29 |
| 3.1 - Introduction | 29 |
| 3.2 - Irish orefield | 30 |
| 3.3 - Study sites | 30 |
| 3.4 - Re-Os Geochronology | 31 |
| 3.5 - Timing and duration of mineralization | 31 |
| 3.6 - Osmium source | 32 |
| 3.7 - A possible link between volcanism and Zn-Pb mineralization | 32 |
| 3.8 - Implication for dating carbonate-hosted Zn-Pb ores | 33 |
| 3.9 - References | 33 |
| 3.10: Appendix | 43 |

| | |
|--|-----------|
| 3.10.1: Sample Descriptions | 43 |
| 3.10.2: Sample Preparation | 46 |
| 3.10.3: Analytical Data | 46 |
| 3.10.4: References: | 47 |
| 4.1: UNDERSTANDING PYRITE RE-OS GEOCHRONOLOGY | 48 |
| PART A: RE-OS SYSTEMATICS OF PYRITE | 48 |
| 4.1.1: Introduction | 48 |
| 4.1.2: Violations of isochron assumptions | 49 |
| 4.1.3: Sample Selection | 50 |
| 4.1.3.1: Study Location 1: Lisheen Deposit | 51 |
| 4.1.3.1.1: Background | 51 |
| 4.1.3.1.2: Mineralization | 51 |
| 4.1.3.1.3: Sample Selection | 52 |
| 4.1.3.2: Study Location 2: Baffin Island | 54 |
| 4.1.3.2.1: Background: | 54 |
| 4.1.3.2.2: Sample Description and Background | 54 |
| 4.1.4: Methods | 55 |
| 4.1.4.1 Sample Preparation | 55 |
| 4.1.4.2: ICP-MS Analysis | 55 |
| 4.1.4.3: Re-Os Analytical Procedure | 56 |
| 4.1.4.4: Sulphur Isotope Sample Preparation | 56 |
| 4.1.4.5: LA- ICPMS Analysis | 57 |
| 4.1.5: Results | 58 |
| 4.1.5.1: Characterization of Mineral Separates | 58 |
| 4.1.5.2: Re-Os Results | 58 |
| 4.1.5.3: SIMS Sulphur Isotope Study | 59 |
| 4.1.5.3.1: Lisheen | 59 |
| 4.1.5.3.2: Baffin Island | 60 |
| 4.1.5.4: Laser Ablation Results | 61 |
| 4.1.6: Discussion | 63 |
| 4.1.6.1: Assessment of Lisheen Re-Os Geochronology | 63 |
| 4.1.6.1.1: Isochron Assumption 2: Variability in initial $^{187}\text{Os}/^{188}\text{Os}$ | 63 |
| 4.1.6.1.2: Isochron Assumptions 3 and 4: Alteration and Impurities | 63 |
| 4.1.6.1.3: Recommended Interpretation of Lisheen Re-Os Geochronology | 66 |
| 4.1.6.2: Assessment of Nanisivik Re-Os Geochronology | 68 |
| 4.1.6.2.1: Isochron Assumption 2: Initial $^{187}\text{Os}/^{188}\text{Os}$ Variation | 68 |
| 4.1.6.2.2: Isochron Assumption 3 and 4: Alteration and Impurities | 68 |
| 4.1.6.2.3: Recommended Interpretation of Nanisivik Re-Os Geochronology | 69 |
| 4.1.6.2.4: Reassessment of Hawker Creek Re-Os Geochronology | 69 |
| 4.1.6.3: Rhenium Systematics within Sulphide Ore | 70 |
| 4.1.6.3.1: Observed Distributions and Potential Hosts | 70 |
| 4.1.6.3.2: Spatial Correlations | 72 |
| 4.1.6.3.3: Alternatives to Re Mapping | 73 |
| 4.1.6.3.4: Sulphur Isotope Distribution | 73 |
| 4.1.6.3.5: General Implications for Re-Os Geochronology | 74 |

| | |
|--|------------|
| 4.1.7: Conclusions | 75 |
| 4.1.8: References | 76 |
| 4.1.9: Appendix: | 119 |
| 4.2: UNDERSTANDING PYRITE RE-OS GEOCHRONOLOGY | 146 |
| PART B: REFINING SAMPLE PROCESSING PROTOCOLS | 146 |
| 4.2.1: Introduction | 146 |
| 4.2.2: Sample Preparation Methods and Characterization. | 147 |
| 4.2.3: Results and Discussion | 149 |
| 4.2.3.1: Mineral separate mineralogy and descriptions | 149 |
| 4.2.3.2: Leaching experiments – bulk mineralogy | 150 |
| 4.2.3.3: Leaching experiments – effect on Re-Os isochrons | 151 |
| 4.2.3.4: Heavy liquid separation, composite grains and effect of low density phases on isochrons | 153 |
| 4.2.3.5: Evaluation of Magnetic Separation, and effects on Re-Os isochrons | 154 |
| 4.2.4: Conclusions | 156 |
| 4.2.5: References | 157 |
| 4.2.6: Appendix | 169 |
| 5.0: PYRITE RE-OS GEOCHRONOLOGY OF CARBONATE-HOSTED ZN-PB ORE DEPOSITS OF THE CANADIAN CORDILLERA | 170 |
| 5.1: Introduction | 170 |
| 5.2: Regional Geologic History | 171 |
| 5.3: Deposit Geology | 173 |
| 5.3.1: Prairie Creek | 173 |
| 5.3.1.1: Geological Context | 173 |
| 5.3.1.2: Mineralization | 174 |
| 5.3.2: Robb Lake | 175 |
| 5.3.2.1: Geological Context | 175 |
| 5.3.2.2: Mineralization | 176 |
| 5.3.3: Salmo district | 177 |
| 5.3.3.1: Geologic Context | 177 |
| 5.3.3.2: Mineralization | 178 |
| 5.3.3.3: Reeves MacDonald Mine | 179 |
| 5.3.3.4: H.B. Mine | 179 |
| 5.4: Methodology | 179 |
| 5.4.1: Sample Selection and Preparation | 179 |
| 5.4.2: Re-Os Analytical Procedure | 180 |
| 5.4.3: Compositional Mapping | 181 |
| 5.5: Results | 182 |

| | |
|---|------------|
| 5.5.1: Sample Characterization | 182 |
| 5.5.1.1: Prairie Creek - MVT-style Mineralization | 182 |
| 5.5.1.2: Prairie Creek - SMS-style Mineralization | 183 |
| 5.5.1.3: Prairie Creek - Vein-style Mineralization | 184 |
| 5.5.1.4: Robb Lake | 185 |
| 5.5.1.5: Salmo district | 186 |
| 5.5.2: Re-Os Geochronology Results | 187 |
| 5.5.2.1: Prairie Creek | 187 |
| 5.5.2.2: Robb Lake | 188 |
| 5.5.2.3: Salmo district | 188 |
| 5.6: Discussion | 189 |
| 5.6.1: Interpretation of Re-Os Isotopic Data | 189 |
| 5.6.1.1: General Considerations | 189 |
| 5.6.1.2: Re-Os Systematics of Prairie Creek | 189 |
| 5.6.1.3: Re-Os Systematics of Robb Lake | 191 |
| 5.6.1.4: Re-Os Systematics of the Salmo district | 193 |
| 5.6.2: Constraints on the relationship between SMS, Vein-Type, and MVT mineralization at Prairie Creek | 194 |
| 5.6.3: Timing of Zn-Pb mineralization in the Canadian Cordillera. | 195 |
| 5.7: Conclusions | 197 |
| 5.8: References | 198 |
| 5.9: Appendix: | 235 |
| | |
| 6.0: RHENIUM-OSMIUM ISOTOPIC SYSTEMATICS OF SURFACE, SHALLOW AND DEEP GROUNDWATER FROM THE WESTERN CANADA SEDIMENTARY BASIN (WCSB) | 243 |
| 6.1: Introduction | 243 |
| 6.2: Re-Os Reservoirs and Transportation | 243 |
| 6.3: Speciation in Aqueous Solutions | 244 |
| 6.4: Sampling Locations | 245 |
| 6.5: Sampling Protocol | 246 |
| 6.6: Analytical Procedures | 247 |
| 6.7: Analysis | 248 |
| 6.8: Results | 249 |
| 6.9: Sample Contamination | 250 |
| 6.10: Discussion | 251 |
| 6.10.1: Re-Os distribution in surface and groundwater | 251 |
| 6.10.2: Water-Oil Interactions | 253 |
| 6.10.3: Implications for Re-Os geochronology of sediment-hosted ore deposits. | 254 |
| 6.10.4: Os Tracing | 255 |

| | |
|---|------------|
| 6.11: Conclusions | 256 |
| 6.12: References | 256 |
| 6.13: Appendix | 271 |
| 7.0: CONCLUSIONS | 273 |
| 7.1: Mineralization in the Irish Orefield | 273 |
| 7.2: Re-Os systematics and the recommended approach to Re-Os geochronology | 273 |
| 7.3: Mineralization in the Canadian Cordillera | 274 |
| 7.4: Sources and Sinks of Re-Os within Sedimentary Basins | 275 |
| 7.5: Future Considerations and Unanswered Questions | 275 |
| BIBLIOGRAPHY | 278 |

List of Tables

| | |
|--|-----|
| Table 3.1: Lisheen Re-Os data..... | 46 |
| Table 3.2: Silvermines Re-Os data | 46 |
| Table 3.3: Re-Os blank data..... | 47 |
| Table 4.1.1: Lisheen Sample Mineralogy | 84 |
| Table 4.1.2: Lisheen Main Zone Re-Os analyses | 85 |
| Table 4.1.3: Lisheen Derryville Zone Re-Os analyses | 86 |
| Table 4.1.4: Lisheen Bog Zone Re-Os analyses | 87 |
| Table 4.1.5: Nanisivik and Hawker Creek Re-Os analyses | 88 |
| Table 4.1.6: ICPMS mineral separate analyses for the Lisheen dataset | 119 |
| Table 4.1.7: ICPMS mineral separate analyses for the Baffin Island dataset..... | 120 |
| Table 4.1.8: SIMS Sulphur isotope analyses of 8S08FW mineral | 121 |
| separates..... | 121 |
| Table 4.1.9: SIMS sulphur isotope analyses of 8S08FW-1 | 122 |
| Table 4.1.10: SIMS sulphur isotope analyses of LK 359 mineral separates | 123 |
| Table 4.1.11: SIMS sulphur isotope analyses of LK 359 rock | 124 |
| fragments..... | 124 |
| Table 4.1.12: SIMS sulphur isotope analyses of LK 451 | 125 |
| mineral separates..... | 125 |
| Table 4.1.13: SIMS sulphur isotope analyses of..... | 126 |
| LK 451 rock fragments | 126 |
| Table 4.1.14: SIMS sulphur isotope analyses of Nanisivik samples | 127 |
| Table 4.1.15: SIMS sulphur isotope analyses of Hawker Creek samples | 128 |
| Table 4.2.1: Lisheen Sample Mineralogy | 160 |
| Table 4.2.2: ICPMS analyses for samples used for leaching experiments | 169 |
| Table 5.1: Re-Os results for Prairie Creek..... | 207 |
| Table 5.2: Re-Os results for Robb Lake | 208 |
| Table 5.3: Re-Os results for the Salmo district..... | 209 |
| Table 5.4: Mineralogy and modal abundance estimates | 210 |
| Table 6.1: Location data | 264 |
| Table 6.2: Analytical data | 265 |
| Table 6.3: ICPMS analyses for samples collected in 2016. Detection limits do not represent uncertainty in the measurement. | 271 |
| Table 6.4: ICPMS analyses for samples collected in 2017. Detection limits do not represent uncertainty in the measurement. | 272 |

List of Figures

| | |
|--|-----|
| Figure 2.1: Hypothetical Isochron | 27 |
| Figure 2.2: Re-Os Reservoirs | 28 |
| Figure 3.1: Geological map of Ireland | 39 |
| Figure 3.2: Stratigraphy of Lisheen and Silvermines | 40 |
| Figure 3.3: Isochrons for Lisheen and Silvermines | 41 |
| Figure 3.4: Summary of ages for the Irish orefield | 42 |
| Figure 3.5: Appendix - Sample locations | 44 |
| Figure 3.6: Appendix - Sample Pictures | 45 |
| Figure 3.7: Appendix - Sample Pictures | 45 |
| Figure 4.1.1: Re-Os comparison | 89 |
| Figure 4.1.2: Lisheen map and cross-section | 90 |
| Figure 4.1.3: Paragenetic sequence - Lisheen | 91 |
| Figure 4.1.4: 8S08FW Rock + BSE + Microscope Pictures | 92 |
| Figure 4.1.5: LK 359 Rock + BSE + Microscope Pictures | 93 |
| Figure 4.1.6: LK 451 Rock + BSE + Microscope Pictures | 94 |
| Figure 4.1.7: Baffin Island map | 95 |
| Figure 4.1.8: Nanisivik paragenesis | 96 |
| Figure 4.1.9: Nanisivik pictures | 97 |
| Figure 4.1.10: Mineral ICPMS | 98 |
| Figure 4.1.11: LK 359 isochron | 99 |
| Figure 4.1.12: LK 451 isochron | 100 |
| Figure 4.1.13: Transect and map locations | 101 |
| Figure 4.1.14: Sulfur isotope histograms - Lisheen | 102 |
| Figure 4.1.15: Sulfur isotope histograms - Nanisivik | 103 |
| Figure 4.1.16: Sulfur isotope transects - Lisheen | 104 |
| Figure 4.1.17: Sulfur isotope transects - Lisheen Bog Zone | 105 |
| Figure 4.1.18: Sulfur isotope transects - Nanisivik | 106 |
| Figure 4.1.19: 8S08FW - trace elements | 107 |
| Figure 4.1.20: LK 359 - trace elements | 108 |
| Figure 4.1.21: LK 451 - trace elements | 109 |
| Figure 4.1.22: NOV-1 - trace elements | 110 |
| Figure 4.1.23: NOV-2 - trace elements | 111 |
| Figure 4.1.24: HC - trace elements | 112 |
| Figure 4.1.25: Assumptions - model ages and initial ratios | 113 |
| Figure 4.1.26: Molybdenite inclusions | 114 |
| Figure 4.1.27: Correlogram- LK 359 | 115 |
| Figure 4.1.28: Trace element scatterplots | 116 |
| Figure 4.1.29: Sulphur vs. Element plots | 117 |
| Figure 4.1.30: Quality Factor | 118 |
| Figure 4.1.31: Appendix: NOV4 - mineral separates | 129 |
| Figure 4.1.32: Appendix: LA-ICMPS supplementary maps - 8S08FW Map 1 | 130 |
| Figure 4.1.33: Appendix: LA-ICMPS supplementary maps - 8S08FW Map 2 | 131 |
| Figure 4.1.34: Appendix: LA-ICMPS supplementary maps - 8S08FW Map 3 | 132 |
| Figure 4.1.35: Appendix: LA-ICMPS supplementary maps - 8S08FW Map 4 | 133 |
| Figure 4.1.36: Appendix: LA-ICMPS supplementary maps - LK359-1 Map 1 | 134 |

| | |
|--|-----|
| Figure 4.1.37: Appendix: LA-ICMPS supplementary maps - LK359-1 Map 2 | 135 |
| Figure 4.1.38: Appendix: LA-ICMPS supplementary maps - LK359-1 Map 3 | 136 |
| Figure 4.1.39: Appendix: LA-ICMPS supplementary maps - LK451 Map 1 | 137 |
| Figure 4.1.40: Appendix: LA-ICMPS supplementary maps - LK451 Map 2 | 138 |
| Figure 4.1.41: Appendix: LA-ICMPS supplementary maps - LK451 Map 3 | 139 |
| Figure 4.1.42: Appendix: LA-ICMPS supplementary maps - NOV4-1 Map 1 | 140 |
| Figure 4.1.43: Appendix: LA-ICMPS supplementary maps - NOV4-1 Map 2 | 141 |
| Figure 4.1.44: Appendix: LA-ICMPS supplementary maps - NOV4-2 Map 1 | 142 |
| Figure 4.1.45: Appendix: LA-ICMPS supplementary maps - NOV4-2 Map 1 | 143 |
| Figure 4.1.46: Appendix: LA-ICMPS supplementary maps - HC Map 1 | 144 |
| Figure 4.1.47: Appendix: LA-ICMPS supplementary maps - HC Map 2 | 145 |
| Figure 4.2.1: Mineral separates | 161 |
| Figure 4.2.2: Leachate composition | 162 |
| Figure 4.2.3: LK 451B leaching image | 163 |
| Figure 4.2.4: 8S08FW isochron | 164 |
| Figure 4.2.5: LK451 isochron | 165 |
| Figure 4.2.6: Calcium map | 166 |
| Figure 4.2.7: Rhenium vs. magnetic susceptibility | 167 |
| Figure 4.2.8: Recommended methodology | 168 |
| Figure 5.1: Cordillera map | 211 |
| Figure 5.2: Cordillera architecture | 212 |
| Figure 5.3: Prairie Creek stratigraphy | 213 |
| Figure 5.4: Prairie Creek map | 214 |
| Figure 5.5: Robb Lake map | 215 |
| Figure 5.6: Salmo district map | 216 |
| Figure 5.7: PC-94-80 pictures | 217 |
| Figure 5.8: PC-94-80 LA-ICPMS maps | 218 |
| Figure 5.9: Paragenesis | 219 |
| Figure 5.10: PC-93-25 pictures | 220 |
| Figure 5.11: PC-93-25 LA-ICPMS maps | 221 |
| Figure 5.12: PC-11-209A pictures | 222 |
| Figure 5.13: PC-11-209A LA-ICPMS maps | 223 |
| Figure 5.14: PCU pictures | 224 |
| Figure 5.15: PCU LA-ICMPS maps | 225 |
| Figure 5.16: Robb Lake pictures | 226 |
| Figure 5.17: Robb Lake LA-ICPMS maps | 227 |
| Figure 5.18: Salmo sample SP pictures | 228 |
| Figure 5.19: Salmo sample SP LA-ICPMS | 229 |
| Figure 5.20: HB pictures | 230 |
| Figure 5.21: Prairie Creek isochrons | 231 |
| Figure 5.22: Robb Lake isochrons | 232 |
| Figure 5.23: Salmo district isochrons | 233 |
| Figure 5.24: Age summary | 234 |
| Figure 5.25: Appendix: PC-94-80 EMPA | 235 |
| Figure 5.26: Appendix: PC-93-25 EMPA | 235 |
| Figure 5.27: Appendix: PC-11-209A EMPA | 236 |

| | |
|--|-----|
| Figure 5.28: Appendix: PCU EMPA | 237 |
| Figure 5.29: Appendix: Robb Lake EMPA | 238 |
| Figure 5.30: Appendix: Salmo EMPA..... | 239 |
| Figure 5.31: Appendix: PC-92-17B sample pictures..... | 240 |
| Figure 5.32: Appendix: Robb Lake deconvoluted LA-ICPMS Mo map..... | 241 |
| Figure 5.33: Appendix: Salmo deconvoluted LA-ICPMS Mo map | 242 |
| Figure 6.1: Re-Os resevoirs | 266 |
| Figure 6.2: Sample map | 267 |
| Figure 6.3: Results | 268 |
| Figure 6.4: Carius tube diagram..... | 269 |
| Figure 6.5: Oil-water disequilibrium | 270 |

1.0 - Introduction:

1.1 - Background

Geochemistry is a field in Earth science that attempts to understand Earth systems processes through measuring chemical signatures present in rocks and fluids and coupling them to physical and chemical processes that can produce them. Isotope geochemistry is one of the most important subsets of geochemistry and is widely used to constrain the history, chemical, and physical characteristics of a geologic system.

Isotope geochemistry is built upon the assumption that observed variations in the ratios between different isotopes (e.g. $^{18}\text{O}/^{16}\text{O}$, $^{34}\text{S}/^{32}\text{S}$, $^{187}\text{Os}/^{188}\text{Os}$) reflect differences in physical or chemical processes. Isotope geochemistry comes in two types, stable isotope geochemistry, and radioactive isotope geochemistry. In stable isotope geochemistry certain reactions preferentially fractionate one isotope from the other, which are often dependent on temperature and pressure of the system and can be catalyzed by certain reaction pathways (e.g. biological reactions). This process of fractionation can modify the isotope ratio of the system at the level of part per thousand (i.e. per-mil) with the magnitude being inversely proportional to the absolute difference in mass between the isotopes. By understanding how different processes (e.g. mineralization, phase transitions, biological reaction) fractionate different isotope systems, geoscientists strive to understand the processes a rock or fluid had experienced during its formation and evolution. This process is generally known as isotopic tracing.

Radioactive isotope systems have one or more isotopes that undergo radioactive decay (i.e. the parent) to a new radiogenic isotope (i.e. the daughter). The accumulation of the daughter product in a closed system through radioactive decay will follow the following equation:

$$D(t) = D_0 + P(e^{\lambda t} - 1) \quad (1)$$

where $D(t)$ is the amount of daughter after some time t , D_0 is the starting amount of daughter in the system, P is the amount of radioactive parent in the system, and λ is the decay constant for the parent isotope. The decay constant, for each radioactive isotope (e.g. ^{235}U , ^{238}U , ^{187}Re , ^{176}Lu , ^{147}Sm , ^{87}Rb , ^{40}K) is unique and fixed. As a result of radioactive decay the degree of variation commonly observed in the stable daughter products may be orders of magnitude greater than that observed through stable isotopic fractionation, which is typically ignored when working with radioactive isotope systems. Isotopic tracing using radiogenic isotopic systems typically involves

correcting for the accumulation of daughter product to determine D_0 and then comparing the D_0 values to known isotopic compositions of different reservoirs (e.g. mantle, crust). Whereas isotopic tracing is clearly useful, the most powerful application of radioactive isotope systems is in their unique ability to provide absolute ages in the rock record. In the field of geochronology absolute ages can be calculated by solving equation (1) for time, with each system being tailored for specific applications depending on the geochemical character of the corresponding parent-daughter pair. In an ideal system, a number of rules need to be satisfied to ensure an accurate age, with all imprecision coming from analytical uncertainty. The following rules will be discussed in detail in Chapter 2, but in short these rules are:

- 1) All samples in a dataset were formed synchronously.
- 2) They formed from a single isotopic reservoir (i.e. all samples started with the same D_0).
- 3) The samples have not been altered since formation (i.e. no gain or loss of parent or daughter).
- 4) The decay constant of the radioactive isotope is accurately and precisely known

1.2 - The Re-Os system

The Rhenium-Osmium (Re-Os) system is based on the beta decay of ^{187}Re to ^{187}Os (half life of 42 billion years; Smoliar et al., 1996) and is unique among radioactive isotopic systems as both Re and Os are classified as siderophile and chalcophile elements. This character allows Re to be preferentially sequestered into minerals not typically amenable to isotopic dating (e.g. sulphides) due to the primarily lithophile nature of all other radiometric systems commonly used (Rb-Sr, Sm-Nd, K-Ar, U-Pb and Lu-Hf). This attribute makes the Re-Os system highly applicable to the field of economic geology, as ore deposits are commonly enriched in sulphide minerals that sequester chalcophile elements. Furthermore, the tectonic models used to explain ore mineralization typically require robust age constraints to be verified or tested, making Re-Os geochronology one of the most valuable isotopic systems in economic geology.

Prior to analytical advancements that allowed precise and accurate isotopic measurements of Re and Os (Creaser et al., 1991; Volkening et al., 1991), the accurate determination of the Re decay constant (Smoliar et al., 1996), and other methodological improvements (Shirey and Walker, 1995; Birck et al., 1997), most ores could not be reliably dated. However, with current isotope dilution methods and negative thermal ionization mass spectrometry (NTIMS), geochronologically useful data can be obtained from minerals that contain > 0.1 parts per billion

(ppb) Re and > 1 parts per trillion Os (ppt), well within the range of concentrations observed for many sulphide minerals formed during ore stage mineralization. Over the past few decades, molybdenite, pyrite, and arsenopyrite have become the cornerstone of Re-Os geochronology due to their proven ability to produce robust ages in many types of ore deposits (e.g., Morelli et al., 2010; Ootes et al., 2011; Li et al., 2017).

1.3- Applications of Re-Os geochronology in ore deposits

The first attempts at applying Re-Os geochronology to crustal ore systems focused on the mineral molybdenite, as it is enriched in Re, with concentrations greater than parts per million (ppm) levels being typical. As a chronometer, molybdenite is a simple system as Os is not incorporated into its structure during mineralization, simplifying equation 1 into:

$$^{187}\text{Os} = ^{187}\text{Re}(e^{\lambda t}-1) \quad (2)$$

Initial attempts at dating molybdenite produced mixed results as some published datasets produced ages that are not geological reasonable (e.g. Luck and Allegre, 1982; McCandless et al., 1993; Suzuki et al., 2000, 2001), whereas other studies showed that molybdenite Re-Os geochronology holds tremendous potential (e.g. Stein et al., 1997; Torrealday et al., 2000). Reconciling these disparate findings required dedicated studies of the molybdenite Re-Os system. Through the use of laser ablation inductively coupled mass spectrometry (LA-ICPMS), it was revealed that Re and Os can end up being decoupled from one another within molybdenite crystals. Essentially, at the scale of individual crystals molybdenite may experience open system behaviour but at the bulk scale will remain closed. Hence, it has been recommended that bulk measurements are used to ensure precise and reproducible ages (e.g. Stein et al., 2003; Selby and Creaser, 2004). Complete open system behaviour, where Re is removed from molybdenite crystals into secondary phases appears to occur in some rare circumstances (e.g. McCandless et al., 1993), however the concerns brought up by Suzuki et al. (2000, 2001, 2004) have been mostly alleviated.

Other sulphide Re-Os systems, primarily based on the minerals pyrite and arsenopyrite, have also been developed and applied to ore systems. The far lower concentrations of Re (~ppb level) and Os (~ppt level) within these minerals delayed the development of pyrite Re-Os geochronology with early work being attempted in the late 1990's (e.g. Stein et al., 1998; Mathur et al., 1999). The major advantage in expanding the Re-Os system to these minerals is that pyrite

in particular is far more common in an ore's paragenetic sequence than molybdenite, and therefore can be used to investigate a far more diverse suite of ore systems. Pyrite is considered a robust mineral for use in geochronology as age information can be preserved through metamorphic regimes of 300-590°C (e.g. Brenan et al., 2000; van Acken et al., 2014; Vernon et al., 2014). The robust nature of the pyrite system has allowed for the precise determination (< 10% error) of many types of ore deposits such as orogenic and epigenetic gold deposits, porphyry, sedimentary exhalative (SEDEX), Mississippi Valley Type (MVT), and Irish-type ore deposits (Arne et al., 2001; Morelli et al., 2004; Kerr and Selby, 2012; Hnatyshin et al., 2015; Hnatyshin et al., 2016; Zhang et al., 2016). However, pyrite ages are typically less precise than molybdenite ages by up to an order of magnitude. This may be partially due to higher analytical errors associated with measuring the lower abundance of Re and Os associated with these sulphides. Further complexities include the presence of common Os in pyrite and arsenopyrite requiring the use of equation (1), which is more sensitive to violations of assumption (2), and the possibility that samples used for analysis also contain minerals that have comparable concentrations of Re and Os to pyrite but with less robust characteristics (e.g. sphalerite, pyrrhotite; Morelli et al., 2004, 2010).

1.4 - Dating of carbonate-hosted Zn-Pb ore deposits

Carbonate-hosted Zn-Pb ore deposits (e.g. MVT-type, Irish-type) are a class of deposits that provide the economically important base metals (Zn + Pb ± Cu ± Ag). These deposits are widespread worldwide with notable examples located throughout the United States, Canada, Ireland, mainland Europe, and Australia, with individual districts occupying up to several thousand square kilometers (Sangster, 1990; Leach et al., 2010). Ore stage mineralization is mineralogically simple, dominated by iron sulphides (pyrite and marcasite), sphalerite, and galena that precipitate from relatively cool (< 200°C) non-magmatic brines that flow through sedimentary basins (Wilkinson et al., 2005; Leach et al., 2010) and replace carbonate rocks. Determining the dominant tectonic processes that give rise to these deposits is complicated by their existence in a wide variety of settings such as orogenic forelands, orogenic fold and thrust belts, and rift basins. Therefore, tying mineralization to specific tectonic events (e.g. orogenesis, rifting) or specific models (e.g. topographic recharge; Garven, 1985) requires proper geochronological constraints. Historically the main constraint preventing the determination of

absolute ages for these deposits was the mineralogy precluded many radioactive dating techniques. With the absence of isotopic constraints many age estimates were derived through paleomagnetism (e.g. Symons and Sangster 1991; Pan and Symons, 1993; Symons et al. 1993). Paleomagnetic techniques get around the limitation of simple mineralogy by determining the orientation of trace magnetic minerals (e.g. single domain magnetite) that are essentially ubiquitous within the ore and the host rock. The orientation of these magnetic grains can be compared to reference curves, known as apparent polar wander paths, to convert the paleomagnetic direction to absolute ages. A major limitation of paleomagnetic techniques is that magnetic directions are susceptible to being reset (i.e. remagnetized) chemically or thermally. A dramatic example of remagnetization is the documentation of Cretaceous-Eocene (Laramide) paleomagnetic ages for Paleozoic sediments hundreds of kilometers from the fold and thrust belts of the Rocky Mountains in Saskatchewan, Canada (Koehler et al., 1997). A competing dating method that was developed to date these ores was sphalerite Rb-Sr geochronology. This dating technique is attractive as an ore stage mineral of known paragenetic affinity is directly dated. One concern about applying Rb-Sr geochronology to sphalerite is that Rb^+ and Sr^{2+} appear to be too large to simply be substituted for Zn^{2+} , making it unclear if these elements are structurally bound to the sphalerite structure (Pettke and Diamond, 1996). Secondly, the fear that sphalerite can become contaminated with clays, which could significantly alter Rb-Sr systematics, has made some authors wary of trusting Rb-Sr data (Leach et al., 2001; Leach et al., 2002; Bradley et al., 2004). When both techniques are applied to the same deposits/district the dates produced between the two methods often diverge resulting in debates on which technique produced reliable ages (e.g. Bradley and Leach, 2003; Kesler et al., 2004; Bradley et al., 2004). As a result both compressional (e.g. Symons et al., 1998; Smethurst et al., 1999) and extensional (Nakai et al., 1993; Nelson et al., 2002) tectonic regimes have been proposed in the literature for the same deposit depending on what dating technique was used.

With these two techniques often at odds the more recent development of the pyrite Re-Os geochronometer provided an alternative method in determining the age of contentiously dated Zn-Pb ores. The first example of pyrite Re-Os geochronology being applied to a carbonate-hosted Zn-Pb ore was for the Lisheen deposit from the Irish orefield. For the Lisheen deposit, and the Irish orefield in general, one proposed genetic model involves the near-surface mixing of seawater with a metal-bearing brine that had risen up from the deep subsurface through a fault

system (Wilkinson, 2010). Confirming this model required an age that places the age of ore within the shallow subsurface, but dating the Irish deposits using sphalerite Rb-Sr geochronology and paleomagnetism resulted in contentious results (e.g. Symons et al., 2002; Schneider et al., 2007; Pannalal et al., 2008). Paleomagnetic dates for the Irish orefield spanned a wide range of possible ages from ~270 - 330 Ma suggesting that mineralization occurred after deep burial (Symons et al., 2002, 2007). A Rb-Sr study (Schneider et al., 2007) in contrast produced a significantly older age of ~360 Ma that was arguably older than the host-rock itself (~350 Ma). The uncertainty in the age of the Irish orefield, and by extension the geologic mechanisms that formed it, was the impetus of designing my previous graduate thesis (Hnatyshin, 2012) around using pyrite Re-Os geochronology to solve the age disputes of select carbonate-hosted Zn-Pb ore deposits. The dataset produced from that thesis and published in Hnatyshin et al. (2015) resulted in one of the most precise ages determined through pyrite Re-Os geochronology which ultimately supports the fluid mixing model described in Wilkinson (2010). Now with key examples of pyrite Re-Os dates established in the literature (e.g. Hnatyshin et al., 2015; Hnatyshin et al., 2016), the methodology of pyrite Re-Os geochronology should be widely applicable to the origin of carbonate hosted Zn-Pb.

1.5 - Objectives and structure of this PhD Thesis

The primary objective of this thesis is to further develop, understand, test and apply pyrite Re-Os geochronology to carbonate hosted Zn-Pb ore systems, in order to test models for their origin. A secondary objective is to measure and characterise the Re-Os abundance and Os isotopic composition of modern sedimentary basinal fluids, to evaluate the potential for Os isotopic tracing. This thesis builds upon knowledge gained from my previous graduate thesis (Hnatyshin, 2012), which demonstrated that precise ages are possible using pyrite Re-Os geochronology. However, other examples are far more complex, with levels of imprecision far greater than expected from analytical uncertainty alone, requiring that at least one of the fundamental assumptions of age dating to have been violated (Hnatyshin, 2012). Understanding why some samples violate these assumptions is vital for fully understanding the pyrite Re-Os system, and evaluating its level of applicability to carbonate-hosted Zn-Pb ores, and other ore types.

The following chapter, Chapter 2, reviews the important theoretical constructs behind robust geochronology and the empirical background material required to apply the Re-Os system to geologic tracing. In Chapter 3, further Re-Os geochronology from the Irish orefield is presented, that was designed to test if the precise pyrite Re-Os dating results from Lisheen (Hnatyshin, 2012) could be replicated at another key deposit in the orefield (Silvermines), thereby permitting wider applicability of the proposed genetic model (e.g. Wilkinson, 2010) within the Irish orefield. In Chapter 4, pyrite from several carbonate-hosted ores is studied in detail using compositional analysis that included LA-ICMPS element mapping and in-situ sulphur isotopic measurements (SIMS) to compliment broad scale mineralogical characterization. This sample characterization is used in conjunction with several highly scrutinized mineral separation and purification methods (e.g. heavy liquid separation, magnetic separation, acid leaching) to understand and explain why some Re-Os ages are precise and geologically meaningful, and others imprecise and geologically meaningless. Chapter 4 aims to unravel why such a continuum of age quality exists and how best to screen and process samples to avoid potentially problematic samples. The closing pyrite Re-Os dating project (Chapter 5) focuses on identifying the large scale tectonic processes responsible for carbonate-hosted Zn-Pb mineralization in the Canadian Cordillera while incorporating the lessons learned from Chapter 4. The final chapter, Chapter 6, moves away from geochronology, and into a broader scale study that attempts to characterize the Re and Os systematic of fluids present within a modern continental sedimentary basins. Chapter 6 aims to evaluate whether Os isotopes can help determine potential sources of metals within sediment-hosted ore deposits, how fluids (e.g. water, petroleum) may affect the transport of Re and Os within the subsurface, and how Os isotopes could potentially be used in isotopic tracing.

1.6 - References

Arne, D. C., Bierlin, F. P., Morgan, J. W., & Stein, H. J. (2001). Re-Os dating of sulfides associated with gold mineralization in central Victoria, Australia. *Economic Geology*, 96(6), 1455-1459.

Birck, J. L., Barman, M. R., & Capmas, F. (1997). Re - Os isotopic measurements at the femtomole level in natural samples. *Geostandards newsletter*, 21(1), 19-27.

Bradley, D. C., & Leach, D. L. (2003). Tectonic controls of Mississippi Valley-type lead–zinc mineralization in orogenic forelands. *Mineralium Deposita*, 38(6), 652-667.

Bradley, D. C., Leach, D. L., Symons, D., Emsbo, P., Premo, W., Breit, G., & Sangster, D. F. (2004). Reply to Discussion on “Tectonic controls of Mississippi Valley-type lead–zinc mineralization in orogenic forelands” by SE Kesler, JT Christensen, RD Hagni, W. Heijlen, JR Kyle, KC Misra, P. Muchez, and R. van der Voo, *Mineralium Deposita*. *Mineralium Deposita*, 39(4), 515-519.

Brenan, J. M., Cherniak, D. J., & Rose, L. A. (2000). Diffusion of osmium in pyrrhotite and pyrite: implications for closure of the Re–Os isotopic system. *Earth and Planetary Science Letters*, 180(3-4), 399-413.

Garven, G. (1985). The role of regional fluid flow in the genesis of the Pine Point deposit, western Canada sedimentary basin. *Economic Geology*, 80(2), 307-324.

Hnatyshin, D. (2012). Geochronology and Trace Element Characteristics of Pyrite from Selected Carbonate Hosted Pb-Zn Ore Deposits. M.Sc. thesis, University of Alberta, Edmonton, Alberta, 138 p.

Hnatyshin, D., Creaser, R. A., Wilkinson, J. J., & Gleeson, S. A. (2015). Re-Os dating of pyrite confirms an early diagenetic onset and extended duration of mineralization in the Irish Zn-Pb ore field. *Geology*, 43(2), 143-146.

Hnatyshin, D., Kontak, D. J., Turner, E. C., Creaser, R. A., Morden, R., & Stern, R. A. (2016). Geochronologic (ReOs) and fluid-chemical constraints on the formation of the Mesoproterozoic-hosted Nanisivik ZnPb deposit, Nunavut, Canada: Evidence for early diagenetic, low-temperature conditions of formation. *Ore Geology Reviews*, 79, 189-217.

Kesler, S. E., Chesley, J. T., Christensen, J. N., Hagni, R. D., Heijlen, W., Kyle, J. R., ... & Van der Voo, R. (2004). Discussion of "Tectonic controls of Mississippi Valley-type lead-zinc mineralization in orogenic forelands" by DC Bradley and DL Leach. *Mineralium Deposita*, 39(4), 512-514.

Koehler, G., Kyser, T. K., Enkin, R., & Irving, E. (1997). Paleomagnetic and isotopic evidence for the diagenesis and alteration of evaporites in the Paleozoic Elk Point Basin, Saskatchewan, Canada. *Canadian Journal of Earth Sciences*, 34(12), 1619-1629.

Leach, D. L., Bradley, D., Lewchuk, M. T., Symons, D. T., de Marsily, G., & Brannon, J. (2001). Mississippi Valley-type lead-zinc deposits through geological time: implications from recent age-dating research. *Mineralium Deposita*, 36(8), 711-740.

Leach, D. L., Bradley, D., Lewchuk, M., Symons, D. T., Premo, W., Brannon, J., & de Marsily, G. (2002). Reply to Discussion on "Mississippi Valley-type lead-zinc deposits through geological time: implications from recent age-dating research" by SE Kesler and CW Carrigan (2001) *Mineralium Deposita* 36: 711-740. *Mineralium Deposita*, 37(8), 803-805.

Leach, D. L., Bradley, D. C., Huston, D., Pisarevsky, S. A., Taylor, R. D., & Gardoll, S. J. (2010). Sediment-hosted lead-zinc deposits in Earth history. *Economic Geology*, 105(3), 593-625.

Li, Y., Selby, D., Condon, D., & Tapster, S. (2017). Cyclic Magmatic-Hydrothermal Evolution in Porphyry Systems: High-Precision U-Pb and Re-Os Geochronology Constraints on the Tibetan Qulong Porphyry Cu-Mo Deposit. *Economic Geology*, 112(6), 1419-1440.

Luck, J. M., & Allègre, C. J. (1982). The study of molybdenites through the 187Re-187Os chronometer. *Earth and Planetary Science Letters*, 61(2), 291-296.

Mathur, R., Ruiz, J., & Tornos, F. (1999). Age and sources of the ore at Tharsis and Rio Tinto, Iberian Pyrite Belt, from Re-Os isotopes. *Mineralium Deposita*, 34(8), 790-793.

McCandless, T. E., Ruiz, J., & Campbell, A. R. (1993). Rhenium behavior in molybdenite in hypogene and near-surface environments: Implications for Re-Os geochronometry. *Geochimica et Cosmochimica Acta*, 57(4), 889-905.

Morelli, R. M., Creaser, R. A., Selby, D., Kelley, K. D., Leach, D. L., & King, A. R. (2004). Re-Os sulfide geochronology of the red dog sediment-hosted Zn-Pb-Ag deposit, Brooks Range, Alaska. *Economic Geology*, 99(7), 1569-1576.

Morelli, R. M., Bell, C. C., Creaser, R. A., & Simonetti, A. (2010). Constraints on the genesis of gold mineralization at the Homestake Gold Deposit, Black Hills, South Dakota from rhenium–osmium sulfide geochronology. *Mineralium Deposita*, 45(5), 461-480.

Nakai, S. I., Halliday, A. N., Kesler, S. E., Jones, H. D., Kyle, J. R., & Lane, T. E. (1993). Rb-Sr dating of sphalerites from Mississippi Valley-type (MVT) ore deposits. *Geochimica et Cosmochimica Acta*, 57(2), 417-427.

Nelson, J., Paradis, S., Christensen, J., & Gabites, J. (2002). Canadian Cordilleran Mississippi Valley-type deposits: A case for Devonian-Mississippian back-arc hydrothermal origin. *Economic Geology*, 97(5), 1013-1036.

Ootes, L., Morelli, R. M., Creaser, R. A., Lentz, D. R., Falck, H., & Davis, W. J. (2011). The timing of Yellowknife gold mineralization: A temporal relationship with crustal anatexis?. *Economic Geology*, 106(4), 713-720.

Pan, H., & Symons, D. T. A. (1993). Paleomagnetism of the Mississippi Valley - type Newfoundland zinc deposit: Evidence for Devonian mineralization and host rock remagnetization in the northern Appalachians. *Journal of Geophysical Research: Solid Earth*, 98(B12), 22415-22427.

Pannalal, S. J., Symons, D. T. A., & Sangster, D. F. (2008). Paleomagnetic evidence for an early Permian age of the Lisheen Zn-Pb deposit, Ireland. *Economic Geology*, *103*(8), 1641-1655.

Petke, T., & Diamond, L. W. (1996). Rb–Sr dating of sphalerite based on fluid inclusion-host mineral isochrons: a clarification of why it works. *Economic Geology*, *91*(951), e956.

Sangster, D. F. (1990). Mississippi Valley-type and sedex lead-zinc deposits: a comparative examination. *Trans. Inst. Mining and Metall.*, *99*, 21-42.

Schneider, J., Quadt, A. V., Wilkinson, J. J., Boyce, A. J., & Andrew, C. J. (2007, August). Age of the Silvermines Irish-type Zn-Pb deposit from direct Rb-Sr dating of sphalerite. In *Digging Deeper: Proceedings of the 9th Biennial Meeting of the Society for Geology Applied to Mineral Deposits, Dublin, Ireland* (pp. 20-23).

Selby, D., & Creaser, R. A. (2004). Macroscale NTIMS and microscale LA-MC-ICP-MS Re-Os isotopic analysis of molybdenite: Testing spatial restrictions for reliable Re-Os age determinations, and implications for the decoupling of Re and Os within molybdenite. *Geochimica et Cosmochimica Acta*, *68*(19), 3897-3908.

Shirey, S. B., & Walker, R. J. (1995). Carius tube digestion for low-blank rhenium-osmium analysis. *Analytical Chemistry*, *67*(13), 2136-2141.

Smethurst, M. T., Sangster, D. F., Symons, D. T. A., & Lewchuk, M. T. (1999). Paleomagnetic age for Zn-Pb mineralization at Robb Lake, northeastern British Columbia. *Bulletin of Canadian Petroleum Geology*, *47*(4), 548-555.

Smoliar, M. I., Walker, R. J., & Morgan, J. W. (1996). Re-Os ages of group IIA, IIIA, IVA, and IVB iron meteorites. *Science*, *271*(5252), 1099-1102.

Stein, H. J., Markey, R. J., Morgan, J. W., Du, A., & Sun, Y. (1997). Highly precise and accurate Re-Os ages for molybdenite from the East Qinling molybdenum belt, Shaanxi Province, China. *Economic Geology*, 92(7-8), 827-835.

Stein, H. J., Sundblad, K., Markey, R. J., Morgan, J. W., & Motuza, G. (1998). Re-Os ages for Archean molybdenite and pyrite, Kuittila-Kivisuo, Finland and Proterozoic molybdenite, Kabeliai, Lithuania: testing the chronometer in a metamorphic and metasomatic setting. *Mineralium Deposita*, 33(4), 329-345.

Stein, H., Scherstén, A., Hannah, J., & Markey, R. (2003). Subgrain-scale decoupling of Re and ¹⁸⁷Os and assessment of laser ablation ICP-MS spot dating in molybdenite. *Geochimica et Cosmochimica Acta*, 67(19), 3673-3686.

Suzuki, K., Kagi, H., Nara, M., Takano, B., & Nozaki, Y. (2000). Experimental alteration of molybdenite: evaluation of the Re-Os system, infrared spectroscopic profile and polytype. *Geochimica et Cosmochimica Acta*, 64(2), 223-232.

Suzuki, K., Feely, M., & O'Reilly, C. (2001). Disturbance of the Re-Os chronometer of molybdenites from the late-Caledonian Galway Granite, Ireland, by hydrothermal fluid circulation. *Geochemical Journal*, 35(1), 29-35.

Suzuki, K. (2004). Reply to "Accurate and precise Re-Os molybdenite dates from the Galway Granite, Ireland" by D. Selby et al.: Critical comment on "Disturbance of the Re-Os chronometer of molybdenites from the late-Caledonian Galway Granite, Ireland, by hydrothermal fluid circulation". *Geochemical Journal*, 38(3), 295-298.

Symons, D. T. A., & Sangster, D. F. (1991). Paleomagnetic age of the central Missouri barite deposits and its genetic implications. *Economic Geology*, 86(1), 1-12.

Symons, D. T. A., Pan, H., Sangster, D. F., & Jowett, E. C. (1993). Paleomagnetism of the Pine Point Zn-Pb deposits. *Canadian Journal of Earth Sciences*, 30(5), 1028-1036.

Symons, D. T. A., Lewchuk, M. T., & Sangster, D. F. (1998). Laramide orogenic fluid flow into the Western Canada sedimentary basin; evidence from paleomagnetic dating of the Kicking Horse Mississippi valley-type ore deposit. *Economic Geology*, 93(1), 68-83.

Symons, D. T. A., Smethurst, M. T., & Ashton, J. H. (2002). Paleomagnetism of the Navan Zn-Pb deposit, Ireland. *Economic Geology*, 97(5), 997-1012.

Symons, D. T. A., Pannalal, S. J., Kawasaki, K., Sangster, D. F., Stanley, G. A., & Andrew, C. J. (2007). Paleomagnetic age of the Magcobar Ba deposit, Silvermines, Ireland. *Mineral exploration and research: Digging deeper: Dublin, Irish Association for Economic Geology*, 377-380.

Torrealday, H. I., Hitzman, M. W., Stein, H. J., Markley, R. J., Armstrong, R., & Broughton, D. (2000). Re-Os and U-Pb dating of the vein-hosted mineralization at the Kansanshi copper deposit, northern Zambia. *Economic Geology*, 95(5), 1165-1170.

Van Acken, D., Su, W., Gao, J., & Creaser, R. A. (2014). Preservation of Re - Os isotope signatures in pyrite throughout low - T, high - P eclogite facies metamorphism. *Terra Nova*, 26(5), 402-407.

Vernon, R., Holdsworth, R. E., Selby, D., Dempsey, E., Finlay, A. J., & Fallick, A. E. (2014). Structural characteristics and Re-Os dating of quartz-pyrite veins in the Lewisian Gneiss Complex, NW Scotland: Evidence of an Early Paleoproterozoic hydrothermal regime during terrane amalgamation. *Precambrian Research*, 246, 256-267.

Völkening, J., Walczyk, T., & Heumann, K. G. (1991). Osmium isotope ratio determinations by negative thermal ionization mass spectrometry. *International Journal of Mass Spectrometry and Ion Processes*, 105(2), 147-159.

Wilkinson, J. J., Eyre, S. L., & Boyce, A. J. (2005). Ore-forming processes in Irish-type carbonate-hosted Zn-Pb deposits: Evidence from mineralogy, chemistry, and isotopic composition of sulfides at the Lisheen mine. *Economic Geology*, *100*(1), 63-86.

Wilkinson, J. J. (2010). A review of fluid inclusion constraints on mineralization in the Irish ore field and implications for the genesis of sediment-hosted Zn-Pb deposits. *Economic Geology*, *105*(2), 417-442.

Zhang, P., Huang, X. W., Cui, B., Wang, B. C., Yin, Y. F., & Wang, J. R. (2016). Re-Os isotopic and trace element compositions of pyrite and origin of the Cretaceous Jinchang porphyry Cu-Au deposit, Heilongjiang Province, NE China. *Journal of Asian Earth Sciences*, *129*, 67-80.

2.0 - Theoretical and empirical background

The Re-Os system is a radioactive isotope system with potential uses in both geochronology and isotope tracing. This chapter reviews the fundamental concepts behind geochronology while providing important background material required to apply Re-Os to geologic tracing. The concepts provided here are not necessarily fully comprehensive but provide the basic framework behind which this thesis is based.

2.1 - Fundamentals of Re-Os geochronology

Re-Os geochronology is a technique based on the beta decay of ^{187}Re to ^{187}Os and the accumulation of ^{187}Os can be calculated by the following equation

$$\left(\frac{^{187}\text{Os}}{^{188}\text{Os}}\right)_{\text{Measured}} = \left(\frac{^{187}\text{Os}}{^{188}\text{Os}}\right)_{\text{Initial}} + \left(\frac{^{187}\text{Re}}{^{188}\text{Os}}\right)_{\text{Measured}} (e^{\lambda t} - 1) \quad (1)$$

where "Measured" refers to the ratio measured today through mass spectrometry (normalized to ^{188}Os), "Initial" refers to the $^{187}\text{Os}/^{188}\text{Os}$ incorporated by the mineral/rock at the time of formation, t is the time elapsed since the system became closed, and λ is the decay constant for Re ($1.666 \times 10^{-11} \text{ yr}^{-1} \pm 0.017$; Smoliar et al., 1996). Typically both the age of the sample and the initial $^{187}\text{Os}/^{188}\text{Os}$ are unknown. This equation is written in the form of a linear equation, that allows for both the initial $^{187}\text{Os}/^{188}\text{Os}$ (y-intercept) and age (slope = $e^{\lambda t} - 1$) to be determined when plotting $^{187}\text{Os}/^{188}\text{Os}_{\text{Measured}}$ vs. $^{187}\text{Re}/^{188}\text{Os}_{\text{Measured}}$ (i.e. a Re-Os isochron diagram). Isochron fitting is typically accomplished using the Excel add-in Isoplot (Ludwig, 2003). Isoplot can be used to determine what are known as Model 1 ages or Model 3 ages, most typically, although Model 2 and Model 4 exist. A Model 1 age is calculated using a modified version of the algorithm published in York (1969) and only applies analytical uncertainties to the regression analysis. Model 1 ages are typically, although arbitrarily, calculated when the probability of fit (p) for the data is $\geq 15\%$. If the probability of fit falls below the Model 1 threshold, Model 3 ages are computed instead. Model 3 ages apply additional corrections to the data assuming that the initial $^{187}\text{Os}/^{188}\text{Os}$ is variable for each data point, resulting in an increase in uncertainty in the slope and intercept of the isochron (Fig. 2.1). Model 3 ages calculated from Isoplot also quote the variability in initial $^{187}\text{Os}/^{188}\text{Os}$ (VIOs) required to fit the data, an important parameter that is typically overlooked in the literature but should be scrutinized for its geologic feasibility.

Due to their siderophile/chalcophile/organophile nature, Re and Os are elements that tend to sequester into metallic iron, sulphides, and organic matter. Rhenium and Os are therefore expected to be enriched, at least with respect to silicate and carbonate minerals, in minerals such as pyrite (FeS₂). However, the concentrations of Re and Os are still typically very low, most commonly in the parts-per-billion (ppb) and parts-per-trillion (ppt) range, respectively. The low concentrations of Re and Os in most (all?) minerals precludes current in-situ dating techniques for crustal sulphides and therefore isotope dilution techniques on bulk material is the most common approach for Re-Os dating of pyrite.

2.2 - Assumptions

Isotopic dating requires that the phase(s) analysed were in isotopic equilibrium with one another during their formation and subsequently became closed with respect to isotopic exchange. This statement can be broken down into a number of fundamental assumptions that when fulfilled will ensure that accurate ages result. In practice, identifying and processing samples that closely fulfill the following assumptions is a fundamental challenge in producing precise and accurate results from pyrite Re-Os geochronology.

2.2.1 - (1) Samples are formed synchronously

The age produced from the isochron method assumes that the data points represent a series of samples that formed at the same time (i.e. t is the same for each data point in equation 1). If assumption (1) is not met, each data point produces a unique evolution curve in Re-Os isotopic space and any isochron produced from the entire dataset will be a result of averaging. Clearly minerals do not crystallize instantaneously, and ore deposits may be the result of numerous distinct episodes of mineralization that may take place over thousands or millions of years (Cathles and Smith, 1983; Garven et al., 1993; Lewchuk and Symons, 1995; Rowan and Goldhaber, 1995; Cathles et al., 1997; von Quadt et al., 2011). As a result, any sample chosen for analysis must be assumed to have formed over a time interval that is negligible with respect to the time elapsed since the Re-Os system has become isotopically closed. What constitutes negligible must be decided based on (1) the age of the deposit, (2) the expected length of the mineralization episode, and (3) the question asked of the data. However, current analytical capabilities introduce uncertainties higher than the probable length of a mineralization at a

simple deposit (< 1 My), therefore violations of assumption (1) have negligible impact in many cases (Fig. 2.1A). Furthermore, current sampling practices emphasize selecting cogenetic samples associated with ore stage mineralization within a restricted range of the paragenetic sequence, minimizing the risk of violating assumption (1).

To determine possible age variations between data points individual ages can be calculated (i.e. model age) by using a fixed initial $^{187}\text{Os}/^{188}\text{Os}$ (e.g. the isochron initial $^{187}\text{Os}/^{188}\text{Os}$). Lower and upper bounds on the age of the sample can be estimated by comparing model ages under the premise that only assumption (1) was violated. Data points that produce older/younger ages are investigated to determine if they can be correlated with specific paragenetic stages. For example, younger model ages are expected to be from mineral separates that contain a higher proportion of later stage crystals.

2.2.2 - (2) Single osmium reservoir

In a given sample, the $(^{187}\text{Os}/^{188}\text{Os})_{\text{measured}}$ is a mixture of radiogenic ingrowth from decay of ^{187}Re and the $^{187}\text{Os}/^{188}\text{Os}$ incorporated from the source fluid(s). In order to use a Model 1 regression it must be assumed that the source fluid contained an invariant $^{187}\text{Os}/^{188}\text{Os}$ (i.e. a invariant initial $^{187}\text{Os}/^{188}\text{Os}$) for the suite of samples analyzed. If this assumption is violated, each data point represents a unique evolution curve, resulting in a series of parallel lines on an $^{187}\text{Re}/^{188}\text{Os}$ vs. $^{187}\text{Os}/^{188}\text{Os}$ diagram and a Model 3 regression may be appropriate (Figs. 2.1C, D). Unfortunately, the bounds on the possible Re-Os isotopic signatures found in mineralization fluids, and how temporally variable they are, is essentially an open question, but is extremely important for validating VIOs used by Model 3 regressions. Isotopic changes in mineralization fluids may be a major concern when fluid mixing processes are responsible for mineralization, as changing mixing ratios will influence isotopic signatures. A prime example of how changing fluid mixing ratios can affect $^{187}\text{Os}/^{188}\text{Os}$ can be seen in modern day hydrothermal vent systems. High temperature (~300°C) hydrothermal fluids from the Juan de Fuca Ridge show spatial variability in $^{187}\text{Os}/^{188}\text{Os}$ (0.148 to 0.312) in active vents situated within a < 1 km² area (Endeavour location from Sharma et al. (2000) and Sharma et al. (2007a)). Fluid mixing with ambient seawater within 1 m from the vent orifice results in an $^{187}\text{Os}/^{188}\text{Os}$ reaching a near sea water $^{187}\text{Os}/^{188}\text{Os}$ value of 0.986. Regional scale (several km²) data from Sharma et al. (2007a) for cooler fluids (~10-62°C) show larger ranges in $^{187}\text{Os}/^{188}\text{Os}$ (0.420 - 1.012), suggesting

different mixing ratios between hydrothermal fluids and seawater. These modern day studies clearly show that spatial variability in $^{187}\text{Os}/^{188}\text{Os}$ exist in marine hydrothermal systems, and it would be expected that temporal and spatial variations also exist in crustal hydrothermal systems forming Zn-Pb ores. Based on these results, a suggestion is that when interpreting a Model 3 regression VIOs should not exceed 1.0 in a system where seawater is a potential component.

Testing for violations of assumption (2) follows the same principle as for assumption (1). In this case, the variation in initial $^{187}\text{Os}/^{188}\text{Os}$ required to explain each data point is determined by using a fixed age (e.g. the isochron age). The entire set of calculations provides the bounds on how much variability of $^{187}\text{Os}/^{188}\text{Os}$ is required to explain the data. Ideally there will also be a clear correlation between the initial $^{187}\text{Os}/^{188}\text{Os}$ and the paragenesis of the sample. For example, mineral separates that contain paragenetically early material may produce initial ratios that are distinct from mineral separates that contain paragenetically late material, if the source of Os in the hydrothermal fluid changed with time. Confidence in this interpretation requires many analyses in addition to well characterized mineral separates. If observed violations required by a Model 3 are within geologic plausibility then the use of a Model 3 age is likely justified. In cases where the geologic plausibility in the VIOs is in question then regression analysis likely provides inaccurate bounds on the age of mineralization and therefore should not be used.

2.2.3 - (3) No alteration

Excess geologic scatter in an isochron may be a result of thermal and/or chemical changes that perturb Re and/or Os in pyrite after formation. In the literature, this is a common way to explain excess scatter in an isochron and is usually presented as a generic loss or gain of Re and/or Os from specific samples, although often without accompanying analytical data for mineral separates causing the scatter (e.g. Lawley et al., 2013; Ding et al., 2016; Jiang et al. 2017).

Thermal effects increase the likelihood of diffusion or the direct removal of Re and/or Os into, or out of, a pyrite crystal, resulting in unpredictable isotopic behaviour. Experimentally, it has been shown that pyrite has a very low diffusion rate for Os at elevated temperatures (Brenan et al., 2000), and preservation of robust pyrite isochrons through 300-590°C metamorphic regimes (e.g. van Acken et al., 2014; Vernon et al., 2014), suggest high thermal stability of pyrite for Re-Os

The chemical stability of pyrite is strongly dependent on the chemical conditions experienced by the pyrite. Complex recrystallization, replacement, and dissolution textures are found in many ore systems suggesting the pyrite is rarely simply precipitated and left undisturbed (Large et al., 2009). If, during any of these processes, Re or Os is preferentially gained or lost then by definition isotopic disturbance has occurred.

2.2.4 - (4) No contamination

Pyrite often coexists with numerous other ore and gangue minerals in hydrothermal ores. Currently, relatively few minerals have been investigated for their Re-Os content, and even less have been proven to be robust systems for dating (e.g., molybdenite Re-Os). Due to this lack of knowledge it should not be assumed that impurities, even silicates and carbonates, contain negligible Re and/or Os. The approach taken when dating organic-rich sediments with Re-Os (e.g. Kendall et al., 2004), which is assuming that silicate (or other) contaminants introduce additional scatter, should be followed. Therefore, for simplicity mineral separates should in practice be pure, or impurities must be shown to have a negligible impact on the Re-Os ratios reported. A clear example of the effect impurities can have on an isochron is illustrated in Kelley et al. (2017). In Kelley et al. (2017) the original pyrite Re-Os isochron produced a meaningless Re-Os age of 156 +/- 1200 Ma. However, by identifying impurities of mudstone within some samples Kelley et al. (2017) was able to justifiably remove some data points, subsequently improving their Re-Os age to 442 +/- 12 Ma, which is geologically feasible for the study area.

2.3 - Current constraints on Re-Os isotopic reservoirs

One other potential use for the Re-Os system is its application as a tracer isotope system, where differences in initial $^{187}\text{Os}/^{188}\text{Os}$ may correspond to different isotopic reservoirs (Fig. 2.2). However, for any isotopic tracing scheme it is important to define the relevant reservoirs and to understand how Re and Os may be transferred between reservoirs, and how the time-integrated Os isotopic composition varies between and within these reservoirs. As both Re and Os are siderophile in nature they will be primarily sequestered into the core (Brenan and McDonough, 2005, 2009), but the next most abundant reservoir on Earth is the mantle. Mantle Re-Os values have been well defined from mantle xenoliths. Current estimates put the $^{187}\text{Os}/^{188}\text{Os}$ composition of the primitive upper mantle at approximately 0.1296 with Os concentrations averaging 2.6 ppb

(Meisel et al., 2001); Re concentrations are lower at ~0.2 ppb and therefore the low Re-Os ratio limits $^{187}\text{Os}/^{188}\text{Os}$ variation observed in typical mantle rocks to roughly between 0.105 and 0.135 (Meisel et al., 2001).

During partial melting of the mantle, Re behaves more incompatibly than Os (Shirey and Walker, 1998) resulting in Re being relatively enriched in crustal material (0.2 to 2 ppb; Peucker-Ehrenbrink and Jahn, 2001; Sun et al., 2003) compared to Os (~50 ppt, Peucker-Ehrenbrink and Jahn, 2001). Due to crustal enrichment of Re, crustal $^{187}\text{Os}/^{188}\text{Os}$ will evolve to a much higher degree than that of the mantle, although the exact values is dependent on the $^{187}\text{Re}/^{188}\text{Os}$ of the system. Whereas the average $^{187}\text{Os}/^{188}\text{Os}$ of the continental crust is poorly constrained, a commonly cited $^{187}\text{Os}/^{188}\text{Os}$ of 1.40 ± 0.30 has been suggested for typical (~2.2 Ga) crust based on Os isotopic measurements of loess that are assumed to be representative of typical crustal material (Peucker-Ehrenbrink and Jahn, 2001).

Subaerial weathering of crustal material results in the mobilization of Re and Os into river systems. River systems contain a diverse range of Os isotopic compositions ($^{187}\text{Os}/^{188}\text{Os}$ 0.17 - 2.94) and concentrations (0.29 - 41.8 ppq) due to the huge variety of potential sources of Os present along the river's flow path (Levasseur et al., 1999; Sharma et al., 1999; Sharma et al., 2007b). Studies from Indian river deltas have shown that the Os isotopic composition of the river water broadly reflect that of upstream sedimentary rocks (Sharma et al., 2007b).

Infiltration of meteoric water or seawater into the subsurface provides a potential source of Os and Re in groundwater. Based on the known ratios for riverine and seawater Os it is expected that prior to any fluid mixing processes and water-rock interactions, groundwater might be expected to have baseline concentrations of ≥ 10 ppq Os. Prior to this thesis, the only constraints available for groundwater Os isotopic compositions come from Paul et al. (2010). In their study of shallow (≤ 74 m) Indian groundwater they found that $^{187}\text{Os}/^{188}\text{Os}$ values closely match that of local rivers and sediments but having much higher concentrations of Os (17 - 192 ppq). A discussion of new Os isotopic data from pore waters contained in confined aquifers as well as additional effects related to the water-rock-petroleum system is the basis for Chapter 6.

Weathering of young oceanic crust and magmatic fluids in ocean basins should have $^{187}\text{Os}/^{188}\text{Os}$ compositions similar to that of the mantle. Direct measurements of active hydrothermal vents from the Juan de Fuca Ridge ($^{187}\text{Os}/^{188}\text{Os} = 0.148 - 0.312$; Sharma et al., 2000; Sharma et al., 2007a) are consistent with mixing of a mantle $^{187}\text{Os}/^{188}\text{Os}$ end member with

ambient seawater values ($^{187}\text{Os}/^{188}\text{Os} = 1.05$, $[\text{Os}] = 10.4$ ppq; Sharma et al., 2007a). Seawater in general is a very homogenous reservoir with $^{187}\text{Os}/^{188}\text{Os}$ values of 1.02 - 1.07 at concentrations of 6.8 to 10.4 ppq being reported in the literature (Woodhouse et al., 1999; Sharma et al., 2007a; Gannoun and Burton, 2014).

The organophile nature of Re and Os can result in localized enrichments of these elements in either sediments or living organisms (e.g. Ravizza et al., 1991; Racionero-Gomez et al., 2017). Organic-rich sediments deposited in anoxic waters are known to accumulate Re and Os from the overlying water column. Upon thermal maturation of the organic matter and the subsequent production of petroleum, Re and Os become preferentially sequestered inside the asphaltene portion of the petroleum products (Selby et al., 2007; Georgiev et al., 2016; DiMarzio et al., 2018). As both Re and Os are also chalcophile in nature they can also be enriched upon the precipitation of sulphides from fluids or magma. Accumulations of sulphides such as found at metallic ore deposits are important local sinks for metals such as Re and Os.

2.4 - References

Acken, D., Su, W., Gao, J., & Creaser, R. A. (2014). Preservation of Re - Os isotope signatures in pyrite throughout low - T, high - P eclogite facies metamorphism. *Terra Nova*, 26(5), 402-407.

Anbar, A. D., Creaser, R. A., Papanastassiou, D. A., & Wasserburg, G. J. (1992). Rhenium in seawater: Confirmation of generally conservative behavior. *Geochimica et Cosmochimica Acta*, 56(11), 4099-4103.

Brenan, J. M., Cherniak, D. J., & Rose, L. A. (2000). Diffusion of osmium in pyrrhotite and pyrite: implications for closure of the Re-Os isotopic system. *Earth and Planetary Science Letters*, 180(3-4), 399-413.

Brenan, J. M., McDonough, W. F., & Ash, R. (2005). An experimental study of the solubility and partitioning of iridium, osmium and gold between olivine and silicate melt. *Earth and Planetary Science Letters*, 237(3-4), 855-872.

Brenan, J. M., & McDonough, W. F. (2009). Core formation and metal–silicate fractionation of osmium and iridium from gold. *Nature Geoscience*, 2(11), 798.

Cathles, L. M., & Smith, A. T. (1983). Thermal constraints on the formation of Mississippi Valley-type lead-zinc deposits and their implications for episodic basin dewatering and deposit genesis. *Economic Geology*, 78(5), 983-1002.

Cathles, L. M., Erendi, A. H. J., & Barrie, T. (1997). How long can a hydrothermal system be sustained by a single intrusive event?. *Economic Geology*, 92(7-8), 766-771.

DiMarzio, J. M., Georgiev, S. V., Stein, H. J., & Hannah, J. L. (2018). Residency of rhenium and osmium in a heavy crude oil. *Geochimica et Cosmochimica Acta*, 220, 180-200.

Ding, C., Nie, F., Bagas, L., Dai, P., Jiang, S., Ding, C., ... & Shao, G. (2016). Pyrite Re–Os and zircon U–Pb dating of the Tugurige gold deposit in the western part of the Xing'an–Mongolia Orogenic Belt, China and its geological significance. *Ore Geology Reviews*, 72, 669-681.

Garven, G., Ge, S., Person, M. A., & Sverjensky, D. A. (1993). Genesis of stratabound ore deposits in the Midcontinent basins of North America; 1, The role of regional groundwater flow. *American Journal of Science*, 293(6), 497-568.

Gannoun, A., & Burton, K. W. (2014). High precision osmium elemental and isotope measurements of North Atlantic seawater. *Journal of Analytical Atomic Spectrometry*, 29(12), 2330-2342.

Georgiev, S. V., Stein, H. J., Hannah, J. L., Galimberti, R., Nali, M., Yang, G., & Zimmerman, A. (2016). Re–Os dating of maltenes and asphaltenes within single samples of crude oil. *Geochimica et Cosmochimica Acta*, 179, 53-75.

Jiang, S. H., Bagas, L., & Liang, Q. L. (2017). Pyrite Re-Os isotope systematics at the Zijinshan deposit of SW Fujian, China: Constraints on the timing and source of Cu-Au mineralization. *Ore Geology Reviews*, *80*, 612-622.

Kelley, K. D., Selby, D., Falck, H., & Slack, J. F. (2017). Re-Os systematics and age of pyrite associated with stratiform Zn-Pb mineralization in the Howards Pass district, Yukon and Northwest Territories, Canada. *Mineralium Deposita*, *52*(3), 317-335.

Kendall, B. S., Creaser, R. A., Ross, G. M., & Selby, D. (2004). Constraints on the timing of Marinoan “Snowball Earth” glaciation by ^{187}Re – ^{187}Os dating of a Neoproterozoic, post-glacial black shale in Western Canada. *Earth and Planetary Science Letters*, *222*(3-4), 729-740.

Lawley, C., Selby, D., & Imber, J. (2013). Re-Os molybdenite, pyrite, and chalcopyrite geochronology, lupa goldfield, southwestern Tanzania: tracing metallogenic time scales at midcrustal shear zones hosting orogenic Au deposits. *Economic Geology*, *108*(7), 1591-1613.

Large, R. R., Danyushevsky, L., Hollit, C., Maslennikov, V., Meffre, S., Gilbert, S., & Singh, B. (2009). Gold and trace element zonation in pyrite using a laser imaging technique: Implications for the timing of gold in orogenic and Carlin-style sediment-hosted deposits. *Economic Geology*, *104*(5), 635-668.

Levasseur, S., Birck, J. L., & Allegre, C. J. (1999). The osmium riverine flux and the oceanic mass balance of osmium. *Earth and Planetary Science Letters*, *174*(1-2), 7-23.

Lewchuk, M. T., & Symons, D. T. A. (1995). Age and duration of Mississippi Valley–type ore-mineralizing events. *Geology*, *23*(3), 233-236.

Ludwig, K. R. (2003). Isoplot 3.00: A geochronological toolkit for Microsoft Excel, 71 pp. *Berkeley Geochronol. Center Spec. Publ.*, *4*.

Meisel, T., Walker, R. J., Irving, A. J., & Lorand, J. P. (2001). Osmium isotopic compositions of mantle xenoliths: a global perspective. *Geochimica et Cosmochimica Acta*, 65(8), 1311-1323.

Paul, M., Reisberg, L., Vigier, N., Zheng, Y., Ahmed, K. M., Charlet, L., & Huq, M. R. (2010). Dissolved osmium in Bengal plain groundwater: Implications for the marine Os budget. *Geochimica et Cosmochimica Acta*, 74(12), 3432-3448.

Peucker - Ehrenbrink, B., & Jahn, B. M. (2001). Rhenium - osmium isotope systematics and platinum group element concentrations: Loess and the upper continental crust. *Geochemistry, Geophysics, Geosystems*, 2(10).

Ravizza, G., Turekian, K. K., & Hay, B. J. (1991). The geochemistry of rhenium and osmium in recent sediments from the Black Sea. *Geochimica et Cosmochimica Acta*, 55(12), 3741-3752.

Racionero-Gómez, B., Sproson, A. D., Selby, D., Gannoun, A., Gröcke, D. R., Greenwell, H. C., & Burton, K. W. (2017). Osmium uptake, distribution, and $^{187}\text{Os}/^{188}\text{Os}$ and $^{187}\text{Re}/^{188}\text{Os}$ compositions in Phaeophyceae macroalgae, *Fucus vesiculosus*: Implications for determining the $^{187}\text{Os}/^{188}\text{Os}$ composition of seawater. *Geochimica et Cosmochimica Acta*, 199, 48-57.

Rowan, E. L., & Goldhaber, M. B. (1995). Duration of mineralization and fluid-flow history of the Upper Mississippi Valley zinc-lead district. *Geology*, 23(7), 609-612.

Selby, D., Creaser, R. A., & Fowler, M. G. (2007). Re–Os elemental and isotopic systematics in crude oils. *Geochimica et Cosmochimica Acta*, 71(2), 378-386.

Sharma, M., & Wasserburg, G. J. (1997). Osmium in the rivers. *Geochimica et cosmochimica Acta*, 61(24), 5411-5416.

Sharma, M., Wasserburg, G. J., Hofmann, A. W., & Chakrapani, G. J. (1999). Himalayan uplift and osmium isotopes in oceans and rivers. *Geochimica et Cosmochimica Acta*, 63(23-24), 4005-4012.

Sharma, M., Wasserburg, G. J., Hofmann, A. W., & Butterfield, D. A. (2000). Osmium isotopes in hydrothermal fluids from the Juan de Fuca Ridge. *Earth and Planetary Science Letters*, 179(1), 139-152.

Sharma, M., Rosenberg, E. J., & Butterfield, D. A. (2007a). Search for the proverbial mantle osmium sources to the oceans: Hydrothermal alteration of mid-ocean ridge basalt. *Geochimica et Cosmochimica Acta*, 71(19), 4655-4667.

Sharma, M., Balakrishna, K., Hofmann, A. W., & Shankar, R. (2007b). The transport of osmium and strontium isotopes through a tropical estuary. *Geochimica et Cosmochimica Acta*, 71(20), 4856-4867.

Shirey, S. B., & Walker, R. J. (1998). The Re-Os isotope system in cosmochemistry and high-temperature geochemistry. *Annual Review of Earth and Planetary Sciences*, 26(1), 423-500.

Smoliar, M. I., Walker, R. J., Morgan, J.W. (1996). Re-Os ages of group IIA, IIIA, IVA, and IVB iron meteorites. *Science*, 271, 1099.

Sun, W., Arculus, R. J., Bennett, V. C., Eggins, S. M., & Binns, R. A. (2003). Evidence for rhenium enrichment in the mantle wedge from submarine arc-like volcanic glasses (Papua New Guinea). *Geology*, 31(10), 845-848.

Vernon, R., Holdsworth, R. E., Selby, D., Dempsey, E., Finlay, A. J., & Fallick, A. E. (2014). Structural characteristics and Re-Os dating of quartz-pyrite veins in the Lewisian Gneiss Complex, NW Scotland: Evidence of an Early Paleoproterozoic hydrothermal regime during terrane amalgamation. *Precambrian Research*, 246, 256-267.

Von Quadt, A., Erni, M., Martinek, K., Moll, M., Peytcheva, I., & Heinrich, C. A. (2011). Zircon crystallization and the lifetimes of ore-forming magmatic-hydrothermal systems. *Geology*, 39(8), 731-734.

Woodhouse, O. B., Ravizza, G., Falkner, K. K., Statham, P. J., & Peucker-Ehrenbrink, B. (1999). Osmium in seawater: vertical profiles of concentration and isotopic composition in the eastern Pacific Ocean. *Earth and Planetary Science Letters*, 173(3), 223-233.

York, D. (1968). Least squares fitting of a straight line with correlated errors. *Earth and planetary science letters*, 5, 320-324.

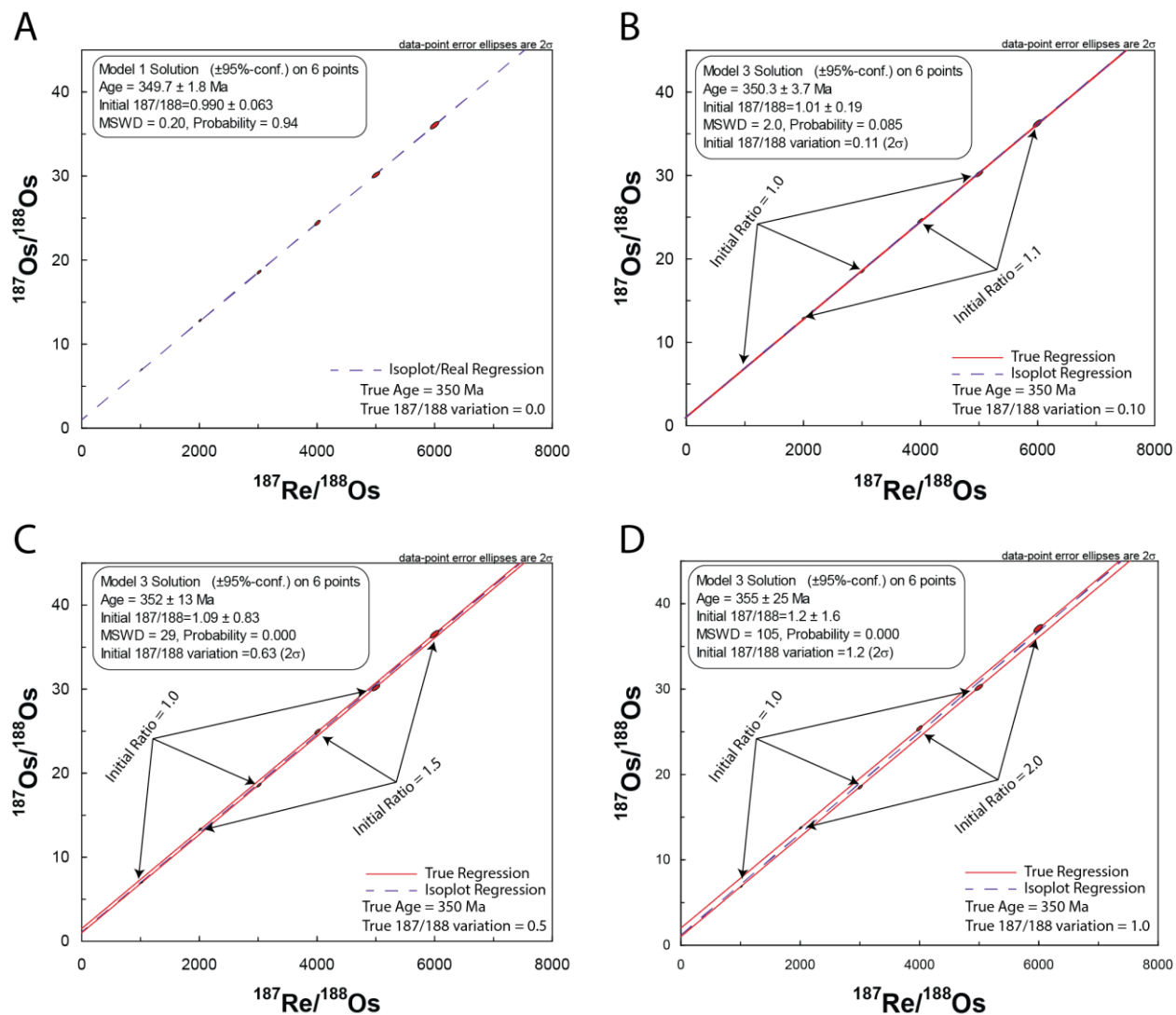


Figure 2.1: Hypothetical dataset with variable VIOs. The $^{187}\text{Re}/^{188}\text{Os}$ values of 1000 - 6000, 2σ errors of 10%, and a rho value of 0.75 were chosen arbitrarily, but fall within normal ranges seen in pyrite analyses. The $^{187}\text{Os}/^{188}\text{Os}$ values are calculated based on these parameters at an age of 350 Ma and then a regression is calculated using Isoplot. (A) VIOs is invariant with each $^{187}\text{Os}/^{188}\text{Os}$ being calculated using an initial $^{187}\text{Os}/^{188}\text{Os}$ of 1.00. (B) $^{187}\text{Os}/^{188}\text{Os}$ is calculated using a initial $^{187}\text{Os}/^{188}\text{Os}$ of 1.00 or 1.10. (C) $^{187}\text{Os}/^{188}\text{Os}$ is calculated using an initial $^{187}\text{Os}/^{188}\text{Os}$ of 1.00 or 1.50. (D) $^{187}\text{Os}/^{188}\text{Os}$ is calculated using an initial $^{187}\text{Os}/^{188}\text{Os}$ of 1.00 or 2.00.

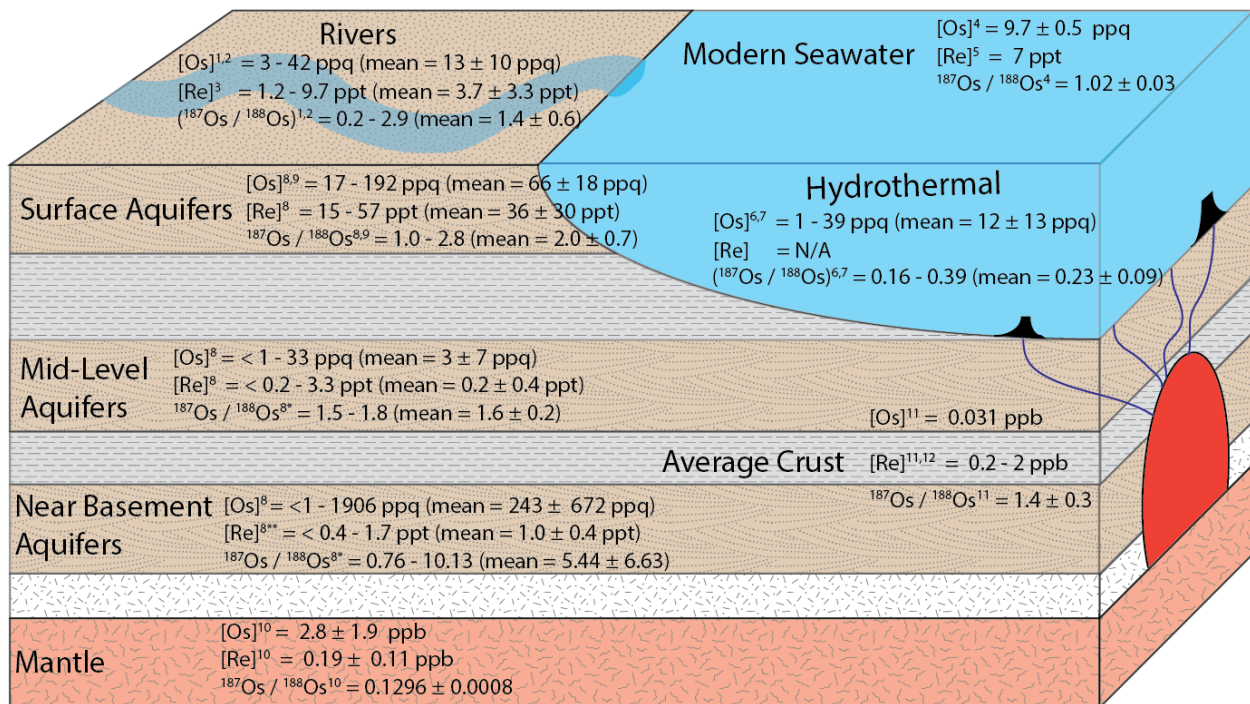


Figure 2.2: Overview of the range of Re-Os values seen in various reservoirs, see Chapter 6 for additional details.

¹Levasseur et al. (1999); ²Sharma and Wasserburg (1997); ³Unpublished; ⁴Gannoun and Burton; ⁵Anbar et al. (1992); ⁶Sharma et al. (2000); ⁷Sharma et al. (2007a); ⁸This Study, ^{8*}Only data with $> 10 \text{ ppq Os}$, ^{8**}High Os samples were not measured for Re content; ⁹Paul et al. (2010); ¹⁰Meisel et al. (2001); ¹¹Peucker-Ehrenbrink and Jahn (2001); ¹²Sun et al. (2003). ppb - parts per billion, ppt - parts per trillion, ppq - parts per quadrillion.

3.0 - Re-Os dating of pyrite confirms an early diagenetic onset and extended duration of mineralization in the Irish Zn-Pb orefield

3.1 - Introduction

Hydrothermal ore deposits hosted by sedimentary rocks supply the majority of the world's lead, zinc, and a significant proportion of copper. Although general models for ore formation are well established (e.g., Gustafson and Williams, 1981; Goodfellow et al., 1993; Leach et al., 2005; Wilkinson, 2014), significant controversy remains over fundamental aspects of their genesis. Some ores are thought to have formed during, or soon after, deposition of the host sediments (syngenetic and/or early diagenetic mineralization), whereas others formed after – in some cases hundreds of millions of years after – lithification of the host rocks (epigenetic mineralization). For a number of Zn-Pb deposits, such as the Carboniferous ores of central Ireland (Hitzman and Beaty, 1996), both models have been proposed. This dichotomy stems from difficulties in determining with confidence the relative timing of sulphide precipitation, and the paucity of hydrothermal minerals amenable to radiogenic isotope dating.

The lack of certainty regarding the timing of Zn-Pb mineralization has numerous impacts, including on the understanding of geodynamic controls on deposit location, on the development of fluid flow models, and on identifying viable sulphide precipitation mechanisms. In a wider context, inferred ages of ore deposition, in particular those obtained by paleomagnetic methods, have been used to argue for a link between the formation of sediment-hosted Zn-Pb deposits and supercontinent assembly cycles (Leach et al., 2001). However, if paleomagnetic methods date orogenic events rather than mineralization, then this interpretation is invalid. Mineral exploration is guided by deposit models: a syngenetic interpretation will focus efforts on specific stratigraphic horizons, whereas an epigenetic model allows for deposits to occur in receptive host rocks of any age.

Here we use Re-Os dating of ore-stage pyrite, an approach not previously applied to carbonate-hosted Zn-Pb ores, to test models for the timing and genesis of mineralization in the Irish ore field – topics that have been vigorously debated for 50 years but have yet to be answered convincingly.

3.2 - Irish orefield

In Ireland during the early Mississippian, a marine transgression across the Laurussian continental margin deposited thick limestone units (Figs. 3.1, 3.2). Hydrothermal fluids subsequently precipitated tens of millions of tons of zinc and lead within these carbonate rocks, making the Irish orefield one of the most intensely mineralized Zn districts on Earth (Singer, 1995). The giant Navan Zn-Pb deposit forms the largest resource, but economic Zn-Pb deposits also formed at Tynagh, Silvermines, Galmoy, and Lisheen (Fig. 3.1).

Early syngenetic models, such as the extension and convection model of Russell (1978), were largely discounted in the 1990s in favor of epigenetic interpretations involving lateral, topographically-driven fluid flow (Hitzman and Beaty, 1996), similar to the widely accepted model for Mississippi Valley-type (MVT) Zn-Pb deposits. It is significant that the past decade has seen movement away from this concept, as new regional data sets and analytical techniques have become available (Wilkinson and Hitzman, 2014).

3.3 - Study sites

Lisheen is the second-largest base-metal deposit in Ireland and has a well-defined geologic setting (e.g., Wilkinson et al., 2005). The Silvermines deposit has been central to the development of syngenetic models (e.g., Boyce et al., 2003) and presents an opportunity to test an existing Rb-Sr sphalerite age (360 ± 5 Ma; Schneider et al., 2007) and a much younger paleomagnetic age (269 ± 4 Ma; Symons et al., 2007).

Sulfide mineralization at Lisheen (Fig. 3.2) occurs principally within a hydrothermal dolomite breccia located at the base of the Waulsortian Limestone Formation (WLF). A minor proportion of ore is hosted by an oolitic unit (Lisduff Oolite Member - LOM) within underlying argillaceous bioclastic limestones (Ballysteen Limestone Formation - BLF). Mineralization forms three stratabound ore bodies: the Main, Derryville, and Bog zones, each of which are controlled by a major normal fault (Hitzman et al., 2002). Mineralization primarily occurs in the hanging walls of these faults within the WLF; footwall mineralization is mainly developed within the LOM.

Sulfide ore at Silvermines is generally restricted to two stratigraphic levels: the upper G and B Zones within the dolomitized base of the WLF (Fig. DR2), and the lower G, K, and P

Zones hosted by dolomitized portions of the BLF (Taylor, 1984). All ore zones are spatially associated with normal faults (Taylor, 1984).

3.4 - Re-Os Geochronology

At Lisheen, massive pyrite from the early main ore-stage in the LOM (sample LK 8S08FW: Panel 8, Stope 8 in the Main Zone orebody) was selected for analysis. At Silvermines, massive pyrite from the B Zone orebody (samples B18, B15) was chosen (see Appendix for sample descriptions). All pyrite separates were produced and analyzed using the procedures described by Morelli et al. (2010); some additional details are described in the Appendix. We analyzed 12 pyrite separates were analyzed from the Lisheen sample, with Re and Os concentrations of 2-8 ppb and 15-280 ppt, respectively. For Silvermines, 12 pyrite separates from B18 and one from B15 were analyzed; these contain 0.5-2.5 ppb Re and 85-400 ppt Os. Detailed analytical results are provided in Tables 3.1, 3.2, and 3.3 in the Appendix.

The Lisheen sample yields a Re-Os isochron age of 346.6 ± 3.0 Ma, whereas the Silvermines samples produce a younger Re-Os isochron age of 334.0 ± 6.1 Ma. (Fig. 3.3) The Silvermines isochron shows some scatter beyond calculated analytical uncertainties (mean square of weighted deviates (MSWD) = 19); this scatter can be accounted for by only a 1% variation in initial $^{187}\text{Os}/^{188}\text{Os}$ (IOs) of the fluid from which pyrite formed.

3.5 - Timing and duration of mineralization

The early ore-stage pyrite samples from both Lisheen and Silvermines yield Early Mississippian Re-Os ages that place the timing of sulfide mineralization within ~15 myr of host rock deposition. The Re-Os age from Lisheen (346 ± 3.0 Ma) overlaps with the probable depositional age range (353-347 Ma; Waters et al. 2011) for the WLF (Fig. 3.4). We conclude that Zn-Pb mineralization at Lisheen most likely developed during the latter depositional stages of the WLF, or during deposition of the overlying Crosspatrick Formation (CF) at a depth of no more than 200 meters below the paleo-seafloor. This interpretation is consistent with arguments that the thickening of the WLF and CF above the ore zone was due to subsidence of the seafloor during mineralization-related host rock dissolution (Wilkinson et al., 2011).

Previous interpretations of the timing of mineralization at Silvermines concluded that syngenetic and near-seafloor mineralization took place based on the occurrence of exhalative features (e.g., Boyce et al. 1983), vent fauna (e.g., Boyce et al., 2003), sedimentary reworking of

sulfides (Lee and Wilkinson, 2002) and a sphalerite Rb-Sr age (Schneider et al., 2007). Our result does not exclude a syngenetic component to the hydrothermal system, but clearly shows that significant mineralization occurred during later stages of host rock burial (e.g. Reed and Wallace, 2004). Likewise, the Re-Os age obtained for Lisheen does not exclude later mineralization at greater burial depths as has been suggested based on sulfur isotope data (Wilkinson et al., 2005). Together, the new Re-Os ages provide concrete evidence for a protracted, and probably episodic, history of mineralization in the Irish Zn-Pb orefield (Wilkinson and Hitzman, 2014).

3.6 - Osmium source

The precise IOs obtained for pyrite isochrons from both Lisheen (0.253 ± 0.045) and Silvermines (0.453 ± 0.006) reflect the source or sources of Os in the hydrothermal fluids that formed the deposits. These relatively low values invite the possibility that the fluids contained a mixture of mantle-derived Os ($^{187}\text{Os}/^{188}\text{Os} \sim 0.13$; Meisel et al., 2001) and crustal Os ($^{187}\text{Os}/^{188}\text{Os} \gg 0.13$; Peucker-Ehrenbrink and Jahn, 2001). Alternatively, the IOs values may reflect derivation of Os from the immediate basement rocks of the Irish deposits, which were largely derived from early Paleozoic (Caledonian) volcanic arcs (480-380 Ma; Chew and Stillman, 2009). We estimate average crustal source rock ages for Os at Lisheen (363 Ma) and Silvermines (412 Ma) by assuming the IOs of the Caledonian arc rocks was 0.2, similar to that reported in porphyry systems (e.g. Zimmerman et al., 2014), combined with a $^{187}\text{Re}/^{188}\text{Os}$ ratio of 190 calculated from average crustal concentrations of Re (2 ppb) and Os (50 ppt) (Peucker-Ehrenbrink and Jahn, 2001; Sun et al., 2003). These estimates are compatible with Os, like Pb and other metals, being sourced from the early Paleozoic basement (Dixon et al., 1990; Wilkinson et al., 2005; Wilkinson, 2014) and/or the overlying Devonian Old Red Sandstone.

3.7 - A possible link between volcanism and Zn-Pb mineralization

The possibility of a genetic link between the Irish orefield and early Carboniferous volcanism (e.g. Strogen, 1995) has been a lingering but largely undocumented issue. However, evidence for a mantle input into the Zn-Pb deposits has recently been proposed based on He isotope data derived from fluid inclusions from all the main ore deposits (Davidheiser-Kroll et al., 2014), and from the intimate association of mineralization and mantle-derived igneous rocks in the Stonepark area, Limerick (Fig. 3.1; McCusker and Reed, 2013). Our Re-Os ages overlap

with these Chadian-Asbian volcanic rocks (Strogen, 1995) and, therefore, are consistent with a new genetic model (Wilkinson and Hitzman, 2014) that invokes magmatic heat derived from underplating and mid-crustal sills as a driver for regional fluid flow. Such a magmatic-related model may explain the unusually high fluid temperatures documented in the province (~70-280°C; Wilkinson, 2010), compared to those documented for sediment-hosted Zn-Pb deposits elsewhere, and the extraordinary regional extent of Zn-Pb mineralization.

3.8 - Implication for dating carbonate-hosted Zn-Pb ores

Paleomagnetic dating at Silvermines (Symons et al., 2007), Galmoy (Pannalal et al., 2008b), and Lisheen (Pannalal et al., 2008a) yields ages of 269 ± 4 , 290 ± 9 Ma, and 277 ± 7 Ma, respectively (Fig. 3.4). However, paleomagnetic studies do not readily discriminate between primary magnetization ages (e.g. mineralization), and remagnetization ages. Consequently, we interpret the disparity between our Re-Os pyrite ages and the systematically younger paleomagnetic ages from the Irish orefield to be a result of widespread remagnetization that took place during Variscan orogenic activity. The preservation of well-defined Re-Os isochrons (Fig. 3.3), despite a Variscan overprint in southern and central Ireland, suggests that the Re-Os isotope system in pyrite was little affected by these tectonothermal processes, and is therefore a robust system for dating weakly metamorphosed, sediment-hosted Zn-Pb deposits.

Globally, paleomagnetic ages have been used to implicate major collisional orogenies that developed during supercontinent assembly cycles as principal drivers for MVT mineralization (Leach et al., 2001). However, if paleomagnetic ages reflect younger orogenic events rather than the age of mineralization, as we observe in the Irish orefield, then this interpretation is invalid. We propose, therefore, that application of pyrite Re-Os geochronology may help resolve the large age discrepancies and competing geodynamic models reported for several MVT districts (e.g., Tennessee, USA and Upper Silesia, Poland: e.g. Leach et al., 2005).

3.9 - References

Anderson, I.K., Ashton, J.H., Boyce, A.J., Fallick, A.E., and Russell, M.J., 1998, Ore depositional processes in the Navan Zn-Pb deposit, Ireland: *Economic Geology*, v. 93, p. 535–563.

Boyce, A.J., Coleman, M.L., and Russell, M.J., 1983, Formation of fossil hydrothermal chimneys and mounds from Silvermines, Ireland: *Nature*, v. 306, p. 545–550.

Boyce, A.J., Litle, C.T.S., Russel, M.J., 2003, A new fossil vent biota in the Balleynoe barite deposit, Silvermines, Ireland: Evidence for intracratonic sea-floor hydrothermal activity about 352 Ma: *Economic Geology*, v.92, p. 649-656.

Chew, D.M., and Stillman, C.J., 2009, Late Caledonian orogeny and magmatism, *in*, Holland, C.H., and Sanders, I.S., eds., *The Geology of Ireland*, 2nd edition: Edinburgh, Dunedin Academic Press, p. 143–173.

Davidheiser-Kroll, B., Stuart, E.M., and Boyce, A.J., 2014, Mantle heat drives hydrothermal fluids responsible for carbonate-hosted base metal deposits: Evidence from $^3\text{He}/^4\text{He}$ ore fluids in the Irish Pb-Zn ore district: *Mineralium Deposita*, v. 49, p. 547–553.

Dixon, P.R., LeHuray, A.P., and Rye, D.M., 1990, Basement geology and tectonic evolution of Ireland as deduced from Pb isotopes: *Journal of the Geological Society [London]*, v. 147, p. 121–132.

Goodfellow, W.D., Lydon, J.W., and Turner, R.J.W., 1993, Geology and genesis of stratiform sediment-hosted (SEDEX) zinc-lead-silver sulphide deposits, *in*, Kirkham, R.V., Sinclair, W.D., Thorpe, R.I., and Duke, J.M., eds., *Mineral Deposit Modeling: Geological Association of Canada Special Paper 40*, p. 201–251.

Gustafson, L.B., and Williams, N., 1981, Sediment-hosted stratiform deposits of copper, lead, and zinc, *in* Skinner, B.J., ed., *Economic Geology 75th Anniversary Volume*: Lancaster, Penn., Lancaster Press, p. 139–178.

Hitzman, M.W., 1999, Extensional faults that localize Irish syndiagenetic Zn-Pb deposits and their reactivation during Variscan compression, *in*, McCaffrey, K.J.W., Lonergan, L., and

Wilkinson, J.J., eds, *Fractures, Fluid Flow and Mineralization*: Geological Society, London Special Publication 155, p. 233–245.

Hitzman, M.W., and Beaty, D.W., 1996, The Irish Zn-Pb-(Ba) orefield, *in* Sangster, D.F., ed., *Carbonate-Hosted Lead-Zinc Deposits*: Littleton, Colo., Society of Economic Geologists, Inc., Special Publication 6, p. 112–143.

Hitzman, M.W., Redmond, P.B., and Beaty, D.W., 2002, The carbonate hosted Lisheen Zn-Pb-Ag deposit, County Tipperary, Ireland: *Economic Geology*, v. 97, p. 1627–1655.

Leach, D.L., Bradley, D., Lewchuk, M.T., Symons, D.T.A., de Marsily, G., and Brannon, J., 2001, Mississippi Valley-type lead-zinc deposits through geological time: Implications from recent age-dating research: *Mineralium Deposita*, v. 36, p. 711–740.

Leach, D.L., Sangster, D.F., Kelley, K.D., Large, R.R., Garven, G., Allen, C.R., Gutzmer, J., and Walters, S., 2005, Sediment-hosted lead-zinc deposits: A global perspective, *in* Hedenquist, J.W., Thompson, J.F.H., Goldfarb, R.J., and Richards, J.P., eds., *Economic Geology One Hundredth Anniversary Volume, 1905–2005*: Littleton, Colo., Society of Economic Geologists, Inc., p. 561–607.

Lee, M.J., and Wilkinson, J.J., 2002, Cementation, hydrothermal alteration, and Zn-Pb mineralization of carbonate breccias in the Irish Midlands: *Economic Geology*, v. 97, p. 653–662.

Ludwig, K.R., 2001, *Isoplot 3.0—A geochronological toolkit for Microsoft Excel*: Berkeley, California, Berkeley Geochronology Center, Special Publication No. 4, 71 p.

McCusker, J., and Reed, C., 2013, The role of intrusions in the formation of Irish-type mineralization: *Mineralium Deposita*, v. 48, p. 687–695.

Meisel, T., Walker, R.J., Irving, A.J., and Lorand, J.-P., 2001, Osmium isotopic compositions of mantle xenoliths: A global perspective: *Geochimica et Cosmochimica Acta*, v. 65, p. 1311–1323.

Morelli, R.M., Bell, C.C., Creaser, R.A., and Simonetti, A., 2010, Constraints on the genesis of gold mineralization at the Homestake gold deposit, Black Hills, South Dakota, from rhenium–osmium sulfide geochronology: *Mineralium Deposita*, v. 45, p. 461–480.

Pannalal, S.J., Symons, D.T.A., and Sangster, D.F., 2008a, Paleomagnetic evidence for an Early Permian age of the Lisheen Zn-Pb deposit, Ireland: *Economic Geology*, v. 103, p. 1641–1655.

Pannalal, S.J., Symons, D.T.A., and Sangster, D.F., 2008b, Paleomagnetic evidence of a Variscan age for the epigenetic Galmoy zinc-lead deposit, Ireland: *Terra Nova*, v. 20, p. 385–393.

Peucker-Ehrenbrink B., and Jahn, B.M., 2001, Rhenium-osmium isotope systematics and platinum group element concentrations: Loess and the upper continental crust: *Geochemistry, Geophysics, Geosystems*, v. 2, DOI: 10.1029/2001GC000172.

Quinn, D., Meere, P.A., and Wartho, J., 2005, A chronology of foreland deformation: Ultra-violet laser $^{40}\text{Ar}/^{39}\text{Ar}$ dating of syn/late-orogenic intrusions from the Variscides of southwest Ireland: *Journal of Structural Geology*, v. 27, p. 1413–1425.

Reed C.P., and Wallace M.W., 2004, Zn-Pb mineralisation in the Silvermines district, Ireland: A product of burial diagenesis: *Mineralium Deposita*, v. 39, p. 87–102.

Russell, M.J., 1978, Downward-excavating hydrothermal cells and Irish-type ore deposits: Importance of an underlying thick Caledonian prism: *Transactions of the Institution of Mining and Metallurgy*, v. 87, sec. B (Applied Earth Science), p. 168–171.

Russell, M.J., Solomon, M., and Walshe, J.L., 1981, The genesis of sediment-hosted exhalative zinc + lead deposits: *Mineralium Deposita*, v. 16, p. 113–127.

Schneider, J., Quadt, A.V., Wilkinson, J.J., and Boyce, A.J., 2007, Age of Silvermines Irish-type Zn-Pb deposit from direct Rb-Sr dating of sphalerite, *in* Andrew, C.J., et al., eds., *Mineral*

Exploration and Research: Digging Deeper: Proceedings of the Ninth Biennial SGA Meeting: Dublin, Irish Association for Economic Geology, p. 373–376.

Singer, D.A., 1995, World class base and precious metal deposits – A quantitative analysis: *Economic Geology*, v. 90, p. 88–104.

Sommerville, I.D., Strogon, P., Jones, G.L., 1992, Biostratigraphy of Dinantian limestones and associated volcanic rocks in the Limerick Syncline, Ireland: *Geological Journal*, v. 27, p. 201–220.

Strogon, P., 1995, Lower Carboniferous volcanic rocks of the Limerick Syncline, *in* Anderson, I.K., Ashton, J., Earls, G., Hitzman, M., and Tear, S., eds. *Irish Carbonate-Hosted Zn-Pb Deposits: Littleton, Colo., Society of Economic Geologists, Inc., Guidebook Series*, v. 21, p.75–79.

Sun, W., Bennett, V.C., Eggins, S.M., Kamenetsky, V.S., and Arculus, R.J., 2003, Enhanced mantle-to-crust rhenium transfer in undegassed arc magmas: *Nature*, v. 422, p. 94–297.

Symons, D.T.A., Smethurst, M.T., and Ashton, J.H., 2002, Paleomagnetism of the Navan Zn-Pb deposit, Ireland: *Economic Geology*, v. 97, p. 997–1012.

Symons, D.T.A., Pannalal, S.J., Kawasaki, K., Sangster, D.F., and Stanley, G.A., 2007, Paleomagnetic age of the Magcobar Ba deposit, Silvermines, Ireland, *in* Andrew, C.J., et al., eds., *Mineral Exploration and Research: Digging Deeper: Dublin, Irish Association for Economic Geology*, p. 377–380.

Taylor, S., 1984, Structural and paleotopographic controls of lead-zinc mineralization in the Silvermines orebodies, Republic of Ireland: *Economic Geology*, v. 79, p. 529–548.

Waters, C.N., Somerville, I.D., Jones, N.S., Cleal, C.K., Collinson, J.D., Waters, R.A., Besly, B.M., Dean, M.T., Stephenson, M.H., Davies, J.R., Freshney, E.C., Jackson, D.I., Mitchell, W.I.,

Powell, J.H., Barclay, W.J., Browne, M.A.E, Leveridge, B.E., Long, S.L., and Maclean, D., 2011, A Revised Correlation of Carboniferous Rocks in the British Isles: The Geological Society of London Special Report 26, 188 p.

Wilkinson, J.J., 2010, A Review of Fluid Inclusion Constraints on Mineralization in the Irish Ore Field and Implications for the Genesis of Sediment-Hosted Zn-Pb Deposits: *Economic Geology*, v. 105, p. 417–442.

Wilkinson, J.J., 2014, Sediment-hosted zinc-lead mineralization: Processes and perspectives, *in* Scott, S.D., ed., *Geochemistry of Mineral Deposits: Treatise on Geochemistry*, 2nd Edition, v. 13, p. 219–249.

Wilkinson, J.J. and Hitzman, M.W, 2014, The Irish Zn-Pb Orefield: The View from 2014. In S.M. Archibald and S.J. Piercey, eds., *Current Perspectives in Zinc Deposits*. Irish Association of Economic Geology, 59-73.

Wilkinson, J.J., Eyre, S.L., and Boyce, A.J., 2005, Ore-forming processes in Irish-type carbonate-hosted Zn-Pb deposits: Evidence from mineralogy, chemistry, and isotopic composition of sulfides at the Lisheen mine: *Economic Geology*, v. 100, p. 63–86.

Wilkinson, J.J., Crowther, H.L., and Coles, B.J., 2011, Chemical mass transfer during hydrothermal alteration of carbonates: Controls of seafloor subsidence, sedimentation and Zn-Pb mineralization in the Irish Carboniferous: *Chemical Geology*, v. 289, p. 55–75.

Zimmerman, A., Stein, H.J., Morgan, J.W., Markey, R.J., and Watanabe, Y., 2014, Re-Os geochronology of the El Salvador porphyry Cu-Mo deposit, Chile: Tracking analytical improvements in accuracy and precision over the past decade: *Geochimica et Cosmochimica Acta*, v. 131, p. 13–32.

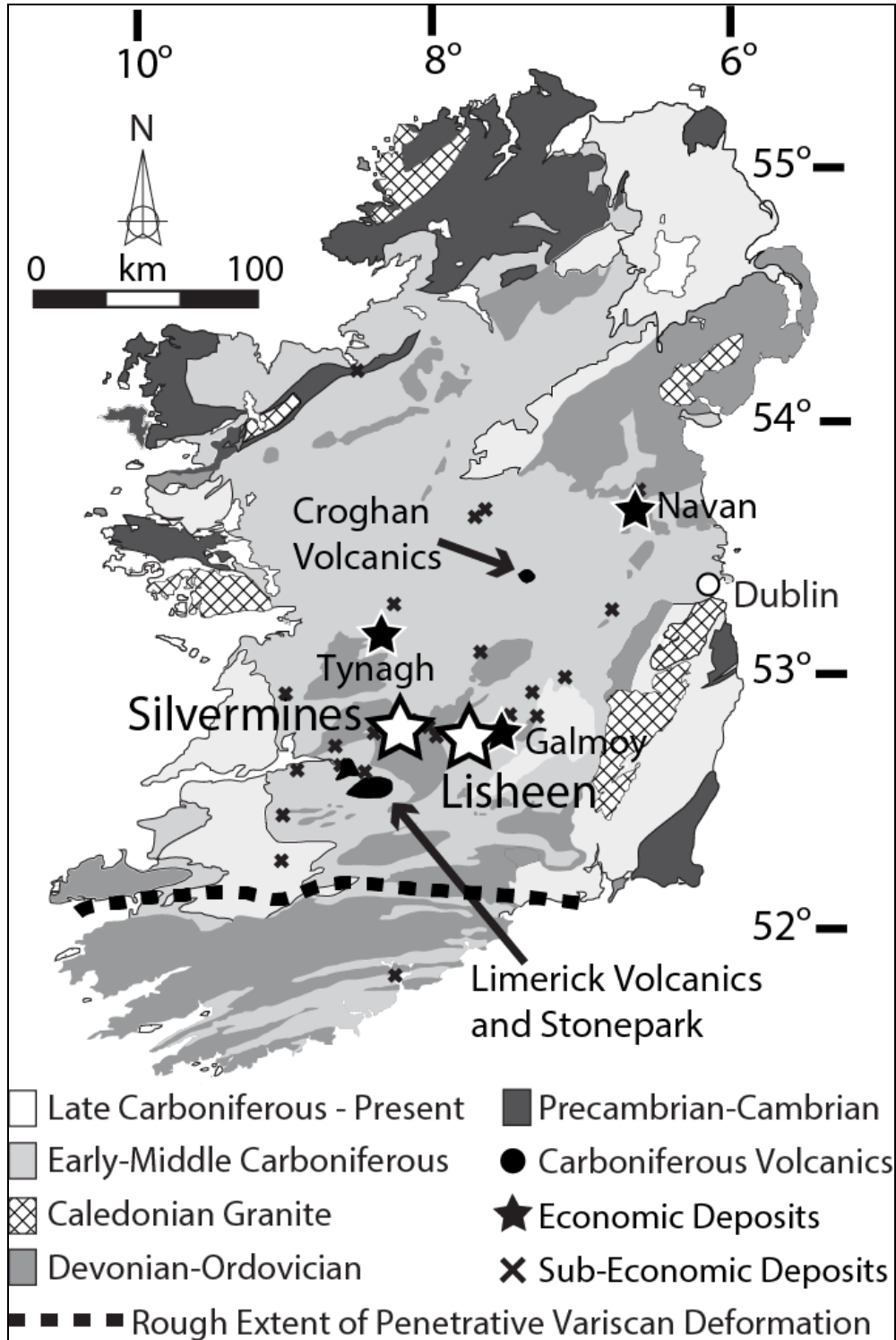


Figure 3.1: Map of Ireland (modified from Wilkinson, 2010) showing selected Zn-Pb ore deposits, volcanic rocks, and approximate northwestern limit of major deformation associated with the Variscan orogeny (Hitzman, 1999).

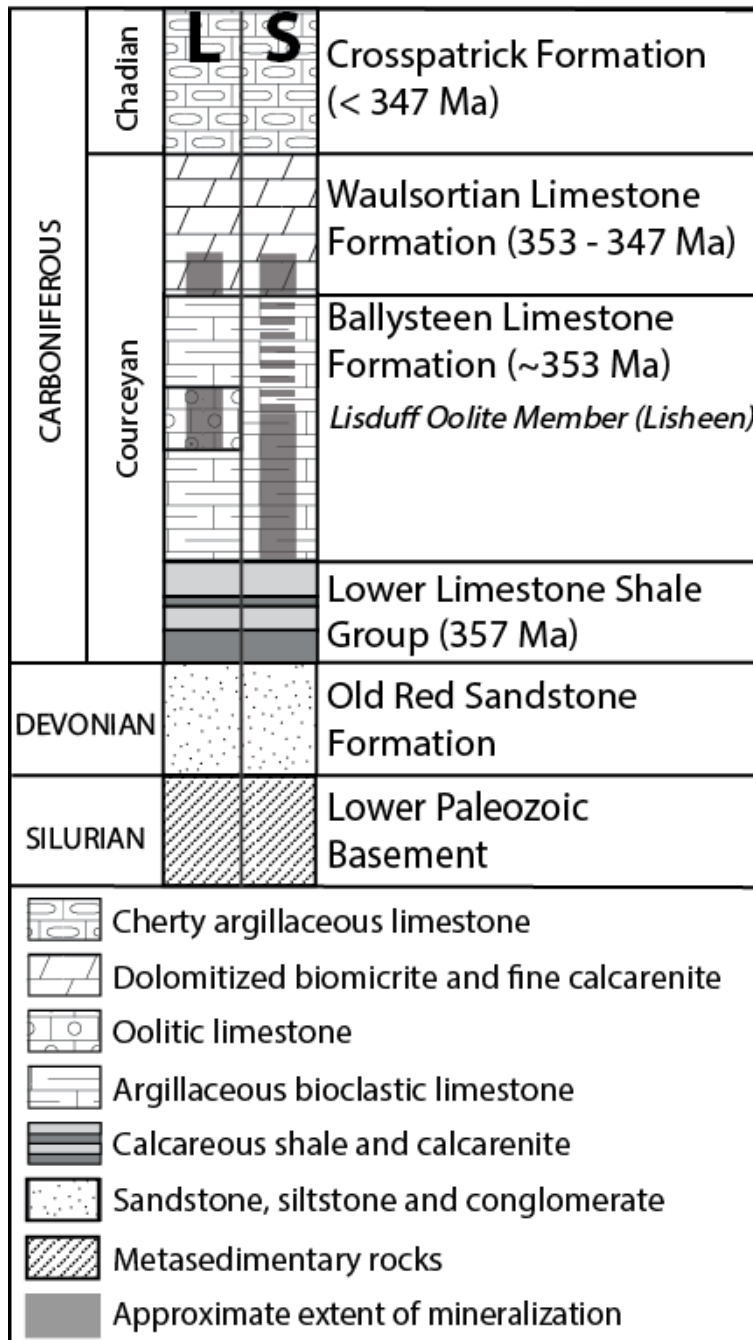


Figure 3.2: Basic stratigraphy of the Lisheen (L) and Silvermines (S) areas (modified from Wilkinson et al., 2005, ages and substages from Waters et al. 2011).

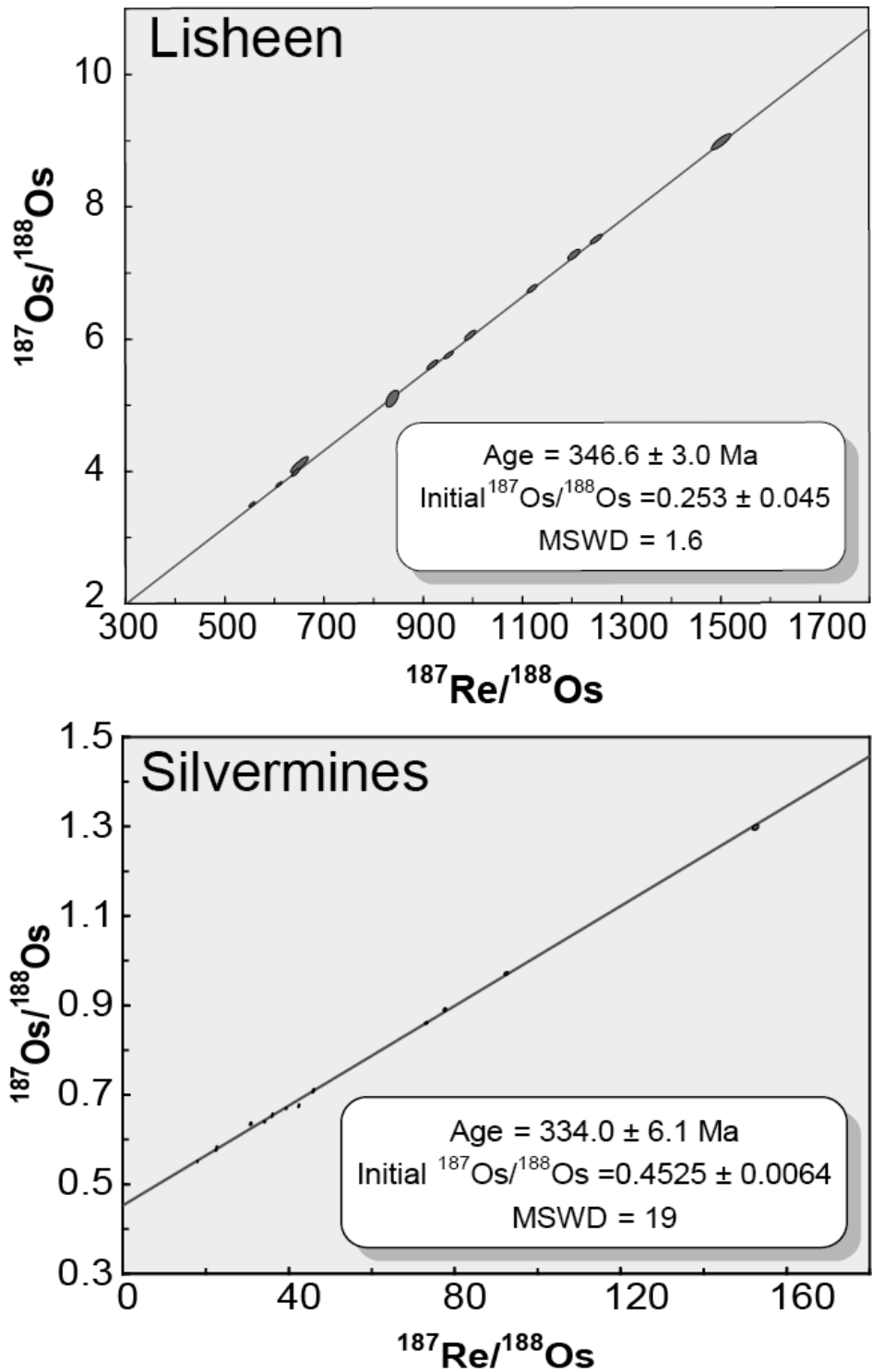


Figure 3.3: Model 3 Re-Os isochron plots based on data for ore-stage pyrite separates from Lisheen (top) and Silvermines (bottom), created using Isoplot v3.00 (Ludwig, 2001). All uncertainties shown are 2σ . MSWD - mean square of weighted deviates.

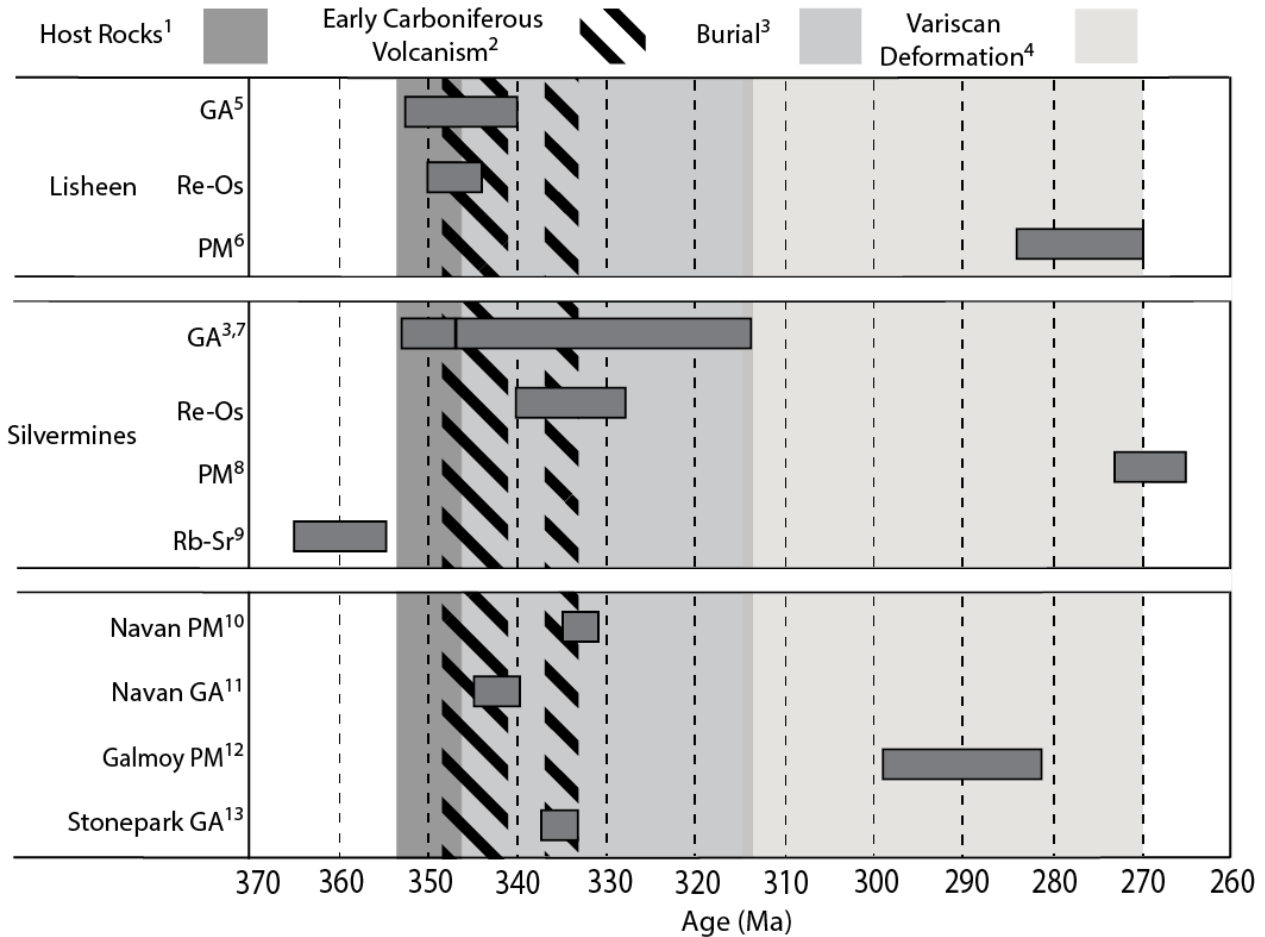


Figure 3.4: Age constraints of major events associated with the Irish Zn-Pb orefield. Key to sources of data: 1 - Waters et al. (2011); 2 - Strogen (1995); Sommerville et al. (1992) 3 - Reed and Wallace (2004); 4 - Quinn et al. (2005); Hitzman (1999); 5 - Hitzman et al. (2002); Wilkinson et al. (2011); 6 - Pannalal et al. (2008a); 7 - Boyce et al. (1983); Lee and Wilkinson (2002); 8 - Symons et al. (2007); 9 - Schneider et al. (2007); 10 - Symons et al. (2002); 11 - Anderson et al. (1998); 12 - Pannalal et al. (2008b); 13 - McCusker and Reed (2013). Methods: Re-Os (rhenium-osmium), Rb-Sr (rubidium-strontium), PM (paleomagnetism), GA (geological arguments).

3.10: Appendix

3.10.1: Sample Descriptions

8S08FW – This sample of massive pyrite was collected by Jamie Wilkinson from the southern part of the Lisheen Main Zone orebody (Panel 8, Stope 8; Fig. DR1) where the ore zone is very thick. The sample came from the footwall of the Killoran Fault at a depth of 176m, within the Lisduff Oolite Member of the Ballysteen Limestone Formation. Ore is locally developed in the footwall oolite at Lisheen and its approximate contiguity with the hangingwall ore zone has been used to argue for a post-faulting timing for mineralization (Hitzman et al., 2002). The sample processed (Fig. DR2) is primarily composed of massive pyrite that is crosscut by calcite veins. A minor amount of sphalerite and fine-grained galena (<10 µm) is observed in thin section and back scattered electron images (Fig. DR2). Such pyrite-rich zones are typical within the high grade cores of the ore lenses at Lisheen (e.g. Fusciardi et al., 2003).

B15 – This sample was collected by John Ashton (Ashton, 1975) from the Silvermines B-zone in the barite ore zone (haulage 4932). The following description is based on his field notes of the sampling locality. The ore zone contains fine-grained massive sulfide composed of ~40-45% pyrite, 5-10% galena, and a variable mixture of barite and sphalerite. Pyrite occurs typically as elongate crystals that occasionally show slight deformation. Sphalerite has replaced pyrite, and galena typically has replaced sphalerite. The sample processed (Fig. DR3) is composed of massive pyrite with cracks infilled by quartz and carbonate. No barite occurs within this sample and galena is present in cracks or as a replacement of pyrite. Pyrite-rich ore was often mined within the B zone at Silvermines, and this pyritic massive sulphide (Taylor and Andrew, 1978) is generally interpreted as an early main stage mineralization ore type.

B18 – This sample was collected by John Ashton (Ashton, 1975) from the Silvermines B-zone (Location: Stope Hanging Wall Drift 48-1S; Fig. DR1). The following description is based on his field notes of the sampling locality. The sample comes from the central part of the B zone in a Pb-rich area close to the B-fault where stratiform massive pyrite and semi-massive pyrite with dolomite breccia overlie siderite- or barite-hosted sulphides. Locally, the massive pyrite is mineralized and was mined. The sample processed (Fig. DR3) is composed primarily of fine-

grained (0.5-2mm), massive pyrite. Sphalerite and galena are present in smaller amounts and show the same general paragenesis as B15, with sphalerite after pyrite and galena typically postdating sphalerite. As with B15, this pyritic massive sulphide is generally interpreted as an early main stage mineralization ore type.

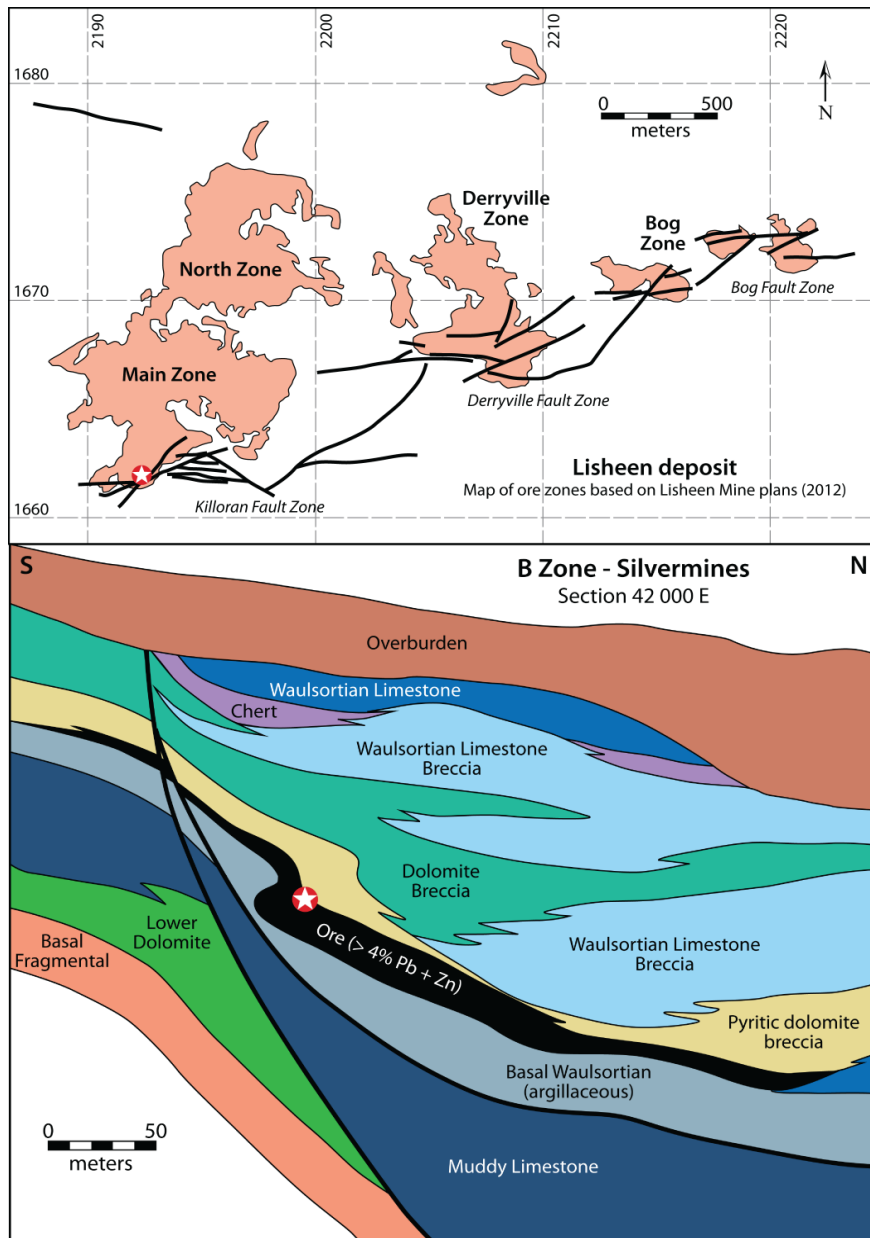


Figure 3.5: Approximate sample locations for Lisheen sample 8S08FW (top) and Silvermines sample B18 (bottom). Modified from Andrew (1986).

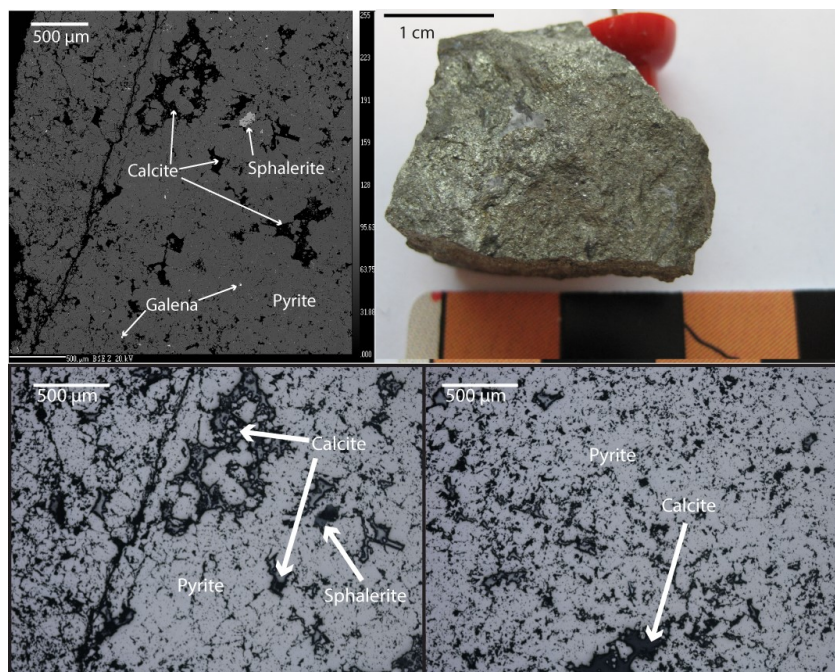


Figure 3.6: Lisheen sample 8S08FW (top right figure) and a representative backscattered electron image (top left figure) and reflected light images (bottom figures).

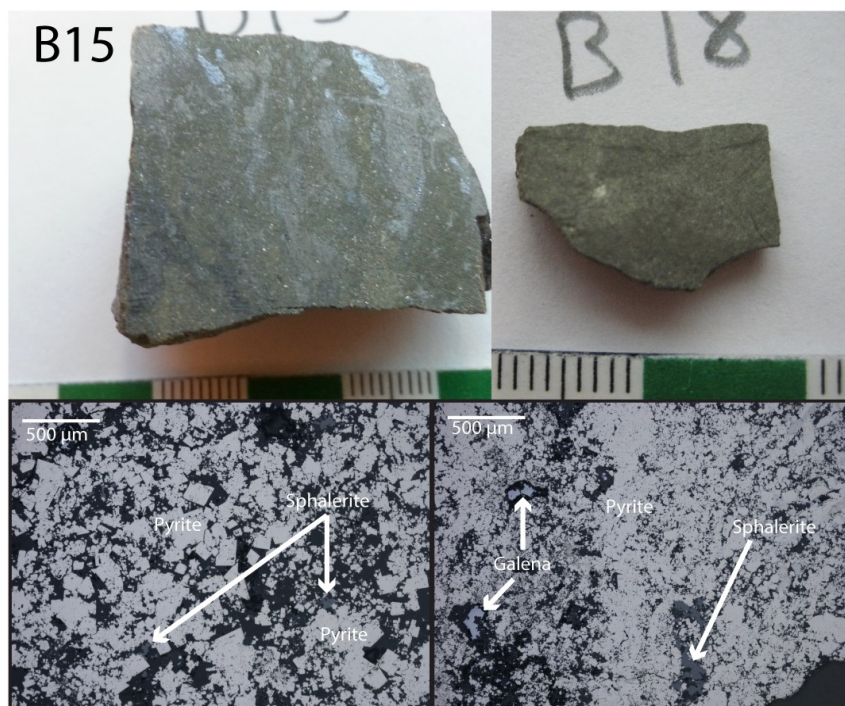


Figure 3.7: Silvermines sample B15 (top left figure) and B18 (top right figure) and representative reflected light images of sample B18 (bottom figures).

3.10.2: Sample Preparation

All samples were prepared using a standardized procedure to ensure that a relatively pure pyrite separate was obtained. A bulk sample containing 5-20g of pyrite was crushed and sieved using metal-free equipment to produce 70-200 μm diameter material containing pyrite and several impurity minerals (e.g. sphalerite, galena, calcite, dolomite, and quartz). Heavy liquid separation using methylene iodide ($\rho = 3.32\text{g/cm}^3$) is used to separate carbonate and silicates from the sulfides. To separate pyrite from galena and sphalerite a Frantz Isodynamic Separator was used. In the sphalerite-pyrite-galena system we typically observe $\chi_{\text{sphalerite}} > \chi_{\text{pyrite}} > \chi_{\text{galena}}$ (χ = magnetic susceptibility). These differences allow separation of pyrite from sphalerite (eliminated at low induced magnetization) and galena (eliminated at high induced magnetization). The final separate contains ~85-100% pyrite. The remaining impurities are typically found as inclusions or are the result of aggregates of multiple minerals not separated by the crushing process.

3.10.3: Analytical Data

Table 3.1: Lisheen Re-Os data

| Sample Name | Re ppb | Os ppt | $^{187}\text{Re} / ^{188}\text{Os}$ | $\pm 2\sigma$ | $^{187}\text{Os} / ^{188}\text{Os}$ | $\pm 2\sigma$ | Rho | % Re Blank | % ^{187}Os Blank | % ^{188}Os Blank |
|------------------|--------|--------|-------------------------------------|---------------|-------------------------------------|---------------|-------|------------|---------------------------|---------------------------|
| 8S08FW | 3.70 | 33.24 | 919.25 | 9.14 | 5.588 | 0.058 | 0.845 | 0.19 | 0.19 | 4.67 |
| 8S08FW M1.0 | 6.18 | 46.72 | 1249.60 | 9.21 | 7.484 | 0.056 | 0.841 | 0.10 | 0.10 | 3.40 |
| 8S08FW M1.0-2 | 5.98 | 47.94 | 1119.67 | 7.98 | 6.735 | 0.052 | 0.778 | 0.10 | 0.10 | 3.15 |
| 8S08FW M1.2 | 5.78 | 44.61 | 1204.48 | 9.68 | 7.254 | 0.067 | 0.758 | 0.11 | 0.11 | 3.51 |
| 8S08FW M1.5 | 3.88 | 33.29 | 995.53 | 9.42 | 6.034 | 0.062 | 0.818 | 0.16 | 0.16 | 4.41 |
| 8S08FW NM1.5 | 2.73 | 31.87 | 609.76 | 5.07 | 3.784 | 0.031 | 0.817 | 0.23 | 0.22 | 3.78 |
| 8S08FW NM1.5-6N | 2.44 | 27.46 | 643.64 | 7.13 | 3.963 | 0.045 | 0.820 | 0.29 | 0.29 | 5.09 |
| 8S08FW NM1.5-10N | 2.28 | 25.53 | 651.82 | 14.85 | 4.077 | 0.098 | 0.869 | 0.50 | 0.93 | 9.56 |
| 8S08FW B | 4.31 | 37.79 | 952.61 | 7.54 | 5.734 | 0.047 | 0.815 | 0.14 | 0.14 | 3.66 |
| 8S08FW B M0.8 | 8.10 | 55.94 | 1501.95 | 16.05 | 8.955 | 0.103 | 0.861 | 0.13 | 0.13 | 5.15 |
| 8S08FW B NM1.0 | 4.14 | 39.18 | 837.80 | 10.33 | 5.076 | 0.104 | 0.561 | 0.15 | 0.15 | 3.36 |
| 8S08FW B NM1.2 | 2.52 | 31.38 | 556.09 | 5.01 | 3.478 | 0.031 | 0.797 | 0.27 | 0.26 | 4.08 |

Table 3.2: Silvermines Re-Os data

| Sample Name | Re ppb | Total Os ppt | 187Re/188 Os | $\pm 2\sigma$ | 187/188 Os | $\pm 2\sigma$ | rho | % Re Blank | % ^{187}Os Blank | % ^{188}Os Blank |
|-------------------|--------|--------------|--------------|---------------|------------|---------------|-------|------------|---------------------------|---------------------------|
| B18 A | 1.28 | 156.97 | 42.106 | 0.185 | 0.6743 | 0.0030 | 0.396 | 0.21 | 0.02 | 0.08 |
| B18 A M0.7-F | 1.37 | 392.10 | 17.719 | 0.085 | 0.5489 | 0.0018 | 0.301 | 0.32 | 0.02 | 0.05 |
| B18 A NM0.7-F | 0.63 | 144.86 | 22.148 | 0.200 | 0.5752 | 0.0022 | 0.188 | 0.79 | 0.05 | 0.15 |
| B18 A NM 0.9 | 0.93 | 156.82 | 30.538 | 0.168 | 0.6335 | 0.0030 | 0.274 | 0.38 | 0.03 | 0.10 |
| B18 A NM 1.0 | 1.24 | 178.58 | 35.616 | 0.180 | 0.6519 | 0.0040 | 0.599 | 0.13 | 0.09 | 0.30 |
| B18 A NM 1.0-F | 1.25 | 189.07 | 33.864 | 0.146 | 0.6380 | 0.0019 | 0.325 | 0.26 | 0.02 | 0.08 |
| B18 A NM 1.2 | 1.21 | 159.77 | 39.011 | 0.173 | 0.6675 | 0.0024 | 0.342 | 0.26 | 0.02 | 0.09 |
| B18 A NM 1.55 | 1.59 | 181.03 | 45.575 | 0.231 | 0.7076 | 0.0042 | 0.628 | 0.12 | 0.09 | 0.33 |
| B18 A NM 1.55-F | 1.25 | 90.99 | 72.681 | 0.294 | 0.8589 | 0.0025 | 0.370 | 0.22 | 0.03 | 0.14 |
| B18 A NM 2.0-10/5 | 1.87 | 108.67 | 92.002 | 0.368 | 0.9701 | 0.0031 | 0.384 | 0.20 | 0.03 | 0.16 |
| B18 A NM 2.0-F | 1.72 | 118.02 | 77.250 | 0.305 | 0.8888 | 0.0031 | 0.390 | 0.18 | 0.02 | 0.12 |
| B18 A NM 2.0-10/3 | 2.32 | 84.80 | 151.998 | 0.571 | 1.2975 | 0.0045 | 0.430 | 0.13 | 0.02 | 0.17 |
| B15 | 0.53 | 120.22 | 22.355 | 0.115 | 0.5811 | 0.0021 | 0.283 | 0.36 | 0.02 | 0.07 |

Table 3.3: Re-Os blank data

| Blank | n(Re) | n(Os) | Re (pg) | $\pm 2\sigma$ | Os (pg) | $\pm 2\sigma$ | 187/188 Os | $\pm 2\sigma$ |
|-------------|-------|-------|---------|---------------|---------|---------------|------------|---------------|
| Lisheen | 4 | 4 | 2.5 | 1.5 | 0.34 | 0.03 | 0.23 | 0.05 |
| Silvermines | 9 | 8 | 1.1 | 0.6 | 0.05 | 0.01 | 0.18 | 0.16 |

n(Re) = number of blank analyses for Re blank determination; n(Os) = number of blank analyses for Os blank determination

3.10.4: References:

Andrew, C. J., 1986, The tectono-stratigraphic controls in mineralization in the Silvermines area, County Tipperary, Ireland, *in*: Andrew, C.J., Crowe, R.W.A., Finlay, S., Pennell, W.M., Pyne, H.F., eds., *Geology and genesis of mineral deposits in Ireland*: Dublin, Irish Association for Economic Geology, p. 377-417.

Ashton, J.H. 1975, A geological study of the B Zone base metal deposit at the Mogul of Ireland mine, Silvermines, Eire: Unpublished B.Sc. Thesis, University of London.

Fusciardi, L.P., Guven, J.F., Stewart, D.R.A., Carboni, V., and Walshe, J.J., 2003, The geology and genesis of the Lisheen Zn-Pb deposit, Co. Tipperary, Ireland, *in* Kelly, J.G., Andrew, C.J., Ashton, J.H., Boland, M.B., Earls, G., Fusciardi, L., and Stanley, G., eds., *Europe's major base metal deposits*: Dublin, Irish Association for Economic Geology, p. 455–481.

Hitzman, M.W., Redmond, P.B., and Beaty, D.W., 2002, The carbonate hosted Lisheen Zn-Pb-Ag deposit, County Tipperary, Ireland: *Economic Geology*, v. 97, p. 1627–1655.

Taylor, S., and Andrew, C. J., 1978, Silvermines orebodies, Co. Tipperary, Ireland: *Inst. Mining Metallurgy Trans.*, v. 87, sec. B, p. 111-124.

4.1: Understanding pyrite Re-Os geochronology

Part A: Re-Os systematics of pyrite

4.1.1: Introduction

Constructing the history and evolution of geologic processes is one of the major tasks assigned to geoscientists and requires accurate and precise geochronology. Economic geology is one discipline in which robust geochronology is required as temporally linking ore mineralization to tectonics, magmatism, and/or sedimentary processes is essential when developing genetic models for ore formation.

Pyrite Re-Os geochronology is an absolute dating technique that is becoming a widely accepted method for dating mineralization associated with many types of ore systems. The usefulness of this technique stems from the almost ubiquity of pyrite and similar minerals (e.g. arsenopyrite) being associated with ore stage mineralization and remaining robust through post-mineralization thermal disturbances (Morelli et al., 2010; van Acken et al., 2014; Vernon et al., 2014). As a result, pyrite Re-Os geochronology has been widely used to successfully date a large assortment of ore types including orogenic gold, porphyry, SEDEX, and MVT deposits resulting in dozens of publications in the past 20 years (e.g. Stein et al., 2000; Morelli et al., 2004; Lawley et al., 2013; Hnatyshin et al., 2015; Zhang et al., 2016), with many examples producing geologically plausible ages with relatively high precision (error < 10%) and low scatter in the data (MSWD < 10).

However, a number of publications, and surely many unpublished datasets, have produced results with high scatter and/or imprecise ages (Fig. 4.1.1). For these datasets, a violation of one or more of the fundamental assumptions of isotopic dating may have occurred (see Chapter 2). Unfortunately, but perhaps unsurprisingly, comparatively little effort has been expended to understanding the fundamental causes of scatter or imprecision found within these datasets and how it may affect the interpretation of the calculated age. This is, in part, due to the lack of understanding of the Re-Os systematics of pyrite. This is in contrast to what is known about the Re-Os systematics associated with molybdenite and organic-rich sediments, for example for molybdenite, several important studies (e.g. Stein et al., 2003, Selby and Creaser, 2004) focused on understanding how Re-Os is distributed within molybdenite crystals. Crucially,

these studies demonstrated that Re and Os can become decoupled in molybdenite crystals implying that bulk sampling procedures should be used to date molybdenite crystals and that in-situ methods should be avoided. For organic-rich sediments, analytical protocols have also evolved over time to reduce the influence of Re and Os liberated from detrital sediment (Selby and Creaser, 2003; Yin et al., 2017). In a similar spirit to these studies, this chapter further develops how pyrite-bearing rocks are screened prior to processing, suggests which processing techniques should be used, and how the results of Re-Os geochronology should ultimately be interpreted.

To accomplish these goals we have split the investigation of pyrite Re-Os systematics into two companion studies. In this chapter (Part A) the focus is on determining how Re is distributed within pyrite-bearing Zb-Pb ores to determine how much petrological context is required to properly judge the accuracy and geologic significance of a geochronological result. This is accomplished by documenting the sample paragenesis, relating it to the known paragenesis of the ore deposit, and then characterizing samples through bulk (Re-Os isotopes, trace elements, magnetic susceptibility) and microanalytical (S isotopes, Re mapping, trace element mapping) techniques, with the objective of determining the behaviour of Re, and hence radiogenic ^{187}Os within the ore. Herein, both published (Hnatyshin et al. (2015) and Hnatyshin et al. (2016)) and unpublished datasets from carbonate hosted Zn-Pb deposits are investigated; Lisheen from Ireland, and two mineralized locations from Baffin Island in Canada (Nanisivik and Hawker Creek). These samples were chosen for their well-documented analytical protocols, sample availability, and their contrasting levels of precision and accuracy. The dataset compiled and discussed in Part A will be used as a reference for Part B, in which several different mineral purification procedures are scrutinized to determine their applicability in producing high quality mineral separates for Re-Os geochronology.

4.1.2: Violations of isochron assumptions

Pyrite Re-Os geochronology is an isotopic dating method that commonly applies the isochron method to determine an age from a set of samples. Isotopic dating using the isochron method requires that the phase(s) analysed were in isotopic equilibrium with one another during their formation and subsequently became closed with respect to isotopic exchange. This can be broken down into the following assumptions (see Chapter 2 for more details), (1) samples are

formed synchronously, (2) samples are formed from a single Os isotopic reservoir (i.e. unique initial $^{187}\text{Os}/^{188}\text{Os}$ signature), (3) the crystals have not been altered with respect to the Re-Os system since closure and (4) the samples analyzed have negligible contamination. With all these requirements satisfied, the errors calculated are purely due to analytical error and will therefore provide accurate ages. However, for this study, violations of assumption (1) are considered negligible as the analytical error of Re-Os analyses (> 1 Ma) is far greater than many estimates of the duration of mineralization episodes (e.g. Cathles and Smith, 1983; Garven et al., 1993; Lewchuk and Symons, 1995; Rowan and Goldhaber, 1995). Violations of assumption (2) will be assessed by evaluating if the observed variation in initial osmium (VIOs) for a given dataset are geologically plausible. In scenarios for which fluid mixing is possible “significant” differences in $^{187}\text{Os}/^{188}\text{Os}$ could occur in time and space. Modern day hydrothermal systems mixing with seawater allow for $^{187}\text{Os}/^{188}\text{Os}$ variations of close to ~ 1 and could be considered a liberal bound on the VIOs, at least until better constraints are able to be determined (Sharma et al., 2000, 2007). Assumption (2) can be ignored when there is negligible common Os (i.e. ^{188}Os) present in the sample (Stein et al., 2000). Contamination and alteration (assumptions 3 and 4) will be identified using petrographic imaging, laser ablation inductively coupled mass spectrometry (LA-ICPMS) compositional mapping, and secondary ionization mass spectrometry (SIMS) sulphur isotope measurements.

4.1.3: Sample Selection

The Lisheen deposit from Ireland was chosen for detailed investigation as pyrite from this deposit produced one of the most precise pyrite Re-Os ages found in the literature (346 ± 3.0 Ma; Fig 4.1.1; Chapter 3). Scrutinizing the sample used to produce this robust age provides insight into which characteristics may make a sample amenable for Re-Os dating. Additionally, this isochron sets a well-defined baseline age of the Lisheen ore-forming system, which can be used for interpreting other ages produced from Lisheen ores. In particular, we have attempted to replicate this age using more paragenetically complex samples to determine how precision and accuracy are influenced when analyzing samples of higher complexity.

The second set of samples is from Zn-Pb mineralization from Baffin Island in Canada (Hnatyshin et al., 2016). Re-Os analysis from the Nanisivik deposit from Hnatyshin et al. (2016) produced an isochron with relatively high scatter (Model 3, 1122 ± 52 Ma, MSWD = 97), but

with an age consistent with sphalerite Rb-Sr geochronology and paleomagnetism (Christensen et al., 1993; Symons et al., 2000). The Hawker Creek prospect from produced non-linear data; hence no isochron could be constructed, although model ages suggested that there may be mixing between two end-members (~1100 Ma and ~400 Ma; Hnatyshin et al., 2016). The Baffin Island samples present an excellent test of our ability to deconstruct the origins of scatter present in a Re-Os pyrite dataset.

4.1.3.1: Study Location 1: Lisheen Deposit

4.1.3.1.1: Background

In Ireland during the early Mississippian, a marine transgression across the Laurussian continental margin deposited thick limestone units. Hydrothermal fluids subsequently precipitated tens of millions of tons of zinc and lead within these carbonate rocks, making the Irish orefield one of the most intensely mineralized Zn districts on Earth (Singer, 1995; Chapter 3). Lisheen is the second-largest base-metal deposit in Ireland and has been described in detail and is summarized below using the descriptions provided by Hitzman et al. (2002) and Wilkinson et al. (2005). It consists of a series of stratabound sulphide lenses divided into the Main Zone, Derryville Zone, and Bog Zone, with each zone being controlled by its own normal fault (Fig. 4.1.2B). Ore is primarily hosted within the Waulsortian Limestone Formation on the hangingwall of normal faults, with a smaller proportion of the ore hosted within the Lisduff oolite of the Ballysteen Limestone Formation on the footwall (Fig. 4.1.2C).

4.1.3.1.2: Mineralization

The onset of mineralization at Lisheen is marked by widespread dolomitization and brecciation of the host limestone. The first stage of sulphide mineralization at Lisheen is represented by small amounts of disseminated pyrite associated within the earliest stages of dolomitization (D1 in Wilkinson et al., 2005) of the Waulsortian Limestone Formation. A later stage of dolomitization (D2) is associated with higher abundances of fine-grained pyrite and sphalerite. Following dolomitization, massive iron sulphide mineralization took place, beginning with the precipitation of trace-element poor pyrite. These pyrites are often overgrown by colloform bands of new iron sulphides (pyrite and marcasite) that contain minor amounts of sphalerite, which preferentially replace individual iron sulphide framboids, dolomite, and galena.

The colloform iron sulphide bands transition into an assemblage that is dominated by colloform sphalerite, and signifies the boundary between pre-ore and main ore stage in Wilkinson et al. (2005). Following the precipitation of colloform sphalerite, is a mixture of sphalerite, galena, tennantite and blocky dolomite. The last major ore stage assemblage is sphalerite \pm galena \pm dolomite \pm quartz \pm barite that fill in either vugs or are found as crosscutting veins. Late stage mineralization sequences also include minor Cu-sulphides, arsenopyrite and tennantite that locally replace other sulphides. The Lisduff oolite mineralization is generally similar to that observed in the Waulsortian Limestone, with the only major difference being that the earliest stage of sulphide mineralization is denoted by massive pyrite replacing the host oolitic limestone. The general paragenesis is provided in Figure 4.1.3A and is constructed using our interpretation of the observations provided by Hitzman et al. (2002), Wilkinson et al. (2005), as well as the smaller sample set used in this study.

4.1.3.1.3: Sample Selection

The sample set used herein, consisting of 3 rocks, contains a variety of textures that cover preore to post-ore stage mineralization as defined by Wilkinson et al. (2005). In Figure 4.1.3 the observed textures are shown split into 8 groups (Lisheen Generation 0 to Lisheen Generation 7, and abbreviated as LG0 to LG7) along with their suggested paragenetic relationships. LG1-LG7 are visually distinctive and fit into the sample descriptions provided by Hitzman et al. (2002) and Wilkinson et al. (2005). LG0 are silicate-rich areas contained within LG6 sphalerite and are interpreted to be the remnants or direct replacement of host rock material due to needle-shaped textures that are interpreted to be primary texture. LGU is the designation given to any texture or phase which has an uncertain place within the paragenetic sequence.

8S08FW

The Re-Os data from 8S08FW used in this Chapter are from Hnatyshin (2012) and published in Hnatyshin et al. (2015), whereas analyses of trace elements and sulphur isotopes were produced for this Chapter to complement the Re-Os dataset.

8S08FW was sampled from the Lisduff oolite member of the Ballysteen Formation at a depth of 176 m. 8S08FW is composed primarily of LG1 pyrite containing small ($<5 \mu\text{m}$) sphalerite and galena inclusions (Fig. 4.1.4C). LG1 pyrite is very rarely crosscut by coarser

galena crystals ($> 100 \mu\text{m}$) that are possibly from LG5, and more commonly cross-cut by calcite veins (LG7?). Localized areas in LG1 pyrite contain silicate-filled fractures with no clear placement in the paragenetic sequence and hence are placed into LGU.

LK 359

LK 359 comprises a different generation of iron sulphide than 8S08FW (LG2 vs. LG1) in addition to being a more paragenetically complex sample (Fig. 4.1.3, Fig. 4.1.5). LK 359 is a Derryville Zone sample collected from massive sulphide ore at a depth of 143.6 m within the Waulsortian Limestone Formation and is composed primarily of pyrite, marcasite, sphalerite, and silicates. Brecciation and replacement of LG2 marcasite by LG6 sphalerite veins is the dominant feature observed in LK 359 (Fig. 4.1.5B). Associated with LG6 sphalerite, are dark fine-grained silicate needles (LG0) which are interpreted to be the remnants of the host rock prior to replacement by sulphides (Fig. 4.1.5B, C). Sulphides representing LG1 and LG3 are uncommon in LK 359 and are often highly fractured. A clear progression of LG1-LG3 can be seen in localized areas (Fig. 4.1.5D) and these anhedral masses of LG1-LG3 are often fractured and in-filled by LG5 sphalerite and dolomite (Fig. 4.1.5B).

LK 451

The Hnatyshin et al. (2015) project was initiated following encouraging preliminary results produced from the Bog Zone sample LK 451 (Creaser et al., 2009). LK 451 was at the time not pursued further due to the textural and mineralogical complexity found in this sample (Fig. 4.1.3, Fig. 4.1.6).

LK 451 was sampled from the Bog Zone at a depth of 139.1 m from massive sulphide hosted within the Waulsortian Limestone Formation and primarily contains pyrite, sphalerite, quartz, and dolomite. The earliest stage of mineralization in LK 451 is LG1 pyrite which appears to have been lightly fractured prior to being overgrown by rims of LG2 and/or LG3 colloform sulphide bands (Figs. 4.1.6B, D, and E). Individual colloform layers are well defined and are typically $< 10 \mu\text{m}$ thick with a total thickness of LG2 bands being $\sim 50 - 100 \mu\text{m}$, while the total thickness of LG3 bands may exceed $250 \mu\text{m}$. The transition from LG1 to LG2/LG3 may be sharp (dashed line in Fig. 4.1.6D) or gradational (right side of Fig. 4.1.6D). LG4 sphalerite, quartz, and carbonate fill in the interstitial spaces between LG1/LG2/LG3 masses (Figs. 4.1.6C, E) but may

also crosscut younger sulphides of LG1-LG3. Some anomalous areas of Si-rich material appear to crosscut all previous phases but it is unclear what its paragenetic affinity is (LGU designation).

4.1.3.2: Study Location 2: Baffin Island

4.1.3.2.1: Background:

The Mesoproterozoic Borden Basin of Baffin Island, Nunavut, Canada is known for its extensive, if underexplored, Zn-Pb mineralization. The past producing mine of Nanisivik is largest known example of Zn-Pb mineralization on the island, whereas smaller base-metal showings occur southeast of Nanisivik (e.g. Hawker Creek; Fig. 4.1.7A). The geologic history of the region is geologically complex and are detailed in the studies of Jackson and Innaelli (1981), Turner (2009, 2011), and Turner et al. (2016).

Mineralization at Nanisivik and Hawker Creek is similar in style, with ore being composed of elongated sulphide bodies with the top surface showing extremely low relief (Sutherland and Dumka, 1995; Turner, 2011; Fig. 4.1.7C). The dominant ore texture found within these massive sulphide lenses is the alternating banding of pyrite, sphalerite, galena, and dolomite that replace the dolostone of the Nanisivik Formation (Olson, 1984; Arne et al., 1991; Turner, 2011). The relative timing of the different sulphides is likely variable depending on the location sampled, as the observations of Olson (1984) reported pyrite replacing sphalerite/galena, whereas observations by Arne et al. (1991) report the opposite sequence (Fig. 4.1.8). A minor proportion of the sulphides are fracture-hosted, vug-filling, or disseminated within the host rock.

4.1.3.2.2: Sample Description and Background

NOV4

Sample NOV4, along with sample 04-N-2, was used by Hnatyshin et al. (2016) to construct an isochron for Nanisivik with a high amount of scatter (Model 3, 1115 ± 52 Ma, MSWD = 99).

NOV4 was collected from the main lens at Nanisivik and at hand sample scale is defined by ~1 cm thick bands of pyrite, sphalerite, and dolomite (Fig. 4.1.9A). The paragenetic sequence follows the general sequence suggested by Olson (1984) with pyrite being replaced by sphalerite

and galena, and then followed by dolomite (Fig. 4.1.8). Finer scale observations from BSE images from Hnatyshin et al. (2016) clearly show zones of fractured and brecciated pyrite that are infilled with galena, silicates, and dolomite. These fractures likely predate dolomite mineralization as they only occur in pyrite.

03-HC-8D

03-HC-8D is one of two samples used in Hnatyshin et al. (2016) to produce Re-Os model ages for Hawker Creek, and is a relatively simple rock consisting primarily of massive pyrite with smaller semi-continuous bands of sphalerite (Fig. 4.1.9B). Sulphides are primarily anhedral with localized areas that are highly fractured and infiltrated by dolomite (Fig. 4.1.9E). BSE images from Hnatyshin et al. (2016) also show areas containing high concentrations of small (< 30 μm) inclusions of sphalerite and pyrrhotite.

The mineral separates analyzed by Hnatyshin et al. (2016) contain a wide range of model ages of 413 Ma to 805 Ma for 03-HC-8D, whereas older ages up to 1083 Ma were obtained for 03-HC-8F. Hnatyshin et al. (2016) suggested that based on these observations, their dataset contains two end members of pyrite formation at ~ 1100 Ma and ~ 400 Ma.

4.1.4: Methods

4.1.4.1 Sample Preparation

Samples chosen for Re-Os geochronology were processed in a similar fashion to that of other Re-Os studies (e.g. Morelli et al., 2010) and are described in Chapter 4B. In short, samples were crushed and sieved to a size of 74-210 μm using metal free equipment to minimize the risk of metallic contamination. Heavy liquid separation and magnetic separation procedures were used to help purify the majority of the samples. Hydrochloric acid (0.2N to 10N) was also used to remove acid-soluble impurities (e.g. calcite, dolomite, sphalerite, galena) for some samples. After acid leaching, the residual acid solutions were collected and stored for ICP-MS analysis.

4.1.4.2: ICP-MS Analysis

Bulk compositions of several mineral separates, leached mineral separates, and the leachates were analyzed for major and minor elements. Prior to analysis of the mineral separates, acid digestion was performed on ~ 200 mg of sample. After digestion, a Perkin Elmer Elan 6000

Quadrupole Inductively Coupled Plasma Mass Spectrometer at the University of Alberta was used to analyze the major, minor, and trace elements using a DNC-1 standard for element calibration. Appropriate dwell times (10 – 20 ms) and integration times (350 – 700 ms) were selected to optimize counting statistics for each element.

4.1.4.3: Re-Os Analytical Procedure

All prepared material for Re-Os analysis were chemically purified and analyzed at the Crustal Re-Os Geochronology Laboratory at the University of Alberta. Chemical purification of Re and Os was accomplished by following the isotope dilution procedure outlined in Hnatyshin et al. (2016). After chemical purification of Re and Os the samples were analyzed using a thermal ionization mass spectrometer (TIMS) running in negative ion mode using the sample preparation and conditions specified in Hnatyshin et al. (2016). All age determinations were performed using Isoplot version 3.00 (Ludwig, 2003).

4.1.4.4: Sulphur Isotope Sample Preparation

Sample preparation and SIMS analysis were carried out at the Canadian Centre for Isotopic Microanalysis (CCIM), University of Alberta. Pyrite mineral separates and rock fragments were co-mounted in 25 mm diameter epoxy assemblies along with fragments of CCIM pyrite reference material S0302A. The mounts were ground and polished with diamond compounds on rotary equipment, cleaned with a lab soap solution and de-ionized H₂O, and then coated with 30 nm of high-purity Au prior to scanning electron microscopy (SEM). SEM characterization was carried out with a Zeiss EVO MA15 instrument using beam conditions of 20kV and 3 – 4 nA. A further 23 nm of Au was subsequently deposited on the mounts prior to SIMS analysis.

Sulphur isotope ratios (³⁴S/³²S) were determined in pyrite using the IMS-1280 multi-collector ion microprobe at the CCIM. Primary beam conditions included the use of 20 keV ¹³³Cs⁺ ions focused to form a probe with diameter ~10 μm and beam current of 1.3 - 2.7 nA. The primary beam was rastered across an 18 x 18 μm area for 30 s prior to analysis, to clean the surface of Au and contaminants, and implant Cs. The normal incidence electron gun was not required. Negative secondary ions were extracted through 10 kV to the grounded secondary column (Transfer section). Conditions for the Transfer section included an entrance slit width of

122 μm , field aperture of 5 x 5 mm, and a field aperture-to-sample magnification of 100 x. Automated tuning of the secondary ions in the Transfer section preceded each analysis. Both $^{32}\text{S}^-$ and $^{34}\text{S}^-$ were analysed simultaneously in Faraday cups (L'2 using $10^{10} \Omega$ amplifier, and FC2 with $10^{11} \Omega$, respectively) at a mass resolution of 2000. Mean count rates for $^{32}\text{S}^-$ and $^{34}\text{S}^-$ were typically $1.2 - 3.6 \times 10^9$ and $0.5 - 1.6 \times 10^8$ counts/s, respectively, determined over a 60 – 75 s counting interval. The analytical protocol interspersed analyses of unknowns with the pyrite reference material (RM, CCIM sample S0302A with $\delta^{34}\text{S}_{\text{VCDT}} = -0.2 \pm 0.2 \text{ ‰}$; R. Stern, unpublished data) in a 4:1 ratio. Instrumental mass fractionation (IMF) for $^{34}\text{S}^-/^{32}\text{S}^-$ was $\sim 4 - 6 \text{ ‰}$, determined for the two analytical sessions by utilizing all the replicate analyses of S0302A pyrite. The standard deviation of $^{34}\text{S}^-/^{32}\text{S}^-$ ratios for S0302A was $0.02 - 0.05 \text{ ‰}$ after small corrections for within-session IMF drift ($< 0.4 \text{ ‰}$). Final uncertainties are reported at 95% confidence level (2σ) and propagate within-spot counting errors, between-spot errors to account for geometric effects (blanket uncertainty of $\pm 0.10 \text{ ‰}$ applied), and between-session error ($\leq \pm 0.02 \text{ ‰}$) that accounts for uncertainty in the mean IMF for the session. The total uncertainties average $\pm 0.120 - 0.135 \text{ ‰}$ (2σ) per spot, not including the absolute uncertainty in the true composition of S0302A pyrite indicated above. No orientation-related biases have been found for SIMS analysis of pyrite at CCIM, consistent with previous findings (Kozdon et al., 2010). The $^{34}\text{S}/^{32}\text{S}$ value of VCDT utilized for normalization was 0.0441626 (Ding et al., 2001).

4.1.4.5: LA- ICPMS Analysis

LA-ICPMS analysis was carried out at the CODES LA-ICPMS facility, University of Tasmania, using a Agilent 7500 ICPMS coupled to a New Wave 213-nm solid state laser using methods similar to that described in Large et al. (2009) and Danyushevsky et al. (2011). The main focus of the LA-ICPMS mapping program was to map the distribution of Re within pyrite at the sub-millimetre scale while maintaining detection limits at the ppb level. To accomplish this goal, dwell times (0.31 s) were biased towards Re with up to 90% of the analysis time allocated to count Re. Compositional maps were produced by rastering across the sample at a rate equal to the spot size (e.g. 10 μm spot size = 10 $\mu\text{m}/\text{s}$ scan rate) using a laser frequency of 10 Hz and a fluence of 2.7 - 3.5 J/cm^2 . Preceding and following each map one to three spot analyses of several external standards (STDGL2b2, BCR-2G, and GSD-1G) were measured for data evaluation. Following the analyses of the standards, but prior to the analysis of the sample, a spot

analysis of quartz was used to clean to system and then a background measurement was taken. In-house data reduction software packages were used to manually quantify the collected data.

4.1.5: Results

4.1.5.1: Characterization of Mineral Separates

Estimates of modal abundances and associated magnetic susceptibility for each mineral separate are provided in Table 4.1.1 and bulk chemistry compositions are provided in Figure 4.1.10, with the full dataset being available in the Appendix (Tables 4.1.6, 4.1.7). Representative petrographic images and backscattered electron images (BSE) of mineral separates for mineral separates can be found in Figures 4.1.4, 4.1.5, 4.1.6, and 4.1.9, in addition to the images provided in Hnatyshin et al. (2016). A more detailed discussion of mineral separate characterization is presented in Chapter 4B.

4.1.5.2: Re-Os Results

A compilation of all the Re-Os results obtained from this study and the relevant data from Chapter 3 and Hnatyshin et al. (2016) is provided in Tables 4.1.2-4.1.6. The isochron produced for 8S08FW (346.6 ± 3.0 , MSWD = 1.6, VIOs = 0.026) can be found in Chapter 3 and is replicated with additional detail in Chapter 4B. For the Lisheen Derryville Zone sample LK 359 two rock fragments were split from an original core were analyzed (LK 359A and LK 359B). Twelve analyses from LK 359A have a range of Re and Os concentrations of 338 - 6259 ppb and 1285 - 23597 ppt, respectively. Nine analyses for LK 359B contain much lower concentrations of 40 - 506 ppb and 204 - 2724 ppt, for Re and Os, respectively. Using all 21 analyses yields a Model 3 age of 322 ± 11 Ma (MSWD = 206) with a mean initial $^{187}\text{Os}/^{188}\text{Os}$ ratio of 0.9 ± 1.4 and a VIOs of 3.0 (Fig. 4.1.11A). Removing the six samples that underwent an acid leaching procedure results in a similar Model 3 regression of 317 ± 11 Ma (MSWD = 181) with a mean initial $^{187}\text{Os}/^{188}\text{Os}$ ratio of 1.0 ± 1.4 , and a VIOs of 2.5 (Fig. 4.1.11B).

Two rock fragments split from Bog Zone sample LK 451 resulted in 36 Re-Os analyses, including 18 acid leached separates, 3 leachate samples, and one low density separate. Excluding the leachate samples and the low density separate, a relatively restricted distribution of 24-74 ppb and 118 - 352 ppt was measured for Re and Os, respectively. A Model 3 regression of the 32 samples produced a Model 3 age of 348 ± 15 Ma (MSWD = 177) with an initial $^{187}\text{Os}/^{188}\text{Os}$ ratio

of -0.1 ± 1.2 (Fig. 4.1.12A) and a VIOs of 1.3. With the 18 leached samples removed the regression produced an age of 348 ± 17 Ma (MSWD = 118) with a mean initial $^{187}\text{Os}/^{188}\text{Os}$ ratio of -0.3 ± 1.3 and a VIOs of 1.1 (Fig. 4.1.12B). The single low density fraction is depleted in Re (27 ppb) and Os (118 ppt), whereas the leachate samples produced through the acid leaching process contain the lowest values of Re (0.18 - 0.47 ppb) and Os (12 - 38 ppt).

4.1.5.3: SIMS Sulphur Isotope Study

The Lisheen and Baffin Island sample sets used for SIMS pyrite sulphur isotopic analysis comprise several rock fragments and mineral separates that are identical to those used for Re-Os geochronology. Mineral separates were chosen based on their spread in Re-Os ratios and rock fragments were analyzed to reveal microscopic variations in sulphur isotope ratios. Prior to SIMS analysis, SEM images were taken to determine areas of interest and to avoid inclusions during SIMS analysis (Fig. 4.1.13). Areas were typically chosen to help reveal any variability in sulphur isotopes present in the rock; therefore the distributions produced likely have a strong bias towards outlier data and therefore do not represent the true distribution of sulphur isotopic ratios found in the rock as a whole. The summary of the measured $\delta^{34}\text{S}$ values are presented in Figures 4.1.14-4.1.15, with the full analytical data being provided in the Appendix (Tables 4.1.8-4.1.15).

4.1.5.3.1: Lisheen

A total of seven different separates spanning the Main Zone (8S08FW M0.8 and 8S08FW NM1.5), Derryville Zone (LK 359A NM0.8 and LK 359B NM1.6), and Bog Zone (LK 451A M1.6, LK 451A M1.8, and LK 451B M1.8) were chosen for analysis. A single Main Zone rock fragment (8S08FW-1), two Derryville rock fragments (LK 359-1, LK 359-2), and a single Bog Zone rock fragment (LK 451-1) were also analyzed (Fig. 4.1.13).

Rock fragment 8S08FW-1 is dominated by massive pyrite (LG1) containing numerous small sphalerite and galena inclusions ($< 10\mu\text{m}$). Calcite veins can be observed crosscutting the sample (LG7?). Two anomalous areas occur in this sample, a larger (200 μm) anhedral galena crystal (LG5) that appears to have replaced pyrite on the left side of the image, while the right-hand side of the sample appears to be more heavily fractured (LGU). For 8S08FW a total of five transects were analyzed (Figs. 4.1.16A-D). Pyrites associated with, or adjacent to LG1, LG5, LG7, and LGU, were measured with the intention to analyze areas that may contain the highest variability in sulphur isotopic composition. The mineral separate 8S08FW NM1.5 contains

primarily clean LG1 pyrite, whereas the more magnetic separate 8S08FW M0.8 contains a higher abundance of inclusions and fractures. The mean $\delta^{34}\text{S}$ for all data points ($n = 99$) is $-31.68 \pm 12.34 \text{ ‰}$; however 8S08FW-1 shows a clear bimodal distribution of data with peaks at approximately -40.0 ‰ and -20.0 ‰ . The bimodal nature is present in both mineral separates; however it is more pronounced in analyses from the more magnetic separate (8S08FW M0.8).

Rock fragments LK 359-1 and LK 359-2 contain pyrite and marcasite (LG1, LG2, LG3) that is replaced, fractured, and heavily infiltrated by sphalerite and carbonate (LG5, LG6). SIMS analysis focused on producing transects that started from the edge of the marcasite masses through to the core (Figs. 4.1.16E-G). As a result, all visually distinctive sections of LK 359 had their iron sulphide sulphur isotopic composition examined. Marcasite crystals from LK 359A-NM0.8 are dominated by the close association of sphalerite (LG6) that replace and crosscut the pyrite, whereas LK 359B-NM1.6 is dominated by marcasite that is heavily fractured. LK 359 displays a mean $\delta^{34}\text{S}$ of $-37.15 \pm 13.70 \text{ ‰}$, and a mode that lies between -47.5 to -50 ‰ ($n = 101$). LK 359A NM0.8 shows a broader span in $\delta^{34}\text{S}$, with a mean of $-29.52 \pm 16.23 \text{ ‰}$ ($n = 24$), while a more restrictive $\delta^{34}\text{S}$ range is observed for LK 359B NM1.6 ($-42.96 \pm 9.01 \text{ ‰}$, $n = 26$).

For sample LK451-1 measurements of sulphur isotopes associated with LG1, LG2, and LG3 pyrite were originally planned. Unfortunately, the scale of zonation in LG2 is too small ($<10 \text{ }\mu\text{m}$) to analyze individual growth zones and therefore each analysis is an average of the many zones ablated in each analysis (Fig. 4.1.17). Furthermore, LG3 was typically avoided due to the high abundance of inclusions. LK 451 displays a mean $\delta^{34}\text{S}$ of $-32.11 \pm 6.98 \text{ ‰}$, and a mode that lies between -35.0 ‰ to -37.5 ‰ ($n = 158$). Mineral separates show comparable mean values of $-30.78 \pm 6.62 \text{ ‰}$ ($n = 24$), $-34.1.49 \pm 4.69 \text{ ‰}$ ($n = 25$), and $-31.07 \pm 11.18 \text{ ‰}$ ($n = 25$), for LK 451A M1.6, LK 451A M1.8, and LK 451B M1.8, respectively.

4.1.5.3.2: Baffin Island

Four mineral separates (04-N-2 NM 2.0, NOV4-B NM 0.6, NOV4-B NM 1.2, and NOV4-B NM 1.2) and three rock fragments (NOV4-1, NOV4-2, NOV4-3) were analyzed from Nanisivik. Two mineral separates (03-HC-8D M0.8 and 03-HC-8D NM0.8) and a single rock fragment (03-HC-8D) from Hawker Creek was also analyzed (Fig. 4.1.13).

The Nanisivik rock fragments contain numerous fractures filled with dolomite and galena, with smaller inclusions of galena, sphalerite, and carbonate. Eight transects were chosen

for SIMS measurements for the three Nanisivik rock fragments. These transects contain homogeneous pyrite as well as pyrite adjacent to inclusions and/or fractures. All four mineral separates contain relatively homogeneous pyrite with few inclusions, and with the exception of the most magnetic sample (NOV4-B NM 0.6), are relatively free of fractures (see Figure 4.1.31 in the Appendix). The Hawker Creek rock fragment 03-HC-8D contains highly fractured crystals between 100 μm and several mm in size, and contains areas with a high density of small sphalerite and pyrrhotite inclusions (typically $<30 \mu\text{m}$ in diameter; Fig. 4.1.13). These inclusion-rich areas represent approximately half of the sample and do not appear to be controlled by crystal shape, fractures, or crystal boundaries. The non-magnetic separate 03-HC-8D NM2.0 is composed of very clean pyrite crystals with minimal inclusions (Fig. 4.1.9G). In contrast, the magnetic separate 03-HC-8D M0.8 contains an abundance of sphalerite and pyrrhotite inclusions and is highly fractured (Fig. 4.1.9F).

Sulphur isotope analyses for Nanisivik pyrite spots ($n=194$) are summarised in Figure 4.1.18, and the Appendix (Table 4.1.14). The Nanisivik samples display a mean $\delta^{34}\text{S}$ of $27.54 \pm 0.72 \text{‰}$ (Fig. 4.1.15A). Mineral separates show insignificant $\delta^{34}\text{S}$ variation between them, with mean values of $27.25 \pm 0.68 \text{‰}$ ($n = 25$), $27.53 \pm 0.63 \text{‰}$ ($n = 25$), $27.59 \pm 0.66 \text{‰}$ ($n=25$), $27.56 \pm 0.94 \text{‰}$ ($n=25$), for NOV4-B NM1.2, NOV4-B NM0.6, NOV4-C NM1.2, 04-N-2 NM2.0, respectively (Figs. 4.1.15 B-E). The sulphur isotope data measured for the eight transects shown in Figure 4.1.13 are presented in Figure 4.1.18.

Sulphur isotope analysis for Hawker Creek pyrite spots ($n=133$) display a slightly higher $\delta^{34}\text{S}$ of $29.09 \pm 0.72 \text{‰}$ compared to Nanisivik (Fig. 4.1.15F, Appendix Table 4.1.15). Different sulphur isotopic ratio distributions are evident in mineral separate 03-HC-8D M0.8 versus 03-HC-8D NM2.0. Sample 03-HC-8D M0.8 appears to be bimodal, with one $\delta^{34}\text{S}$ peak at between 28.0‰ and 28.5‰ and another between 29.5‰ and 30.0‰ (Fig. 4.1.15G). Sample 03-HC-8D NM2.0 shows an approximately normal distribution, with a mean of $28.98 \pm 0.65 \text{‰}$ that lies between the two peaks of 03-HC-8D M0.8 (Fig. 4.1.15F). Data points located on the four 03-HC-8D transects labelled in Figure 4.1.13 are shown in Figure 4.1.18.

4.1.5.4: Laser Ablation Results

Trace element maps were produced for the rock fragments of 8S08FW-1, LK 359-1, LK451-1, NOV-1, NOV-2, and HC with all locations analyzed shown in Figure 4.1.13. The

focus of this study was to map Re distributions, many other elements were mapped to characterize the sample. The major phases in these rocks include pyrite \pm sphalerite \pm galena \pm calcite \pm dolomite, therefore the distribution of the major phases could be mapped by measuring Fe, Zn, Pb, S, Ca, Mg, and Mn. Common trace elements associated with sulphide mineralization, including Ni, Co, Cu, Ag, Sb, and As, were also mapped to resolve chemical zonation within sulphide phases. Elements that could be associated with the host rock or alteration phases included Si, Al, and K. Molybdenum was selected for analysis due to its known association with Re (e.g. in molybdenite). Maps of Re, Mo, Co, As, Al, and Ca for each sample are shown in Figures 4.1.19-4.1.24 while the full dataset is presented in the Appendix (Figs. 4.1.31-4.1.47). It should be emphasized that comparisons between phases should be done cautiously as the standards were chosen for pyrite analysis. Observed differences in concentrations of less than an order of magnitude, especially at levels close to the detection limit, should also be interpreted with caution.

To improve confidence in the Re concentration produced by LA-ICPMS, we compare these results with that produced through TIMS analysis. 8S08FW being comparatively simple and homogeneous will provide the best comparison as it likely provides the best potential scalability between element maps and TIMS analysis. From Table 4.1.2, bulk sulphide material (8S08FW) has a Re concentration of 3.70 ppb, and the minimum concentration observed for an unleached separate is 2.52 ppb (8S08FWB NM1.2). Map 1 and Map 2 from 8S08FW-1 (Fig. 4.1.19), which have the lowest detection limits, contain mean Re concentrations of 1.3 ppb. For the purposes of this study, this is considered very good agreement between both methods, as there is still the question of scalability, as well as some concern in the precision of LA-ICPMS analyses at such low concentrations. Therefore, we cautiously suggest that the accuracy of LA-ICPMS measurements at low concentrations (< 2 orders of magnitude above detection limits), may be within a factor of 2-3 of the true concentration. For higher concentrations of Re, the accuracy is likely to improve, as the data produced at these concentrations is much more continuous.

4.1.6: Discussion

4.1.6.1: Assessment of Lisheen Re-Os Geochronology

4.1.6.1.1: Isochron Assumption 2: Variability in initial $^{187}\text{Os}/^{188}\text{Os}$

To determine the required VIOs required to explain the dataset, the initial $^{187}\text{Os}/^{188}\text{Os}$ is solved for in Equation (1) for each data point without correlated errors. For consistency, an age of 347 Ma is used for these calculations, and is assumed to be the true age of the ore deposit based on the results of 8S08FW.

For sample 8S08FW, the calculated initial ratios are identical within analytical uncertainty (Fig. 4.1.25D, MSWD = 0.28, probability of fit = 99%), justifying the application of a Model 3 regression (VIOs 0.026). Separates for LK 359 and LK451 show substantial variation (> 1) in initial ratio (Figs. 4.1.25E, F) and similarly high VIOs from the Model 3 regressions at 2.5 and 1.3, respectively. No clear trend is observed between initial $^{187}\text{Os}/^{188}\text{Os}$'s and the magnetic susceptibility of a sample, a proxy for its composition, suggesting variability is not strongly controlled by the relative proportions of major phases. The Model 3 regressions for LK 359 and LK 451 therefore do not likely provide accurate bounds on the possible age for those samples.

4.1.6.1.2: Isochron Assumptions 3 and 4: Alteration and Impurities

8S08FW

8S08FW is dominated by massive LG1 pyrite that is characterized by having few fractures and $\delta^{34}\text{S}$ values of < 35 ‰. Local alteration of LG1 pyrite associated with LG5 galena, LG6, and LGU silicate-filled fractures is identified by anomalous sulphur isotope and/or trace element patterns in the vicinity of these phases. LG5 veins of galena are rare but alter the sulphur isotope signature of LG1 pyrite to higher $\delta^{34}\text{S}$ values (~ -20 ‰) in the direct vicinity of the vein (100 – 200 μm ; Fig. 4.1.16A). Calcite veins of LG7 are much more common and are occasionally associated with trace element enrichment (e.g. Fig. 4.1.19, Map 2), but do not show anomalous $\delta^{34}\text{S}$. Disruption of the Re-systematics appears minor as Re concentrations near LG5 or LG7 veins are unchanged. Pyrite adjacent to LGU fractures (e.g. Figs. 4.1.13, 4.1.19, Map 2) contain enrichment of all trace elements, including Re, and containing the highest values of $\delta^{34}\text{S}$

in 8S08FW, with values approaching +10 ‰ (Figs. 4.1.16B, C). Together this may suggest that LGU is associated with alteration of the primary pyrite.

The spatial data, as well as bulk chemical analysis, reveal that the separates with lower magnetic susceptibility are correlated with lower trace element concentrations (Fig. 4.1.10), a lower density of fractures (Fig. 4.1.4), and contain less carbonates (Table 4.1.1). This implies that they contain a higher proportion of unaltered pyrite than more magnetic samples, and contain fewer impurities (e.g. sphalerite, and calcite). No trend between distribution of data points along the isochron and the amount of impurities and alteration contained in the sample is evident. This suggests that alteration associated with LG5, LG7, and LGU, as well as the calcite and sphalerite impurities have a negligible effect on the robustness of the 8S08FW isochron.

LK 359

LK 359 is a complicated sample containing pre-ore silicates (LG0) and altered LG1-LG3 pyrite and marcasite. The fractured areas within LG1-LG3 iron sulphides show high variability in sulphur isotopes that do not clearly follow textural relationships (Figs. 4.1.16E, F). Unfractured areas containing low $\delta^{34}\text{S}$ (< -40 ‰) signatures are plausible locations where primary sulphide may have been preserved (Figs. 4.1.18F, G). Extrapolating these observations to the LA-ICPMS images (Fig. 4.1.20) it appears that the core regions of the iron sulphide masses often contain fewer fractures, inclusions and trace element concentrations. These regions also appear to have the lowest Re contents (< 10 ppb). During the precipitation of LG6 sphalerite, the associated fluids have altered the iron sulphides resulting in enriched trace element profiles and elevated $\delta^{34}\text{S}$ values (> -40 ‰). Possible molybdenite crystals (Figs. 4.1.26A, B) are imbedded within these zones. Silicates that are assumed to be preore (LG0) contain several hundred ppb Re and probably represent the major reservoir of Re within this rock.

Based on the calculated modal mineralogy (Table 4.1.1) for the prepared separates, it appears that the majority of silicate material has been removed for samples analyzed for Re-Os. However, the high concentration of Re associated with these phases means that they still can significantly influence the measured Re-Os isotopic ratios. Furthermore, since these silicates are not related to ore stage mineralization the mixing lines they create negatively impact the usability of the Re-Os results. The elevated Re content of LK 359A vs. LK359B is likely due to the

mineralogy present in each sample. For LK 359A, the much higher Re contents are probably a consequence of this sample containing more LG0 silicates and LG6 sphalerite. This is consistent with the higher and more variable $\delta^{34}\text{S}$ measured for LK 359A NM1.6 ($-29.52 \pm 16.23 \text{ ‰}$) compared to LK 359B NM1.6 ($-42.96 \pm 9.02 \text{ ‰}$). No mineral separate contains pure unaltered pyrite; all contain appreciable sphalerite and a minor amount of silicates.

LK 451

LK451 has a paragenetic sequence that progresses from LG1-LG4 with progressive replacement between each generation (Fig. 4.1.6B). LG1 pyrite has comparable $\delta^{34}\text{S}$ values to 8S08FW and LK 359 with values being $< -35 \text{ ‰}$. The LG2 pyrite replacing cores of LG1 pyrite have higher values between -10 ‰ to -30 ‰ . LG3 sphalerite replaces LG2 pyrite through preferential replacement of individual framboidal crystals. The associated pyrite was rarely measured for $\delta^{34}\text{S}$ but appears to be comparable to LG2 ($\sim -20 \text{ ‰}$). Outside the normal paragenesis of LG1-LG4 are localized areas of silicate-rich material (LGU; Fig 4.1.21, LK 451 Map 3). These areas can be associated with higher levels of Re and may potentially host inclusions of molybdenite (Figs. 4.1.26 C, D).

Based on the TIMS analysis, it appears that all mineral separates, which contain $\sim 50 \text{ ppb}$ Re, must be a combination of low Re ($< 10 \text{ ppb}$) sulphides (LG1-LG4) and the enriched LGU material ($> 100 \text{ ppb}$). Some differences are seen between magnetic separates, sphalerite for example is enriched in more magnetic separates whereas pyrite is enriched in non-magnetic separates. The observed scatter seen in the LK 451 dataset cannot be clearly attributed to specific phases as the variably leached LK451B M1.6 does not demonstrate correlations between scatter and mineralogy. However, the fact that the sample LK 451 M1.6 Low Density plots significantly below the isochron suggests that material associated with carbonates and/or silicates will significantly influence the isochron. This is a notable observation as silicates and carbonates contribute 10-25% to the total volume of these samples. Ultimately, the data suggests that the robustness of the LK 451 is dictated by the influence of LGU areas. If LGU is associated with ore mineralization then any imparted scatter will still likely keep the age produced by the isochron at roughly the true age of mineralization. If unrelated to mineralization the produced scatter will greatly obscure the age of ore mineralization due to the mixing lines produced.

4.1.6.1.3: Recommended Interpretation of Lisheen Re-Os Geochronology

The Main Zone sample 8S08FW gives the most precise estimate for the age of Lisheen (Model 3, 346.6 ± 3.0 Ma, initial $^{187}\text{Os}/^{188}\text{Os} = 0.253 \pm 0.045$, $\text{VIOs} = 0.026$). Closer inspection of the original dataset from Chapter 3 identifies several important aspects that made 8S08FW a successful candidate for pyrite Re-Os geochronology. The homogeneity observed in the Re maps produced for 8S08FW, coupled with the observation that alteration is localized and has not significantly modified the Re concentration (i.e. by orders of magnitude) gives us confidence that 8S08FW retains age information from ore mineralization. Additionally, all isochron assumptions have been, in our opinion, passed to a reasonable degree, with the majority, if not all, observed scatter being related to the analytical errors. We conclude that the interpretations from Chapter 3 are upheld for Lisheen based on our analysis of 8S08FW. Derryville and Bog Zone samples should presumably produce similar ages (~ 347 Ma) to that of the Main Zone sample 8S08FW, assuming a general contemporaneity of ore forming mechanisms at Lisheen. Similar initial $^{187}\text{Os}/^{188}\text{Os}$ may be expected, but are not required, as current models for the Irish ore field require a fluid mixing model for ore formation (Wilkinson 2010; Wilkinson et al., 2014) which may allow for some variability in isotopic composition through space and time.

The calculated Model 3 age for LK 359 (322 ± 11 Ma) is statistically much younger than 8S08FW (346.6 ± 3.0 Ma) but there are many issues with the dataset which makes the LK 359 age suspect. Clear differences in Re-Os systematics (Table 4.1.3, Fig. 4.1.25E) between LK 359A and LK 359B are observed, with higher scatter (LK 359A) being correlated with a higher proportion of LG6 (sphalerite in Table 4.1.1), and likely by extension LG0, impurities. In particular, it appears that incorporation of LG6 and LG0 has made the calculated initial Os ratio impossibly low (assuming a 347 Ma age) for the majority of samples, and excessively variable (violation of assumption 2). By focusing on the samples with the least impurities (LK 359B NM1.6, samples leached in 10N HCl) may result in a more accurate age estimate. Assuming an initial $^{187}\text{Os}/^{188}\text{Os}$ of 0.25 the mean model age for these samples is 340 ± 8 Ma, which is in much better agreement with the expected age of ~ 347 Ma. Even within these separates, there are still impurities and altered pyrite present so it is suggested that this estimate may be a lower bound on the age. Together with the age of the host rock (~ 353 Ma, Waters, 2011) the best estimate for the age of the LK 359 is 332 – 353 Ma. However, this estimate requires a lot of assumptions and is considered nowhere nearly as robust as the age determined for 8S08FW. It is important to

emphasize that the Model 3 isochron created from the dataset is considered useless, and only through vast amount of supplementary data were we able to determine a more realistic estimate.

LK 451 produced a Model 3 age of 348 ± 15 Ma, nominally matching the age of 8S08FW (346.6 ± 3.0 Ma). However, this age and particularly the error bounds are probably invalidated because of the high VIOs required (1.3). The closeness in age between these two rocks may suggest that geochronologic information has been preserved in LK 451. Much like LK 359, it appears that LGU has significant influence on the Re-Os systematics as the LG1-LG4 sulphides have very low Re (<10 ppb) whereas LGU may have > 100 ppb and a mixture of these groups is required to explain the TIMS results of ~50 ppb. Separates that underwent extreme leaching (10N HCl) while in a finely powdered state (LK 451A M1.8 10N Fine Hot, LK 451B M1.8 10N Fine) are clear outliers in the dataset. It is speculated that under these conditions preferential leaching of Re is occurring and therefore these data points should be discarded. Other outlier points (LK 451B M1.6 0.2N rpt, LK 451B M1.6 1N) have been repeated and produced much different isotopic ratios suggesting that micro-scale heterogeneities might be controlling scatter in these points. Finally, LK 451 M1.0 is an outlier but beyond its high magnetic susceptibility it is unclear what is controlling its position on the isochron diagram. Violations of isochron assumption (2) does not account for the observed scatter and therefore the fundamental cause of scatter in LK 451 is likely due to limited open system behaviour. The open system behaviour is considered limited as age information appears to be preserved since the mean age for LK 451 closely matches that of 8S08FW, however such a conclusion requires a preconceived notion of the age of the deposit. The cause of open system behaviour is unclear but alteration by LGU fluids is the simplest explanation. Under the assumption that the initial $^{187}\text{Os}/^{188}\text{Os}$ is 0.25 and we can ignore the outlier data points it is suggested that LK 451 is reported to be supportive of an age > 336 Ma. The Model 3 age produced by Isoplot does agree with this recommendation, but requires an unrealistic VIOs and therefore the age of 348 ± 15 Ma should not be reported as necessarily accurate

Although not as robust as 8S08FW both LK 359 and LK 451 Re-Os ages are consistent with the age reported from 8S08FW. However, this conclusion requires some assumptions about the dataset and needed the full suite of analyses provided by this study to entirely support such a conclusion. The timing of open system behaviour and/or alteration associated with LGU and LG6 phases cannot be determined precisely, as they produce mixing lines with LG1 pyrite.

However, the youngest ages implied at by the model ages are ~ 310 Ma, a time which Ireland was beginning to experience the heating and tectonic activity associated with the Variscan orogeny (Quinn et al., 2005). During this time the Irish Midlands underwent extensive reverse faulting and folding (Woodcock and Strachan, 2000; Graham, 2001), while older normal faults were reactivated (Chadwick et al., 1993). Reverse faulting in the Lisheen area resulted in the deformation of the Lisheen ore (Fusciardi et al., 2003; Carboni et al., 2003). Vitrinite reflectance values and conodont alteration indexes suggest that much of the orefield underwent extensive heating post-deposition during the Variscan orogeny (Clayton et al., 1980; Jones, 1992). This heating may be responsible for the remagnetization of magnetic grains found at Lisheen and other Irish deposits. Therefore, it could be speculated that fluids may have migrated into the Lisheen deposit during the Variscan orogeny in response to heating and/or tectonic activity, leading to the precipitation of LGU phases and the alteration seen in LK 359 and LK 451.

4.1.6.2: Assessment of Nanisivik Re-Os Geochronology

4.1.6.2.1: Isochron Assumption 2: Initial $^{187}\text{Os}/^{188}\text{Os}$ Variation

For the Nanisivik dataset a large variation in initial $^{187}\text{Os}/^{188}\text{Os}$ is observed assuming an age of 1100Ma, and results in a isochron requiring an unreasonable VIOs of 2.0. The incorporation of different paragenetic stages of pyrite and impurities are not controlling the scatter in this dataset as there is no correlation between scatter and magnetic susceptibility (Table 4.1.5). Too fully scrutinize this dataset additional images of NOV4 mineral separates would need to be captured to determine the exact mineralogy of each separate. However, this was determined not to be worth pursuing as the range in initial $^{187}\text{Os}/^{188}\text{Os}$ required is deemed too high to be associated with violation of assumption (2).

4.6.2.2: Isochron Assumption 3 and 4: Alteration and Impurities

In both NOV4-1 and NOV-2 when pyrite bounds later stage mineralization (e.g. galena and dolomite) enrichment in some trace elements (e.g. As) is observed. Rhenium and Mo do not appear to be greatly influenced, although this may be an artefact of the limit of detection. It is not clear whether the observed trace element pattern is natural zonation in the pyrite or is associated with alteration of primary pyrite which shows low trace element concentrations. Fractured areas are associated with an increase in concentration of many different elements in NOV4-2. Of

particular concern is the enrichment of Re from < 10 ppb in pyrite cores to up to > 100 ppb in the vicinity of fractures (Fig. 4.1.23A). The host of Re in these areas is unclear but may include both pyrite and molybdenite (Figs. 4.1.26E, F). The fractures themselves seem to postdate the pyrite, but do not crosscut dolomite, likely bracketing the fracturing between the precipitation of these two phases. Highly fractured areas, such as the central part of NOV4-1, the right-hand side of transect 1 in sample NOV4-2, and transect 2 in sample NOV4-2, contain a notable variation in $\delta^{34}\text{S}$ values (from 26.5 ‰ to 30 ‰, Fig. 4.1.18), compared to areas that are not fractured. These fractured areas are considered to be high risk for possible disturbances in the Re-Os system. Minerals separates with higher magnetic susceptibility have higher abundances of trace elements (e.g. Re, Table 4.1.5) and therefore may preferentially source fractured areas.

4.1.6.2.3: Recommended Interpretation of Nanisivik Re-Os Geochronology

The paragenetic location of the fractures appears to be within ore stage mineralization (Fig. 4.1.8) which may have limited the magnitude of scatter produced through putative open system behaviour. The fact that the number of fractures contained in a mineral separate does not have a clear impact on the model age or initial $^{187}\text{Os}/^{188}\text{Os}$ (Table 4.1.5) may indicate that pyrite fracturing had only a minor impact of the Re-Os systematics of the ore. Open system behaviour and/or the influence of high Re phases coupled with possible violations of assumption (2) is the only reasonable explanation for the isochron scatter based on our dataset. The Re-Os systematics of sample NOV4, even with minor disturbances, still require a >1 Ga age even if the precision from the isochron and model ages is poor (1122 ± 52 Ma and 1093 ± 24 Ma respectively; Hnatyshin et al., 2016), and therefore the general interpretations of Hnatyshin et al (2016) are still valid.

4.1.6.2.4: Reassessment of Hawker Creek Re-Os Geochronology

The Hawker Creek dataset did not produce a well-defined regression (Hnatyshin et al., 2016). The correlation between chemical and physical properties (e.g., Re concentration, magnetic susceptibility) and calculated Model Ages suggests mineral separates are sampling, to varying degrees, two end members of combined Re-Os and magnetic characteristic. Examples of the magnetic and non-magnetic end-members in the sample set are 03-HC-8D M0.8 and 03-HC-8D NM 2.0, respectively. Back-scattered electron images of these two samples show clear differences (Figs. 4.1.9F, G). The non-magnetic sample shows unfractured, pure pyrite, whereas

the more magnetic sample contains highly fractured crystals with small inclusions of sphalerite and pyrrhotite. Direct evidence for chemical differences between these two end-members exists in the LA-ICPMS compositional maps and sulphur isotope data. The distribution of $\delta^{34}\text{S}$ values shows that the magnetic sample has a bimodal distribution of $\delta^{34}\text{S}$ peaks at 28.0 ‰ - 28.5‰ and 29.5‰ - 30.0‰, whereas the non-magnetic sample has a normal distribution with a peak at $\delta^{34}\text{S} = 29$ ‰ (Figs. 4.1.15G, H). For rock fragment 03-HC-8D (Fig. 4.1.24) highly fractured material contains the bulk of Re (> 100 ppb) while the unaltered pyrite cores have much lower concentrations (< 1 ppb). The fractured areas also contain general trace element enrichment. The clean pyrite cores represent primary mineralization at ~ 1 Ga by correlating the LA-ICPMS mapping to that of the Re-Os model ages. The boundaries of these pyrite crystals have been highly fractured and are enveloped in trace element-enriched material and result in model ages that bottom out at ~ 400 Ma. These 400 Ma Re-Os model ages and an Ar-Ar age of 461 Ma from adularia alteration at Nanisivik (Sherlock et al. 2004) suggests that the Borden Basin experienced fluid flow in the Paleozoic. There is sparse evidence of major fluid flow occurring this time, however it has been speculated that deposition of evaporites to the northwest may have initiated deep-crustal brine convection during this time (Turner, 2011; Hnatyshin et al., 2016). Dense brines from the evaporites may have migrated to the Nanisivik deposit, resulting in alteration, and ultimately the Paleozoic ages reported in Sherlock et al. (2004) and this study.

4.1.6.3: Rhenium Systematics within Sulphide Ore

4.1.6.3.1: Observed Distributions and Potential Hosts

Rhenium concentrations are observed to range from low ppb levels to exceeding ppm levels in many of the samples (LK 359, LK 451, NOV-2), a range exceeding that suggested through TIMS analysis. Such an observation is unsurprising due to the bulk, nature of samples used in TIMS analysis. Nevertheless, this striking range of concentrations underscores the potential complexity of Re-Os systematics as a whole, but for simplicity we have grouped Re distributions into four general categories.

Category 0 is defined as the Re signal produced by phases that are not directly associated with paragenesis of the ore, such as any material from host-rock (e.g. LG0). For host-rocks the elemental signature will be dependent on the lithology and may be highly altered by mineralization fluids, but should be correlated with lithophile elements such as Si, Al, K, and Ca.

LK 359 is the only sample that appears to have residual silicates, potentially associated with pre-sulphide dolomitization (D1, D2) and brecciation. These areas appear to be highly enriched in trace elements in LK 359 and may have been conduits for later fluids that cause the alteration in surrounding sulphides.

Category 1 is defined as Re that appears to be contained within unaltered crystals of ore-stage sulphide minerals (excluding molybdenite), typically characterized by low Re concentrations (<10 ppb). These regions exist in all samples, even LK 359 and LK 451, which through TIMS analysis produced measurements almost exclusively > 30 ppb (Figs. 4.1.19-4.1.24). However, in these samples and the Hawker Creek samples unaltered pyrite is encased in altered material.

Category 2 is defined by small localized areas (< 100 μm^2) containing anomalously high levels of Re (> 1 ppm) correlated with very high concentrations of Mo (> 1000 ppm). Category 2 is easily identified in maps due to these elevated levels of Re and Mo clearly standing out over the background concentrations (Fig. 4.1.26). Micron scale molybdenite crystals are the mostly likely explanation for the observations and although molybdenite is not a commonly reported mineral in sediment-hosted Zn-Pb ores, few other minerals are known substitute such high levels of Mo and Re within their structure.

Category 3 is defined as Re associated with the alteration, fracturing, and recrystallization of primary phases. Category 3 in this study is often identified by anomalous zoning of Re (or other elements) typically at levels greater than Category 1 material. Category 3 material in this study are observed to contain several hundred ppb Re, and are correlated with elements associated with silicates (e.g. K, Si, Al). Localized enrichment of other trace elements (e.g. Ni, Co, Mo, As) are also commonly observed. This is demonstrated particularly well LK 359 where LG2 marcasite in close proximity of LG6 have highly enriched trace element values (Fig. 4.1.20). However, it is important to note that not all fractured areas show clear evidence of Re disturbance (e.g. Fig. 4.1.22, NOV-1).

Rhenium concentrations for other phases (e.g. sphalerite, calcite) are likely not accurate due to the standard being chosen for analysis of pyrite. However, broad scale observations are likely to be of use and are probably best used when comparing concentrations at the log scale. With that in mind when calcite was analyzed (e.g. Fig. 4.1.23, NOV-2) Re concentrations were

close to or below detection limits. Sphalerite analyses, in particular for LK 359, show that Re concentrations are comparable to that of pyrite.

4.1.6.3.2: Spatial Correlations

Through visual inspection (Figs. 4.1.19-4.1.24) spatial association between Re and Mo and to a lesser degree other elements (e.g. K, Co, As) is observed. This observation is supported through more detailed spatial analysis of Map 1 from LK 359 (Fig. 4.1.20), a sample chosen for the continuous nature of its dataset. Correlograms were produced in both pyrite and sphalerite-rich areas to determine how well different elements predict the concentration of Re up to a range of 200 μm (Fig. 4.1.27A). A Re vs. Re analysis was carried out to ensure that Re is a good predictor of itself and therefore is a useful baseline to compare other elements to. For simpler visualization the Re vs. Re curve was used to normalize the data (Fig. 4.1.27B). Molybdenum shows the strongest correlation with Re for both pyrite and sphalerite whereas all other elements have modest (e.g. Co) or insignificant (e.g. As) correlations (Fig. 4.1.27A). Curiously, K is a reasonable predictor of Re distribution in sphalerite and likely reflects the silicate-rich phases (LG0) embedded within sphalerite. A series of scatter plots shows the relationship Re has with other elements (Fig. 4.1.28; Mo, Sb, As, Co, and K) for each pixel in the LA-ICPMS maps. Molybdenum shows the tightest correlation, corroborating observations made by visual inspection and spatial analysis. At high concentrations of Sb, there also appears to be a positive relationship with Re, although much weaker than Mo. Other elements (e.g. Co, As, K) that in Figures 4.1.19-4.1.24 suggest positive correlations at local scales do not have a well-correlated nature at a bulk scale (Fig. 4.1.28A). This is emphasized in Figure 4.1.28B where the data is normalized by taking the Re concentration and dividing out "Element X's" concentrations. The Mo/Re values produced are relatively restricted ($\sim 100 - 1000$) and are almost independent of Re concentration, but all other elements show a much wider variability and higher dependence on the Re concentration. A unique characteristic of the Mo-Re ratio is that it is insensitive to ore locality, as all samples from Lisheen and Nanisivik show overlapping patterns even though each sample is composed of a different mineral assemblage with diverse bulk chemistry (Fig. 4.1.10). This behaviour implies that Re is substituting exclusively into Mo-rich minerals (e.g. molybdenite) as was speculated for Re Category 2 and/or is incorporated into pyrite in a similar fashion to Mo (Category 1?), which is thought in some cases to adsorb on the pyrite surfaces as

Fe-Mo-S cuboidal clusters (Vorliceck et al., 2004; Helz et al., 2014), as opposed to following other lattice bound elements such as Ni, Co, or As.

The apparent association between silicates and Re for Categories 0/3 is enigmatic due to the low resolution of the LA-ICPMS analysis. It is speculated that Re is still hosted in sulphides since there is scant evidence to suggest otherwise (e.g. peculiar correlations). However, it cannot be totally discounted that Re may be hosted in a silicate phase (e.g. clay minerals) until higher resolution data is able to be produced. The only sample that appears to show unusual behaviour of Re is Hawker Creek. Examination of the Hawker Creek data points with enriched Re contents (>10 ppb), which for context is binned into Re Category 3, reveals a Mo/Re ratio that is much lower than all other locations (Fig. 4.1.28B). The reason for this is unclear but it may be a consequence of Re being hosted in a different phase or being incorporated into minerals in a different fashion than the other samples. Alternatively, the trend followed by the Lisheen, Nanisivik, and low Re Hawker Creek samples may represent dissimilar fluid compositions (i.e. ore fluids) than that of phases associated with high Re Hawker Creek samples (i.e. non-ore fluids).

4.1.6.3.3: Alternatives to Re Mapping

Although mapping Re directly is preferred prior to Re-Os geochronology, it requires specialized instrumentation and standards to detect the low concentration (ppb level) of Re found in sulphides, which is not widely available. Even with this capability, current technology limits the resolution available for mapping. For example, this study used spot sizes between 15 μm to 100 μm , which even at the largest spot sizes limits detection to ~0.5 - 1.0 ppb Re and the collected data only becomes pseudo-continuous at roughly one order of magnitude greater than this. The discrete nature of Re-measurements near the detection limit undoubtedly hides some of the complexity that may be present. Based on the strong Re-Mo correlation documented here, measurement of Mo as a Re proxy may identify high risk areas or samples (e.g. alteration associated with silicates), and may be sufficient to evaluate the potential Re distribution within a rock.

4.1.6.3.4: Sulphur Isotope Distribution

Variability in the mineralization fluids can result in variability in sulphur isotope signatures, which can subsequently be used to fingerprint the sources of these fluids and their

influence on sulphide mineralization. Figures 4.1.14-4.1.18 show a non-random distribution of sulphur isotopic compositions in these rocks and are clearly correlated with specific textures (Fig. 4.1.14), but not necessarily with the composition of the pyrite (Fig. 4.1.29). Due to the scattered nature of data seen in Figure 4.1.29, sulphur isotope ratios cannot by itself be used to predict the chemistry of pyrite. Furthermore, the absolute range in sulphur isotopes is not useful in determining if a sample will produce a highly precise isochron. For example 8S08FW's variation in $\delta^{34}\text{S}$ exceeds 40 ‰ but produced a precise isochron (MSWD = 1.6), whereas Nanisivik produced an isochron with far greater scatter (MSWD = 97) with only ~ 5 ‰ variation. The usefulness of analyzing sulphur isotopes therefore lies in its ability to test for possible sources of mineralizing fluids and identifying paragenetically distinct areas within a sample that can be scrutinized using other methods (e.g. LA-ICPMS).

4.1.6.3.5: General Implications for Re-Os Geochronology

Category 1 material is of primary interest for pyrite Re-Os geochronology, as it is defined as the relatively unaltered cores of pyrite. This is substantiated by the successful dating of 8S08FW where the mineral separates used to produce the 8S08FW isochron appear to be almost pure Category 1 pyrite. Although far more complicated, the Hawker Creek samples agree with this proposal, with Category 1 material yielding geologically useful data at ca. 1.1 Ga, and Category 3 material produced data that postdates ore stage mineralization. In studied samples Category 1 material typically contains low concentrations of Re and therefore was at high risk of being co-analyzed by any high Re phases that exist within the rock.

Category 2 is composed of micron scale molybdenite inclusions that are of a later paragenetic stage than Category 1 for the samples analyzed in this study (Fig. 4.1.26). Molybdenite crystals are expected to have a negligible common Os signature and therefore can result in very high $^{187}\text{Re}/^{188}\text{Os}$ and $^{187}\text{Os}/^{188}\text{Os}$ of any affected pyrite mineral separate. The unexpected observation of molybdenite existing in the low temperature (<300°C) environments of sediment-hosted Zn-Pb deposits, suggests molybdenite contamination may be a wider issue associated with pyrite Re-Os geochronology. In the literature there are many examples of pyrite, chalcopyrite, and arsenopyrite being extremely radiogenic in nature (e.g. Barra et al., 2003; Morelli et al., 2007; Zhang et al., 2005; Selby et al., 2009; Lawley et al., 2013). It is plausible

that in many of these publications that molybdenite inclusions, not pyrite, is being dated, which consequently may compromise their interpretation of their calculated ages.

Category 3 materials are inherently problematic by its association with fracturing, recrystallization, and alteration of primary crystals. Whenever this is observed local open system behaviour may have been present, resulting in the isotopic composition of the precursor sulphide being modified in an unpredictable fashion. Identification of these Category 3 areas should at least be carried out at the petrographic level, but can often be seen chemically through zonation or peculiar chemical/isotopic signatures.

Based on these results it is crucial to properly screen for suitable samples beforehand and scrutinizing the separates used to produce Re-Os isotopic data. The most illustrative example that emphasizes this is the dataset from Hawker Creek. The Hawker Creek sample is clearly divided between Category 1 pyrite cores and secondary Category 3 phases found in fractures and interstitial spaces between pyrite crystals. Through hand sample and petrographic analysis these observations could not be made, therefore necessitating LA-ICPMS to identify these two categories. In fact, it would be expected that the petrographically simple nature of this ore would provide high quality material for Re-Os geochronology. Clearly this is not the case due to the 2-4 orders of magnitude difference in concentrations present between these two groups, so even a slight contamination of Category 3 material will create mixing trends that result in erroneous ages. Such erroneous ages can be seen in many of the separates produced from Hawker Creek (Table 4.1.5) and could easily be misinterpreted without the availability of LA-ICPMS Re spatial data

4.1.7: Conclusions

The LA-ICMPS compositional maps provided in this study demonstrate that the Re distribution with Zn-Pb ores is complex. Pyrite that has a relatively homogeneous Re profile with negligible alteration (i.e. Category 1) is shown to produce high-quality Re-Os isochrons, such as the 8S08FW sample from the main zone at Lisheen. For the other Lisheen samples and the Nanisivik samples, Category 1 material was often associated with altered material (Category 3) with trace element enrichment, as well as with probable molybdenite inclusions (Category 2). This complexity resulted in great difficulty in interpreting the Re-Os data from the Derryville (LK 359) and Bog Zone's (LK 451). These samples were determined to consistent with that of

the Main Zone (8S08FW) but did not provide a precise estimate of the age of Lisheen. For the Hawker Creek sample LA-ICPMS compositional maps resolved the meaning of the highly variable Re-Os model ages as a mixture of two discrete events, which were not discernible through petrographic observation.

These case studies emphasizes the importance of providing petrographic and chemical context for samples being dated through Re-Os geochronology. The clear link between Mo and Re with all samples investigated allows us to recommend providing Mo (or Re) compositional maps whenever sulphides are dated using Re-Os geochronology. When datasets are created and produced Model 3 ages with unrealistic variations in initial ratio's (e.g. > 1) the samples should be carefully scrutinized petrographically and chemically, with age recommendations being expressed in more generic terms (e.g. LK 359 and LK 451 in this study). To help categorize the quality of a publish dataset it may be helpful to assign a quality factor based on how much supplemental information is provided and the perceived accuracy of the data (Fig. 4.1.30).

4.1.8: References

Acken, D., Su, W., Gao, J., & Creaser, R. A. (2014). Preservation of Re - Os isotope signatures in pyrite throughout low - T, high - P eclogite facies metamorphism. *Terra Nova*, 26(5), 402-407.

Arne, D. C., Curtis, L. W., & Kissin, S. A. (1991). Internal zonation in a carbonate-hosted Zn-Pb-Ag deposit, Nanisivik, Baffin Island, Canada. *Economic Geology*, 86(4), 699-717.

Barra, F., Ruiz, J., Mathur, R., & Titley, S. (2003). A Re-Os study of sulfide minerals from the Bagdad porphyry Cu-Mo deposit, northern Arizona, USA. *Mineralium Deposita*, 38(5), 585-596.

Carboni, V., Walsh, J. J., Stewart, D. R. A., Güven, J. F., & Eliopoulos, D. G. (2003). Timing and geometry of normal faults and associated structures at the Lisheen Zn/Pb deposit, Ireland—investigating their role in the transport and the trapping of metals. In *Mineral Exploration and Sustainable Development: Proceedings of the 7th Biennial SGA Meeting* (pp. 665-668).

Cathles, L. M., & Smith, A. T. (1983). Thermal constraints on the formation of Mississippi Valley-type lead-zinc deposits and their implications for episodic basin dewatering and deposit genesis. *Economic Geology*, 78(5), 983-1002.

Chadwick, R. A., Evans, D. J., & Holliday, D. W. (1993). The Maryport fault: the post-Caledonian tectonic history of southern Britain in microcosm. *Journal of the Geological Society*, 150(2), 247-250.

Christensen, J. N., Halliday, A. N., Kesler, S. E., & Sangster, D. F. (1993). Further evaluation of the Rb-Sr dating of sphalerite: the Nanisivik Precambrian MVT deposit, Baffin Island, Canada. In *Abstracts with Programs-Geological Society of America* (Vol. 25, p. 471).

Clayton, G., Haughey, N., Sevastopulo, G. D., & Burnett, R. (1989). *Thermal maturation levels in the Devonian and Carboniferous rocks of Ireland*. Geological Survey of Ireland.

Creaser, R. A., Wilkinson, J. J., & Hnatyshin, D. (2009). Re-Os dating of sulfide mineralization (pyrite) from the Lisheen Pb-Zn deposit, Ireland. In *2009 Portland GSA Annual Meeting*.

Danyushevsky, L. V., Robinson, P., Gilbert, S.E. (2011). Routine quantitative multi-element analysis of sulphide minerals by laser ablation ICP-MS: Standard development and consideration of matrix effects. *Geochemistry Exploration Environment Analysis*, 11(1), 51-60.

Ding, T., Valkiers, S., Kipphardt, H., De Bièvre, P., Taylor, P. D. P., Gonfiantini, R., & Krouse, R. (2001). Calibrated sulfur isotope abundance ratios of three IAEA sulfur isotope reference materials and V-CDT with a reassessment of the atomic weight of sulfur. *Geochimica et Cosmochimica Acta*, 65(15), 2433-2437.

Fusciardi, L. P., Guven, J. F., Stewart, D. R. A., Carboni, V., & Walshe, J. J. (2003). The geology and genesis of the Lisheen Zn-Pb deposit, Co. Tipperary, Ireland. *Europe's major base metal deposits: Dublin, Irish Association for Economic Geology*, 455-481.

Garven, G., Ge, S., Person, M. A., & Sverjensky, D. A. (1993). Genesis of stratabound ore deposits in the Midcontinent basins of North America; 1, The role of regional groundwater flow. *American Journal of Science*, 293(6), 497-568.

Ghazban, F., Schwarcz, H. P., & Ford, D. C. (1990). Carbon and sulfur isotope evidence for in situ reduction of sulfate, Nanisivik lead-zinc deposits, Northwest Territories, Baffin Island, Canada. *Economic Geology*, 85(2), 360-375.

Graham, J.R., 2001, Variscan structures, in Holland, C.H., ed., *The geology of Ireland: Edinburgh, Dunedin Academic Press*, p. 312–330.

Helz, G. R., Erickson, B. E., & Vorlicek, T. P. (2014). Stabilities of thiomolybdate complexes of iron; implications for retention of essential trace elements (Fe, Cu, Mo) in sulfidic waters. *Metallomics*, 6(6), 1131-1140.

Hitzman, M.W., Redmond, P.B., and Beaty, D.W. (2002), The carbonate hosted Lisheen Zn-Pb-Ag deposit, County Tipperary, Ireland: *Economic Geology*, 97, 1627–1655.

Hnatyshin, D., Creaser, R. A., Wilkinson, J. J., & Gleeson, S. A. (2015). Re-Os dating of pyrite confirms an early diagenetic onset and extended duration of mineralization in the Irish Zn-Pb ore field. *Geology*, 43(2), 143-146.

Hnatyshin, D., Kontak, D. J., Turner, E. C., Creaser, R. A., Morden, R., & Stern, R. A. (2016). Geochronologic (Re Os) and fluid-chemical constraints on the formation of the Mesoproterozoic-hosted Nanisivik Zn Pb deposit, Nunavut, Canada: Evidence for early diagenetic, low-temperature conditions of formation. *Ore Geology Reviews*, 79, 189-217.

Jackson, G. D., & Iannelli, T. R. (1981). Rift-related cyclic sedimentation in the Neohelikian Borden Basin, northern Baffin Island. *Geological Survey of Canada, Paper*, 81-10.

Jones, G. L. (1992). Irish Carboniferous conodonts record maturation levels and the influence of tectonism, igneous activity and mineralization. *Terra nova*, 4(2), 238-244.

Kampschulte, A., & Strauss, H. (2004). The sulfur isotopic evolution of Phanerozoic seawater based on the analysis of structurally substituted sulfate in carbonates. *Chemical Geology*, 204(3-4), 255-286.

Kozdon, R., Kita, N. T., Huberty, J. M., Fournelle, J. H., Johnson, C. A., & Valley, J. W. (2010). In situ sulfur isotope analysis of sulfide minerals by SIMS: Precision and accuracy, with application to thermometry of ~ 3.5 Ga Pilbara cherts. *Chemical Geology*, 275(3), 243-253.

Large, R. R., Danyushevsky, L., Hollit, C., Maslennikov, V., Meffre, S., Gilbert, S., ... & Singh, B. (2009). Gold and trace element zonation in pyrite using a laser imaging technique: Implications for the timing of gold in orogenic and Carlin-style sediment-hosted deposits. *Economic Geology*, 104(5), 635-668.

Lawley, C., Selby, D., & Imber, J. (2013). Re-Os molybdenite, pyrite, and chalcopyrite geochronology, Lupa goldfield, southwestern Tanzania: tracing metallogenic time scales at midcrustal shear zones hosting orogenic Au deposits. *Economic Geology*, 108(7), 1591-1613.

Lewchuk, M. T., & Symons, D. T. A. (1995). Age and duration of Mississippi Valley-type ore-mineralizing events. *Geology*, 23(3), 233-236.

Ludwig, K. R. (2003). Isoplot 3.00: A geochronological toolkit for Microsoft Excel, 71 pp. *Berkeley Geochronol. Center Spec. Publ.*, 4.1.

Morelli, R. M., Creaser, R. A., Selby, D., Kelley, K. D., Leach, D. L., & King, A. R. (2004). Re-Os sulfide geochronology of the red dog sediment-hosted Zn-Pb-Ag deposit, Brooks Range, Alaska. *Economic Geology*, 99(7), 1569-1576.

Morelli, R., Creaser, R. A., Seltmann, R., Stuart, F. M., Selby, D., & Graupner, T. (2007). Age and source constraints for the giant Muruntau gold deposit, Uzbekistan, from coupled Re-Os-He isotopes in arsenopyrite. *Geology*, 35(9), 795-798.

Morelli, R. M., Bell, C. C., Creaser, R. A., & Simonetti, A. (2010). Constraints on the genesis of gold mineralization at the Homestake Gold Deposit, Black Hills, South Dakota from rhenium–osmium sulfide geochronology. *Mineralium Deposita*, 45(5), 461-480.

Olson, R. A. (1984). Genesis of paleokarst and strata-bound zinc-lead sulfide deposits in a Proterozoic dolostone, northern Baffin Island, Canada. *Economic Geology*, 79(5), 1056-1103.

Patterson, K. M., & Powis, K. (2002). Structural and stratigraphic controls on Zn-Pb-Ag mineralization at the Nanisivik Mississippi Valley-type deposit, northern Baffin Island, Nunavut. Natural Resources Canada, Geological Survey of Canada.

Patterson, K. M., Powis, K., Sutherland, R. A., & Turner, E. C. (2003). Stratigraphy and structural geology of the Nanisivik area, northern Baffin Island: Geological Survey of Canada Open File 1552.

Quinn, D., Meere, P. A., & Wartho, J. A. (2005). A chronology of foreland deformation: Ultra-violet laser $^{40}\text{Ar}/^{39}\text{Ar}$ dating of syn/late-orogenic intrusions from the Variscides of southwest Ireland. *Journal of Structural Geology*, 27(8), 1413-1425.

Rowan, E. L., & Goldhaber, M. B. (1995). Duration of mineralization and fluid-flow history of the Upper Mississippi Valley zinc-lead district. *Geology*, 23(7), 609-612.

Selby, D., & Creaser, R. A. (2003). Re–Os geochronology of organic rich sediments: an evaluation of organic matter analysis methods. *Chemical Geology*, 200(3), 225-240.

Selby, D., & Creaser, R. A. (2004). Macroscale NTIMS and microscale LA-MC-ICP-MS Re-Os isotopic analysis of molybdenite: Testing spatial restrictions for reliable Re-Os age

determinations, and implications for the decoupling of Re and Os within molybdenite. *Geochimica et Cosmochimica Acta*, 68(19), 3897-3908.

Selby, D., Kelley, K. D., Hitzman, M. W., & Zieg, J. (2009). Re-Os sulfide (bornite, chalcopyrite, and pyrite) systematics of the carbonate-hosted copper deposits at Ruby Creek, southern Brooks Range, Alaska. *Economic Geology*, 104(3), 437-444.1.

Sharma, M., Wasserburg, G. J., Hofmann, A. W., & Butterfield, D. A. (2000). Osmium isotopes in hydrothermal fluids from the Juan de Fuca Ridge. *Earth and Planetary Science Letters*, 179(1), 139-152.

Sharma, M., Rosenberg, E. J., & Butterfield, D. A. (2007). Search for the proverbial mantle osmium sources to the oceans: Hydrothermal alteration of mid-ocean ridge basalt. *Geochimica et Cosmochimica Acta*, 71(19), 4655-4667.

Sherlock, R. L., Lee, J. K., & Cousens, B. L. (2004). Geologic and geochronologic constraints on the timing of mineralization at the Nanisivik zinc-lead Mississippi Valley-type deposit, northern Baffin Island, Nunavut, Canada. *Economic Geology*, 99(2), 279-293.

Singer, D.A. (1995). World class base and precious metal deposits—A quantitative analysis: *Economic Geology and the Bulletin of the Society of Economic Geologists*, 90, 88–104.1.

Stein, H. J., Morgan, J. W., & Scherstén, A. (2000). Re-Os dating of low-level highly radiogenic (LLHR) sulfides: The Harnas gold deposit, southwest Sweden, records continental-scale tectonic events. *Economic Geology*, 95(8), 1657-1671.

Stein, H., Scherstén, A., Hannah, J., & Markey, R. (2003). Subgrain-scale decoupling of Re and ¹⁸⁷Os and assessment of laser ablation ICP-MS spot dating in molybdenite. *Geochimica et Cosmochimica Acta*, 67(19), 3673-3686.

Sutherland, R. A., & Dumka, D. (1995). Geology of Nanisivik mine, NWT, Canada. *Carbonate-hosted Lead-Zinc-Fluorite-Barite Deposits of North America*. Edited by KC Misra. *Society of Economic Geologists, Guide Book Series*, 22, 4-12.

Symons, D. T. A., Symons, T. B., & Sangster, D. F. (2000). Paleomagnetism of the Society Cliffs dolostone and the age of the Nanisivik zinc deposits, Baffin Island, Canada. *Mineralium Deposita*, 35(7), 672-682.

Turner, E. C. (2009). Mesoproterozoic carbonate systems in the Borden Basin, Nunavut. *Canadian Journal of Earth Sciences*, 46(12), 915-938.

Turner, E. C. (2011). Structural and stratigraphic controls on carbonate-hosted base metal mineralization in the Mesoproterozoic Borden Basin (Nanisivik District), Nunavut. *Economic Geology*, 106(7), 1197-1223.

Turner, E. C., Long, D. G., Rainbird, R. H., Petrus, J. A., & Rayner, N. M. (2016). Late Mesoproterozoic rifting in Arctic Canada during Rodinia assembly: impactogens, trans - continental far - field stress and zinc mineralisation. *Terra Nova*, 28(3), 188-194.1.

Vernon, R., Holdsworth, R. E., Selby, D., Dempsey, E., Finlay, A. J., & Fallick, A. E. (2014). Structural characteristics and Re–Os dating of quartz-pyrite veins in the Lewisian Gneiss Complex, NW Scotland: Evidence of an Early Paleoproterozoic hydrothermal regime during terrane amalgamation. *Precambrian Research*, 246, 256-267.

Vorliceck, T. P., Kahn, M. D., Kasuya, Y., & Helz, G. R. (2004). Capture of molybdenum in pyrite-forming sediments: role of ligand-induced reduction by polysulfides 1. *Geochimica et Cosmochimica Acta*, 68(3), 547-556.

Waters, C. N. (2011). A revised correlation of Carboniferous rocks in the British Isles. Geological Society of London.

Wilkinson, J. J., Eyre, S. L., Boyce, A. J. (2005). Ore-Forming Processes in Irish-Type Carbonate-Hosted Zn-Pb Deposits: Evidence from Mineralogy, Chemistry, and Isotopic Composition of Sulfides at the Lisheen Mine. *Economic Geology*, 100 (1), 63–86.

Wilkinson, J.J., 2010, A Review of Fluid Inclusion Constraints on Mineralization in the Irish Ore Field and Implications for the Genesis of Sediment-Hosted Zn-Pb Deposits: *Economic Geology*, v. 105, p. 417–442.

Wilkinson, J.J.. and Hitzman, M.W, 2014, The Irish Zn-Pb Orefield: The View from 2014.1. In S.M. Archibald and S.J. Piercey, eds., *Current Perspectives in Zinc Deposits*. Irish Association of Economic Geology, 59-73.

Wu, N., Farquhar, J., & Strauss, H. (2014). $\delta^{34}\text{S}$ and $\Delta^{33}\text{S}$ records of Paleozoic seawater sulfate based on the analysis of carbonate associated sulfate. *Earth and Planetary Science Letters*, 399, 44-51.

Woodcock, N., and Strachan, R., 2000, *Geological history of Britain and Ireland: Oxford, Blackwell Science*, 423 p.

Yin, L., Li, J., Liu, J., Li, C., Sun, S., Liang, H., & Xu, J. (2017). Precise and accurate Re–Os isotope dating of organic-rich sedimentary rocks by thermal ionization mass spectrometry with an improved $\text{H}_2\text{O}_2\text{-HNO}_3$ digestion procedure. *International Journal of Mass Spectrometry*, 421, 263-270.

Zhang, L., Xiao, W., Qin, K., Qu, W., & Du, A. (2005). Re–Os isotopic dating of molybdenite and pyrite in the Baishan Mo–Re deposit, eastern Tianshan, NW China, and its geological significance. *Mineralium Deposita*, 39(8), 960-969.

Zhang, P., Huang, X. W., Cui, B., Wang, B. C., Yin, Y. F., & Wang, J. R. (2016). Re-Os isotopic and trace element compositions of pyrite and origin of the Cretaceous Jinchang porphyry Cu-Au deposit, Heilongjiang Province, NE China. *Journal of Asian Earth Sciences*, 129, 67-80.

Table 4.1.1: Lisheen Sample Mineralogy

| Mineral Separate | Qualitative χ | Mineralogy (Modal Abundance) | | | | |
|--------------------------|--------------------|------------------------------|------------|--------|-----------|-----------|
| | | Pyrite* | Sphalerite | Galena | Silicates | Carbonate |
| 8S08FW M1.0 | 4 | 83.2% | 5.4% | 0.1% | 2.1% | 9.1% |
| 8S08FW M1.2 | 3 | XX | X | X | X | X |
| 8S08FW M1.5 | 2 | XX | X | X | X | X |
| 8S08FW NM1.5 | 1 | 94.3% | 0.4% | <0.1% | 3.0% | 2.3% |
| 8S08FW B M0.8 | 3 | 81.2% | 8.8% | X | X | (10%) |
| 8S08FW B NM1.0 | 2 | XX | X | X | X | X |
| 8S08FW B NM1.2 | 1 | XX | X | X | X | X |
| LK 359A M0.6 | 6 | XX | XX | X | X | X |
| LK 359A NM 0.8 | 5 | 47.2% | 47.3% | 0.50% | X | X |
| LK 359A NM 1.0 | 4 | 39.6% | 54.3% | 0.30% | 4.7% | 1.2% |
| LK 359A M1.2 | >3 | XX | XX | X | X | X |
| LK 359A NM 1.2 | 3 | XX | XX | X | X | X |
| LK 359A NM 1.6 | 2 | XX | XX | X | X | X |
| LK 359A NM 1.8 | 1 | 9.0% | 69.1% | 19.0% | 2.5% | 0.4% |
| LK 359B M0.6 | 5 | XX | XX | X | X | X |
| LK 359B NM 1.2 | 4 | 74.2% | 24.1% | 0.3% | 0.9% | 0.5% |
| LK 359B NM 1.4 | 3 | XX | XX | X | X | X |
| LK 359B NM 1.6 | 2 | 81.1% | 17.9% | X | X | X |
| LK 359B NM 1.8 | 1 | 4.3% | 93.8% | 1.6% | 0.3% | <0.1% |
| LK 451A M1.6 | 4 | 49.3% | 25.2% | 0.2% | (<5%) | 21.7% |
| LK 451A M1.8 | 3 | 77.9% | 6.5% | 1.1% | (<5%) | 14.5% |
| LK 451A M2.0 | 2 | XX | XX | X | XX | XX |
| LK 451A NM2.0 | 1 | XX | XX | X | XX | XX |
| LK 451B M1.0 | 5 | XX | XX | X | XX | 8.4% |
| LK 451B M1.6 | 4 | XX | XX | X | XX | 10.6% |
| LK 451B M1.6 Low Density | 4 | XX | XX | X | XX | XX |
| LK 451B M1.8 | 3 | 81.8% | 6.6% | 0.3% | X | 11.3% |
| LK 451B M2.0 | 2 | XX | XX | X | XX | XX |
| LK 451B NM2.0 | 1 | XX | XX | X | XX | XX |

The concentrations of these phases should be taken as upper estimates as not all phases are accounted for. A designation of "x" means the abundance of that phase is expected to be < 5%, while a designation of "xx" means the phase is expected to be > 5%. Rock fragments that cannot be compared via χ are separated by a dotted border or an empty row. *Includes marcasite. Bracketed values are estimated values based known trends and observations. The relative magnetic susceptibility (χ) between rocks or rock fragments is given in the second column where higher values refer to higher χ values.

Table 4.1.2: Lisheen Main Zone Re-Os analyses

Lisheen Main Zone

| Sample Name | Separation Procedure | Qualitative χ | Re ppb | Os ppt | $^{87}\text{Re} / ^{188}\text{O}$: | $\pm 2\sigma$ | $^{87}\text{Os} / ^{188}\text{O}$: | $\pm 2\sigma$ | Rho | Model Age | $\pm 2\sigma$ | Initial Ratio | $\pm 2\sigma$ |
|-----------------------------|------------------------------|--------------------------------------|---------------|---------------|--|---------------------------------|--|---------------------------------|------------|------------------|---------------------------------|----------------------|---------------------------------|
| 8S08FW | 74-210 | N/A | 3.70 | 33.24 | 919 | 9.142 | 5.588 | 0.058 | 0.845 | 347.40 | 2.10 | 0.26 | 0.08 |
| 8S08FW M1.0 | 74-210 / Mag | 4 | 6.18 | 46.72 | 1250 | 9.210 | 7.484 | 0.056 | 0.841 | 346.30 | 1.40 | 0.24 | 0.08 |
| 8S08FW M1.0-2 | 74-210 / Mag | 4 | 5.98 | 47.94 | 1120 | 7.981 | 6.735 | 0.052 | 0.778 | 346.50 | 1.70 | 0.24 | 0.07 |
| 8S08FW M1.2 | 74-210 / Mag | 3 | 5.78 | 44.61 | 1204 | 9.685 | 7.254 | 0.067 | 0.758 | 347.90 | 2.10 | 0.27 | 0.09 |
| 8S08FW M1.5 | 74-210 / Mag | 2 | 3.88 | 33.29 | 996 | 9.423 | 6.034 | 0.062 | 0.818 | 347.50 | 2.10 | 0.26 | 0.08 |
| 8S08FW NM1.5 | 74-210 / Mag | 1 | 2.73 | 31.87 | 610 | 5.069 | 3.784 | 0.031 | 0.817 | 346.60 | 1.70 | 0.25 | 0.04 |
| 8S08FW NM1.5-6N | 74-210 / Mag / 6N HCl | 1 | 2.44 | 27.46 | 644 | 7.132 | 3.963 | 0.045 | 0.820 | 345.00 | 2.40 | 0.23 | 0.06 |
| 8S08FW NM1.5-10N Hot | 74-210 / Mag / 10N HCl @ 80C | 1 | 2.28 | 25.53 | 652 | 14.845 | 4.077 | 0.098 | 0.869 | 351.10 | 4.40 | 0.30 | 0.13 |
| 8S08FW B | 74-210 | N/A | 4.31 | 37.79 | 953 | 7.542 | 5.734 | 0.047 | 0.815 | 344.40 | 1.70 | 0.21 | 0.06 |
| 8S08FW B M0.8 | 74-210 | 3 | 8.10 | 55.94 | 1502 | 16.048 | 8.955 | 0.103 | 0.861 | 346.80 | 2.20 | 0.25 | 0.14 |
| 8S08FW B NM1.0 | 74-210 | 2 | 4.14 | 39.18 | 838 | 10.327 | 5.076 | 0.104 | 0.561 | 344.50 | 6.00 | 0.22 | 0.12 |

All data and blank corrections are from Chapter 3. Model ages are determined using an initial Os ratio of 0.25. Initial ratio calculations are based off an age of 347Ma. In the "Separation Procedure" column the first value reported is the grain size of the mineral separate in μm . If the sample has undergone magnetic separation the designation "Mag" is given. If the sample has undergone acid leaching the concentration of HCl used for the leaching procedure is given, and if the temperature was elevated beyond room temperature the temperature is also given. For example the designation "74-210 / Mag / 10N HCl @ 80C" states that the sample contains grains 74-210 μm in size, has underwent magnetic separation, and has been leached with 10N HCl at 80°C. All samples unless otherwise stated have underwent heavy liquid separation. The relative magnetic susceptibility (χ) between rocks or rock fragments is given in the third column where higher values refer to higher χ values.

| Sample Name | Reference | Separation Procedure | Qualitative χ | Re ppb | Os ppt | $^{187}\text{Re} / ^{188}\text{Os}$ | $\pm 2\sigma$ | $^{187}\text{Os} / ^{188}\text{Os}$ | $\pm 2\sigma$ | Rho | Model Age | $\pm 2\sigma$ | Initial Ratio | $\pm 2\sigma$ |
|-----------------------|------------|------------------------------|--------------------|--------|--------|-------------------------------------|---------------|-------------------------------------|---------------|-------|-----------|---------------|---------------|---------------|
| LK 359A M0.6* | This Study | 74-210 / Mag | 6 | 6259 | 23597 | 13346.97 | 61.24 | 72.53 | 0.35 | 0.657 | 324.10 | 1.20 | -4.86 | 0.50 |
| LK 359A NM 0.8* | This Study | 74-210 / Mag | 5 | 1933 | 7670 | 10801.83 | 36.00 | 60.66 | 0.20 | 0.430 | 334.70 | 1.20 | -1.97 | 0.29 |
| LK 359A NM 0.8-10N* | This Study | 74-210 / Mag / 10N HCl | 5 | 3499 | 14078 | 11190.26 | 43.78 | 64.09 | 0.29 | 0.499 | 341.50 | 1.40 | -0.78 | 0.39 |
| LK 359A NM 1.0** | This Study | 74-210 / Mag | 4 | 1092 | 4284 | 10108.91 | 43.05 | 55.55 | 0.30 | 0.515 | 327.50 | 1.50 | -3.06 | 0.39 |
| LK 359A M1.2-6N * | This Study | 74-210 / Mag / 6N HCl | >3 | 1215 | 4749 | 9192.28 | 39.76 | 49.60 | 0.28 | 0.510 | 321.40 | 1.60 | -3.70 | 0.36 |
| LK 359A NM 1.2-10N * | This Study | 74-210 / Mag / 10N HCl | >3 | 1179 | 4867 | 9438.71 | 127.63 | 54.47 | 0.74 | 0.958 | 343.80 | 1.30 | -0.26 | 1.05 |
| LK 359A M1.2-10N Hot* | This Study | 74-210 / Mag / 10N HCl @ 80C | >3 | 1201 | 4815 | 9073.76 | 47.24 | 50.31 | 0.32 | 0.621 | 330.20 | 1.70 | -2.29 | 0.42 |
| LK 359A NM 1.2** | This Study | 74-210 / Mag | 3 | 497 | 1920 | 8813.78 | 29.83 | 46.61 | 0.15 | 0.447 | 314.90 | 1.10 | -4.49 | 0.23 |
| LK 359A NM 1.2-2* | This Study | 74-210 / Mag | 3 | 454 | 1855 | 8177.66 | 78.05 | 45.64 | 0.68 | 0.594 | 332.20 | 3.90 | -1.77 | 0.82 |
| LK 359A NM 1.6** | This Study | 74-210 / Mag / MI | 2 | 520 | 1938 | 10640.60 | 51.39 | 55.59 | 0.40 | 0.485 | 311.40 | 2.00 | -6.10 | 0.50 |
| LK 359A NM 1.6-2* | This Study | 74-210 / Mag | 2 | 554 | 2048 | 11009.60 | 46.89 | 57.15 | 0.28 | 0.565 | 309.40 | 1.30 | -6.68 | 0.39 |
| LK 359A NM 1.8** | This Study | 74-210 / Mag / MI | 1 | 338 | 1285 | 11440.38 | 45.58 | 61.62 | 0.25 | 0.571 | 321.10 | 1.20 | -4.71 | 0.37 |
| LK 359B M0.6* | This Study | 74-210 / Mag | 5 | 506 | 2724 | 2768.80 | 13.47 | 16.20 | 0.09 | 0.642 | 344.70 | 1.50 | 0.14 | 0.12 |
| LK 359B NM 1.2** | This Study | 74-210 / Mag | 4 | 137 | 709 | 3128.94 | 10.95 | 18.23 | 0.07 | 0.462 | 343.90 | 1.20 | 0.09 | 0.09 |
| LK 359B NM 1.4** | This Study | 74-210 / Mag | 3 | 92 | 468 | 2893.23 | 19.78 | 15.79 | 0.16 | 0.581 | 321.50 | 2.60 | -0.98 | 0.20 |
| LK 359B NM 1.4 10N * | This Study | 74-210 / Mag / 10N HCl | 3 | 77 | 419 | 2724.76 | 21.34 | 16.14 | 0.17 | 0.649 | 349.00 | 2.80 | 0.34 | 0.21 |
| LK 359B NM 1.6** | This Study | 74-210 / Mag | 2 | 73 | 385 | 2792.90 | 17.32 | 15.74 | 0.12 | 0.699 | 331.90 | 1.80 | -0.45 | 0.15 |
| LK 359B NM 1.6-2* | This Study | 74-210 / Mag | 2 | 71 | 389 | 2754.99 | 16.90 | 16.36 | 0.11 | 0.752 | 349.90 | 1.60 | 0.39 | 0.15 |
| LK 359B NM 1.6 10N* | This Study | 74-210 / Mag / 10N HCl | 2 | 62 | 332 | 2697.83 | 23.60 | 15.25 | 0.16 | 0.746 | 332.80 | 2.40 | -0.39 | 0.21 |
| LK 359B NM 1.8** | This Study | 74-210 / Mag | 1 | 41 | 207 | 2844.91 | 30.46 | 15.37 | 0.19 | 0.809 | 318.10 | 2.30 | -1.12 | 0.26 |
| LK 359B NM 1.8rpt* | This Study | 74-210 / Mag | 1 | 40 | 204 | 2934.94 | 19.01 | 16.06 | 0.14 | 0.617 | 322.50 | 2.30 | -0.95 | 0.18 |

Table 4.1.3: Lisheen Derryville Zone Re-Os analyses

Model ages are determined using an initial Os ratio of 0.25. Initial ratio calculations are based off an age of 347Ma. * Os Blank = 0.05 ± 0.01 pg, $^{187}\text{Re}/^{188}\text{Os} = 0.18 \pm 0.06$, Re Blank = 1.1 ± 0.6 pg. **Os Blank = 0.34 ± 0.03 pg, $^{187}\text{Re}/^{188}\text{Os} = 0.23 \pm 0.05$, Re Blank = 2.5 ± 1.5 pg. In the "Separation Procedure" column the first value reported is the grain size of the mineral separate in μm . If the sample has undergone magnetic separation the designation "Mag" is given. If the sample has undergone acid leaching the concentration of HCl used for the leaching procedure is given, and if the temperature was elevated beyond room temperature the temperature is also given. For example the designation "74-210 / Mag / 10N HCl @ 80C" states that the sample contains grains 74-210 μm in size, has undergone magnetic separation, and has been leached with 10N HCl at 80°C. All samples unless otherwise stated have undergone heavy liquid separation. The relative magnetic susceptibility (χ) between rocks or rock fragments is given in the third column where higher values refer to higher χ values.

Table 4.1.4: Lisheen Bog Zone Re-Os analyses

| Sample Name | Separation Procedure | Qualitative χ | Re ppb | Os ppt | $^{187}\text{Re} / ^{188}\text{Os}$ | $\pm 2\sigma$ | $^{187}\text{Os} / ^{188}\text{Os}$ | $\pm 2\sigma$ | Rho | Model Age | $\pm 2\sigma$ | Initial Ratio | $\pm 2\sigma$ |
|----------------------------|------------------------------|--------------------|--------|--------|-------------------------------------|---------------|-------------------------------------|---------------|-------|-----------|---------------|---------------|---------------|
| LK 451A Bulk 1*** | 74-210 | N/A | 54 | 237 | 5999.24 | 40.65 | 34.54 | 0.22 | 0.72 | 342.10 | 1.60 | -0.24 | 0.32 |
| LK 451A Bulk 2*** | 74-210 | N/A | 55 | 244 | 6131.48 | 44.09 | 35.82 | 0.28 | 0.64 | 347.20 | 2.20 | 0.27 | 0.38 |
| LK 451A Bulk 3*** | 74-210 | N/A | 53 | 234 | 6101.30 | 45.22 | 35.22 | 0.29 | 0.65 | 343.00 | 2.20 | -0.15 | 0.39 |
| LK 451A M1.0** | 74-210 | 5 | 53 | 238 | 5712.32 | 15.45 | 33.11 | 0.12 | 0.60 | 344.27 | 0.99 | -0.01 | 0.15 |
| LK 451A M1.6 0.2N* | 74-210 / Mag / 0.2N HCl | 4 | 54 | 241 | 5681.56 | 35.43 | 33.15 | 0.20 | 0.81 | 346.60 | 1.30 | 0.21 | 0.29 |
| LK 451A M1.8 0.2N* | 74-210 / Mag / 0.2N HCl | 3 | 55 | 245 | 6007.36 | 32.47 | 35.12 | 0.18 | 0.76 | 347.40 | 1.30 | 0.29 | 0.26 |
| LK 451A M1.8 Fine 10N Hot* | <74 / Mag / 10N HCl @ 80C | 3 | 50 | 233 | 5385.56 | 28.78 | 32.57 | 0.17 | 0.73 | 359.20 | 1.40 | 1.35 | 0.24 |
| LK 451A M2.0*** | 74-210 / Mag | 2 | 55 | 279 | 3320.87 | 20.29 | 19.42 | 0.11 | 0.64 | 345.50 | 1.70 | 0.17 | 0.16 |
| LK 451A M2.0 0.2N* | 74-210 / Mag / 0.2N HCl | 2 | 55 | 244 | 6012.12 | 16.63 | 35.17 | 0.12 | 0.65 | 347.65 | 0.69 | 0.32 | 0.15 |
| LK 451A NM2.0*** | 74-210 / Mag | 1 | 40 | 176 | 5998.92 | 131.40 | 34.32 | 0.77 | 0.94 | 339.90 | 2.50 | -0.46 | 1.08 |
| LK 451 B Bulk 1*** | 74-210 | N/A | 45 | 223 | 3742.90 | 22.45 | 21.86 | 0.14 | 0.56 | 345.60 | 2.00 | 0.16 | 0.19 |
| LK 451 B Bulk 2*** | 74-210 | N/A | 47 | 225 | 3857.77 | 22.18 | 22.13 | 0.12 | 0.57 | 339.40 | 1.70 | -0.24 | 0.18 |
| LK 451B M1.0 ** | 74-210 / Mag | 5 | 48 | 218 | 4137.05 | 23.38 | 22.13 | 0.12 | 0.76 | 316.60 | 1.20 | -1.86 | 0.18 |
| LK 451B M1.0 0.2N* | 74-210 / Mag / 0.2N HCl | 5 | 47 | 227 | 4106.03 | 20.31 | 23.83 | 0.11 | 0.74 | 343.70 | 1.20 | 0.03 | 0.16 |
| LK 451B M1.6** | 74-210 / Mag | 4 | 57 | 261 | 4586.93 | 23.44 | 26.17 | 0.13 | 0.69 | 338.30 | 1.30 | -0.42 | 0.19 |
| LK 451B M1.6 0.2N* | 74-210 / Mag / 0.2N HCl | 4 | 62 | 275 | 5193.18 | 27.49 | 29.40 | 0.15 | 0.75 | 335.90 | 1.20 | -0.71 | 0.22 |
| LK 451B M1.6 0.2N rpt* | 74-210 / Mag / 0.2N HCl | 4 | 61 | 266 | 4937.02 | 27.78 | 26.71 | 0.16 | 0.72 | 320.80 | 1.30 | -1.91 | 0.22 |
| LK 451B M1.6 0.2N rpt2* | 74-210 / Mag / 0.2N HCl | 4 | 67 | 309 | 4915.27 | 24.16 | 28.75 | 0.13 | 0.71 | 347.00 | 1.30 | 0.25 | 0.19 |
| LK 451B M1.6 1N* | 74-210 / Mag / 1N HCl | 4 | 56 | 264 | 5063.22 | 27.92 | 30.30 | 0.16 | 0.77 | 355.20 | 1.30 | 0.94 | 0.23 |
| LK 451B M1.6 1N rpt* | 74-210 / Mag / 1N HCl | 4 | 57 | 259 | 4823.90 | 24.72 | 27.47 | 0.14 | 0.73 | 337.70 | 1.20 | -0.50 | 0.20 |
| LK 451B M1.6 2N* | 74-210 / Mag / 2N HCl | 4 | 60 | 273 | 4981.23 | 28.18 | 28.54 | 0.15 | 0.79 | 340.00 | 1.20 | -0.34 | 0.22 |
| LK 451B M1.6 2N rpt* | 74-210 / Mag / 2N HCl | 4 | 65 | 295 | 5360.69 | 29.72 | 31.27 | 0.17 | 0.77 | 346.30 | 1.20 | 0.19 | 0.24 |
| LK 451B M1.6 6N* | 74-210 / Mag / 2N HCl | 4 | 67 | 310 | 4863.96 | 23.35 | 28.34 | 0.12 | 0.72 | 345.60 | 1.20 | 0.14 | 0.18 |
| LK 451B M1.6 10N* | 74-210 / Mag / 10N HCl | 4 | 65 | 309 | 4396.45 | 20.45 | 25.89 | 0.11 | 0.71 | 349.00 | 1.20 | 0.40 | 0.16 |
| LK 451B M1.6 10N Hot* | 74-210 / Mag / 10N HCl @ 80C | 4 | 74 | 352 | 4517.53 | 20.03 | 26.63 | 0.11 | 0.66 | 349.50 | 1.20 | 0.44 | 0.16 |
| LK 451B M1.6 Low Density* | 74-210 / Mag / Low Density* | 4 | 27 | 118 | 4837.13 | 18.46 | 25.67 | 0.08 | 0.55 | 314.60 | 1.00 | -2.37 | 0.13 |
| LK 451B M1.8** | 74-210 / Mag | 3 | 55 | 274 | 3536.37 | 27.18 | 20.31 | 0.25 | 0.54 | 339.50 | 3.50 | -0.19 | 0.30 |
| LK 451B M1.8 0.2N* | 74-210 / Mag / 0.2N HCl | 3 | 55 | 272 | 3536.32 | 24.94 | 20.49 | 0.19 | 0.65 | 342.60 | 2.40 | -0.01 | 0.24 |
| LK 451B M1.8 Fine 6N* | <74 / Mag / 6N HCl | 3 | 52 | 262 | 3518.02 | 25.90 | 20.55 | 0.15 | 0.85 | 345.30 | 1.40 | 0.15 | 0.21 |
| LK 451B M1.8 Fine 10N* | <74 / Mag / 10N HCl | 3 | 46 | 245 | 3368.35 | 17.81 | 20.70 | 0.10 | 0.75 | 363.40 | 1.30 | 1.17 | 0.15 |
| LK 451B M2.0 *** | 74-210 / Mag | 2 | 47 | 231 | 3751.1 | 29.0 | 21.82 | 0.20 | 0.636 | 344.20 | 2.50 | 0.08 | 0.26 |
| LK 451B M2.0 rpt* | 74-210 / Mag | 2 | 46 | 219 | 3903.08 | 22.59 | 22.26 | 0.13 | 0.77 | 337.50 | 1.30 | -0.37 | 0.18 |
| LK 451B NM2.0*** | 74-210 / Mag | 1 | 24 | 123 | 3068.99 | 47.67 | 17.76 | 0.28 | 0.91 | 341.60 | 2.20 | -0.03 | 0.39 |
| LK 451A Leachate* | Leachate | N/A | 0.18 | 12 | 167.81 | 7.50 | 10.49 | 0.28 | 0.57 | 3554.00 | 120.00 | 9.51 | 0.28 |
| LK 451A M1.0 Leachate* | Leachate | N/A | 0.47 | 38 | 87.49 | 3.80 | 3.63 | 0.07 | 0.32 | 2272.00 | 91.00 | 3.12 | 0.07 |
| LK 451B Leachate* | Leachate | N/A | 0.30 | 23 | 109.82 | 2.90 | 6.35 | 0.07 | 0.42 | 3245.00 | 74.00 | 5.71 | 0.07 |

In the "Separation Procedure" column the first value reported is the grain size of the mineral separate in μm . If the sample has undergone magnetic separation the designation "Mag" is given. If the sample has undergone acid leaching the concentration of HCl used for the leaching procedure is given, and if the temperature was elevated beyond room temperature the temperature is also given. For example the designation "74-210 / Mag / 10N HCl @ 80C" states that the sample contains grains 74-210 μm in size, has underwent magnetic separation, and has been leached with 10N HCl at 80°C. All samples unless otherwise stated have underwent heavy liquid separation. The term "Low Density" refers to material that is less dense than the heavy liquid used for heavy liquid separation (i.e. < 3.32 g/cm³). The relative magnetic susceptibility (χ) between rocks or rock fragments is given in the second column where higher values refer to higher χ values. Model ages are determined using an initial Os ratio of 0.25. Initial ratio calculations are based off an age of 347Ma. *Os Blank = 0.05 \pm 0.01 pg, 187/188 = 0.18 \pm 0.06, Re Blank = 1.1 \pm 0.6pg. **Os Blank = 0.34 \pm 0.03 pg, 187/188 = 0.23 \pm 0.05, Re Blank = 2.5 \pm 1.5pg. ***Os Blank = 0.37 \pm 0.043 pg, 187/188 = 1.8 \pm 0.5, Re Blank = 2.5 \pm 1.5pg.

Table 4.1.5: Nanisivik and Hawker Creek Re-Os analyses

| Sample Name | Separation Procedure | Qualitative χ | Re ppb | Os ppt | $^{187}\text{Re} / ^{188}\text{Os}$ | $\pm 2\sigma$ | $^{187}\text{Os} / ^{188}\text{Os}$ | $\pm 2\sigma$ | Rho | Model Age | $\pm 2\sigma$ | Initial Ratio | $\pm 2\sigma$ |
|-------------------------|------------------------------|--------------------------------------|---------------|---------------|---|---------------------------------|---|---------------------------------|------------|------------------|---------------------------------|----------------------|---------------------------------|
| NOV4-B NM0.6 | 74-210 / Mag / 0.2N HCl | 4 | 12.54 | 176.71 | 2076.47 | 14.51 | 39.03 | 0.34 | 0.62 | 1128 | 47 | 0.63 | 0.69 |
| NOV4-B NM0.9 | 74-210 / Mag / 0.2N HCl | 3 | 9.02 | 130.74 | 1987.22 | 13.99 | 38.31 | 0.32 | 0.66 | 1118 | 43 | 1.55 | 0.64 |
| NOV4-B NM1.2 | 74-210 / Mag / 0.2N HCl | 2 | 4.27 | 61.48 | 1933.19 | 16.86 | 36.79 | 0.39 | 0.70 | 1124 | 46 | 1.04 | 0.79 |
| NOV4-B NM1.2-2 | 74-210 / Mag | 2 | 3.81 | 56.71 | 1963.47 | 26.19 | 38.96 | 0.74 | 0.66 | 1109 | 22 | 2.64 | 1.48 |
| NOV4-B NM1.95 | 74-210 / Mag / 0.2N HCl | 1 | 2.37 | 34.87 | 1936.85 | 33.85 | 37.81 | 0.69 | 0.92 | 1019 | 23 | 1.98 | 1.38 |
| NOV4-C NM0.6 | 74-210 / Mag / 10N HCl @ 80C | 3 | 2.40 | 48.52 | 621.64 | 4.51 | 12.49 | 0.10 | 0.69 | 1021 | 24 | 0.99 | 0.19 |
| NOV4-C NM1.2 | 74-210 / Mag / 10N HCl @ 80C | 2 | 0.88 | 16.82 | 702.03 | 10.16 | 13.90 | 0.23 | 0.76 | 1038 | 24 | 0.92 | 0.47 |
| NOV4-C NM2.0 | 74-210 / Mag / 10N HCl @ 80C | 1 | 0.62 | 12.19 | 671.41 | 19.51 | 13.39 | 0.38 | 0.89 | 1055 | 25 | 0.97 | 0.77 |
| NOV4-D NM0.6 | 74-210 / Mag / 10N HCl @ 80C | 5 | 10.80 | 165.69 | 1430.73 | 9.50 | 27.39 | 0.24 | 0.57 | 1098 | 16 | 0.93 | 0.49 |
| NOV4-D NM0.9 | 74-210 / Mag / 10N HCl @ 80C | 4 | 6.26 | 90.96 | 1370.56 | 13.01 | 24.16 | 0.28 | 0.71 | 1125 | 16 | -1.19 | 0.56 |
| NOV4-D NM1.1 | 74-210 / Mag / 10N HCl @ 80C | 3 | 3.60 | 53.28 | 1287.91 | 10.52 | 22.80 | 0.23 | 0.67 | 1110 | 17 | -1.02 | 0.46 |
| NOV4-D NM1.5 | 74-210 / Mag / 10N HCl @ 80C | 2 | 2.11 | 31.99 | 1239.63 | 12.68 | 22.32 | 0.26 | 0.78 | 1158 | 22 | -0.60 | 0.51 |
| NOV4-D NM2.0 | 74-210 / Mag / 10N HCl @ 80C | 1 | 1.60 | 24.72 | 1190.48 | 14.86 | 21.80 | 0.29 | 0.84 | 1139 | 17 | -0.21 | 0.59 |
| 04-N-2 M1.6 | 74-210 / Mag | 3 | 0.80 | 20.45 | 365.42 | 6.43 | 7.24 | 0.11 | 0.79 | 1065 | 80 | 0.48 | 0.23 |
| 04-N-2 NM1.6 | 74-210 / Mag | 2 | 0.60 | 16.15 | 344.78 | 7.68 | 7.14 | 0.14 | 0.79 | 1111 | 85 | 0.76 | 0.27 |
| 04-N-2 NM2.0 | 74-210 / Mag | 1 | 0.21 | 6.10 | 307.64 | 18.00 | 6.47 | 0.31 | 0.78 | 1115 | 100 | 0.78 | 0.62 |
| 03-HC-8D M0.8 | 74-210 / Mag | 4 | 20.34 | 93.69 | 19239.41 | 594.08 | 133.46 | 4.31 | 0.95 | 413 | 6 | - | - |
| 03-HC-8D M1.25 | 74-210 / Mag | 3 | 3.62 | 22.85 | 10634.60 | 1005.87 | 99.15 | 9.55 | 0.98 | 553 | 11 | - | - |
| 03-HC-8D M1.25-2 | 74-210 / Mag | 3 | 3.55 | 20.90 | 10327.38 | 973.47 | 89.16 | 8.57 | 0.98 | 512 | 10 | - | - |
| 03-HC-8D M2.0 | 74-210 / Mag | 2 | 1.18 | 9.07 | 6478.95 | 1130.85 | 71.77 | 12.59 | 0.99 | 655 | 14 | - | - |
| 03-HC-8D M2.0-2 | 74-210 / Mag | 2 | 1.60 | 12.12 | 9080.00 | 1648.17 | 102.13 | 18.54 | 1.00 | 667 | 7 | - | - |
| 03-HC-8D NM2.0 | 74-210 / Mag | 1 | 0.44 | 4.65 | 2380.18 | 408.73 | 32.83 | 5.62 | 0.99 | 805 | 21 | - | - |
| 03-HC-8F M1.2 | 74-210 / Mag | 2 | 8.37 | 88.47 | 8281.62 | 290.34 | 131.78 | 4.65 | 0.99 | 943 | 4 | - | - |
| 03-HC-8F NM1.2 | 74-210 / Mag | 1 | 1.75 | 22.06 | 4509.50 | 381.59 | 82.80 | 7.20 | 0.97 | 1083 | 23 | - | - |

All data and blank corrections are from Hnatyshin et al. (2016). Model ages are determined using an initial Os ratio of 0.7. Initial ratio calculations are based off an age of 1100 Ma. In the "Separation Procedure" column the first value reported is the grain size of the mineral separate in μm . If the sample has undergone magnetic separation the designation "Mag" is given. If the sample has undergone acid leaching the concentration of HCl used for the leaching procedure is given, and if the temperature was elevated beyond room temperature the temperature is also given. For example the designation "74-210 / Mag / 10N HCl @ 80C" states that the sample contains grains 74-210 μm in size, has undergone magnetic separation, and has been leached with 10N HCl at 80°C. All samples unless otherwise stated have undergone heavy liquid separation. The relative magnetic susceptibility (χ) between rocks or rock fragments is given in the second column where higher values refer to higher χ values.

Distribution of Sulfide Re-Os Geochronology Datasets

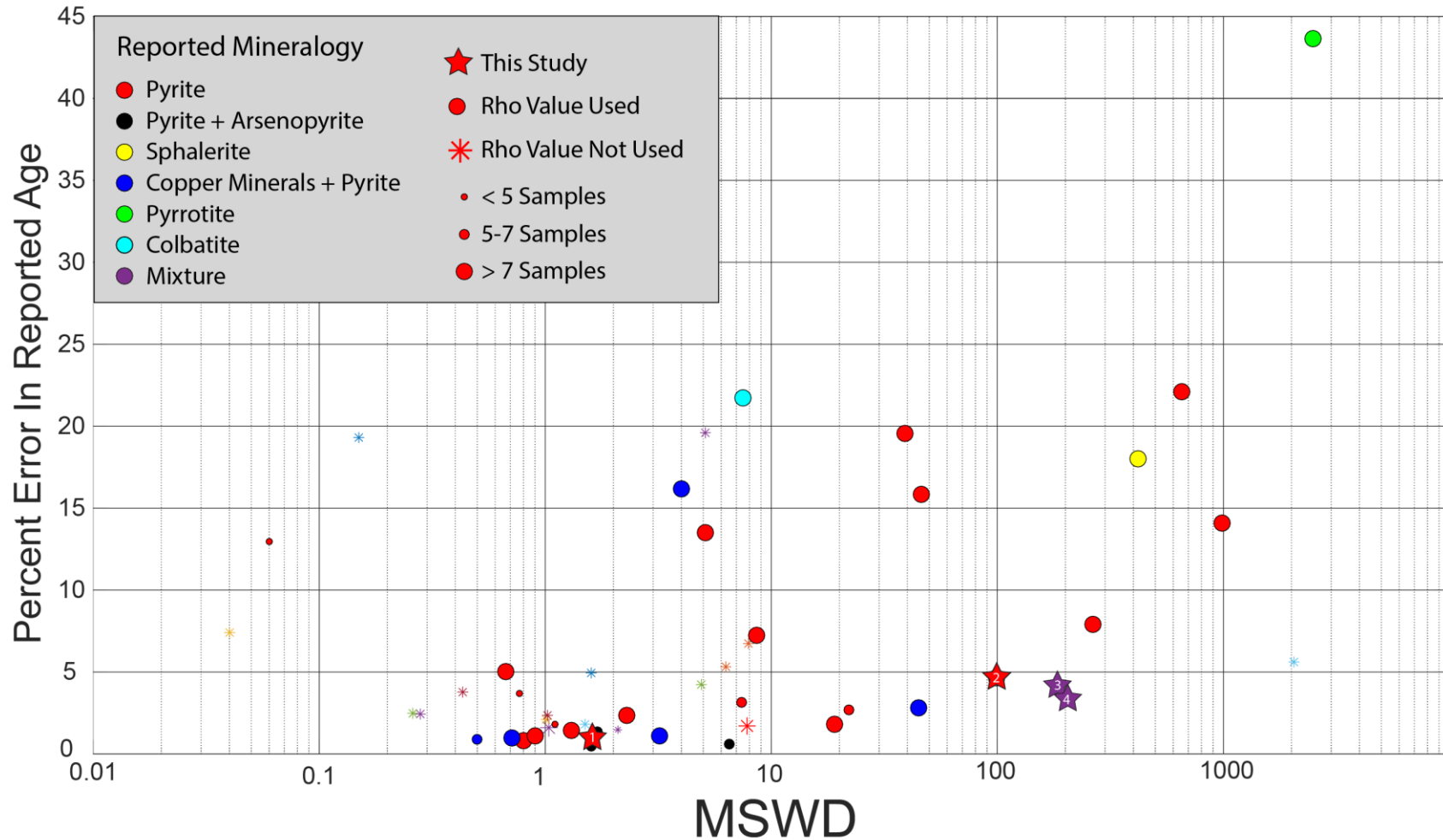


Figure 4.1.1: The distribution of scatter and precision of some sulphide Re-Os publications in addition to personal unpublished results. Published data is expected to skew too much lower errors and MSWD than what is expected from an unbiased sample population. Datasets that do not use rho in statistical calculations will artificially skew to lower MSWD values. The stars designate samples used in this study: 1 - 8S08FW (Lisheen Main Zone), 2 - NOV4 (Nanisivik), 3 - LK 451 (Lisheen Bog Zone), 4 - LK 359 (Lisheen Derryville Zone).

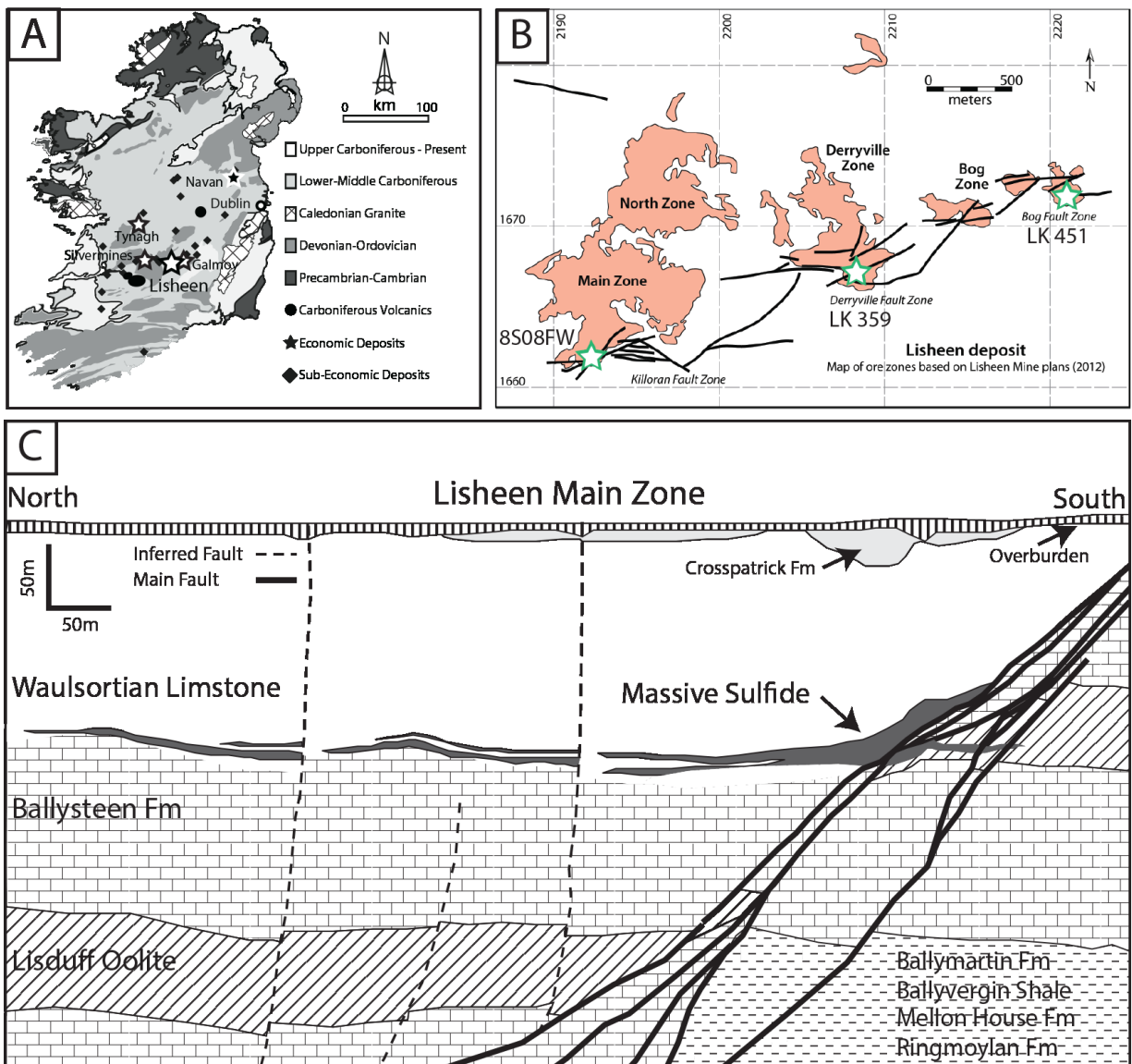


Figure 4.1.2: (A) Map of Ireland showing Zn-Pb mineralization (modified from Wilkinson, 2010) (B) Sampling locations (C) Geologic Cross-section of the Lisheen Main Zone showing the basic stratigraphy, location of massive sulphide, and faults (modified from Hitzman et al., 2002).

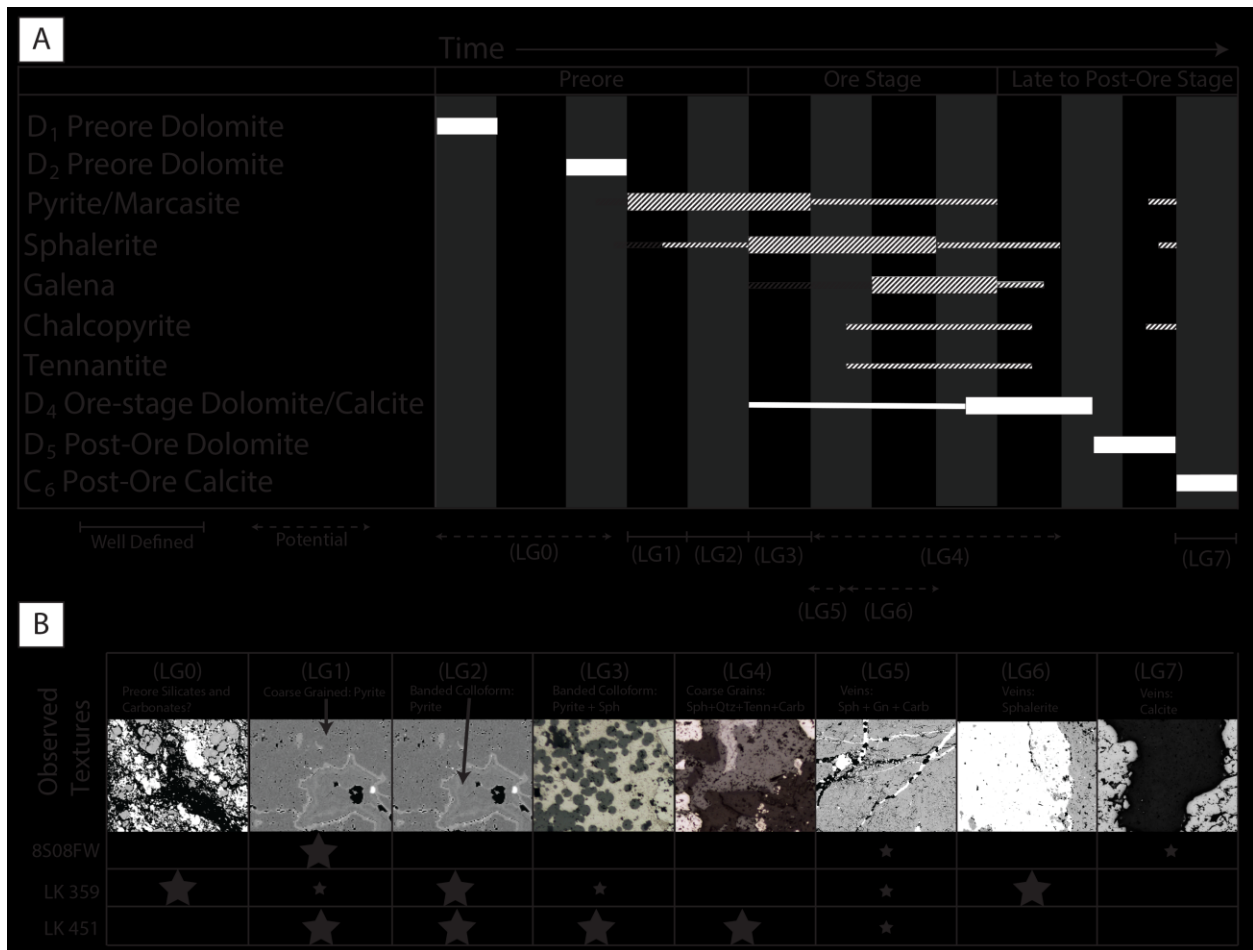


Figure 4.1.3: Paragenetic sequence for Lisheen (A) The generalized paragenetic sequence and the subjective location of the various observed textures seen in processed samples (B) Observed textures – LG0/LG5/LG6 (Backscattered electron (BSE) image from LK 359), LG1/LG2 (BSE image from LK 451), LG3/LG4 (Reflected light image from LK 451), LG7 (BSE image from 8S08FW). Large star = major component, small star = minor component. An eighth texture (LGU - not shown) refers to any texture/phase whose paragenetic relation is uncertain.

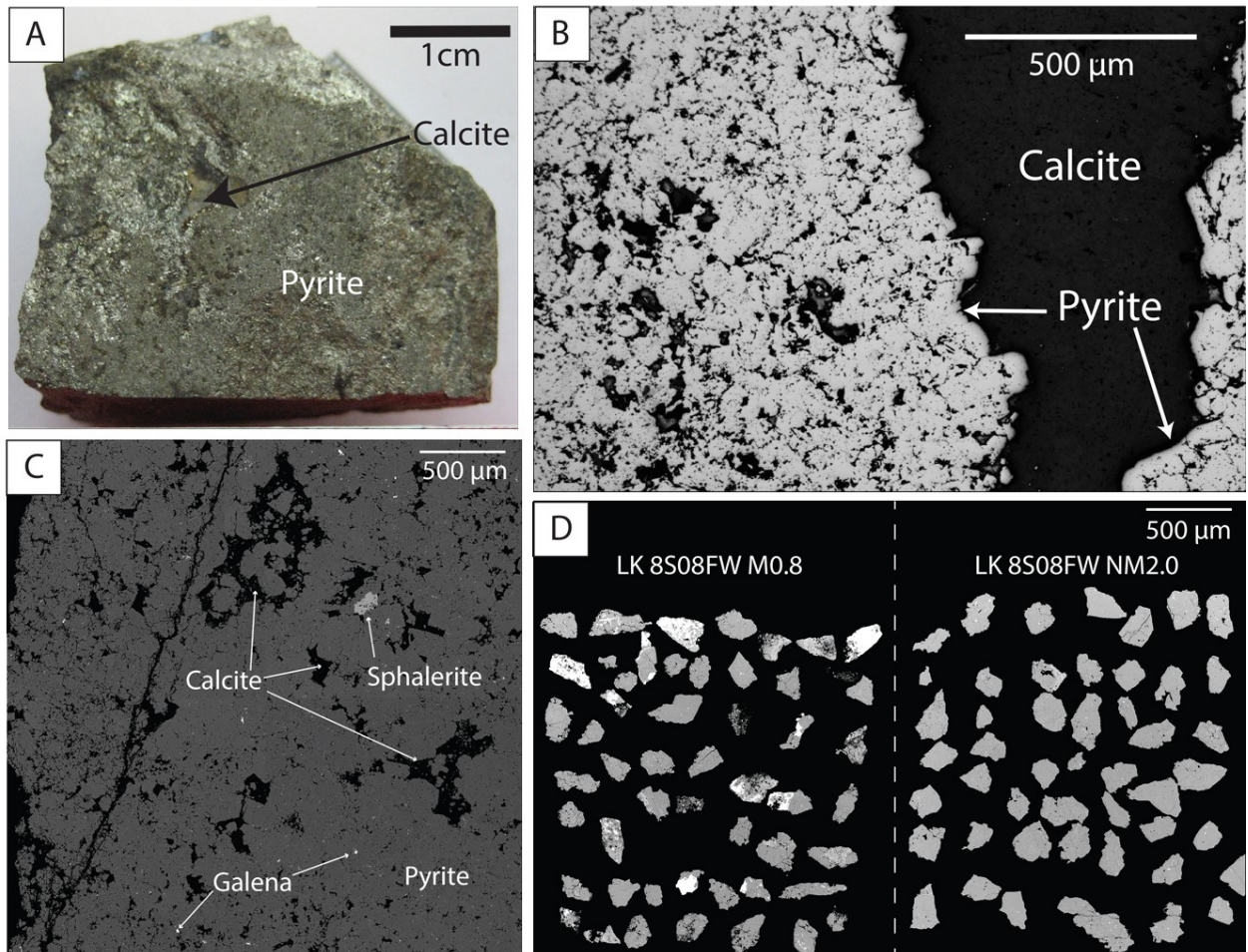


Figure 4.1.4: (A) Hand sample of 8S08FW (B) Reflected light image showing LG1 pyrite and LG7 calcite (C) BSE image emphasizing the different phases present (D) Representative BSE images of mineral separates used for Re-Os geochronology.

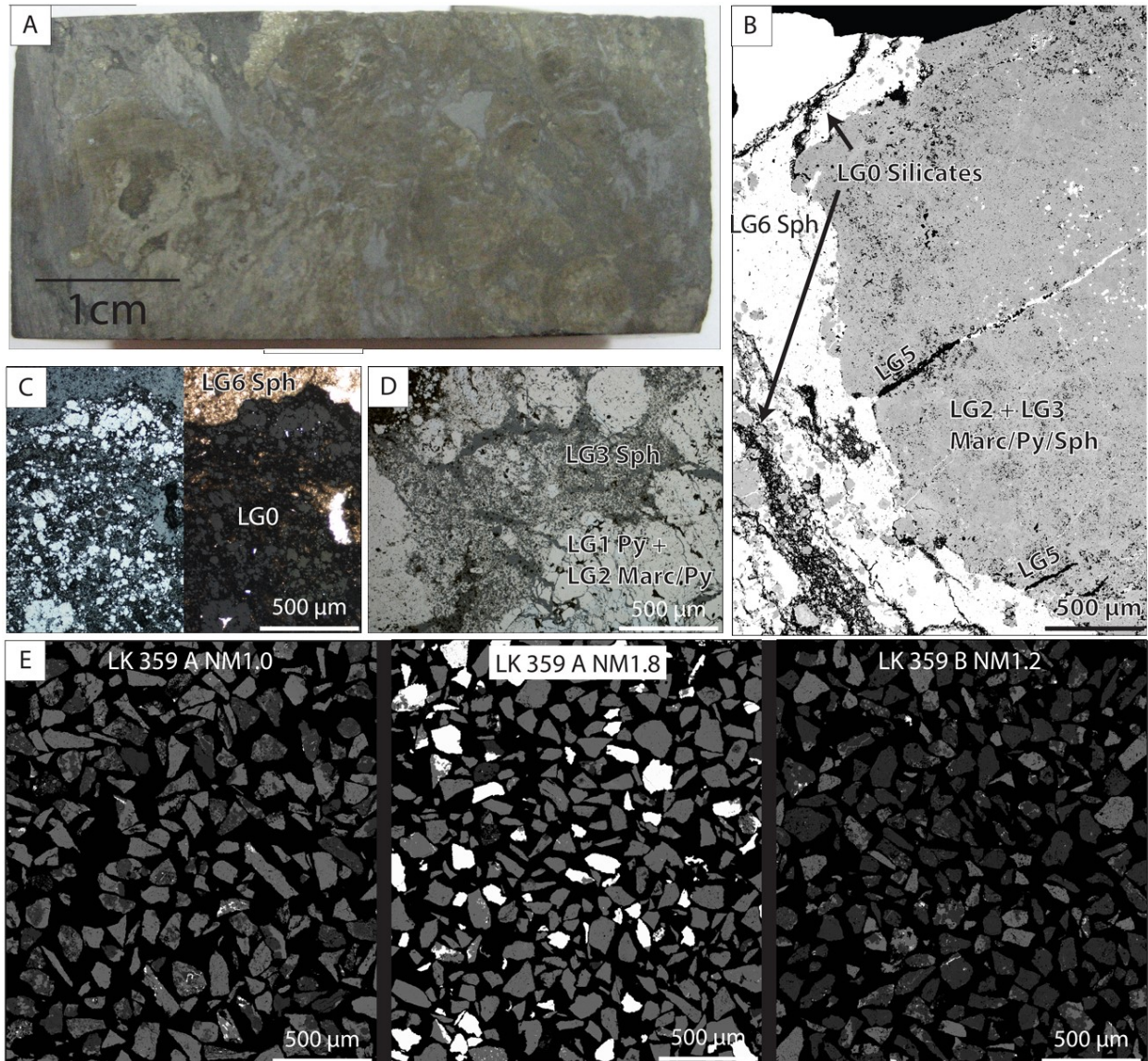


Figure 4.1.5: (A) Hand sample LK 359 (B) Representative BSE image of LK 359 (C) Reflected light on the left side of the image and transmitted light on the right side of the image showing the boundary between LG6 sphalerite and LG0 silicates intermixed with LG1-LG3 pyrite (D) Reflected light image showing the transitions between LG1-LG3 (E) Representative BSE images of mineral separates used of Re-Os geochronology.

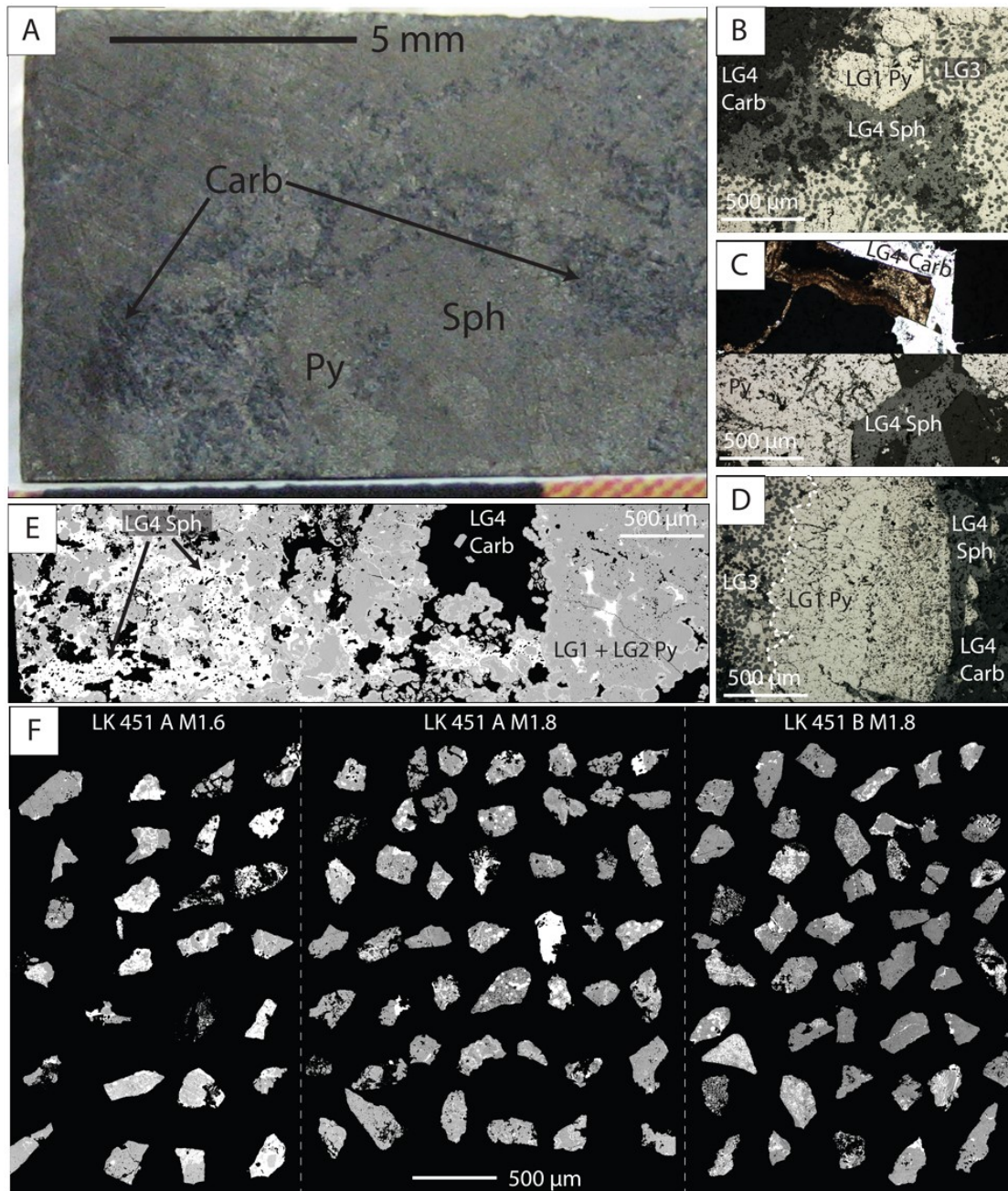


Figure 4.1.6: (A) Hand sample LK 451 (B) Reflected light image showing the paragenetic transition through LG1-LG3-LG4 (C) Reflected light on the bottom side of the image and transmitted light on the top side on the image showing the sphalerite zoning (D) Reflected light image showing the paragenetic transition through LG1-LG3-LG4, dashed line outlines the boundary between LG1 and LG3 (E) Representative BSE image of LK 451 outlining the distribution of iron sulphides, sphalerite, and carbonates (F) Representative BSE images of mineral separates used for Re-Os geochronology.

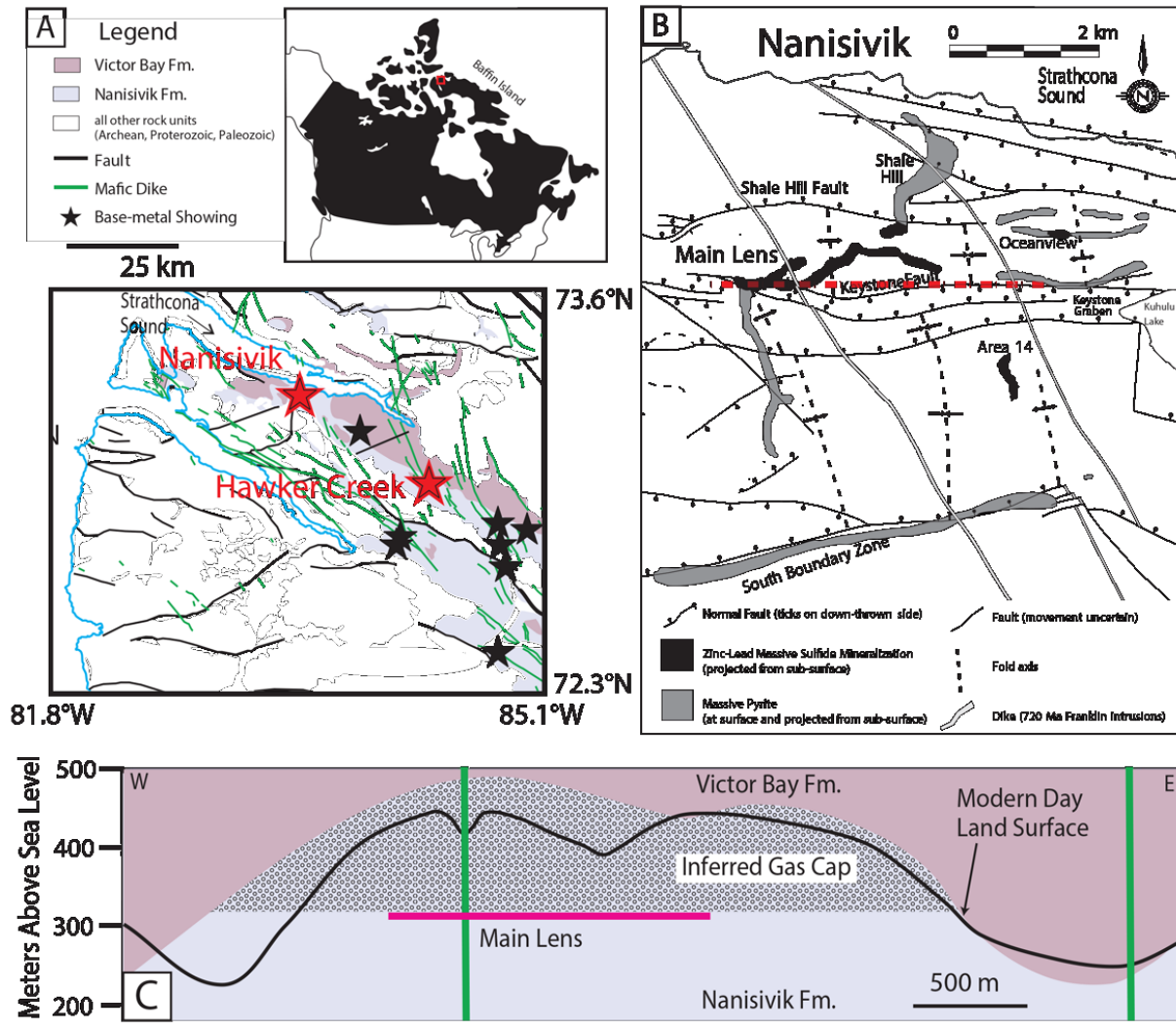


Figure 4.1.7: (A) Location of Nanisivik and Hawker Creek (modified from Turner, 2011) (B) Structures near Nanisivik; modified from Sutherland and Dumka (1995), Patterson and Powis (2002), Patterson et al. (2003), and Sherlock et al. (2004) (C) East-West cross-section (red dashed line from B) of the Main Lens of the Nanisivik ore body (modified from Turner, 2011).

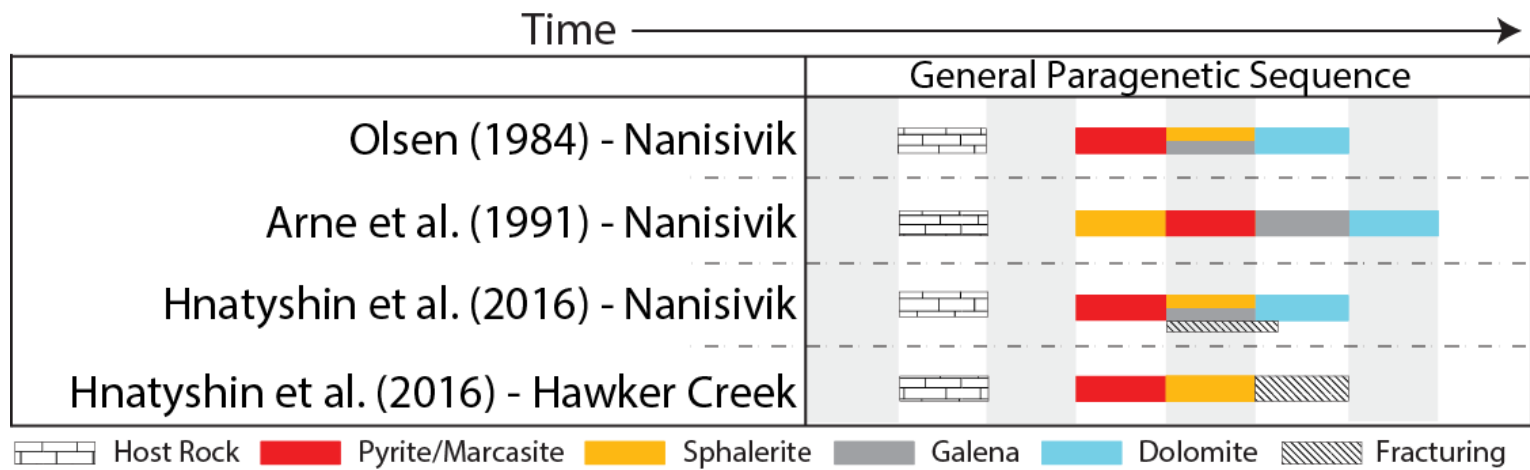


Figure 4.1.8: Paragenesis of Nanisivik and Hawker Creek.

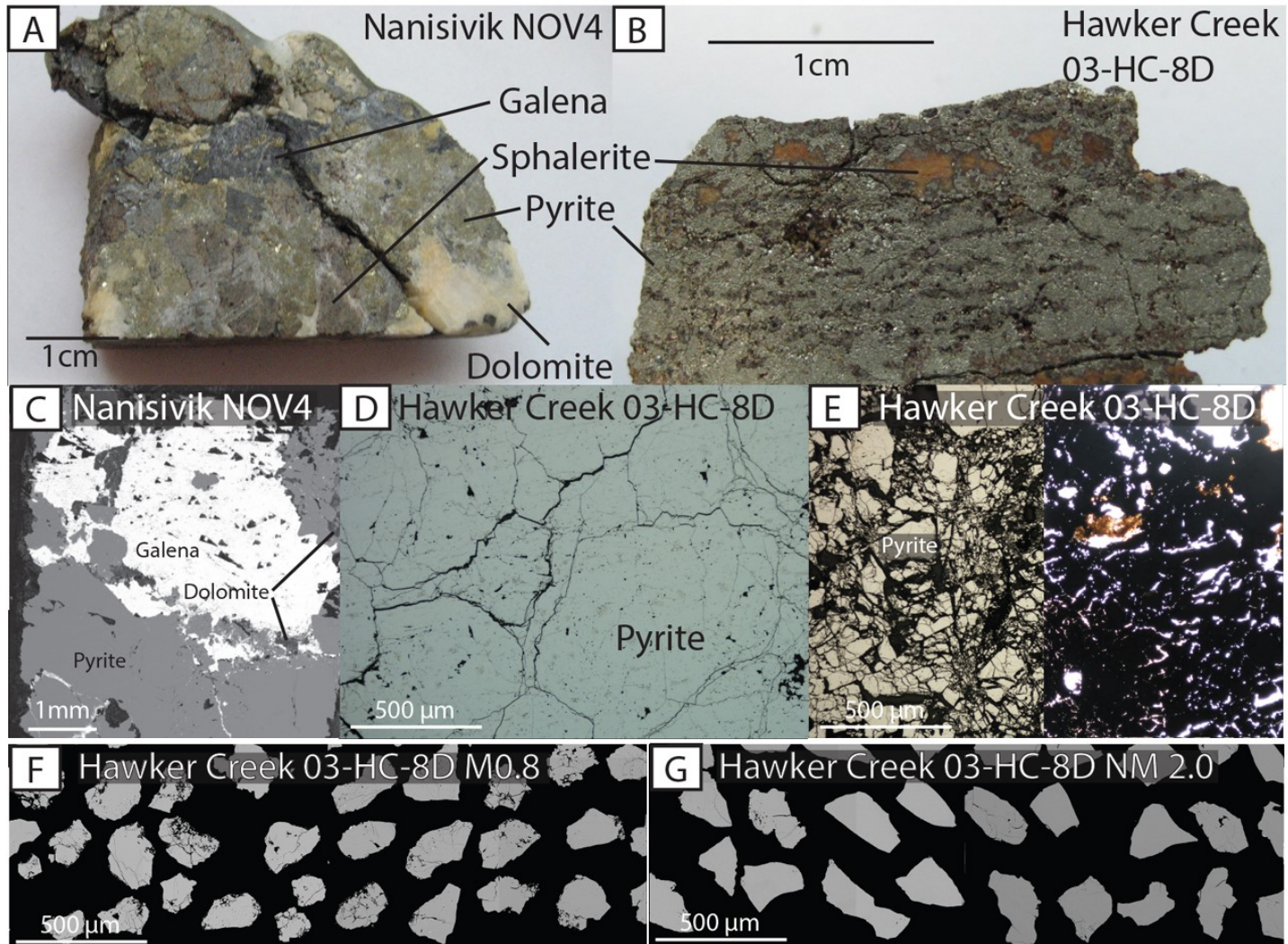


Figure 4.1.9: (A) Hand sample of NOV4 from Nanisivik (B) Hand Sample of 03-HC-8D from Hawker Creek (C) BSE image of NOV4 (D) Reflected light image of 03-HC-8D showing clean pyrite cores (E) Highly fractured area in 03-HC-8D infilled with silicates and other minerals. (F) Mineral separate with the highest magnetic susceptibility from 03-HC-8D (G) Mineral separate with the lowest magnetic susceptibility from 03-HC-8D.

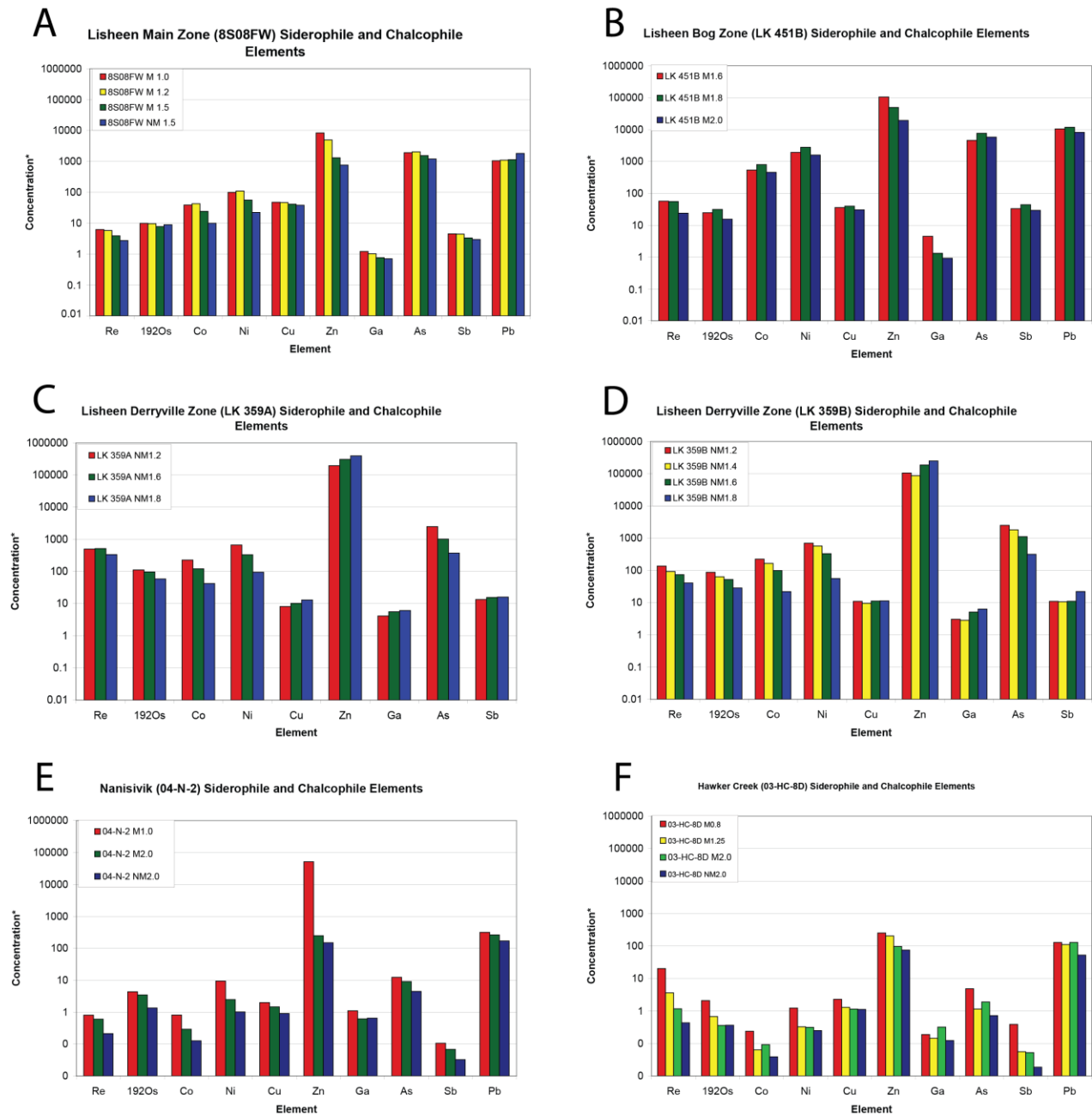


Figure 4.1.10: ICPMS analyses of mineral separates (A) 8S08FW (B) LK 451 (C) LK 359A (D) LK 359B (E) 04-N-2 (F) 03-HC-8D.

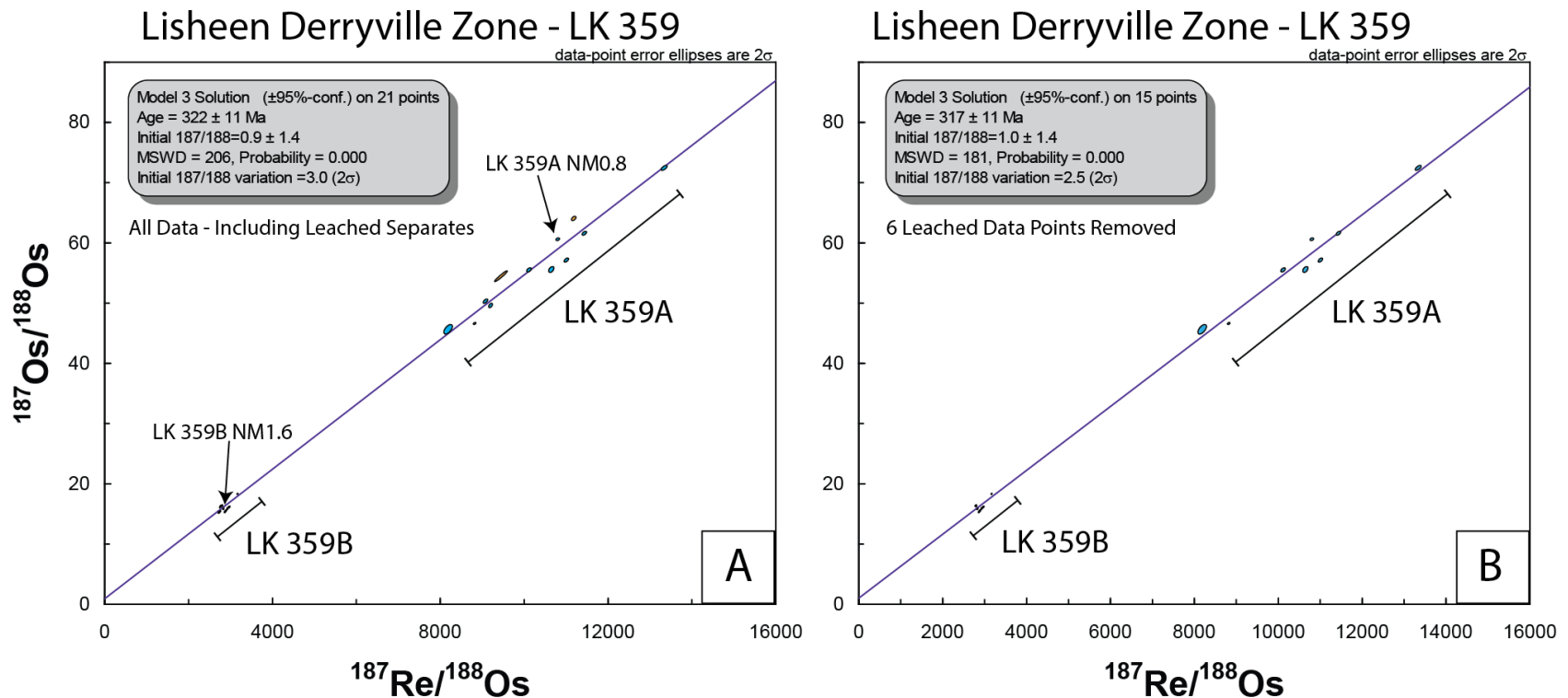


Figure 4.1.11: (A) Model 3 Isochron for LK 359. Samples selected for SIMS sulphur isotope measurements are indicated (B) Model 3 isochron after removal of points that represented mineral separates that underwent leaching procedures. Orange ellipses represent leached data points, blue ellipses represent non-leached data points, and grey ellipses represent low density data points. Orange ellipses represent leached data points and blue ellipses represent non-leached data points.

Lisheen Bog Zone - LK 451

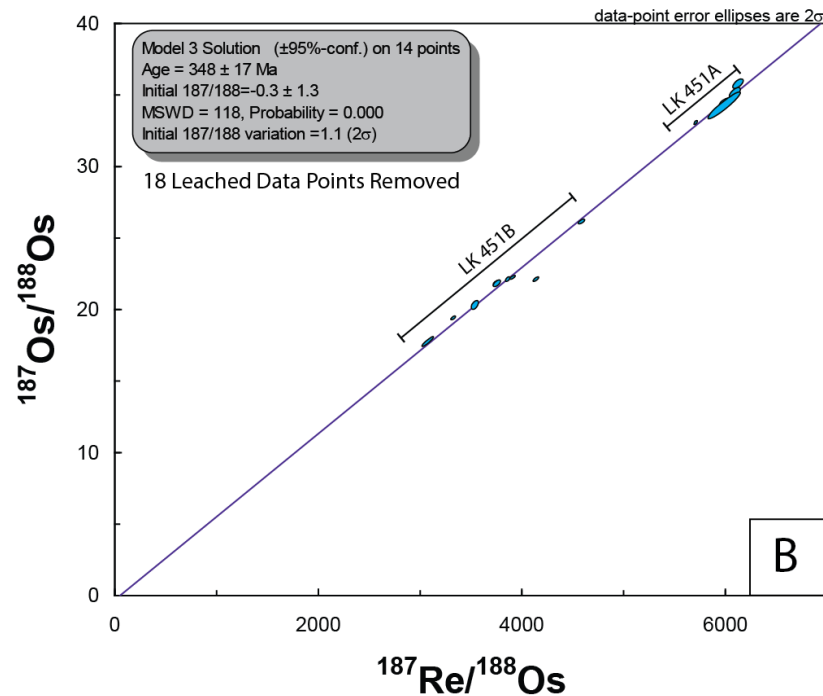
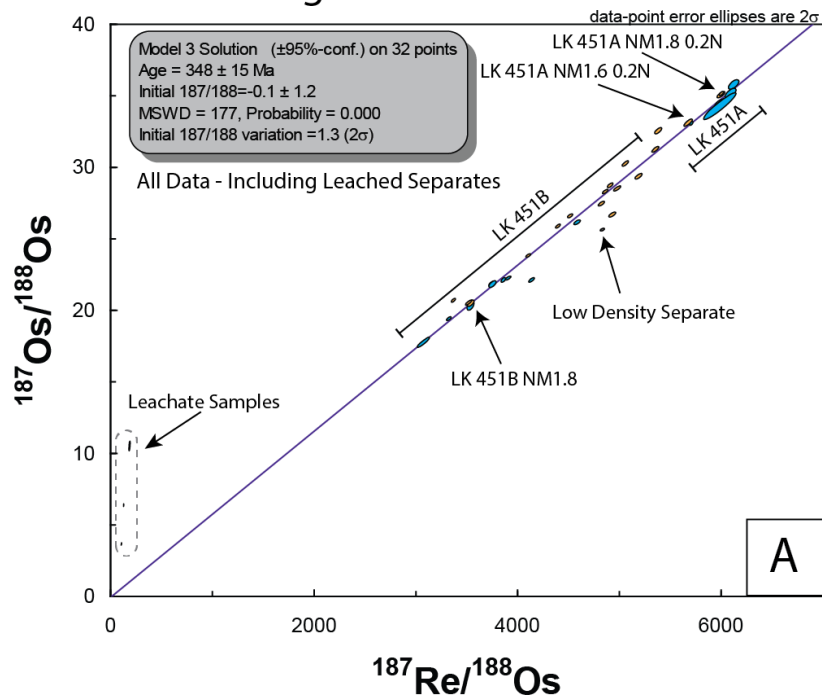


Figure 4.1.12: (A) Model 3 isochron for LK 451. Three data points with SIMS sulphur isotope data (LK 451A NM1.6 0.2N, LK 451A NM1.8 0.2N, LK 451B NM1.8) are indicated (B) Model 3 Isochron for LK 451 when ignoring all mineral separates that underwent leaching. Orange ellipses represent leached data points, blue ellipses represent non-leached data points, and grey ellipses represent low density data points.

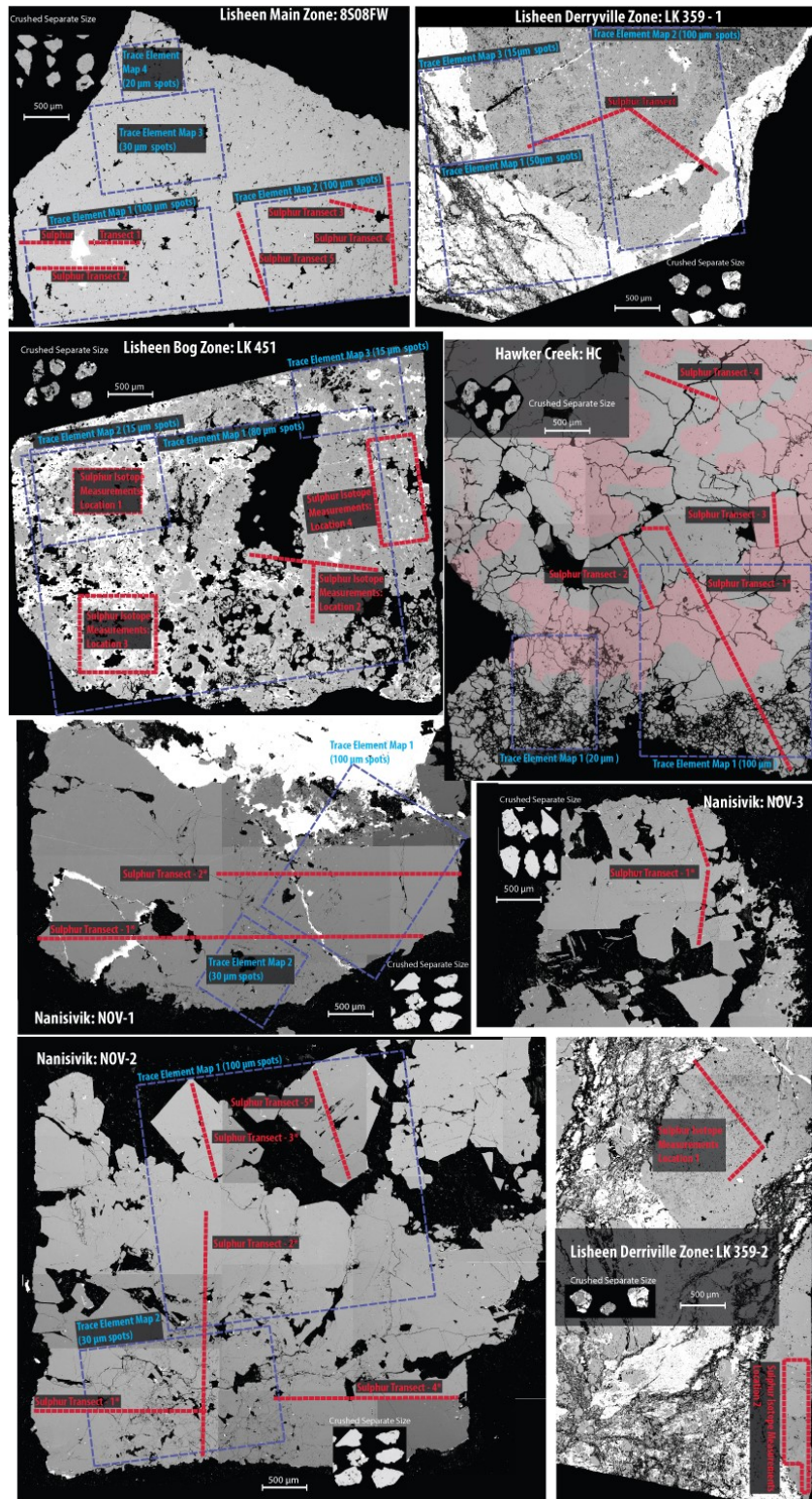


Figure 4.1.13: Areas chosen for SIMS sulphur isotope measurements and LA-ICPMS compositional mapping. All images are scaled to the same size.

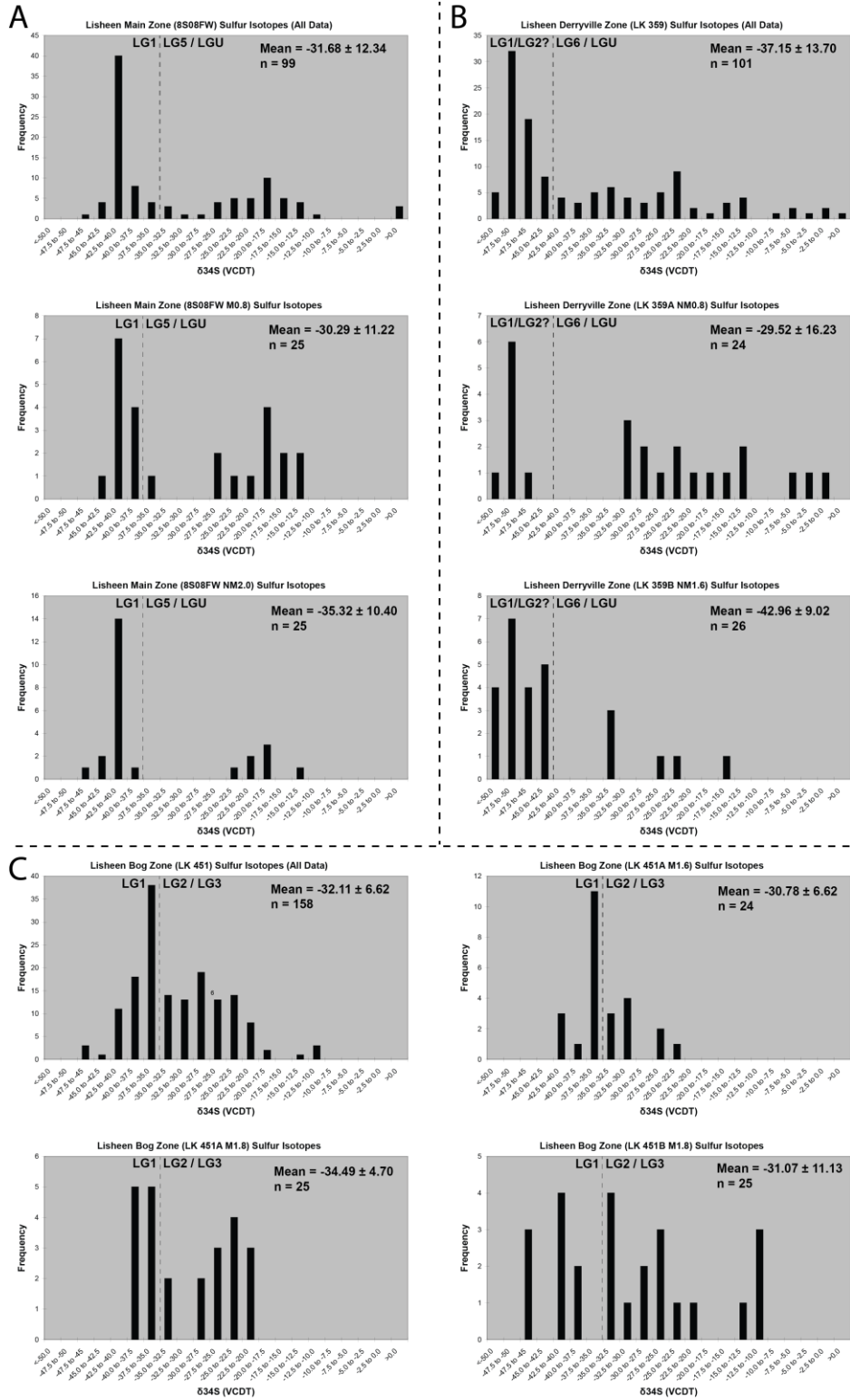


Figure 4.1.14: Histograms of SIMS sulphur isotope measurements for Lisheen. Lightly dashed lines indicates interpreted divisions between specific generations. (A) Main Zone sample 8S08FW (B) Derryville Sample LK 359 (C) Bog Zone Sample LK 451. Carboniferous seawater has a value of 16 ± 3 (Kampschulte and Strauss, 2004; Wu et al., 2014)

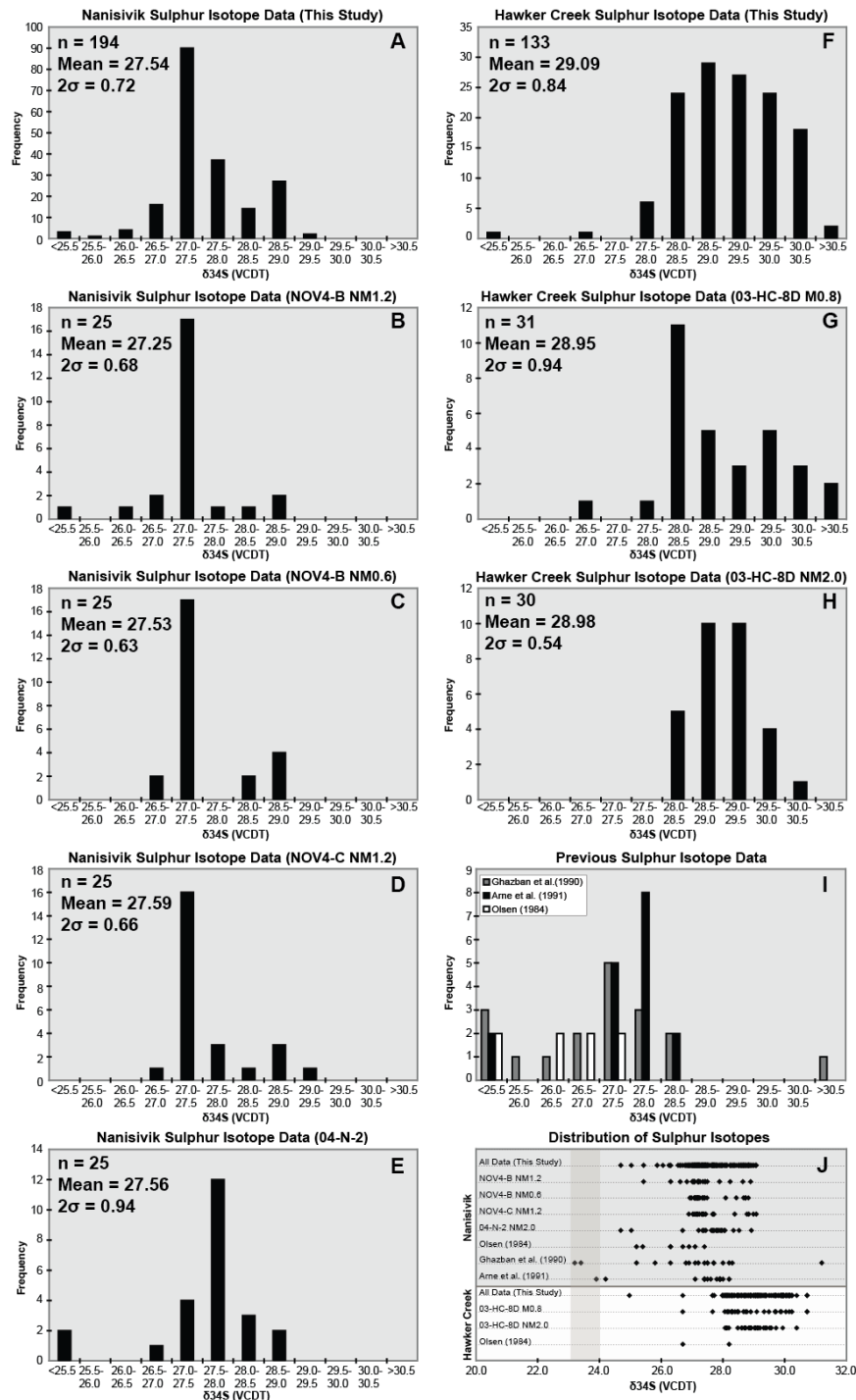


Figure 4.1.15: Compilation of sulphur isotope data for Nanisivik pyrite. (A) - Histogram for all Nanisivik analyses in this study (rock fragments and mineral separates). (B) to (E) - Histogram for individual Nanisivik mineral separates. (F) - Histogram for all Hawker Creek analyses in current study (rock fragment and mineral separates). (G) Histogram for Hawker Creek sample 03-HC-8D-M0.8. (H) Histogram for Hawker Creek sample 03-HC-8D-NM2.0. (I) - Histogram for Previous Studies. (J) - Plot containing all pyrite sulphur isotope analyses from Nanisivik and Hawker Creek. The shaded region indicates Nanisivik Formation gypsum (23.7 ± 0.5 ; Olson, 1984)

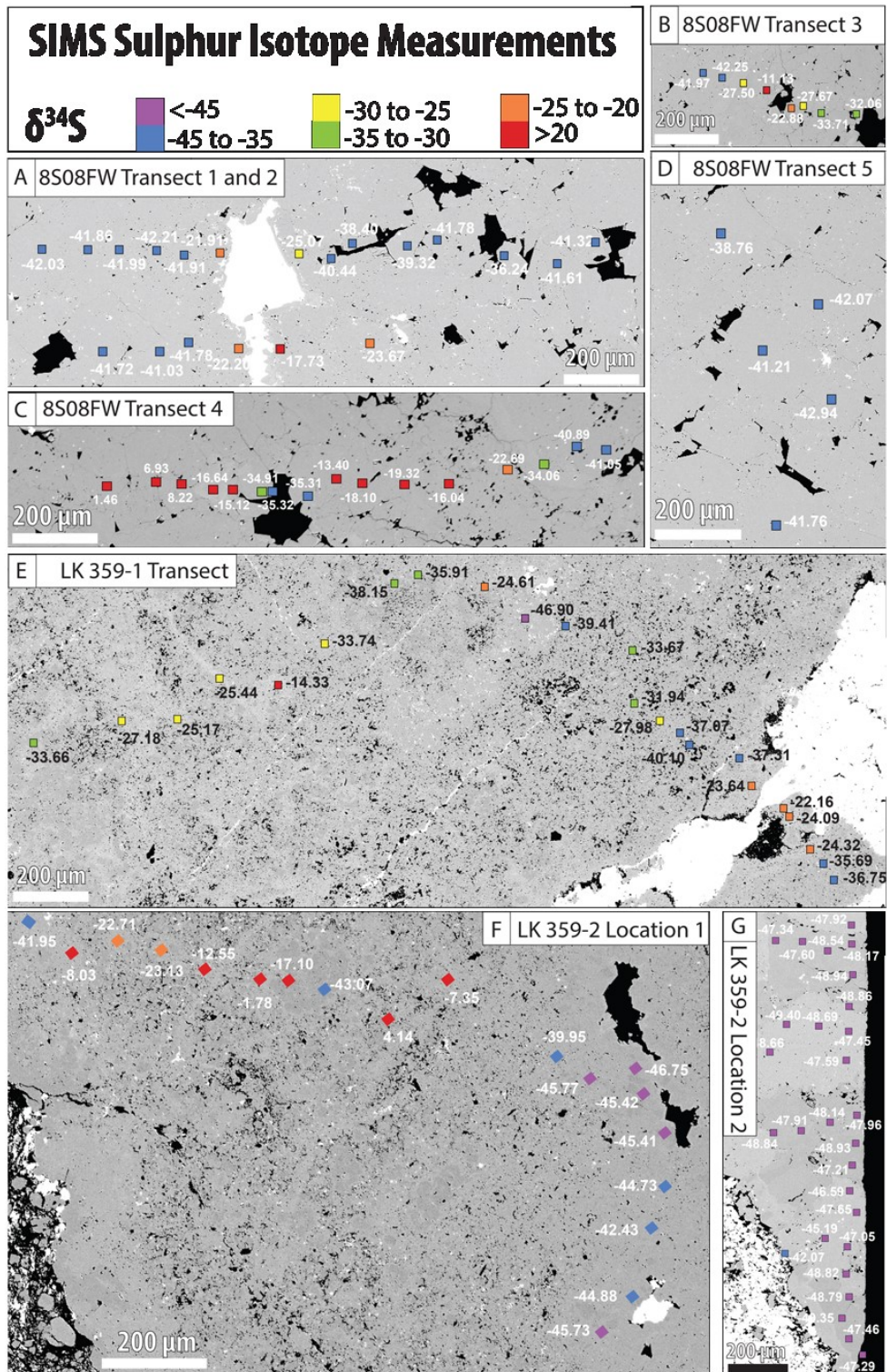


Figure 4.1.16: SIMS sulphur isotope measurements for the Main Zone and Derryville Zones along transects highlighted in Figure 4.1.13. (A)-(D) Main Zone sample 8S08FW-1 (E)-(G) Derryville samples LK 359-1 and LK 359-2. Data points are scaled to the sizes of SIMS spots.

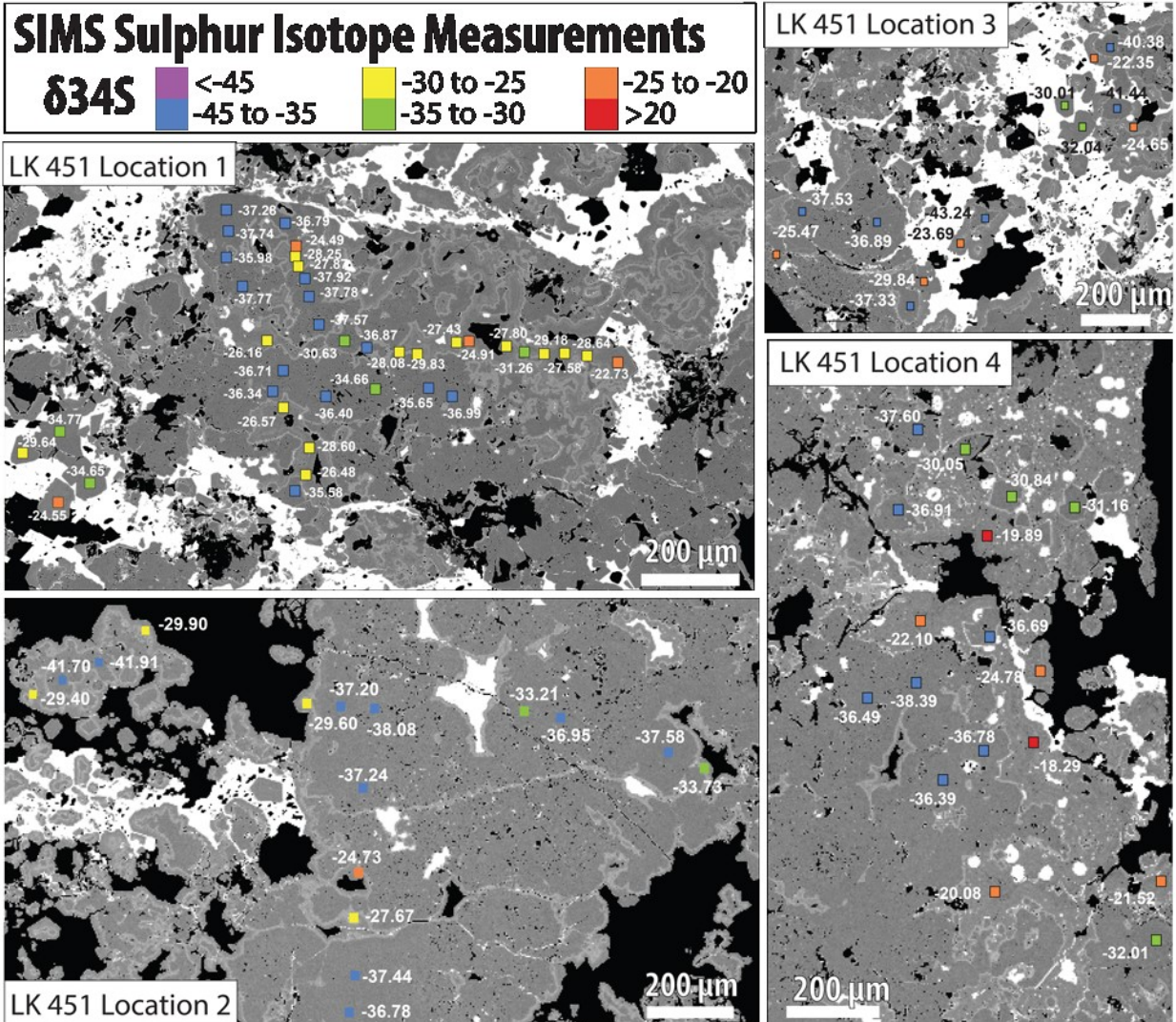


Figure 4.1.17: SIMS sulphur isotope measurements for the Bog Zone sample LK 451 along transects highlighted in Figure 4.1.13. Data points are scaled to the sizes of SIMS spots.

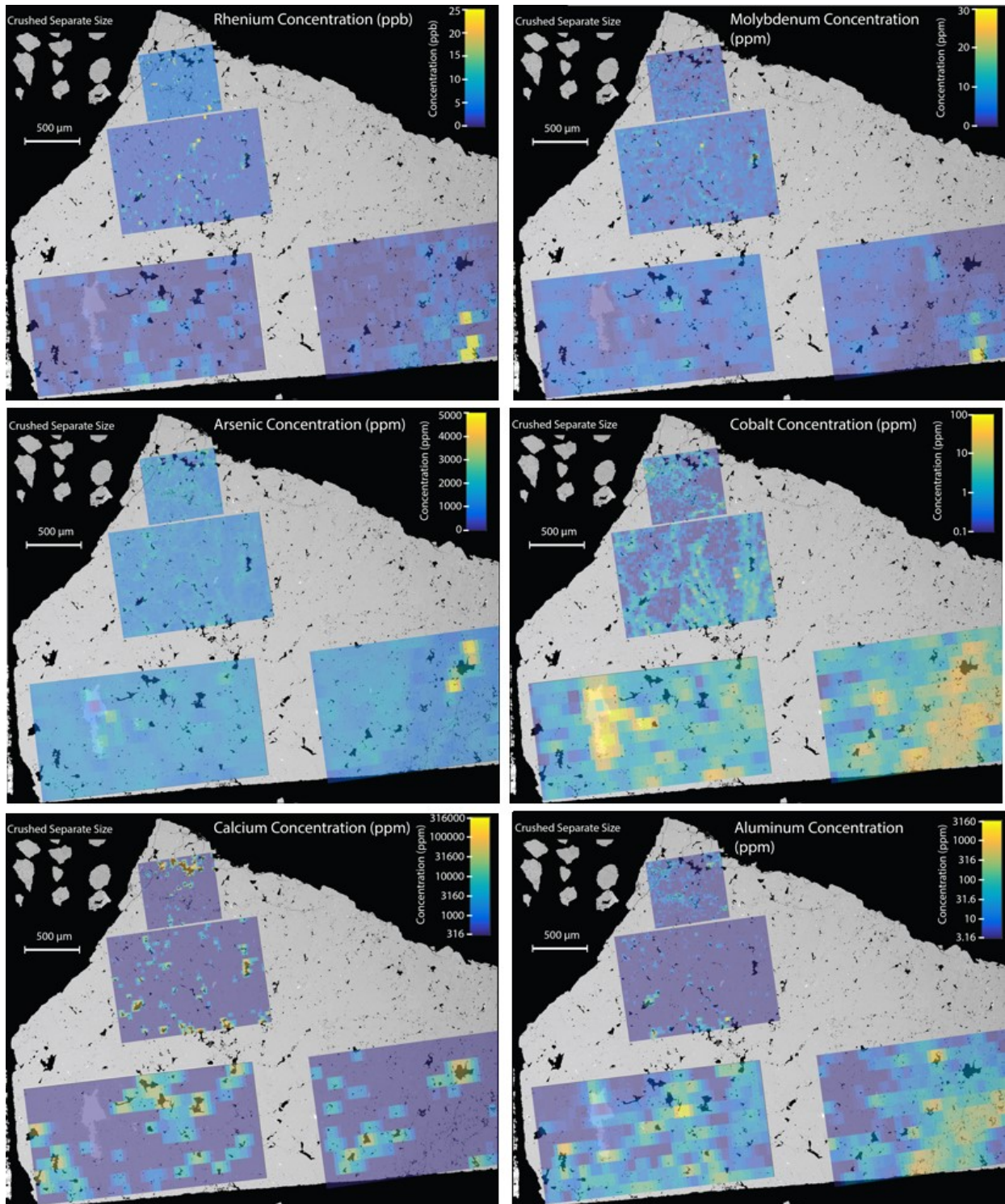


Figure 4.1.19: LA-ICPMS images for Lisheen Main Zone sample 8S08FW-1

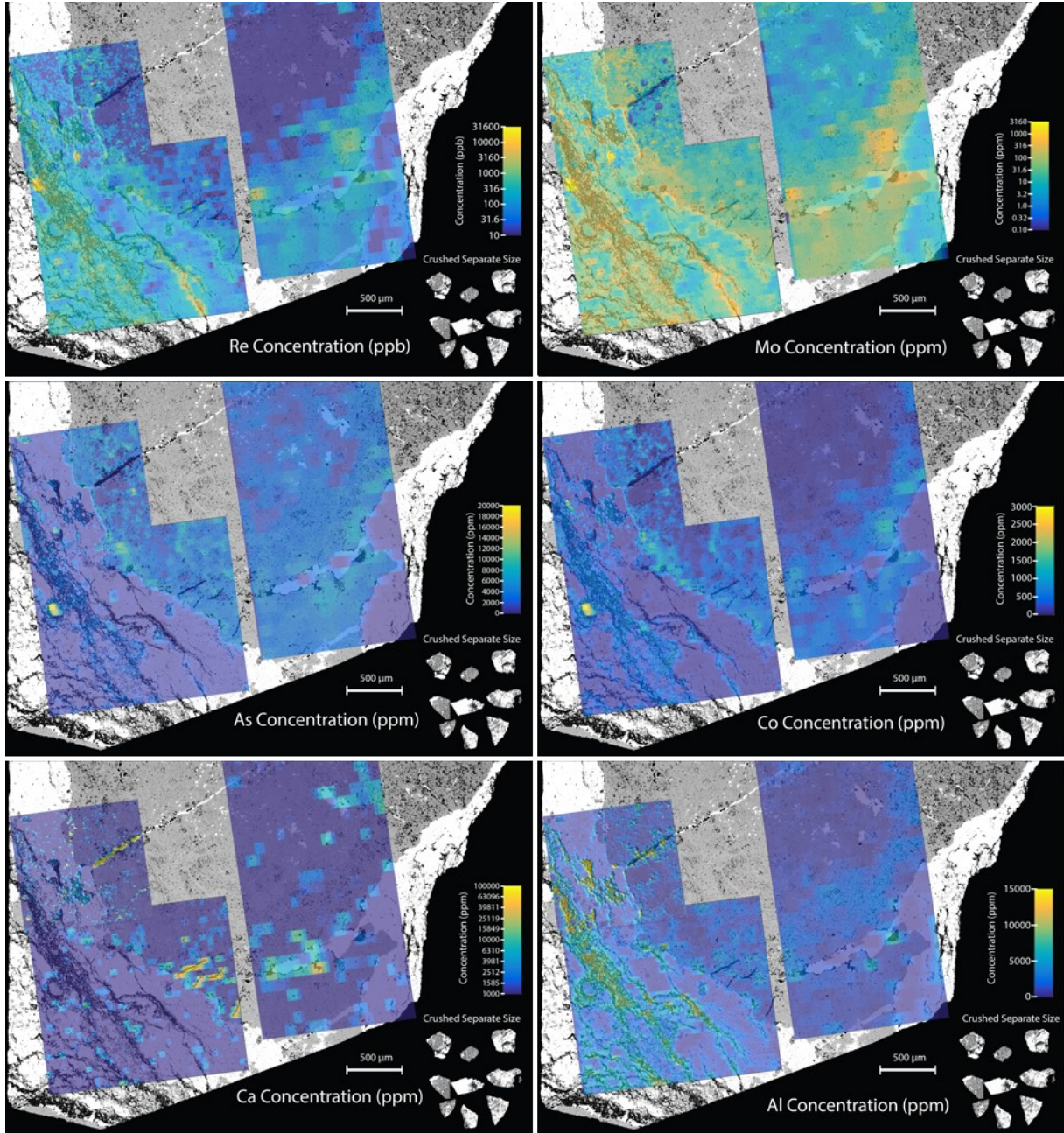


Figure 4.1.20: LA-ICPMS images for Lisheen Derryville Zone sample LK 359-1.

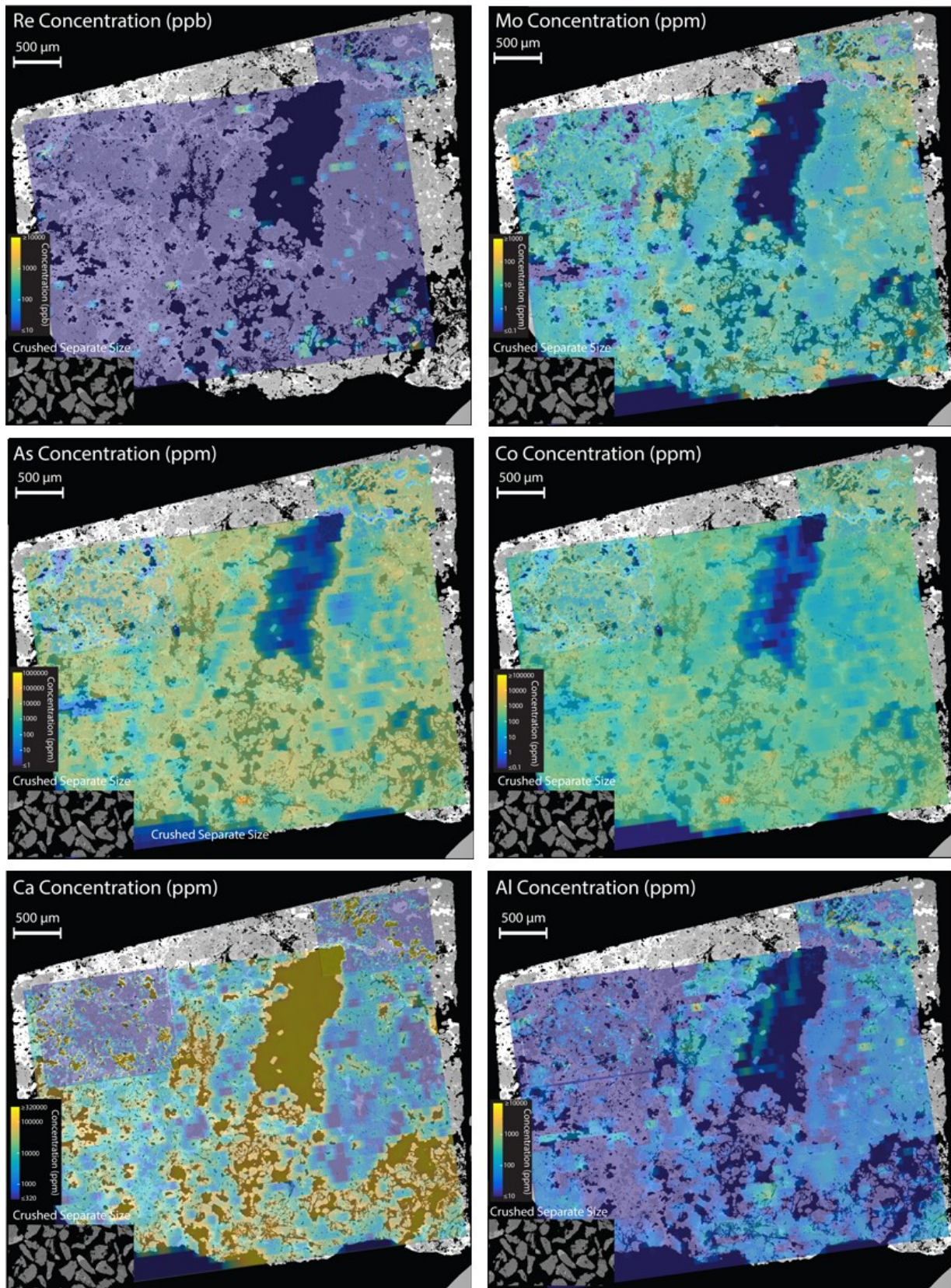


Figure 4.1.21: LA-ICPMS images for Lisheen Bog Zone sample LK 451.

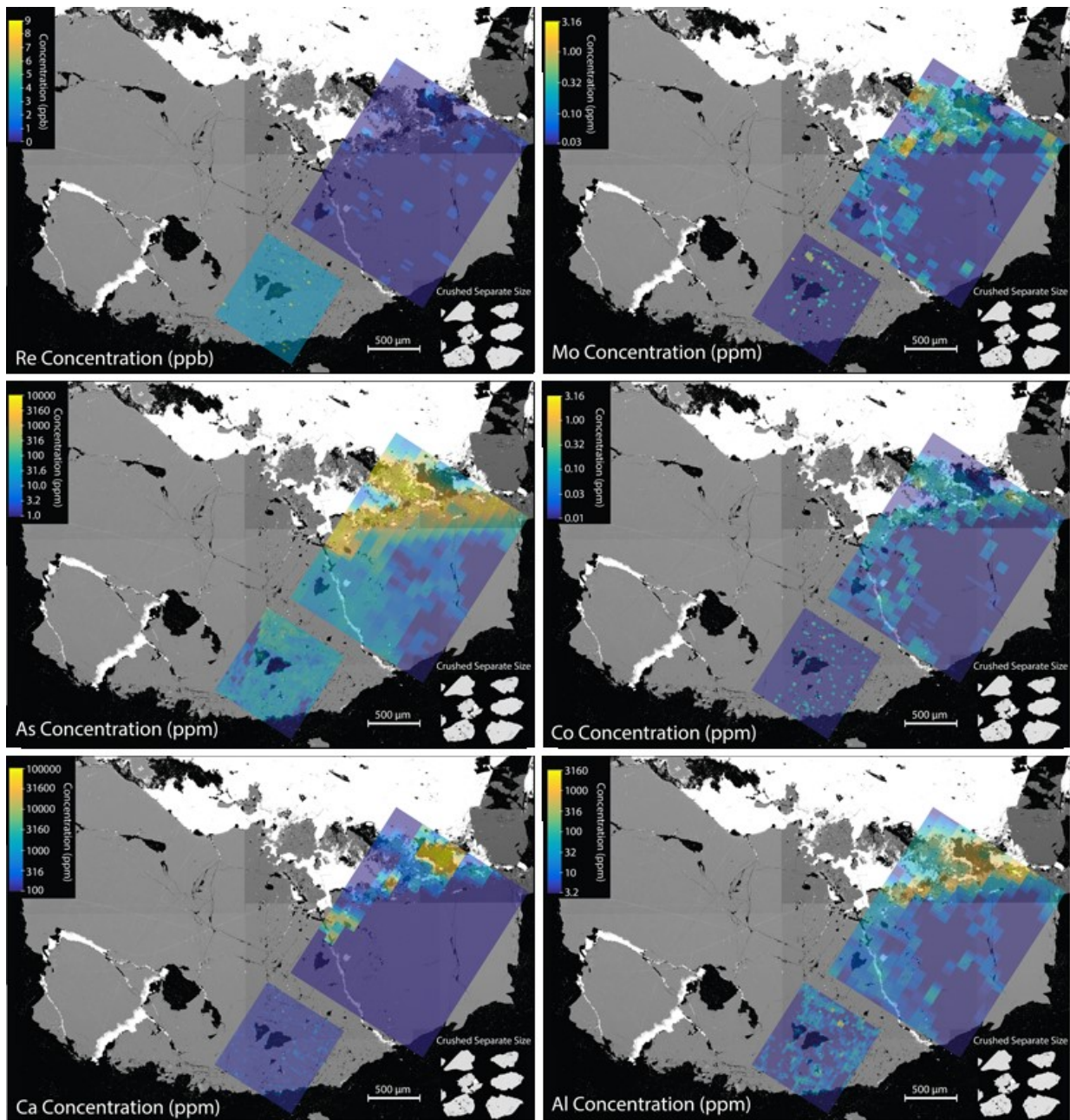


Figure 4.1.22: LA-ICPMS images for Nanisivik sample NOV-1.

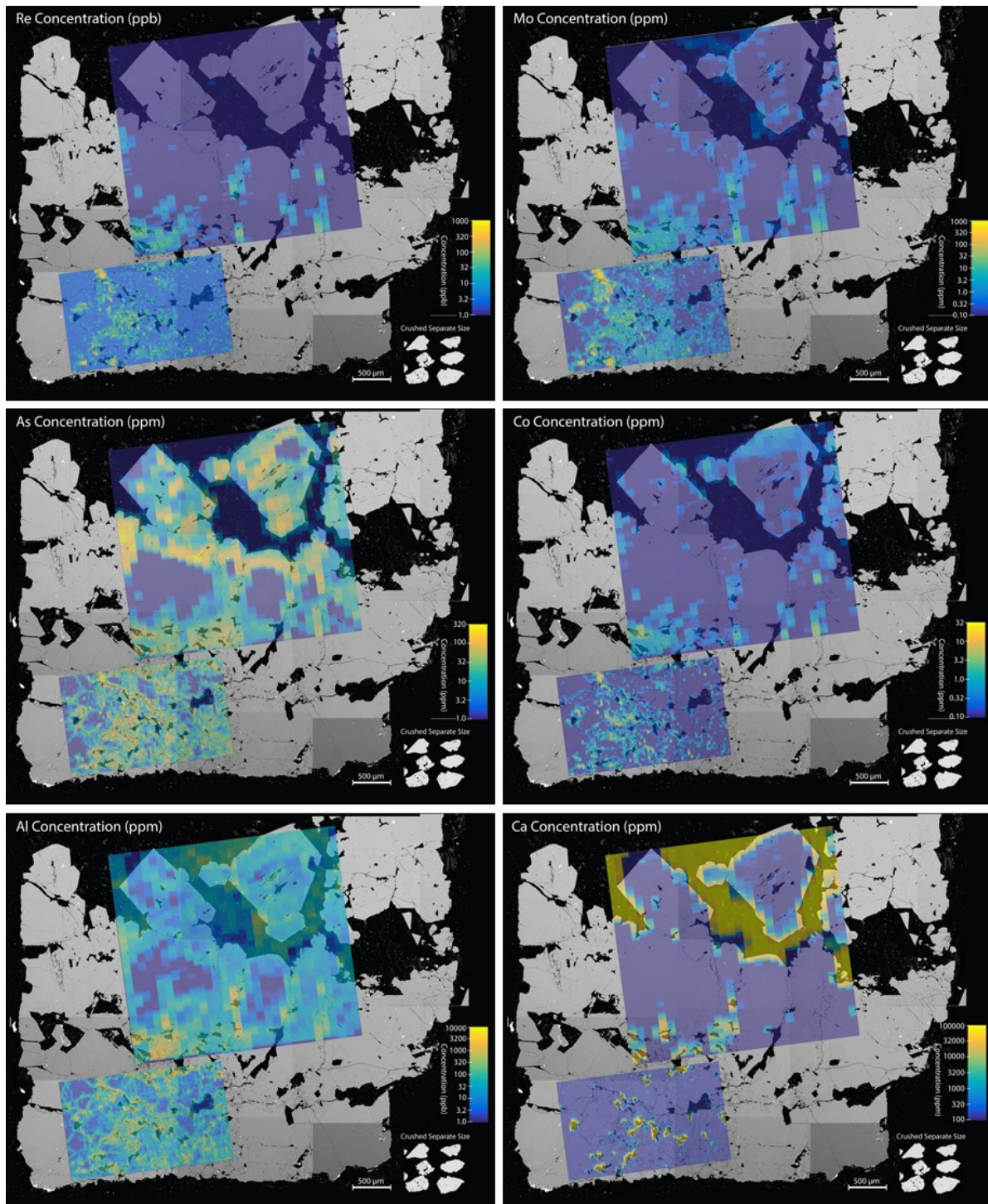


Figure 4.1.23: LA-ICPMS images for Nanisivik sample NOV-2.

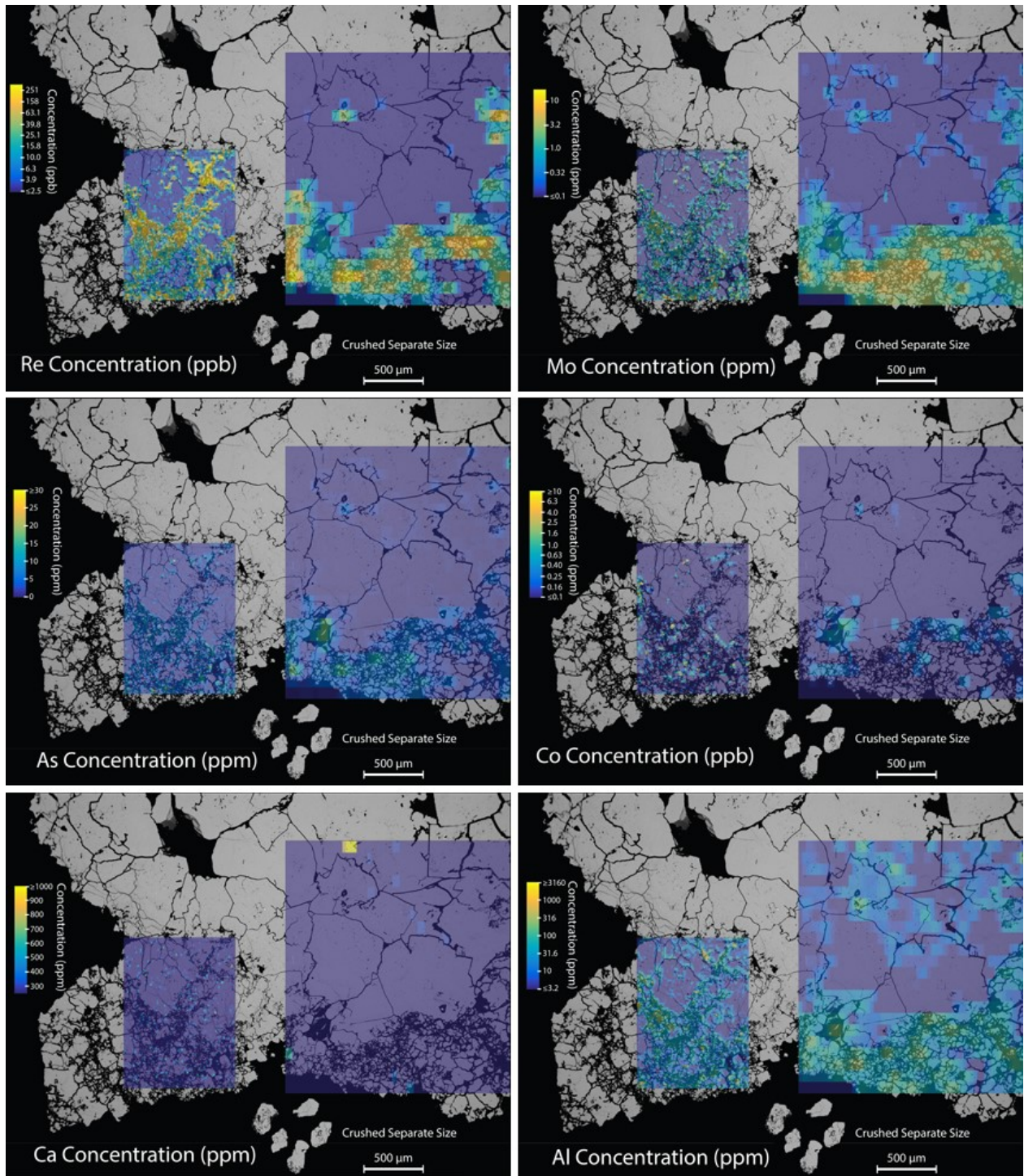


Figure 4.1.24: LA-ICPMS images for Hawker Creek sample HC.

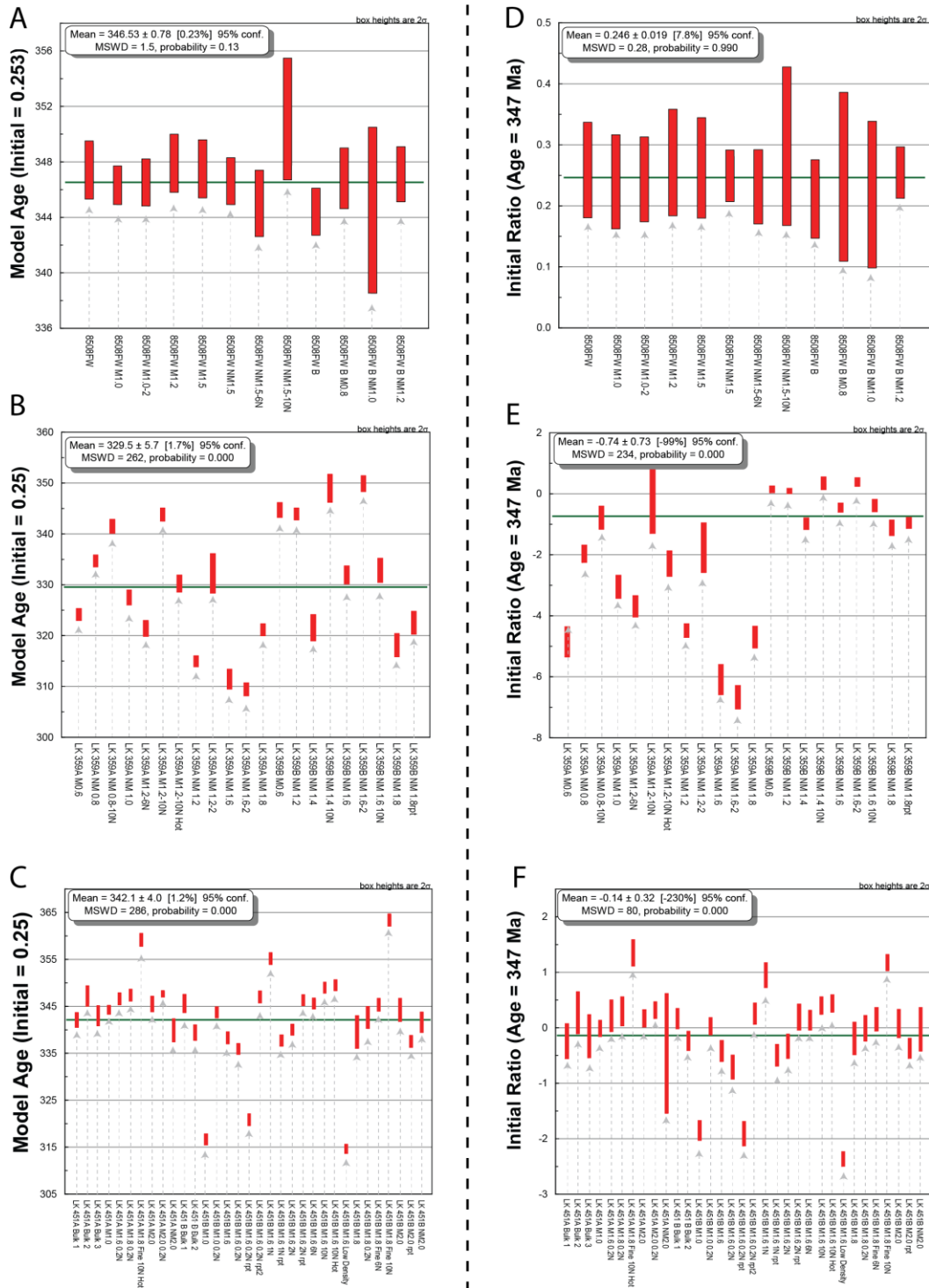


Figure 4.1.25: (A) Model age calculations for Main Zone sample 8S08FW (B) Model age calculations for Derryville Zone sample LK 359 (C) Model age calculations for Bog Zone sample LK 451 (D) Initial $^{187}\text{Os}/^{188}\text{Os}$ calculations for Main Zone sample 8S08FW (E) Initial $^{187}\text{Os}/^{188}\text{Os}$ calculations for Derryville Zone sample LK 359 (F) Initial $^{187}\text{Os}/^{188}\text{Os}$ calculations for Bog Zone sample LK 451. Dashed line separates Model Age calculations from Initial $^{187}\text{Os}/^{188}\text{Os}$ calculations.

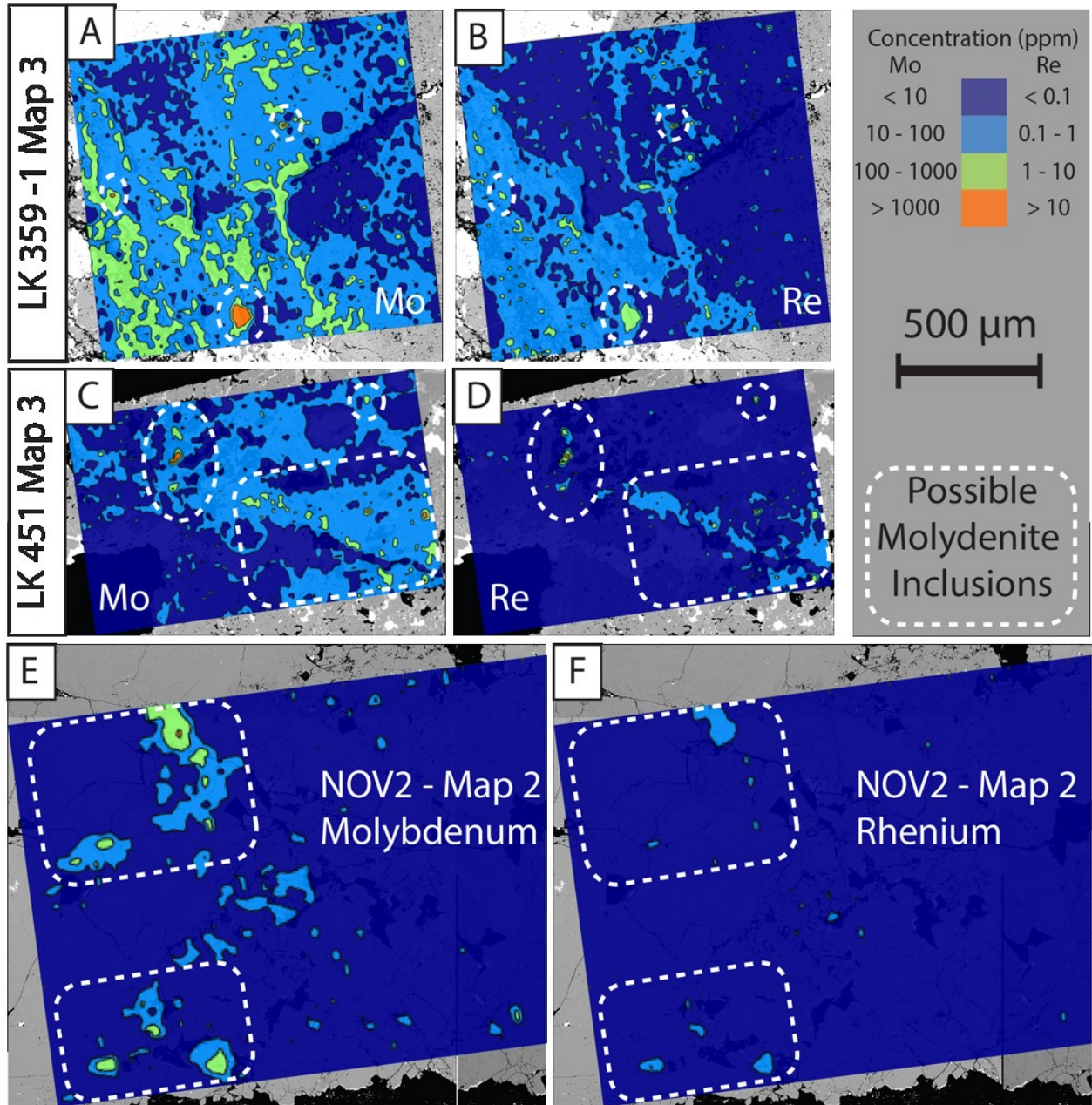


Figure 4.1.26: Areas containing anomalous Mo and Re contents that may indicate micron scale molybdenite crystals, (A) and (B) Derryville Zone sample LK 359-1 Map Location 3, (C) and (D) Bog Zone sample LK 451 Map Location 3, (E) and (F) Nanisivik sample NOV-1 Map Location 2. See Figure 4.1.13 for map locations.

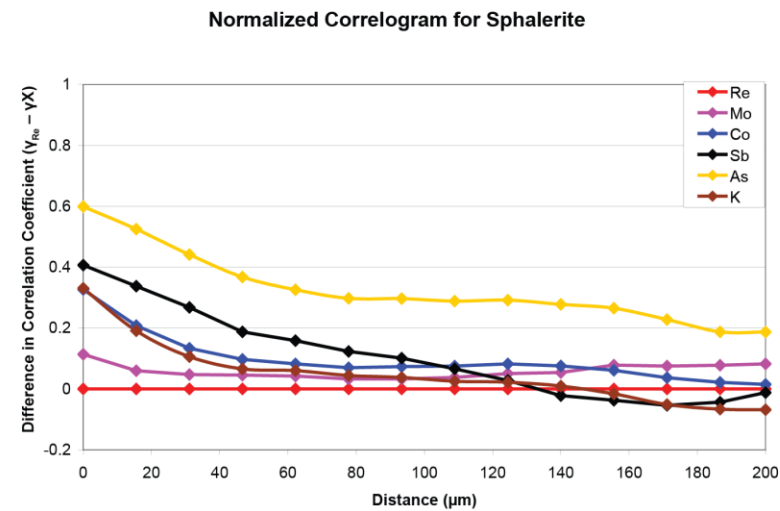
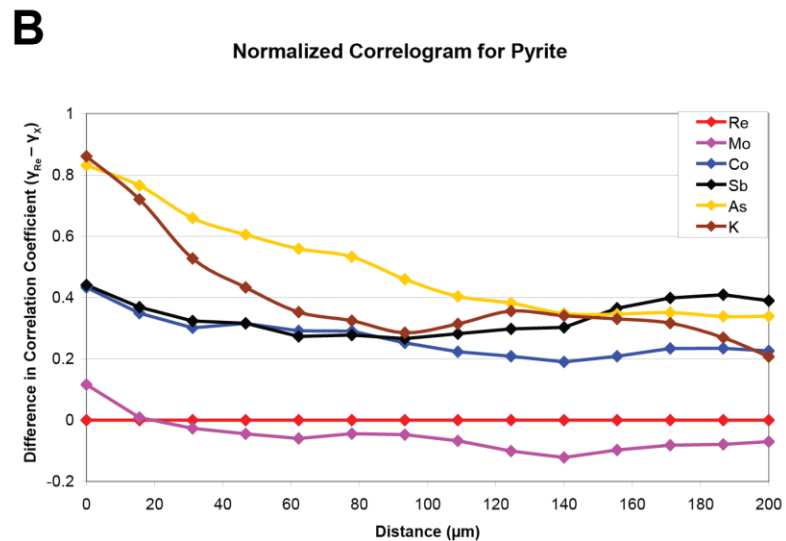
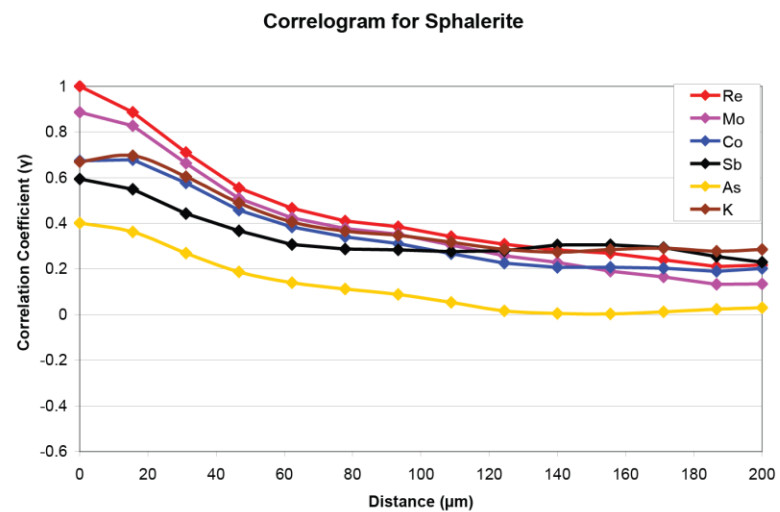
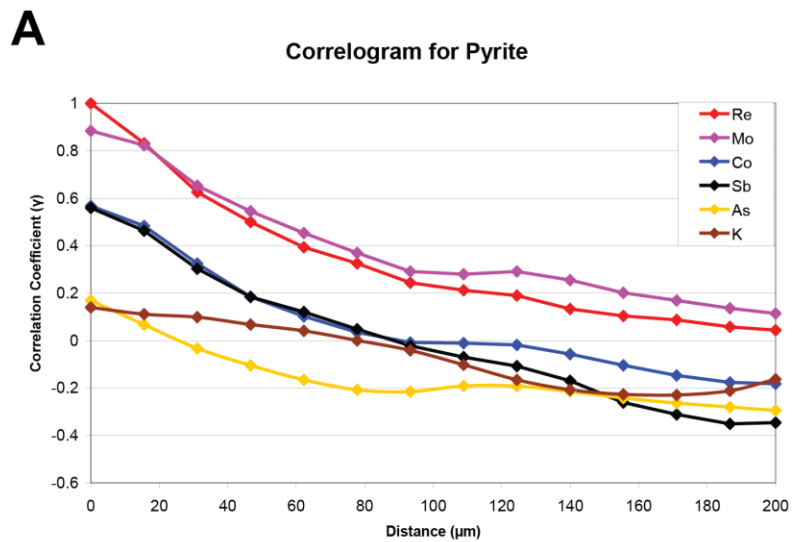


Figure 4.1.27: Correlograms for Derryville Sample LK 359. (A) Non-normalized. (B) Normalized to Re (Concentration of Re - Concentration of element X).

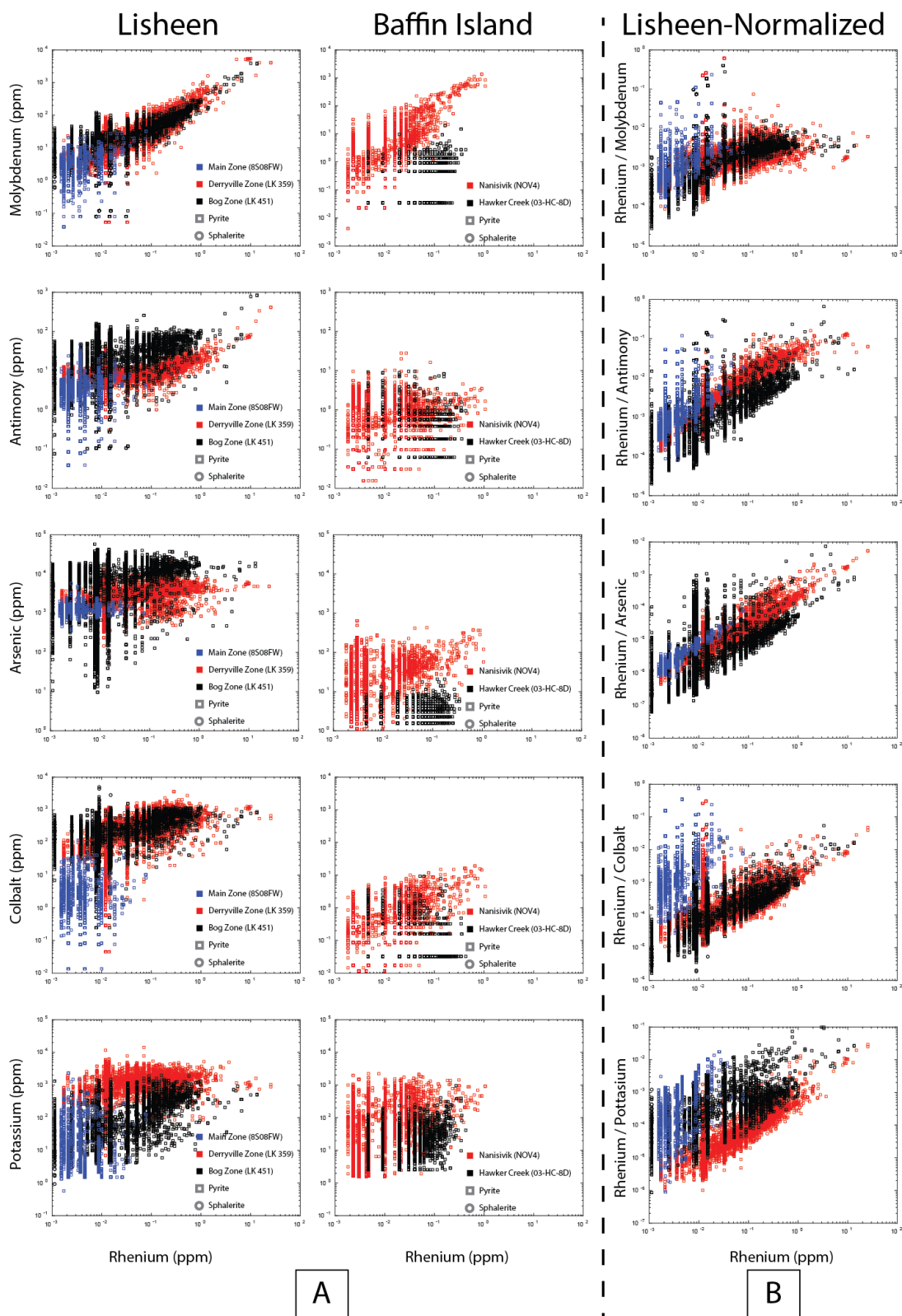


Figure 4.1.28: (A) Single pixel concentrations of selected elements (Mo, Sb, Co, As, and K) vs. Re from LA-ICPMS maps (B) Normalized y-axis (Re Concentration / Element X Concentration).

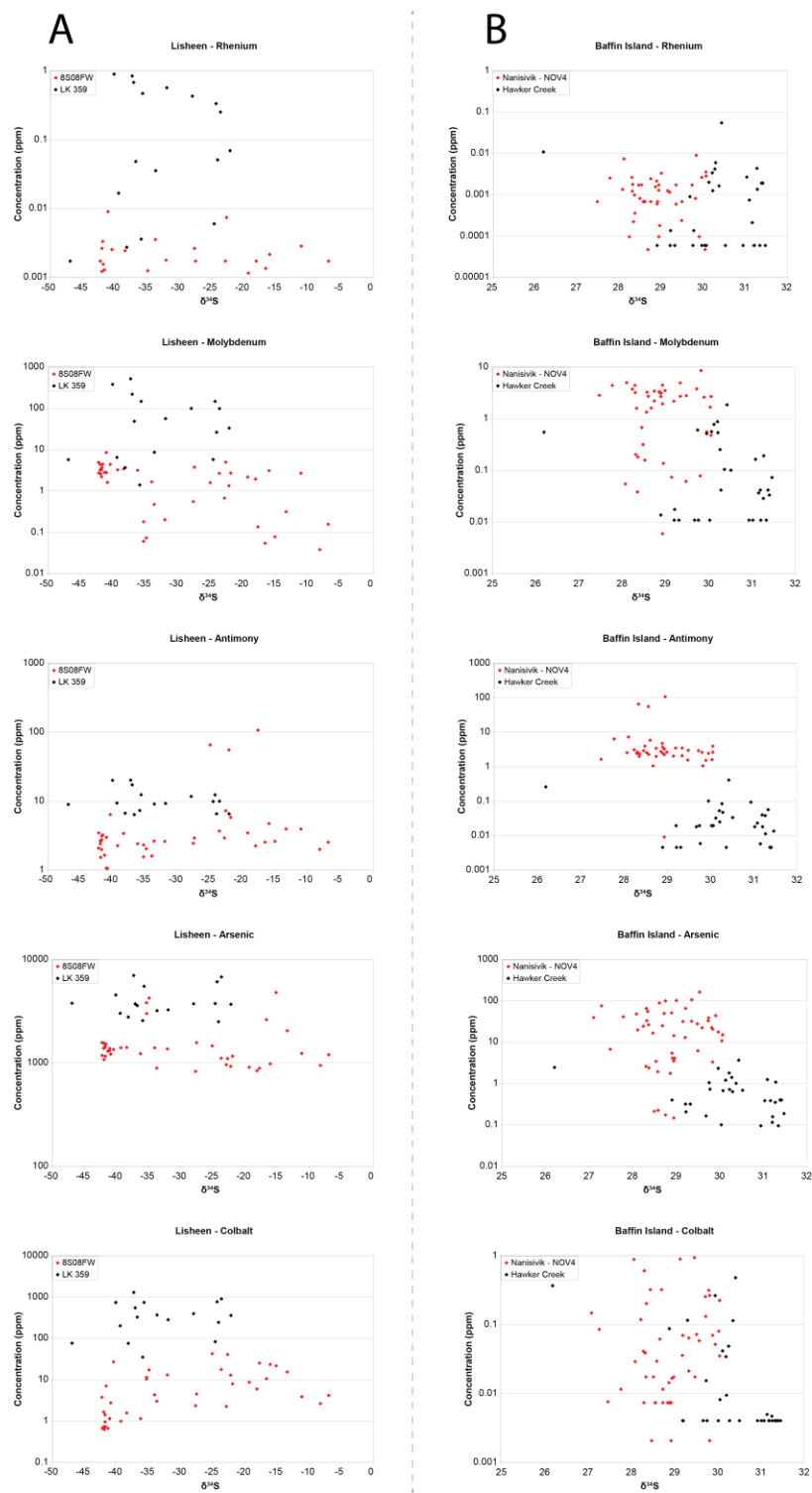


Figure 4.1.29: Sulphur Isotope Measurements vs. Trace Element Concentrations. Trace element concentrations were taken from the location that SIMS sulphur isotope measurements were taken. (A) Lisheen Data (B) Baffin Island Data.

Context and Information Provided

| Level Provided | 0 | 1 | 2 |
|---------------------------------------|---|---|---|
| (P) Paragenetic Context Knowledge | | | |
| (M) Mineral Separate Mineralogy Known | | | |
| (I) Isochron Assumptions Testing | | | |

Level 0 = Not documented
 Level 1 = Marginal: Some supplementary information given
 Level 2 = Well Documented: includes relevant supplementary information directly related to (P), (M), and (I) (e.g. petrographic, compositional images, ect...)

Quality Factor = Sum of levels + Result Type

Result Type

| | |
|---------------------------|---|
| Model 1 | A |
| Model 3 - Reasonable VIOs | B |
| Other | C |

A B

Lisheen Main Zone - 8S08FW

| Context and Information Provided | 0 | 1 | 2 |
|---------------------------------------|---|---|---|
| (P) Paragenetic Context Knowledge | | | ★ |
| (M) Mineral Separate Mineralogy Known | | | ★ |
| (I) Isochron Assumptions Testing | | | ★ |

| Result Type | |
|---------------------------|---|
| Model 1 | A |
| Model 3 - Reasonable VIOs | B |
| Other | C |

Quality Factor = 6B

Lisheen Derryville Zone - LK 359

| Context and Information Provided | 0 | 1 | 2 |
|---------------------------------------|---|---|---|
| (P) Paragenetic Context Knowledge | | | ★ |
| (M) Mineral Separate Mineralogy Known | | | ★ |
| (I) Isochron Assumptions Testing | | | ★ |

| Result Type | |
|---------------------------|---|
| Model 1 | A |
| Model 3 - Reasonable VIOs | B |
| Other | C |

Quality Factor = 6C

Nanisivik

| Context and Information Provided | 0 | 1 | 2 |
|---------------------------------------|---|---|---|
| (P) Paragenetic Context Knowledge | | | ★ |
| (M) Mineral Separate Mineralogy Known | | | ★ |
| (I) Isochron Assumptions Testing | | | ★ |

| Result Type | |
|---------------------------|---|
| Model 1 | A |
| Model 3 - Reasonable VIOs | B |
| Other | C |

Quality Factor = 6C

Hawker Creek

| Context and Information Provided | 0 | 1 | 2 |
|---------------------------------------|---|---|---|
| (P) Paragenetic Context Knowledge | | ★ | |
| (M) Mineral Separate Mineralogy Known | | | ★ |
| (I) Isochron Assumptions Testing | | | ★ |

| Result Type | |
|---------------------------|---|
| Model 1 | A |
| Model 3 - Reasonable VIOs | B |
| Other | C |

Quality Factor = 5C

Lisheen Bog Zone - LK 451

| Context and Information Provided | 0 | 1 | 2 |
|---------------------------------------|---|---|---|
| (P) Paragenetic Context Knowledge | | | ★ |
| (M) Mineral Separate Mineralogy Known | | | ★ |
| (I) Isochron Assumptions Testing | | | ★ |

| Result Type | |
|---------------------------|---|
| Model 1 | A |
| Model 3 - Reasonable VIOs | B |
| Other | C |

Quality Factor = 6C

Figure 4.1.30: Calculating a quality factor for the data provided in a publication (A) Description (B) Quality Factor for samples in this study.

4.1.9: Appendix:

Table 4.1.6: ICPMS mineral separate analyses for the Lisheen dataset

| Sample Name | | 8S08FW M1.0 | 8S08FW M1.2 | 8S08FW M1.5 | 8S08FW NM1.5 | LK 359A NM1.2 | LK 359A NM1.6 | LK 359A NM1.8 | LK 359B NM1.2 | LK 359B NM1.4 | LK 359B NM1.6 | LK 359B NM1.8 | LK 451B M1.6 | LK 451B M1.8 | LK 451B M2.0 |
|-------------|------------------|-------------|-------------|-------------|--------------|---------------|---------------|---------------|---------------|---------------|---------------|---------------|--------------|--------------|--------------|
| Analyte | Detection Limits | | | | | | | | | | | | | | |
| Re | ppb | 6.18 | 5.78 | 3.88 | 2.73 | 497.12 | 519.68 | 338.18 | 137.03 | 92.42 | 73.44 | 40.86 | 56.60 | 55.30 | 23.81 |
| 192Os | ppt | 9.84 | 9.54 | 7.76 | 8.91 | 112.21 | 97.16 | 58.81 | 87.13 | 63.55 | 52.31 | 28.57 | 24.55 | 31.11 | 15.43 |
| Li | 0.3 ppm | 0.62 | 3.55 | <DL | 0.49 | 3.74 | 5.48 | 9.73 | 2.44 | 2.41 | 4.35 | 4.27 | 9.95 | 2.91 | 2.66 |
| Be | 0.1 ppm | <DL | <DL | <DL | <DL | 0.62 | 0.64 | 3.03 | 0.27 | 0.33 | 1.09 | 1.37 | 0.44 | 0.13 | 0.12 |
| B | 2 ppm | <DL | <DL | <DL | <DL | <DL | <DL | <DL | <DL | <DL | <DL | <DL | 5.75 | <DL | <DL |
| V | 0.05 ppm | 3.92 | 3.32 | 1.74 | 1.08 | 28.04 | 20.73 | 9.64 | 41.96 | 36.84 | 30.19 | 7.70 | 114.40 | 56.07 | 43.45 |
| Cr | 0.05 ppm | 1.85 | 1.66 | 1.06 | 0.79 | 8.21 | 5.78 | 3.08 | 8.23 | 6.93 | 7.25 | 2.06 | 15.86 | 4.68 | 3.44 |
| Co | 0.03 ppm | 38.77 | 42.55 | 24.12 | 9.93 | 228.10 | 121.06 | 42.59 | 224.29 | 165.11 | 98.60 | 21.98 | 537.55 | 793.76 | 455.27 |
| Ni | 0.06 ppm | 99.38 | 108.94 | 55.89 | 22.25 | 668.88 | 333.63 | 94.95 | 698.31 | 570.78 | 330.71 | 56.02 | 1923.74 | 2772.55 | 1590.35 |
| Cu | 0.03 ppm | 47.56 | 46.61 | 41.27 | 37.92 | 8.14 | 10.25 | 13.05 | 10.98 | 9.48 | 11.17 | 11.35 | 35.86 | 39.39 | 30.29 |
| Zn | 0.08 ppm | 8338 | 4946 | 1307 | 758 | 196643 | 308117 | 396620 | 105045 | 86691 | 185392 | 249523 | 105209 | 49424 | 19208 |
| Ga | 0.01 ppm | 1.21 | 1.02 | 0.76 | 0.70 | 4.14 | 5.60 | 6.14 | 3.04 | 2.84 | 5.10 | 6.30 | 4.48 | 1.31 | 0.92 |
| As | 0.06 ppm | 1912 | 2034 | 1539 | 1195 | 2484 | 1021 | 373 | 2502 | 1812 | 1118 | 316 | 4560 | 7612 | 5802 |
| Rb | 0.04 ppm | 2.25 | 1.80 | 0.90 | 0.50 | 5.55 | 3.85 | 2.01 | 7.53 | 7.61 | 6.44 | 1.98 | 31.73 | 7.73 | 5.07 |
| Sr | 0.03 ppm | 48.16 | 33.48 | 26.93 | 57.15 | 3.00 | 2.08 | 0.90 | 4.46 | 4.68 | 4.52 | 1.07 | 23.25 | 6.15 | 6.55 |
| Y | 0.02 ppm | 0.25 | 0.16 | 0.09 | 0.20 | 0.95 | 0.72 | 0.36 | 1.86 | 1.81 | 1.86 | 0.50 | 1.79 | 0.51 | 0.48 |
| Zr | 0.09 ppm | 7.59 | 8.78 | 5.05 | 3.80 | 10.18 | 5.85 | 2.75 | 10.72 | 8.81 | 6.24 | 2.22 | 18.39 | 15.89 | 11.99 |
| Nb | 0.04 ppm | 0.22 | 0.19 | 0.10 | 0.05 | 0.47 | 0.39 | 0.24 | 0.57 | 0.44 | 0.37 | 0.16 | 1.61 | 0.34 | 0.22 |
| Sb | 0.01 ppm | 4.51 | 4.41 | 3.31 | 2.96 | 13.52 | 15.65 | 16.03 | 11.00 | 10.60 | 11.05 | 22.10 | 33.09 | 43.97 | 29.08 |
| Ba | 0.03 ppm | 78.02 | 70.99 | 54.09 | 51.48 | 58.82 | 33.93 | 10.51 | 75.31 | 71.71 | 61.18 | 4.10 | 125.73 | 20.18 | 14.07 |
| La | 0.03 ppm | 0.46 | 0.29 | 0.16 | 0.39 | 0.48 | 0.42 | 0.20 | 1.37 | 1.37 | 1.39 | 0.33 | 1.55 | 0.49 | 0.46 |
| Nd | 0.03 ppm | 0.24 | 0.15 | 0.10 | 0.30 | 0.74 | 0.58 | 0.29 | 1.75 | 1.86 | 2.08 | 0.55 | 1.60 | 0.56 | 0.58 |
| Eu | 0.03 ppm | 0.07 | 0.06 | 0.04 | 0.06 | 0.04 | 0.03 | 0.03 | 0.08 | 0.08 | 0.09 | <DL | 0.09 | <DL | <DL |
| Gd | 0.03 ppm | 0.05 | 0.03 | <DL | 0.06 | 0.20 | 0.15 | 0.07 | 0.38 | 0.39 | 0.44 | 0.11 | 0.32 | 0.11 | 0.12 |
| Dy | 0.04 ppm | 0.04 | <DL | <DL | <DL | 0.15 | 0.12 | <DL | 0.28 | 0.29 | 0.32 | 0.09 | 0.34 | 0.10 | 0.10 |
| Ho | 0.02 ppm | <DL | <DL | <DL | <DL | 0.03 | 0.02 | <DL | 0.06 | 0.05 | 0.06 | <DL | 0.07 | 0.02 | 0.02 |
| Yb | 0.05 ppm | <DL | <DL | <DL | <DL | 0.06 | 0.05 | <DL | 0.07 | 0.07 | 0.07 | <DL | 0.21 | 0.05 | <DL |
| Pb | 0.03 ppm | 1047 | 1098 | 1137 | 1810 | N/A | 10458 | 11741 | 8125 |

Table 4.1.7: ICPMS mineral separate analyses for the Baffin Island dataset

| Sample Name | | 04-N-2 M1.0 | 04-N-2 M2.0 | 04-N-2 NM2.0 | 03-HC-8D M0.8 | 03-HC-8D M1.25 | 03-HC-8D M2.0 | 03-HC-8D NM2.0 |
|-------------|------------------|-------------|-------------|--------------|---------------|----------------|---------------|----------------|
| Analyte | Detection Limits | | | | | | | |
| Re | ppb | 0.80 | 0.60 | 0.21 | 20.34 | 3.62 | 1.18 | 0.44 |
| 192Os | ppt | 4.35 | 3.46 | 1.35 | 2.08 | 0.65 | 0.34 | 0.08 |
| Li | 0.3 ppm | <DL | <DL | <DL | <DL | <DL | <DL | <DL |
| Be | 0.1 ppm | N/A | N/A | N/A | N/A | N/A | N/A | N/A |
| B | 2 ppm | N/A | N/A | N/A | N/A | N/A | N/A | N/A |
| V | 0.05 ppm | 3.36 | 1.79 | 1.57 | 0.40 | 0.61 | 0.45 | 0.29 |
| Cr | 0.05 ppm | 0.57 | 0.65 | 0.58 | 1.59 | 0.85 | 0.40 | 0.41 |
| Co | 0.03 ppm | 0.81 | 0.29 | 0.13 | 0.24 | 0.06 | 0.09 | 0.04 |
| Ni | 0.06 ppm | 9.37 | 2.48 | 1.01 | 1.23 | 0.33 | 0.31 | 0.25 |
| Cu | 0.03 ppm | 2.00 | 1.46 | 0.91 | 2.30 | 1.30 | 1.15 | 1.12 |
| Zn | 0.08 ppm | 51580 | 249 | 150 | 254 | 205 | 97 | 76 |
| Ga | 0.01 ppm | 1.10 | 0.62 | 0.65 | 0.19 | 0.15 | 0.32 | 0.12 |
| As | 0.06 ppm | 12.36 | 9.09 | 4.46 | 4.86 | 1.16 | 1.91 | 0.73 |
| Rb | 0.04 ppm | 0.12 | 0.05 | <DL | <DL | <DL | 0.03 | <DL |
| Sr | 0.03 ppm | 15.78 | 4.41 | 1.83 | 0.65 | 0.67 | 0.84 | 0.47 |
| Y | 0.02 ppm | 0.45 | 0.11 | 0.06 | 0.01 | 0.01 | 0.02 | 0.01 |
| Zr | 0.09 ppm | 0.37 | 0.27 | 0.18 | 0.21 | <DL | 0.19 | <DL |
| Nb | 0.04 ppm | 0.05 | <DL | <DL | <DL | <DL | <DL | <DL |
| Sb | 0.01 ppm | 0.11 | 0.07 | 0.03 | 0.39 | 0.06 | 0.05 | 0.02 |
| Ba | 0.03 ppm | 2.87 | 1.92 | 1.48 | 0.54 | 0.63 | 0.70 | 0.38 |
| La | 0.03 ppm | 0.12 | 0.03 | <DL | <DL | <DL | 0.04 | <DL |
| Nd | 0.03 ppm | 0.24 | 0.06 | 0.06 | <DL | <DL | <DL | <DL |
| Eu | 0.03 ppm | N/A | N/A | N/A | N/A | N/A | N/A | N/A |
| Gd | 0.03 ppm | 0.13 | 0.03 | <DL | <DL | <DL | 0.01 | <DL |
| Dy | 0.04 ppm | 0.08 | <DL | <DL | <DL | <DL | <DL | <DL |
| Ho | 0.02 ppm | N/A | N/A | N/A | N/A | N/A | N/A | N/A |
| Yb | 0.05 ppm | N/A | N/A | N/A | N/A | N/A | N/A | N/A |
| Pb | 0.03 ppm | 316.07 | 263.83 | 170.82 | 129.36 | 111.57 | 129.03 | 52.91 |

Table 4.1.8: SIMS Sulphur isotope analyses of 8S08FW mineral separates

| Name | Type | Session | $^{34}\text{S}/^{32}\text{S}$ | 1σ (%) intra- session | $\delta^{34}\text{S}$ (VCDT) | 2σ (%) inter- session |
|--------------|------|---------|-------------------------------|------------------------------------|---------------------------------|------------------------------------|
| 8S08FW M0.8 | MS | 1 | 0.04223708 | 0.00687 | -43.60 | 0.14 |
| 8S08FW M0.8 | MS | 1 | 0.04232883 | 0.00659 | -41.52 | 0.13 |
| 8S08FW M0.8 | MS | 1 | 0.04312045 | 0.00643 | -23.60 | 0.13 |
| 8S08FW M0.8 | MS | 1 | 0.04234759 | 0.00702 | -41.10 | 0.14 |
| 8S08FW M0.8 | MS | 1 | 0.04243688 | 0.00709 | -39.08 | 0.14 |
| 8S08FW M0.8 | MS | 1 | 0.04241291 | 0.00713 | -39.62 | 0.14 |
| 8S08FW M0.8 | MS | 1 | 0.04298212 | 0.00672 | -26.73 | 0.13 |
| 8S08FW M0.8 | MS | 1 | 0.04256229 | 0.00668 | -36.24 | 0.13 |
| 8S08FW M0.8 | MS | 1 | 0.04233773 | 0.00821 | -41.32 | 0.16 |
| 8S08FW M0.8 | MS | 1 | 0.04250238 | 0.00644 | -37.59 | 0.13 |
| 8S08FW M0.8 | MS | 1 | 0.04244052 | 0.01310 | -38.99 | 0.26 |
| 8S08FW M0.8 | MS | 1 | 0.04344540 | 0.00717 | -16.24 | 0.14 |
| 8S08FW M0.8 | MS | 1 | 0.04236389 | 0.00776 | -40.73 | 0.16 |
| 8S08FW M0.8 | MS | 1 | 0.04342828 | 0.00834 | -16.63 | 0.17 |
| 8S08FW M0.8 | MS | 1 | 0.04232621 | 0.00720 | -41.58 | 0.14 |
| 8S08FW M0.8 | MS | 1 | 0.04233870 | 0.00655 | -41.30 | 0.13 |
| 8S08FW M0.8 | MS | 1 | 0.04332298 | 0.01146 | -19.01 | 0.23 |
| 8S08FW M0.8 | MS | 1 | 0.04333522 | 0.00573 | -18.73 | 0.12 |
| 8S08FW M0.8 | MS | 1 | 0.04319016 | 0.00789 | -22.02 | 0.16 |
| 8S08FW M0.8 | MS | 1 | 0.04336437 | 0.00697 | -18.07 | 0.14 |
| 8S08FW M0.8 | MS | 1 | 0.04357137 | 0.00770 | -13.39 | 0.15 |
| 8S08FW M0.8 | MS | 1 | 0.04301199 | 0.00746 | -26.05 | 0.15 |
| 8S08FW M0.8 | MS | 1 | 0.04229405 | 0.00760 | -42.31 | 0.15 |
| 8S08FW M0.8 | MS | 1 | 0.04335833 | 0.00594 | -18.21 | 0.12 |
| 8S08FW M0.8 | MS | 1 | 0.04356498 | 0.00771 | -13.53 | 0.15 |
| 8S08FW NM2.0 | MS | 1 | 0.04331996 | 0.00750 | -19.08 | 0.15 |
| 8S08FW NM2.0 | MS | 1 | 0.04235396 | 0.00742 | -40.95 | 0.15 |
| 8S08FW NM2.0 | MS | 1 | 0.04236496 | 0.00751 | -40.70 | 0.15 |
| 8S08FW NM2.0 | MS | 1 | 0.04232130 | 0.00689 | -41.69 | 0.14 |
| 8S08FW NM2.0 | MS | 1 | 0.04228204 | 0.00708 | -42.58 | 0.14 |
| 8S08FW NM2.0 | MS | 1 | 0.04230218 | 0.00667 | -42.13 | 0.13 |
| 8S08FW NM2.0 | MS | 1 | 0.04328041 | 0.00735 | -19.97 | 0.15 |
| 8S08FW NM2.0 | MS | 1 | 0.04225457 | 0.00711 | -43.20 | 0.14 |
| 8S08FW NM2.0 | MS | 1 | 0.04230801 | 0.00646 | -41.99 | 0.13 |
| 8S08FW NM2.0 | MS | 1 | 0.04247885 | 0.00917 | -38.13 | 0.18 |
| 8S08FW NM2.0 | MS | 1 | 0.04356880 | 0.01010 | -13.44 | 0.20 |
| 8S08FW NM2.0 | MS | 1 | 0.04238436 | 0.00787 | -40.26 | 0.16 |
| 8S08FW NM2.0 | MS | 1 | 0.04309481 | 0.00973 | -24.18 | 0.19 |
| 8S08FW NM2.0 | MS | 1 | 0.04337386 | 0.01081 | -17.86 | 0.22 |
| 8S08FW NM2.0 | MS | 1 | 0.04229901 | 0.00741 | -42.20 | 0.15 |
| 8S08FW NM2.0 | MS | 1 | 0.04234783 | 0.00675 | -41.09 | 0.14 |
| 8S08FW NM2.0 | MS | 1 | 0.04237418 | 0.00695 | -40.50 | 0.14 |
| 8S08FW NM2.0 | MS | 1 | 0.04325964 | 0.00703 | -20.45 | 0.14 |
| 8S08FW NM2.0 | MS | 1 | 0.04230793 | 0.00709 | -42.00 | 0.14 |
| 8S08FW NM2.0 | MS | 1 | 0.04233280 | 0.00700 | -41.43 | 0.14 |
| 8S08FW NM2.0 | MS | 1 | 0.04234041 | 0.00687 | -41.26 | 0.14 |
| 8S08FW NM2.0 | MS | 1 | 0.04327751 | 0.00625 | -20.04 | 0.13 |
| 8S08FW NM2.0 | MS | 1 | 0.04231157 | 0.00710 | -41.91 | 0.14 |
| 8S08FW NM2.0 | MS | 1 | 0.04235935 | 0.00689 | -40.83 | 0.14 |
| 8S08FW NM2.0 | MS | 1 | 0.04216705 | 0.00667 | -45.19 | 0.13 |

*MS = Mineral Separate

Table 4.1.9: SIMS sulphur isotope analyses of 8S08FW-1

| Name | Type | Session | $^{34}\text{S}/^{32}\text{S}$ | 1σ (%) intra- session | $\delta^{34}\text{S}$ (VCDT) | 2σ (‰) inter- session |
|---------------------|------|---------|-------------------------------|------------------------------------|---------------------------------|------------------------------------|
| 8S08FW - Transect 1 | RF | 2 | 0.042306 | 0.00566 | -42.03 | 0.11 |
| 8S08FW - Transect 1 | RF | 2 | 0.042314 | 0.00657 | -41.86 | 0.13 |
| 8S08FW - Transect 1 | RF | 2 | 0.042308 | 0.00544 | -41.99 | 0.11 |
| 8S08FW - Transect 1 | RF | 2 | 0.042298 | 0.00633 | -42.21 | 0.13 |
| 8S08FW - Transect 1 | RF | 2 | 0.042312 | 0.00639 | -41.91 | 0.13 |
| 8S08FW - Transect 1 | RF | 2 | 0.043195 | 0.00581 | -21.91 | 0.12 |
| 8S08FW - Transect 1 | RF | 2 | 0.043055 | 0.00698 | -25.07 | 0.14 |
| 8S08FW - Transect 1 | RF | 2 | 0.042376 | 0.00564 | -40.44 | 0.11 |
| 8S08FW - Transect 1 | RF | 2 | 0.042467 | 0.00664 | -38.40 | 0.13 |
| 8S08FW - Transect 1 | RF | 2 | 0.042426 | 0.00580 | -39.32 | 0.12 |
| 8S08FW - Transect 1 | RF | 2 | 0.042318 | 0.00600 | -41.78 | 0.12 |
| 8S08FW - Transect 1 | RF | 2 | 0.042562 | 0.00538 | -36.24 | 0.11 |
| 8S08FW - Transect 1 | RF | 2 | 0.042325 | 0.00590 | -41.61 | 0.12 |
| 8S08FW - Transect 1 | RF | 2 | 0.042338 | 0.00654 | -41.32 | 0.13 |
| 8S08FW - Transect 2 | RF | 2 | 0.04232 | 0.00598 | -41.72 | 0.12 |
| 8S08FW - Transect 2 | RF | 2 | 0.042351 | 0.00818 | -41.03 | 0.16 |
| 8S08FW - Transect 2 | RF | 2 | 0.042317 | 0.00694 | -41.78 | 0.14 |
| 8S08FW - Transect 2 | RF | 2 | 0.043182 | 0.00687 | -22.20 | 0.14 |
| 8S08FW - Transect 2 | RF | 2 | 0.04338 | 0.00644 | -17.73 | 0.13 |
| 8S08FW - Transect 2 | RF | 2 | 0.043117 | 0.00621 | -23.67 | 0.12 |
| 8S08FW - Transect 3 | RF | 2 | 0.042309 | 0.00698 | -41.97 | 0.14 |
| 8S08FW - Transect 3 | RF | 2 | 0.042297 | 0.00670 | -42.25 | 0.13 |
| 8S08FW - Transect 3 | RF | 2 | 0.042948 | 0.01150 | -27.50 | 0.23 |
| 8S08FW - Transect 3 | RF | 2 | 0.043671 | 0.00614 | -11.13 | 0.12 |
| 8S08FW - Transect 3 | RF | 2 | 0.043152 | 0.00715 | -22.88 | 0.14 |
| 8S08FW - Transect 3 | RF | 2 | 0.042941 | 0.00832 | -27.67 | 0.17 |
| 8S08FW - Transect 3 | RF | 2 | 0.042674 | 0.01312 | -33.71 | 0.26 |
| 8S08FW - Transect 3 | RF | 2 | 0.042747 | 0.01764 | -32.06 | 0.35 |
| 8S08FW - Transect 4 | RF | 2 | 0.044227 | 0.00831 | 1.46 | 0.17 |
| 8S08FW - Transect 4 | RF | 2 | 0.044469 | 0.00698 | 6.93 | 0.14 |
| 8S08FW - Transect 4 | RF | 2 | 0.044525 | 0.00591 | 8.22 | 0.12 |
| 8S08FW - Transect 4 | RF | 2 | 0.043428 | 0.00591 | -16.64 | 0.12 |
| 8S08FW - Transect 4 | RF | 2 | 0.043495 | 0.00849 | -15.12 | 0.17 |
| 8S08FW - Transect 4 | RF | 2 | 0.042621 | 0.00636 | -34.91 | 0.13 |
| 8S08FW - Transect 4 | RF | 2 | 0.042603 | 0.00739 | -35.32 | 0.15 |
| 8S08FW - Transect 4 | RF | 2 | 0.042603 | 0.00535 | -35.31 | 0.11 |
| 8S08FW - Transect 4 | RF | 2 | 0.043571 | 0.00641 | -13.40 | 0.13 |
| 8S08FW - Transect 4 | RF | 2 | 0.043363 | 0.00554 | -18.10 | 0.11 |
| 8S08FW - Transect 4 | RF | 2 | 0.043309 | 0.00623 | -19.32 | 0.12 |
| 8S08FW - Transect 4 | RF | 2 | 0.043454 | 0.00676 | -16.04 | 0.14 |
| 8S08FW - Transect 4 | RF | 2 | 0.043161 | 0.01001 | -22.69 | 0.20 |
| 8S08FW - Transect 4 | RF | 2 | 0.042658 | 0.00594 | -34.06 | 0.12 |
| 8S08FW - Transect 4 | RF | 2 | 0.042357 | 0.00597 | -40.89 | 0.12 |
| 8S08FW - Transect 4 | RF | 2 | 0.04235 | 0.00672 | -41.05 | 0.13 |
| 8S08FW - Transect 5 | RF | 2 | 0.042451 | 0.00841 | -38.76 | 0.17 |
| 8S08FW - Transect 5 | RF | 2 | 0.042305 | 0.00613 | -42.07 | 0.12 |
| 8S08FW - Transect 5 | RF | 2 | 0.042343 | 0.00572 | -41.21 | 0.11 |
| 8S08FW - Transect 5 | RF | 2 | 0.042266 | 0.00873 | -42.94 | 0.17 |
| 8S08FW - Transect 5 | RF | 2 | 0.042318 | 0.00652 | -41.76 | 0.13 |

Raw sulphur isotope data from SIMS analysis. See Figure 4.1.13 for transect locations. *RF = Rock Fragment.

Table 4.1.10: SIMS sulphur isotope analyses of LK 359 mineral separates

| Name | Type | Session | $^{34}\text{S}/^{32}\text{S}$ | 1σ (%) intra- session | $\delta^{34}\text{S}$ (VCDT) | 2σ (‰) inter- session |
|---------------|------|---------|-------------------------------|------------------------------------|---------------------------------|------------------------------------|
| LK 359A NM0.8 | MS | 1 | 0.04211248 | 0.00919 | -46.42 | 0.18 |
| LK 359A NM0.8 | MS | 1 | 0.04180765 | 0.00955 | -53.32 | 0.19 |
| LK 359A NM0.8 | MS | 1 | 0.04196206 | 0.00653 | -49.83 | 0.13 |
| LK 359A NM0.8 | MS | 1 | 0.04205835 | 0.00727 | -47.65 | 0.15 |
| LK 359A NM0.8 | MS | 1 | 0.04275719 | 0.01517 | -31.82 | 0.30 |
| LK 359A NM0.8 | MS | 1 | 0.04277271 | 0.00981 | -31.47 | 0.20 |
| LK 359A NM0.8 | MS | 1 | 0.04294546 | 0.01765 | -27.56 | 0.35 |
| LK 359A NM0.8 | MS | 1 | 0.04295127 | 0.00752 | -27.43 | 0.15 |
| LK 359A NM0.8 | MS | 1 | 0.04338021 | 0.00772 | -17.71 | 0.15 |
| LK 359A NM0.8 | MS | 1 | 0.04391438 | 0.00742 | -5.62 | 0.15 |
| LK 359A NM0.8 | MS | 1 | 0.04359814 | 0.00697 | -12.78 | 0.14 |
| LK 359A NM0.8 | MS | 1 | 0.04355439 | 0.00665 | -13.77 | 0.13 |
| LK 359A NM0.8 | MS | 1 | 0.04310493 | 0.01441 | -23.95 | 0.29 |
| LK 359A NM0.8 | MS | 1 | 0.04405122 | 0.00688 | -2.52 | 0.14 |
| LK 359A NM0.8 | MS | 1 | 0.04406171 | 0.00673 | -2.28 | 0.14 |
| LK 359A NM0.8 | MS | 1 | 0.04294171 | 0.00586 | -27.64 | 0.12 |
| LK 359A NM0.8 | MS | 1 | 0.04276680 | 0.00694 | -31.60 | 0.14 |
| LK 359A NM0.8 | MS | 1 | 0.04202693 | 0.00617 | -48.36 | 0.12 |
| LK 359A NM0.8 | MS | 1 | 0.04342079 | 0.00606 | -16.80 | 0.12 |
| LK 359A NM0.8 | MS | 1 | 0.04320300 | 0.00744 | -21.73 | 0.15 |
| LK 359A NM0.8 | MS | 1 | 0.04315286 | 0.00725 | -22.86 | 0.15 |
| LK 359A NM0.8 | MS | 1 | 0.04200740 | 0.00772 | -48.80 | 0.15 |
| LK 359A NM0.8 | MS | 1 | 0.04199767 | 0.00686 | -49.02 | 0.14 |
| LK 359A NM0.8 | MS | 1 | 0.04206220 | 0.00604 | -47.56 | 0.12 |
| LK 359B NM1.6 | MS | 1 | 0.04193138 | 0.00681 | -50.52 | 0.14 |
| LK 359B NM1.6 | MS | 1 | 0.04204957 | 0.00711 | -47.85 | 0.14 |
| LK 359B NM1.6 | MS | 1 | 0.04204556 | 0.00619 | -47.94 | 0.12 |
| LK 359B NM1.6 | MS | 1 | 0.04193744 | 0.00724 | -50.38 | 0.15 |
| LK 359B NM1.6 | MS | 1 | 0.04209490 | 0.00719 | -46.82 | 0.14 |
| LK 359B NM1.6 | MS | 1 | 0.04267050 | 0.01058 | -33.79 | 0.21 |
| LK 359B NM1.6 | MS | 1 | 0.04218516 | 0.00800 | -44.78 | 0.16 |
| LK 359B NM1.6 | MS | 1 | 0.04201374 | 0.00806 | -48.66 | 0.16 |
| LK 359B NM1.6 | MS | 1 | 0.04209314 | 0.00672 | -46.86 | 0.14 |
| LK 359B NM1.6 | MS | 1 | 0.04192126 | 0.00612 | -50.75 | 0.12 |
| LK 359B NM1.6 | MS | 1 | 0.04200379 | 0.00722 | -48.88 | 0.14 |
| LK 359B NM1.6 | MS | 1 | 0.04201418 | 0.00638 | -48.65 | 0.13 |
| LK 359B NM1.6 | MS | 1 | 0.04310833 | 0.00929 | -23.87 | 0.19 |
| LK 359B NM1.6 | MS | 1 | 0.04205424 | 0.00660 | -47.74 | 0.13 |
| LK 359B NM1.6 | MS | 1 | 0.04204144 | 0.00627 | -48.03 | 0.13 |
| LK 359B NM1.6 | MS | 1 | 0.04194539 | 0.00641 | -50.20 | 0.13 |
| LK 359B NM1.6 | MS | 1 | 0.04221053 | 0.01085 | -44.20 | 0.22 |
| LK 359B NM1.6 | MS | 1 | 0.04218209 | 0.00627 | -44.84 | 0.13 |
| LK 359B NM1.6 | MS | 1 | 0.04217782 | 0.00708 | -44.94 | 0.14 |
| LK 359B NM1.6 | MS | 1 | 0.04262274 | 0.02541 | -34.87 | 0.51 |
| LK 359B NM1.6 | MS | 1 | 0.04210953 | 0.00581 | -46.49 | 0.12 |
| LK 359B NM1.6 | MS | 1 | 0.04223655 | 0.00708 | -43.61 | 0.14 |
| LK 359B NM1.6 | MS | 1 | 0.04264960 | 0.00835 | -34.26 | 0.17 |
| LK 359B NM1.6 | MS | 1 | 0.04303142 | 0.00995 | -25.61 | 0.20 |
| LK 359B NM1.6 | MS | 1 | 0.04217293 | 0.00654 | -45.05 | 0.13 |
| LK 359B NM1.6 | MS | 1 | 0.04339996 | 0.00551 | -17.27 | 0.11 |

Raw sulphur isotope data from SIMS analysis. See Figure 4.1.13 for transect locations. *MS = Mineral Separate.

Table 4.1.11: SIMS sulphur isotope analyses of LK 359 rock fragments

| Name | Type | Session | $^{34}\text{S}/^{32}\text{S}$ | 1σ (%) intra-session | $\delta^{34}\text{S}$ (VCDT) | 2σ (‰) inter-session |
|-----------------------|------|---------|-------------------------------|--------------------------------|---------------------------------|--------------------------------|
| LK 359-1 - Transect | RF | 2 | 0.04253961 | 0.00967 | -36.75 | 0.19 |
| LK 359-1 - Transect | RF | 2 | 0.04258656 | 0.00889 | -35.69 | 0.18 |
| LK 359-1 - Transect | RF | 2 | 0.04308867 | 0.00746 | -24.32 | 0.15 |
| LK 359-1 - Transect | RF | 2 | 0.0430986 | 0.00724 | -24.09 | 0.15 |
| LK 359-1 - Transect | RF | 2 | 0.04318403 | 0.00666 | -22.16 | 0.13 |
| LK 359-1 - Transect | RF | 2 | 0.04311874 | 0.00566 | -23.64 | 0.11 |
| LK 359-1 - Transect | RF | 2 | 0.04251502 | 0.01343 | -37.31 | 0.27 |
| LK 359-1 - Transect | RF | 2 | 0.04239176 | 0.00860 | -40.10 | 0.17 |
| LK 359-1 - Transect | RF | 2 | 0.04252541 | 0.00553 | -37.07 | 0.11 |
| LK 359-1 - Transect | RF | 2 | 0.04292702 | 0.00581 | -27.98 | 0.12 |
| LK 359-1 - Transect | RF | 2 | 0.04275205 | 0.00614 | -31.94 | 0.12 |
| LK 359-1 - Transect | RF | 2 | 0.04267559 | 0.00649 | -33.67 | 0.13 |
| LK 359-1 - Transect | RF | 2 | 0.04242229 | 0.00637 | -39.41 | 0.13 |
| LK 359-1 - Transect | RF | 2 | 0.04209134 | 0.00549 | -46.90 | 0.11 |
| LK 359-1 - Transect | RF | 2 | 0.04307558 | 0.02444 | -24.61 | 0.49 |
| LK 359-1 - Transect | RF | 2 | 0.04257657 | 0.00687 | -35.91 | 0.14 |
| LK 359-1 - Transect | RF | 2 | 0.04247786 | 0.00761 | -38.15 | 0.15 |
| LK 359-1 - Transect | RF | 2 | 0.04267251 | 0.01189 | -33.74 | 0.24 |
| LK 359-1 - Transect | RF | 2 | 0.04352959 | 0.00717 | -14.33 | 0.14 |
| LK 359-1 - Transect | RF | 2 | 0.04303884 | 0.02292 | -25.44 | 0.46 |
| LK 359-1 - Transect | RF | 2 | 0.04305091 | 0.00576 | -25.17 | 0.12 |
| LK 359-1 - Transect | RF | 2 | 0.04296206 | 0.00552 | -27.18 | 0.11 |
| LK 359-1 - Transect | RF | 2 | 0.04267603 | 0.00585 | -33.66 | 0.12 |
| LK 359-2 - Location 1 | RF | 2 | 0.04231014 | 0.00602 | -41.95 | 0.12 |
| LK 359-2 - Location 1 | RF | 2 | 0.04380798 | 0.00965 | -8.03 | 0.19 |
| LK 359-2 - Location 1 | RF | 2 | 0.04315957 | 0.02536 | -22.71 | 0.51 |
| LK 359-2 - Location 1 | RF | 2 | 0.04314116 | 0.01303 | -23.13 | 0.26 |
| LK 359-2 - Location 1 | RF | 2 | 0.04360851 | 0.01572 | -12.55 | 0.31 |
| LK 359-2 - Location 1 | RF | 2 | 0.04408393 | 0.00591 | -1.78 | 0.12 |
| LK 359-2 - Location 1 | RF | 2 | 0.04340741 | 0.01164 | -17.10 | 0.23 |
| LK 359-2 - Location 1 | RF | 2 | 0.04226057 | 0.00886 | -43.07 | 0.18 |
| LK 359-2 - Location 1 | RF | 2 | 0.04434533 | 0.00701 | 4.14 | 0.14 |
| LK 359-2 - Location 1 | RF | 2 | 0.04383813 | 0.02348 | -7.35 | 0.47 |
| LK 359-2 - Location 1 | RF | 2 | 0.0423982 | 0.00540 | -39.95 | 0.11 |
| LK 359-2 - Location 1 | RF | 2 | 0.04214119 | 0.00593 | -45.77 | 0.12 |
| LK 359-2 - Location 1 | RF | 2 | 0.04209815 | 0.00662 | -46.75 | 0.13 |
| LK 359-2 - Location 1 | RF | 2 | 0.04215668 | 0.00620 | -45.42 | 0.12 |
| LK 359-2 - Location 1 | RF | 2 | 0.04215698 | 0.00604 | -45.41 | 0.12 |
| LK 359-2 - Location 1 | RF | 2 | 0.04218696 | 0.00657 | -44.73 | 0.13 |
| LK 359-2 - Location 1 | RF | 2 | 0.04228886 | 0.00649 | -42.43 | 0.13 |
| LK 359-2 - Location 1 | RF | 2 | 0.04218056 | 0.00557 | -44.88 | 0.11 |
| LK 359-2 - Location 1 | RF | 2 | 0.04214314 | 0.00652 | -45.73 | 0.13 |
| LK 359-2 - Location 2 | RF | 2 | 0.04204611 | 0.00686 | -47.92 | 0.14 |
| LK 359-2 - Location 2 | RF | 2 | 0.04203513 | 0.00575 | -48.17 | 0.12 |
| LK 359-2 - Location 2 | RF | 2 | 0.04200137 | 0.00620 | -48.94 | 0.12 |
| LK 359-2 - Location 2 | RF | 2 | 0.04200498 | 0.00699 | -48.86 | 0.14 |
| LK 359-2 - Location 2 | RF | 2 | 0.04206713 | 0.00642 | -47.45 | 0.13 |
| LK 359-2 - Location 2 | RF | 2 | 0.04206085 | 0.00543 | -47.59 | 0.11 |
| LK 359-2 - Location 2 | RF | 2 | 0.04204463 | 0.00599 | -47.96 | 0.12 |
| LK 359-2 - Location 2 | RF | 2 | 0.04200183 | 0.00635 | -48.93 | 0.13 |
| LK 359-2 - Location 2 | RF | 2 | 0.04207782 | 0.00680 | -47.21 | 0.14 |
| LK 359-2 - Location 2 | RF | 2 | 0.0421052 | 0.00595 | -46.59 | 0.12 |
| LK 359-2 - Location 2 | RF | 2 | 0.04205829 | 0.00634 | -47.65 | 0.13 |
| LK 359-2 - Location 2 | RF | 2 | 0.04208483 | 0.00611 | -47.05 | 0.12 |
| LK 359-2 - Location 2 | RF | 2 | 0.04200658 | 0.00652 | -48.82 | 0.13 |
| LK 359-2 - Location 2 | RF | 2 | 0.04200797 | 0.00608 | -48.79 | 0.12 |
| LK 359-2 - Location 2 | RF | 2 | 0.04198309 | 0.00637 | -49.35 | 0.13 |
| LK 359-2 - Location 2 | RF | 2 | 0.04206667 | 0.00596 | -47.46 | 0.12 |
| LK 359-2 - Location 2 | RF | 2 | 0.04207407 | 0.00603 | -47.29 | 0.12 |
| LK 359-2 - Location 2 | RF | 2 | 0.0420189 | 0.00675 | -48.54 | 0.14 |
| LK 359-2 - Location 2 | RF | 2 | 0.04206027 | 0.00616 | -47.60 | 0.12 |
| LK 359-2 - Location 2 | RF | 2 | 0.04207187 | 0.00687 | -47.34 | 0.14 |
| LK 359-2 - Location 2 | RF | 2 | 0.04201206 | 0.00577 | -48.69 | 0.12 |
| LK 359-2 - Location 2 | RF | 2 | 0.04198105 | 0.00581 | -49.40 | 0.12 |
| LK 359-2 - Location 2 | RF | 2 | 0.04201343 | 0.00609 | -48.66 | 0.12 |
| LK 359-2 - Location 2 | RF | 2 | 0.04203674 | 0.00566 | -48.14 | 0.11 |
| LK 359-2 - Location 2 | RF | 2 | 0.04204674 | 0.00594 | -47.91 | 0.12 |
| LK 359-2 - Location 2 | RF | 2 | 0.04200552 | 0.00608 | -48.84 | 0.12 |
| LK 359-2 - Location 2 | RF | 2 | 0.04216676 | 0.00586 | -45.19 | 0.12 |
| LK 359-2 - Location 2 | RF | 2 | 0.04230458 | 0.00573 | -42.07 | 0.11 |

Raw sulphur isotope data from SIMS analysis. See Figure 4.1.13 for transect locations. *RF = Rock Fragment.

Table 4.1.12: SIMS sulphur isotope analyses of LK 451 mineral separates

| Name | Type | Session | $^{34}\text{S}/^{32}\text{S}$ | 1σ (%) intra- session | $\delta^{34}\text{S}$ (VCDT) | 2σ (‰) inter- session |
|--------------|------|---------|-------------------------------|------------------------------------|---------------------------------|------------------------------------|
| LK 451A M1.8 | MS | 1 | 0.04254506 | 0.00677 | -36.63 | 0.14 |
| LK 451A M1.8 | MS | 1 | 0.04263364 | 0.00684 | -34.62 | 0.14 |
| LK 451A M1.8 | MS | 1 | 0.04315020 | 0.00533 | -22.92 | 0.11 |
| LK 451A M1.8 | MS | 1 | 0.04312078 | 0.00611 | -23.59 | 0.12 |
| LK 451A M1.8 | MS | 1 | 0.04255591 | 0.00668 | -36.38 | 0.13 |
| LK 451A M1.8 | MS | 1 | 0.04299150 | 0.00592 | -26.52 | 0.12 |
| LK 451A M1.8 | MS | 1 | 0.04263506 | 0.00811 | -34.59 | 0.16 |
| LK 451A M1.8 | MS | 1 | 0.04319400 | 0.00606 | -21.93 | 0.12 |
| LK 451A M1.8 | MS | 1 | 0.04258784 | 0.00675 | -35.66 | 0.14 |
| LK 451A M1.8 | MS | 1 | 0.04247163 | 0.00733 | -38.29 | 0.15 |
| LK 451A M1.8 | MS | 1 | 0.04307125 | 0.00678 | -24.71 | 0.14 |
| LK 451A M1.8 | MS | 1 | 0.04243433 | 0.00742 | -39.13 | 0.15 |
| LK 451A M1.8 | MS | 1 | 0.04246850 | 0.00744 | -38.36 | 0.15 |
| LK 451A M1.8 | MS | 1 | 0.04287513 | 0.00757 | -29.15 | 0.15 |
| LK 451A M1.8 | MS | 1 | 0.04319936 | 0.00756 | -21.81 | 0.15 |
| LK 451A M1.8 | MS | 1 | 0.04305337 | 0.00801 | -25.12 | 0.16 |
| LK 451A M1.8 | MS | 1 | 0.04318468 | 0.00748 | -22.14 | 0.15 |
| LK 451A M1.8 | MS | 1 | 0.04255619 | 0.00720 | -36.37 | 0.14 |
| LK 451A M1.8 | MS | 1 | 0.04297250 | 0.00958 | -26.95 | 0.19 |
| LK 451A M1.8 | MS | 1 | 0.04245503 | 0.00871 | -38.66 | 0.17 |
| LK 451A M1.8 | MS | 1 | 0.04256560 | 0.00983 | -36.16 | 0.20 |
| LK 451A M1.8 | MS | 1 | 0.04315817 | 0.01393 | -22.74 | 0.28 |
| LK 451A M1.8 | MS | 1 | 0.04246346 | 0.00684 | -38.47 | 0.14 |
| LK 451A M1.8 | MS | 1 | 0.04293462 | 0.00603 | -27.80 | 0.12 |
| LK 451A M1.6 | MS | 1 | 0.04280181 | 0.00674 | -30.81 | 0.14 |
| LK 451A M1.6 | MS | 1 | 0.04309221 | 0.00534 | -24.24 | 0.11 |
| LK 451A M1.6 | MS | 1 | 0.04240178 | 0.00673 | -39.87 | 0.14 |
| LK 451A M1.6 | MS | 1 | 0.04251792 | 0.00587 | -37.24 | 0.12 |
| LK 451A M1.6 | MS | 1 | 0.04260253 | 0.00657 | -35.32 | 0.13 |
| LK 451A M1.6 | MS | 1 | 0.04305546 | 0.00766 | -25.07 | 0.15 |
| LK 451A M1.6 | MS | 1 | 0.04233478 | 0.00729 | -41.39 | 0.15 |
| LK 451A M1.6 | MS | 1 | 0.04282261 | 0.00669 | -30.34 | 0.13 |
| LK 451A M1.6 | MS | 1 | 0.04261109 | 0.00817 | -35.13 | 0.16 |
| LK 451A M1.6 | MS | 1 | 0.04260804 | 0.00722 | -35.20 | 0.14 |
| LK 451A M1.6 | MS | 1 | 0.04254899 | 0.00673 | -36.54 | 0.14 |
| LK 451A M1.6 | MS | 1 | 0.04258972 | 0.00778 | -35.61 | 0.16 |
| LK 451A M1.6 | MS | 1 | 0.04297505 | 0.00757 | -26.89 | 0.15 |
| LK 451A M1.6 | MS | 1 | 0.04278201 | 0.00661 | -31.26 | 0.13 |
| LK 451A M1.6 | MS | 1 | 0.04270853 | 0.00677 | -32.92 | 0.14 |
| LK 451A M1.6 | MS | 1 | 0.04230327 | 0.00654 | -42.10 | 0.13 |
| LK 451A M1.6 | MS | 1 | 0.04229602 | 0.00889 | -42.27 | 0.18 |
| LK 451A M1.6 | MS | 1 | 0.04271417 | 0.01517 | -32.80 | 0.30 |
| LK 451A M1.6 | MS | 1 | 0.04254500 | 0.00693 | -36.63 | 0.14 |
| LK 451A M1.6 | MS | 1 | 0.04273236 | 0.00626 | -32.38 | 0.13 |
| LK 451A M1.6 | MS | 1 | 0.04257969 | 0.00718 | -35.84 | 0.14 |
| LK 451A M1.6 | MS | 1 | 0.04267546 | 0.00669 | -33.67 | 0.13 |
| LK 451A M1.6 | MS | 1 | 0.04258920 | 0.00703 | -35.63 | 0.14 |
| LK 451A M1.6 | MS | 1 | 0.04252764 | 0.00825 | -37.02 | 0.17 |
| LK 451A M1.6 | MS | 1 | 0.04256702 | 0.00674 | -36.13 | 0.14 |
| LK 451B M1.8 | MS | 1 | 0.04270038 | 0.00548 | -33.11 | 0.11 |
| LK 451B M1.8 | MS | 1 | 0.04241594 | 0.00702 | -39.55 | 0.14 |
| LK 451B M1.8 | MS | 1 | 0.04237736 | 0.00660 | -40.42 | 0.13 |
| LK 451B M1.8 | MS | 1 | 0.04268980 | 0.00709 | -33.35 | 0.14 |
| LK 451B M1.8 | MS | 1 | 0.04370059 | 0.00640 | -10.46 | 0.13 |
| LK 451B M1.8 | MS | 1 | 0.04265465 | 0.00768 | -34.14 | 0.15 |
| LK 451B M1.8 | MS | 1 | 0.04296234 | 0.00697 | -27.18 | 0.14 |
| LK 451B M1.8 | MS | 1 | 0.04350643 | 0.00651 | -14.86 | 0.13 |
| LK 451B M1.8 | MS | 1 | 0.04275632 | 0.00647 | -31.84 | 0.13 |
| LK 451B M1.8 | MS | 1 | 0.04233569 | 0.00687 | -41.37 | 0.14 |
| LK 451B M1.8 | MS | 1 | 0.04369034 | 0.00671 | -10.69 | 0.13 |
| LK 451B M1.8 | MS | 1 | 0.04366358 | 0.00615 | -11.30 | 0.12 |
| LK 451B M1.8 | MS | 1 | 0.04294148 | 0.00868 | -27.65 | 0.17 |
| LK 451B M1.8 | MS | 1 | 0.04302639 | 0.00607 | -25.73 | 0.12 |
| LK 451B M1.8 | MS | 1 | 0.04325606 | 0.00553 | -20.53 | 0.11 |
| LK 451B M1.8 | MS | 1 | 0.04306025 | 0.00628 | -24.96 | 0.13 |
| LK 451B M1.8 | MS | 1 | 0.04292986 | 0.00616 | -27.91 | 0.12 |
| LK 451B M1.8 | MS | 1 | 0.04295984 | 0.00737 | -27.23 | 0.15 |
| LK 451B M1.8 | MS | 1 | 0.04262823 | 0.00712 | -34.74 | 0.14 |
| LK 451B M1.8 | MS | 1 | 0.04229360 | 0.00690 | -42.32 | 0.14 |
| LK 451B M1.8 | MS | 1 | 0.04248778 | 0.00810 | -37.92 | 0.16 |
| LK 451B M1.8 | MS | 1 | 0.04216717 | 0.00640 | -45.18 | 0.13 |
| LK 451B M1.8 | MS | 1 | 0.04217322 | 0.00600 | -45.05 | 0.12 |
| LK 451B M1.8 | MS | 1 | 0.04231305 | 0.00700 | -41.88 | 0.14 |
| LK 451B M1.8 | MS | 1 | 0.04207003 | 0.00681 | -47.38 | 0.14 |

Raw sulphur isotope data from SIMS analysis. See Figure 4.1.13 for transect locations. *MS = Mineral Separate.

Table 4.1.13: SIMS sulphur isotope analyses of LK 451 rock fragments

| Name | Type | Session | ³⁴ S/ ³² S | 1σ (%) intra- session | δ ³⁴ S (VCDT) | 2σ (%) inter- session |
|---------------------|------|---------|----------------------------------|-----------------------------|-----------------------------|-----------------------------|
| LK 451 - Location 1 | RF | 2 | 0.04285366 | 0.00635 | -29.64 | 0.13 |
| LK 451 - Location 1 | RF | 2 | 0.04262716 | 0.00688 | -34.77 | 0.14 |
| LK 451 - Location 1 | RF | 2 | 0.04263249 | 0.00691 | -34.65 | 0.14 |
| LK 451 - Location 1 | RF | 2 | 0.04307842 | 0.00548 | -24.55 | 0.11 |
| LK 451 - Location 1 | RF | 2 | 0.04251612 | 0.00616 | -37.28 | 0.12 |
| LK 451 - Location 1 | RF | 2 | 0.0424959 | 0.00679 | -37.74 | 0.14 |
| LK 451 - Location 1 | RF | 2 | 0.04257354 | 0.00705 | -35.98 | 0.14 |
| LK 451 - Location 1 | RF | 2 | 0.04249433 | 0.00796 | -37.77 | 0.16 |
| LK 451 - Location 1 | RF | 2 | 0.04300737 | 0.00554 | -26.16 | 0.11 |
| LK 451 - Location 1 | RF | 2 | 0.04254136 | 0.00645 | -36.71 | 0.13 |
| LK 451 - Location 1 | RF | 2 | 0.04255757 | 0.00702 | -36.34 | 0.14 |
| LK 451 - Location 1 | RF | 2 | 0.04298905 | 0.00801 | -26.57 | 0.16 |
| LK 451 - Location 1 | RF | 2 | 0.04289941 | 0.00543 | -28.60 | 0.11 |
| LK 451 - Location 1 | RF | 2 | 0.04299324 | 0.00596 | -26.48 | 0.12 |
| LK 451 - Location 1 | RF | 2 | 0.04259124 | 0.00564 | -35.58 | 0.11 |
| LK 451 - Location 1 | RF | 2 | 0.04253802 | 0.00616 | -36.79 | 0.12 |
| LK 451 - Location 1 | RF | 2 | 0.04308118 | 0.00598 | -24.49 | 0.12 |
| LK 451 - Location 1 | RF | 2 | 0.04291479 | 0.01173 | -28.25 | 0.23 |
| LK 451 - Location 1 | RF | 2 | 0.04293153 | 0.00878 | -27.87 | 0.18 |
| LK 451 - Location 1 | RF | 2 | 0.04248794 | 0.00564 | -37.92 | 0.11 |
| LK 451 - Location 1 | RF | 2 | 0.04249397 | 0.00762 | -37.78 | 0.15 |
| LK 451 - Location 1 | RF | 2 | 0.04250342 | 0.00707 | -37.57 | 0.14 |
| LK 451 - Location 1 | RF | 2 | 0.0428098 | 0.01109 | -30.63 | 0.22 |
| LK 451 - Location 1 | RF | 2 | 0.04253447 | 0.00579 | -36.87 | 0.12 |
| LK 451 - Location 1 | RF | 2 | 0.04292226 | 0.00805 | -28.08 | 0.16 |
| LK 451 - Location 1 | RF | 2 | 0.0428453 | 0.00611 | -29.83 | 0.12 |
| LK 451 - Location 1 | RF | 2 | 0.04295123 | 0.00770 | -27.43 | 0.15 |
| LK 451 - Location 1 | RF | 2 | 0.04306232 | 0.00556 | -24.91 | 0.11 |
| LK 451 - Location 1 | RF | 2 | 0.04293469 | 0.00902 | -27.80 | 0.18 |
| LK 451 - Location 1 | RF | 2 | 0.04278202 | 0.00720 | -31.26 | 0.14 |
| LK 451 - Location 1 | RF | 2 | 0.04287405 | 0.00808 | -29.18 | 0.16 |
| LK 451 - Location 1 | RF | 2 | 0.04294445 | 0.00594 | -27.58 | 0.12 |
| LK 451 - Location 1 | RF | 2 | 0.04289759 | 0.00807 | -28.64 | 0.16 |
| LK 451 - Location 1 | RF | 2 | 0.04315874 | 0.00598 | -22.73 | 0.12 |
| LK 451 - Location 1 | RF | 2 | 0.04255512 | 0.00655 | -36.40 | 0.13 |
| LK 451 - Location 1 | RF | 2 | 0.04263199 | 0.00664 | -34.66 | 0.13 |
| LK 451 - Location 1 | RF | 2 | 0.042588 | 0.00750 | -35.65 | 0.15 |
| LK 451 - Location 1 | RF | 2 | 0.04252891 | 0.00688 | -36.99 | 0.14 |
| LK 451 - Location 2 | RF | 2 | 0.04286408 | 0.00802 | -29.40 | 0.16 |
| LK 451 - Location 2 | RF | 2 | 0.04232095 | 0.00633 | -41.70 | 0.13 |
| LK 451 - Location 2 | RF | 2 | 0.04231178 | 0.00634 | -41.91 | 0.13 |
| LK 451 - Location 2 | RF | 2 | 0.04284195 | 0.00604 | -29.90 | 0.12 |
| LK 451 - Location 2 | RF | 2 | 0.04285547 | 0.00639 | -29.60 | 0.13 |
| LK 451 - Location 2 | RF | 2 | 0.04251964 | 0.00559 | -37.20 | 0.11 |
| LK 451 - Location 2 | RF | 2 | 0.04248096 | 0.00900 | -38.08 | 0.18 |
| LK 451 - Location 2 | RF | 2 | 0.04269611 | 0.00929 | -33.21 | 0.19 |
| LK 451 - Location 2 | RF | 2 | 0.04253096 | 0.00564 | -36.95 | 0.11 |
| LK 451 - Location 2 | RF | 2 | 0.04250293 | 0.00659 | -37.58 | 0.13 |
| LK 451 - Location 2 | RF | 2 | 0.04267297 | 0.01436 | -33.73 | 0.29 |
| LK 451 - Location 2 | RF | 2 | 0.0425179 | 0.00714 | -37.24 | 0.14 |
| LK 451 - Location 2 | RF | 2 | 0.04307021 | 0.00691 | -24.73 | 0.14 |
| LK 451 - Location 2 | RF | 2 | 0.04294049 | 0.00558 | -27.67 | 0.11 |
| LK 451 - Location 2 | RF | 2 | 0.04250893 | 0.00684 | -37.44 | 0.14 |
| LK 451 - Location 2 | RF | 2 | 0.04253828 | 0.00735 | -36.78 | 0.15 |
| LK 451 - Location 3 | RF | 2 | 0.04303754 | 0.00578 | -25.47 | 0.12 |
| LK 451 - Location 3 | RF | 2 | 0.04250505 | 0.00691 | -37.53 | 0.14 |
| LK 451 - Location 3 | RF | 2 | 0.04253324 | 0.00572 | -36.89 | 0.11 |
| LK 451 - Location 3 | RF | 2 | 0.04251404 | 0.00632 | -37.33 | 0.13 |
| LK 451 - Location 3 | RF | 2 | 0.04284459 | 0.00583 | -29.84 | 0.12 |
| LK 451 - Location 3 | RF | 2 | 0.04311632 | 0.00648 | -23.69 | 0.13 |
| LK 451 - Location 3 | RF | 2 | 0.04225313 | 0.00838 | -43.24 | 0.17 |
| LK 451 - Location 3 | RF | 2 | 0.04283727 | 0.00599 | -30.01 | 0.12 |
| LK 451 - Location 3 | RF | 2 | 0.04317533 | 0.00649 | -22.35 | 0.13 |
| LK 451 - Location 3 | RF | 2 | 0.04237911 | 0.00599 | -40.38 | 0.12 |
| LK 451 - Location 3 | RF | 2 | 0.04274742 | 0.00619 | -32.04 | 0.12 |
| LK 451 - Location 3 | RF | 2 | 0.04233267 | 0.00567 | -41.44 | 0.11 |
| LK 451 - Location 3 | RF | 2 | 0.04307409 | 0.00609 | -24.65 | 0.12 |
| LK 451 - Location 4 | RF | 2 | 0.0425021 | 0.00822 | -37.60 | 0.16 |
| LK 451 - Location 4 | RF | 2 | 0.0428356 | 0.00633 | -30.05 | 0.13 |
| LK 451 - Location 4 | RF | 2 | 0.04280048 | 0.00589 | -30.84 | 0.12 |
| LK 451 - Location 4 | RF | 2 | 0.04278641 | 0.00630 | -31.16 | 0.13 |
| LK 451 - Location 4 | RF | 2 | 0.04253236 | 0.00659 | -36.91 | 0.13 |
| LK 451 - Location 4 | RF | 2 | 0.04328411 | 0.00605 | -19.89 | 0.12 |
| LK 451 - Location 4 | RF | 2 | 0.04255118 | 0.00667 | -36.49 | 0.13 |
| LK 451 - Location 4 | RF | 2 | 0.04246728 | 0.00966 | -38.39 | 0.19 |
| LK 451 - Location 4 | RF | 2 | 0.04318639 | 0.00594 | -22.10 | 0.12 |
| LK 451 - Location 4 | RF | 2 | 0.04254202 | 0.00605 | -36.69 | 0.12 |
| LK 451 - Location 4 | RF | 2 | 0.04306835 | 0.00644 | -24.78 | 0.13 |
| LK 451 - Location 4 | RF | 2 | 0.04335502 | 0.00537 | -18.29 | 0.11 |
| LK 451 - Location 4 | RF | 2 | 0.04253831 | 0.00626 | -36.78 | 0.13 |
| LK 451 - Location 4 | RF | 2 | 0.04255533 | 0.00605 | -36.39 | 0.12 |
| LK 451 - Location 4 | RF | 2 | 0.04327594 | 0.00567 | -20.08 | 0.11 |
| LK 451 - Location 4 | RF | 2 | 0.04321212 | 0.00650 | -21.52 | 0.13 |
| LK 451 - Location 4 | RF | 2 | 0.04274894 | 0.00604 | -32.01 | 0.12 |

Raw sulphur isotope data from SIMS analysis. See Figure 4.1.13 for transect locations. *RF = Rock Fragment.

Table 4.1.14: SIMS sulphur isotope analyses of Nanisivik samples

| Name | Type | Session | ³⁴ S/ ³² S | 1σ (%) intra-session | δ ³⁴ S (VCDT) | 2σ (%) inter-session | Name | Type | Session | ³⁴ S/ ³² S | 1σ (%) intra-session | δ ³⁴ S (VCDT) | 2σ (%) inter-session |
|--------------|------|---------|----------------------------------|----------------------|--------------------------|----------------------|-------------------|------|---------|----------------------------------|----------------------|--------------------------|----------------------|
| 04-N-2 NM2.0 | MS | 2 | 0.045424314 | 0.00561 | 27.34 | 0.11 | NOV4-1 Transect 1 | RF | 2 | 0.04542 | 0.00593 | 27.24 | 0.12 |
| 04-N-2 NM2.0 | MS | 2 | 0.045494059 | 0.00552 | 28.92 | 0.11 | NOV4-1 Transect 1 | RF | 2 | 0.045427 | 0.00580 | 27.39 | 0.12 |
| 04-N-2 NM2.0 | MS | 2 | 0.045426298 | 0.00551 | 27.39 | 0.11 | NOV4-1 Transect 1 | RF | 2 | 0.045423 | 0.00586 | 27.31 | 0.12 |
| 04-N-2 NM2.0 | MS | 2 | 0.045440403 | 0.00590 | 27.71 | 0.12 | NOV4-1 Transect 1 | RF | 2 | 0.045424 | 0.00545 | 27.33 | 0.11 |
| 04-N-2 NM2.0 | MS | 2 | 0.045418607 | 0.00544 | 27.21 | 0.11 | NOV4-1 Transect 1 | RF | 2 | 0.045427 | 0.00566 | 27.41 | 0.11 |
| 04-N-2 NM2.0 | MS | 2 | 0.04547643 | 0.00553 | 28.52 | 0.11 | NOV4-1 Transect 1 | RF | 2 | 0.045431 | 0.00566 | 27.49 | 0.11 |
| 04-N-2 NM2.0 | MS | 2 | 0.045451327 | 0.00561 | 27.95 | 0.11 | NOV4-1 Transect 1 | RF | 2 | 0.045416 | 0.00628 | 27.15 | 0.13 |
| 04-N-2 NM2.0 | MS | 2 | 0.045307237 | 0.00685 | 24.69 | 0.14 | NOV4-1 Transect 1 | RF | 2 | 0.045416 | 0.00575 | 27.15 | 0.12 |
| 04-N-2 NM2.0 | MS | 2 | 0.045456242 | 0.00573 | 28.06 | 0.12 | NOV4-1 Transect 1 | RF | 2 | 0.045392 | 0.00558 | 26.61 | 0.11 |
| 04-N-2 NM2.0 | MS | 2 | 0.04544356 | 0.00530 | 27.78 | 0.11 | NOV4-1 Transect 1 | RF | 2 | 0.045438 | 0.00583 | 27.65 | 0.12 |
| 04-N-2 NM2.0 | MS | 2 | 0.04544899 | 0.00560 | 27.90 | 0.11 | NOV4-1 Transect 1 | RF | 2 | 0.045432 | 0.00579 | 27.52 | 0.12 |
| 04-N-2 NM2.0 | MS | 2 | 0.045322297 | 0.00678 | 25.03 | 0.14 | NOV4-1 Transect 1 | RF | 2 | 0.045389 | 0.00685 | 26.55 | 0.14 |
| 04-N-2 NM2.0 | MS | 2 | 0.045428807 | 0.00587 | 27.44 | 0.12 | NOV4-1 Transect 1 | RF | 2 | 0.045414 | 0.01121 | 27.11 | 0.22 |
| 04-N-2 NM2.0 | MS | 2 | 0.045395671 | 0.00560 | 26.69 | 0.11 | NOV4-1 Transect 1 | RF | 2 | 0.045491 | 0.00548 | 28.85 | 0.11 |
| 04-N-2 NM2.0 | MS | 2 | 0.045439121 | 0.00569 | 27.68 | 0.11 | NOV4-1 Transect 1 | RF | 2 | 0.0454 | 0.00566 | 26.79 | 0.11 |
| 04-N-2 NM2.0 | MS | 2 | 0.045455148 | 0.00598 | 28.04 | 0.12 | NOV4-1 Transect 1 | RF | 2 | 0.045376 | 0.00619 | 26.25 | 0.12 |
| 04-N-2 NM2.0 | MS | 2 | 0.045438163 | 0.00589 | 27.65 | 0.12 | NOV4-1 Transect 1 | RF | 2 | 0.045441 | 0.00593 | 27.71 | 0.12 |
| 04-N-2 NM2.0 | MS | 2 | 0.04544489 | 0.00581 | 27.81 | 0.12 | NOV4-1 Transect 1 | RF | 2 | 0.045439 | 0.00603 | 27.68 | 0.12 |
| 04-N-2 NM2.0 | MS | 2 | 0.045451597 | 0.00595 | 27.96 | 0.12 | NOV4-1 Transect 1 | RF | 2 | 0.045437 | 0.00570 | 27.63 | 0.11 |
| 04-N-2 NM2.0 | MS | 2 | 0.045451596 | 0.00576 | 27.96 | 0.12 | NOV4-1 Transect 1 | RF | 2 | 0.045425 | 0.00550 | 27.35 | 0.11 |
| 04-N-2 NM2.0 | MS | 2 | 0.045446414 | 0.00544 | 27.84 | 0.11 | NOV4-1 Transect 1 | RF | 2 | 0.045399 | 0.00554 | 26.77 | 0.11 |
| 04-N-2 NM2.0 | MS | 2 | 0.045436784 | 0.00579 | 27.62 | 0.12 | | | | | | | |
| 04-N-2 NM2.0 | MS | 2 | 0.045468466 | 0.00530 | 28.34 | 0.11 | NOV4-1 Transect 2 | RF | 2 | 0.045444 | 0.00565 | 27.79 | 0.11 |
| 04-N-2 NM2.0 | MS | 2 | 0.045445789 | 0.00548 | 27.83 | 0.11 | NOV4-1 Transect 2 | RF | 2 | 0.045483 | 0.00612 | 28.66 | 0.12 |
| NOV4B-NM1.2 | MS | 2 | 0.045463632 | 0.00556 | 28.23 | 0.11 | NOV4-1 Transect 2 | RF | 2 | 0.045496 | 0.00551 | 28.97 | 0.11 |
| NOV4B-NM1.2 | MS | 2 | 0.045428058 | 0.00590 | 27.43 | 0.12 | NOV4-1 Transect 2 | RF | 2 | 0.045405 | 0.00577 | 26.91 | 0.12 |
| NOV4B-NM1.2 | MS | 2 | 0.045418937 | 0.00580 | 27.22 | 0.12 | NOV4-1 Transect 2 | RF | 2 | 0.045426 | 0.00585 | 27.38 | 0.12 |
| NOV4B-NM1.2 | MS | 2 | 0.045418202 | 0.00572 | 27.20 | 0.11 | NOV4-1 Transect 2 | RF | 2 | 0.045483 | 0.00561 | 28.67 | 0.11 |
| NOV4B-NM1.2 | MS | 2 | 0.045448517 | 0.00570 | 27.89 | 0.11 | NOV4-1 Transect 2 | RF | 2 | 0.045459 | 0.00646 | 28.12 | 0.13 |
| NOV4B-NM1.2 | MS | 2 | 0.045417459 | 0.00590 | 27.19 | 0.12 | NOV4-1 Transect 2 | RF | 2 | 0.045413 | 0.00580 | 27.08 | 0.12 |
| NOV4B-NM1.2 | MS | 2 | 0.045427658 | 0.00578 | 27.42 | 0.12 | NOV4-1 Transect 2 | RF | 2 | 0.045443 | 0.00572 | 27.77 | 0.11 |
| NOV4B-NM1.2 | MS | 2 | 0.045392245 | 0.00652 | 26.61 | 0.13 | NOV4-1 Transect 2 | RF | 2 | 0.045441 | 0.00569 | 27.71 | 0.11 |
| NOV4B-NM1.2 | MS | 2 | 0.045411768 | 0.00546 | 27.06 | 0.11 | NOV4-1 Transect 2 | RF | 2 | 0.045439 | 0.00590 | 27.67 | 0.12 |
| NOV4B-NM1.2 | MS | 2 | 0.04541793 | 0.00579 | 27.20 | 0.12 | NOV4-1 Transect 2 | RF | 2 | 0.045441 | 0.00544 | 27.73 | 0.11 |
| NOV4B-NM1.2 | MS | 2 | 0.045410136 | 0.00532 | 27.02 | 0.11 | NOV4-1 Transect 2 | RF | 2 | 0.045424 | 0.00557 | 27.34 | 0.11 |
| NOV4B-NM1.2 | MS | 2 | 0.045412776 | 0.00567 | 27.08 | 0.11 | NOV4-1 Transect 2 | RF | 2 | 0.045432 | 0.00552 | 27.52 | 0.11 |
| NOV4B-NM1.2 | MS | 2 | 0.045481823 | 0.00601 | 26.64 | 0.12 | NOV4-1 Transect 2 | RF | 2 | 0.045430 | 0.00547 | 27.56 | 0.11 |
| NOV4B-NM1.2 | MS | 2 | 0.045378582 | 0.00830 | 26.31 | 0.17 | NOV4-2 Transect 1 | RF | 2 | 0.045439 | 0.00572 | 27.68 | 0.12 |
| NOV4B-NM1.2 | MS | 2 | 0.045417326 | 0.00594 | 27.18 | 0.12 | NOV4-2 Transect 1 | RF | 2 | 0.045429 | 0.00582 | 27.46 | 0.12 |
| NOV4B-NM1.2 | MS | 2 | 0.045431072 | 0.00610 | 27.49 | 0.12 | NOV4-2 Transect 1 | RF | 2 | 0.045428 | 0.00589 | 27.42 | 0.12 |
| NOV4B-NM1.2 | MS | 2 | 0.045419072 | 0.00570 | 27.22 | 0.11 | NOV4-2 Transect 1 | RF | 2 | 0.045424 | 0.00569 | 27.33 | 0.11 |
| NOV4B-NM1.2 | MS | 2 | 0.04542069 | 0.00599 | 27.26 | 0.12 | NOV4-2 Transect 1 | RF | 2 | 0.045413 | 0.00556 | 27.09 | 0.11 |
| NOV4B-NM1.2 | MS | 2 | 0.045492919 | 0.00584 | 28.89 | 0.12 | NOV4-2 Transect 1 | RF | 2 | 0.045465 | 0.00631 | 28.26 | 0.13 |
| NOV4B-NM1.2 | MS | 2 | 0.045424751 | 0.00573 | 27.35 | 0.12 | NOV4-2 Transect 1 | RF | 2 | 0.04541 | 0.00554 | 27.01 | 0.11 |
| NOV4B-NM1.2 | MS | 2 | 0.045409632 | 0.00636 | 27.01 | 0.13 | NOV4-2 Transect 1 | RF | 2 | 0.045412 | 0.00608 | 27.07 | 0.12 |
| NOV4B-NM1.2 | MS | 2 | 0.045339812 | 0.01100 | 25.43 | 0.22 | NOV4-2 Transect 1 | RF | 2 | 0.045459 | 0.00595 | 28.12 | 0.12 |
| NOV4B-NM1.2 | MS | 2 | 0.045411793 | 0.00566 | 27.06 | 0.11 | NOV4-2 Transect 1 | RF | 2 | 0.045476 | 0.00647 | 28.50 | 0.13 |
| NOV4B-NM1.2 | MS | 2 | 0.045412858 | 0.00604 | 27.08 | 0.12 | NOV4-2 Transect 1 | RF | 2 | 0.04549 | 0.00550 | 28.83 | 0.11 |
| NOV4B-NM1.2 | MS | 2 | 0.045401827 | 0.00588 | 26.83 | 0.12 | | | | | | | |
| NOV4B NM0.6 | MS | 2 | 0.045427505 | 0.00547 | 27.41 | 0.11 | NOV4-2 Transect 2 | RF | 2 | 0.045429 | 0.00553 | 27.44 | 0.11 |
| NOV4B NM0.6 | MS | 2 | 0.045412807 | 0.00590 | 27.08 | 0.12 | NOV4-2 Transect 2 | RF | 2 | 0.04542 | 0.00612 | 27.23 | 0.12 |
| NOV4B NM0.6 | MS | 2 | 0.045418036 | 0.00581 | 27.20 | 0.12 | NOV4-2 Transect 2 | RF | 2 | 0.045486 | 0.00649 | 28.73 | 0.13 |
| NOV4B NM0.6 | MS | 2 | 0.045406184 | 0.00563 | 26.93 | 0.11 | NOV4-2 Transect 2 | RF | 2 | 0.04549 | 0.00554 | 28.83 | 0.11 |
| NOV4B NM0.6 | MS | 2 | 0.04541852 | 0.00572 | 27.21 | 0.11 | NOV4-2 Transect 2 | RF | 2 | 0.045413 | 0.00708 | 27.09 | 0.14 |
| NOV4B NM0.6 | MS | 2 | 0.045408254 | 0.00596 | 26.98 | 0.11 | NOV4-2 Transect 2 | RF | 2 | 0.045422 | 0.00594 | 27.30 | 0.12 |
| NOV4B NM0.6 | MS | 2 | 0.045423981 | 0.00571 | 27.33 | 0.11 | NOV4-2 Transect 2 | RF | 2 | 0.045415 | 0.00523 | 27.13 | 0.13 |
| NOV4B NM0.6 | MS | 2 | 0.045472544 | 0.00585 | 28.43 | 0.12 | NOV4-2 Transect 2 | RF | 2 | 0.045403 | 0.00936 | 26.95 | 0.17 |
| NOV4B NM0.6 | MS | 2 | 0.045483013 | 0.00545 | 28.67 | 0.11 | NOV4-2 Transect 2 | RF | 2 | 0.045479 | 0.00527 | 28.58 | 0.11 |
| NOV4B NM0.6 | MS | 2 | 0.045420378 | 0.00532 | 27.25 | 0.11 | NOV4-2 Transect 2 | RF | 2 | 0.045476 | 0.00613 | 28.52 | 0.12 |
| NOV4B NM0.6 | MS | 2 | 0.045417845 | 0.00585 | 27.19 | 0.11 | NOV4-2 Transect 2 | RF | 2 | 0.04545 | 0.00577 | 27.92 | 0.12 |
| NOV4B NM0.6 | MS | 2 | 0.045457247 | 0.00550 | 28.09 | 0.11 | NOV4-2 Transect 2 | RF | 2 | 0.045464 | 0.00560 | 28.25 | 0.11 |
| NOV4B NM0.6 | MS | 2 | 0.045416609 | 0.00580 | 27.17 | 0.12 | NOV4-2 Transect 2 | RF | 2 | 0.045415 | 0.00567 | 27.14 | 0.11 |
| NOV4B NM0.6 | MS | 2 | 0.04541223 | 0.00611 | 27.07 | 0.12 | NOV4-2 Transect 2 | RF | 2 | 0.045421 | 0.00567 | 27.26 | 0.11 |
| NOV4B NM0.6 | MS | 2 | 0.045416647 | 0.00569 | 27.17 | 0.11 | NOV4-2 Transect 2 | RF | 2 | 0.04544 | 0.00598 | 27.71 | 0.12 |
| NOV4B NM0.6 | MS | 2 | 0.045415036 | 0.00554 | 27.13 | 0.11 | NOV4-2 Transect 3 | RF | 2 | 0.04548 | 0.00582 | 28.60 | 0.12 |
| NOV4B NM0.6 | MS | 2 | 0.045417905 | 0.00572 | 27.20 | 0.12 | NOV4-2 Transect 3 | RF | 2 | 0.045429 | 0.00574 | 27.45 | 0.12 |
| NOV4B NM0.6 | MS | 2 | 0.04541448 | 0.00560 | 27.12 | 0.11 | NOV4-2 Transect 3 | RF | 2 | 0.045489 | 0.00565 | 28.81 | 0.11 |
| NOV4B NM0.6 | MS | 2 | 0.045489785 | 0.00557 | 28.82 | 0.11 | NOV4-2 Transect 3 | RF | 2 | 0.045404 | 0.00533 | 26.88 | 0.11 |
| NOV4B NM0.6 | MS | 2 | 0.045413475 | 0.00559 | 27.10 | 0.11 | NOV4-2 Transect 3 | RF | 2 | 0.045438 | 0.00555 | 27.66 | 0.11 |
| NOV4B NM0.6 | MS | 2 | 0.04542631 | 0.00578 | 27.39 | 0.12 | NOV4-2 Transect 3 | RF | 2 | 0.045452 | 0.00569 | 27.97 | 0.11 |
| NOV4B NM0.6 | MS | 2 | 0.045430595 | 0.00569 | 27.48 | 0.11 | | | | | | | |
| NOV4B NM0.6 | MS | 2 | 0.04542442 | 0.00553 | 27.34 | 0.11 | NOV4-2 Transect 4 | RF | 2 | 0.045404 | 0.00567 | 26.89 | 0.11 |
| NOV4B NM0.6 | MS | 2 | 0.045485622 | 0.00616 | 28.73 | 0.12 | NOV4-2 Transect 4 | RF | 2 | 0.045422 | 0.00575 | 27.30 | 0.12 |
| NOV4B NM0.6 | MS | 2 | 0.045485712 | 0.00562 | 28.73 | 0.11 | NOV4-2 Transect 4 | RF | 2 | 0.045418 | 0.00561 | 27.21 | 0.11 |
| NOV4C NM1.2 | MS | 2 | 0.045415331 | 0.00595 | 27.14 | 0.12 | NOV4-2 Transect 4 | RF | 2 | 0.045411 | 0.00591 | 27.04 | 0.12 |
| NOV4C NM1.2 | MS | 2 | 0.045410424 | 0.00547 | 27.03 | 0.11 | NOV4-2 Transect 4 | RF | 2 | 0.045409 | 0.00601 | 26.99 | 0.12 |
| NOV4C NM1.2 | MS | 2 | 0.04541481 | 0.00585 | 27.13 | 0.12 | NOV4-2 Transect 4 | RF | 2 | 0.045428 | 0.00542 | 27.42 | 0.12 |
| NOV4C NM1.2 | MS | 2 | 0.045423988 | 0.00573 | 27.33 | 0.12 | NOV4-2 Transect 4 | RF | 2 | 0.045464 | 0.00570 | 28.23 | 0.11 |
| NOV4C NM1.2 | MS | 2 | 0.04543937 | 0.00568 | 27.68 | 0.11 | NOV4-2 Transect 4 | RF | 2 | 0.045479 | 0.00545 | 28.58 | 0.11 |
| NOV4C NM1.2 | MS | 2 | 0.045490298 | 0.00567 | 28.84 | 0.11 | NOV4-2 Transect 4 | RF | 2 | 0.045407 | 0.00567 | 26.95 | 0.11 |
| NOV4C NM1.2 | MS | 2 | 0.045417088 | 0.00578 | 27.18 | 0.12 | NOV4-2 Transect 4 | RF | 2 | 0.045422 | 0.00613 | 27.29 | 0.12 |
| NOV4C NM1.2 | MS | 2 | 0.045428364 | 0.00571 | 27.43 | 0.11 | NOV4-2 Transect 4 | RF | 2 | 0.045415 | 0.00586 | 27.13 | 0.12 |
| NOV4C NM1.2 | MS | 2 | 0.045501043 | 0.00585 | 29.08 | 0.12 | NOV4-2 Transect 4 | RF | 2 | 0.045413 | 0.00555 | 27.08 | 0.11 |
| NO | | | | | | | | | | | | | |

Table 4.1.15: SIMS sulphur isotope analyses of Hawker Creek samples

| Name | Type | Session | $^{34}\text{S}/^{32}\text{S}$ | 1σ (%) intra-session | $\delta^{34}\text{S}$ (VCDT) | 2σ (%) inter-session | Name | Type | Session | $^{34}\text{S}/^{32}\text{S}$ | 1σ (%) intra-session | $\delta^{34}\text{S}$ (VCDT) | 2σ (%) inter-session |
|-----------------|------|---------|-------------------------------|--------------------------------|---------------------------------|--------------------------------|---------------------|------|---------|-------------------------------|--------------------------------|---------------------------------|--------------------------------|
| 03-HC-8D M0.8 | MS | 1 | 0.045543 | 0.00639 | 30.04 | 0.13 | 03-HC-8D Transect 1 | RF | 1 | 0.045493 | 0.00589 | 28.90 | 0.12 |
| 03-HC-8D M0.8 | MS | 1 | 0.045552 | 0.00590 | 30.23 | 0.12 | 03-HC-8D Transect 1 | RF | 1 | 0.045497 | 0.00615 | 28.98 | 0.12 |
| 03-HC-8D M0.8 | MS | 1 | 0.045574 | 0.00589 | 30.72 | 0.12 | 03-HC-8D Transect 1 | RF | 1 | 0.045506 | 0.00562 | 29.20 | 0.11 |
| 03-HC-8D M0.8 | MS | 1 | 0.045537 | 0.00595 | 29.89 | 0.12 | 03-HC-8D Transect 1 | RF | 1 | 0.04532 | 0.00567 | 24.97 | 0.12 |
| 03-HC-8D M0.8 | MS | 1 | 0.045462 | 0.00577 | 28.19 | 0.12 | 03-HC-8D Transect 1 | RF | 1 | 0.045499 | 0.00596 | 29.04 | 0.12 |
| 03-HC-8D M0.8 | MS | 1 | 0.045529 | 0.00585 | 29.71 | 0.12 | 03-HC-8D Transect 1 | RF | 1 | 0.045477 | 0.00589 | 28.54 | 0.12 |
| 03-HC-8D M0.8 | MS | 1 | 0.045471 | 0.00574 | 28.39 | 0.12 | 03-HC-8D Transect 1 | RF | 1 | 0.04555 | 0.00589 | 30.18 | 0.12 |
| 03-HC-8D M0.8 | MS | 1 | 0.045474 | 0.00592 | 28.47 | 0.12 | 03-HC-8D Transect 1 | RF | 1 | 0.045548 | 0.00607 | 30.15 | 0.12 |
| 03-HC-8D M0.8 | MS | 1 | 0.045574 | 0.00672 | 30.72 | 0.14 | 03-HC-8D Transect 1 | RF | 1 | 0.045489 | 0.00639 | 28.80 | 0.13 |
| 03-HC-8D M0.8 | MS | 1 | 0.04546 | 0.00662 | 28.15 | 0.13 | 03-HC-8D Transect 1 | RF | 1 | 0.045473 | 0.00671 | 28.45 | 0.14 |
| 03-HC-8D M0.8 | MS | 1 | 0.045474 | 0.00594 | 28.47 | 0.12 | 03-HC-8D Transect 1 | RF | 1 | 0.045453 | 0.01208 | 27.99 | 0.24 |
| 03-HC-8D M0.8 | MS | 1 | 0.045465 | 0.00589 | 28.27 | 0.12 | 03-HC-8D Transect 1 | RF | 1 | 0.045544 | 0.00597 | 30.05 | 0.12 |
| 03-HC-8D M0.8 | MS | 1 | 0.045439 | 0.00876 | 27.66 | 0.18 | 03-HC-8D Transect 1 | RF | 1 | 0.045539 | 0.00617 | 29.93 | 0.13 |
| 03-HC-8D M0.8 | MS | 1 | 0.045476 | 0.00820 | 28.50 | 0.17 | 03-HC-8D Transect 1 | RF | 1 | 0.045439 | 0.00727 | 27.67 | 0.15 |
| 03-HC-8D M0.8 | MS | 1 | 0.045483 | 0.00578 | 28.67 | 0.12 | 03-HC-8D Transect 1 | RF | 1 | 0.045458 | 0.00577 | 28.09 | 0.12 |
| 03-HC-8D M0.8 | MS | 1 | 0.045456 | 0.00580 | 28.06 | 0.12 | 03-HC-8D Transect 1 | RF | 1 | 0.045504 | 0.00593 | 29.14 | 0.12 |
| 03-HC-8D M0.8 | MS | 1 | 0.045535 | 0.00618 | 29.86 | 0.13 | 03-HC-8D Transect 1 | RF | 1 | 0.0455 | 0.00664 | 29.06 | 0.13 |
| 03-HC-8D M0.8 | MS | 1 | 0.045493 | 0.00807 | 28.90 | 0.16 | 03-HC-8D Transect 1 | RF | 1 | 0.045544 | 0.00568 | 30.04 | 0.12 |
| 03-HC-8D M0.8 | MS | 1 | 0.045548 | 0.00577 | 30.15 | 0.12 | 03-HC-8D Transect 1 | RF | 1 | 0.045533 | 0.00626 | 29.80 | 0.13 |
| 03-HC-8D M0.8 | MS | 1 | 0.045488 | 0.00585 | 28.77 | 0.12 | 03-HC-8D Transect 1 | RF | 1 | 0.04551 | 0.00722 | 29.29 | 0.15 |
| 03-HC-8D M0.8 | MS | 1 | 0.045528 | 0.00682 | 29.68 | 0.14 | 03-HC-8D Transect 1 | RF | 1 | 0.045535 | 0.00628 | 29.86 | 0.13 |
| 03-HC-8D M0.8 | MS | 1 | 0.045396 | 0.00592 | 26.70 | 0.12 | 03-HC-8D Transect 1 | RF | 1 | 0.04554 | 0.00599 | 29.97 | 0.12 |
| 03-HC-8D M0.8 | MS | 1 | 0.045519 | 0.00920 | 29.49 | 0.19 | 03-HC-8D Transect 1 | RF | 1 | 0.045539 | 0.00580 | 29.94 | 0.12 |
| 03-HC-8D M0.8 | MS | 1 | 0.045502 | 0.00594 | 29.09 | 0.12 | 03-HC-8D Transect 1 | RF | 1 | 0.045543 | 0.00593 | 30.04 | 0.12 |
| 03-HC-8D M0.8 | MS | 1 | 0.045486 | 0.00594 | 28.73 | 0.12 | 03-HC-8D Transect 1 | RF | 1 | 0.045538 | 0.00581 | 29.92 | 0.12 |
| 03-HC-8D M0.8 | MS | 1 | 0.045512 | 0.00596 | 29.33 | 0.12 | 03-HC-8D Transect 1 | RF | 1 | 0.045538 | 0.00581 | 29.92 | 0.12 |
| 03-HC-8D M0.8 | MS | 1 | 0.045467 | 0.00570 | 28.31 | 0.12 | 03-HC-8D Transect 1 | RF | 1 | 0.045539 | 0.00628 | 29.94 | 0.13 |
| 03-HC-8D M0.8 | MS | 1 | 0.045467 | 0.00598 | 28.31 | 0.12 | 03-HC-8D Transect 1 | RF | 1 | 0.045537 | 0.00617 | 29.90 | 0.12 |
| 03-HC-8D M0.8 | MS | 1 | 0.045529 | 0.00594 | 29.70 | 0.12 | 03-HC-8D Transect 1 | RF | 1 | 0.045505 | 0.00573 | 29.18 | 0.12 |
| 03-HC-8D M0.8 | MS | 1 | 0.04546 | 0.00577 | 28.14 | 0.12 | 03-HC-8D Transect 1 | RF | 1 | 0.045479 | 0.00581 | 28.59 | 0.12 |
| 03-HC-8D M0.8 | MS | 1 | 0.045466 | 0.00573 | 28.28 | 0.12 | | | | | | | |
| 03-HC-8D NM 2.0 | MS | 1 | 0.045456 | 0.00590 | 28.07 | 0.12 | 03-HC-8D Transect 2 | RF | 1 | 0.045485 | 0.00575 | 28.71 | 0.12 |
| 03-HC-8D NM 2.0 | MS | 1 | 0.045485 | 0.00580 | 28.71 | 0.12 | 03-HC-8D Transect 2 | RF | 1 | 0.045546 | 0.00596 | 30.09 | 0.12 |
| 03-HC-8D NM 2.0 | MS | 1 | 0.045494 | 0.00794 | 28.91 | 0.16 | 03-HC-8D Transect 2 | RF | 1 | 0.045497 | 0.00605 | 28.99 | 0.12 |
| 03-HC-8D NM 2.0 | MS | 1 | 0.045459 | 0.00588 | 28.13 | 0.12 | 03-HC-8D Transect 2 | RF | 1 | 0.04547 | 0.00549 | 28.37 | 0.11 |
| 03-HC-8D NM 2.0 | MS | 1 | 0.0455 | 0.00571 | 29.06 | 0.12 | 03-HC-8D Transect 2 | RF | 1 | 0.045527 | 0.00703 | 29.66 | 0.14 |
| 03-HC-8D NM 2.0 | MS | 1 | 0.045506 | 0.00581 | 29.20 | 0.12 | 03-HC-8D Transect 2 | RF | 1 | 0.045465 | 0.00685 | 28.26 | 0.14 |
| 03-HC-8D NM 2.0 | MS | 1 | 0.045498 | 0.00595 | 29.02 | 0.12 | 03-HC-8D Transect 2 | RF | 1 | 0.045532 | 0.00590 | 29.78 | 0.12 |
| 03-HC-8D NM 2.0 | MS | 1 | 0.045481 | 0.00594 | 28.62 | 0.12 | 03-HC-8D Transect 2 | RF | 1 | 0.045507 | 0.00971 | 29.22 | 0.20 |
| 03-HC-8D NM 2.0 | MS | 1 | 0.045516 | 0.00529 | 29.41 | 0.11 | 03-HC-8D Transect 2 | RF | 1 | 0.045464 | 0.00622 | 28.23 | 0.13 |
| 03-HC-8D NM 2.0 | MS | 1 | 0.045504 | 0.00600 | 29.15 | 0.12 | 03-HC-8D Transect 2 | RF | 1 | 0.045552 | 0.00590 | 30.24 | 0.12 |
| 03-HC-8D NM 2.0 | MS | 1 | 0.045529 | 0.00600 | 29.72 | 0.12 | 03-HC-8D Transect 2 | RF | 1 | 0.045541 | 0.00592 | 29.98 | 0.12 |
| 03-HC-8D NM 2.0 | MS | 1 | 0.045475 | 0.00564 | 28.48 | 0.11 | 03-HC-8D Transect 2 | RF | 1 | 0.045453 | 0.00586 | 27.98 | 0.12 |
| 03-HC-8D NM 2.0 | MS | 1 | 0.045503 | 0.00575 | 29.12 | 0.12 | 03-HC-8D Transect 2 | RF | 1 | 0.045547 | 0.00581 | 30.11 | 0.12 |
| 03-HC-8D NM 2.0 | MS | 1 | 0.045503 | 0.00595 | 29.13 | 0.12 | 03-HC-8D Transect 2 | RF | 1 | 0.045529 | 0.00933 | 29.71 | 0.19 |
| 03-HC-8D NM 2.0 | MS | 1 | 0.045462 | 0.00581 | 28.19 | 0.12 | 03-HC-8D Transect 3 | RF | 1 | 0.045548 | 0.00581 | 30.14 | 0.12 |
| 03-HC-8D NM 2.0 | MS | 1 | 0.045523 | 0.00588 | 29.56 | 0.12 | 03-HC-8D Transect 3 | RF | 1 | 0.045493 | 0.00830 | 28.89 | 0.17 |
| 03-HC-8D NM 2.0 | MS | 1 | 0.04549 | 0.00600 | 28.84 | 0.12 | 03-HC-8D Transect 3 | RF | 1 | 0.045514 | 0.00586 | 29.37 | 0.12 |
| 03-HC-8D NM 2.0 | MS | 1 | 0.045512 | 0.00564 | 29.32 | 0.11 | 03-HC-8D Transect 3 | RF | 1 | 0.045469 | 0.00612 | 28.34 | 0.12 |
| 03-HC-8D NM 2.0 | MS | 1 | 0.045493 | 0.00615 | 29.91 | 0.12 | 03-HC-8D Transect 3 | RF | 1 | 0.045441 | 0.00753 | 27.72 | 0.15 |
| 03-HC-8D NM 2.0 | MS | 1 | 0.045514 | 0.00588 | 28.97 | 0.12 | 03-HC-8D Transect 3 | RF | 1 | 0.045453 | 0.00595 | 27.98 | 0.12 |
| 03-HC-8D NM 2.0 | MS | 1 | 0.04552 | 0.00592 | 29.51 | 0.12 | 03-HC-8D Transect 3 | RF | 1 | 0.045474 | 0.00605 | 28.47 | 0.12 |
| 03-HC-8D NM 2.0 | MS | 1 | 0.045459 | 0.00563 | 28.12 | 0.11 | 03-HC-8D Transect 3 | RF | 1 | 0.045479 | 0.00610 | 28.58 | 0.12 |
| 03-HC-8D NM 2.0 | MS | 1 | 0.0455 | 0.00599 | 29.06 | 0.12 | 03-HC-8D Transect 3 | RF | 1 | 0.045494 | 0.00607 | 28.91 | 0.12 |
| 03-HC-8D NM 2.0 | MS | 1 | 0.045559 | 0.00597 | 30.39 | 0.12 | | | | | | | |
| 03-HC-8D NM 2.0 | MS | 1 | 0.045485 | 0.00590 | 28.72 | 0.12 | 03-HC-8D Transect 4 | RF | 1 | 0.045549 | 0.00617 | 30.17 | 0.13 |
| 03-HC-8D NM 2.0 | MS | 1 | 0.045539 | 0.00732 | 29.94 | 0.15 | 03-HC-8D Transect 4 | RF | 1 | 0.045544 | 0.00585 | 30.05 | 0.12 |
| 03-HC-8D NM 2.0 | MS | 1 | 0.04548 | 0.00585 | 28.61 | 0.12 | 03-HC-8D Transect 4 | RF | 1 | 0.045552 | 0.00587 | 30.23 | 0.12 |
| 03-HC-8D NM 2.0 | MS | 1 | 0.045486 | 0.00585 | 28.73 | 0.12 | 03-HC-8D Transect 4 | RF | 1 | 0.045525 | 0.00618 | 29.63 | 0.13 |
| 03-HC-8D NM 2.0 | MS | 1 | 0.045484 | 0.00590 | 28.70 | 0.12 | 03-HC-8D Transect 4 | RF | 1 | 0.045509 | 0.00612 | 29.25 | 0.12 |
| 03-HC-8D NM 2.0 | MS | 1 | 0.045492 | 0.00603 | 28.87 | 0.12 | 03-HC-8D Transect 4 | RF | 1 | 0.045515 | 0.00572 | 29.39 | 0.12 |
| 03-HC-8D NM 2.0 | MS | 1 | 0.0455 | 0.00590 | 29.05 | 0.12 | 03-HC-8D Transect 4 | RF | 1 | 0.045509 | 0.00584 | 29.26 | 0.12 |
| 03-HC-8D NM 2.0 | MS | 1 | 0.045455 | 0.00607 | 28.04 | 0.12 | 03-HC-8D Transect 4 | RF | 1 | 0.045539 | 0.00585 | 29.94 | 0.12 |
| 03-HC-8D NM 2.0 | MS | 1 | 0.045486 | 0.00591 | 28.73 | 0.12 | 03-HC-8D Transect 4 | RF | 1 | 0.04555 | 0.00600 | 30.18 | 0.12 |
| 03-HC-8D NM 2.0 | MS | 1 | 0.045476 | 0.00580 | 28.52 | 0.12 | 03-HC-8D Transect 4 | RF | 1 | 0.045549 | 0.00604 | 30.16 | 0.12 |
| 03-HC-8D NM 2.0 | MS | 1 | 0.04549 | 0.00598 | 28.84 | 0.12 | 03-HC-8D Transect 4 | RF | 1 | 0.045515 | 0.00629 | 29.39 | 0.13 |
| 03-HC-8D NM 2.0 | MS | 1 | 0.045497 | 0.00594 | 28.99 | 0.12 | 03-HC-8D Transect 4 | RF | 1 | 0.045502 | 0.00759 | 29.11 | 0.15 |

Raw sulphur isotope data from SIMS analysis. See Figure 4.1.13 for transect locations. *MS = Mineral Separate, RF = Rock Fragment.

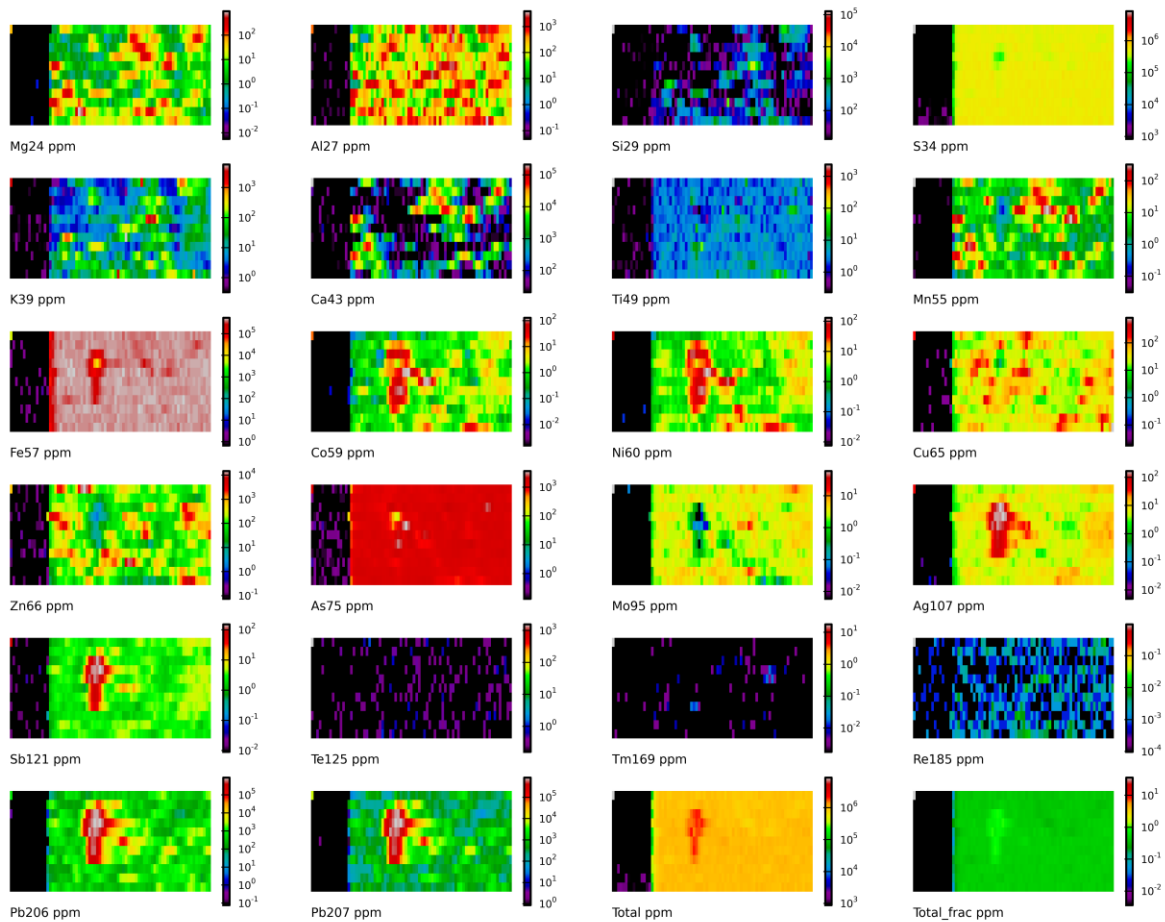


Figure 4.1.32: LA-ICPMS elemental maps for 8S08FW Map 1.

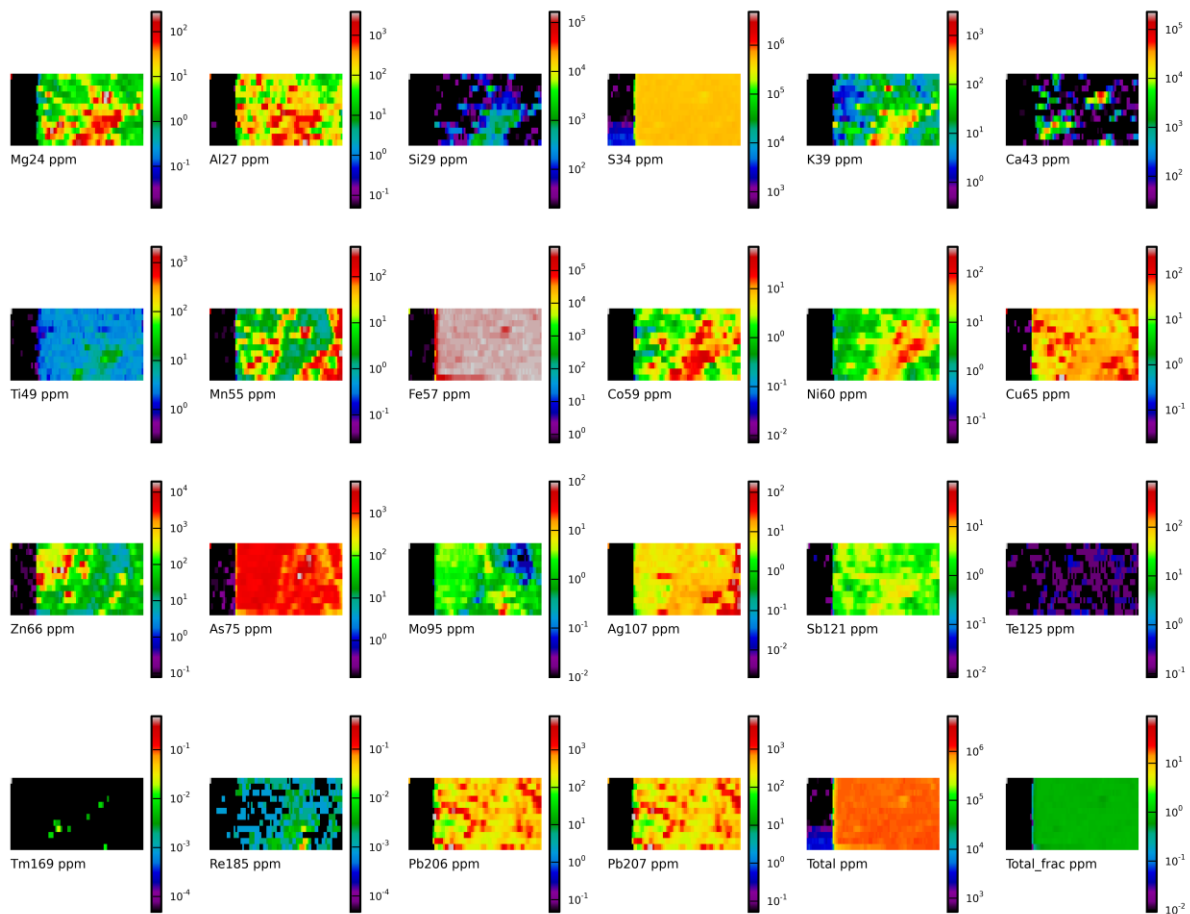


Figure 4.1.33: LA-ICPMS elemental maps for 8S08FW Map 2.

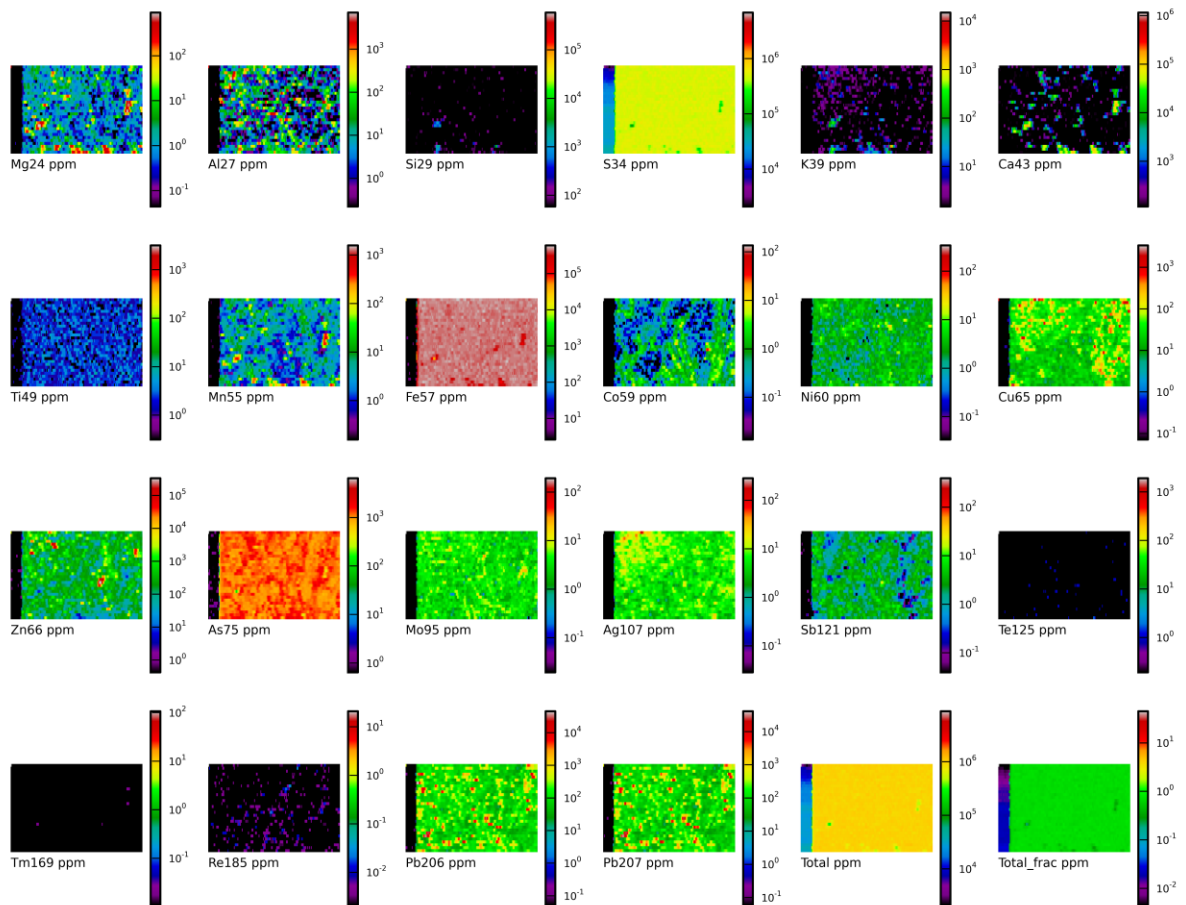


Figure 4.1.34: LA-ICPMS elemental maps for 8S08FW Map 3.

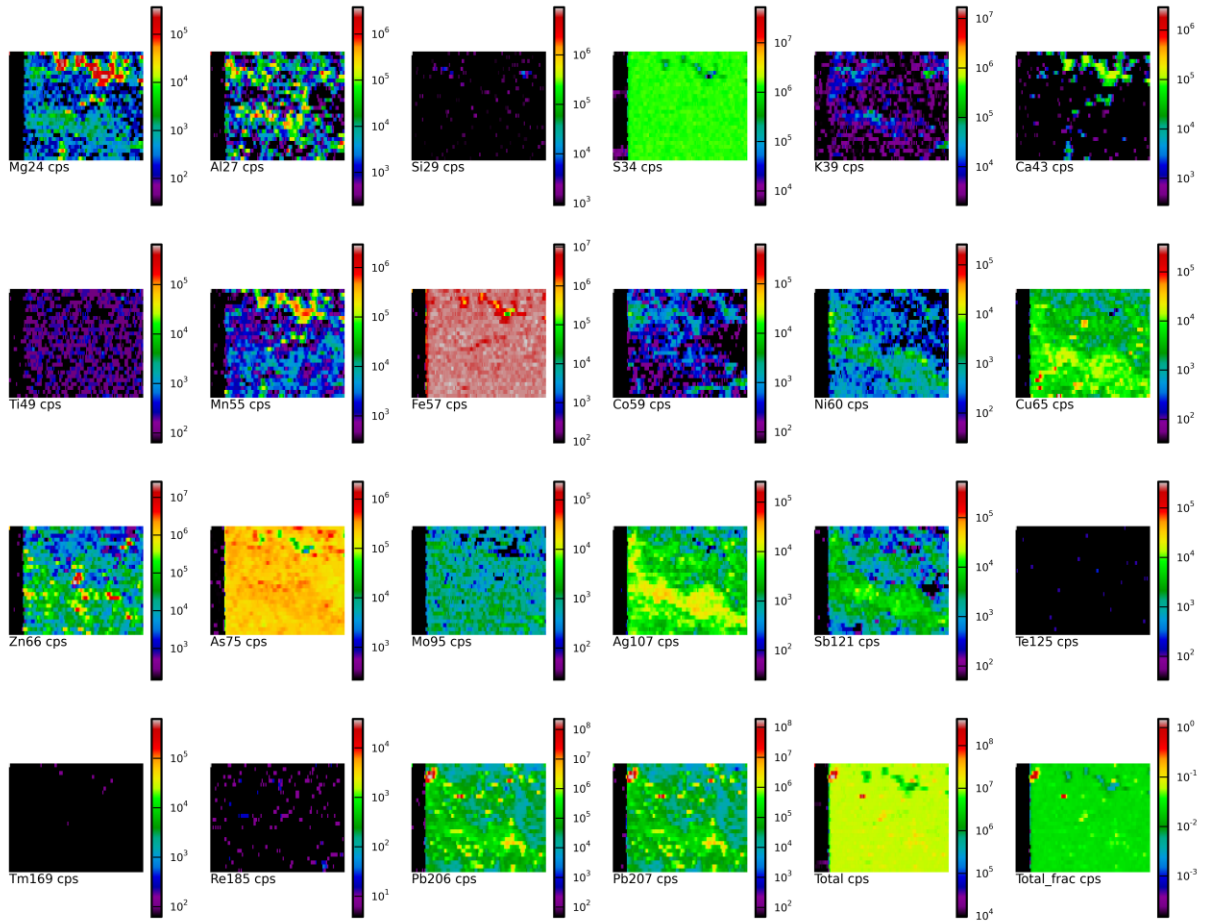


Figure 4.1.35: LA-ICPMS elemental maps for 8S08FW Map 4.

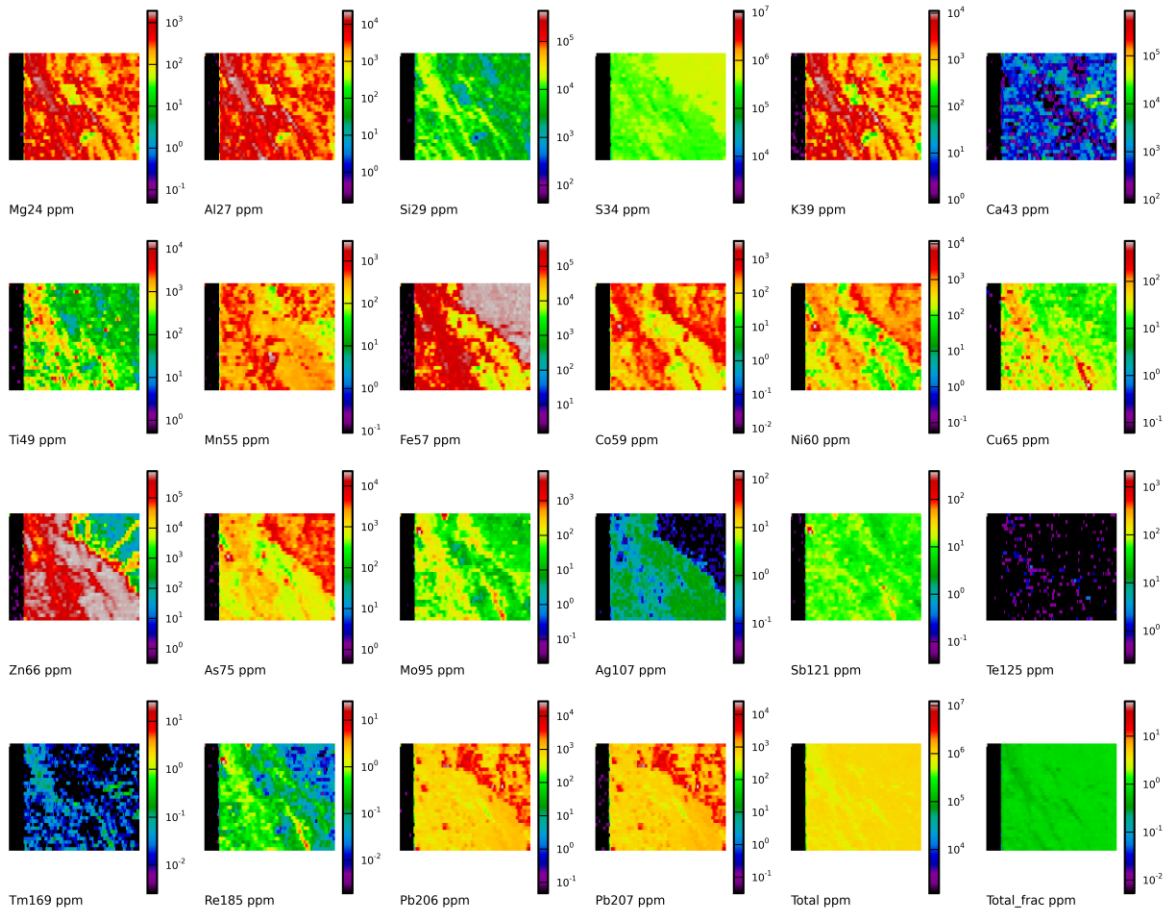


Figure 4.1.36: LA-ICPMS elemental maps for LK 359-1 Map 1.

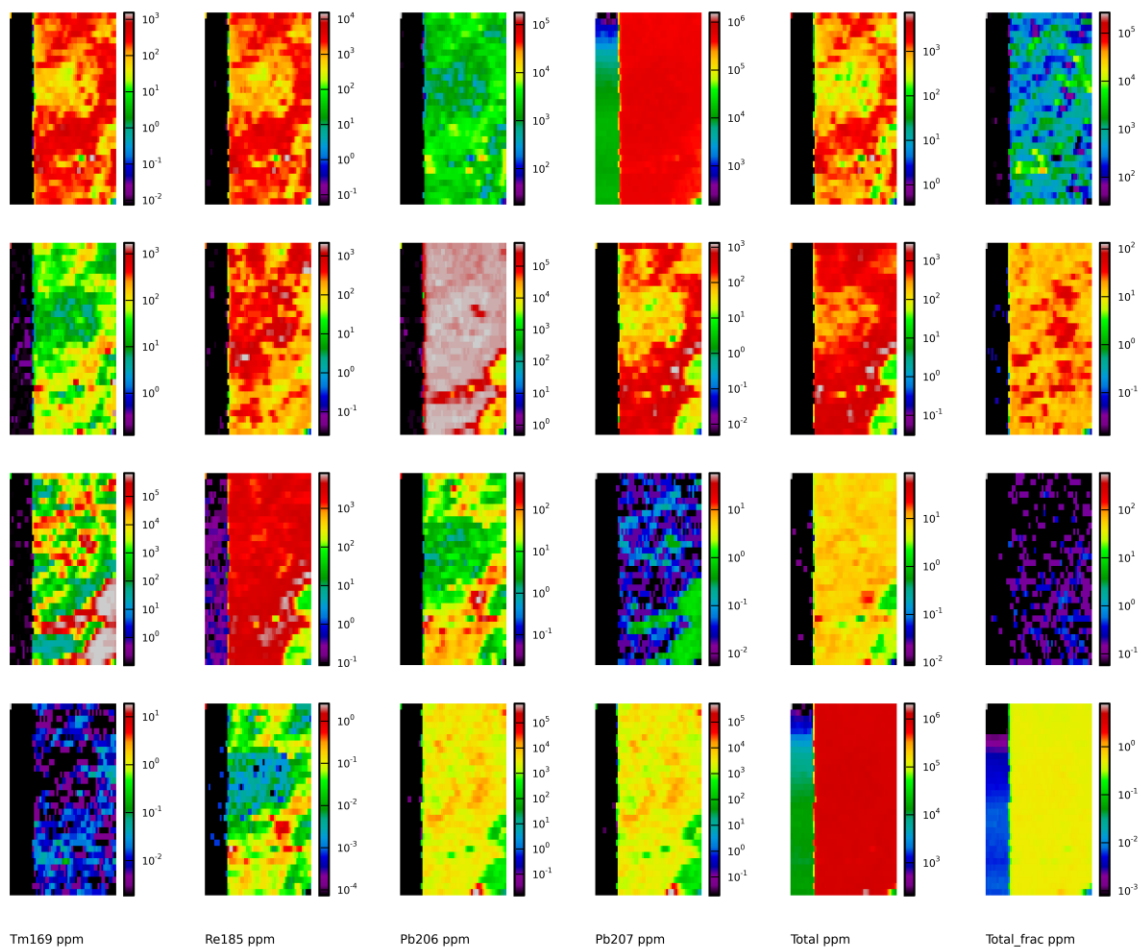


Figure 4.1.37: LA-ICPMS elemental maps for LK 359-1 Map 2.

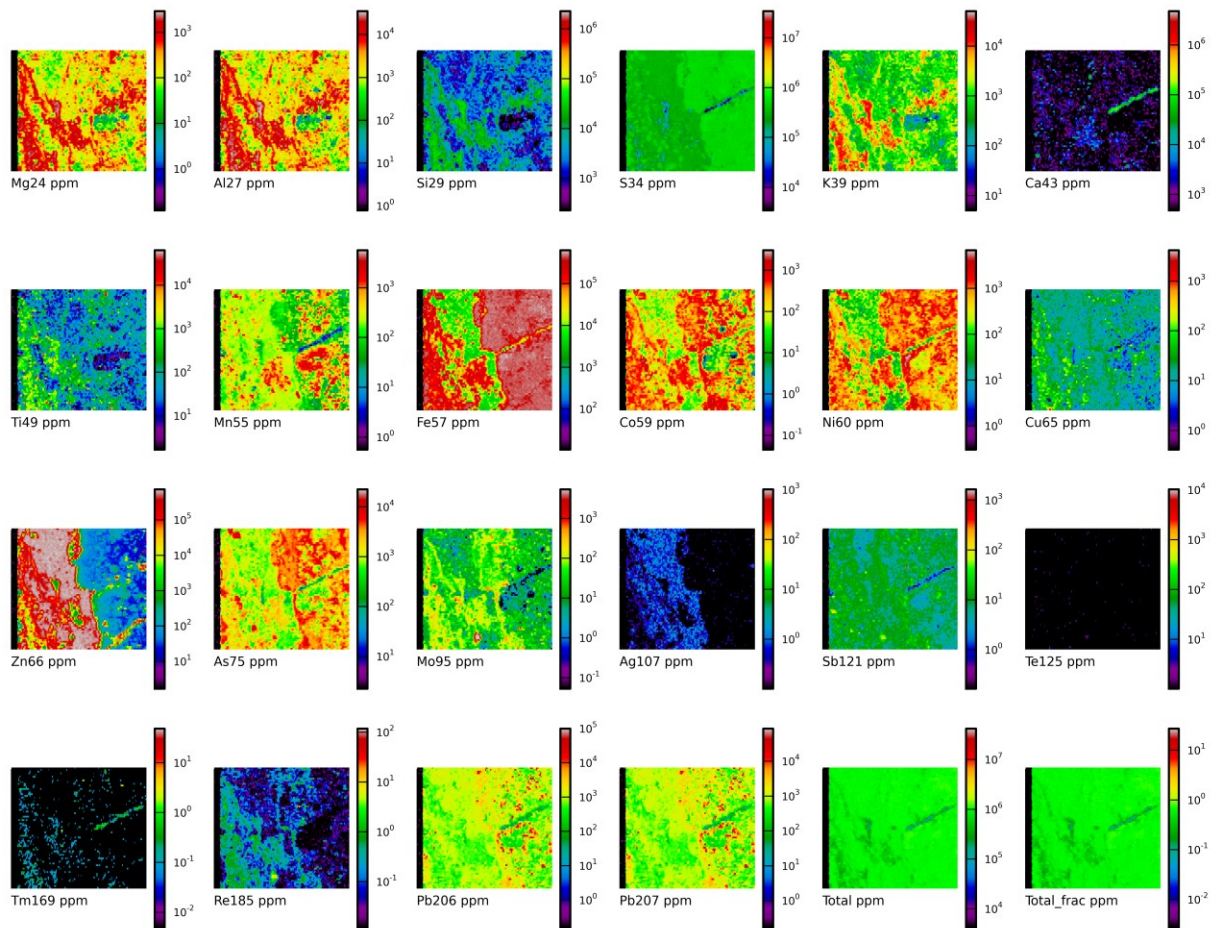


Figure 4.1.38: LA-ICPMS elemental maps for LK 359-1 Map 3.

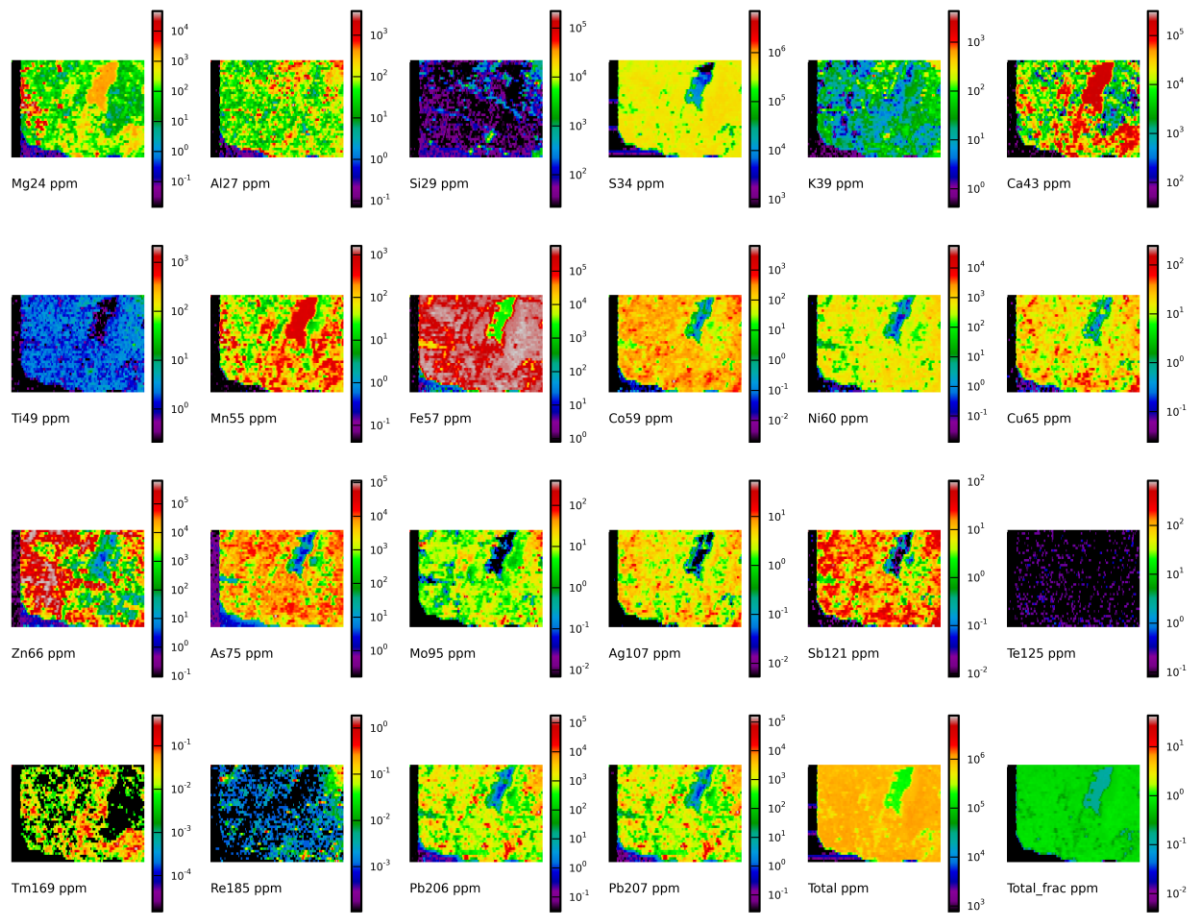


Figure 4.1.39: LA-ICPMS elemental maps for LK 451 Map 1.

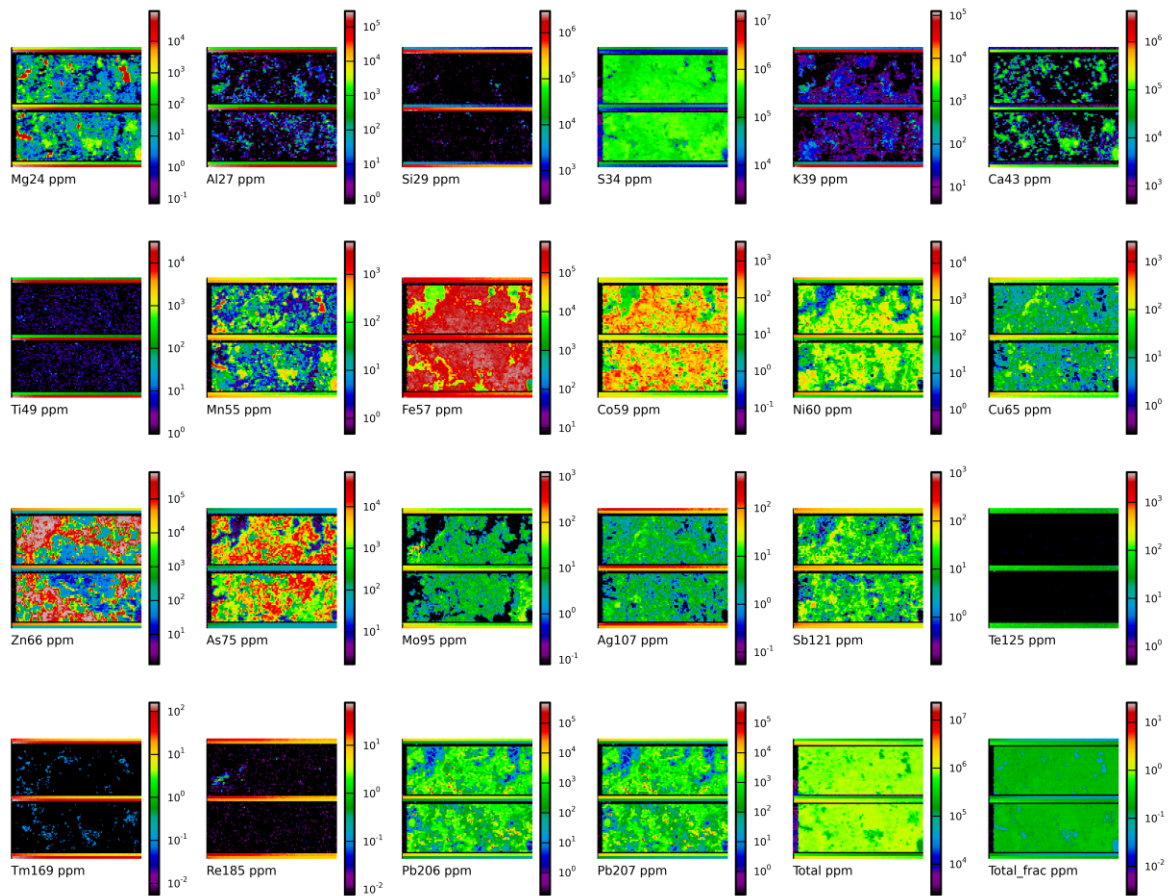


Figure 4.1.40: LA-ICPMS elemental maps for LK 451 Map 2.

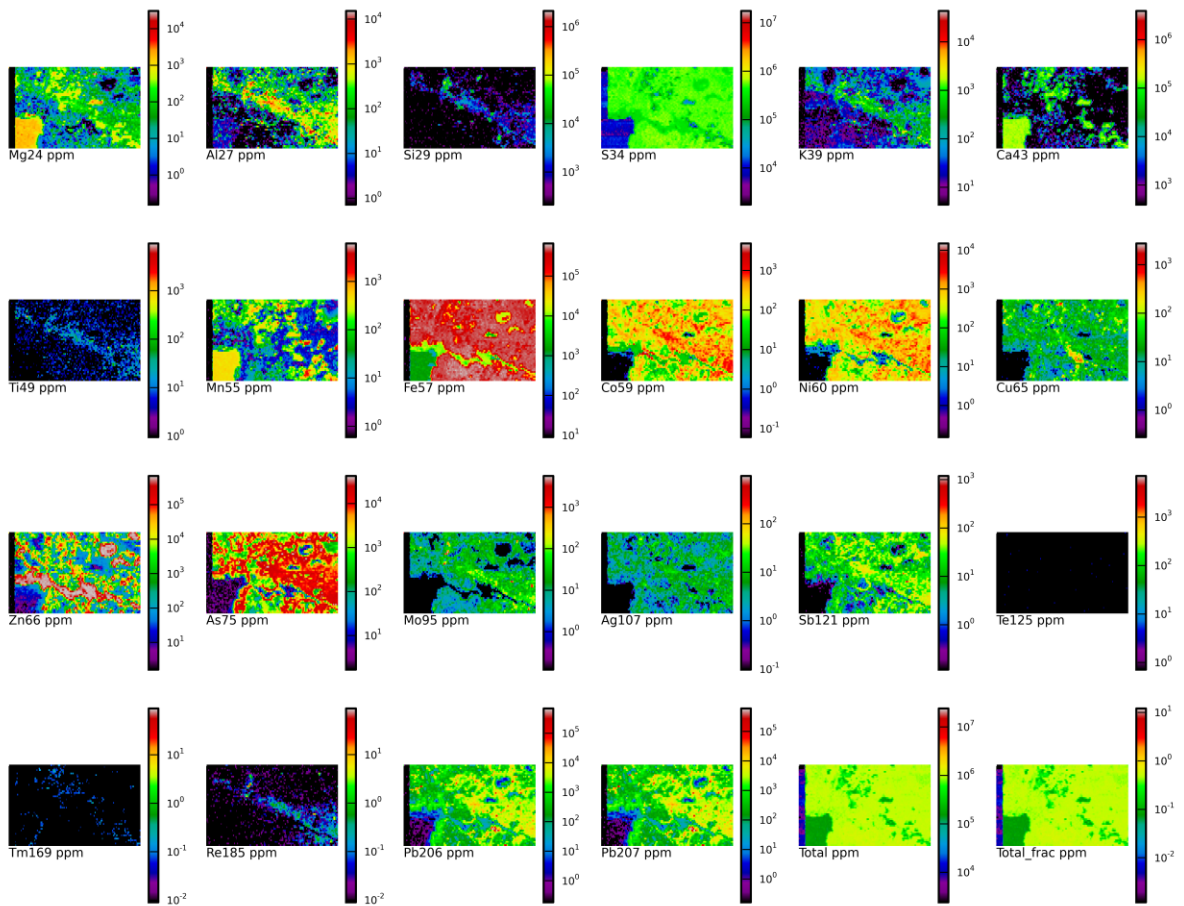


Figure 4.1.41: LA-ICPMS elemental maps for LK 451 Map 3.

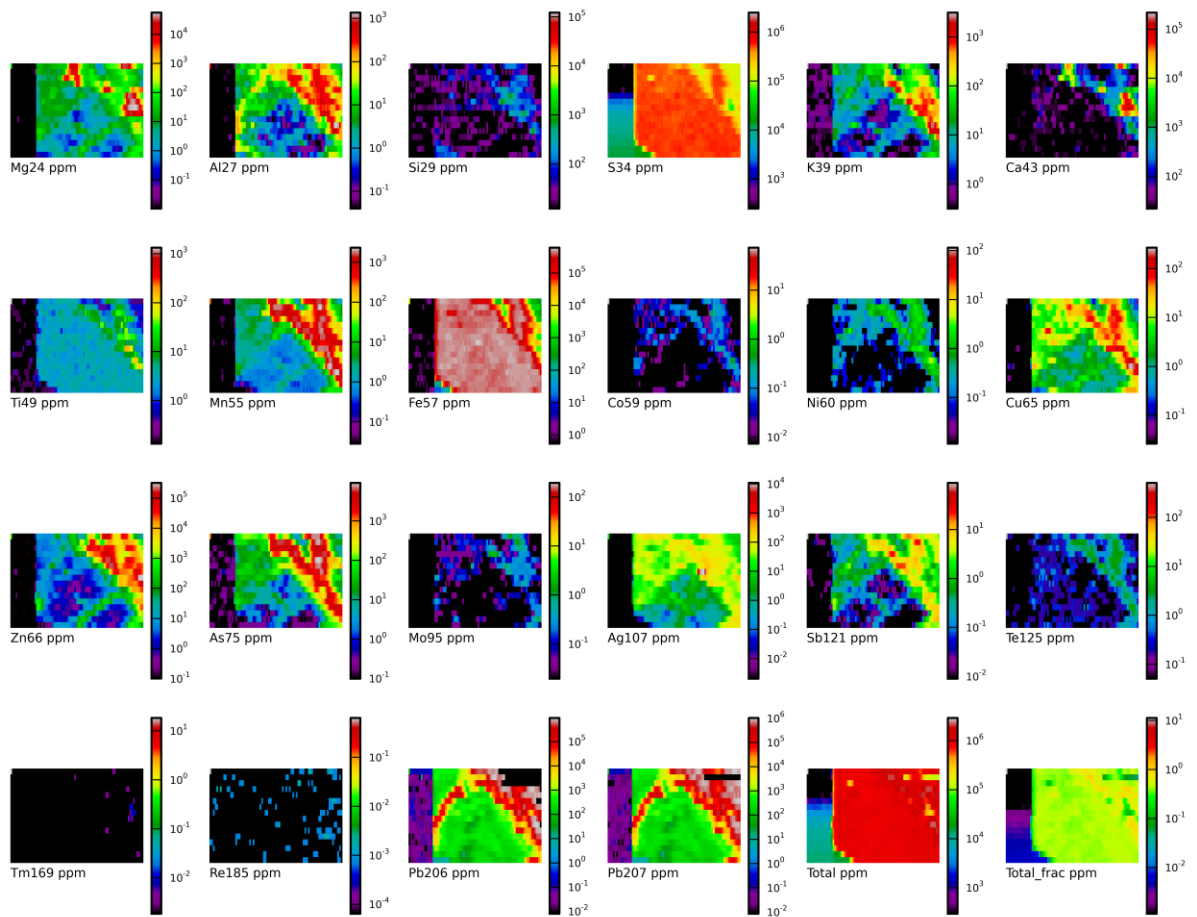


Figure 4.1.42: LA-ICPMS elemental maps for NOV-1 Map 1.

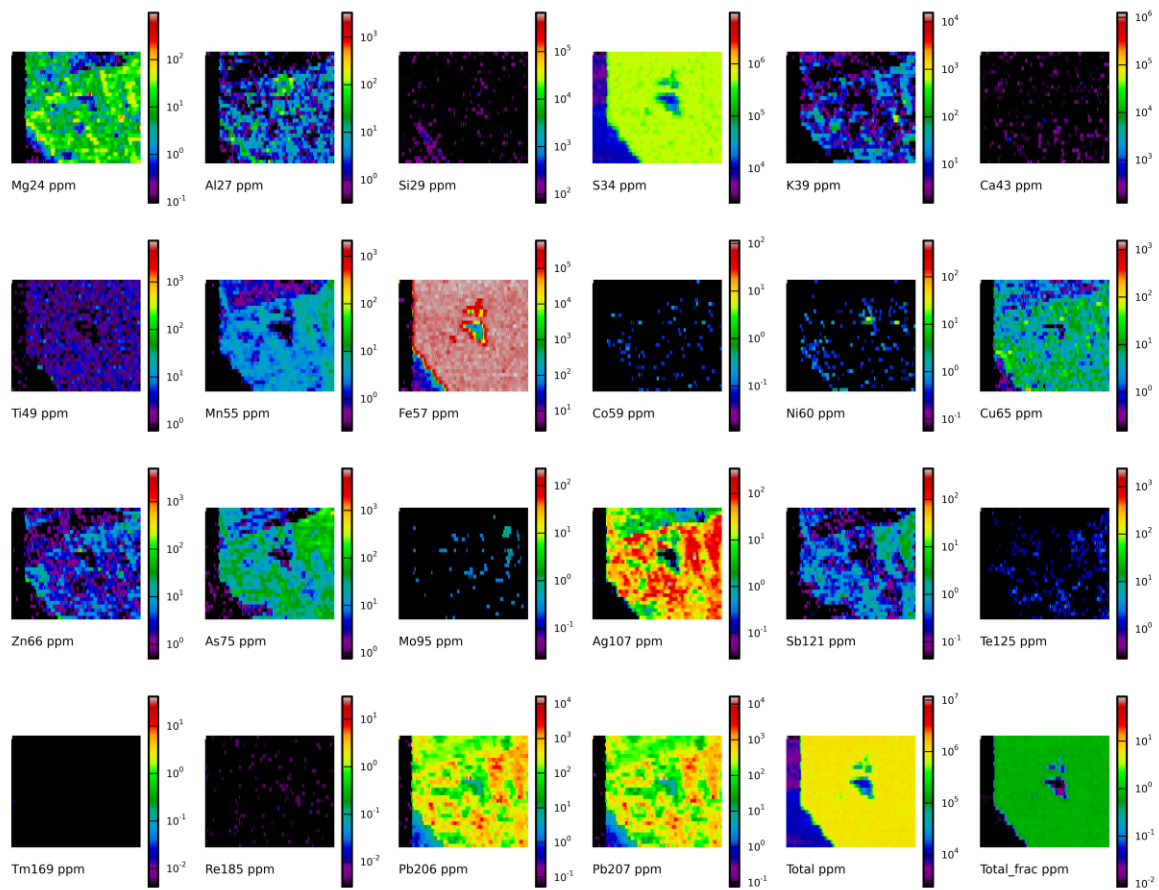


Figure 4.1.43: LA-ICPMS elemental maps for NOV-1 Map 2.

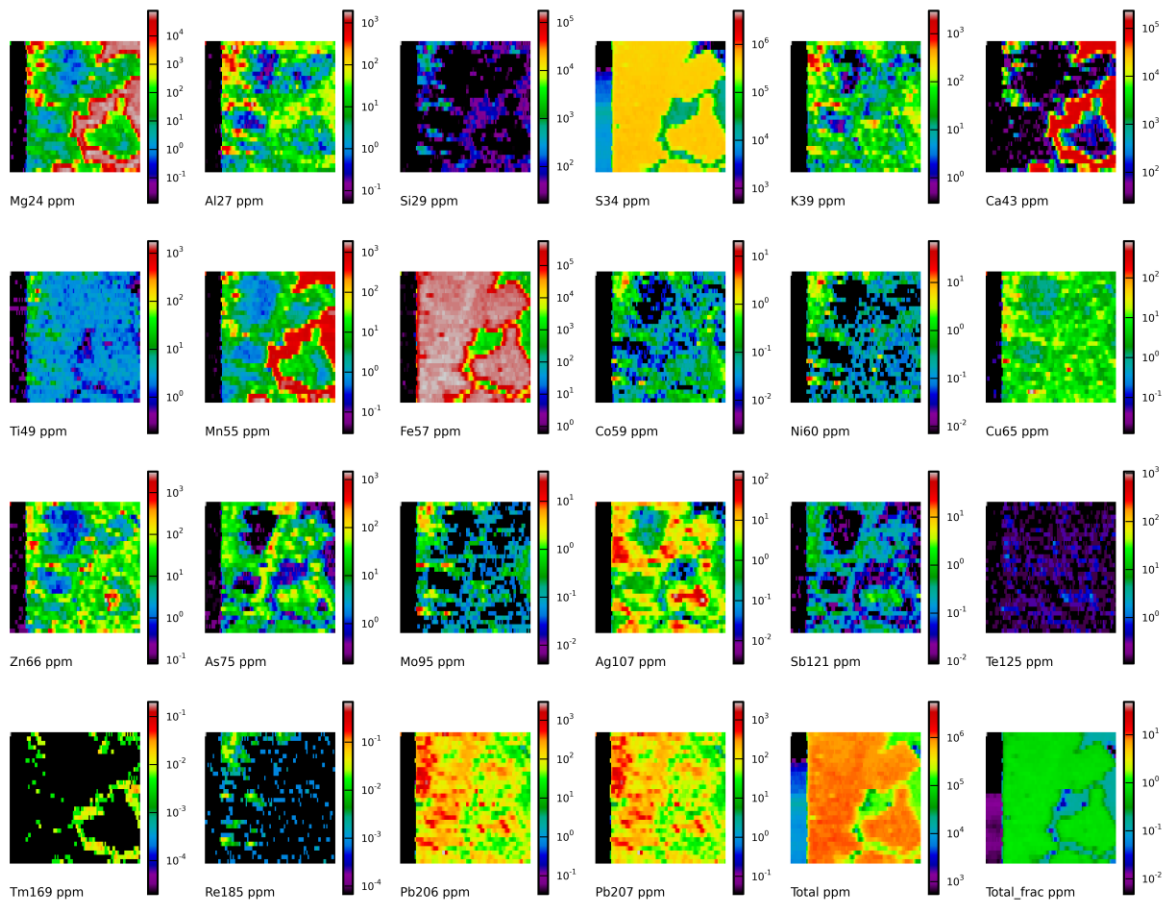


Figure 4.1.44: LA-ICPMS elemental maps for NOV-2 Map 1.

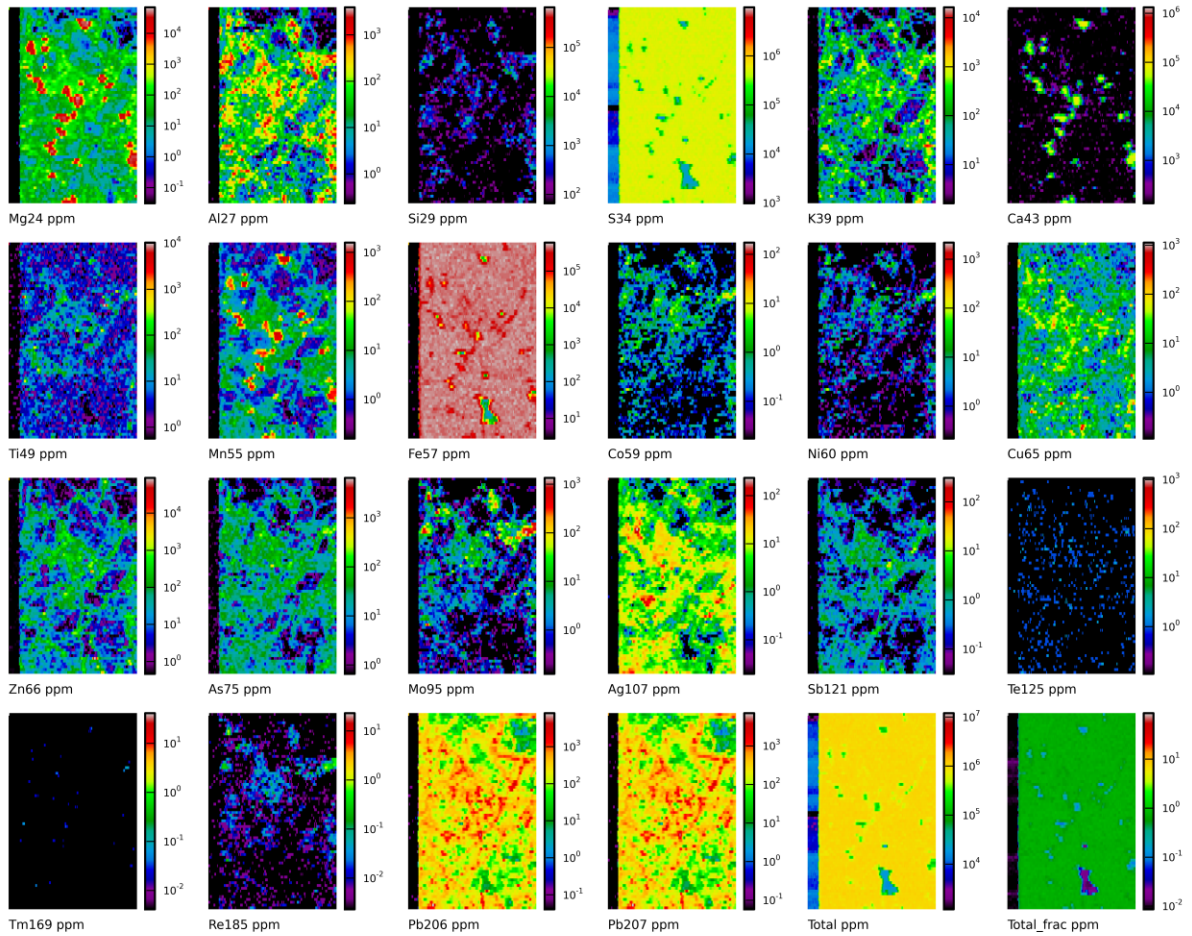


Figure 4.1.45: LA-ICPMS elemental maps for NOV-2 Map 2.

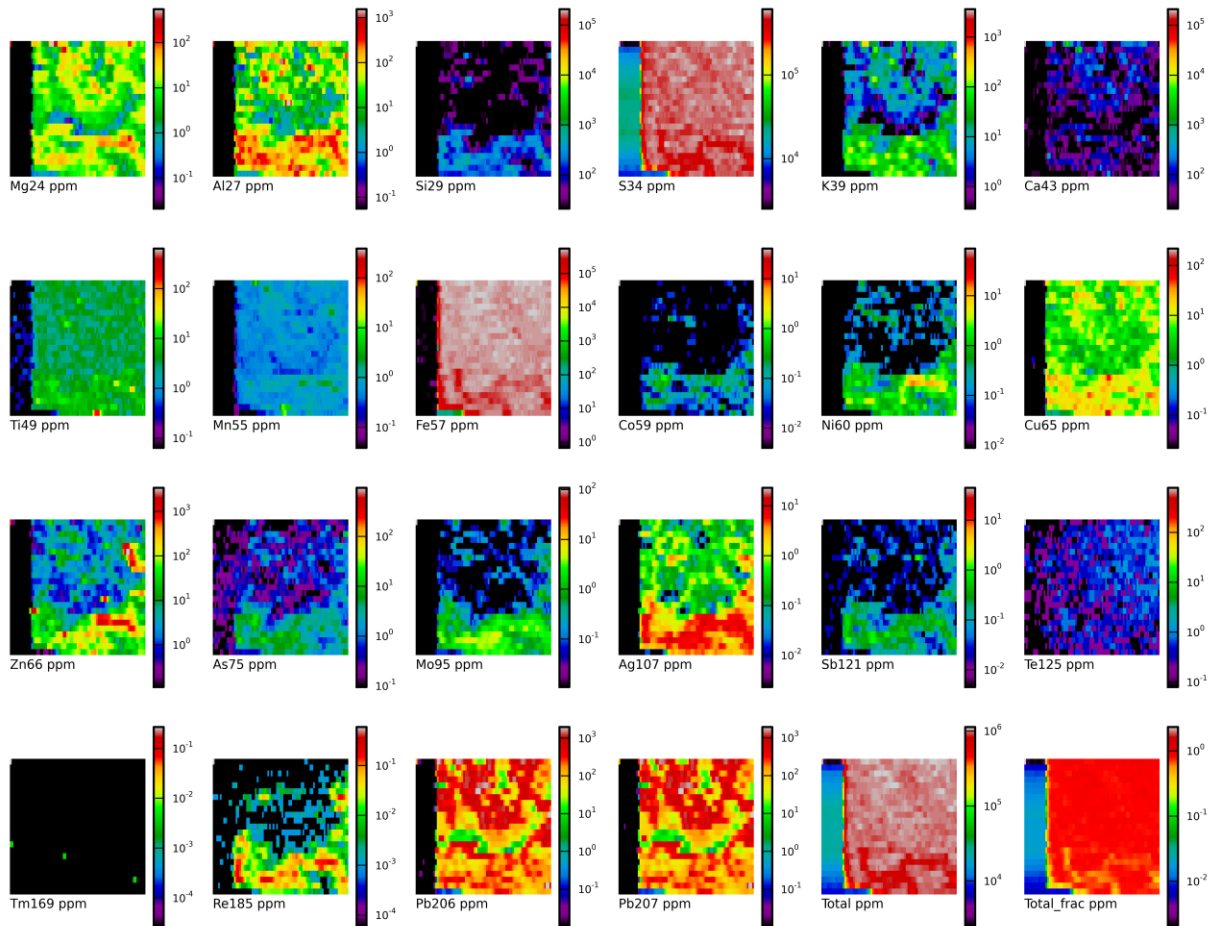


Figure 4.1.46: LA-ICPMS elemental maps for HC Map 1.

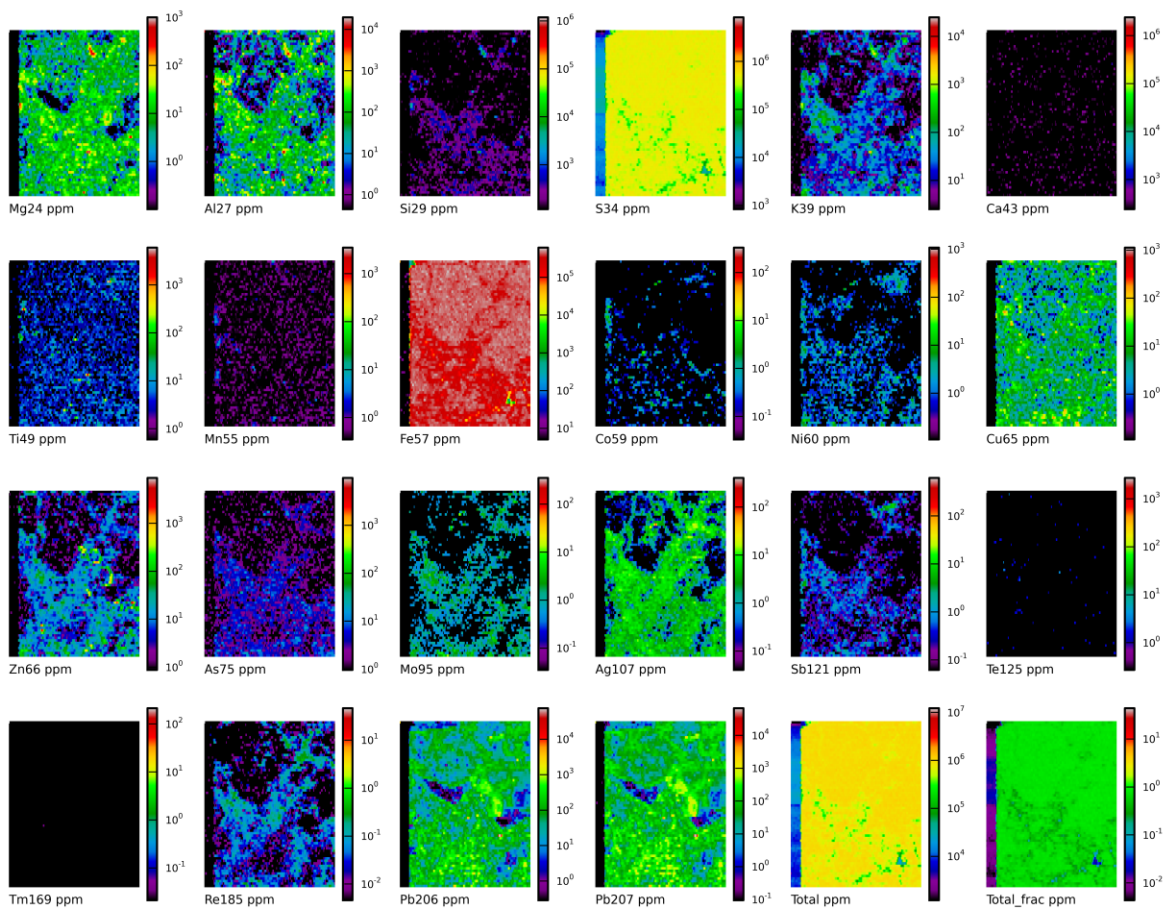


Figure 4.1.47: LA-ICPMS elemental maps for HC Map 2.

4.2: Understanding pyrite Re-Os geochronology

Part B: Refining sample processing protocols

4.2.1: Introduction

Sample preparation is a critical process required to ensure that samples have low abundances of impurities and that any isotopic analyses subsequently performed are constrained within the paragenetic sequence of the ore deposit. In the literature, many different approaches are used to prepare mineral separates, but rarely are protocols discussed, and in some cases no protocol is referenced (e.g. Arne et al., 2001; Munha et al., 2005; Liu et al., 2012). Crushing of ore and hand-picking of the material is a common way to collect the several hundred milligrams of material necessary for analysis (e.g. Mathur et al., 1999; Barra et al., 2003; Huang et al., 2013), and in many studies crushed samples are further purified through magnetic or heavy liquid separation (e.g. Selby et al., 2009; Lawley et al., 2013). Whereas each of these methods may be useful in different circumstances the true efficiency of these mineral separation procedures are typically not reported and are presumably never, or rarely, tested.

In Chapter 4A, it was shown that the Re-Os systematics of pyrite from Zn-Pb ores can be complex with variable levels of Re found throughout the sampled rock. Geochronology requires the use of unaltered ore stage pyrite (Category 1), however as was shown in Chapter 4A this pyrite is often closely associated with altered material (i.e. Category 3), secondary phases (e.g. molybdenite, sphalerite), or material unrelated to sulphide mineralization (Category 0), which often contain significant amounts of Re. Extracting Category 1 pyrite from impurities is a challenging task and may require the application of several different mineral processing techniques. In this chapter we have evaluated heavy liquid separation, magnetic separation, and acid dissolution (leaching) procedures, to a greater extent than is typically provided in the literature in order to determine how well each process isolates Category 1 pyrite. Magnetic separation is also explored as a method to separate different generations of pyrite into different mineral separates, which may expand the range of Re-Os ratios used in geochronology. Using the sample set from Chapter 4A (8S08FW, LK 359, LK 451, NOV4, 03-HC-8D) we provide recommendations on how to most effectively process and document samples used for pyrite Re-Os geochronology.

4.2.2: Sample Preparation Methods and Characterization.

Samples chosen for Re-Os geochronology are crushed and sieved in a manner to minimize the use of metallic components, which minimizes the risk of contamination by steel, which may contain ppb level Re and hundreds of ppt Os (R.A. Creaser, pers comm. 2018). Samples of sufficient size to produce several grams of pyrite are removed from unwanted material (e.g. host rock) using a rock saw. The remaining sample is then polished to remove weathering products and any contaminants ingrained into the rock from the rock saw. The sample is then wrapped in plastic and then broken up to a size of $\sim 1 \text{ cm}^2$ using a Duck Tape wrapped hammer. An Alumina Ceramic grinding mill (SPEX 8505) further crushes the sample until passes through a disposable nylon sieve material (74-210 μm particle size) held between disposable HDPE food containers. This size distribution was chosen to allow grains to be easily filtered when being processed through heavy liquid procedures, as well as being an appropriate size for magnetic separation using a Frantz isodynamic separator. Directly following the crushing procedure a hand magnetic was passed over the sample to remove highly magnetic minerals (e.g. magnetite).

To remove the majority of silicates and carbonates from a crushed sample, a heavy liquid separation procedure was used to exploit differences in mineral densities. For this study, methylene iodide (CH_2I_2) was used due to its high density of 3.32 g/cm^3 . Heavy liquid separation involves introducing the crushed sample into a separatory funnel containing CH_2I_2 . Minerals with higher density than CH_2I_2 (e.g. sulphides and oxides) will tend to sink, while minerals with lower density than CH_2I_2 will float (e.g. calcite, dolomite, quartz). The design of the separatory funnel allows for the extraction of a high density and low density fraction. To determine the efficiency of heavy liquid separation the modal abundance of representative mineral separates were calculated.

To take advantage of the potential differences in magnetic susceptibility between different minerals, the sample is passed through a Frantz isodynamic separator to produce a variety of mineral separates, each with a different bulk magnetic susceptibility. Minerals that are dominated by their diamagnetic nature (e.g. quartz, and calcite) are expected to have low magnetic susceptibilities, while paramagnetic/ferromagnetic/ferrimagnetic (e.g. pyrrhotite, hematite, magnetite) are expected to have higher magnetic susceptibilities. However, within single crystals, variation in minor elements, trace elements, grain size, and crystal structure can

cause variations in magnetic susceptibility (Burgardt and Seehra, 1977; Dekkers, 1988). Mineral impurities, especially magnetite and pyrrhotite, also strongly influence the magnetic susceptibility of a sample. Therefore, in practice it is expected that individual minerals will be extracted over a range of magnetic susceptibility. To determine how effectively magnetic separation works at separating common ore minerals, the modal abundance of representative mineral separates for each sample was calculated. To determine the distribution of different paragenetic stages of iron sulphide within the mineral separates they are visually inspected using petrographic and backscattered electron (BSE) images. In conjunction with visual inspection, bulk chemistry and SIMS sulphur isotope measurements are used to help determine the paragenetic character of individual mineral separates.

The final purification step applied to some samples involved using hydrochloric acid (0.2N to 10N) to dissolve impurities from the mineral separate (e.g. calcite, dolomite, sphalerite, galena). Leaching procedures were first tested on pure mineral separates provided by the Mineralogy and Petrology Collection from the University of Alberta to test the efficacy of leaching on various minerals (pyrite, sphalerite, galena, and magnetite). Following these tests, the procedure was applied to several Re-Os samples. During the leaching process acids were added to a crushed sample and were allowed to react in a 22 mL glass vial, either at either room temperature ($\sim 21^{\circ}\text{C}$) or $\sim 80^{\circ}\text{C}$. After ~ 24 hrs, the acid was decanted and the sample was rinsed a total of 4 times, 3 times with milli-Q water, and a final rinse with ethanol to ensure no residual acid was present. The decanted acid and subsequent rinses (together known as the leachate solution) were then filtered through a 1 μm glass filter and stored for ICPMS and Re-Os analysis. Leaching experiments are divided into two groups. To test how well hydrochloric acid removes impurities, the sample LK 451B M1.6 was used, as it contains a mix of pyrite, sphalerite, and carbonate. For this sample, experiments using 0.2N, 1N, 2N, 6N, and 10N HCl at room temperature as well as an additional experiment using 10N HCl at $\sim 80^{\circ}\text{C}$ were carried out. To test for possible effects of HCl on the Re-Os isotope system, the sample 8S08FW NM 1.5 was chosen. This sample yields the robust 347 Ma isochron from the Lisheen Main Zone, so any preferential leaching of Re or Os from pyrite during HCl reaction should be evidenced by plotting these analyses relative to the unleached isochron samples.

Representative petrographic images and backscattered electron images (BSE) of mineral separates used for this study are compiled in Figure 4.2.1 and complement the images found in

Hnatyshin et al. (2015, 2016). Together these and other images were used to estimate modal abundances of some mineral separates using pixel counting. The pixel counting method required converting either reflected light images, BSE images, or compositional maps of mineral separates into greyscale images. Modal abundances are then calculated by counting pixels of specific intensities for up to several hundred individual grains and then assigning them to a specific mineral (e.g. brightest mineral in BSE is galena). Additional estimations were completed by back calculating modal abundances from the leached samples. For leached samples, the amount of material removed from using 0.2-6N HCl was assumed to be from carbonate dissolution. Further leaching of these mineral separates using 10N HCl was used to estimate the amount of sphalerite in these samples using the difference in mass between 6N and 10N leaching.

4.2.3: Results and Discussion

4.2.3.1: Mineral separate mineralogy and descriptions

The modal abundances estimated for each mineral separate used are presented in Table 4.2.1. However, these values are treated as semi-quantitative, and are used to reveal general trends. Representative bulk minor and trace compositions for mineral separates are provided in Figure 4.1.10 in Chapter 4A, and the full dataset is available in the Appendix for Chapter 4A (Tables 4.1.6 and 4.1.7).

The Lisheen Main Zone sample 8S08FW is dominated by pyrite in all mineral separates, however there are slight differences in mineralogy between the most magnetic (8S08FW M1.0) and least magnetic (8S08FW NM1.5) end members. Pyrite with minimal fracturing is the dominant phase in 8S08FW NM1.5 (Figure 4.2.1) with an estimated modal abundance of ~94%. The main impurities are found as small inclusions within the pyrite and are dominated by carbonates (~2%) and silicates (~3%). In 8S08FW M1.0 the pyrite is much more fractured and is complexly intergrown with other minerals such as galena and sphalerite. Pyrite is still the dominant phase (~ 83%) but this mineral separate has a higher abundance of sphalerite (~ 5%) and carbonate are present (~9%) compared to 8S08FW NM1.5. Sample 8S08FW B was sourced from the same rock as 8S08FW and is assumed to follow the same mineralogical behaviour as 8S08FW.

The Lisheen Derryville samples are complex, with very different mineralogical profiles between rock fragments LK 359A and LK 359B, even though they were processed from the same core. In LK 359A iron sulphides are enriched in the more magnetic end members (~47% for LK 359A NM0.8) and drops to ~9% for the least magnetic separate (LK 359A NM1.8). Sphalerite is an important phase in all mineral separates making up ~69% in LK 359A NM1.8 and dropping to ~47% for LK 359A NM0.8. Galena is strongly enriched in the least magnetic separate (~19 %) but is likely only present at abundances of < 1% in all other separates. In LK 359B iron sulphide is likely the dominant phase in all mineral separates except for the least magnetic separate (LK 359B NM1.8). Sphalerite is highly concentrated in LK359B NM1.8 (~94%) and is an important component of all other separates (> 10%) where it is complexly intergrown with iron sulphide (Fig. 4.2.1). Silicates and carbonates make up a minor proportion of LK 359A and LK 359B (< 10%), but are positively correlated with sphalerite content as a result of it being commonly associated with sphalerite on the whole rock scale (Fig. 4.1.20).

Bog Zone sample LK 451A is defined by being composed of iron sulphide from multiple generations (LG1-LG3, Chapter 4A), highlighted by relative differences in BSE images (Fig. 4.2.1). Iron sulphide makes up the majority of the samples (49 - 78% in characterized separates), but sphalerite and carbonates are both important impurities. Carbonates are typically at levels of 10-20% whereas sphalerite is slightly more variable (~7-25%). Galena is a negligible impurity in all characterized separates but is suspected to be enriched in the least magnetic separates (LK 451A NM2.0, LK 451B NM2.0).

The Nanisivik sample NOV4 will be a mix of pyrite, sphalerite, and galena based on hand sample observations (Fig. 4.1.9). However, pyrite is expected to be the dominant phase based on Figure 4.1.31. Hawker Creek likely has pyrite contents in excess of 90% based on images of 03-HC-8D M0.8 and 03-HC-8D NM2.0 (Fig. 4.2.1). For both Baffin Island samples a higher proportion of fractures are observed in more magnetic separates (i.e. NOV4B NM0.6, Fig 4.1.31; 03-HC-8D NM2.0, Fig. 4.2.1).

4.2.3.2: Leaching experiments – bulk mineralogy

The results of the leaching experiments are presented in Figures 4.2.2-4.2.3, and demonstrate that dissolution is enhanced at higher HCl concentrations and elevated temperatures. For sample LK 451B M1.6, leaching experiments used 0.2N, 1N, 2N, 6N, 10N HCl at room

temperature, as well 10N HCl at ~80°C, to monitor the dissolution of different phases. Visually, in all samples that were leached, there are no carbonate minerals remaining (Figs. 4.2.3C-H), at 10N HCl sphalerite has been partially removed at room temperature (Fig. 4.2.3I), and appears to be completely removed at 80°C (Fig. 4.2.3H). Visible dissolution of pyrite does not appear to have occurred and through mass balance calculations it was determined that < 2% of the pyrite had dissolved in the conditions tested (Figure 4.2.2A). However, at HCl concentrations of 6N and 10N the leachate solution turns from clear to a yellow-orange colour likely signally the presence of FeCl_4^- , presumably from the partial dissolution of pyrite, sphalerite, and/or iron oxides. These observations are reinforced by trace element analysis of the leachate solutions (see Appendix for data, Figure 4.2.3B), in which the Fe and Zn concentrations both increase in 6-10N HCl. At lower concentrations (0.2N - 2N HCl), Ca is the dominant cation present (Figs. 4.2.2C-E), while at higher concentrations (6N - 10N HCl) Zn and Ca are the dominant cations (Figs. 4.2.2F-H).

4.2.3.3: Leaching experiments – effect on Re-Os isochrons

The premise of this experimental method is to dissolve material that may negatively impact a pyrite Re-Os isochron (e.g. carbonates, sphalerite). Observations from the experiments on LK 451B M1.6 show that pyrite remains resistant to HCl attack, that carbonates are removed at low concentrations of HCl (0.2N), and sphalerite begins to be removed at 2N HCl (Figs. 4.2.2B-H). Leaching with HCl therefore appears to be an efficient route to remove select impurities. However, it is critical to establish whether HCl leaching may preferentially leach out Re or Os from pyrite, thereby changing the Re-Os ratio of residual pyrite and altering otherwise isochronous behaviour of pyrite.

Lisheen Main Zone sample 8S08FW NM1.5, for which the mineral separate is of high purity (94% pyrite, Table 4.1.1), and from which a precise ca. 347 Ma Re-Os isochron was obtained (Chapter 3, Fig. 4.2.4A), underwent leaching experiments to test if preferential leaching of Re or Os was occurring. The results of leaching 8S08FW NM1.5 with 6N (at ~21°C) and 10N HCl (at ~80°C) show the leached pyrite separates do not deviate from the 347 Ma isochron, suggesting that any preferential leaching of Re from Os taking place is negligible. Therefore, HCl leaching of pyrite, even using conditions as strong as 10N HCl at elevated temperatures, does not appear to negatively impact the ability to produce a Re-Os isochron.

However, the results of the leaching experiments and Re-Os analyses conducted on the LK 451 samples are much more complex, due to the multiphase nature of the separates analyzed (Table 4.2.1, Figs. 4.2.1, 4.2.5). Leachate solution analyses from LK 451 using 0.2N HCl show that the material removed through leaching (primarily carbonate) has distinctive Re-Os characteristics (Table 4.1.4 from Chapter 4A). Compared to the sulphides, the leachate solutions have very low $^{187}\text{Re}/^{188}\text{Os}$ and lower $^{187}\text{Os}/^{188}\text{Os}$ and plot to the left of the isochron (Fig. 4.2.5A). The mean Re concentration is extremely low in the leachate compared to the sulphides (~0.3 ppb vs. ~54 ppb) whereas Os is comparably less depleted (~23 ppt vs. ~250 ppt). Carbonates, in principle, could contain sufficient Re-Os abundances to explain these results, as carbonates have been documented to have to contain > 10 ppt Os, while remaining depleted in Re (< 1 ppb) (Pierson-Wickmann et al., 2002; Dalai and Ravizza, 2006). If the dissolved carbonates are the sole source of Os, then carbonates contain significant Os, which is not isochronous with pyrite, emphasizing the need to remove carbonate impurities. Minor amounts of sulphide or other minerals could also be contributing to the Os as evidenced by the ICPMS analyses (Fig. 4.2.2). For all the samples a small quantity of Fe, Zn, and Pb are present in leachate solutions. This suggests that either small amounts of sulphide or oxides have been dissolved, or that microscopic crystals were released into suspension during the dissolution of carbonate. However, if these impurities were the primary source of Os it would be expected the data points would lie close to the sulphide isochron, which is not the case. A third possibility is that Os has been preferentially leached out of sulphides over Re, a possibility that will artificially lower the Re-Os ratio of the leachate, and requiring the residual sulphides to have a higher $^{187}\text{Re}/^{188}\text{Os}$, plotting to the right of its true location on a isochron diagram. A major counterpoint to leaching of Os possibility is that the observed $^{187}\text{Os}/^{188}\text{Os}$ of the leachate samples (3.63 – 10.49) is much lower than the bulk sulphide values ($^{187}\text{Os}/^{188}\text{Os} = 17.76 - 35.82$), suggesting that Os is not being sourced exclusively, if at all, from the bulk sulphide material. A similar suggestion that arguably fits the data is that only radiogenic ^{187}Os is being leached from the mineral separate and is mixed with that of the dissolved carbonates. The carbonates, presumably would have low $^{187}\text{Re}/^{188}\text{Os}$ and $^{187}\text{Os}/^{188}\text{Os}$, would be mixed with radiogenic ^{187}Os being released during the leaching process, artificially increasing the $^{187}\text{Os}/^{188}\text{Os}$ to the levels observed (3.63 – 10.49). Finally, it is possible that the carbonates incorporated a radiogenic signature long after the ore formed. As was briefly discussed in Chapter 4A, younger fluids may have permeated the ore in response to the Variscan

orogeny (~270 - 310Ma; Quinn et al., 2005). If these fluids acquired radiogenic Os from some older source (e.g. the ore sulphides), and then precipitated or recrystallized carbonates within the ore deposit, it may explain the Re-Os systematics of the carbonates dissolved in the leachate. The carbonates produced in such a process will have elevated $^{187}\text{Os}/^{188}\text{Os}$ values but do not evolve to the high values seen in the sulphides, as the $^{187}\text{Re}/^{188}\text{Os}$ for carbonates are generally much lower. Such a mechanism is not unprecedented as Pierson-Wickmann et al. (2002) proposed a similar mechanism to explain impossibly old model ages from marbles in the Himalayas. In that case, it was proposed that metamorphism caused by orogenesis altered older rock that contained radiogenic Os (e.g. black shales), which was then mobilized by metamorphic fluids, and then subsequently precipitated marbles with extremely radiogenic Os, and low Re/Os ratios.

Removing carbonate impurities appears to be safe to attempt based on the negligible impact leaching had on analyses of 8S08FW. However, the observation that the acid solution begins to turn yellow when 6N HCl is used suggests that a mild reaction with the pyrite is occurring even if a negligible (< 1 %) amount of pyrite is dissolved. Therefore we consider it safe to prepare the mineral separates to a size of > 74 μm and then use low concentration of HCl (i.e. 0.2N) to dissolve carbonate crystals out of the mineral separate. Finer grained material has not been rigorously tested, but the higher surface area induces a much higher risk for Re and/or Os loss, as has apparently occurred in LK 451A M1.8 Fine 10N Hot and LK 451B M1.8 Fine 10N (Fig. 4.2.5A). For complex mineral separates (e.g. LK 451) the utility of using acid to remove other impurities (e.g. sphalerite) is less clear cut. One application of leaching is that it can reveal relative isotopic differences between various phases (Figure 4.2.5B). Based on the experiments conducted, it is not possible to determine with certainty if Re or Os is preferentially leached from sphalerite. Under the assumption that preferential leaching is occurring within sphalerite, it would only be safe to attempt leaching if 100% of the sphalerite is dissolved. If phases such as sphalerite are required to be removed it is recommended that this leaching procedure be applied with extreme caution, at least until more experiments are undertaken.

4.2.3.4: Heavy liquid separation, composite grains and effect of low density phases on isochrons

The leached separates clearly show that the efficiency of heavy liquid separation is highly variable as both carbonates and silicates can still be present in mineral separates and can

contribute > 10% of the total volume of the sample in some separates (Table 4.2.1). This results mainly from the crushing process which can create composite grains of different minerals, or monomineralic grains that contain multiple generations within the general paragenetic sequence (see insets in Fig. 4.2.1). Sample LK 451 contains the highest proportion of carbonate, with calcite and dolomite intergrown with sulphides at a scale (~100 μm) similar to the size of crushed material (Fig. 4.2.6). For any finer grained disseminated ore, impurity minerals present as composite grains are at high risk in being incorporated into bulk analyses after crushing and sieving.

The effect on a Re-Os isochron of impure mineral separates containing low density minerals is illustrated by fraction LK 451B M1.6 Low Density (Fig. 4.2.5B), which plots far below the sulphide isochron (Fig. 4.2.5B). Considering the results of Chapter 4A, in which silicates and carbonates are commonly associated with Category 0, 2, 3 material (i.e. material not conducive to high quality geochronology) the placement of this low density separate is unsurprising. Similarly, the LK 451 leachate samples containing easily dissolved or leached material (e.g. carbonates) also plot significantly away the sulphide isochron (Fig. 4.2.5A).

Although heavy liquid separation is not perfect in removal of low density minerals it is an efficient method for removing most low density impurities. We also suggest that impurities also be tested for their Re-Os isotopic composition (e.g. the low density fraction after heavy liquid separation) to assess any possible effects these impurities may have on a sulphide Re-Os isochron, rather than assuming that these minerals have a negligible impact.

4.2.3.5: Evaluation of Magnetic Separation, and effects on Re-Os isochrons

The use of magnetic separation clearly influences the modal mineralogy of mineral separates (Table 4.2.1; Fig. 4.2.1), but is far from perfect, even within a single deposit. For example, sphalerite is preferentially extracted from highly magnetic fractions in 8S08FW but it is extracted at the lowest magnetic fractions in LK 359. Galena appears to have very low magnetic susceptibility (Table 4.2.1) resulting in its concentration in the separate with the lowest magnetic susceptibility. Pyrite should be at the lower end of the magnetic susceptibility scale, together with minerals such as galena, however this is not what is observed (Table 4.2.1). Elemental impurities (e.g. Ni) could be a major factor influencing in the magnetic susceptibility of pyrite (e.g. Beegart and Seehra, 1977; Dekkers, 1988), which can be evaluated using pyrite studied

here. The Hawker Creek sample 03-HC-8D M2.0 and Lisheen sample LK 451B M2.0 have similar magnetic susceptibilities, however when comparing their bulk element chemistry (Fig. 4.1.10) the Lisheen sample has trace element concentrations orders of magnitude higher than that of Hawker Creek. Therefore, bulk composition doesn't appear to be controlling magnetic susceptibility in pyrite. Sulphide ore in general may be expected to contain small magnetic minerals as paleomagnetic dating studies on ore deposits require and indirectly document the existence of small magnetic crystals within sulphide ores. For example, in the Irish orefield and at Nanisivik, the ore and/or the surrounding host-rock contains single domain magnetite crystals (e.g. Pannalal et al., 2008). These magnetite crystals could be the source of the magnetic susceptibility and their small size ($\sim 1 \mu\text{m}$) could easily allow them to be overlooked.

The Hawker Creek dataset is an extremely important example in showing the potential application of magnetic separation on the retrieval of Re-Os age information from pyrite. The Hawker Creek mineral separates show extreme physical differences (Fig. 4.2.1), which allow them to be correlated with compositional imaging (Fig. 4.1.24). The least magnetic separates are composed of clean non-fractured pyrite crystals that represent primary mineralization at Hawker Creek, producing ages approaching ~ 1100 Ma (Hnatyshin et al. 2016). The magnetic fraction (03-HC-8D M0.8) is associated with fractured pyrite enveloped by areas containing secondary phases of unclear mineralogical makeup containing high concentrations of Re and other elements. The model ages for 03-HC-8D M0.8 returned model ages of close to 400 Ma, recording events much younger than primary ore mineralization, suggesting these are areas of intense alteration. The Hawker Creek dataset shows it is possible in some circumstances to separate out different generations of pyrite through differences in magnetic susceptibility. The control on magnetic susceptibility in the Hawker Creek sample is likely due to the production of magnetic minerals during alteration or were precipitated directly from the fluids causing alteration.

One trend observed in the magnetic susceptibility data is a positive correlation between relative magnetic susceptibility and the bulk concentration of Re within prepared mineral separates (Figs. 4.1.10, 4.2.7). In most of the published datasets where this information is available, a similar correlation between magnetic susceptibility and Re concentrations exists, (e.g. van Acken et al., 2014; Hnatyshin et al., 2015; Hnatyshin et al., 2016). This observation could be used to select pyrite with higher Re concentrations in future studies, which is useful for

reducing the amount of blank correction or the amount of sample needed for analysis. Speculatively, if an increase in magnetic susceptibility is caused through alteration (e.g. Hawker Creek), then this trend could be indicative of Re being mobilized out of the pyrite and concentrated into secondary phases with higher magnetic susceptibility (e.g. pyrrhotite, iron oxides). However, in the majority of samples there appears to be no clear correlation with the amount of scatter a data point experiences with its magnetic susceptibility. Until a dedicated study is undertaken, perhaps one that integrates LA-ICPMS and scanning SQUID microscopy, the cause of the observed Re vs. χ correlation remains enigmatic.

Magnetic separation can have a significant effect on the quality of age information produced from isochron analysis. For example, in Lisheen sample 8S08FW, the two mineral separates that did not undergo magnetic separation had a very restricted range of Re-Os ratios (919 - 953) but this range expanded to 556 - 1502 when accounting for variation in magnetic susceptibility (Fig. 4.2.4A). The large range in Re/Os ratio is in part responsible for the highly precise age of this sample.

4.2.4: Conclusions

The characterization of samples from Chapter 3 and Hnatyshin et al. (2016) shows that commonly used mineral separation procedures (e.g. heavy liquid and magnetic separation) produce variable quality mineral separates. The crushing procedure can produce composite grains with silicates and carbonates still comprising > 20% of some mineral fractions. Removal of these impurities is required because low density minerals do not plot isochronously with sulphides. Removal of carbonates is relatively straightforward, as applying mild leaching (e.g. 0.2N HCl) appears effective, and does not influence the Re-Os systematics of pyrite. Removal of silicates remains more problematic, but for future work, HF leaching could be adopted for testing, similar to that used by Lawley and Selby (2012).

Magnetic separation can help remove impurities, and magnetic end members may preferentially remove altered sulphide material, as shown by the Hawker Creek samples where magnetic separation clearly separated younger altered pyrite from unaltered older cores. Another benefit of magnetic separation is that it may expand the range of Re-Os ratio in a dataset, which can potentially greatly improve the statistics of isochron regressions. It is recommended that

future Re-Os sulphide dating studies attempt to follow the basic procedures outlined in this study, as summarized in Figure 4.2.8.

4.2.5: References

Acken, D., Su, W., Gao, J., & Creaser, R. A. (2014). Preservation of Re-Os isotope signatures in pyrite throughout low-T, high-P eclogite facies metamorphism. *Terra Nova*, 26(5), 402-407.

Arne, D. C., Bierlin, F. P., Morgan, J. W., & Stein, H. J. (2001). Re-Os dating of sulfides associated with gold mineralization in central Victoria, Australia. *Economic Geology*, 96(6), 1455-1459.

Barra, F., Ruiz, J., Mathur, R., & Titley, S. (2003). A Re–Os study of sulfide minerals from the Bagdad porphyry Cu–Mo deposit, northern Arizona, USA. *Mineralium Deposita*, 38(5), 585-596.

Burgardt, P., & Seehra, M. S. (1977). Magnetic susceptibility of iron pyrite (FeS₂) between 4.2 and 620 K. *Solid State Communications*, 22(2), 153-156.

Dalai, T. K., & Ravizza, G. (2006). Evaluation of osmium isotopes and iridium as paleoflux tracers in pelagic carbonates. *Geochimica et Cosmochimica Acta*, 70(15), 3928-3942.

Dekkers, M. J. (1988). Magnetic properties of natural pyrrhotite Part I: Behaviour of initial susceptibility and saturation-magnetization-related rock-magnetic parameters in a grain-size dependent framework. *Physics of the Earth and Planetary Interiors*, 52(3-4), 376-393.

Hnatyshin, D., Creaser, R. A., Wilkinson, J. J., & Gleeson, S. A. (2015). Re-Os dating of pyrite confirms an early diagenetic onset and extended duration of mineralization in the Irish Zn-Pb ore field. *Geology*, 43(2), 143-146.

Hnatyshin, D., Kontak, D. J., Turner, E. C., Creaser, R. A., Morden, R., & Stern, R. A. (2016). Geochronologic (Re Os) and fluid-chemical constraints on the formation of the

Mesoproterozoic-hosted Nanisivik Zn Pb deposit, Nunavut, Canada: Evidence for early diagenetic, low-temperature conditions of formation. *Ore Geology Reviews*, 79, 189-217.

Huang, X. W., Qi, L., Gao, J. F., & Zhou, M. F. (2013). First Reliable Re–Os Ages of Pyrite and Stable Isotope Compositions of Fe (- Cu) Deposits in the Hami Region, Eastern Tianshan Orogenic Belt, NW China. *Resource Geology*, 63(2), 166-187.

Jackson, G. D., & Iannelli, T. R. (1981). Rift-related cyclic sedimentation in the Neohelikian Borden Basin, northern Baffin Island. *Geological Survey of Canada, Paper*, 81-10.

Lawley, C. J. M., & Selby, D. (2012). Re-Os geochronology of quartz-enclosed ultrafine molybdenite: Implications for ore geochronology. *Economic Geology*, 107(7), 1499-1505.

Lawley, C., Selby, D., & Imber, J. (2013). Re-Os molybdenite, pyrite, and chalcopyrite geochronology, lupa goldfield, southwestern Tanzania: tracing metallogenic time scales at midcrustal shear zones hosting orogenic Au deposits. *Economic Geology*, 108(7), 1591-1613.

Liu, J., Wu, G., Li, Y., Zhu, M., & Zhong, W. (2012). Re–Os sulfide (chalcopyrite, pyrite and molybdenite) systematics and fluid inclusion study of the Duobaoshan porphyry Cu (Mo) deposit, Heilongjiang Province, China. *Journal of Asian Earth Sciences*, 49, 300-312.

Mathur, R., Ruiz, J., & Tornos, F. (1999). Age and sources of the ore at Tharsis and Rio Tinto, Iberian Pyrite Belt, from Re-Os isotopes. *Mineralium Deposita*, 34(8), 790-793.

Munhá, J., Relvas, J. M. R. S., Barriga, F. J. A. S., Conceição, P., Jorge, R. C. G. S., Mathur, R., ... & Tassinari, C. C. G. (2005). Osmium isotope systematics in the Iberian Pyrite Belt. In *Mineral deposit research: Meeting the global challenge* (pp. 663-666). Springer, Berlin, Heidelberg.

Pannalal, S. J., Symons, D. T. A., & Sangster, D. F. (2008). Paleomagnetic evidence for an early Permian age of the Lisheen Zn-Pb deposit, Ireland. *Economic Geology*, 103(8), 1641-1655.

Pierson-Wickmann, A. C., Reisberg, L., & France-Lanord, C. (2002). Impure marbles of the Lesser Himalaya: another source of continental radiogenic osmium. *Earth and Planetary Science Letters*, 204(1-2), 203-214.

Quinn, D., Meere, P. A., & Wartho, J. A. (2005). A chronology of foreland deformation: Ultra-violet laser $^{40}\text{Ar}/^{39}\text{Ar}$ dating of syn/late-orogenic intrusions from the Variscides of southwest Ireland. *Journal of Structural Geology*, 27(8), 1413-1425.

Selby, D., Kelley, K. D., Hitzman, M. W., & Zieg, J. (2009). Re-Os sulfide (bornite, chalcopyrite, and pyrite) systematics of the carbonate-hosted copper deposits at Ruby Creek, southern Brooks Range, Alaska. *Economic Geology*, 104(3), 437-444.

Table 4.2.1: Lisheen Sample Mineralogy

| Mineral Separate | Qualitative χ | Mineralogy (Modal Abundance) | | | | |
|--------------------------|--------------------|------------------------------|------------|--------|-----------|-----------|
| | | Pyrite* | Sphalerite | Galena | Silicates | Carbonate |
| 8S08FW M1.0 | 4 | 83.2% | 5.4% | 0.1% | 2.1% | 9.1% |
| 8S08FW M1.2 | 3 | XX | X | X | X | X |
| 8S08FW M1.5 | 2 | XX | X | X | X | X |
| 8S08FW NM1.5 | 1 | 94.3% | 0.4% | <0.1% | 3.0% | 2.3% |
| 8S08FW B M0.8 | 3 | 81.2% | 8.8% | X | X | (10%) |
| 8S08FW B NM1.0 | 2 | XX | X | X | X | X |
| 8S08FW B NM1.2 | 1 | XX | X | X | X | X |
| LK 359A M0.6 | 6 | XX | XX | X | X | X |
| LK 359A NM 0.8 | 5 | 47.2% | 47.3% | 0.50% | X | X |
| LK 359A NM 1.0 | 4 | 39.6% | 54.3% | 0.30% | 4.7% | 1.2% |
| LK 359A M1.2 | >3 | XX | XX | X | X | X |
| LK 359A NM 1.2 | 3 | XX | XX | X | X | X |
| LK 359A NM 1.6 | 2 | XX | XX | X | X | X |
| LK 359A NM 1.8 | 1 | 9.0% | 69.1% | 19.0% | 2.5% | 0.4% |
| LK 359B M0.6 | 5 | XX | XX | X | X | X |
| LK 359B NM 1.2 | 4 | 74.2% | 24.1% | 0.3% | 0.9% | 0.5% |
| LK 359B NM 1.4 | 3 | XX | XX | X | X | X |
| LK 359B NM 1.6 | 2 | 81.1% | 17.9% | X | X | X |
| LK 359B NM 1.8 | 1 | 4.3% | 93.8% | 1.6% | 0.3% | <0.1% |
| LK 451A M1.6 | 4 | 49.3% | 25.2% | 0.2% | (<5%) | 21.7% |
| LK 451A M1.8 | 3 | 77.9% | 6.5% | 1.1% | (<5%) | 14.5% |
| LK 451A M2.0 | 2 | XX | XX | X | XX | XX |
| LK 451A NM2.0 | 1 | XX | XX | X | XX | XX |
| LK 451B M1.0 | 5 | XX | XX | X | XX | 8.4% |
| LK 451B M1.6 | 4 | XX | XX | X | XX | 10.6% |
| LK 451B M1.6 Low Density | 4 | XX | XX | X | XX | XX |
| LK 451B M1.8 | 3 | 81.8% | 6.6% | 0.3% | X | 11.3% |
| LK 451B M2.0 | 2 | XX | XX | X | XX | XX |
| LK 451B NM2.0 | 1 | XX | XX | X | XX | XX |

The concentrations of these phases should be taken as upper estimates as not all phases are accounted for. A designation of "x" means the abundance of that phase is expected to be < 5%, while a designation of "xx" means the phase is expected to be > 5%. Rock fragments that cannot be compared via χ are separated by a dotted border or an empty row. Bracketed values are estimated values based known trends and observations. *Includes marcasite.

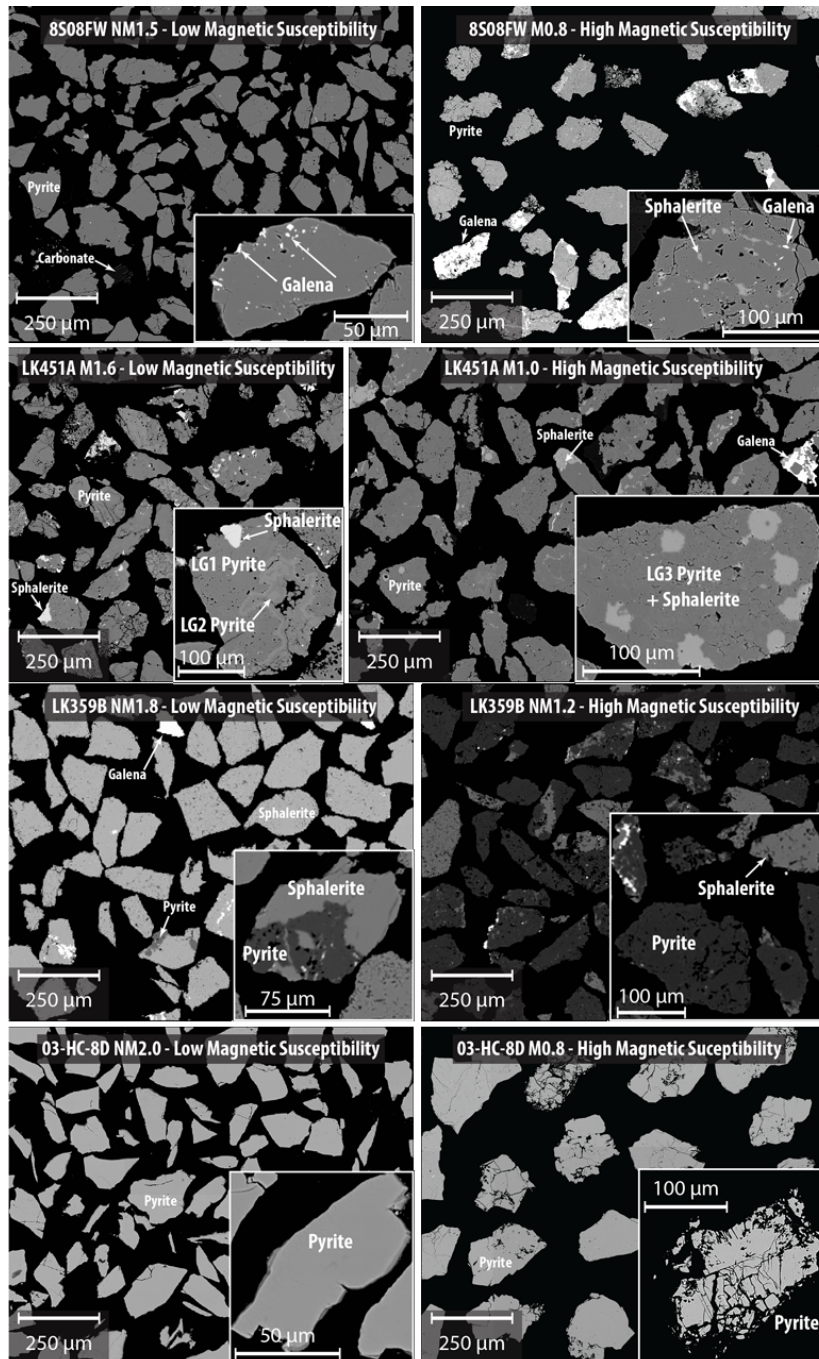


Figure 4.2.1: Representative images of mineral separates that have undergone heavy liquid separation and magnetic separation. Sample 8S08FW is from the Main Zone of the Lisheen deposit. Sample LK 359 is from the Derryville Zone of the Lisheen deposit. Sample LK 451 is from the Bog Zone of the Lisheen deposit. Sample 03-HC-8D is from the Hawker Creek prospect of Baffin Island. See Chapter 4A for additional details.

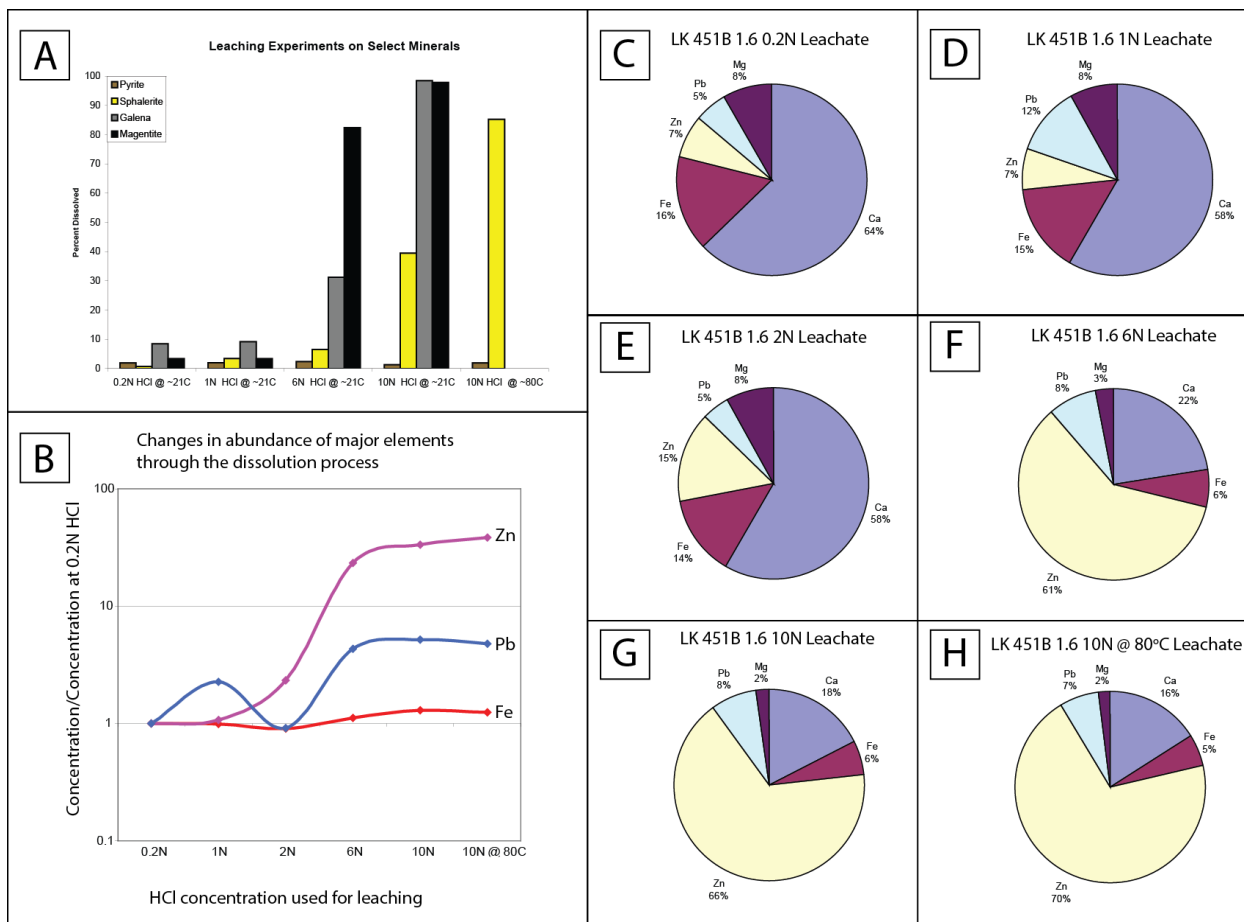


Figure 4.2.2: (A) Leaching experiments using pure mineral samples obtained from the Mineralogy and Petrology Collection at the University of Alberta (B) ICPMS analyses LK 451B M1.6 leachate samples normalized against the concentration of Ca found in the 0.2N HCl leachate solution. It was assumed that the amount of Ca released is constant through all experiments. This plot shows that Zn begins to be released into solution in greater quantities at 2N HCl, whereas galena and pyrite increase at 6N HCl. The Pb seen at 1N HCl may be an analytical artefact or caused by contamination of the leachate solution. (C)-(H) The leachate solution composition for each experiment on LK 451B M1.6.

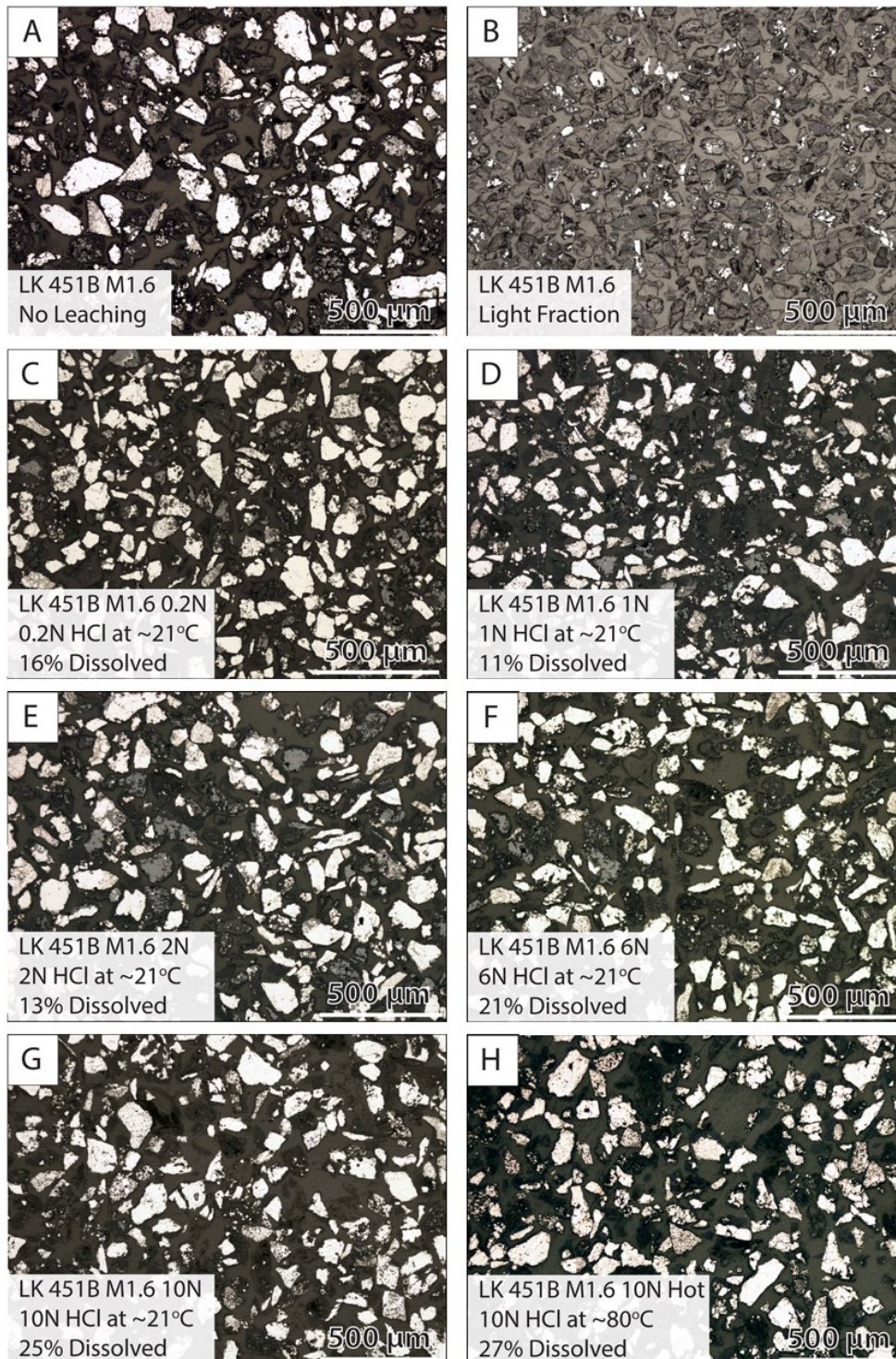


Figure 4.2.3: Reflected light images of material used for leaching experiments. (A) Original material from LK 451B M1.6 (B) Low density mineral separate associated with LK 451B M1.6 (C)-(H) Various mineral separates produced under different acid leaching conditions.

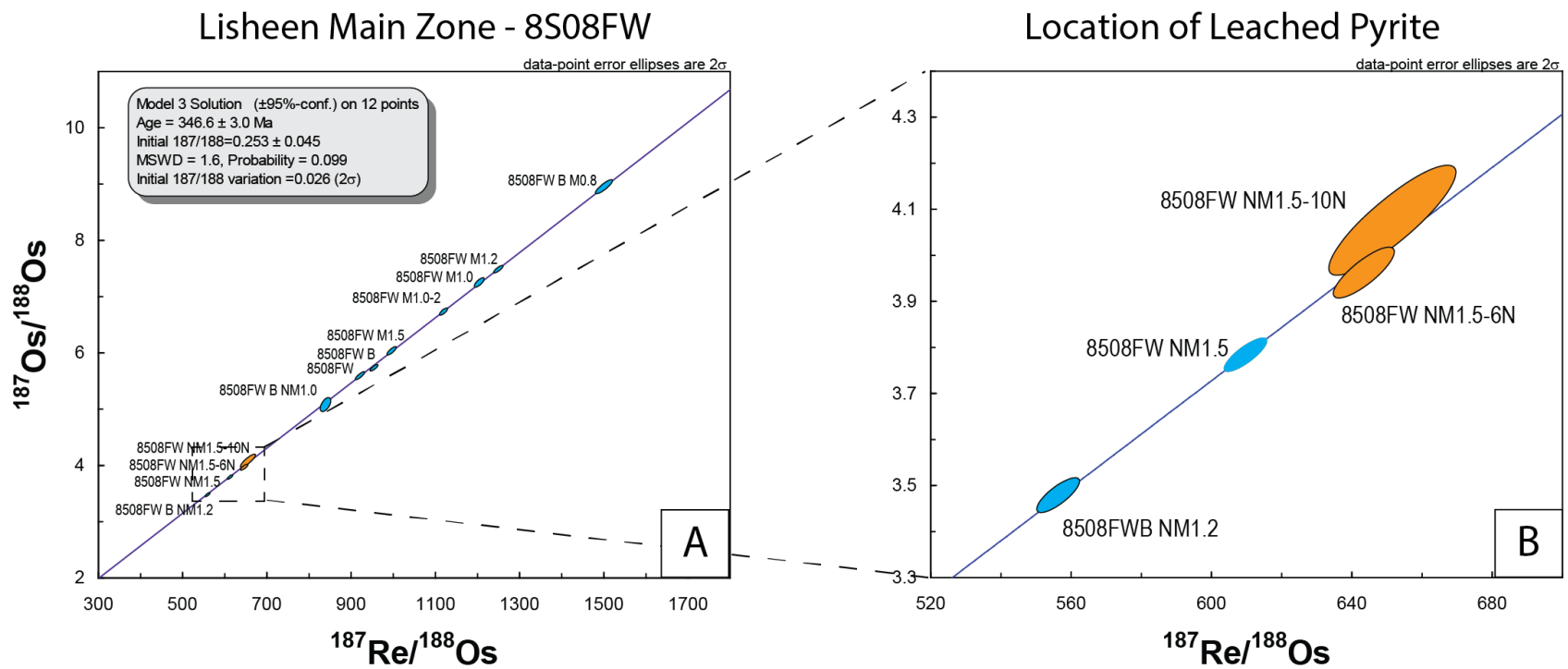


Figure 4.2.4: (A) Model 3 isochron for 8S08FW (B) Expanded region for the samples that have undergone HCl leaching procedures, showing that they do not deviate from the regression line of the isochron. Orange ellipses represent leached data points and blue ellipses represent non-leached data points.

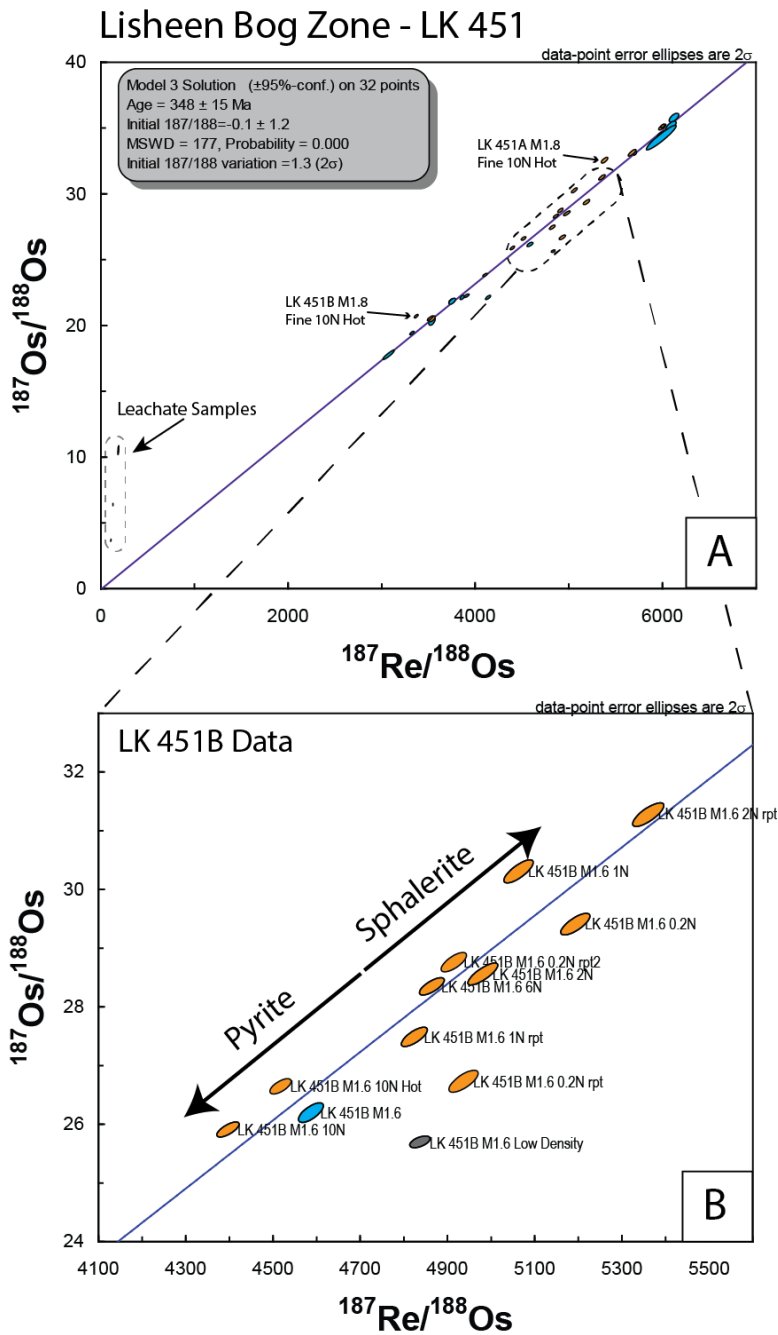


Figure 4.2.5: (A) Model 3 Isochron for LK 451 with important areas highlighted. (B) Expanded image highlighting the location of the LK 451B NM1.6 mineral separates used for the leaching experiments. The arrows indicate the direction of increasing modal abundance in analyzed separate (excluding LK 451B NM1.6 Low Density). LK 451B NM1.6 Low Density represents the mineral separate contained in the low density fraction of heavy liquid separation and primarily contains carbonate and silicates. Orange ellipses represent leached data points, blue ellipses represent non-leached data points, and grey ellipses represent data points from low density mineral separates.

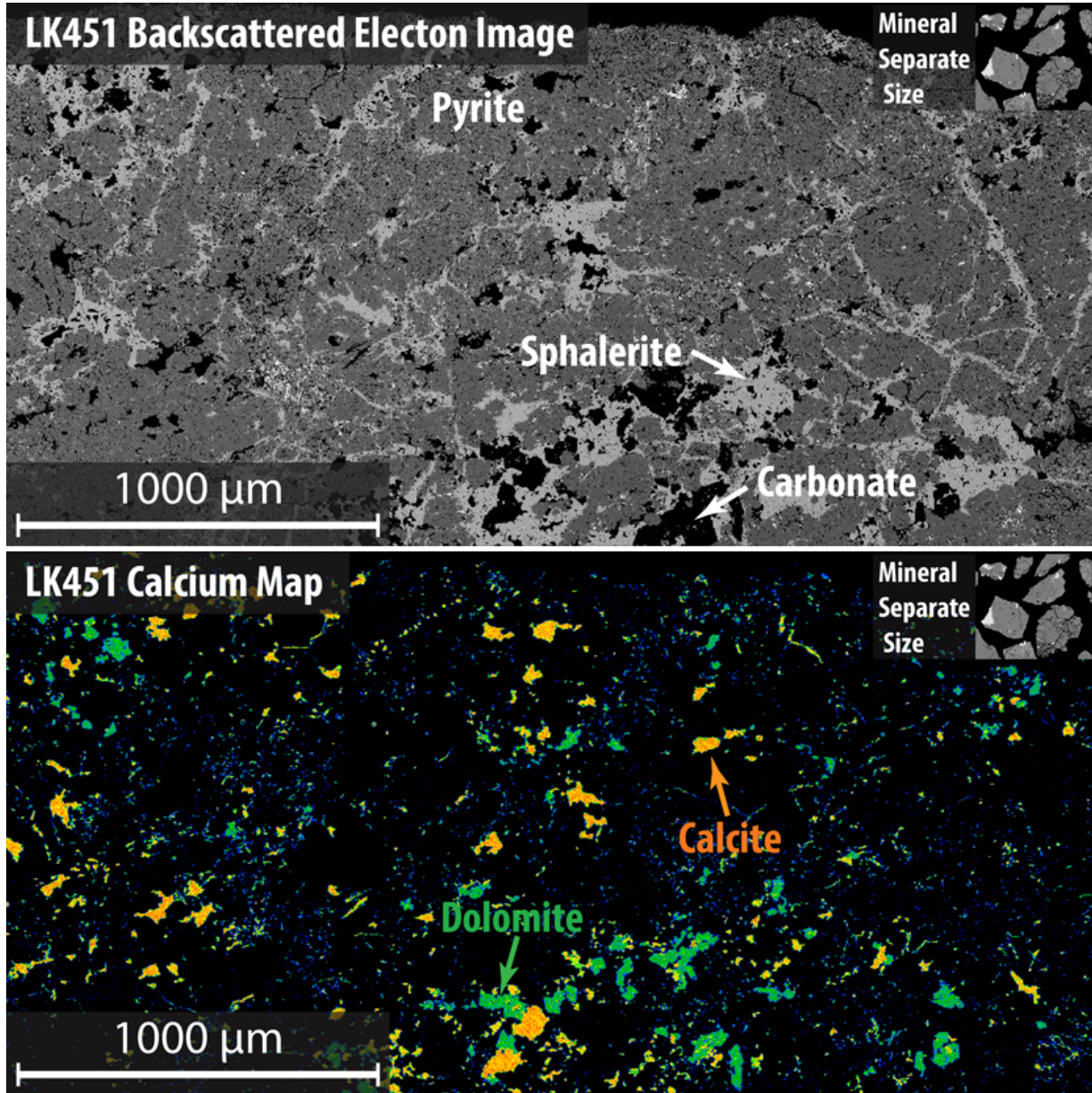


Figure 4.2.6: Representative image of the sample LK 451 showing the relative scale of carbonate crystals compared to the size of mineral separates created through the mineral separation process. Top Image: BSE image. Bottom Image: Calcium map created from electron microprobe analysis.

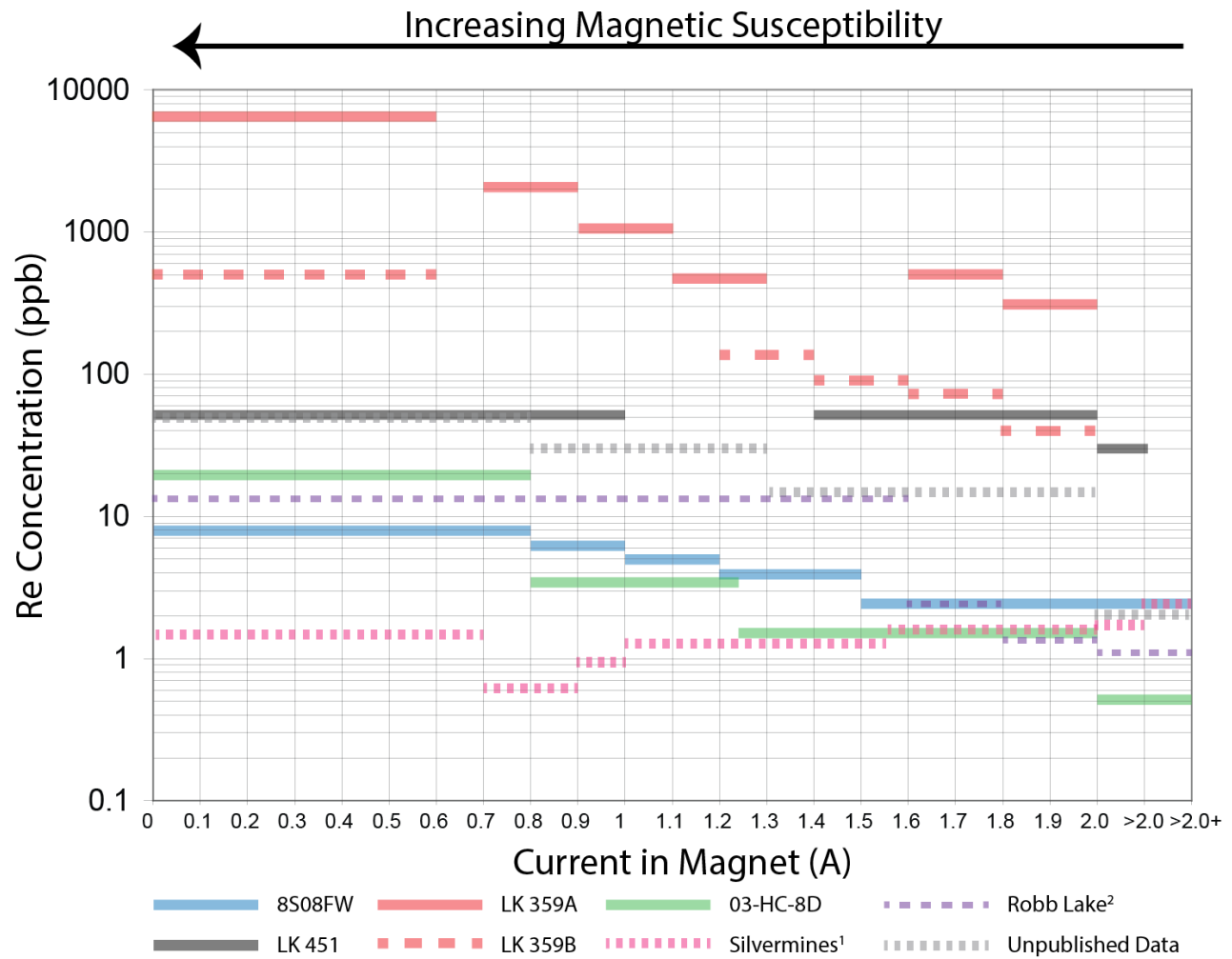


Figure 4.2.7: Rhenium concentration as a function of the magnetic susceptibility of the mineral separate. For these samples, the Frantz isodynamic separator was run at identical settings with the horizontal axis represents the current used. Data in the 0 - 2.0 amp range used a side slope of 5°. Data in the > 2.0 amp band are mineral separates that remain non-magnetic at 2.0 amps and a side slope at 5°. Separates in the >2.0+ amp band remain non-magnetic at 2.0 amps and a side slope of 3°. The coloured horizontal bars represent the range in magnetic susceptibility within a single mineral separate. ¹Hnatyshin et al. (2015), ²van Acken et al. (2014).

| | Step One: Sample Collection | Step Two: Screening of Samples | Step Three: Choosing Samples | Step Four: Processing/Samples | Step 5: Interperet Data |
|----------------|---|--|---|--|---|
| Recommendation | <ol style="list-style-type: none"> 1) Collect a variety of samples related to ore stage mineralization 2) Emphasize collection of paragenetically simple samples 3) Avoid samples with obvious contaminants (e.g. organic rich host rocks) | <ol style="list-style-type: none"> 1) Petrographically examine each sample and determine the paragenetic sequence. 2) Identify any areas with alteration, recrystalization, or contaminants 3) Follow up with compositioning mapping (e.g. EMPA , LA-ICPMS), empahsizing Re, Mo, Si, Al, K 4) Place the updated paragenetic sequence into the broader context of the deposit | <ol style="list-style-type: none"> 1) Select samples that have Category 1 material 2) Choose samples that have minimal Category 0/2/3 material. | <ol style="list-style-type: none"> 1) Crush/Cut/Hand Pick unaltered pyrite 2) Use heavy liquid and magnetic seperation 3) Use leaching if remaining contaminants will compromise the Re-Os data 4) Petrographically analyze processed separates 5) Identify highest quality separates and process through chemistry | <ol style="list-style-type: none"> 1) Test all assumptions using available information (e.g. petrography, compositional mapping) 2) For regressions that require unreasonable or impossible initial ratio's or variations of them, it is preferable that more generalized interpretations be reported. 3) Use the resultant age information to answer geologic questions |
| Reasoning | By collecting samples in this manner there is a higher probability that a high quality sample was collected. | <ol style="list-style-type: none"> 1 and 4) Important to verify that ore stage material is being dated and can be used to help correlate between locations and samples. 2 and 3) Allows for screening (Step 3) and is important for interpretation of data (Step 5). | Focus on material that has the highest chance of success. | <ol style="list-style-type: none"> 1/2/3) Using all these methods will give the best chance of obtaining separates that have minimal impurities. 4) Important for interpretation of the .data (Step 5). | <ol style="list-style-type: none"> 1) Testing for all assumptions is required to determine the quality and accuracy of the data. Using as much supplemental data as possible helps with testing these assumptions. 2) Regressions producing or requiring unrealistic values are inherently flawed and must be treated carefully. |

Figure 4.2.8: Basic methodology that is recommended to be followed to ensure the highest chance of success at Re-Os Geochronology.

4.2.6: Appendix

Table 4.2.2: ICPMS analyses for samples used for leaching experiments

| Sample Name | | LK 451B M1.6 | LK 451B M1.6 0.2N | LK 451B M1.6 1N | LK 451B M1.6 2N | LK 451B M1.6 6N | LK 451B M1.6 10N | LK 451B M1.6 10N Hot |
|-------------|------------------------|------------------|-------------------|-----------------|-----------------|-----------------|------------------|----------------------|
| Sample Type | | Mineral Separate | Leachate | Leachate | Leachate | Leachate | Leachate | Leachate |
| Element | Detection Limits (ppm) | | | | | | | |
| Li | 0.05 | 6.14 | 1.22 | 1.19 | 1.43 | 2.75 | 2.79 | 3.66 |
| Be | 0.1 | <DL | 0.61 | 0.66 | 0.67 | 0.39 | 0.28 | 0.39 |
| B | 2 | 106.54 | 115.42 | 79.57 | 121.39 | 48.14 | 29.59 | 27.49 |
| Na | 0.5 | 772.75 | 1241.55 | 712.90 | 958.32 | 436.72 | 391.49 | 294.11 |
| Mg | 2 | 3234.18 | 29282.19 | 29784.52 | 30264.21 | 15790.22 | 11229.09 | 11303.20 |
| Al | 0.2 | 1182.25 | 1385.19 | 1328.99 | 1304.18 | 772.57 | 558.20 | 1267.58 |
| P | 5 | 279.96 | 1123.52 | 1127.83 | 1049.88 | 599.75 | 406.59 | 391.75 |
| K | 6 | 848.50 | 1209.18 | 1229.36 | 1333.05 | 833.34 | 543.57 | 937.79 |
| Ca | 31 | 21955 | 218489 | 215485 | 219009 | 116227 | 92049 | 93760 |
| Ti | 0.09 | 42.68 | 13.51 | 10.40 | 9.38 | 6.05 | 5.61 | 11.02 |
| V | 0.05 | 11.94 | 19.92 | 19.24 | 19.40 | 11.22 | 8.67 | 12.91 |
| Cr | 0.05 | 1.41 | 5.93 | 1.90 | 3.44 | 3.16 | 0.94 | 1.85 |
| Fe | 3.7 | 279891 | 55862 | 54670 | 50851 | 33004 | 30369 | 29906 |
| Mn | 0.03 | 179.90 | 1285.82 | 1369.39 | 1448.51 | 765.45 | 574.52 | 582.24 |
| Co | 0.03 | 460.02 | 605.13 | 575.58 | 517.16 | 312.31 | 275.74 | 254.10 |
| Ni | 0.06 | 1656.75 | 1745.14 | 1646.09 | 1502.70 | 875.61 | 757.49 | 689.64 |
| Cu | 0.03 | 40.70 | 2.48 | 0.60 | 0.77 | 1.77 | 21.56 | 40.36 |
| Zn | 0.08 | 59519 | 24816 | 26295 | 57919 | 308869 | 349458 | 407085 |
| Ga | 0.01 | 0.90 | 0.87 | 0.79 | 0.99 | 1.67 | 1.77 | 2.27 |
| Ge | 0.02 | 0.33 | <DL | <DL | <DL | <DL | <DL | <DL |
| As | 0.06 | 3348.26 | 1930.88 | 1008.84 | 18.04 | 7.31 | 3.52 | 33.21 |
| Se | 0.2 | 1.52 | 4.55 | 3.69 | 3.84 | 3.27 | 3.00 | 3.60 |
| Rb | 0.04 | 5.31 | 3.28 | 3.55 | 3.93 | 3.09 | 2.18 | 3.86 |
| Sr | 0.03 | 26.07 | 242.56 | 249.13 | 247.25 | 127.38 | 96.95 | 98.58 |
| Y | 0.02 | 1.56 | 13.78 | 13.56 | 14.01 | 7.32 | 5.45 | 5.86 |
| Zr | 0.09 | 15.07 | 9.22 | 15.89 | 17.37 | 10.71 | 8.42 | 15.69 |
| Nb | 0.04 | 0.36 | 0.14 | 0.10 | 0.09 | 0.04 | 0.04 | 0.07 |
| Mo | 0.02 | 39.39 | 18.85 | 19.79 | 1.22 | 0.40 | 1.37 | 7.06 |
| Ru | 0.01 | <DL | 0.31 | 0.32 | 0.28 | 0.17 | 0.13 | 0.13 |
| Pd | 0.01 | 1.53 | 0.72 | 0.84 | 0.96 | 0.20 | 0.07 | 0.18 |
| Ag | 0.01 | 10.31 | 1.23 | 0.96 | 0.88 | 2.68 | 17.30 | 19.40 |
| Cd | 0.06 | 69.46 | 13.60 | 16.90 | 41.16 | 210.05 | 235.50 | 285.51 |
| Sn | 0.06 | 0.96 | 0.70 | 2.05 | 1.34 | 2.65 | 2.44 | 2.72 |
| Sb | 0.01 | 13.14 | 14.73 | 17.51 | 0.15 | 28.18 | 51.48 | 55.83 |
| Te | 0.02 | <DL | <DL | <DL | <DL | <DL | <DL | <DL |
| Cs | 0.02 | 1.29 | 0.41 | 0.49 | 0.66 | 1.09 | 0.99 | 1.16 |
| Ba | 0.03 | 107.27 | 123.89 | 93.61 | 132.93 | 63.94 | 56.03 | 54.47 |
| La | 0.03 | 1.34 | 6.83 | 7.22 | 7.54 | 3.95 | 3.05 | 4.21 |
| Ce | 0.03 | 4.89 | 16.24 | 16.73 | 17.23 | 9.20 | 7.08 | 9.08 |
| Pr | 0.04 | 0.37 | 2.51 | 2.59 | 2.64 | 1.41 | 1.08 | 1.29 |
| Nd | 0.03 | 1.54 | 11.14 | 11.34 | 11.59 | 6.19 | 4.75 | 5.34 |
| Sm | 0.04 | 0.34 | 2.77 | 2.80 | 2.93 | 1.54 | 1.16 | 1.24 |
| Eu | 0.03 | <DL | 0.48 | 0.46 | 0.49 | 0.27 | 0.20 | 0.21 |
| Gd | 0.03 | 0.35 | 3.02 | 2.97 | 3.08 | 1.59 | 1.18 | 1.27 |
| Tb | 0.03 | <DL | 0.44 | 0.45 | 0.47 | 0.24 | 0.18 | 0.19 |
| Dy | 0.04 | 0.31 | 2.72 | 2.82 | 2.88 | 1.52 | 1.12 | 1.21 |
| Ho | 0.02 | <DL | 0.53 | 0.54 | 0.57 | 0.29 | 0.22 | 0.25 |
| Er | 0.04 | 0.18 | 1.48 | 1.50 | 1.54 | 0.80 | 0.61 | 0.69 |
| Tm | 0.06 | <DL | 0.21 | 0.22 | 0.23 | 0.12 | 0.09 | 0.10 |
| Yb | 0.05 | 0.16 | 1.19 | 1.20 | 1.28 | 0.67 | 0.50 | 0.61 |
| Lu | 0.04 | <DL | 0.17 | 0.17 | 0.18 | 0.09 | 0.08 | 0.10 |
| Hf | 0.05 | 0.25 | 0.14 | 0.45 | 0.62 | 0.39 | 0.28 | 0.52 |
| Ta | 0.02 | 0.11 | <DL | <DL | <DL | <DL | <DL | <DL |
| W | 0.08 | 3.49 | 1.59 | 0.93 | 1.82 | 0.46 | 0.27 | 0.69 |
| Re | 0.03 | <DL | <DL | <DL | <DL | <DL | <DL | <DL |
| Os | 0.08 | 1.04 | 0.46 | 0.22 | 0.14 | 0.07 | 0.10 | 0.06 |
| Ir | 0.04 | 0.57 | <DL | <DL | <DL | <DL | <DL | <DL |
| Pt | 0.01 | <DL | <DL | <DL | <DL | <DL | <DL | <DL |
| Au | 0.01 | | 1.85 | 0.97 | 0.76 | 0.71 | 0.84 | 0.70 |
| Tl | 0.05 | 380.31 | 59.21 | 55.69 | 31.32 | 47.04 | 53.62 | 56.15 |
| Pb | 0.03 | 9745 | 18986 | 42576 | 17344 | 43805 | 41254 | 38814 |
| Th | 0.01 | 1.25 | 3.89 | 4.82 | 5.51 | 3.19 | 2.55 | 3.87 |
| U | 0.03 | 2.21 | 6.24 | 7.01 | 8.28 | 5.19 | 4.72 | 7.45 |

5.0: Pyrite Re-Os Geochronology of carbonate-hosted Zn-Pb ore deposits of the Canadian Cordillera

5.1: Introduction

The Canadian Cordillera contains extensive mineralization from southern British Columbia through to the Yukon and Northwest Territories, with a suite of volcanogenic sulphide deposits (VMS/VHMS), sedimentary exhalative (SEDEX), and carbonate-hosted base metal (i.e. Zn-Pb ± Ag) sulphides (e.g. MVT deposits) being present (Fig. 5.1). Devonian-Mississippian VHMS/VMS deposits are associated with arc magmatism in the pericratonic terranes and basinal facies of the North American continental margin. SEDEX deposits related to intracontinental rifting are of similar age and are located more inboard within the basinal shales of the Selwyn Basin, and Kechika Trough (McClay et al., 1989; Paradis et al., 1998; Nelson and Colpron, 2007). Carbonate-hosted Zn-Pb mineralization occurs throughout the Rocky Mountains, Mackenzie Mountains, and the Western Canadian Sedimentary Basin within platform carbonates deposited during Cambrian through to the Devonian (Fyles and Hewlett, 1959; Olson et al., 1994). The carbonate-hosted Zn-Pb deposits are typically located directly east of many of the SEDEX deposits, which has led some authors to speculate if MVT systems have a genetic relationship to SEDEX and VMS/VHMS mineralization systems within the Cordillera (e.g. Goodfellow et al., 1993; Nelson et al., 2002; Paradis and Simandl, 2017). However, since MVT deposits do not require a link to magmatic activity they may be a genetically distinct suite of deposits. Currently, the constraints on the timing of mineralization are relatively weak, with contradictory datasets existing in the literature (Nakai et al., 1993; Symons et al. 1993; Smethurst et al., 1999; Nelson et al., 2002)

Due to their simple mineralogy (pyrite, sphalerite, galena) the types of dating techniques applicable to carbonate-hosted deposits have been mainly restricted to either paleomagnetism or sphalerite Rb-Sr geochronology. Unfortunately, when these two methods are applied to ores within the Canadian Cordillera they produced disparate ages. Paleomagnetic dating typically produces young ages (<100 Ma) implying that these deposits formed in response to compression during the Laramide orogeny (Symons et al., 1993; Lewchuk et al., 1997; Smethurst et al., 1999). Such a compressional tectonic regime is required by the topographic recharge model used by

Garven (1985) to explain mineralization of the Pine Point MVT deposit in the Northwest Territories. Fluid flow associated with the Laramide orogeny has also been used as a mechanism to explain the extensive dolomitization found in western Canada (Amthor et al., 1993; Drivet and Mountjoy, 1997; Machel and Mountjoy, 1987). Sphalerite Rb-Sr isotopic dating has produced ages older than paleomagnetism (~350 Ma), a period of time closely associated with widespread extensional tectonics along the continental margin (Nelson et al., 2006). Alternatively, a potential compressional regime in the far south associated with the Late Devonian - Mississippian Antler orogeny has also been suggested as the driver for fluid flow and related mineralization episodes (Amthor et al., 1993; Nesbitt and Muehlenbachs, 1994; Mountjoy et al., 1999).

The primary objective of this study is to resolve the age dispute between isotopic and paleomagnetic ages through the application of pyrite Re-Os geochronology. Due to the proven reliability of this technique in the similarly age-contentious Zn-Pb deposits from the Irish Midlands (Hnatyshin et al., 2015) this could be the ideal isotopic system for settling the age debate. Several mineralization sites were chosen for isotopic dating including the Salmo district in southern British Columbia, Robb Lake from northern British Columbia, and Prairie Creek from the Northwest Territories (Fig. 5.1A). These locations were chosen due to their large, potentially economic sizes, and their widespread spatial distribution within the Cordillera. These deposits, compared to previously dated carbonate-hosted ores (e.g. Hnatyshin et al., 2015; Hnatyshin et al., 2016), have more extensive post-mineralization modifications. These deposits, to varying degrees, underwent folding, brecciation, regional metamorphism, contact metamorphism, and large scale oxidation. Therefore, a secondary objective of this study is to test the robustness of the pyrite Re-Os system when sulphide ores have undergone substantial post-formation modification. Samples chosen for Re-Os geochronology have been compositionally mapped using an electron microprobe microanalyzer (EMPA) and a Laser Ablation ICPMS (LA-ICPMS) system, as per the recommendations discussed in Chapter 4.

5.2: Regional Geologic History

The Cordillera of western North America is a tectonically complex orogenic belt built up by many episodes of terrane accretion throughout the Palaeozoic and Mesozoic (Coney et al., 1980; Monger and Nokleberg, 1996; Colpron et al., 2007). During the early Palaeozoic, Cambrian-Devonian platform carbonates, a number of basal units, and fringing

parautochthonous pericratonic terranes (e.g. Cassiar and Kootenay) were deposited along an ancient North American miogeocline (Colpron and Price, 1995; Colpron et al., 2007). Tectonic activity along the western margin became widespread during the Devonian and is associated with an east facing subduction zone, located to the west of the continental margin (Fig. 5.2). Inboard of this subduction zone, both the continental margin and the pericratonic Yukon-Tanana terrane (YTT) show initiation of volcanism at ~390 Ma with peak magmatic activity occurring from ca. 350 - 370 Ma (Rubin et al., 1990; Nelson et al., 2006). During this period, the majority of VHMS, VMS and SEDEX deposits were formed along the continental margin and associated terranes (e.g. Kootenay, Cassiar, YTT). Based on their relationships to various magmatic episodes and host sedimentary rocks, VHMS and VMS deposits are thought to have formed in back-arc and intra-arc settings, whereas SEDEX deposits were formed towards the edges of the back-arc basins. A marginal rift basin that formed during the Late Devonian created the Slide Mountain ocean (Slide Mountain terrane) detaching the YTT away from ancestral North America (Fig. 5.2; Nelson et al., 2006). The maximum span of the ocean is not known with certainty but may have stretched over 1000 km in width by the Pennsylvanian based on fossil evidence (Belasky et al., 2002). During the expansion of the Slide Mountain ocean magmatism along the continental margin ceased by ~340 Ma, but the rifted YTT showed continued magmatic activity throughout the Carboniferous. Farther south, the Antler orogenic belt of the western United States developed during the Late Devonian - Early Mississippian. The influence that the Antler compression had on the Canadian Cordillera is unclear but at least minor development of a fold and thrust belt in the southern Western Canadian Sedimentary Basin appears to have been created (Klepachy and Wheeler, 1985; Root, 2001). The closure of the Slide Mountain Ocean during the Permian marks the initiation of large scale magmatism within the YTT and lead to the eventual accretion of YTT and other intermontane terranes onto the continental margin during the Mesozoic (Nelson and Colpron, 2007). The more exotic Insular and Alaska terranes likely migrated from a more northerly position and began to accrete during the Jurassic. During the Cretaceous and into the early Paleogene the Cordillera experienced extensive plutonism throughout its length in response to the compression and continued accretion along the orogen.

5.3: Deposit Geology

5.3.1: Prairie Creek

5.3.1.1: Geological Context

Prairie Creek is an area of extensive Zn-Pb-Ag±Cu mineralization located in the southern Mackenzie Mountains of the south-western Northwest Territories (Fig. 5.1). Below is a brief geologic description based on the work of Morrow and Cook (1987). The southern Mackenzie Mountains are a tectonically complex region containing lower Paleozoic carbonates deposited in a shelf environment (Mackenzie Shelf) on the western edge of the ancient North American miogeocline. An intrashelf basin within the Mackenzie Shelf, the Root River Basin, contains significant Zn-Pb-Ag±Cu mineralization within a paleo-depression (Prairie Creek Embayment) at the basin's southern end (Morrow, 1984).

The southern Root River Basin is divided into three general assemblages that mark important facies changes within the basin (Fig. 5.3). The first, known as the Root River Assemblage, is dominated by Ordovician-Silurian subtidal sediments, deep water argillaceous carbonates, and shales of the Esbatottine, Whittaker, and Road River formations. Uplift during the Late Silurian - Early Devonian is thought to have resulted in the formation of the Prairie Creek Embayment and marked the beginning of deposition of the shallow water Prairie Creek Assemblage. The Prairie Creek Assemblage includes the Cadillac Formation siltstones, Vera Formation limestones, the Camsell Formation dolostones and evaporites, as well as the dolostones of the Sombre and Arnica Formations. The Prairie Creek Embayment itself is filled primarily with the Cadillac Formation, Sombre Formation, and the Arnica Formation. Overlaying the Arnica Formation is the Early to Middle Devonian Funeral-Headless Assemblage and marks the disappearance of the Prairie Creek Embayment as a feature within the Root River Basin.

The southern Mackenzie Mountains are defined by north to northeast trending structures that form faulted anticlines and synclines that are thought to have been created through transcurrent movement (De Wit et al., 1973). Structural modification of the Prairie Creek Embayment itself mirrors that observed in the Mackenzie Mountains as a whole. The most important features are the many steeply west-dipping, north-south trending, reverse faults that

cut through Ordovician - Late Devonian folded strata (Cook, 1977). More recent interpretations of the Prairie Creek Embayment fault system by Earls (1995) and Fraser (1996) suggest that these reverse faults were originally normal faults that were subsequently reactivated during the Laramide orogeny. The latest tectonic features observed at Prairie Creek are thrust faults that crosscut the earlier reverse faults. Both sets of faults are associated with minor folding (Morrow and Cook, 1987). The dominant tectonic feature in the vicinity of mineralization is the Prairie Creek anticline which trends to the northeast and is bounded by reverse faults, the Prairie Creek Fault to the east and to the west by the Gate Fault (Fig. 5.4A).

Volcanic rocks have not been described at Prairie Creek but extensive heating during the Middle Devonian (300 - 480°C) is known from conodont colour alteration indexes (CAI) from carbonates in the Prairie Creek area (CAI = 5, n = 10) and vitrinite reflectance values (~4.50 %) from the Laird Basin directly to the south (Morrow et al., 1990; Morrow et al., 1993). By the Carboniferous the region cooled to < 90°C based on lower CAI and vitrinite reflectance values of 1.5 and 0.30%, respectively.

5.3.1.2: Mineralization

The Prairie Creek deposit comprises three distinct styles of mineralization that total 8.1 Mt of economic sulphide ore (Canada Zinc, 2017). These include stratabound massive sulphides (SMS), quartz-carbonate-sulphide veins (Vein-Type) that are known to cross-cut SMS sulphides, and currently sub-economic Mississippi Valley-type (MVT) mineralization. Below is a description of the ore system based on the work of Fraser (1996), Paradis (2007), and Canadian Zinc (2017).

SMS mineralization is characterized by five irregularly shaped lenses of sulphide that replace dolostone in the Upper Whittaker Formation. The larger bodies have lateral dimensions of 400 m x 100 m with a thickness of up to 28 m (Earls, 1995; Findlay, 2000). They are spatially associated with the Prairie Creek Fault and the fold axis of the Prairie Creek Anticline (Figs. 5.4B,C). Mineralogy of the sulphide bodies is simple, primarily consisting of sphalerite, galena, pyrite, iron oxides, quartz, and carbonates. Sulphides of the SMS bodies replaced the host dolostone through the precipitation of massive aggregates of sulphides and finely laminated banded sulphide layers. Later stage mineralization includes veins of coarse-grained sphalerite crosscutting the massive sulphide aggregates. Brecciated sulphides are often in-filled by galena

with any remaining open space filled by carbonate. Oxidation of sulphides into their respective oxides is common close to the surface creating a complicated mineralogical assemblage often enriched in trace elements (Stavinga, 2014).

Widespread discontinuous sulphide-filled fractures (Vein-Type) typically trend parallel to regional faults and the Prairie Creek Anticline over a distance of ~16 km. Stratigraphically, they cross-cut all formations and the SMS ore-bodies (Fig. 5.4C). Vein-Type sulphides commonly show shearing textures and brecciation suggesting the mineralization was either contemporaneous with, or predates, tectonic activity. Mineralogy is dominated by sphalerite and galena, with lesser amounts of pyrite, tetrahedrite, and tennantite. Sulphides may be found as massive aggregates or as disseminated crystals within a matrix of quartz, calcite, and/or dolomite. Following sulphide mineralization, carbonates fill in remaining fractures and open spaces. Nearer to the surface a significant proportion of the sulphides have been oxidized.

Poorly explored and described, MVT-style mineralization occurs in the Silurian Root River Formation to the northeast of the SMS and Vein-Type mineralization (Fig 5.4A). Over a half dozen showings are known over a length of ~10 km with sulphides infilling fractures, breccias, vugs, and pore spaces within the host dolostone. Normal faulting proximal to known MVT showings is suspected to have focused fluids into the Root River Formation resulting in the formation of breccia and the precipitation of sulphides in open spaces. Pyrite and sphalerite have been documented to form colloform textures within open-spaces as well as directly replacing dolomite cement as fine to medium grain aggregates.

5.3.2: Robb Lake

5.3.2.1: Geological Context

The Robb Lake Zn-Pb deposit is the largest and best described site of mineralization within a band of north-south trending MVT showings in north-eastern British Columbia (Fig. 5.1A). The Robb Lake area contains many sulphide and breccia bodies located within an area of approximately 8 km² (Fig. 5.5B). The geologic descriptions below are summaries of previously published work by Nelson et al. (1999) with additional background material provided by Thompson (1989). At Robb Lake, the Silurian-Devonian dolostones of the Muncho-McConnell Formation host the majority of sulphides with a minor proportion of ore hosted in the overlying

Stone and Dunedin formations (Fig. 5.5). Near mineralization sites the Muncho-McConnell Formation is divided into an upper and a lower unit based on the physical characteristics of the dolostone. The lower unit is composed of blocky dolostone with subtle bedding patterns, whereas the upper unit has well defined bedding with distinct carbonaceous laminations. The boundary between the upper and lower units is an important marker for mineralization as the boundary contains brecciated rock that is in-filled with the sulphides that comprise the Robb Lake deposit. Structurally, the Robb Lake deposit is located in the footwall of the nearby thrust faults which divide the area into two distinct stratigraphic sequences (Fig. 5.5C). The Muncho-McConnell Formation along with other Silurian - Devonian platform carbonate units are found in the footwall of the thrust fault, and typically older Devonian to Cambrian basinal units compose the hanging wall. Subsequent compression has folded both the ore deposit and thrust faults producing the current geometry of the deposit (Fig. 5.5C).

5.3.2.2: Mineralization

Brecciation and mineralization at the boundary of the Upper and Lower Muncho-McConnell Formation is extensive, with over 6.5 Mt of sulphide over 200m of stratigraphic section. The Robb Lake deposit is primarily composed of stratabound sulphide bodies found within this breccia with minor ore filling fractures and veins. Due to the importance of this breccia with respect to mineralization it has been previously studied in detail (Sangster, 1973; MacQueen and Thompson, 1978; Manns, 1981). Breccia subtypes that are closely associated with mineralization are classified as dolomite-cemented crackle breccia, mosaic and rubble breccias, and the rock-matrix breccias. In particular the dolomite cement of the mosaic and crackle breccias contain the majority of ore at Robb Lake. Rock-matrix breccias are the most voluminous of the breccia types and have a matrix composed of quartz, carbonaceous dolostone, and small fragments of pyrobituminous shales. Sulphides are found disseminated within the matrix or as fracture fill. Textural observations by Nelson et al. (1999) suggest a complicated paragenetic relationship between the different styles of breccia and sulphide mineralization. However, it is expected that the breccias and sulphides were formed contemporaneously as each sub-type of breccia can locally be observed crosscutting each another, with remobilized sulphide clasts contained within the breccias.

The mineralogy of deposit primarily consists of sphalerite, galena, and iron sulphides. Sphalerite crystals are found within the dolomite cement of the various breccias described above and may form rims around dolostone clasts. Individual sphalerite crystals are typically anhedral and are commonly fractured. Galena can be found either as euhedral crystals or as anhedral aggregates with the matrix of the breccias. Iron sulphides are found as disseminated crystals within the matrix or as massive aggregates concentrated along bedding planes and stylolites or within fractures. Pyrobitumen is a minor phase present within the breccia bodies and often infills fractures. Late stage quartz veins are known to crosscut all previous phases of mineralization.

5.3.3: Salmo district

5.3.3.1: Geologic Context

The Salmo district is located in a ~25 km² area in south-eastern British Columbia directly north of the Canada-US border. Numerous occurrences of Zn-Pb±Ag±Au±W mineralization exist within the district, some of which were developed into mines in the early and middle 20th century (Fig. 5.1B). Recent interest in the area is concerned with oxide ores formed from more recent oxidation of primary sulphides (Simandl and Paradis, 2009; Paradis and Simandl, 2010; Keevil, 2011; Paradis et al., 2015). The following descriptions are a summarization of the work of Fyles and Hewlett (1959) and were updated using observations provided in Macdonald (1973). The Salmo district lies in the southern end of the Kootenay terrane, a pericratonic terrane located in the south-eastern portion of the Canadian Cordillera west of the ancient Paleozoic North American miogeocline. The stratigraphy of the Salmo district is dominated by conformable Cambrian formations (Quartzite Range, Reno, Laib, and Nelway Fms,) which overlie Precambrian basement rocks (Fig. 5.6A). The Reeves Member near the base of the Laib Formation is the lowest carbonate within this sequence and is the host of Zn-Pb±W mineralization. The Reeves Member is composed of banded limestone containing minor amounts of quartz, muscovite, with localized occurrences of tremolite, garnet, and pyroxene. Dolomitization is widespread in the vicinity of the ore bodies. Disconformably overlying the Cambrian formations is the Ordovician Active Formation that is composed primarily of metamorphosed argillaceous sediments.

Structurally, the Salmo district is complex with primary overturned and isoclinal folds re-folded into secondary folded complexes. Thrust faulting in the area likely originated during the first episodes of folding and movement continued through the development of secondary folds. Three major thrust faults, known as the Waneata, Argillite, and Black Bluff faults, occur in the Salmo district, whereas smaller faults that follow bedding and foliation are also common. The most prominent structural features in the mineralized area are isoclinal folds known as the Jersey anticline, the Jack Pot anticline, and the Salmo River anticline. Cretaceous-Eocene Granitic activity is common in the area (Fig. 5.1B) and postdate these tectonic episodes and are themselves crosscut by late stage faults that offset the fold and thrust complexes. Regional metamorphism at Salmo reached greenschist facies producing the many foliated rocks found in the area. Contact metamorphism by the granitic bodies and later stage Eocene lamprophyre dykes/sills overprint pre-existing metamorphic textures.

5.3.3.2: Mineralization

The Salmo district contains over ten discrete occurrences of Zn-Pb mineralization that total over 6 Mt in sulphide and oxide ore. Only limited descriptions of the ore are currently available in the literature, therefore the following brief descriptions are primarily from Fyles and Hewlett (1959). For this study we have investigated the Reeves MacDonald and HB mines and the following descriptions are most relevant to those properties. However, Zn-Pb mineralization throughout the district is very similar in mineralogy, shape, and are located at the same stratigraphic level. All mineralization within the district represents replacement of the dolomitized Reeves Member of the Laib Formation by sphalerite, galena, and pyrite. Sulphides take many forms including lens shaped ore bodies, bedding-parallel banded sulphides, or as disseminated grains within dolomitized limestone. Both the host rock and the ore bodies contain shearing textures and may have been brecciated during the deformation associated with younger tectonism. These breccias commonly host sulphides in the form coarse-grained coatings on the fragments of the brecciated host rock. Sphalerite is typically found as mm-scale crystals that either coat dolomite crystals or are found intergrown with pyrite and galena. Galena is less common than sphalerite but when observed is typically intimately associated with sphalerite. Pyrite is typically found as disseminated grains or as masses of fine-grained crystals associated with minor sphalerite and galena. Oxidation of the ore is common near the surface at all deposits

and complete or partial oxidation of the orebody may extend over 100 m below the surface and is believed to have possibly occurred as recently as ~ 10000 BP (Simandl and Paradis, 2009).

5.3.3.3: Reeves MacDonald Mine

The ore bodies of the Reeves-Macdonald mine are found within a secondary fold known as the Reeves syncline, which is in turn part of the regional Salmo River Anticline. The Reeves MacDonald mine is composed of numerous ore bodies that result in an elongated mineralized zone that plunges into the subsurface for > 800 m (Fig. 5.6B). Sulphide mineralization is primarily composed of discontinuous banding of sulphides found within the trough of the Reeves syncline. Small veins composed of carbonates, quartz with minor amounts of sphalerite and galena crosscut the banded ore. A smaller proportion of the ore is hosted in breccia primarily located in the limbs of the Reeves syncline.

5.3.3.4: H.B. Mine

The area surrounding the H.B. mine is defined by isoclinal folding containing thrust faulting with secondary folds being rare. The mineralized zone at the H.B. mine is dominated by steeply dipping lenticular ore bodies that can extend for more than 900 m in the subsurface (Fig. 5.6C). Pyrite and sphalerite are typically fine grained and occur as disseminated crystals within the dolomitized limestone, as irregular lenses, or as narrow banded sulphides. Galena is relatively rare within these ore bodies.

5.4: Methodology

5.4.1: Sample Selection and Preparation

Samples from Prairie Creek, Robb Lake and the Salmo district, were chosen based on the availability of samples containing high pyrite abundances and minimal oxidation. Pre-screening of pyrite also included testing the Re concentration prior to full Re-Os analysis to ensure that Re concentrations was high enough (~ 0.5 ppb) for reliable isotopic measurements by thermal ionization mass spectrometry (TIMS) given the expected age and amount of radiogenic ¹⁸⁷Os produced. Additional samples from the Pine Point deposit located in the Northwest Territories were tested for their Re contents but were found to contain < 0.2 ppb Re and therefore were not pursued further.

Selected samples were put through a mineral separation process to help eliminate impurities (e.g. carbonates, silicates, sphalerite). All samples were first crushed to a size of 74-210 μm using metal free equipment to prevent metallic contamination. This size range was chosen as it optimizes further mineral separation procedures. Most quartz and carbonates were removed through heavy liquid (methylene iodide) separation. Magnetic separation was used to remove additional impurities and to produce several mineral separates of differing magnetic susceptibility, which is known to expand the range of $^{187}\text{Re}/^{188}\text{Os}$ produced in analyses (e.g. Hnatyshin et al., 2015, Hnatyshin et al., 2016). The majority of samples also underwent an acid leaching procedure to remove residual carbonates ($\geq 0.2\text{N HCl}$) and/or oxidation products (6N HCl). The leaching procedure used requires exposing the mineral separates to acid for a period of 24 hours in a 22mL borosilicate glass vial. All samples were then rinsed with Milli-Q water three times and ethanol once to ensure complete removal of the acid. The acid and water rinses together form the leachate which is stored for future analysis. The exact process used for each mineral separate are presented in Tables 5.1-5.3, and for more details on the mineral separation process used in this study refer to Chapter 4B.

5.4.2: Re-Os Analytical Procedure

Re-Os isotopic analysis on several hundred milligrams of sample was carried out at the Crustal Re-Os Geochronology Laboratory at the University of Alberta following the isotope dilution procedure of Hnatyshin et al. (2016). Isotopic measurements on chemically purified Re and Os were carried out using negative-TIMS using a ThermoScientific Triton instrument. For TIMS analysis, Re samples were loaded onto a Ni filament and coated in a saturated solution of $\text{Ba}(\text{NO}_3)_2$ activator to improve the ionization efficiency. The Ni filaments were heated to $\sim 750\text{-}820^\circ\text{C}$ in ~ 5 min to create a stable beam of ReO_4^- . Osmium samples were loaded in 9N HBr onto a Pt filament and coated in a saturated solution of $\text{Ba}(\text{OH})_2$ and were heated to $\sim 650\text{-}720^\circ\text{C}$ over ~ 20 min in an oxygen enriched environment ($\sim 3 \times 10^{-7}$ mbar) to obtain a stable beam of OsO_3^- . One hundred simultaneous measurements of ^{185}Re and ^{187}Re were collected using Faraday cup detectors, whereas a secondary electron multiplier was used to collect 96 measurements of each isotope of Os through peak hopping. Isoplot version 3.00 (Ludwig, 2003) was used to calculate all ages reported by using a decay constant of 1.666e^{-11} (Smoliar et al., 1996).

5.4.3: Compositional Mapping

To complement the Re-Os dating, representative samples from each deposit were further characterized through compositional mapping using EMPA and LA-ICPMS analysis.

EMPA compositional mapping used a CAMECA SX100 located in the Electron Microprobe Laboratory at the University of Alberta Department of Earth and Atmospheric Sciences. Backscattered Electron Images (BSE), compositional maps of major (Ca, S) and minor elements (As, Co, Al) were initially produced followed by the more sensitive but lower resolution LA-ICPMS analyses. Calcium and S were chosen as they are useful at identifying the major phases found in the samples (carbonates and sulphides). Arsenic and Co are potentially useful for identifying zonation within sulphides, whereas Al is useful for determining areas enriched in silicates. All maps produced through EMPA analysis are presented in the Appendix (Figs 5.25-5.30).

LA-ICPMS compositional analysis on preselected locations from EMPA compositional maps used a Thermo Scientific iCAP-Q mass spectrometer interfaced with a New Wave UP-213 laser at the ICMPS Facility of the Canadian Center for Isotopic Microanalysis at the University of Alberta. LA-ICPMS analysis focused on the Mo distribution, as Mo and Re are strongly correlated and are useful in interpreting the Re-Os isotopic data (see Chapter 4). A total sweep time of 0.30 - 0.35 s was used during analysis with ~0.20 - 0.25 s of dwell time being allocated for Mo, with the remaining time split between As, Co, and Fe. Compositional maps were produced using a spot size diameter of 15 μm or 30 μm with scan rates equal to that of the spot size (e.g. 30 μm spot size = 30 $\mu\text{m}/\text{s}$ scan rate) using a laser frequency of 20 Hz, a fluence of 2.5 - 3.0 J/cm^2 , and a He flow rate of 0.5 L/min. Maps were produced through rastering, with each line offset by the spot size. Prior to, and following each line, ablation background measurements were taken over a period of 10 seconds. For semi-quantitative analysis a MASS1 external standard was measured every 10 scans using the same ablation parameters used for the sample. To visualize the raw data, the software program Iolite v3.6 (Paton et al., 2011) was used to convert sweeps into compositional maps. Due to the relatively long wash out time (~10 s) for this laser ablation system it was necessary to deconvolute some images using a simple deconvolution scheme based on modeling the decay of signals using an exponential decay curve and applying a correction for all data points. Due to the semi-quantitative nature of the maps produced and the smearing effects of the long washout times, the concentrations produced are

approximate and interpretations made cautiously. All analytical data is available as a .xls file on request.

5.5: Results

5.5.1: Sample Characterization

Each sample was characterized using hand sample observations, reflected light petrography, and supplemented by EMPA and LA-ICPMS compositional analysis. Representative petrographic images of select mineral separates were used to estimate the modal abundance of the various sulphides found within the mineral separates by pixel counting different phases in petrographic images. The leaching procedure was used to determine the abundance of carbonates originally found within the mineral separate. Micro-inclusions and/or nano-inclusions of molybdenite in some samples are tentatively identified in LA-ICPMS images when localized spikes of Mo concentrations are observed. The estimated mineralogical distribution of each mineral separate used for Re-Os isotopic analysis is provided in Table 5.4.

5.5.1.1: Prairie Creek - MVT-style Mineralization

Sample PC-94-80 (Fig. 5.7) was collected from the Zebra MVT showing at Prairie Creek (Fig. 5.1A) and was chosen for Re-Os analysis based on Re content (> 1 ppb). In hand sample (Fig. 5.7A) PC-94-80 is composed of sub-mm pyrite crystals that have replaced the host dolostone with carbonate veins crosscutting the pyrite aggregates (e.g. top of Figure 5.7A). Pyrite is highly fractured throughout the sample and fractures are in-filled with a mix of carbonates, silicates and oxides. Oxides in fractured areas are often enriched in trace elements such as Co and Mo, up to several orders of magnitude compared to the cores of pyrite crystals (Fig. 5.8). Oxides that stain carbonates can be found within the larger fractures as well as grain boundaries. The timing of oxidation is unclear but it appears oxidation must occur after the fracturing of the pyrite grains. Sphalerite is occasionally observed in the mineral separates but was not observed in thin section, hence the paragenetic relationship between pyrite and sphalerite is unclear. Observations from other studies (e.g. Paradis, 2007) suggest that sphalerite and pyrite form together in aggregate masses. There is minimal evidence of molybdenite crystals in this sample as the Mo compositional maps do not show the extremely localized spikes of Mo. A generalized evolution of PC-94-80 is provided in Figure 5.9.

The mineral separates created from PC-94-80 show subtle differences, with more magnetic fractions (e.g. PC-94-80 NM0.6; Fig. 5.7C) containing a higher density of fractures than that of less magnetic fractions (e.g. PC-94-80 NM 1.1; Fig. 5.7E). Leaching of PC-94-80 separates also show that more magnetic fractions tend to be associated with higher abundances of carbonates (Table 5.4). As fractures are commonly filled with carbonates it may explain why carbonates are concentrated within the more magnetic mineral separates. Based on these observations an estimation of the sampling location of different mineral separates is highlighted in Figure 5.7B.

5.5.1.2: Prairie Creek - SMS-style Mineralization

All samples of SMS-style mineralization at Prairie Creek were collected in the vicinity of the mine site (Fig. 5.4A). All samples from this style of mineralization contain low Re concentrations (< 0.5 ppb), therefore to ensure there is sufficient range of Re-Os ratios to produce an isochron several rocks were processed. The general paragenesis of the SMS sulphides is provided in Figure 5.9.

Sample PC-93-25 is composed of sulphides and silicates that have almost completely replaced the host dolostone (Fig. 5.10). Quartz grains host an interconnected network of anhedral pyrite crystals and irregularly shaped sphalerite that postdates pyrite (Fig. 5.10B). Al-bearing phases are closely associated with sphalerite mineralization but do not crosscut either pyrite or sphalerite (Fig. 5.11). The close association of the Al-rich phases with sphalerite suggest that these silicates represent replacement of original quartz crystal during a phase of sphalerite mineralization. The rims of pyrite crystals are enriched in As and possibly other elements, however the concentrations of other elements are too low for the EMPA to detect, and the LA-ICPMS images are too low of resolution to determine if core-rim zonation occurs in Co or Mo. Molybdenum spikes in LA-ICPMS images exist but do not appear to correlate with a specific phase. The relatively low concentrations (~ 10 ppm) of these spikes could be explained by nano-scale molybdenite crystals being distributed throughout the rock. Oxidation of sulphide material is present around the perimeter of sulphides as well in the grain boundaries between quartz crystals. Mineral separates with the lowest magnetic susceptibility accumulate sphalerite (i.e. PC-93-23 NM 1.95; Fig. 5.10E), whereas more magnetic separates (e.g. Figs. 5.10C,D) appear to

contain almost pure (> 90%) pyrite. Carbonates are rare in this sample but become enriched in the most magnetic separate.

Sample PC-11-209A is composed of massive aggregates of pyrite replacing quartz crystals (Fig. 5.12B). These pyrite crystals have been fractured and infilled by later silicates (Fig. 5.13C). Figure 5.12B and Figure 5.13 show that pyrite is found either as massive aggregates that are > 1 mm in size or smaller aggregates associated with quartz. In reflected light, three possible growth zones in pyrite can be distinguished (Fig. 5.12B), an inner pristine core, an inclusion-filled / fractured internal zone, and a clean outer rim. The As map in Figure 5.13B defines a fourth outermost zone enriched in As, similar to that seen in PC-93-25. The fractures show enrichment in Mo and Al (Fig. 5.13), and represent a stage of fluid flow that occurred after the primary pyrite masses were formed, and may be responsible for the outmost As-rich zone, similar to what was observed in PC-93-25. Quartz is present within the fractures and grain boundaries of the pyrite crystals. Any evidence of molybdenite in PC-11-209A is not present as the Mo compositional map does not show localized spikes of Mo. Other sulphides, such as sphalerite and galena, were not observed in thin section or the mineral separates, and carbonates are very rare. Fractures found within the pyrite crystals contain Fe-oxides and are enriched in Co, As, Mo, and Al, comparable to what was observed in PC-94-80. Mineral separates made from PC-11-209A show a similar fracture abundance pattern to that of PC-94-80, with fractures being more common among the more magnetic end members.

Sample PC-92-17B is characterized by massive aggregates of pyrite similar to PC-11-209A (Appendix Fig. 5.31). This sample did not undergo extensive characterization as it appeared similar to PC-11-209A in hand sample, and was only used for two bulk Re-Os analyses that didn't change the interpretation of the Re-Os system for SMS sulphides.

5.5.1.3: Prairie Creek - Vein-style Mineralization

Sample PCU (Fig. 5.14) represent Vein-style mineralization at Prairie Creek and was collected in the vicinity of the mine site (Fig. 5.4A). This sample was chosen for analysis as it was the only Vein-style sample that contained > 0.5 ppb Re within pyrite. Sample PCU was sliced into several smaller pieces that were processed for use in Re-Os isotopic analysis (e.g. PCU-23, contains material from slices 2 and 3). Slices chosen for further processing contain the highest proportion of pyrite. PCU contains silicates, pyrite and sphalerite that have replaced the

host dolomite (Fig. 5.14). The pyrite crystals show trace element zonation in As, Co, and potentially Mo. Most clearly visible in the As compositional map (Fig. 5.15B), pyrite cores contain trace element concentrations below detection limits, but a narrow internal band shows an increase in trace element concentration of over an order of magnitude before decreasing below detection limits. This zonation pattern is broadly similar to that seen in the SMS samples described above. Sphalerite replaces, crosscuts, and fills in some interstitial spaces within the pyrite crystals. Fractures, as seen in many of the previous samples, contain enrichments of As, Mo and Al. Molybdenum enrichment within these fractures appear to be localized into single pixels in deconvoluted images and may signal the presence of nano-scale molybdenite crystals. Oxidation products, as with the other Prairie Creek samples, also occur within the fractures. Late stage carbonates appear between the grain boundaries of quartz crystals. In the mineral separates the relationship between magnetic susceptibility and modal abundances is similar to that of PC-93-25 with sphalerite concentrating in the sample with the lowest magnetic susceptibility (e.g. PCU-23-NM2.0/3) and occurring in minor amounts in all other separates (Table 5.4). Carbonate contents and the abundance of fractures also appear to slightly increase at higher degrees of magnetic susceptibility (Table 5.4; Figs. 5.14C-E).

5.5.1.4: Robb Lake

Sample DDH 726 (Fig. 5.16) was sampled from the Robb Lake deposit (Fig. 5.5) and was chosen for its Re content (> 1 ppb). This sample is composed of mm-scale dolomite crystals that have been replaced by small ($\sim <100$ μm) crystals of pyrite (Fig. 5.16A). Pyrite is the dominant sulphide phase, forming semi-parallel bands or being disseminated along the grain boundaries of carbonate crystals (Fig. 5.16B). Al-rich phases and oxidation products are found along grain boundaries of pyrite and nearby dolomite crystals. Dolomite crystal boundaries distal to pyrite have a much lower abundance of Al-rich phases suggesting a relationship between pyrite and Al-phases. Arsenic and Co are enriched along certain areas of pyrite bands and grain boundaries (Figs. 5.17B,C). Unfortunately, the resolution of these LA-ICPMS images cannot discern if these enrichments only occur between crystals or are also enriched within the pyrite crystals themselves. The Mo compositional map (Fig. 5.17A) shows similar behaviour to that of Co and As, and deconvolution of the Mo images suggests that Mo spikes occur between pyrite crystals and not within them (see Appendix Figure 5.32 for deconvoluted image). Together it is

envisioned that Al, Co, As, and Mo are enriched between pyrite crystals by fluids exploiting the same flow paths as the fluids that produced pyrite and sphalerite mineralization, although perhaps at a later stage in the paragenesis (Fig. 5.9). Mineral separates produced for DDH have a substantial proportion of carbonates (9-25%; Table 5.4), likely as a result of the small grain size and disseminated nature of the pyrite crystals.

5.5.1.5: Salmo district

Samples collected from the Salmo district were composed of disseminated pyrite and were visually very similar, providing little basis to discriminate between samples for Re-Os analysis. Two samples, 07SP-21-1 from the Reeves-Macdonald Mine, and HB from the H.B. mine, were selected due to their contrasting Re concentration, 07SP-21-1 having > 100 ppb Re and HB having < 100 ppb Re.

Sample 07SP-21-1, originally composed of a single rock (Fig. 5.18a), was broken into separate pieces labelled A through I prior to mineral separation. Sample 07SP-21-1 contains pyrite crystals up to 1 mm in size that are disseminated within a quartz crystal matrix (Fig. 5.18B). Galena and Al-rich phases are common along grain boundaries and fractures within pyrite and to a lesser degree along quartz grain boundaries (Figs. 5.18B and 5.19D). Pyrite crystals show clear zonation in As and Co, although As and Co appear slightly offset (Figs. 5.19B,C). Molybdenum spikes of concentrations up to five orders of magnitude higher than the background grains are clearly visible and are distributed throughout the sample. Deconvoluted images appear to show that these Mo spikes occur most commonly close to fractures and grain boundaries as opposed to the center of large clean pyrite crystals (see Appendix Figure 5.33 for deconvoluted image). Carbonates are relatively rare within 07SP-21-1 but are enriched, along with galena, in the least magnetic end member of the mineral separates. Fracture abundance does not appear to be correlated with magnetic susceptibility in this sample.

As with 07-SP-21-1, Sample HB is composed of disseminated sulphide (Fig. 5.20A). However, in contrast to 07-SP-21-1, HB mineral separates contains significantly more carbonate and other sulphides (Figs. 5.20B-D) and are particularly enriched in separates that have higher magnetic susceptibilities (Table 5.4).

5.5.2: Re-Os Geochronology Results

5.5.2.1: *Prairie Creek*

Results from Re-Os isotopic analysis of *Prairie Creek* samples are summarized in Table 5.1. A total of 15 sulphide mineral separates were analyzed from a sample (PC-94-80) associated with MVT-style mineralization at *Prairie Creek*, with a single low density separate (PC-94-80 Low Density) and its associated leachate product also being analyzed. Rhenium concentrations range from 2.5 - 7.7 ppb and Os concentrations range from 13 to 52 ppt. A 15-point, Model 3 regression of sulphide data yields an age of 330 ± 19 Ma with a mean initial Os ratio of 4.3 ± 1.4 (Fig. 5.21A; MSWD = 75, variation in initial osmium (VIOs) = 1.4). Removing data with carbonate impurities results in a similar age (319 ± 18 Ma), less scatter (MSWD = 16), higher initial ratio (5.3 ± 1.1), and a smaller VIOs (0.54). The low density separate contains 0.5 ppb Re and 6 ppt Os, whereas the leachate produced through the dissolution of this separate contains 0.1 ppb Re and 2 ppt Os. Compared to the sulphide mineral separates, these have much lower $^{187}\text{Re}/^{188}\text{Os}$ and $^{187}\text{Os}/^{188}\text{Os}$, and plot significantly below the regression line.

Samples of *Prairie Creek* SMS mineralization contain significantly lower concentrations of Re and Os compared to the MVT mineralization, and approach the lower limits of reliable measurement using current analytical protocols. Sulphides from PC-93-25 contain 0.07 - 0.47 ppb Re and 5.3 - 24 ppt Os, PC-11-209A contains 0.13 - 0.55 ppb Re and 7.2 - 32 ppt Os, and PC-92-17B contains ~ 0.2 ppb Re and ~ 16 ppt Os. Two populations of data appear to exist in the SMS dataset. Regression of 9 data points from PC-93-25 produce a nearly horizontal array of data points (Fig. 5.21C; 50 ± 74 Ma). Regression of 7 data points from PC-11-209A and PC-92-17B produced a Model 3 age of 292 ± 47 Ma with an initial Os ratio of 0.806 ± 0.089 (Fig. 5.21D; MSWD = 18, VIOs = 0.051). Low density separates for PC-93-25 and PC-11-209A also were analyzed and contain comparable Re (0.12 ppb and 0.13 ppb, respectively) and Os (6.8 ppt and 9.4 ppt, respectively) concentrations to the sulphide mineral separates, but plot significantly away from the corresponding sulphide separates on the isochron diagram.

Sample PCU from the Vein-style mineralization at *Prairie Creek* contains 0.27 - 0.88 ppb Re and 6.8 - 21 ppt Os. A Model 3 regression on 12 sulphide data points yields an age of 302 ± 59 Ma with a corresponding initial Os ratio of 0.87 ± 0.31 (Fig. 5.21E; MSWD = 39, VIOs = 0.13). Two sphalerite separates of the type PCU-NM2.0-10/3 were also analyzed, but as

sphalerite is considered an impurity thus were not included in the regression. These sphalerite data points plot well below the regression line produced from pyrite dominated separates.

Due to the similarity in age and initial Os ratio of the Vein-style and SMS regressions, the combined data yield an age of 321 ± 15 Ma (Fig. 5.21F; Model 3, MSWD = 37, VIOs = 0.11).

5.5.2.2: *Robb Lake*

Re-Os results (Table 5.2) from Robb Lake can be divided into three distinct sets; unleached separates (n = 13), leached separates (n = 18), and leachate analyses (n = 7). The mineral separates contain 1.0 - 22 ppb Re and 16 to 180 ppt Os, and the leachates contain 0.15 ppb to 12 ppb Re and 3.7 to 300 ppt Os. The leached dataset produces a slightly different Model 3 regression of 350 ± 31 Ma with an initial Os ratio of 0.84 ± 0.64 (Fig. 5.22A; MSWD = 415, VIOs = 0.74). The non-leached dataset produces a Model 3 solution corresponding to an age of 401 ± 41 Ma with an initial Os ratio of 0.71 ± 0.78 (Fig. 5.22B; MSWD = 113, VIOs = 0.48). The leachate data plots at much lower $^{187}\text{Re}/^{188}\text{Os}$ values than the mineral separates but at comparable $^{187}\text{Os}/^{188}\text{Os}$ values (Fig. 5.22c).

5.5.2.3: *Salmo district*

Table 5.3 contains the Re-Os analyses from both the Reeves-Macdonald mine (07SP-21-1) and H.B mine (HB). Mineral separates from 07-SP-21-1 contain a range of Re concentrations from 190 to 1100 ppb Re and 1.4 ppb to 17 ppb Os, 2-3 orders of magnitude higher than those of Prairie Creek and Robb Lake. Together 22 data points result in a Model 3 age of 334 ± 52 Ma with an initial Os ratio of 1.25 ± 0.36 (Fig. 5.23A; MSWD = 1098, VIOs = 0.26). The HB mineral separates contains lower concentrations of Re and Os with values of 17 - 28 ppb and 220 - 430 ppt, respectively. A similar age (359 ± 67 Ma) and initial Os ratio (1.32 ± 0.66) is produced from this dataset (Fig. 5.23B; Model 3, n = 8, MSWD = 342, VIOs = 0.37).

5.6: Discussion

5.6.1: Interpretation of Re-Os Isotopic Data

5.6.1.1: General Considerations

All regressions of Re-Os isotopic data resulted in Model 3 ages with relatively low precision ($> 5\%$) and elevated MSWD's (37-1098) and as such, interpretation of the age significance of these results is treated cautiously. As a general rule, Re-Os isotopic dating requires three assumptions to be true: (1) That any mineral phase analyzed are coeval, (2) that these phases have an identical initial Os ratio, and (3) that these phases have remained closed since formation. Clearly one or more of these assumptions must have been violated to produce the observed dataset. Using the arguments presented in Chapter 4, the Mo compositional maps can be used as a proxy for the distribution of Re in these samples. These Mo maps, when used in conjunction with other compositional maps and petrographic images, provide important context for the acquired Re-Os isotopic data. To help identify outliers in the Re-Os datasets, model ages using a fixed initial Os ratio, and initial Os ratio calculations using a fixed age, are also used (Tables 5.1-5.3). These data are used for testing for a violation of assumption 2 and hence tests the applicability of using Model 3 regressions on these datasets.

5.6.1.2: Re-Os Systematics of Prairie Creek

Pyrite from the Prairie Creek samples contains Mo at levels < 0.1 ppm, which likely corresponds to Re concentrations at the low or sub ppb level according to the trends presented in Chapter 4A. However, all samples show localized areas that are dramatically enriched (10-100 ppm) in Mo, and therefore likely also correlate to spikes in Re concentration. In PC-94-80 (MVT) and PC-11-209A (SMS) enrichments are purely along fractures, whereas in PC-93-25 (SMS) and PCU (Vein-style) enrichments are extremely localized and may indicate the presence of Mo-rich inclusions such as nano-scale molybdenite crystals. Trace element enrichment along fractures is associated with Al-rich zones and oxide staining suggesting that trace element enrichment is associated with alteration of pyrite and the introduction of silicate material. The exact relationship that the putative molybdenite has with mineralization or alteration is difficult to ascertain due to technical limitations related to detection limits and wash out times. Together,

both the putative molybdenite crystals and fracture hosted Mo likely represent areas that hold a significant proportion of the Re budget for some of these samples.

In the mineral separates, the magnetic end member is enriched in carbonates, and likely by association, the silicate phases, as well as being commonly associated with more fractures. The most magnetic separate also commonly contains the highest concentrations of Re, as would be expected if they were incorporating fractured and altered pyrite. Mineral separates that contain the high abundances of impurities, such as the low density separates (i.e. PC-94-80 Low Density, PC-11-209A Low Density, and PC-93-25 Low Density), and the sphalerite mineral separates from PCU, plot well away from pyrite dominated separates on the Re-Os isochron diagram (Fig. 5.21). This emphasizes the need to remove these impurities from the mineral separates prior to analysis. Sphalerite impurities are the largest concern with PCU mineral separates, as many separates contain > 10% sphalerite, and therefore probably contribute to the isochron scatter observed in that sample (Fig. 5.21E). Carbonate and oxide impurities are likely problematic in the most magnetic separates of the Prairie Creek samples as these separates probably accumulate these phases to higher degrees as indicated by their higher Re and fracture contents. Curiously, in samples PC-11-209A (SMS) and PCU (Vein-style) there appears to be no clear correlation between magnetic susceptibility and the amount of scatter that an individual data point contributes to the isochron. One possible explanation is that although these samples have experienced alteration and potentially Re-Os remobilization, the rock as a whole remains in a pseudo-closed system, preserving much of the age information of the Re-Os system. The sample PC-93-25 (SMS) is different to all other samples in that the Re-Os data points plot on a pseudo-horizontal trend (Fig. 5.21C). Explaining the stark contrast between PC-93-25 (SMS) and the other samples is difficult as they appear visually very similar. It is speculated that the smaller grain size and disseminated nature of this sample resulted in more intense alteration and larger scale remobilization of Re-Os. Together, impurities and pyrite oxidation are likely candidates for the observed scatter. Ultimately, we cautiously reject the data produced from PC-93-25 as the age produced is far too young and imprecise to have geological significance.

The Model 3 ages produced from Prairie Creek require VIOs of 1.4, 0.051, 0.13, to explain the scatter for PC-94-80 (MVT), PC-11-209A (SMS), and PCU (Vein-Type), respectively. Both PC-11-209A (SMS) and PCU (Vein-Type) show a relatively restricted VIOs which appear geologically plausible. For both PCU (Vein-Type) and PC-11-209 (SMS) there is

clear evidence for multiple growth zones within the pyrite, but through visual inspection of the mineral separates there is no clear evidence that different pyrite zones correlate with specific magnetic separates. As such, it is unclear that any relationship between magnetic susceptibility and the initial Os ratio between different mineral separates should exist, and in fact no such relationship can be seen in the dataset (Table 5.1). Alternatively, the VIOs required by the Model 3 ages are invalid and the isochron scatter is due to the other factors discussed previously. In comparison, PC-94-80 has a much more variable VIOs and is outside the range of simple mixing observed in some modern hydrothermal settings (e.g. Sharma et al., 2007). However, there appears to be a relationship between magnetic susceptibility and initial Os ratios for a certain set of mineral separates. The mineral separates that contain the fewest impurities (PC-94-80 X 0.2N, where X = NM0.6 0.2N, NM0.75 0.2N, NM0.9 0.2N, NM1.0 0.2N, NM1.1 0.2N, NM1.5 0.2N) trend from a initial Os ratio of 5.1 ± 0.2 for PC-94-80 NM0.6 0.2N to a value 4.3 ± 0.4 for PC-94-80 NM0.6 0.2N (Table 5.1). Sample PC-94-80 NM1.5 0.2N contains a much higher error (4.5 ± 1.8) but is consistent with this trend. Regressing only these data points produces an age of 319 ± 18 Ma (Fig. 5.21B; Model 3, $n = 6$, Initial Os = 5.3 ± 1.1 , VIOs = 0.54, MSWD = 16).

The Model 3 ages determined for PCU (302 ± 59 Ma, VIOs = 0.13), PC-11-209A+PC-92-17B (292 ± 47 , VIOs = 0.051), PCU+PC-11-209A+PC (321 ± 21 Ma; VIOs 0.11), and PC-94-80 (319 ± 18 Ma; VIOs 0.54) can be considered close approximations of the mineralization if we assume the rock has remained close to an closed system and that much of the scatter is due to the relatively geological reasonable VIOs required by the Model 3 ages. In summary, a conservative approach to the Prairie Creek dataset is that the Re-Os isotopic data indicate that mineralization occurred broadly in the Carboniferous, with no clear differentiation in the timing between the different styles of mineralization beyond the geological requirement that SMS style mineralization postdates Vein-style mineralization.

5.6.1.3: *Re-Os Systematics of Robb Lake*

The pyrite of the Robb Lake sample DDH 726 contains very low trace element concentrations, and a similar paragenetic evolution as the Prairie Creek samples (Fig. 5.17, Fig. 5.9). Pyrite grains contain very low Mo concentrations (< 1 ppm) which likely correspond to low to sub ppb concentrations of Re. The interstitial areas between pyrite crystals contain enrichment in Mo (> 10 ppm), Co, and Al. The Mo peaks in particular could either be

general enrichments associated with Al-phases and oxides, or as nano-scale molybdenite crystals, unfortunately the resolution in the LA-ICPMS images are too low to make a clear distinction between these options. The Re abundances shown in Table 5.2 show that magnetic susceptibility is positively correlated with Re concentration, indicating that these mineral separates contain a higher proportion of interstitial material. In general all mineral separates appear to contain substantial carbonate impurities (9 - 25%). The high abundance of impurities is due to the small grain sizes (typically < 100 μm) of the disseminated pyrite grains, as composite grains of pyrite and carbonate will be common for the samples size of produced through mineral separation (74-210 μm). Carbonates are considered a high risk impurity at Robb Lake as the host carbonates of the Muncho-McConnell Formation are carbonaceous and may contain significant of Re and/or Os. The Re-Os dataset produced for Robb Lake is very complex (Fig. 5.22). Samples containing a higher proportion of carbonates, silicates, and oxides (i.e. non-leached data) produced an regression age of 401 ± 41 Ma. Leaching of the samples eliminates the carbonates and likely liberates some of the silicate and oxides phases, and results in sulphide mineral separates that yield a younger age of 350 ± 31 Ma. It can be argued, as it was for Prairie Creek, that late stage alteration associated with silicates and oxides have remobilized Re/Os but not to a great enough extent to completely destroy the age information contained within the rock.

The leachate analyses will contain primarily carbonate and any sub-micron crystals that were liberated during the process. The high levels of Re and Os within the leachate material, up to 12 ppb and 119 ppt, respectively, may suggest that the trace element enriched fine-grained interstitial material seen in the LA-ICPMS images (Fig. 5.17) has been partially sampled. The leachate analyses themselves plot as an array corresponding to an age older than the Silurian-Devonian host rock but likely has no significance as it is composed of Re-Os from the host rock, interstitial particulates, and/or Re-Os leached from insoluble materials.

The leached pyrite age of ~ 350 Ma may represent the best estimate of age for the Robb Lake deposit due to the reduction in impurities present in these separates. However, the VIOs required by the pyrite regression is large for a rock that appears to have a single stage of disseminated pyrite growth. Therefore, the Model 3 age produced by Isoplot may not give an accurate portrayal of the uncertainty in the age of Robb Lake, and may be better captured in the range of model ages produced (314-387 Ma), as the assumption of a static initial Os ratio of 0.84 may be more reasonable than that of a highly variable VIOs for DDH 726.

5.6.1.4: *Re-Os Systematics of the Salmo district*

These isochron diagrams show the largest scatter of all the isochrons produced in this study (Fig. 5.23). Such extreme scatter suggests a heavily disturbed isotopic system. The Re systematics of sample 07SP-21-1 (Reeves-Macdonald mine) is dominated by the homogenous distribution of molybdenite crystals. A deconvoluted image of the Mo composition map presented in Figure 5.19A (i.e. Appendix Figure 5.33) suggest that these crystals are primarily within the cracks and the quartz crystals that contain the disseminated pyrite grains. Compared to other suspected molybdenite crystals found in other samples, the Mo concentrations seen in this sample peak much higher (>10000 ppm) suggesting that crystals may be much larger in this sample. The existence of molybdenite crystals may help to explain the high values of Re observed in this sample (>100 ppb). However, this cannot explain the observations that Os in this sample is not particularly radiogenic, as there is large common Os component (> 1 ppb). Molybdenite crystals cannot contain this level of common Os, yet the Mo maps suggest the Re is almost completely coupled to molybdenite in this sample. These observations necessitate that Re and common Os are mineralogically decoupled within this sample. Supporting this suggestion is that the leachate also appear to show extreme decoupling. The Re concentrations of leachate data are low for this sample (1 - 22 ppb), yet contain significant Os concentrations (1 - 3 ppb). A decoupled Re and Os system likely requires that this sample has undergone intense remobilization of Re and Os. If some fluid had liberated Re from the rock it could be speculated that the Re was reincorporated at some later time during the crystallization of small molybdenite crystals, leaving the bulk of the rock enriched in common Os and depleted in Re. The Salmo district mines have experienced greenschist facies metamorphism, are bordered by large granite bodies (Fig. 5.1B), have been cross-cut by lamprophyre dikes (Fyles and Hewlett, 1959; Macdonald, 1973), and have hypothesized to have been oxidized as recently as 10000 BP (Paradis et al., 2015). Any of these events could be responsible for the disturbance in the Re-Os system. While the HB sample from the H.B. mine was not studied to the degree that 07SP-21-1 was, it is assumed that the scatter observed can be explained in a similar way. However, even with the noted complications, a broad Paleozoic age is indicated by the datasets. It is unlikely a Model 3 age is appropriate for this sample as the scatter observed in this sample is almost certainly not a result of a variable initial Os ratio. Therefore a crude estimate of the age of the Salmo district mines are encompassed in the model age ranges produced from their respective

datasets. For the Reeves-Macdonald mine sample 07SP-21-1 this ranges from 307 - 375 Ma, assuming an initial Os ratio of 1.25. For the H.B. mine sample HB the age ranges from 343 to 393 Ma, assuming an initial Os ratio of 1.32. These model ages are heavily influenced by the chosen initial Os ratio and if different initial Os ratio is chosen, different age bounds can be created. We chose the initial Os ratio based on the regression presented in Figure 5.23. In general however, the median of model ages will lie close to 350 Ma for any reasonable initial Os ratio, which suggests a Late Devonian to Early Carboniferous age for the Salmo district Re-Os mineralization.

5.6.2: Constraints on the relationship between SMS, Vein-Type, and MVT mineralization at Prairie Creek

Prior constraints on the relationship between SMS, Vein-Type, and MVT mineralization are based on both physical observations and limited isotopic work (e.g. Paradis, 2007). Sulphur isotopes from the different styles of mineralization overlap with each other (10 - 26‰), and overlap with or are slightly lower than Ordovician - Late Devonian evaporites (Claypool et al., 1980). Although the dataset is limited, these results are consistent with there being a single source of sulphur for the Prairie Creek mineralization. Galena lead isotope analyses for Prairie Creek (Morrow and Cumming, 1982; Fraser, 1996; Paradis, 2007) cluster in two distinct groups. The SMS and MVT sulphides have comparable Pb isotope signatures and overlap with lead isotope signatures of Devonian SEDEX deposits from the Selwyn basin (Godwin et al., 1988; Cousens, 2006). Using the three stage lead evolution model of Godwin and Sinclair (1982) for the northern Canadian Cordillera it has been interpreted that the Pb for the MVT and SMS mineralization is originally derived from the Canadian Shield and are compatible with a Devonian age of mineralization. Vein-Type sulphides however are isotopically distinct and indicate an age as young as 250 Ma if the same evolution curve is used. However, the Re-Os isotopic data obtained in this study for SMS and Vein-Type mineralization are essentially indistinguishable. The data obtained for SMS mineralization indicate an age of 292 ± 47 Ma, compared to an age of 302 ± 59 Ma for the Vein-Type mineralization. They also essentially require the same initial Os ratio, with values of 0.806 ± 0.089 and 0.87 ± 0.31 calculated for SMS and Vein-Type, respectively. The isochron produced from the combined dataset (Fig. 5.21F) produces a more precise age and initial Os ratio of 321 ± 15 Ma and 0.761 ± 0.067 ,

respectively. It is known that Vein-style mineralization postdates SMS mineralization from the observed crosscutting relationships, however if the difference in timing between these mineralization episodes were on the order of 10 Ma or less then this dataset would be indistinguishable as long as they were sourced from identical Os reservoirs, as appears to be the case. Alternatively, the fluids associated with Vein-style mineralization could have wholesale reset the SMS Re-Os systematics at ~ 321 Ma. However, the lack of precedent of such an instance occurring makes us favour the first interpretation. The source of Os for this deposit must be decoupled from the base metals since lead isotopes require that SMS and Vein-Type mineralization have dissimilar sources of lead. It is possible that the Os in this case is sourced from seawater, or seawater derived sources, similar to that of the sulphur in the system, while base metals are leached from siliciclastic crustal material. The observation that all three styles of mineralization have indistinguishable Re-Os ages, suggest that they may be genetically related. It is speculated that regional structures of the Prairie Creek Embayment enabled the confluence of several similar hydrothermal fluids systems that ultimately formed the range of different mineralization styles seen at Prairie Creek.

5.6.3: Timing of Zn-Pb mineralization in the Canadian Cordillera.

The Re-Os age data provided here are the first radiometric constraints on the Prairie Creek and Salmo district mineralization, and significantly improve existing age constraints of the Robb Lake deposit. Although there is significant complexity in the Re-Os data obtained in this study it is clear that mineralization associated with carbonate-hosted Zn-Pb deposits is broadly Late Devonian to Carboniferous in age. Paleomagnetic dating of the Robb Lake deposit, which indicated an Eocene age for Robb Lake (Smethurst et al., 1999), appears to only date regional remagnetization associated with the Laramide orogeny. This then means that the Late Cretaceous paleomagnetic dates for the Monarch-Kicking Horse MVT deposit in southern British Columbia (Symons et al., 1998) and the Pine Point deposit in the Northwest Territories (Symons et al., 1993) may also record Laramide remagnetization. Fluid flow associated with Laramide compression is known to have pervasively remagnetized magnetic minerals throughout the Western Canadian Sedimentary Basin and well beyond the limit of deformation associated with Cordilleran deformation (Gillen et al., 1999; Enkin et al., 2000). Previous sphalerite Rb-Sr dates for Pine Point (361 ± 13 Ma; Nakai et al., 1993) and Robb Lake (348 ± 130 Ma; Nelson et al.,

2002) are consistent with the Re-Os presented in this study. The EMPA images produced in this study show that Al-rich phases (phyllosilicates?) are pervasive and intimately associated with sulphides in all the deposits, including at Robb Lake. The imprecise nature of the sphalerite analyses from Nelson et al. (2002) may be the result of incorporation of these Al-rich phases within their analyzed material, as they can contain problematic amounts of Rb-Sr (Nakai et al., 1993).

The Re-Os ages determined here, despite complexity, support a Paleozoic age for Zn-Pb mineralization at Prairie Creek, Robb Lake, and Salmo. This leads to discussion about the possible tectonic regime that may have been present, and how this relates to fluid flow and mineralization. One explanation is that fluid flow driven by thermal gradients associated with back-arc extension and the opening of the Slide Mountain ocean provided the mechanism for fluid to be directed to the east. The current understanding is that the VMS/VHMS and SEDEX deposits of the eastern Canadian Cordillera are intimately associated with such a mechanism (Nelson et al., 2002). Plausibly, these fluids cooled and moved east into the carbonate platform where they were focused through faults where they interacted with carbonates and produced the carbonated-hosted Zn-Pb±Ag deposits of the Ancestral North American terrane of the Canadian Cordillera.

There is also an ongoing debate about how connected these carbonate-hosted systems are to the SEDEX and the more distal VMS/VHMS deposits (Goodfellow et al., 1993; Nelson et al., 2002; Paradis and Simandl, 2017). This cannot be definitively answered due to the imprecision and complexity of Re-Os pyrite ages produced in this study. The Robb Lake deposit has been suggested to be the eastward expression of hydrothermal fluid flow occurring in the Kechika Trough, the host of a number of SEDEX deposits (Nelson et al., 2002). A spatial relationship is clearly evident as both the location of the SEDEX deposits and MVT deposits run parallel to one another (Fig. 5.1). Although imprecise, the Robb Lake deposit has an age that overlaps with the known SEDEX deposits in the Kechika Trough, consistent with the proposal that they may be related to the same regional hydrothermal system (Nelson et al., 2002). At Prairie Creek such a connection is not as easily made as the mineralization appears younger (~ 320 Ma) than the SEDEX deposits to the west in the Selwyn basin (> 350 Ma; Abbot et al., 1986; Paradis et al., 1998). It is possible that the Prairie Creek sulphides have been partially reset, making the calculated ages simply a minimum age, although what event a potential reset could be related to

is unclear. Perhaps a more reasonable explanation is that the SEDEX deposits and the carbonate-hosted deposits are only tangentially related, being connected only through the general extensional tectonic regime, while not being directly related to the same hydrothermal system.

A second possible mechanism is that compression associated with the Antler orogeny was the driving force behind mineralization (Amthor et al., 1993; Nesbitt and Muehlenbachs, 1994; Mountjoy et al., 1999). However, based on the known tectonics of the Cordillera during the Late Devonian and Mississippian it appears that an extensional regime was dominant and that compressional tectonics are limited to only the southernmost Cordillera (Klepacky and Wheeler, 1985; Root, 2001). Therefore, if the Antler orogeny did play a role in the formation in Zn-Pb mineralization it may be limited to mineralization at the Salmo district and other nearby deposits in the southern Cordillera.

5.7: Conclusions

The primary objective of this study was to test Late Mesozoic versus Paleozoic mineralization ages for carbonate-hosted Zn-Pb mineralization within the Canadian Cordillera. The Re-Os data produced clearly show that all deposits are 300-400 Ma in age indicating that Laramide compression is not the driver of mineralization as suggested by paleomagnetic studies. The different mineralization styles at Prairie Creek are indistinguishable with an age of 319 ± 18 Ma estimated for the MVT mineralization and 321 ± 21 Ma for the SMS and Vein-style mineralization. The Robb Lake deposit is estimated to be 314-387 Ma in age and overlaps with the ages determined for SEDEX deposits in the Kechika Trough, consistent with both sets of deposits being related to a common hydrothermal system. The Salmo district ores show a Re-Os system that is heavily disturbed, likely driven by mineralogical decoupling of Re and Os. However, some age information appears to have survived and a Late Devonian to Early Carboniferous age seems probable. Collectively, these deposits appear to have formed in response to an active margin that existed along the western margin of North America during the Paleozoic, not Laramide compression.

The secondary objective was to test the applicability of pyrite Re-Os geochronology in ore deposits that have undergone complex post-mineralization modification. In all rocks studied there is some level of oxidation of sulphide material as well as the introduction of later Al-rich and silicate phases. Molybdenum compositional maps were used as a proxy for Re in this study

and indicate that the Re budget of these rocks can be skewed towards alteration phases and putative nano to micron scale molybdenite crystals. Given the macro-scale nature of Re-Os sulphide analyses – up to 400 mg of pyrite per analysis - all sulphide separates should be evaluated using Mo and Al compositional maps prior to selecting material to be used for Re-Os isotope analysis.

5.8: References

Abbott, J. G. (1986). Setting of sediment-hosted stratiform lead-zinc deposits in Yukon and northeastern British Columbia. *Mineral Deposits of the Northern Cordillera. Canadian Inst. Mining Metal.*, 37, 1-18.

Amthor, J. E., Mountjoy, E. W., & Machel, H. G. (1993). Subsurface dolomites in Upper Devonian Leduc Formation buildups, central part of Rimbey-Meadowbrook reef trend, Alberta, Canada. *Bulletin of Canadian Petroleum Geology*, 41(2), 164-185.

Belasky, P., Stevens, C. H., & Hanger, R. A. (2002). Early Permian location of western North American terranes based on brachiopod, fusulinid, and coral biogeography. *Palaeogeography, Palaeoclimatology, Palaeoecology*, 179(3-4), 245-266.

Canadian Zinc Corporation 2010. *Main Report for Developer's Assessment Report*, Canadian Zinc Corporation submission to Mackenzie Valley Review Board in support of Environmental Assessment of Prairie Creek Mine EA 0809-002.

Canadian Zinc Corporation 2017. *Prairie Creek Property Feasibility Study NI 43-101 Technical Report*.

Claypool, G. H., Holster, W. T., Kaplan, I. R., Saki, H., & Zak, I. (1980). The age curves for sulphur and oxygen isotopes in marine sulphur and their interpretation. *Chemical Geology*, 54, 149-155.

Colpron, M., & Nelson, J. L. (Eds.). (2006). Paleozoic evolution and metallogeny of pericratonic terranes at the ancient Pacific margin of North America, Canadian and Alaskan Cordillera. Geological Association of Canada.

Coney, P. J., Jones, D. L., & Monger, J. W. (1980). Cordilleran suspect terranes. *Nature*, 288(5789), 329.

Cousens, B. L. (2007). Radiogenic isotope studies of Pb-Zn mineralization in the Howards Pass area, Selwyn Basin. *Mineral and Energy Resource Potential of the Proposed Expansion to the Nahanni National Park Reserve, North Cordillera, Northwest Territories: Geological Survey of Canada, Open File, 5344*, 14.

Cook, D.G. (1977). Two stages of faulting, Virginia Falls map-area, District of Mackenzie; Report of Activities, Part A, Geological Survey of Canada, Paper 77-1A, 113-115.

de Wit, R., Gronberg, E.C., Richards, W.B., & Richmond, W.O. (1973). Tathlina area, District of MacKenzie; *in* The Future Petroleum Provinces of Canada – Their Geology and Potential, (ed.) R.G. McCrossan; Canadian Society of Petroleum Geologists, Memoir 1, 187-212.

Drivet, E., & Mountjoy, E. W. (1997). Dolomitization of the Leduc Formation (Upper Devonian), southern Rimbey-Meadowbrook reef trend, Alberta. *Journal of Sedimentary Research*, 67(3).

Earls, G. (1995). A Review of the Prairie Creek Deposit, NWT, Canada; Internal Report, San Andreas Resources Corporation, 36 p.

Enkin, R. J., Osadetz, K. G., Baker, J., & Kisilevsky, D. (2000). Orogenic remagnetizations in the Front Ranges and Inner Foothills of the southern Canadian Cordillera: Chemical harbinger and thermal handmaiden of Cordilleran deformation. *Geological Society of America Bulletin*, 112(6), 929-942.

Findlay, A. (2000). Geology and Exploration Potential of the Stratabound Massive Sulphides, Prairie Creek Mine, NWT; Internal Report, Canadian Zinc Corporation, 17 p.

Fraser, S. C., (1996). Geology and Geochemistry of the Prairie Creek Zn, Pb, Ag Deposits, Southern Mackenzie Mountains, NWT; M.Sc. thesis, University of Alberta, Edmonton, Alberta, 146 p.

Fyles, J. T., & Hewlett, C. G. (1959). *Stratigraphy and structure of the Salmo lead-zinc area*. Department of Mines.

Garven, G. (1985). The role of regional fluid flow in the genesis of the Pine Point deposit, western Canada sedimentary basin. *Economic Geology*, 80(2), 307-324.

Gillen, K. P., Van der Voo, R., & Thiessen, J. H. (1999). Late Cretaceous-early Tertiary remagnetization of the Devonian Swan Hills Formation recorded in carbonate cores from the Caroline gas field, Alberta, Canada. *AAPG bulletin*, 83(8), 1223-1235.

Godwin, C. I., Gabites, J. E., & Andrew, A. (1988). *LEADTABLE: A galena lead isotope data base for the Canadian Cordillera, with a guide to its use by explorationists*. Province of British Columbia, Ministry of Energy, Mines and Petroleum Resources.

Goodfellow, W. D. (1993). Geology and genesis of stratiform sediment-hosted (SEDEX) zinc-lead-silver sulphide deposits. *Geol. Assoc. Can. Spec. Paper*, 40, 201-252.

Hnatyshin, D., & Kravchinsky, V. A. (2014). Paleomagnetic dating: Methods, MATLAB software, example. *Tectonophysics*, 630, 103-112.

Hnatyshin, D., Creaser, R. A., Wilkinson, J. J., & Gleeson, S. A. (2015). Re-Os dating of pyrite confirms an early diagenetic onset and extended duration of mineralization in the Irish Zn-Pb ore field. *Geology*, 43(2), 143-146.

Hnatyshin, D., Kontak, D. J., Turner, E. C., Creaser, R. A., Morden, R., & Stern, R. A. (2016). Geochronologic (ReOs) and fluid-chemical constraints on the formation of the Mesoproterozoic-hosted Nanisivik ZnPb deposit, Nunavut, Canada: Evidence for early diagenetic, low-temperature conditions of formation. *Ore Geology Reviews*, 79, 189-217.

Keevil, H. K. (2011). Mineralogical and Geochemical Characterization of Supergene Carbonate-hosted Nonsulphide Zn-Pb Mineralization in Southern and Central British Columbia.

Klepacki, D. W., & Wheeler, J. O. (1985). Stratigraphic and structural relations of the Milford, Kaslo and Slocan groups, Goat Range, Lardeau and Nelson map areas, British Columbia. *Current research, part A. Geological Survey of Canada, Paper*, 277-286.

Lewchuk, M. T., Symons, D. T., & Sangster, D. F. (1997). Paleomagnetism of the Monarch-Kicking Horse Pass Mississippi Valley-type (MVT) Ore Deposits in Southeastern British Columbia and Laramide Fluid Flow in the Western Canada Sedimentary Basin (WCSB).

Ludvigsen, R. (1975). Ordovician formations and faunas, southern Mackenzie Mountains. *Canadian Journal of Earth Sciences*, 12(4), 663-697.

Ludwig, K. R. (2003). User's manual for isoplot 3.00, a geochronological toolkit for microsoft excel. *Berkeley Geochronl. Cent. Spec. Publ.*, 4, 25-32.

Macdonald, A. S. (1973). The Salmo lead-zinc deposits: A study of their deformation and metamorphic features. Ph.D. thesis, University of British Columbia, Vancouver, British Columbia, p. 258.

Machel, H. G., & Mountjoy, E. W. (1987). General constraints on extensive pervasive dolomitization--and their application to the Devonian carbonates of western Canada. *Bulletin of Canadian Petroleum Geology*, 35(2), 143-158.

Macqueen, R. W., & Thompson, R. I. (1978). Carbonate-hosted lead–zinc occurrences in northeastern British Columbia with emphasis on the Robb Lake deposit. *Canadian Journal of Earth Sciences*, 15(11), 1737-1762.

Manns, F.T. (1981). Stratigraphic aspects of the Silurian-Devonian sequence hosting zinc and lead mineralization near Robb Lake, northeastern British Columbia. Ph.D. thesis, University of Toronto, Toronto, Ontario, p. 252.

McClay, K. R., Insley, M. W., & Anderton, R. (1989). Inversion of the Kechika Trough, Northeastern British Columbia, Canada. *Geological Society, London, Special Publications*, 44(1), 235-257.

Monger, J. W., Nokleberg, W. J., Coyner, A. R., & Fahey, P. L. (1996). Evolution of the northern North American Cordillera: generation, fragmentation, displacement and accretion of successive North American plate-margin arcs. *Geology and Ore Deposits of the American Cordillera. Geological Society of Nevada*, 1133-1152.

Morrow, D. W. (1984). Sedimentation in Root Basin and Prairie Creek Embayment--Siluro-Devonian, Northwest Territories. *Bulletin of Canadian Petroleum Geology*, 32(2), 162-189.

Morrow, D. W., & Cumming, G. L. (1982). Interpretation of lead isotope data from zinc–lead mineralization in the northern part of the western Canadian Cordillera. *Canadian Journal of Earth Sciences*, 19(5), 1070-1078.

Morrow, D. W., & Cook, D. G. (1987). The Prairie Creek embayment and Lower Paleozoic strata of the southern Mackenzie mountains. *Memoir/Canada. Geological survey*.

Morrow, D. W., Cumming, G. L., & Aulstead, K. L. (1990). *The Gas-bearing Devonian Manetoe Facies, Yukon, and Northwest Territories* (No. 400). Geological Survey of Canada.

Morrow, D. W., Potter, J., Richards, B., & Goodarzi, F. (1993). Paleozoic burial and organic maturation in the Liard Basin region, northern Canada. *Bulletin of Canadian Petroleum Geology*, 41(1), 17-31.

Mountjoy, E. W., Machel, H. G., Green, D., Duggan, J., & Williams-Jones, A. E. (1999). Devonian matrix dolomites and deep burial carbonate cements: a comparison between the Rimbey-Meadowbrook reef trend and the deep basin of west-central Alberta. *Bulletin of Canadian Petroleum Geology*, 47(4), 487-509.

Nakai, S. I., Halliday, A. N., Kesler, S. E., Jones, H. D., Kyle, J. R., & Lane, T. E. (1993). Rb-Sr dating of sphalerites from Mississippi Valley-type (MVT) ore deposits. *Geochimica et Cosmochimica Acta*, 57(2), 417-427.

Nelson, J. L., Paradis, S., & Zantvoort, W. (1998). The Robb Lake carbonate-hosted lead-zinc deposit, northeastern British Columbia: a Cordilleran MVT deposit. *Geological Fieldwork*, 1999-1.

Nelson, J., Paradis, S., Christensen, J., & Gabites, J. (2002). Canadian Cordilleran Mississippi Valley-type deposits: A case for Devonian-Mississippian back-arc hydrothermal origin. *Economic Geology*, 97(5), 1013-1036.

Nelson, J. L., Colpron, M., Piercey, S. J., Dusel-Bacon, C., Murphy, D. C., & Roots, C. F. (2006). Paleozoic tectonic and metallogenic evolution of pericratonic terranes in Yukon, northern British Columbia and eastern Alaska. *Paleozoic evolution and metallogeny of pericratonic terranes at the ancient Pacific margin of North America, Canadian and Alaskan Cordillera: Geological Association of Canada Special Paper*, 45, 323-360.

Nelson, J., & Colpron, M. (2007). Tectonics and metallogeny of the British Columbia, Yukon and Alaskan Cordillera, 1.8 Ga to the present. *Mineral Deposits of Canada: A Synthesis of Major Deposit-Types, District Metallogeny, the Evolution of Geological Provinces, and Exploration*

Methods. Edited by WD Goodfellow. Geological Association of Canada, Mineral Deposits Division, Special Publication, 5, 755-791.

Nesbitt, B. E., & Muehlenbachs, K. (1994). Paleohydrogeology of the Canadian Rockies and origins of brines, Pb-Zn deposits and dolomitization in the Western Canada Sedimentary Basin. *Geology*, 22(3), 243-246.

Norris, A.W., & Uyeno, T. T. (1981). *Lower Devonian (Lochkovian) Brachiopods and Conodonts from the 'Delorme' Formation, Cathedral Mountain, Southwestern District of Mackenzie*. Geological survey of Canada.

Olson, R. A., Dufresne, M. B., Eccles, D. R., Freeman, M. E., & Richardson, R. J. H. (1994). *Regional metallogenic evaluation of Alberta*. Research Council of Alberta.

Paradis, S., Nelson, J. L., & Irwin, S. E. (1998). Age constraints on the Devonian shale-hosted Zn-Pb-Ba deposits, Gataga District, northeastern British Columbia, Canada. *Economic Geology*, 93(2), 184-200.

Paradis, S. J. (2007). *Carbonate-hosted Zn-Pb Deposits in Southern British Columbia: Potential for Irish-type Deposits*. Geological Survey of Canada.

Paradis, S., & Simandl, G. J. (2010) Carbonate-hosted sulphide and nonsulphide Pb-Zn Mineralization, British Columbia, Canada; focus on new exploration criteria.

Paradis, S., Keevil, H., Simandl, G. J., & Raudsepp, M. (2015). Carbonate-hosted nonsulphide Zn-Pb mineralization of southern British Columbia, Canada. *Mineralium Deposita*, 50(8), 923-951.

Paradis, S., & Simandl, G. J. (2016). Is there a genetic link between the SEDEX and MVT deposits of the Canadian Cordillera?. *Targeted Geoscience Initiative*, 107-113.

Paton, C., Hellstrom, J., Paul, B., Woodhead, J., & Hergt, J. (2011). Iolite: Freeware for the visualisation and processing of mass spectrometric data. *Journal of Analytical Atomic Spectrometry*, 26(12), 2508-2518.

Root, K. G. (2001). Devonian Antler fold and thrust belt and foreland basin development in the southern Canadian Cordillera: implications for the Western Canada Sedimentary Basin. *Bulletin of Canadian Petroleum Geology*, 49(1), 7-36.

Rubin, C. M., Miller, M. M., & Smith, G. M. (1990). Tectonic development of Cordilleran mid-Paleozoic volcano-plutonic complexes; Evidence for convergent margin tectonism.

Sangster, D.F. (1973): Geology of Canadian lead and zinc deposits; *Geological Survey of Canada*, Paper 73-1, Part A, 129-130.

Sangster, D. F. (1993). Evidence for, and implications of, a genetic relationship between MVT and SEDEX zinc-lead deposits. In *World Zinc 93: Proceedings of the International Symposium on Zinc*, Australasian Institute of Mining and Metallurgy, Publication Series (Vol. 7, p. 93).

Sharma, M., Balakrishna, K., Hofmann, A. W., & Shankar, R. (2007). The transport of osmium and strontium isotopes through a tropical estuary. *Geochimica et Cosmochimica Acta*, 71(20), 4856-4867.

Silberling, N.J., Jones, D.L., Monger, J.W.H., Coney, P.J., Berg, H.C. and Plafker, G. (1994). Lithotectonic terrane map of Alaska and adjacent parts of Canada, in Plafker, G. and Berg, H.C., eds., *The Geology of Alaska: Geological Society of America, The Geology of North America*, v. G-1, Plate 3, scale 1:2,500,000.

Simandl, G. J., & Paradis, S. (2008). Carbonate-hosted, nonsulphide, zinc-lead deposits in the southern Kootenay arc, British Columbia (NTS 082F/03). *Geological Fieldwork*, 2009-1.

Smethurst, M. T., Sangster, D. F., Symons, D. T. A., & Lewchuk, M. T. (1999). Paleomagnetic age for Zn-Pb mineralization at Robb Lake, northeastern British Columbia. *Bulletin of Canadian Petroleum Geology*, 47(4), 548-555.

Smoliar, M. I., Walker, R. J., Morgan, J.W. (1996). Re-Os ages of group IIA, IIIA, IVA, and IVB iron meteorites. *Science*, 271, 1099.

Stravinga, D.B. (2014). Trace element geochemistry and metal mobility of oxide mineralization at the Prairie Creek Zinc-Lead-Silver Deposit, NWT. M.Sc. thesis, Queen's University, Kingston, Ontario, 294 p.

Symons, D. T. A., Pan, H., Sangster, D. F., & Jowett, E. C. (1993). Paleomagnetism of the Pine Point Zn-Pb deposits. *Canadian Journal of Earth Sciences*, 30(5), 1028-1036.

Symons, D. T. A., MacDonald, M., Lewchuk, M. R., & Sangster, D. F. (1996). Late Cretaceous age for the Monarch-Kicking Horse Mississippi Valley-type deposit in the southern Rocky Mountains of Canada from paleomagnetism. *EOS*, 77, 160.

Thompson, R. I. (1989). Stratigraphy, tectonic evolution and structural analysis of the Halfway River map area (94B), northern Rocky Mountains, British Columbia. *Geological Survey of Canada*, 425, 1-119.

Wheeler, J.O. & McFeely, P. 1991. Tectonic assemblage map of the Canadian Cordillera and adjacent parts of the United States of America: Geological Survey of Canada, Map 1712A, scale 1:2,000,000.

Table 5.1: Re-Os results for Prairie Creek

| Sample Name | Separation Procedure | Qualitative χ | Re ppb | Os ppt | 187Re / 188Os $\pm 2s$ | 187Os / 188Os $\pm 2s$ | Rho | Model Age | $\pm 2\sigma$ | Initial Ratio | $\pm 2\sigma$ | | |
|-------------------------------|------------------------------|--------------------|--------|--------|------------------------|------------------------|--------|-----------|---------------|---------------|---------------|------|------|
| PC-94-80 Bulk | 74-210 | - | 3.91 | 24.33 | 2637.09 | 106.62 | 18.562 | 0.756 | 0.99 | 331 | 4 | 4.0 | 1.0 |
| PC-94-80 NM0.6 | 74-210 / Mag | 8 | 6.29 | 33.76 | 3686.71 | 91.02 | 23.965 | 0.606 | 0.97 | 324 | 3 | 3.6 | 0.8 |
| PC-94-80 NM0.6 | 74-210 / Mag | 7 | 6.02 | 33.02 | 3449.93 | 56.72 | 22.568 | 0.444 | 0.83 | 322 | 4 | 3.5 | 0.5 |
| PC-94-80 NM0.75 | 74-210 / Mag | 6 | 5.44 | 30.19 | 3420.39 | 83.36 | 22.673 | 0.576 | 0.96 | 327 | 3 | 3.8 | 0.7 |
| PC-94-80 NM0.9 | 74-210 / Mag | 5 | 4.46 | 22.74 | 4578.68 | 183.55 | 29.623 | 1.196 | 0.99 | 335 | 3 | 4.4 | 1.6 |
| PC-94-80 NM1.1 | 74-210 / Mag | 3 | 3.44 | 17.32 | 5062.15 | 285.59 | 33.016 | 1.909 | 0.98 | 343 | 6 | 5.1 | 2.5 |
| PC94-80 NM1.3 | 74-210 / Mag | 2 | 3.01 | 14.53 | 4666.14 | 108.35 | 28.248 | 0.716 | 0.91 | 311 | 4 | 2.5 | 0.9 |
| PC-94-80 NM1.5 | 74-210 / Mag | 1 | 2.48 | 11.34 | 6989.16 | 634.25 | 43.310 | 3.980 | 0.99 | 337 | 6 | 4.8 | 5.3 |
| PC-94-80 NM0.6 0.2N | 74-210 / Mag / 0.2N HCl | 8 | 7.73 | 52.46 | 2182.43 | 12.09 | 16.013 | 0.095 | 0.67 | 330 | 2 | 4.0 | 0.1 |
| PC-94-80 NM0.6 0.2N | 74-210 / Mag / 0.2N HCl | 7 | 6.63 | 44.64 | 2438.37 | 15.88 | 18.592 | 0.124 | 0.78 | 358 | 2 | 5.1 | 0.2 |
| PC-94-80 NM0.75 0.2N | 74-210 / Mag / 0.2N HCl | 6 | 5.79 | 37.56 | 2587.28 | 17.50 | 19.155 | 0.133 | 0.79 | 351 | 2 | 4.9 | 0.2 |
| PC-94-80 NM0.9 0.2N | 74-210 / Mag / 0.2N HCl | 5 | 4.72 | 28.42 | 3014.11 | 27.23 | 21.349 | 0.190 | 0.91 | 345 | 2 | 4.7 | 0.2 |
| PC-94-80 NM1.0 0.2N | 74-210 / Mag / 0.2N HCl | 4 | 3.60 | 21.02 | 3160.14 | 37.16 | 21.852 | 0.268 | 0.90 | 338 | 2 | 4.4 | 0.3 |
| PC-94-80 NM1.1 0.2N | 74-210 / Mag / 0.2N HCl | 3 | 3.85 | 21.08 | 3699.26 | 46.78 | 24.719 | 0.319 | 0.93 | 335 | 2 | 4.3 | 0.4 |
| PC-94-80 NM1.5 0.2N | 74-210 / Mag / 0.2N HCl | 1 | 2.71 | 13.02 | 5677.60 | 208.54 | 35.771 | 1.320 | 0.99 | 345 | 3 | 4.5 | 1.8 |
| PC-94-80 Low Density | 74-210 / Low Density* | - | 0.54 | 6.30 | 633.42 | 9.56 | 4.299 | 0.066 | 0.97 | 28 | 6 | 0.8 | 0.1 |
| PC-94-80 Low Density Leachate | Leachate | - | 0.07 | 2.46 | 194.12 | 8.10 | 3.458 | 0.162 | 0.87 | -168 | 55 | 2.4 | 0.2 |
| PC-93-25 Bulk | 74-210 | - | 0.47 | 23.50 | 115.45 | 4.12 | 1.554 | 0.026 | 0.41 | 386 | 15 | 0.99 | 0.03 |
| PC-93-25 NM0.9 | 74-210 / Mag | 4 | 0.18 | 6.92 | 149.63 | 3.30 | 1.712 | 0.035 | 0.47 | 361 | 12 | 0.98 | 0.04 |
| PC-93-25 NM1.1 | 74-210 / Mag | 3 | 0.17 | 6.42 | 150.12 | 3.35 | 1.671 | 0.026 | 0.49 | 343 | 9 | 0.94 | 0.03 |
| PC-93-25 NM1.3 | 74-210 / Mag | 2 | 0.16 | 6.69 | 136.17 | 3.94 | 1.681 | 0.030 | 0.45 | 383 | 13 | 1.02 | 0.04 |
| PC-93-25 NM0.9 0.2N | 74-210 / Mag / 0.2N HCl | 4 | 0.10 | 6.88 | 87.31 | 2.59 | 1.592 | 0.047 | 0.88 | 535 | 19 | 1.17 | 0.05 |
| PC-93-25 NM1.1 0.2N | 74-210 / Mag / 0.2N HCl | 3 | 0.15 | 8.56 | 97.44 | 2.39 | 1.586 | 0.041 | 0.86 | 476 | 16 | 1.11 | 0.04 |
| PC-93-25 NM1.3 0.2N | 74-210 / Mag / 0.2N HCl | 2 | 0.19 | 9.56 | 111.83 | 2.73 | 1.653 | 0.044 | 0.86 | 451 | 15 | 1.11 | 0.05 |
| PC-93-25 NM1.95 0.2N | 74-210 / Mag / 0.2N HCl | 1 | 0.07 | 5.29 | 74.53 | 3.51 | 1.651 | 0.076 | 0.87 | 673 | 36 | 1.29 | 0.08 |
| PC-93-25 NM1.95 10N | 74-210 / Mag / 10N HCl @ 80C | 1 | 0.11 | 10.37 | 59.84 | 3.65 | 1.626 | 0.093 | 0.84 | 813 | 57 | 1.33 | 0.10 |
| PC-93-25 Low Density | 74-210 / Low Density* | - | 0.12 | 6.81 | 99.07 | 1.20 | 1.481 | 0.021 | 0.80 | 405 | 9 | 1.00 | 0.02 |
| PC-93-25 NM1.95 10N Leachate | Leachate | 1 | -0.17 | 1.53 | -542.28 | -203.53 | 0.020 | 0.205 | 0.04 | - | - | 2.66 | 1.14 |
| PC-11-209A NM1.45 FG 6N | 74-210 / Mag / 6N HCl | 4 | 0.55 | 31.64 | 96.04 | 0.67 | 1.262 | 0.006 | 0.32 | 282 | 4 | 0.79 | 0.01 |
| PC-11-209A NM1.7 FG 6N | 74-210 / Mag / 6N HCl | 3 | 0.27 | 15.80 | 96.07 | 1.82 | 1.282 | 0.017 | 0.34 | 294 | 10 | 0.81 | 0.02 |
| PC-11-209A NM2.0 CG 6N | 74-210 / Mag / 6N HCl | 2 | 0.35 | 17.96 | 108.48 | 1.15 | 1.311 | 0.007 | 0.37 | 277 | 4 | 0.78 | 0.01 |
| PC-11-209A NM2.0 FG 6N | 74-210 / Mag / 6N HCl | 2 | 0.19 | 6.85 | 162.91 | 3.22 | 1.640 | 0.020 | 0.54 | 305 | 6 | 0.85 | 0.03 |
| PC-11-209A NM2.0/2 FG 6N | 74-210 / Mag / 6N HCl | 1 | 0.20 | 7.23 | 154.65 | 3.75 | 1.530 | 0.021 | 0.53 | 279 | 7 | 0.78 | 0.03 |
| PC-11-209A Low Density | 74-210 / Low Density* | - | 0.13 | 9.41 | 79.40 | 1.72 | 1.597 | 0.013 | 0.30 | 592 | 13 | 1.21 | 0.02 |
| PC-92-17B-1 0.2N | 74-210 / 0.2N HCl | - | 0.23 | 16.85 | 76.38 | 1.06 | 1.185 | 0.008 | 0.29 | 294 | 6 | 0.81 | 0.01 |
| PC-92-17B-2 0.2N | 74-210 / 0.2N HCl | - | 0.19 | 14.35 | 74.31 | 1.20 | 1.184 | 0.011 | 0.27 | 302 | 9 | 0.82 | 0.01 |
| PCU-1-NM1.2-10/5 | 74-210 / Mag / 0.2N HCl | 5 | 0.88 | 14.82 | 386.95 | 3.08 | 2.770 | 0.023 | 0.64 | 294 | 3 | 0.82 | 0.02 |
| PCU-1-NM1.6-10/5 | 74-210 / Mag / 0.2N HCl | 4 | 0.80 | 13.51 | 389.02 | 4.06 | 2.859 | 0.038 | 0.61 | 306 | 5 | 0.90 | 0.04 |
| PCU-1-NM2.0-10/5 | 74-210 / Mag / 0.2N HCl | 2 | 0.79 | 14.28 | 351.44 | 3.12 | 2.612 | 0.025 | 0.63 | 297 | 3 | 0.84 | 0.03 |
| PCU-1-NM2.0-10/3 | 74-210 / Mag / 0.2N HCl | 1 | 0.86 | 20.71 | 245.48 | 1.97 | 1.834 | 0.015 | 0.53 | 235 | 3 | 0.60 | 0.02 |
| PCU-5-M1.7-10/5 | 74-210 / Mag / 0.2N HCl | - | 0.57 | 13.38 | 259.74 | 2.40 | 2.121 | 0.019 | 0.59 | 288 | 4 | 0.81 | 0.02 |
| PCU-23-M1.0-10/5 | 74-210 / Mag / 0.2N HCl | 7 | 0.83 | 16.73 | 309.69 | 2.87 | 2.355 | 0.026 | 0.59 | 287 | 4 | 0.79 | 0.03 |
| PCU-23-NM1.0-10/5 | 74-210 / Mag / 0.2N HCl | 6 | 0.48 | 9.90 | 305.78 | 3.60 | 2.504 | 0.030 | 0.65 | 320 | 4 | 0.96 | 0.03 |
| PCU-23-NM1.2-10/5 | 74-210 / Mag / 0.2N HCl | 5 | 0.43 | 8.73 | 303.74 | 3.92 | 2.382 | 0.034 | 0.62 | 298 | 5 | 0.85 | 0.03 |
| PCU-23-NM1.6-10/5 | 74-210 / Mag / 0.2N HCl | 4 | 0.33 | 6.39 | 334.25 | 5.77 | 2.663 | 0.036 | 0.68 | 321 | 5 | 0.98 | 0.04 |
| PCU-23-NM1.8-10/5 | 74-210 / Mag / 0.2N HCl | 3 | 0.44 | 8.92 | 305.14 | 4.19 | 2.313 | 0.033 | 0.66 | 283 | 5 | 0.77 | 0.03 |
| PCU-23-NM2.0-10/5 | 74-210 / Mag / 0.2N HCl | 2 | 0.39 | 8.83 | 269.59 | 3.80 | 2.221 | 0.033 | 0.60 | 300 | 6 | 0.86 | 0.03 |
| PCU-23-NM2.0-10/5 rpt | 74-210 / Mag / 0.2N HCl | 2 | 0.46 | 10.42 | 270.83 | 2.84 | 2.233 | 0.019 | 0.68 | 301 | 3 | 0.87 | 0.02 |
| PCU-23-NM2.0-10/5 10N | 74-210 / Mag / 10N HCl | 2 | 0.47 | 11.37 | 251.47 | 2.67 | 2.192 | 0.018 | 0.66 | 315 | 3 | 0.92 | 0.02 |
| PCU-23-NM2.0-10/3 | 74-210 / Mag / 0.2N HCl | 1 | 0.27 | 6.80 | 231.72 | 3.72 | 1.806 | 0.023 | 0.63 | 242 | 5 | 0.64 | 0.02 |

In the "Separation Procedure" column the first value reported is the grain size of the mineral separate in μm . If the sample has undergone magnetic separation the designation "Mag" is given. If the sample has undergone acid leaching the concentration of HCl used for the leaching procedure is given, and if the temperature was elevated beyond room temperature the temperature is also given. For example the designation "74-210 / Mag / 10N HCl @ 80C" states that the sample contains grains 74-210 μm in size, has underwent magnetic separation, and has been leached with 10N HCl at 80°C. All samples unless otherwise stated have underwent heavy liquid separation. The term "Low Density" refers to material that is less dense than the heavy liquid used for heavy liquid separation (i.e. < 3.32 g/cm³). The relative magnetic susceptibility (χ) between rocks or rock fragments is given in the second column where higher values refer to higher χ values. These values are purely qualitative and cannot be used to compare between different rocks or rock fragments. For clarity different rock are divided by a solid border (top section = MVT-style, middle section = SMS-style, bottom section = Vein-style) while rock fragments within the same mineralization that cannot be compared via χ are separated by a dashed border. Model ages are determined using an initial Os ratio of 4.0, 0.81, and 0.87 for MVT, SMS, and Vein-style mineralization, respectively. Initial ratio calculations are based off ages of 330 Ma, 292 Ma, and 302 Ma for MVT, SMS, and Vein-style mineralization, respectively.

Table 5.2: Re-Os results for Robb Lake

| Sample Name | Separation Procedure | Qualitative χ | Re ppb | Os ppt | $^{37}\text{Re} / ^{187}\text{C}$ | $\pm 2\sigma$ | $^{37}\text{Os} / ^{187}\text{C}$ | $\pm 2\sigma$ | Rho | Model Age (Initial = 0.84) | $\pm 2\sigma$ | Initial Ratio (350 Ma) | $\pm 2\sigma$ |
|----------------------------|-------------------------|--------------------|--------|--------|-----------------------------------|---------------|-----------------------------------|---------------|-------|----------------------------|---------------|------------------------|---------------|
| DDH726A | 74-210 | - | 5.10 | 41.3 | 1330.64 | 26.92 | 9.604 | 0.197 | 0.981 | 394 | 2 | 1.8 | 0.25 |
| DDH726A M1.6 | 74-210 / Mag | 4 | 22.34 | 183.7 | 1354.26 | 7.04 | 10.183 | 0.071 | 0.701 | 413 | 2 | 2.3 | 0.08 |
| DDH726A NM1.6 | 74-210 / Mag | <3 | 4.96 | 39.4 | 1336.31 | 14.64 | 9.349 | 0.110 | 0.918 | 381 | 2 | 1.5 | 0.14 |
| DDH726B | 74-210 | - | 2.24 | 22.8 | 859.00 | 22.64 | 6.376 | 0.171 | 0.979 | 386 | 3 | 1.4 | 0.22 |
| DDH726B M1.6 | 74-210 / Mag | 4 | 13.95 | 167.7 | 877.00 | 3.44 | 5.407 | 0.043 | 0.599 | 404 | 3 | 1.4 | 0.05 |
| DDH726B NM1.6 | 74-210 / Mag | <3 | 2.85 | 29.8 | 817.52 | 8.84 | 6.044 | 0.076 | 0.845 | 380 | 3 | 1.3 | 0.09 |
| DDH726C | 74-210 | - | 2.67 | 23.8 | 1159.19 | 18.08 | 8.907 | 0.143 | 0.962 | 416 | 2 | 2.1 | 0.18 |
| DDH726C rpt | 74-210 | - | 2.45 | 23.9 | 939.31 | 17.92 | 7.039 | 0.213 | 0.627 | 395 | 10 | 1.5 | 0.24 |
| DDH726C rpt 2 | 74-210 | - | 2.47 | 20.7 | 1227.18 | 26.36 | 8.816 | 0.201 | 0.940 | 389 | 3 | 1.6 | 0.25 |
| DDH726C M1.6 | 74-210 / Mag | 4 | 3.06 | 26.1 | 1227.72 | 21.10 | 9.125 | 0.163 | 0.954 | 404 | 2 | 1.9 | 0.20 |
| DDH726C NM1.6 | 74-210 / Mag | 3 | 1.91 | 15.5 | 1307.57 | 98.00 | 9.308 | 0.702 | 0.993 | 388 | 5 | 1.7 | 0.91 |
| DDH726C NM1.8 | 74-210 / Mag | 2 | 2.50 | 22.5 | 1080.51 | 18.14 | 7.907 | 0.201 | 0.656 | 391 | 8 | 1.6 | 0.23 |
| DDH726C NM1.8 rpt | 74-210 / Mag | 2 | 1.97 | 17.1 | 1128.73 | 26.52 | 8.019 | 0.192 | 0.980 | 381 | 2 | 1.4 | 0.25 |
| DDH726A Bulk 1N | 74-210 / 1N HCl | - | 12.81 | 98.50 | 1412.39 | 4.93 | 9.74 | 0.03 | 0.39 | 377 | 1 | 1.5 | 0.04 |
| DDH726B Bulk 1N | 74-210 / 1N HCl | - | 5.46 | 58.03 | 802.18 | 2.77 | 6.03 | 0.02 | 0.45 | 387 | 1 | 1.3 | 0.02 |
| DDH726C Bulk 0.2N | 74-210 / 0.2N HCl | - | 2.24 | 18.06 | 1216.27 | 8.20 | 8.03 | 0.06 | 0.81 | 354 | 2 | 0.9 | 0.07 |
| DDH726A M1.6 0.2N | 74-210 / Mag / 0.2N HCl | 2 | 24.5 | 170.7 | 1672.61 | 7.79 | 11.037 | 0.061 | 0.779 | 365 | 1 | 1.3 | 0.08 |
| DDH726A NM1.6 0.2N | 74-210 / Mag / 0.2N HCl | 1 | 4.06 | 28.4 | 1520.33 | 23.80 | 9.354 | 0.157 | 0.929 | 335 | 2 | 0.5 | 0.21 |
| DDH726A NM1.6 0.2N rpt | 74-210 / Mag / 0.2N HCl | 1 | 4.64 | 34.11 | 1478.40 | 9.19 | 9.753 | 0.084 | 0.577 | 361 | 3 | 1.1 | 0.10 |
| DDH726B M1.6 0.2N | 74-210 / Mag / 0.2N HCl | 4 | 13.81 | 139.1 | 832.26 | 3.65 | 5.800 | 0.027 | 0.857 | 357 | 1 | 0.9 | 0.03 |
| DDH726B NM1.6 0.2N | 74-210 / Mag / 0.2N HCl | 3 | 3.16 | 31.73 | 853.69 | 3.56 | 6.081 | 0.026 | 0.535 | 367 | 2 | 1.1 | 0.03 |
| DDH726B NM1.80.2N | 74-210 / Mag / 0.2N HCl | 2 | 1.51 | 14.3 | 897.14 | 31.41 | 6.010 | 0.212 | 0.988 | 345 | 3 | 0.8 | 0.28 |
| DDH726B NM2.0 0.2N | 74-210 / Mag / 0.2N HCl | 1 | 1.20 | 13.1 | 745.89 | 15.46 | 5.446 | 0.122 | 0.920 | 370 | 4 | 1.1 | 0.15 |
| DDH726B NM2.0 0.2N rpt | 74-210 / Mag / 0.2N HCl | 1 | 1.25 | 11.99 | 837.12 | 36.57 | 5.250 | 0.232 | 0.987 | 315 | 4 | 0.4 | 0.32 |
| DDH726B NM2.0 Fine 0.2N | <74 / Mag / 0.2N HCl | 1 | 0.95 | 8.81 | 898.31 | 49.98 | 5.504 | 0.313 | 0.987 | 314 | 5 | 0.3 | 0.43 |
| DDH726C M0.8 0.2N | 74-210 / Mag / 0.2N HCl | 5 | 22.4 | 141.3 | 1900.12 | 9.95 | 11.502 | 0.078 | 0.730 | 336 | 2 | 0.4 | 0.10 |
| DDH726C NM0.8 0.2N | 74-210 / Mag / 0.2N HCl | 4 | 8.47 | 61.47 | 1486.91 | 25.05 | 9.621 | 0.165 | 0.978 | 353 | 2 | 0.9 | 0.22 |
| DDH726C M1.6 0.2N | 74-210 / Mag / 0.2N HCl | 3 | 14.18 | 96.0 | 1649.92 | 8.42 | 10.240 | 0.054 | 0.909 | 341 | 1 | 0.6 | 0.07 |
| DDH726C M1.8 0.2N | 74-210 / Mag / 0.2N HCl | 2 | 2.66 | 21.24 | 1240.57 | 9.12 | 8.231 | 0.064 | 0.810 | 357 | 2 | 1.0 | 0.08 |
| DDH726C M1.8 Fine 0.2N | <74 / Mag / 0.2N HCl | 2 | 2.24 | 21.37 | 887.92 | 17.20 | 5.915 | 0.116 | 0.979 | 342 | 2 | 0.7 | 0.15 |
| DDH726C NM1.8 Fine 0.2N | <74 / Mag / 0.2N HCl | 1 | 2.18 | 20.11 | 898.80 | 46.46 | 5.637 | 0.295 | 0.985 | 320 | 4 | 0.4 | 0.40 |
| DDH726A M1.6 Leachate | Leachate | - | 12.01 | 298.5 | 383.77 | 3.70 | 7.638 | 0.076 | 0.949 | 1054 | 4 | 5.4 | 0.08 |
| DDH726A NM1.6 Leachate | Leachate | - | 2.79 | 58.16 | 485.26 | 27.85 | 8.571 | 0.492 | 0.994 | 949 | 8 | 5.7 | 0.52 |
| DDH726B M1.6 Leachate | Leachate | - | 1.96 | 46.3 | 362.23 | 16.77 | 6.037 | 0.280 | 0.988 | 855 | 9 | 3.9 | 0.30 |
| DDH726B NM2.0 Leachate rpt | Leachate | - | 0.63 | 12.93 | 486.02 | 65.01 | 8.239 | 1.104 | 0.994 | 907 | 19 | 5.4 | 1.17 |
| DDH726C NM0.8 Leachate | Leachate | - | 2.13 | 52.8 | 374.78 | 6.63 | 7.262 | 0.130 | 0.979 | 1020 | 5 | 5.1 | 0.14 |
| DDH726C M1.6 Leachate | Leachate | - | 5.03 | 118.6 | 385.75 | 3.42 | 6.929 | 0.066 | 0.910 | 940 | 4 | 4.7 | 0.07 |
| DDH726C NM1.8 Leachate | Leachate | - | 0.15 | 3.65 | 395.37 | 35.08 | 7.895 | 0.700 | 0.994 | 1062 | 15 | 5.6 | 0.73 |

In the "Separation Procedure" column the first value reported is the grain size of the mineral separate in μm . If the sample has undergone magnetic separation the designation "Mag" is given. If the sample has undergone acid leaching the concentration of HCl used for the leaching procedure is given, and if the temperature was elevated beyond room temperature the temperature is also given. For example the designation "74-210 / Mag / 10N HCl @ 80C" states that the sample contains grains 74-210 μm in size, has underwent magnetic separation, and has been leached with 10N HCl at 80°C. All samples unless otherwise stated have underwent heavy liquid separation. The term "Low Density" refers to material that is less dense than the heavy liquid used for heavy liquid separation (i.e. < 3.32 g/cm³). The relative magnetic susceptibility (χ) between rocks or rock fragments is given in the second column where higher values refer to higher χ values. These values are purely qualitative and cannot be used to compare between different rocks or rock fragments. For clarity rock fragments that cannot be compared via χ are separated by a dashed border. Model ages are determined using an initial Os ratio of 0.84. Initial ratio calculations are based on an age of 350 Ma.

Table 5.3: Re-Os results for the Salmo district

| Sample Name | Separation Procedure | Qualitative χ | Re ppb | Os ppt | 187Re / 188Os | $\pm 2s$ | 187Os / 188Os | $\pm 2s$ | Rho | Model Age | $\pm 2\sigma$ | Initial Ratio | $\pm 2\sigma$ |
|---------------------------|-------------------------|--------------------|--------|--------|---------------|----------|---------------|----------|-------|-----------|---------------|---------------|---------------|
| 07SP-21-1A | 74-210 | - | 572 | 8402 | 494.874 | 1.911 | 4.0302 | 0.0058 | 0.155 | 336 | 1 | 1.3 | 0.01 |
| 07SP-21-1B | 74-210 | - | 789 | 12192 | 463.641 | 1.866 | 3.8661 | 0.0091 | 0.229 | 338 | 2 | 1.3 | 0.01 |
| 07SP-21-1C | 74-210 | - | 556 | 8496 | 470.210 | 2.241 | 3.8958 | 0.0178 | 0.397 | 337 | 2 | 1.3 | 0.02 |
| 07SP-21-1D | 74-210 | - | 834 | 13663 | 423.191 | 1.790 | 3.4923 | 0.0119 | 0.267 | 317 | 2 | 1.1 | 0.02 |
| 07SP-21-1E | 74-210 | - | 1074 | 16835 | 443.339 | 1.775 | 3.5215 | 0.0086 | 0.203 | 307 | 2 | 1.0 | 0.01 |
| 07SP-21-1F | 74-210 | - | 305 | 4662 | 474.904 | 1.054 | 4.0124 | 0.0103 | 0.627 | 348 | 1 | 1.4 | 0.01 |
| 07SP-21-1G M1.0 0.2N | 74-210 / Mag / 0.2N HCl | 5 | 225 | 4457 | 337.232 | 0.651 | 3.1035 | 0.0065 | 0.529 | 329 | 1 | 1.2 | 0.01 |
| 07SP-21-1G NM1.0 0.2N | 74-210 / Mag / 0.2N HCl | 4 | 212 | 4338 | 325.947 | 0.639 | 3.0701 | 0.0065 | 0.532 | 334 | 1 | 1.3 | 0.01 |
| 07SP-21-1G NM1.2 0.2N | 74-210 / Mag / 0.2N HCl | 3 | 228 | 4533 | 336.587 | 0.657 | 3.0946 | 0.0066 | 0.531 | 328 | 0 | 1.2 | 0.01 |
| 07SP-21-1G NM1.5 0.2N | 74-210 / Mag / 0.2N HCl | 2 | 290 | 5592 | 347.503 | 0.696 | 3.1207 | 0.0070 | 0.539 | 322 | 1 | 1.2 | 0.01 |
| 07SP-21-1G NM1.8 0.2N | 74-210 / Mag / 0.2N HCl | 1 | 450 | 8673 | 345.079 | 0.692 | 3.0362 | 0.0069 | 0.528 | 310 | 1 | 1.1 | 0.01 |
| 07SP-21-1G NM1.8 0.2N rpt | 74-210 / Mag / 0.2N HCl | 1 | 466 | 9276 | 332.112 | 0.853 | 2.9889 | 0.0106 | 0.529 | 314 | 2 | 1.1 | 0.01 |
| 07SP-21-1G | 74-210 | - | 348 | 6296 | 372.123 | 1.607 | 3.1586 | 0.0173 | 0.485 | 307 | 2 | 1.1 | 0.02 |
| 07SP-21-1G rpt | 74-210 | - | 324 | 6053 | 358.884 | 0.752 | 3.1182 | 0.0078 | 0.581 | 312 | 1 | 1.1 | 0.01 |
| 07SP-21-1H M1.3 0.2N | 74-210 / Mag / 0.2N HCl | 5 | 196 | 3534 | 386.884 | 0.780 | 3.5559 | 0.0081 | 0.534 | 357 | 1 | 1.4 | 0.01 |
| 07SP-21-1H NM1.3 0.2N | 74-210 / Mag / 0.2N HCl | 4 | 187 | 3398 | 383.209 | 0.794 | 3.5650 | 0.0085 | 0.534 | 362 | 1 | 1.4 | 0.01 |
| 07SP-21-1H NM1.8 0.2N | 74-210 / Mag / 0.2N HCl | 3 | 197 | 3570 | 386.202 | 0.773 | 3.5825 | 0.0080 | 0.534 | 361 | 1 | 1.4 | 0.01 |
| 07SP-21-1H M2.0 0.2N | 74-210 / Mag / 0.2N HCl | 2 | 219 | 4218 | 360.375 | 0.704 | 3.5061 | 0.0074 | 0.533 | 375 | 1 | 1.5 | 0.01 |
| 07SP-21-1H NM2.0 0.2N | 74-210 / Mag / 0.2N HCl | 1 | 418 | 7084 | 418.171 | 0.820 | 3.7234 | 0.0081 | 0.530 | 354 | 1 | 1.4 | 0.01 |
| 07SP-21-1H | 74-210 | - | 350 | 4521 | 580.933 | 2.273 | 4.3828 | 0.0163 | 0.556 | 323 | 1 | 1.1 | 0.02 |
| 07SP-21-1H rpt | 74-210 | - | 286 | 4217 | 490.846 | 1.173 | 3.9678 | 0.0123 | 0.584 | 331 | 1 | 1.2 | 0.01 |
| 07SP-21-1I | 74-210 | - | 355 | 5796 | 432.564 | 2.654 | 3.7072 | 0.0356 | 0.515 | 340 | 4 | 1.3 | 0.04 |
| 07SP-21-1 I Leachate | Leachate | - | 22 | 3301 | 41.308 | 0.318 | 2.3536 | 0.0061 | 0.198 | - | - | 2.1 | 0.01 |
| 07SP-21-1 I Leachate | Leachate | - | 1.2 | 1448 | 5.333 | 0.329 | 2.3619 | 0.0065 | 0.026 | - | - | 2.3 | 0.01 |
| HB-A 0.2N | 74-210 / 0.2N HCl | - | 17 | 261 | 467.49 | 1.86 | 4.0314 | 0.0138 | 0.408 | 347 | 2 | 1.2 | 0.02 |
| HB-A NM 0.6 0.2N | 74-210 / Mag / 0.2N HCl | 3 | 26 | 431 | 435.98 | 1.67 | 3.9979 | 0.0120 | 0.381 | 368 | 2 | 1.4 | 0.02 |
| HB-A NM 1.1 0.2N | 74-210 / Mag / 0.2N HCl | 2 | 26 | 429 | 436.14 | 1.78 | 3.9121 | 0.0160 | 0.386 | 356 | 2 | 1.3 | 0.02 |
| HB-A NM 1.9 0.2N | 74-210 / Mag / 0.2N HCl | 1 | 24 | 390 | 432.42 | 1.64 | 3.8196 | 0.0109 | 0.378 | 346 | 2 | 1.2 | 0.01 |
| HB-B 0.2N | 74-210 / 0.2N HCl | - | 18 | 235 | 629.89 | 2.49 | 5.4607 | 0.0188 | 0.398 | 393 | 2 | 1.7 | 0.02 |
| HB-B NM 0.7 0.2N | 74-210 / Mag / 0.2N HCl | 3 | 28 | 357 | 613.91 | 2.37 | 5.1041 | 0.0158 | 0.397 | 369 | 2 | 1.4 | 0.02 |
| HB-B NM 1.1 0.2N | 74-210 / Mag / 0.2N HCl | 2 | 21 | 223 | 836.81 | 3.28 | 6.2877 | 0.0195 | 0.422 | 355 | 2 | 1.3 | 0.03 |
| HB-B NM 1.6 0.2N | 74-210 / Mag / 0.2N HCl | 1 | 19 | 216 | 714.93 | 4.18 | 5.4120 | 0.0435 | 0.509 | 343 | 3 | 1.1 | 0.05 |

In the "Separation Procedure" column the first value reported is the grain size of the mineral separate in μm . If the sample has undergone magnetic separation the designation "Mag" is given. If the sample has undergone acid leaching the concentration of HCl used for the leaching procedure is given, and if the temperature was elevated beyond room temperature the temperature is also given. For example the designation "74-210 / Mag / 10N HCl @ 80C" states that the sample contains grains 74-210 μm in size, has undergone magnetic separation, and has been leached with 10N HCl at 80°C. All samples unless otherwise stated have undergone heavy liquid separation. The term "Low Density" refers to material that is less dense than the heavy liquid used for heavy liquid separation (i.e. $< 3.32 \text{ g/cm}^3$). The relative magnetic susceptibility (χ) between rocks or rock fragments is given in the second column where higher values refer to higher χ values. These values are purely qualitative and cannot be used to compare between different rocks or rock fragments. For clarity rock fragments that cannot be compared via χ are separated by a dashed border. The Reeves-Macdonald mine and H.B. mine samples are separated by a solid border. Model ages are determined using an initial Os ratio of 1.25 for the Reeves-MacDonald mine and 1.32 for the H.B. mine. Initial ratio calculations are based on an age of 334 Ma for the Reeves-Macdonald mine and 359 Ma for the H.B. mine.

Table 5.4: Mineralogy and modal abundance estimates

| Deposit | Sample | Qualitative χ | Mineralogy (Modal Abundance) | | | | | |
|--------------------------|--------------------------|--------------------|------------------------------|------------|--------|-----------|-----------|-------------|
| | | | Pyrite | Sphalerite | Galena | Silicates | Carbonate | Molybdenite |
| Prairie Creek - MVT | PC-94-80 Whole Rock | - | Y | Y | N | Y | Y | N |
| Prairie Creek - MVT | PC-94-80 M0.6 | 8 | 90% | X | X | X | 10% | - |
| Prairie Creek - MVT | PC-94-80 NM0.6 | 7 | 94% | < 1% | < 0.1% | X | 6% | - |
| Prairie Creek - MVT | PC-94-80 NM0.75 | 6 | 95% | X | X | X | 5% | - |
| Prairie Creek - MVT | PC-94-80 NM0.9 | 5 | 97% | < 1% | < 0.1% | X | 3% | - |
| Prairie Creek - MVT | PC-94-80 NM1.0 | 4 | 98% | X | X | X | 4% | - |
| Prairie Creek - MVT | PC-94-80 NM1.1 | 3 | 97% | < 1% | < 0.1% | X | 3% | - |
| Prairie Creek - MVT | PC94-80 NM1.3 | 2 | 97% | X | X | X | 3% | - |
| Prairie Creek - MVT | PC-94-80 NM1.5 | 1 | 98% | X | X | X | 2% | - |
| Prairie Creek - MVT | PC-93-25 Low Density | - | X | X | X | X | 98% | - |
| Prairie Creek - SMS | PC-93-25 Whole Rock | - | Y | Y | N | Y | Y | Y |
| Prairie Creek - SMS | PC-93-25 NM0.9 | 4 | 84% | 5.3% | < 0.1% | X | 11% | - |
| Prairie Creek - SMS | PC-93-25 NM1.1 | 3 | 88% | 9% | < 0.1% | X | 2% | - |
| Prairie Creek - SMS | PC-93-25 NM1.3 | 2 | xx | xx | X | X | 2% | - |
| Prairie Creek - SMS | PC-93-25 NM1.95 | 1 | 9% | 88% | < 0.1% | X | 3% | - |
| Prairie Creek - SMS | PC-11-209A Whole Rock | - | Y | Y | N | Y | Y | N |
| Prairie Creek - SMS | PC-11-209A NM1.45 FG 6N | 4 | xx | x | < 0.1% | X | 1% | - |
| Prairie Creek - SMS | PC-11-209A NM1.7 FG 6N | 3 | xx | x | < 0.1% | X | 2% | - |
| Prairie Creek - SMS | PC-11-209A NM2.0 CG 6N | 2 | xx | x | < 0.1% | X | 1% | - |
| Prairie Creek - SMS | PC-11-209A NM2.0 FG 6N | 2 | xx | x | < 0.1% | X | 1% | - |
| Prairie Creek - SMS | PC-11-209A NM2.0/2 FG 6N | 1 | xx | x | < 0.1% | X | 1% | - |
| Prairie Creek - SMS | PC-92-17B Whole Rock | - | Y | N/A | N/A | N/A | Y | N/A |
| Prairie Creek - SMS | PC-92-17B-1 | - | xx | N/A | N/A | N/A | 1% | - |
| Prairie Creek - SMS | PC-92-17B-2 | - | xx | N/A | N/A | N/A | 2% | - |
| Prairie Creek - Vein | PCU Whole Rock | - | Y | Y | N | Y | Y | Y |
| Prairie Creek - Vein | PCU M1.0-10/5 | 8 | xx | xx | < 0.1% | X | 10% | - |
| Prairie Creek - Vein | PCU NM1.0-10/5 | 7 | 77% | 20% | < 0.1% | X | 3% | - |
| Prairie Creek - Vein | PCU NM1.2-10/5 | 6 | 91% | 6% | < 0.1% | X | 3% | - |
| Prairie Creek - Vein | PCU NM1.6-10/5 | 5 | xx | xx | < 0.1% | X | 3% | - |
| Prairie Creek - Vein | PCU NM1.8-10/5 | 4 | xx | xx | < 0.1% | X | 2% | - |
| Prairie Creek - Vein | PCU NM2.0-10/5 | 2 | 84% | 13% | < 0.1% | X | 3% | - |
| Prairie Creek - Vein | PCU NM2.0-10/3 | 1 | 42% | 56% | < 0.1% | X | 1% | - |
| Prairie Creek - Vein | PCU-5-M1.7-10/5 | - | xx | xx | < 0.1% | X | 8% | - |
| Robb Lake | DDH726 Whole Rock | - | Y | Y | N | Y | Y | Y |
| Robb Lake | DDH726A M1.6 | 2 | 85% | X | < 0.1% | X | 15% | - |
| Robb Lake | DDH726A NM1.6 | 1 | 91% | X | < 0.1% | X | 9% | - |
| Robb Lake | DDH726B M1.6 | 4 | 88% | X | < 0.1% | X | 14% | - |
| Robb Lake | DDH726B NM1.6 | 3 | 88% | X | < 0.1% | X | 12% | - |
| Robb Lake | DDH726B NM1.8 | 2 | 88% | X | < 0.1% | X | 12% | - |
| Robb Lake | DDH726B NM2.0 | 1 | 88% | X | < 0.1% | X | 12% | - |
| Robb Lake | DDH726C M0.8 | 6 | 77% | X | < 0.1% | X | 23% | - |
| Robb Lake | DDH726C NM0.8 | 5 | 75% | X | < 0.1% | X | 25% | - |
| Robb Lake | DDH726C M1.6 | 4 | 75% | X | < 0.1% | X | 75% | - |
| Robb Lake | DDH726C M1.8 | 3 | 83% | X | < 0.1% | X | 17% | - |
| Robb Lake | DDH726C NM1.8 | 2 | xx | x | < 0.1% | X | xx | - |
| Salmo - Reeves Macdonald | 07-SP-21-1 Whole Rock | - | Y | N | Y | Y | Y | Y |
| Salmo - Reeves Macdonald | 07SP-21-1G M1.0 0.2N | 5 | 98% | X | X | X | 2% | - |
| Salmo - Reeves Macdonald | 07SP-21-1G NM1.0 0.2N | 4 | 95% | X | X | X | 5% | - |
| Salmo - Reeves Macdonald | 07SP-21-1G NM1.2 0.2N | 3 | 96% | X | X | X | 4% | - |
| Salmo - Reeves Macdonald | 07SP-21-1G NM1.5 0.2N | 2 | 97% | X | X | X | 3% | - |
| Salmo - Reeves Macdonald | 07SP-21-1G NM1.8 0.2N | 1 | 92% | X | X | X | 8% | - |
| Salmo - Reeves Macdonald | 07SP-21-1H M1.3 0.2N | 5 | 94% | X | X | X | 6% | - |
| Salmo - Reeves Macdonald | 07SP-21-1H NM1.3 0.2N | 4 | 93% | X | X | X | 7% | - |
| Salmo - Reeves Macdonald | 07SP-21-1H NM1.8 0.2N | 3 | 95% | X | X | X | 5% | - |
| Salmo - Reeves Macdonald | 07SP-21-1H M2.0 0.2N | 2 | 94% | X | X | X | 6% | - |
| Salmo - Reeves Macdonald | 07SP-21-1H NM2.0 0.2N | 1 | 87% | X | X | X | 13% | - |
| Salmo - H.B. Mine | HB Whole Rock | - | Y | Y | N/A | Y | Y | N/A |
| Salmo - H.B. Mine | HB-A NM 0.6 0.2N | 3 | xx | x | N/A | X | 18% | - |
| Salmo - H.B. Mine | HB-A NM 1.1 0.2N | 2 | xx | x | N/A | X | 13% | - |
| Salmo - H.B. Mine | HB-A NM 1.9 0.2N | 1 | xx | x | N/A | X | 10% | - |
| Salmo - H.B. Mine | HB-B NM 0.7 0.2N | 3 | xx | x | N/A | X | 18% | - |
| Salmo - H.B. Mine | HB-B NM 1.1 0.2N | 2 | xx | x | N/A | X | 10% | - |
| Salmo - H.B. Mine | HB-B NM 1.6 0.2N | 1 | xx | x | N/A | X | 6% | - |

Estimated mineralogy of mineral separates prior to leaching. Modal abundances are determined through leaching and pixel counting of petrographic images. The first row of each sample (i.e. "Whole Rock") represents the basic mineralogy of the sample. If a sample is thought to contain > 0.1% then a "Y" is shown in the cell, if < 0.1% then a "N" is shown, if there is insufficient information to make a determination then "N/A" is shown. Molybdenite is an exception to this rule as grains are not directly observed but localized Mo spikes in laser ablation images are thought to represent evidence for small crystals of molybdenite. All samples are thought to contain some silicate material based on EMPA analyses but the abundances in the mineral separates were not quantified but are expected to exist at concentrations of < 5%. The concentrations of pyrite and sphalerite should be taken as upper estimates as not all phases are accounted for. A designation of "x" means the abundance of that phase is expected to be < 5%, while a designation of "xx" means the phase is expected to be > 5%. Rock fragments that cannot be compared via χ are separated by a dotted border or an empty row.

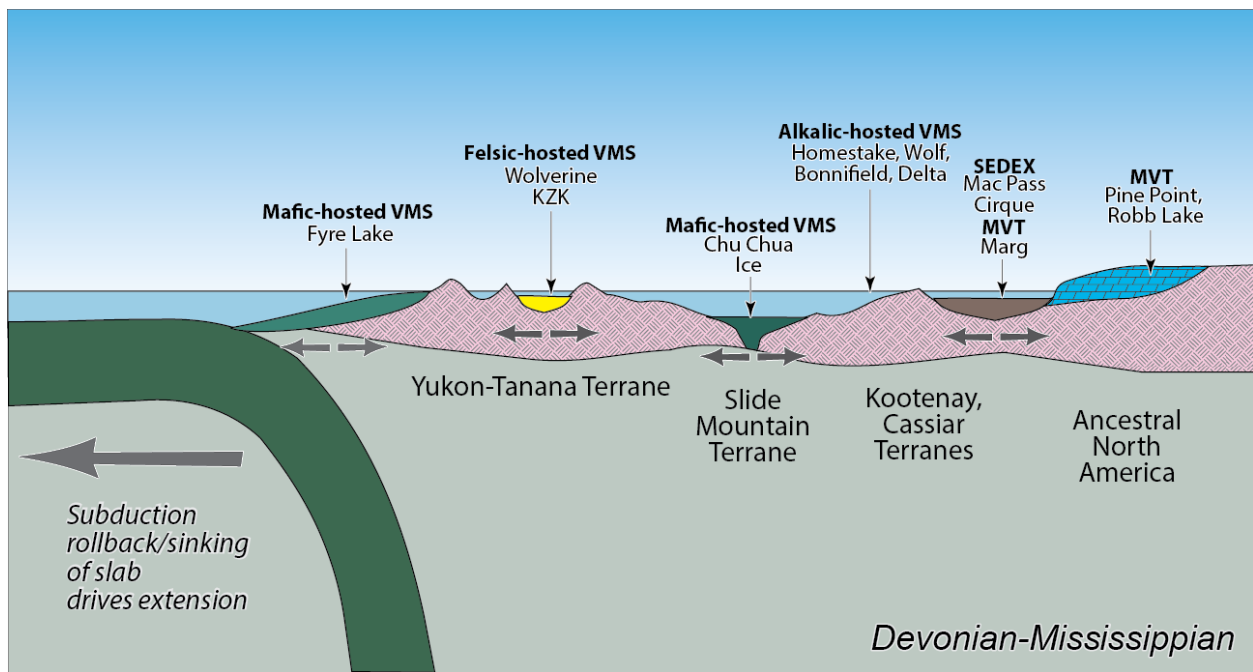


Figure 5.2: Cross-section of the basic tectonic architecture and metallogeny of the Canadian Cordillera during the Late Devonian - Mississippian (modified from Nelson et al., 2006).

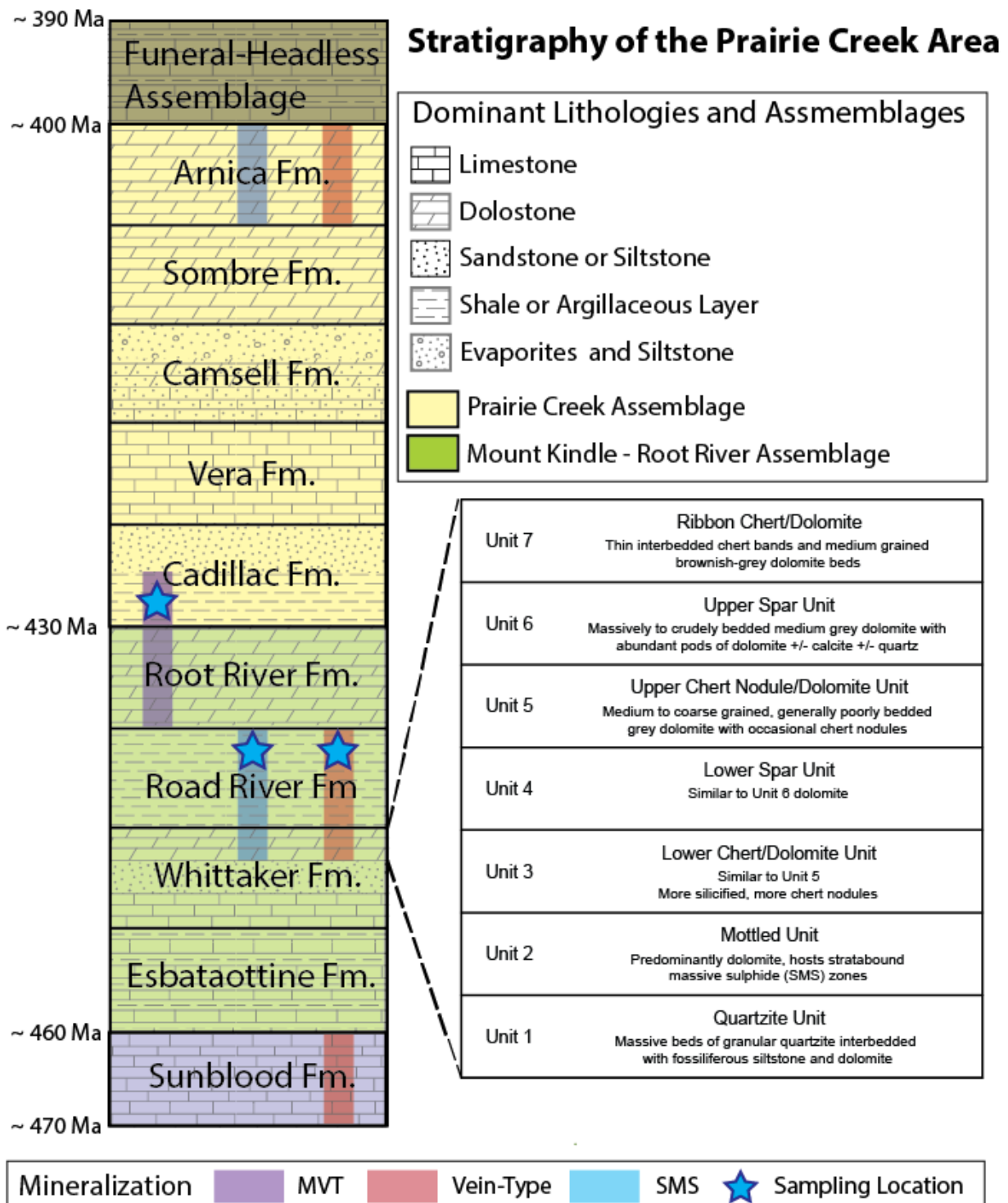


Figure 5.3: (A) Simplified stratigraphy of the Prairie Creek area based on the descriptions of Morrow and Cook (1987). Additional biostratigraphic ages are provided by Ludvigsen (1975) and Norris and Uyeno (1981). Ages are approximate, but formations are generally conformable between the Mount Kindle - Root River, Prairie Creek and Funeral-Headless Assemblages. The upper Whittaker Formation is divided into seven units near the mine site (from Canadian Zinc, 2010).

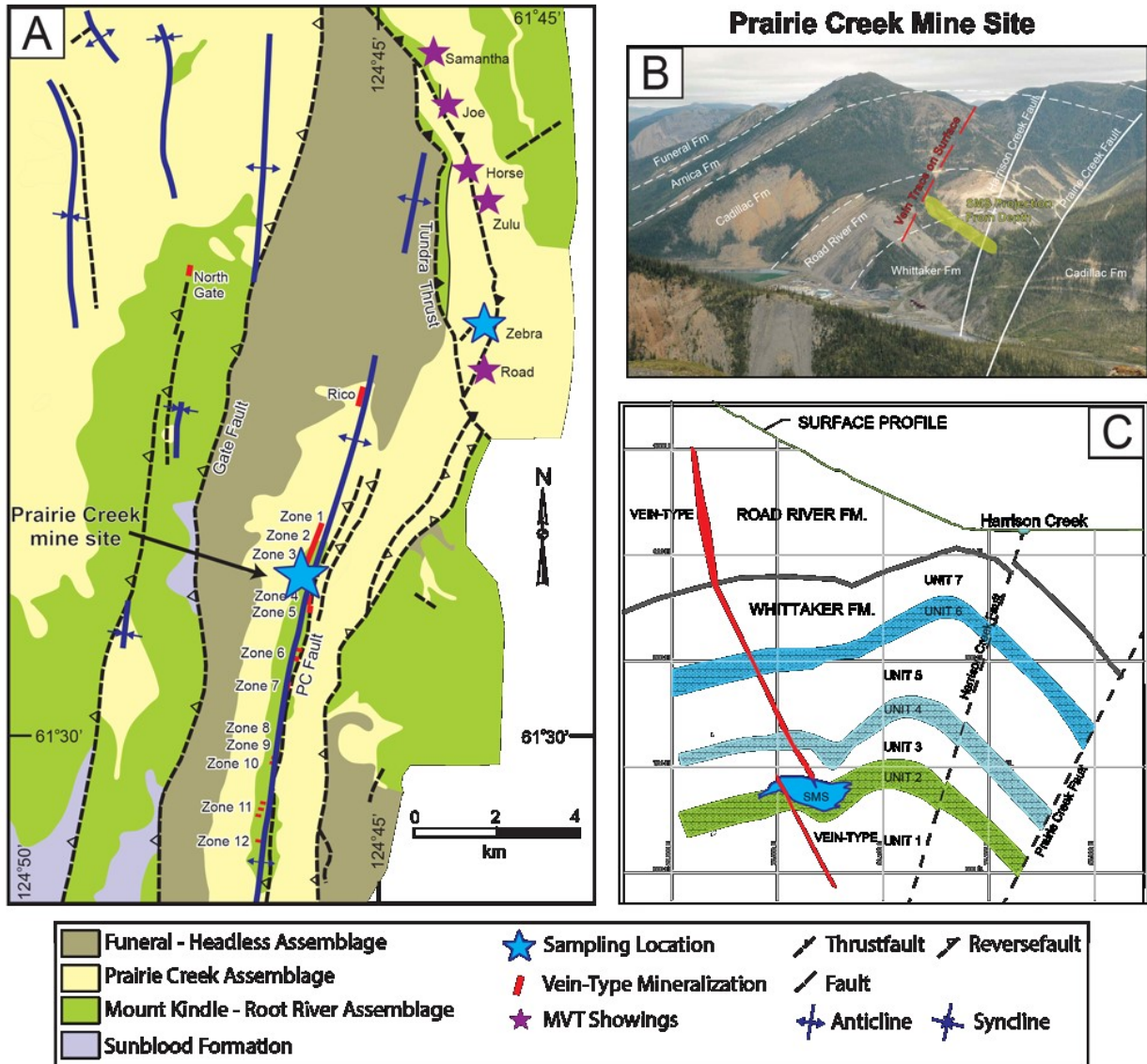


Figure 5.4: (A) Mineralization and major structures associated with the Prairie Creek area. Each numbered zone indicates the location of known Vein-Type mineralization (Morrow and Cook, 1987; Canadian Zinc Corporation, 2010; Figure modified from Paradis, 2007). (B) Stratigraphy and major structures looking north from Zone 6 (modified from Canada Zinc, 2010). (C) Cross section through the Mine Site showing the seven units of the upper Whittaker Formation and their relationship to the Vein-Type and SMS mineralization styles. No vertical exaggeration (modified from Canadian Zinc, 2010).

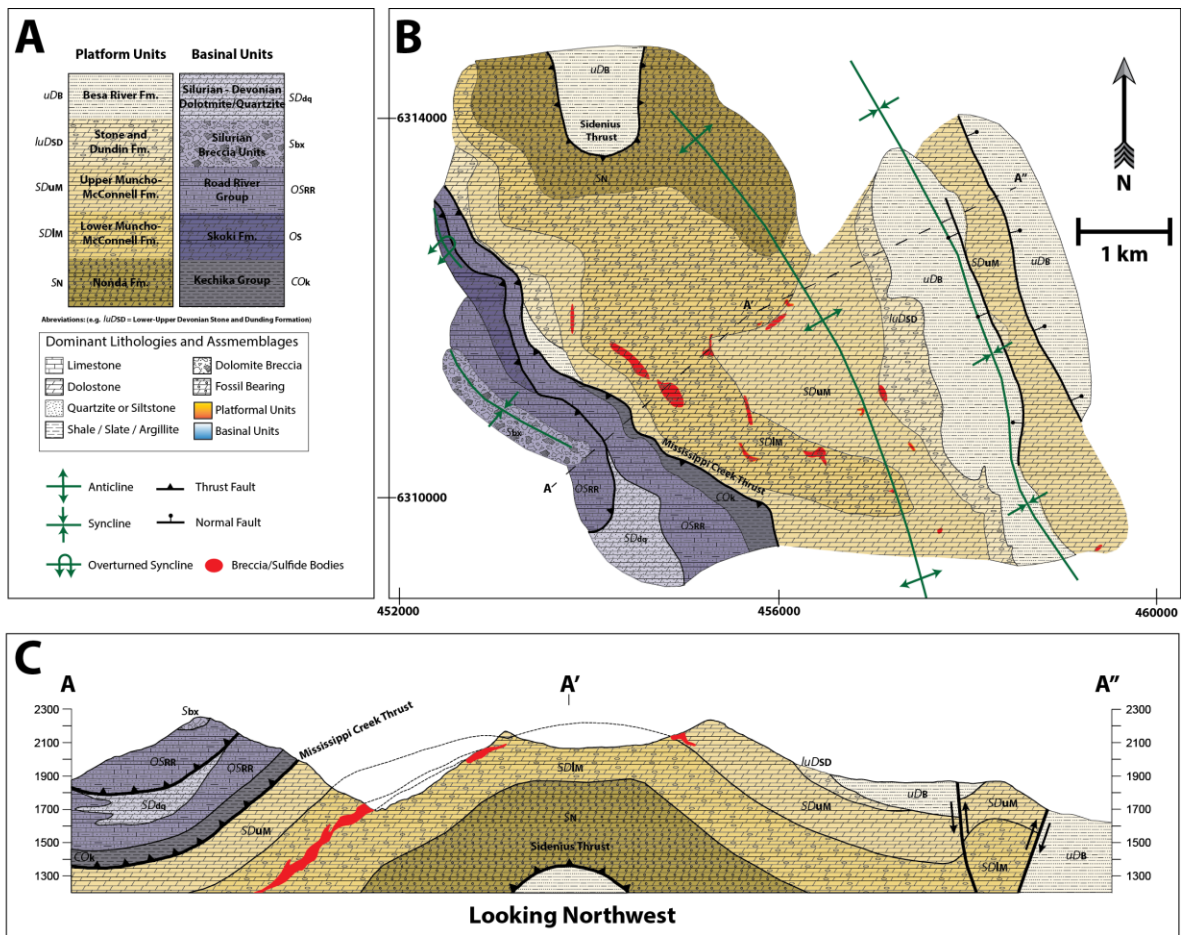


Figure 5.5: (A) Basic stratigraphy of the Robb Lake area as described by Nelson et al. (2000). (B) Location of mineralization/breccia zones (modified from Nelson et al., 1999) (C) Cross-section through A-A'' as shown in Figure B (modified from Nelson et al., 2000).

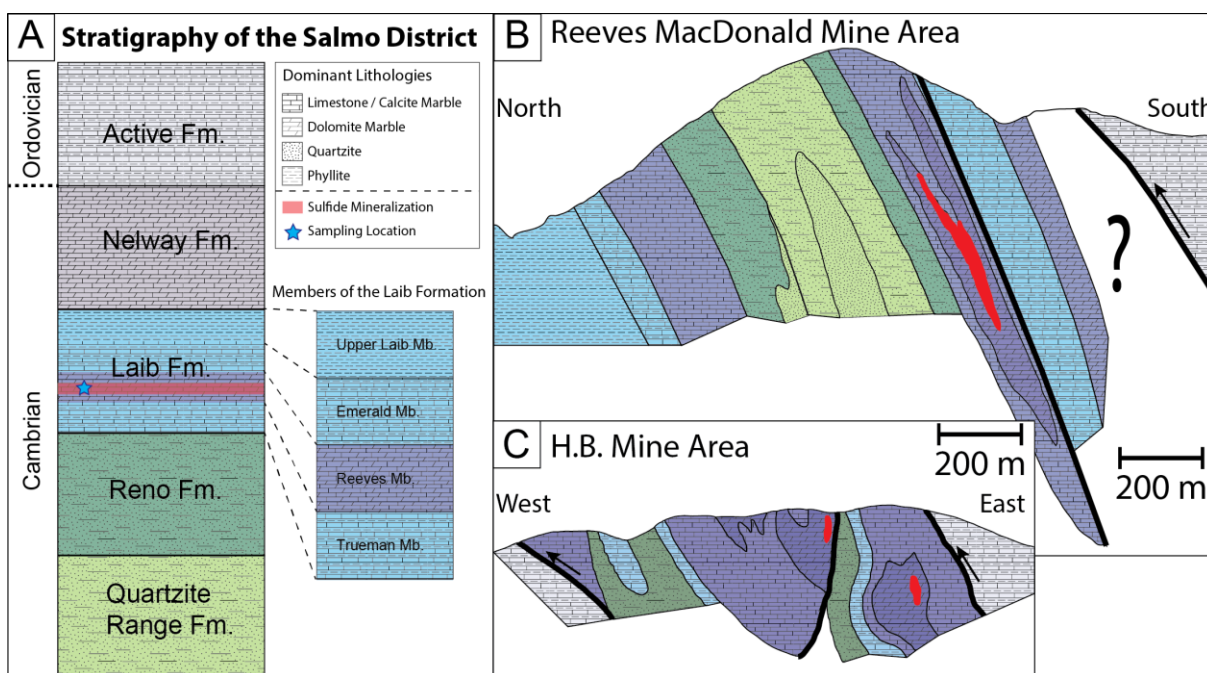


Figure 5.6: (A) Basic stratigraphy of the Salmo district as described by Fyles and Hewlett (1959). (B) North-south cross-section through of the Reeves - Macdonald mine area (modified from Fyles and Hewlett, 1959). (C) East-west cross-section through the H.B. mine area (modified from Fyles and Hewlett, 1959).

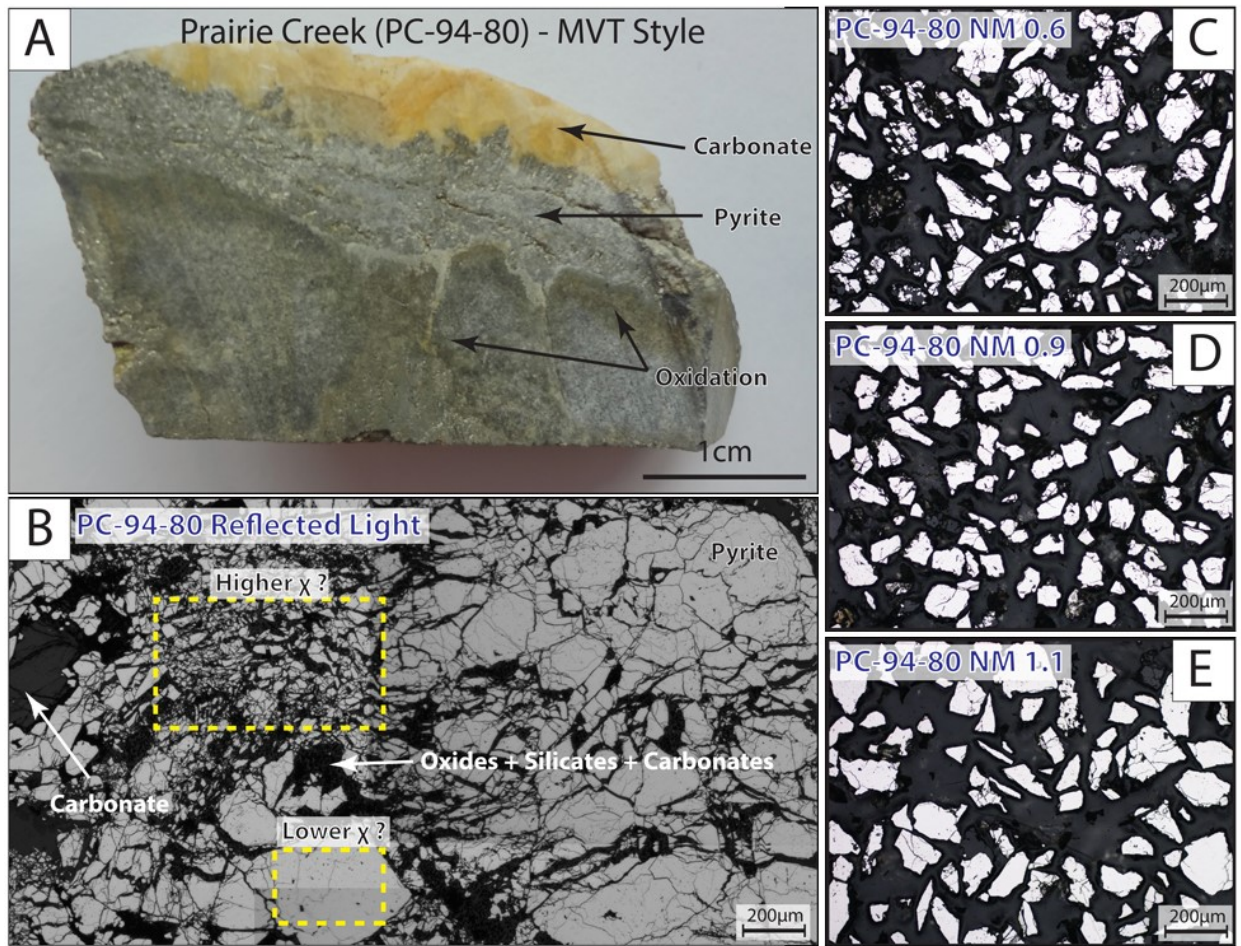


Figure 5.7: Sample PC-94-80 from MVT mineralization at Prairie Creek. (A) Hand sample specimen showing pyrite and carbonate. (B) Reflected light image showing fractured pyrite. (C)-(E) Reflected light images of mineral separates (pyrite). Observations of these mineral separates appear to show a correlation between magnetic susceptibility and fractures, with higher fracturing correlating with higher magnetic susceptibility. Possible locations of the different magnetic separates are highlighted in (B). The scaling of Figures B-E is identical.

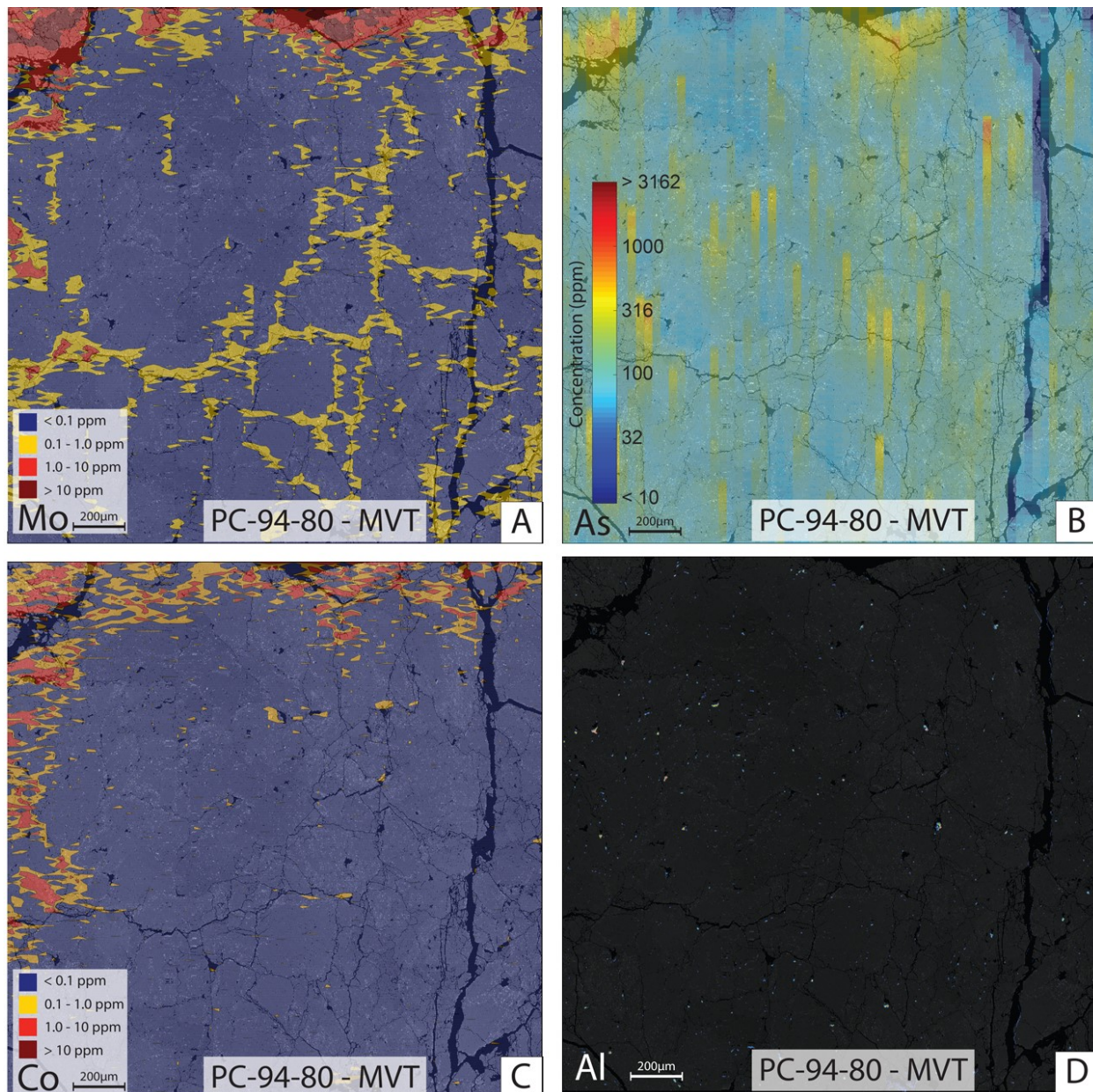


Figure 5.8: Compositional maps for sample PC-94-80 (Prairie Creek - MVT-style). (A) LA-ICPMS molybdenum contour map that has been deconvoluted to enhance clarity (B) LA-ICPMS arsenic map (C) LA-ICPMS cobalt contour map that has been deconvoluted to enhance clarity (D) EMPA aluminium map with hotter colours representing higher concentrations.

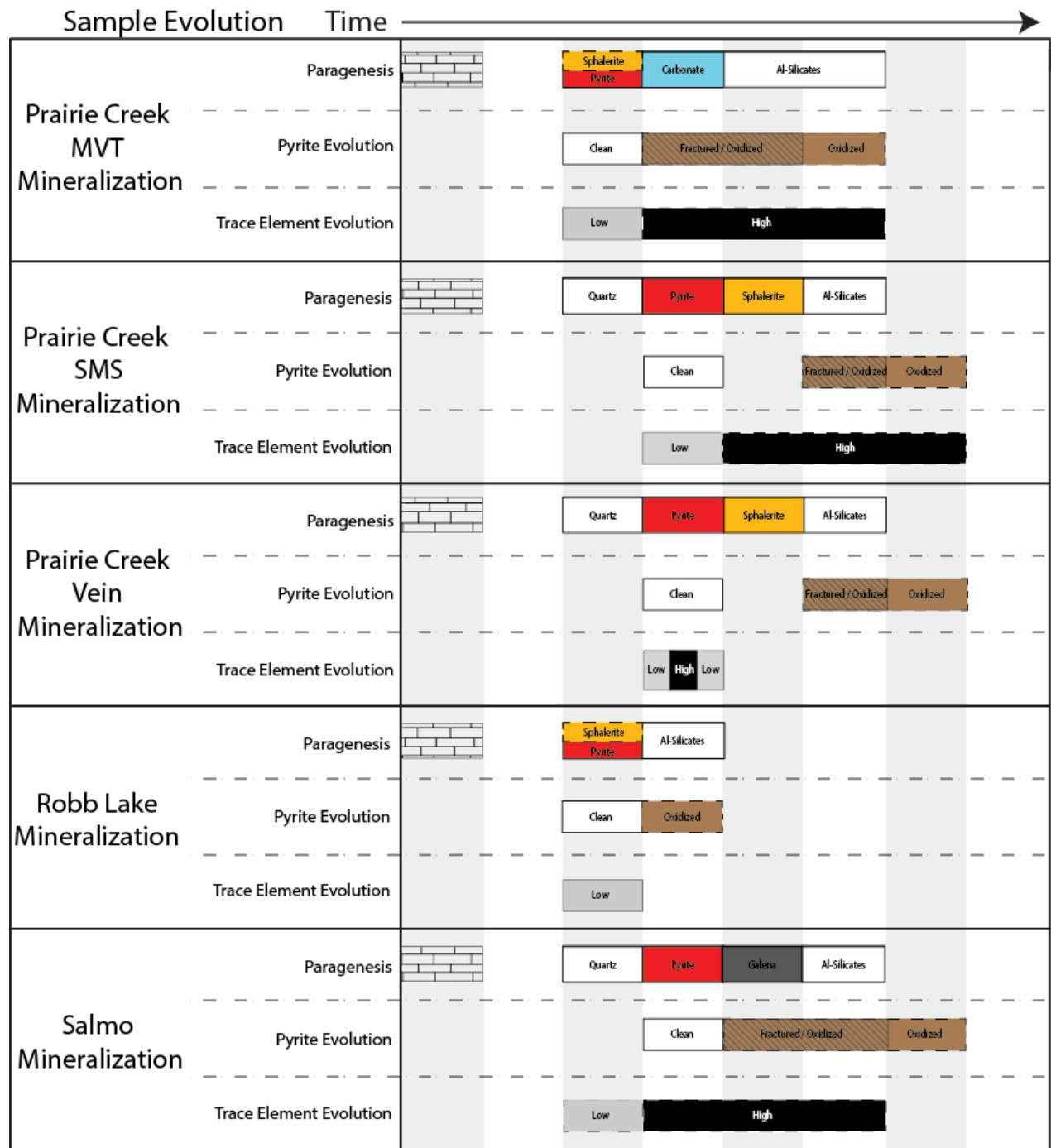


Figure 5.9: The evolution of samples studied in this project. The paragenesis of these samples are based on observations made in this study and do not necessarily represent the deposit as a whole. Paragenesis: The ordering of major minerals within each sample; Pyrite Evolution: Shows the approximate temporal location of fractures and oxidation in pyrite; Trace Element Evolution: The estimated temporal evolution of trace element concentration within pyrite. If there is some uncertainty in the timing of certain features of minerals then the outlined is dashed.

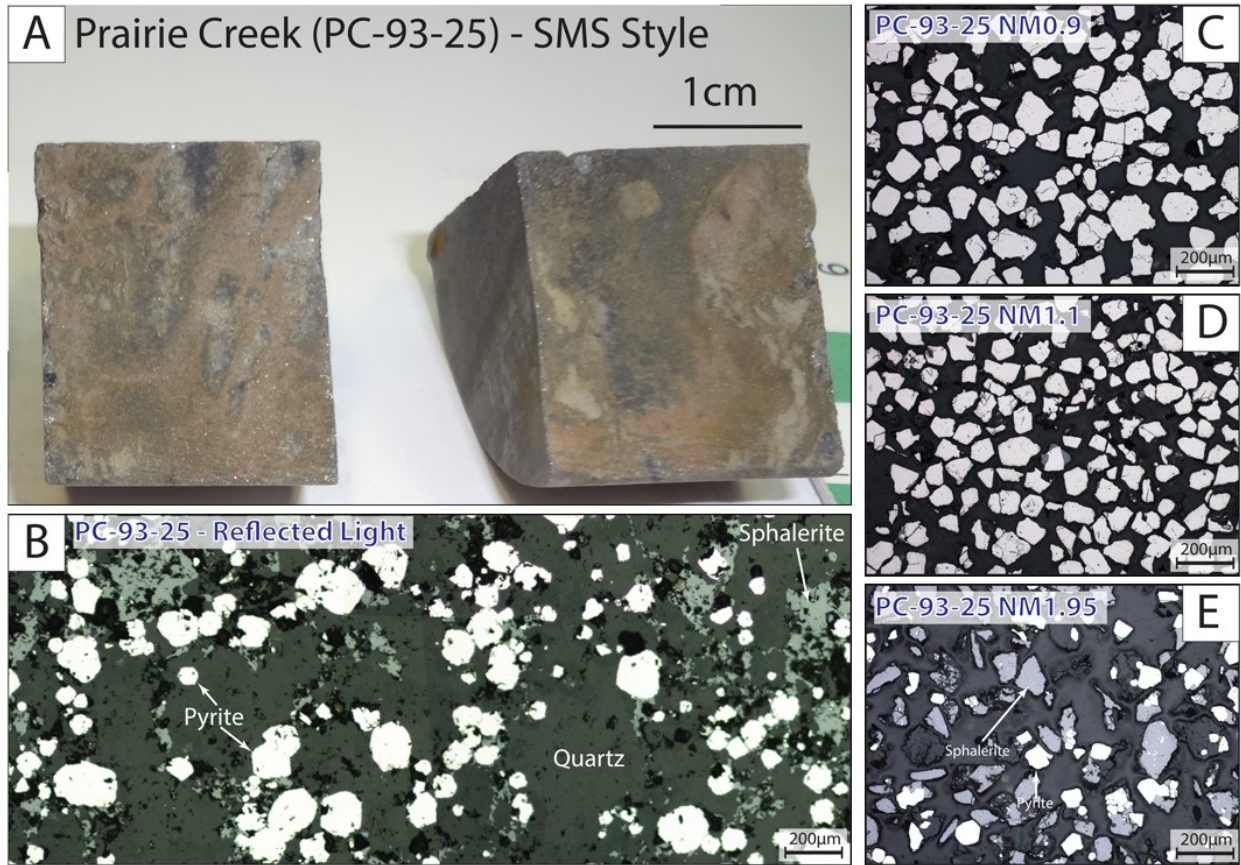


Figure 5.10: Sample PC-93-25 from the SMS mineralization at Prairie Creek. (A) Hand sample specimen showing disseminated sulphides within quartz. (B) Reflected light image showing disseminated sulphides. Sulphides are found commonly along the grain boundaries of quartz crystals. (C)-(E) Reflected light images of mineral separates. There are no substantial differences between PC-93-25 NM0.9 and PC-93-25 NM1.1, however PC-93-25 NM1.95 contains the majority of sphalerite. The scaling of Figures B-E is identical.

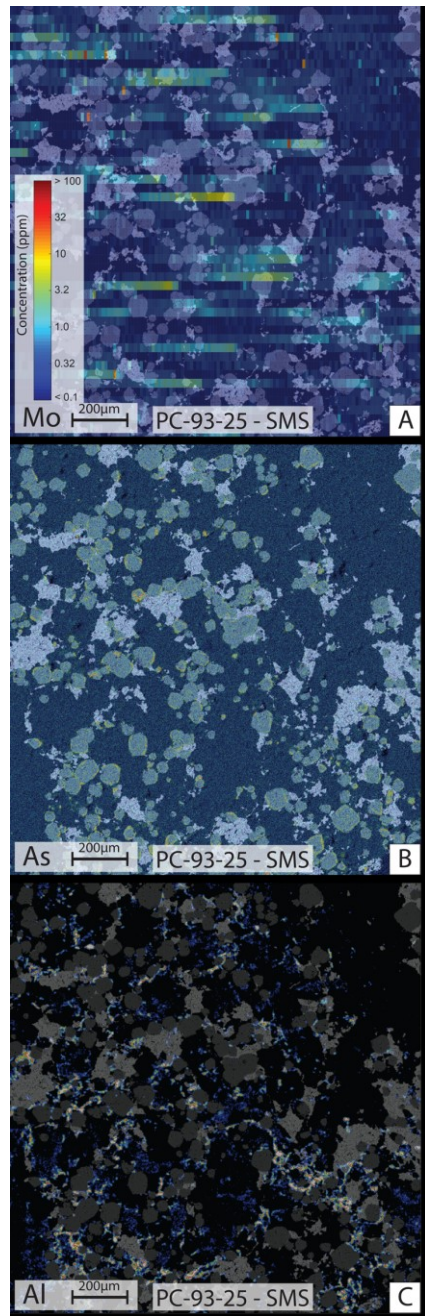


Figure 5.11: Compositional maps for sample PC-93-25 (Prairie Creek - SMS-style). (A) LA-ICPMS molybdenum map. The horizontal smearing of the images is an artefact of the sample acquisition. These smeared out lines likely represent single pixel spikes in Mo concentrations located near on right edge of each line. (B) EMPA arsenic map. (C) EMPA aluminium map. Hotter colours represent higher concentrations in EMPA maps.

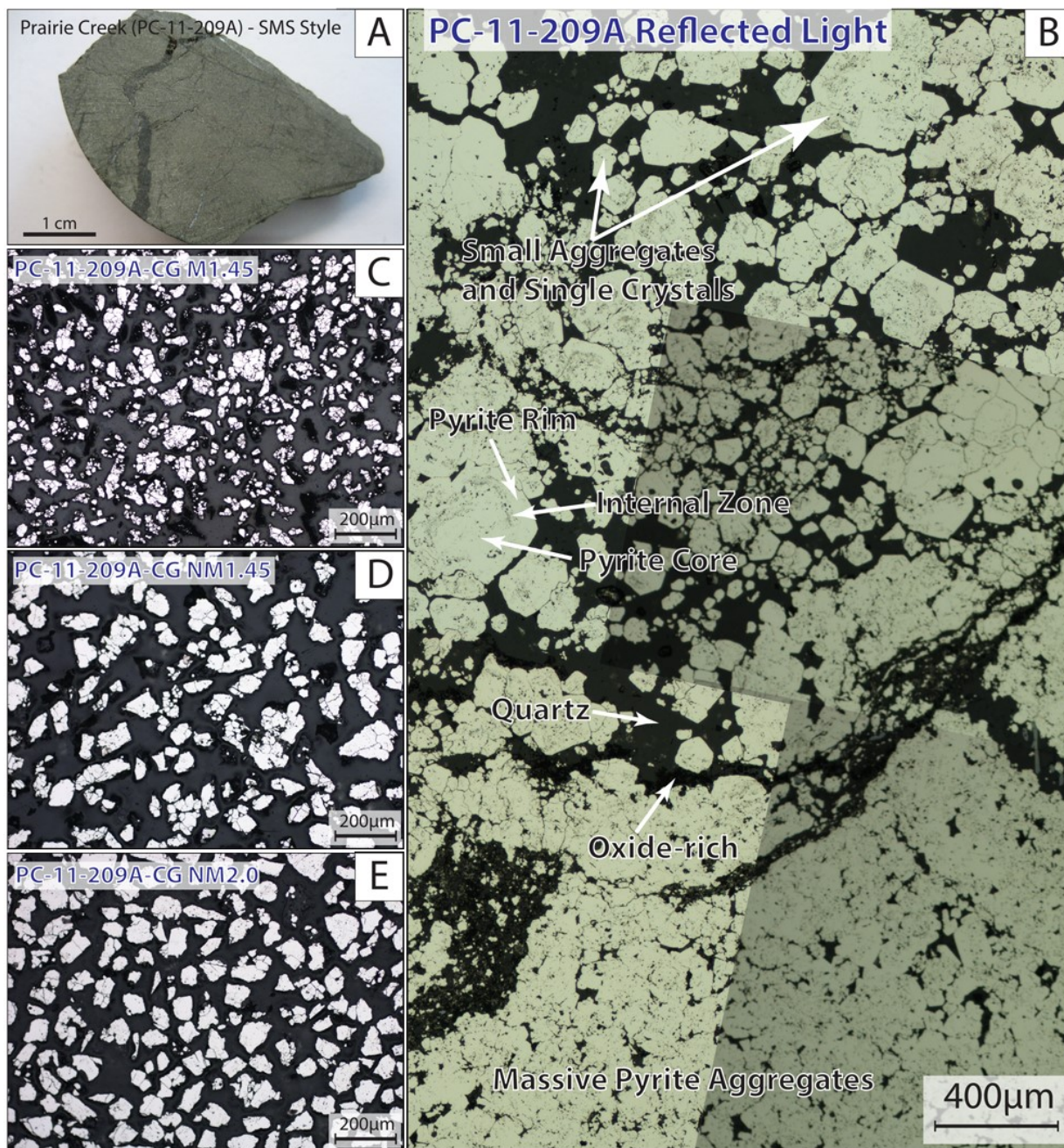


Figure 5.12: Sample PC-11-209A from the SMS-style of mineralization at Prairie Creek. (A) Hand sample specimen showing pyrite masses and crosscutting veins. (B) Reflected light image of PC-11-209A. Pyrite crystals that create large aggregate masses (several mm in size) can be observed at the bottom of the image, while individual crystals and smaller aggregates that replace quartz can be observed in the top part of the image. (C)-(E) Reflected light images of mineral separates. The most magnetic separate (Figure C; PC-11-209A M1.45) contain the highest abundance of fractures. The scaling of Figures B-E is identical.

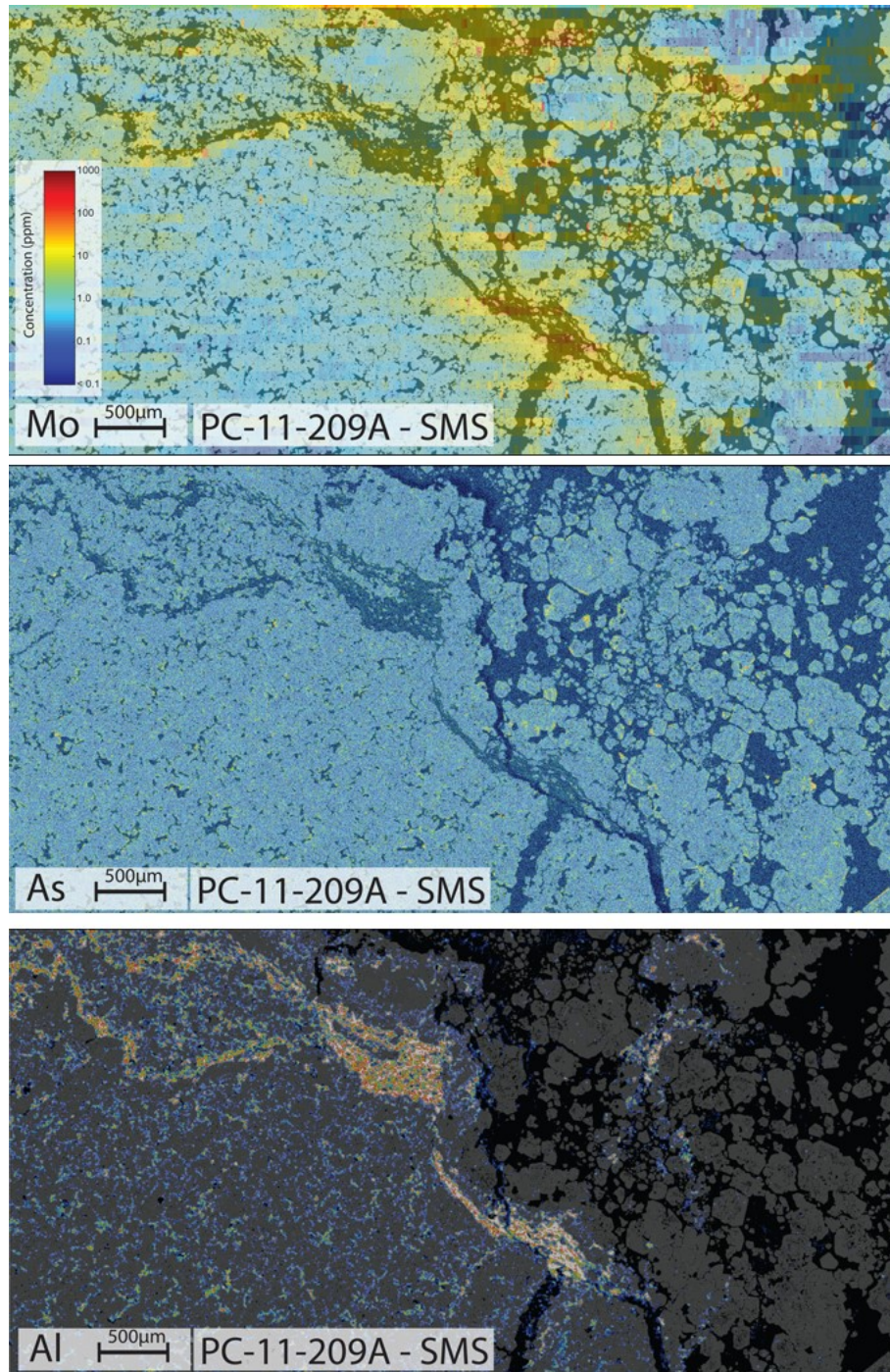


Figure 5.13: Compositional maps for sample PC-11-209A (Prairie Creek - SMS-style). (A) LA-ICPMS molybdenum map. (B) EMPA arsenic map. (C) EMPA aluminium map. Hotter colours represent higher concentrations in EMPA maps.

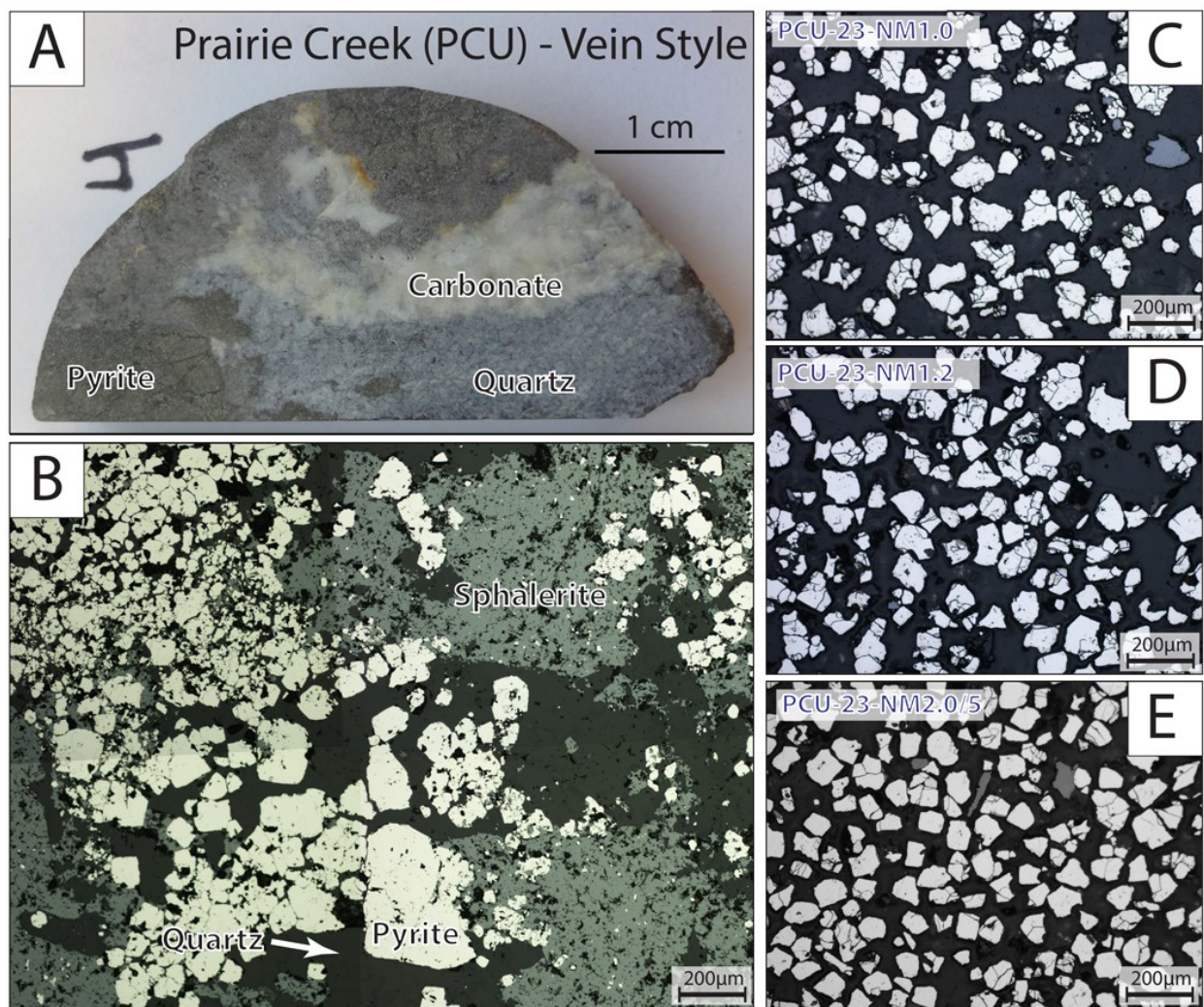


Figure 5.14: Sample PCU from Vein-style mineralization at Prairie Creek. (A) Hand sample specimen showing pyrite aggregates, quartz crystals and a cross-cutting carbonate vein (B) Reflected light image of PCU showing the relationship between pyrite, sphalerite, and quartz. (C)-(E) Reflected light images of mineral separates. The scaling of Figures B-E is identical.

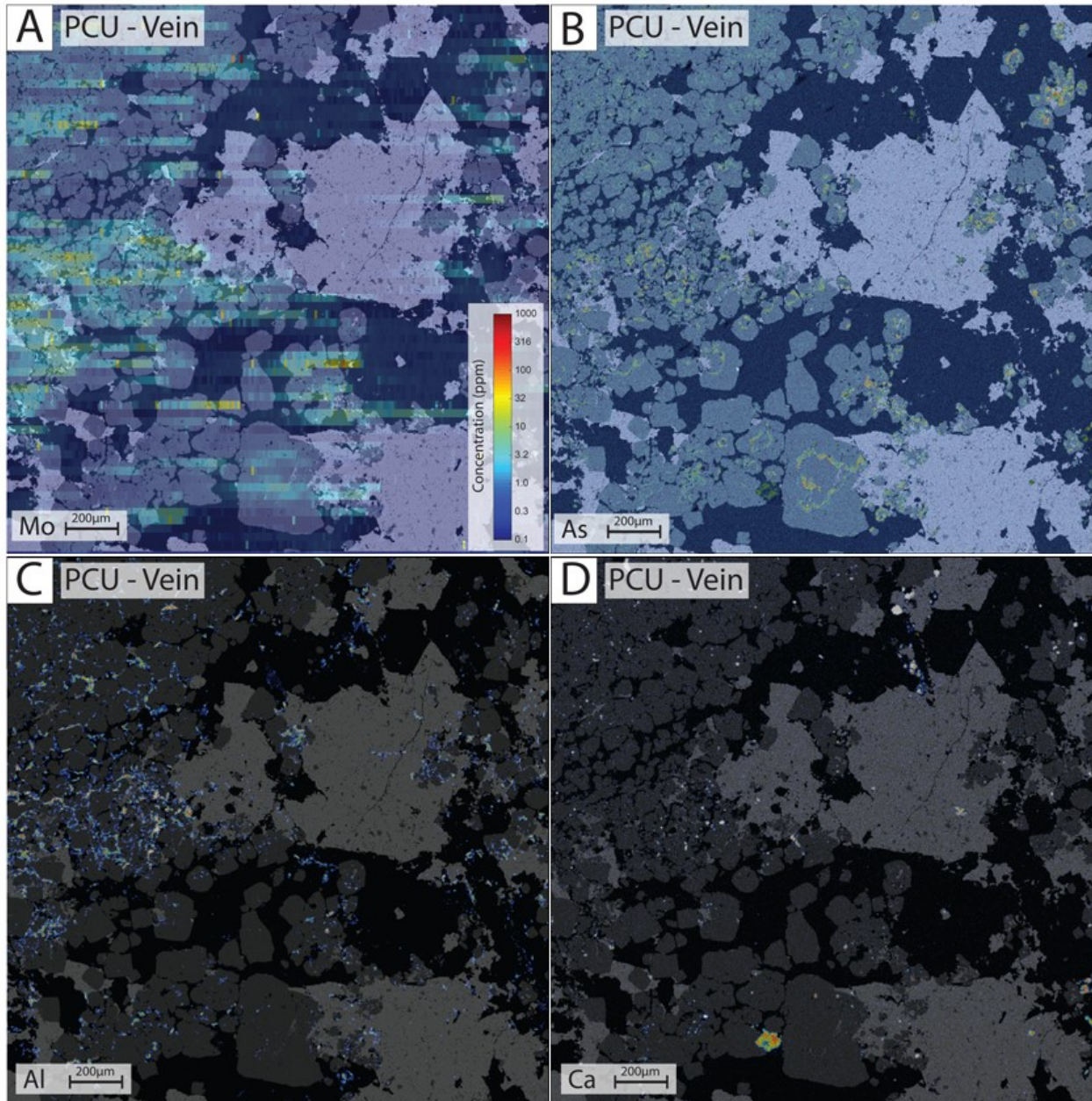


Figure 5.15: Compositional maps for sample PCU (Prairie Creek - Vein-Type). (A) LA-ICPMS molybdenum map. (B) EMPA arsenic map. (C) EMPA aluminium map. (D) EMPA calcium map. Hotter colours represent higher concentrations in EMPA maps.

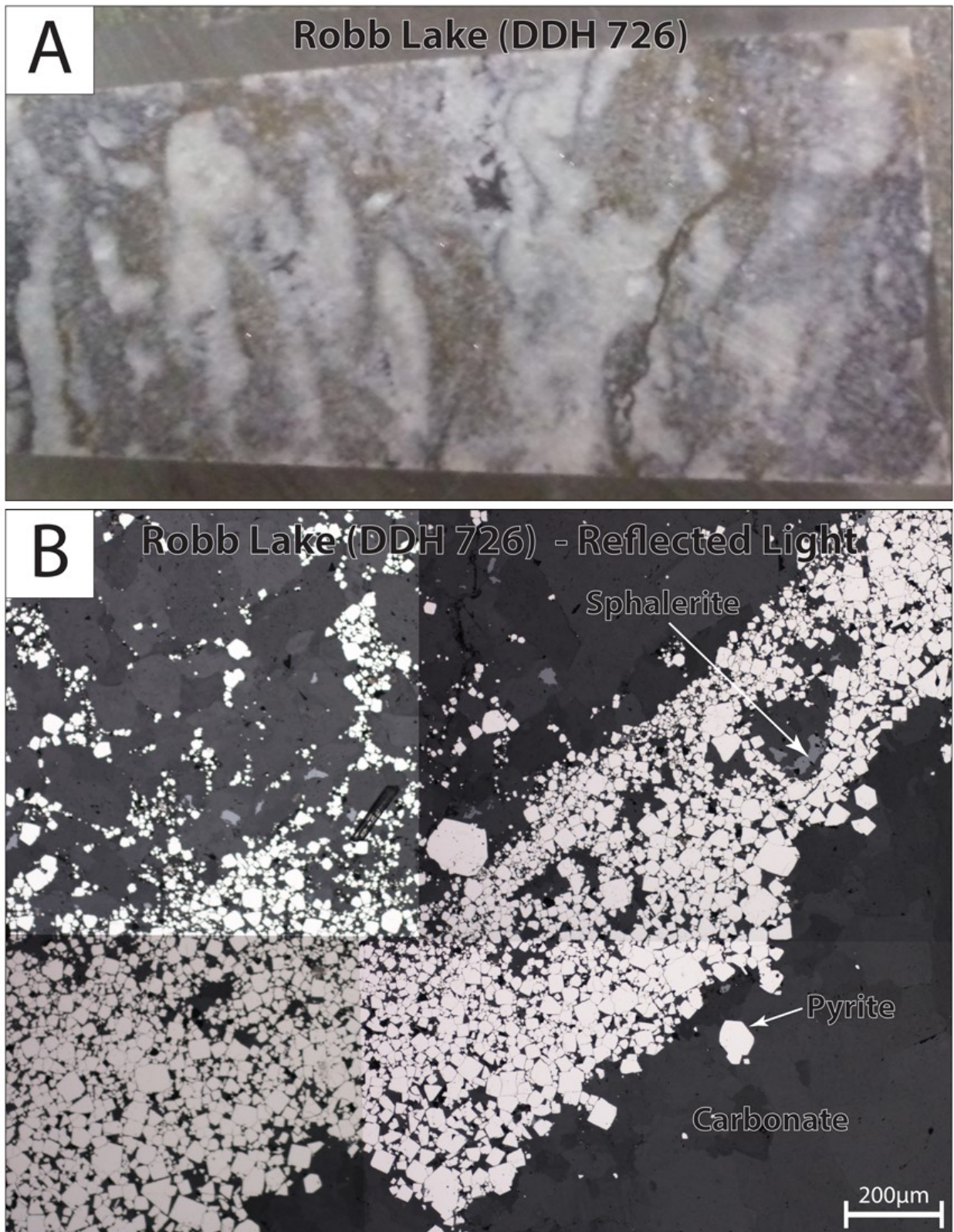


Figure 5.16: Sample DDH 726 from Robb Lake (A) Hand sample specimen showing pyrite running semi-parallel to bedding (B) Reflected light image of DDH 726.

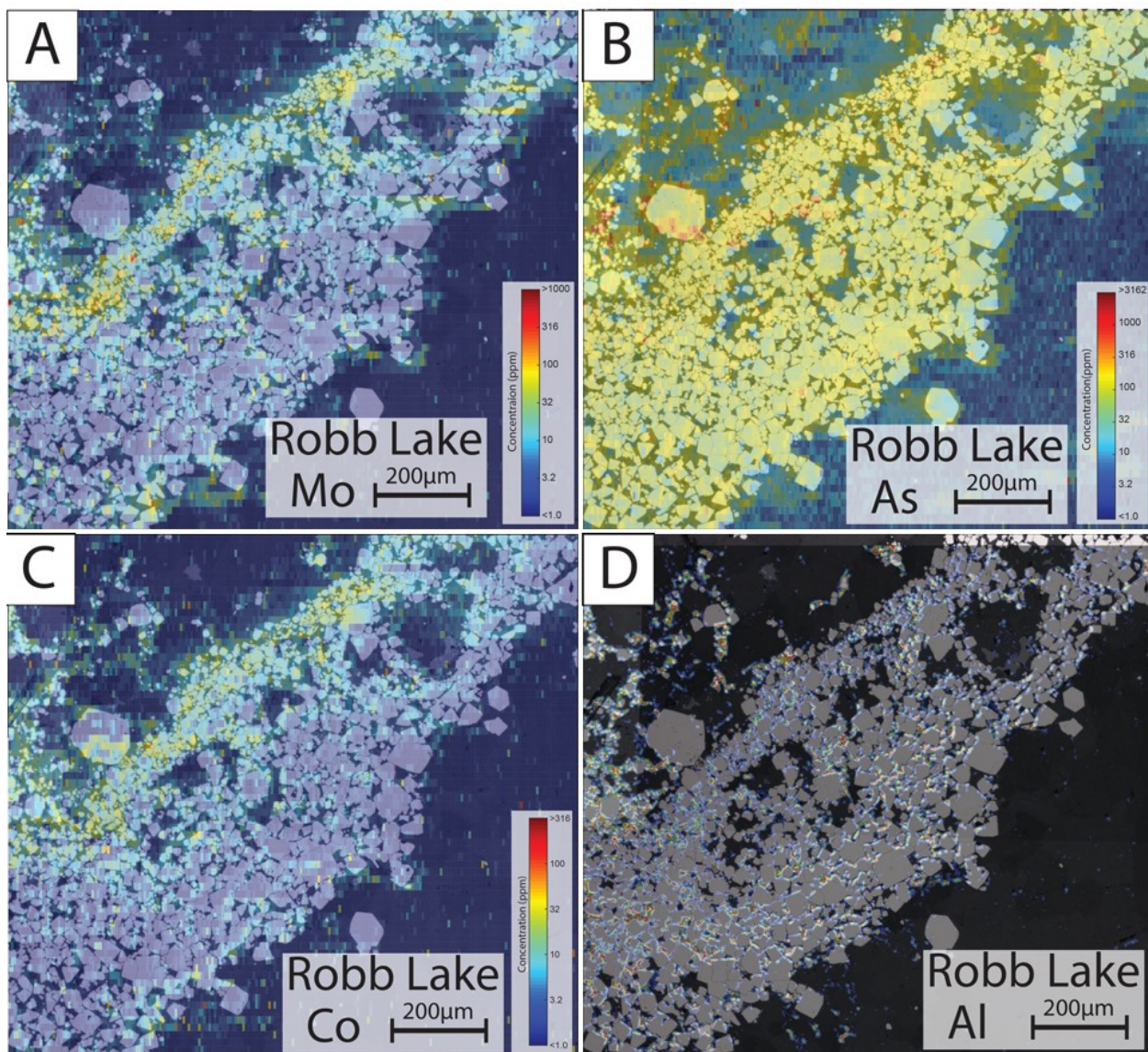


Figure 5.17: Compositional maps for sample DDH 726 from Robb Lake. (A) LA-ICPMS molybdenum map. (B) LA-ICPMS arsenic map. (C) LA-ICPMS cobalt map. (D) EMPA aluminium map. Hotter colours represent higher concentrations.

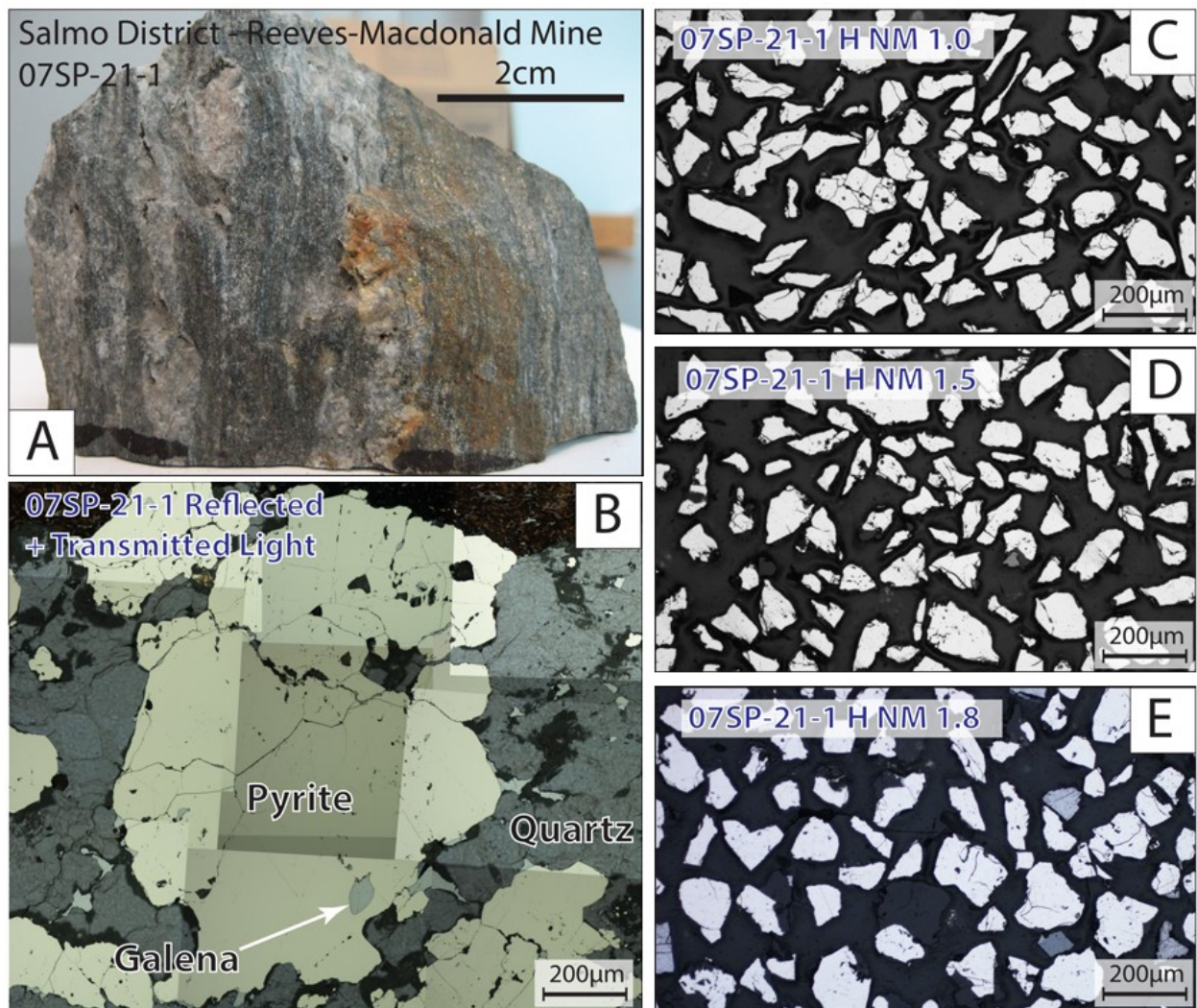


Figure 5.18: Sample 07SP-21-1 from the Reeves-Macdonald mine from the Salmo district (A) Hand sample specimen (B) Reflected light + transmitted light image of 07SP-21-1. (C)-(E) Reflected light images of mineral separates. The scaling of Figures B-E is identical.

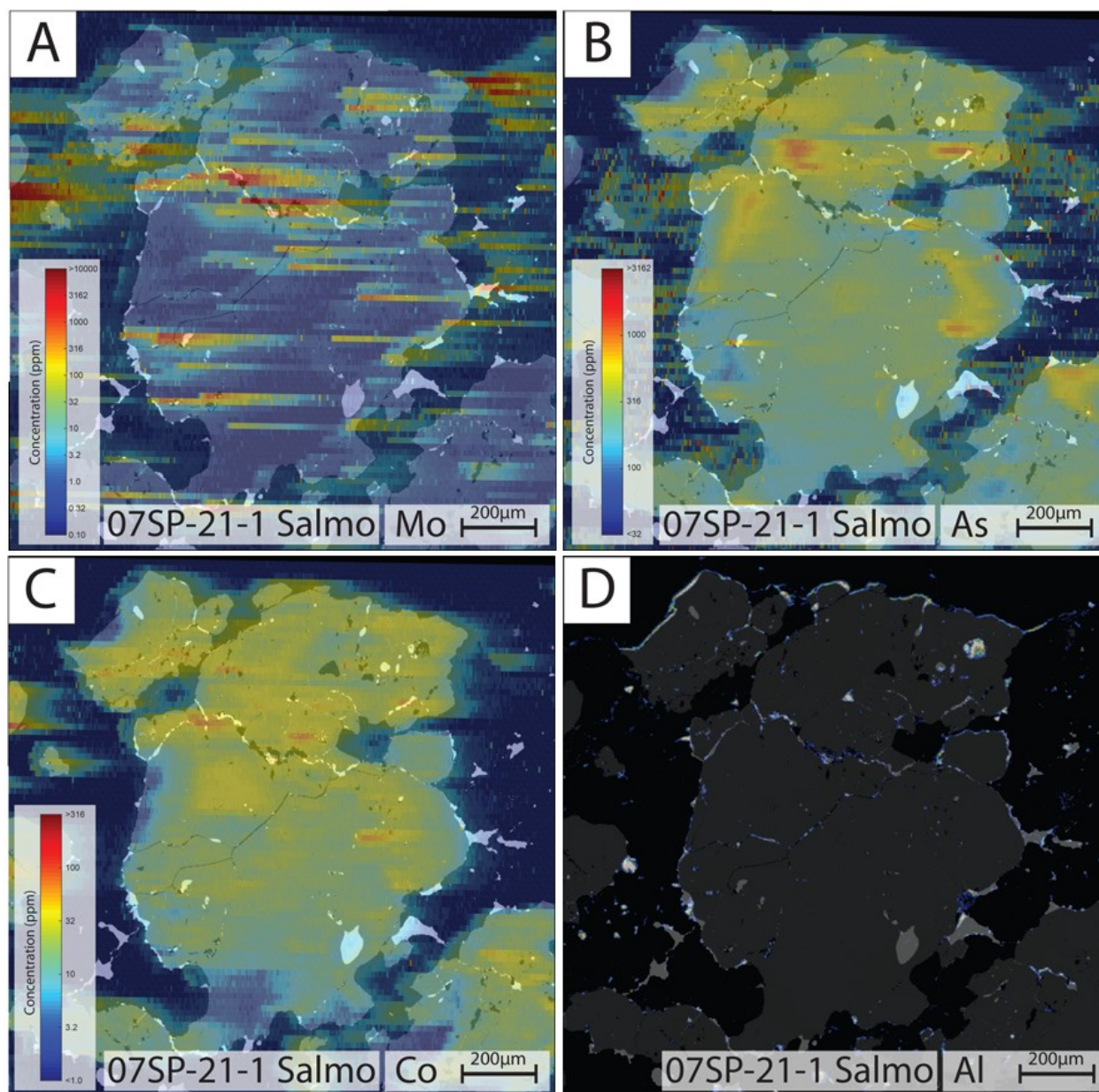


Figure 5.19: Compositional maps for 07SP-21-1 from the Reeves-Macdonald mine from the Salmo district. (A) LA-ICPMS molybdenum map. The horizontal smearing of the images is an artefact of the sample acquisition. These smeared out lines likely represent single pixel spikes in Mo concentrations located near on left edge of each line. (B) LA-ICPMS arsenic map. (C) LA-ICPMS cobalt map. (D) EMPA aluminium map. Hotter colours represent higher concentrations.

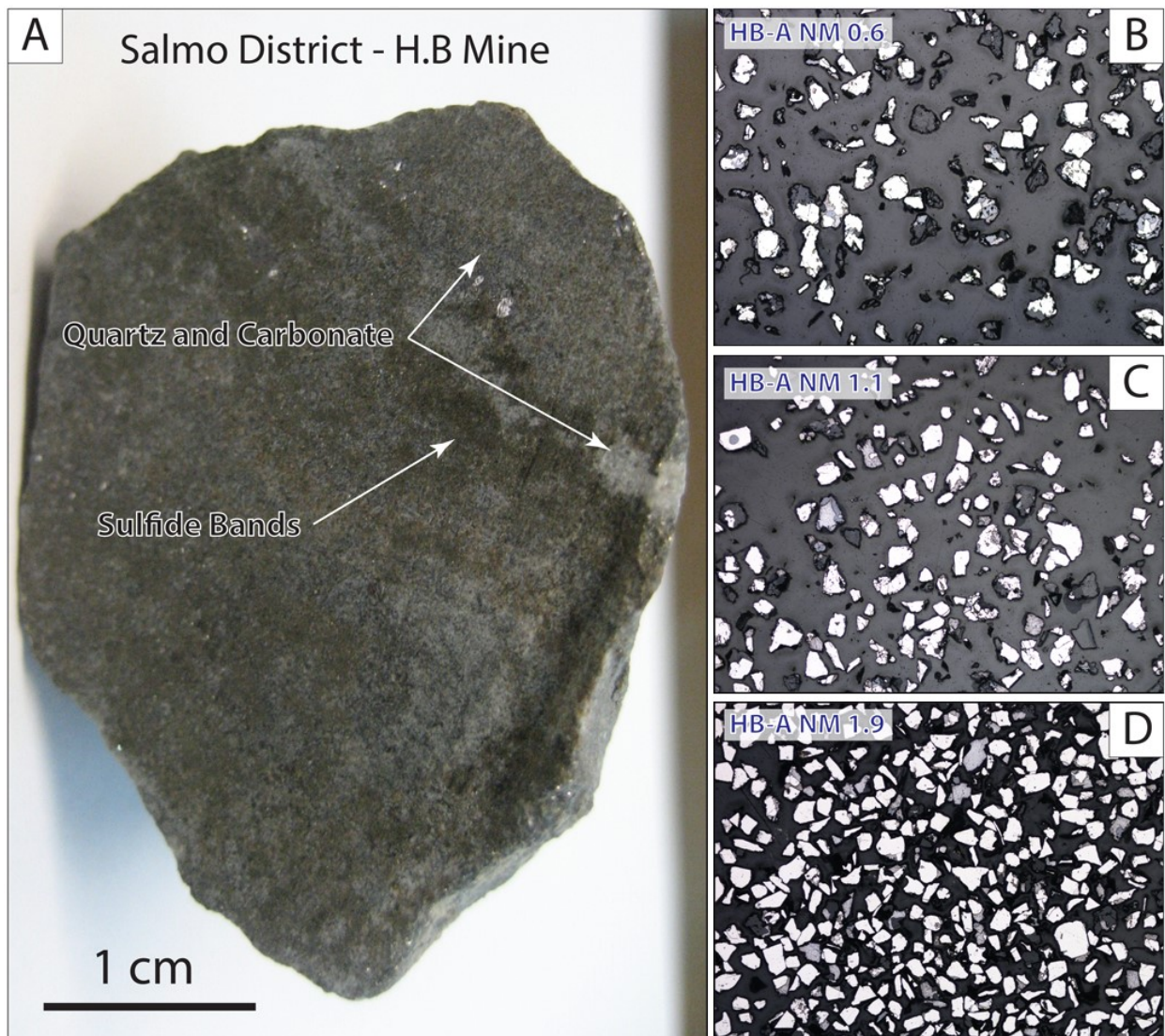


Figure 5.20: Sample HB from the H.B. mine from the Salmo district (A) Hand sample specimen (B) Reflected light image of mineral separates. All mineral separates contain significant impurities.

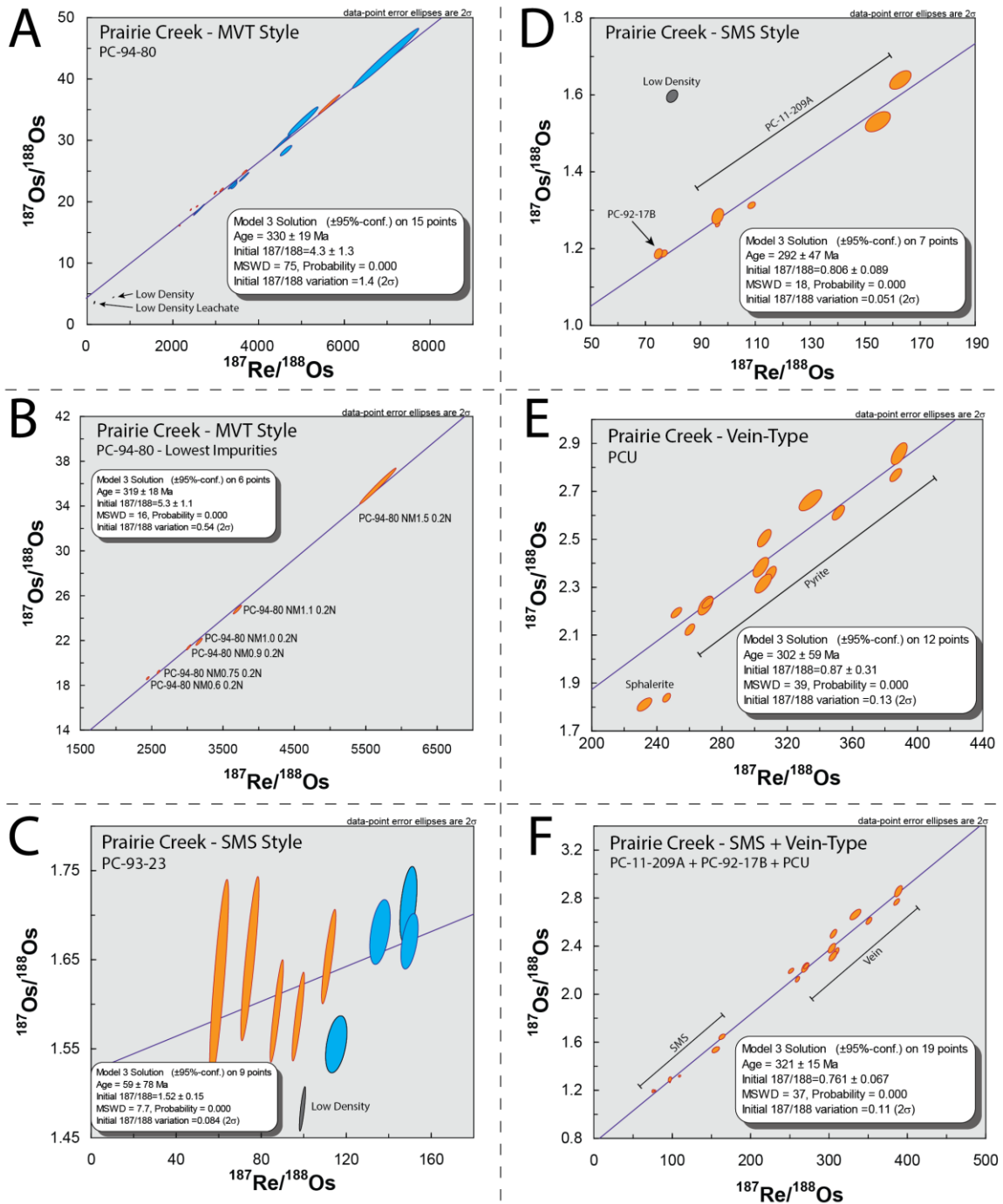


Figure 5.21: (A) Model 3 isochron for Prairie Creek sample PC-94-80 (MVT) excluding the "Low Density" and "Low Density Leachate" data points. (B) Model 3 isochron of sample PC-94-80 (MVT) using only samples that are considered to have the lowest abundance of impurities. (C) Model 3 Isochron for Prairie Creek sample PC-93-25 (SMS) excluding the "Low Density" data point. (D) Model 3 isochron for Prairie Creek sample PC-11-209A (SMS) excluding the "Low Density" data point. (E) Model 3 isochron for Prairie Creek sample PCU (Vein-Type) excluding the sphalerite data points. (F) Model 3 isochron using the combined data from SMS and Vein-Type mineralization, excluding sample PC-93-25. Orange ellipses represent leached data points, blue ellipses represent non-leached data points, and grey ellipses represent data points from low density mineral separates.

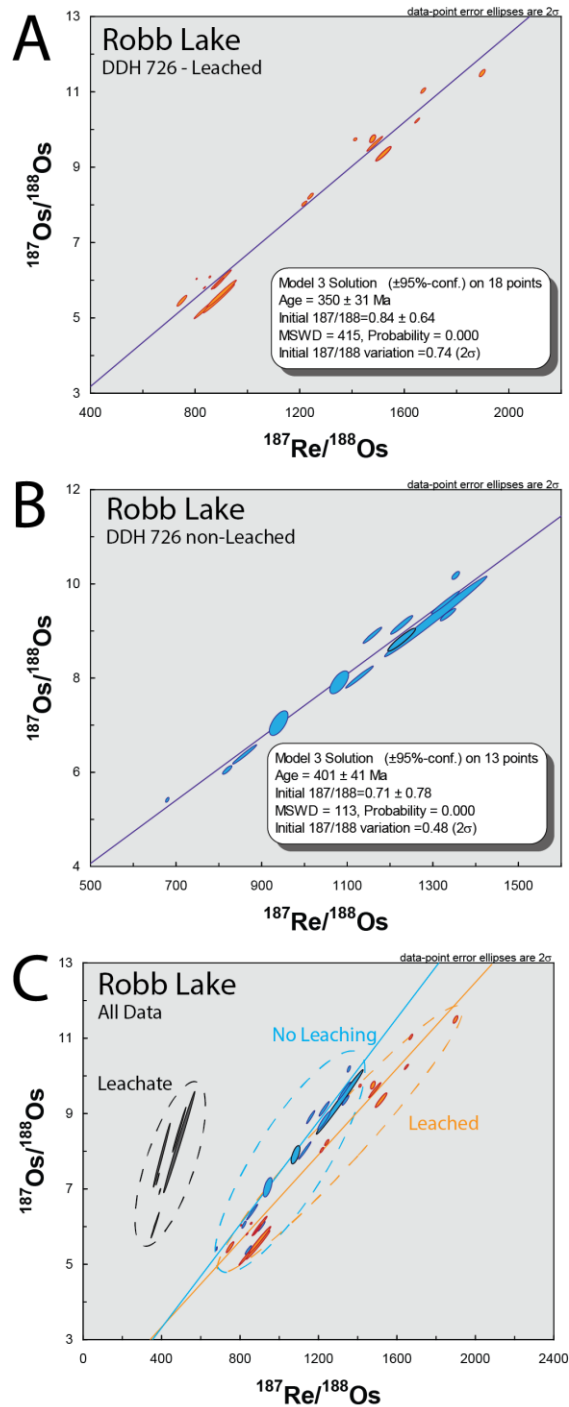


Figure 5.22: (A) Model 3 isochron for Robb Lake sample DDH 726 for leached data points. (B) Model 3 isochron for Robb Lake sample DDH 726 for non-leached data points. (C) Compiled data of leached data, non-leached data, and leachate data. Orange ellipses represent leached data points, blue ellipses represent non-leached data points, and grey ellipses represent leachate data points.

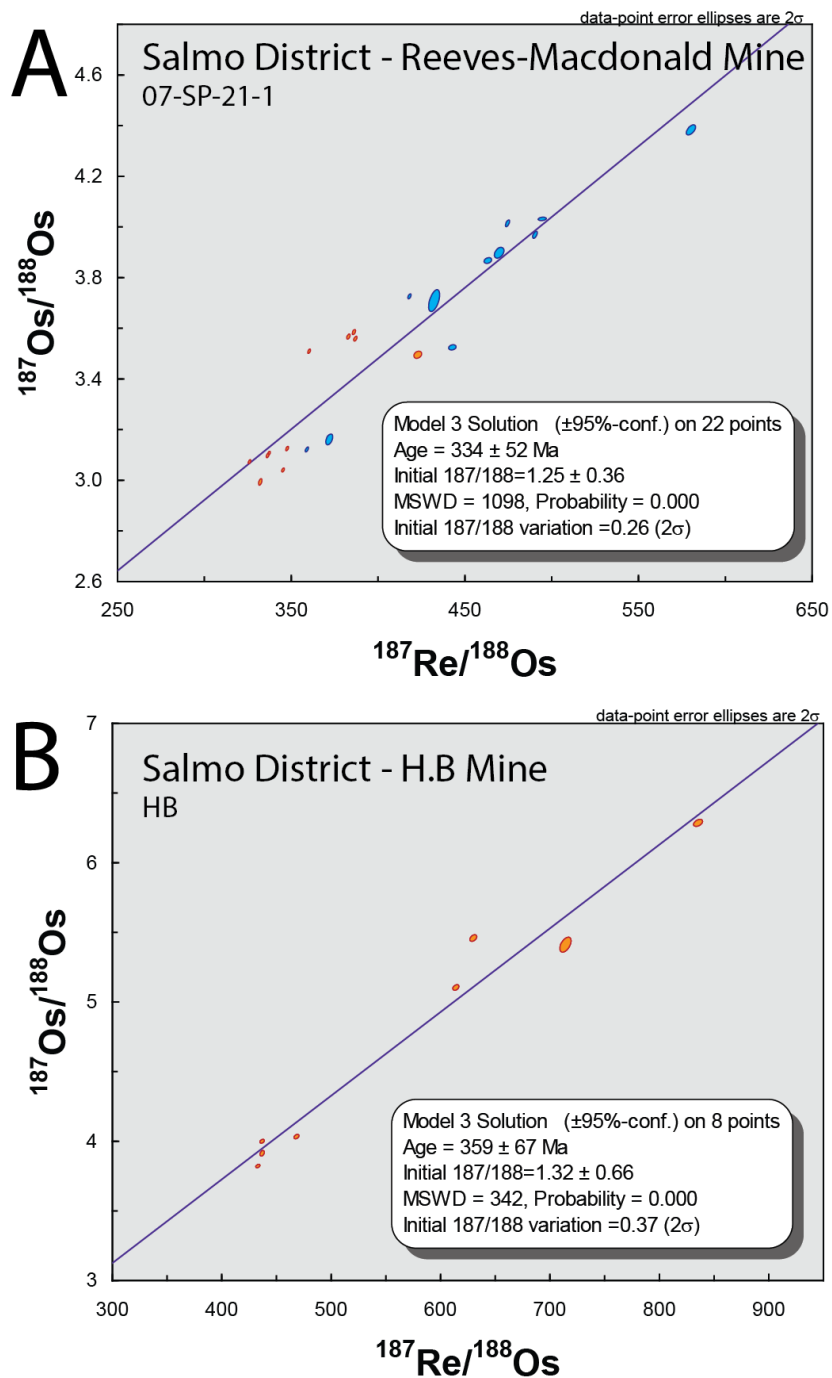


Figure 5.23: (A) Model 3 isochron for the Reeves-Macdonald mine (B) Model 3 isochron for the H.B. mine. Orange ellipses represent leached data points, blue ellipses represent non-leached data points.

Select Geologic Events of the Phanerozoic Canadian Cordillera

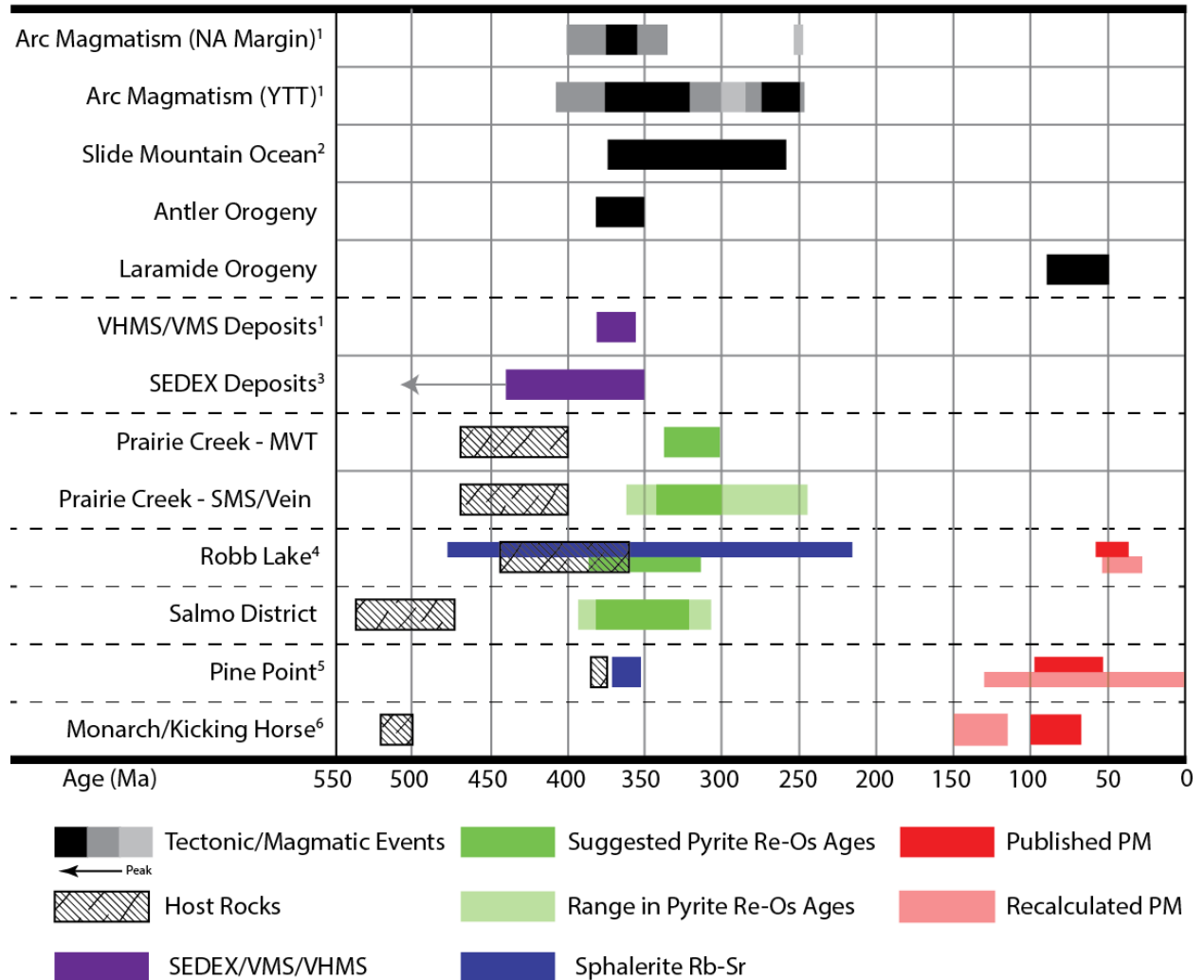


Figure 5.24: Summary of important geologic events associated with Zn-Pb mineralization within and around the Canadian Cordillera. All Re-Os data was collected in this study. Published PM refers to paleomagnetic dates as originally published. Recalculated PM refers to the recalculation of the paleomagnetic dates using approaches of Hnatyshin and Kravchinsky (2014). ¹From data compiled by Nelson et al. (2006), ²From data compiled by Nelson and Colpron (2007), ³Abbot et al. (1986) & Paradis et al. (1998), ⁴Rb-Sr dating by Nelson et al. (2002), paleomagnetic dating by Smethurst et al. (1999), ⁵Rb-Sr dating by Nakai et al. (1993), paleomagnetic dating by Symons et al. (1993), ⁶paleomagnetic dating by Symons et al. (1996).

5.9: Appendix:

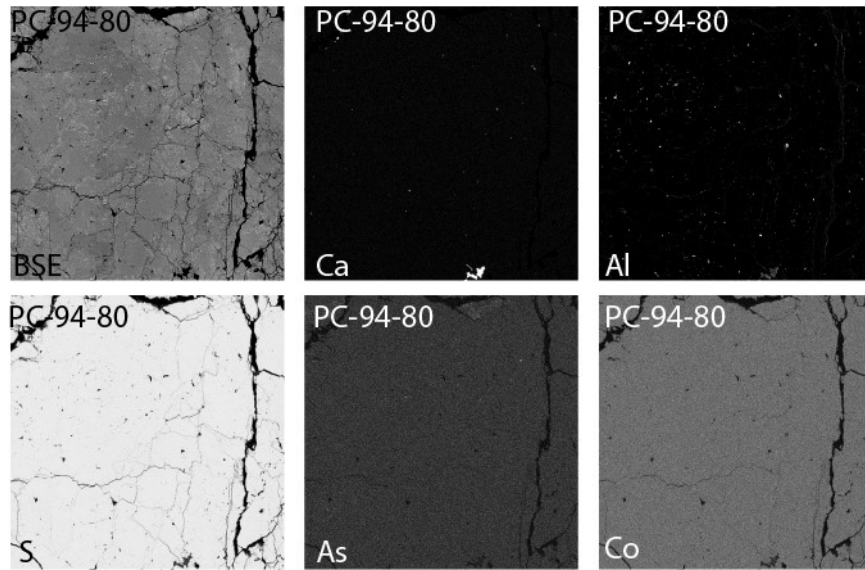


Figure 5.25: Greyscale EMPA images for Prairie Creek sample PC-94-80.

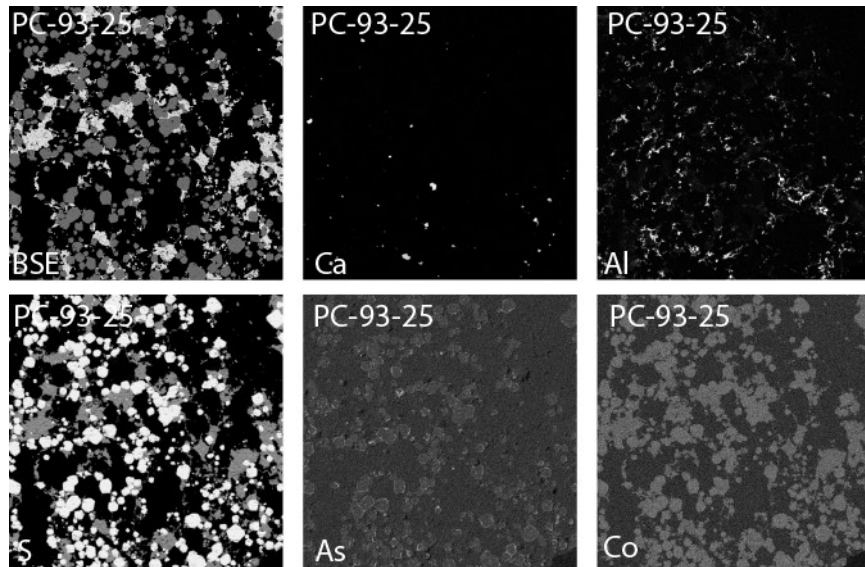


Figure 5.26: Greyscale EMPA images for Prairie Creek sample PC-93-25.

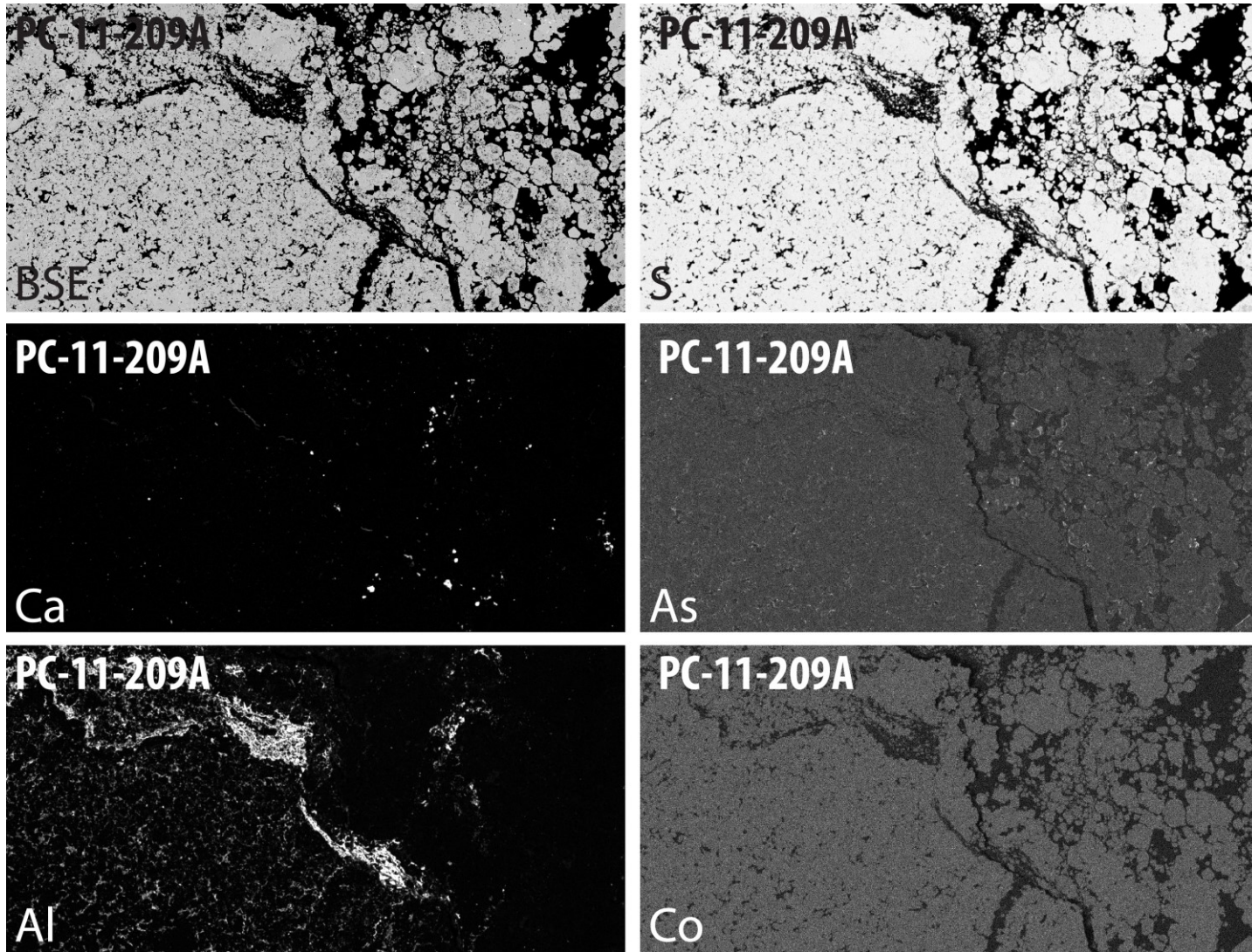


Figure 5.27: Greyscale EMPA images for Prairie Creek sample PC-93-25.

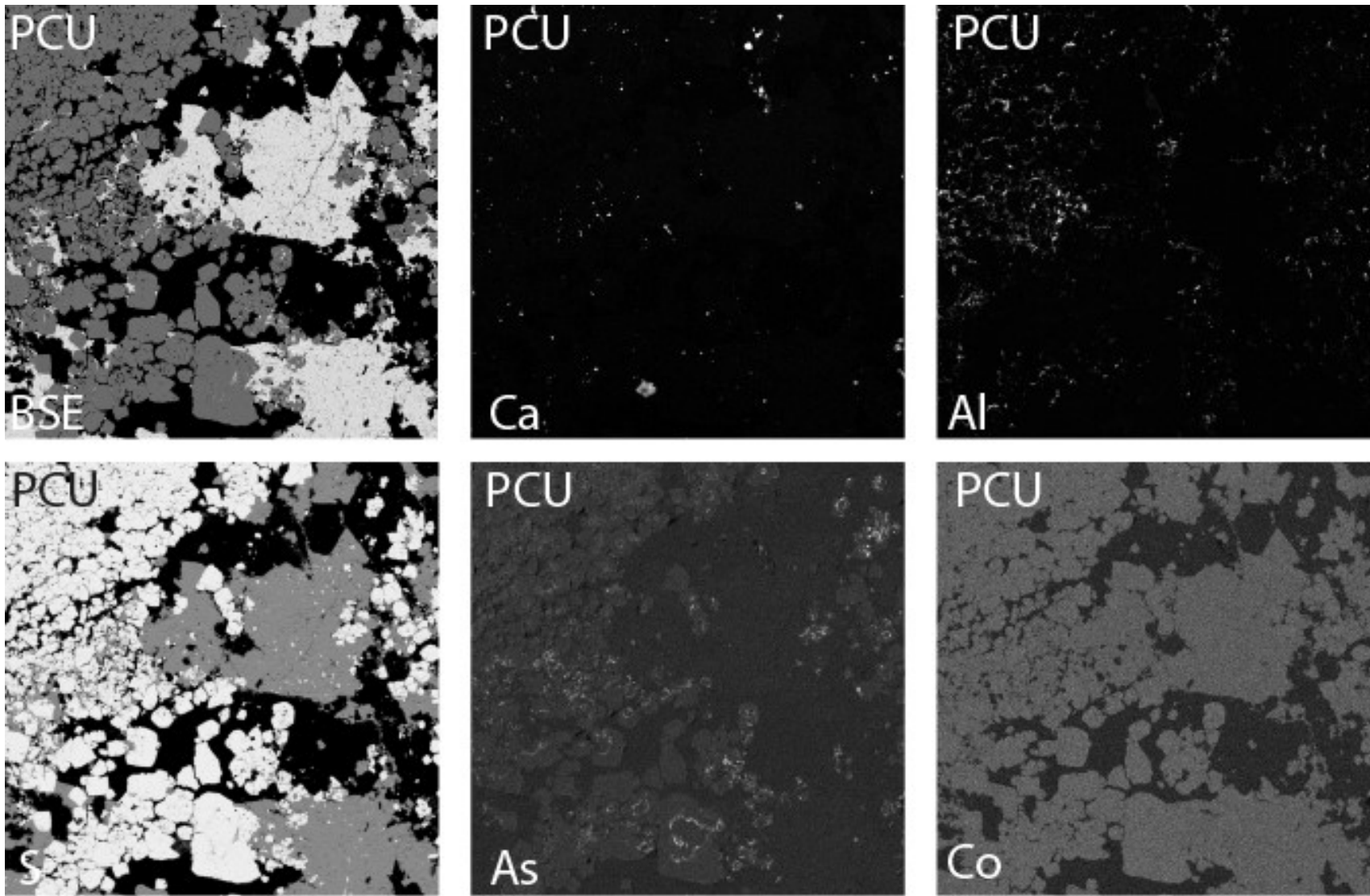


Figure 5.28: Greyscale EMPA images for Prairie Creek sample PCU.

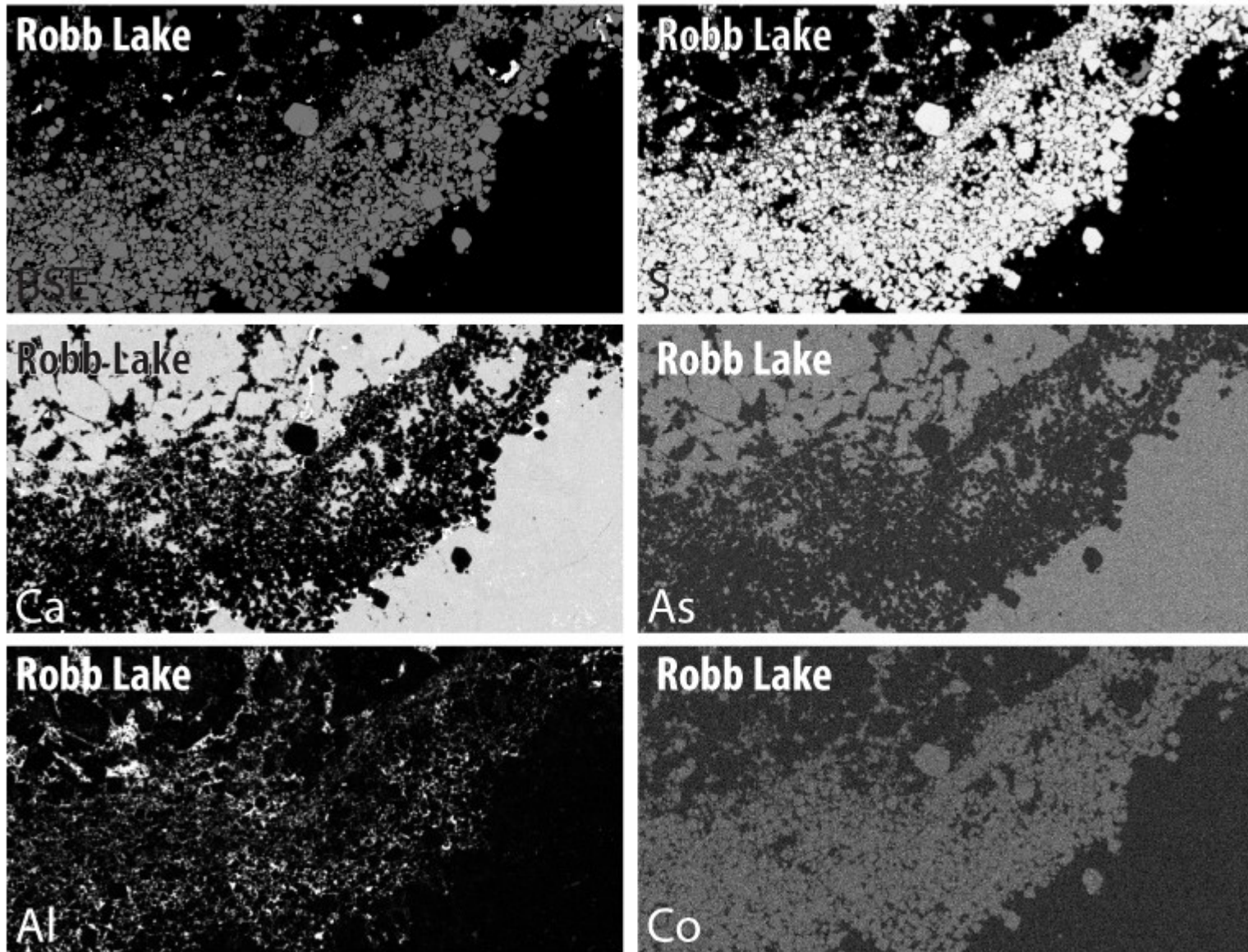


Figure 5.29: Greyscale EMPA images for Robb Lake sample DDH.

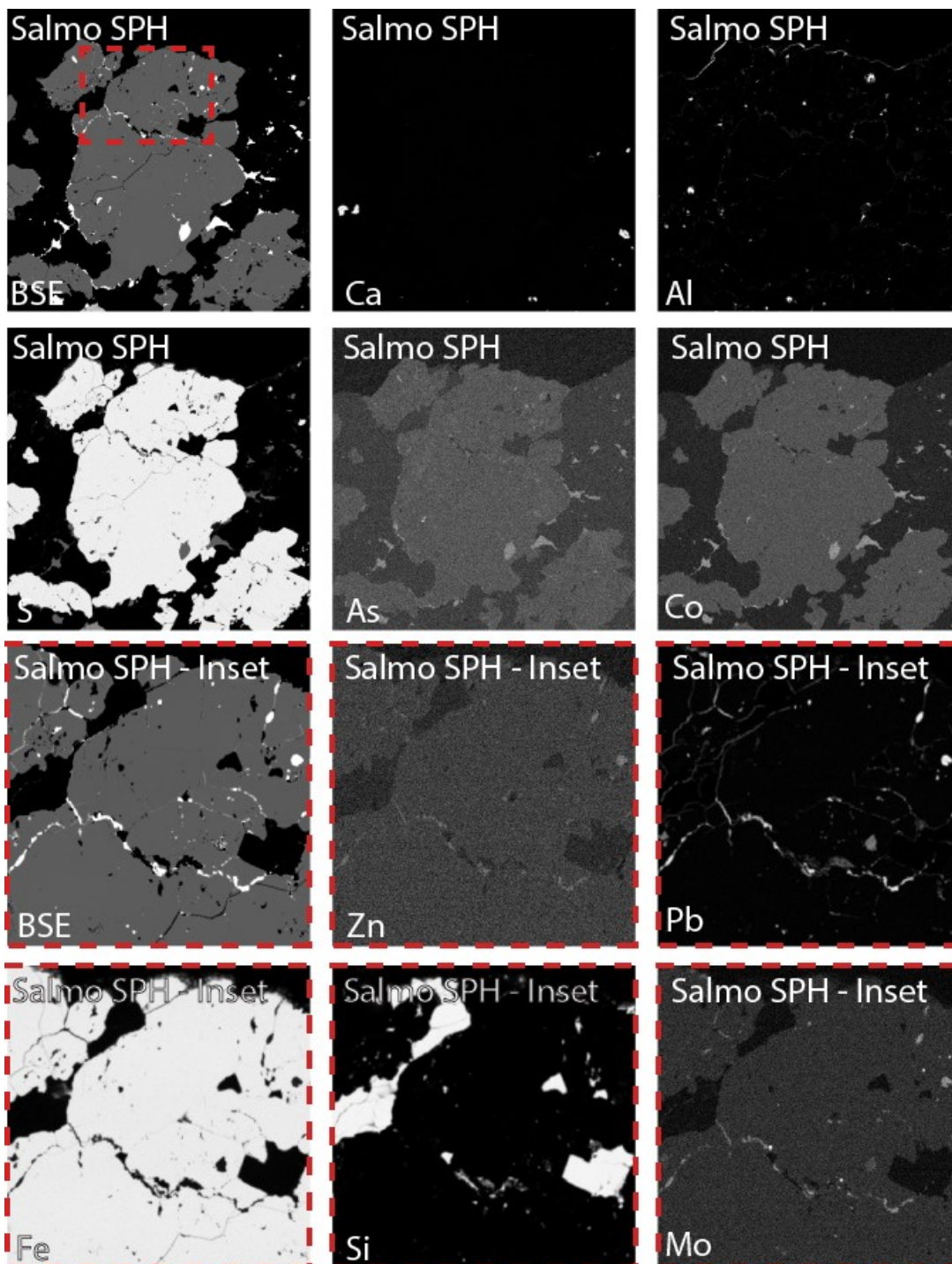


Figure 5.30: Greyscale EMPA images for Salmo district sample SPH. Images bounded by a red dashed box indicate inset images, with the location indicated on the BSE image.

Prairie Creek sample 92-17B - SMS mineralization

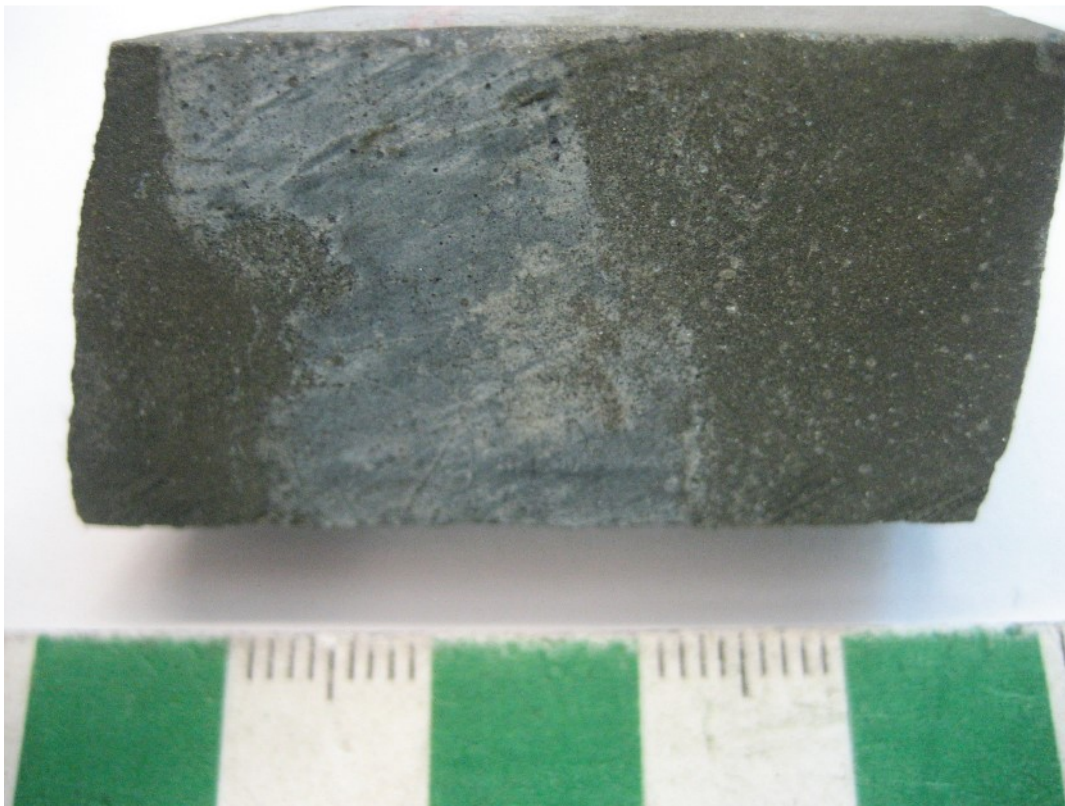


Figure 5.31: Hand sample of Prairie Creek sample 92-17B from SMS-style mineralization.

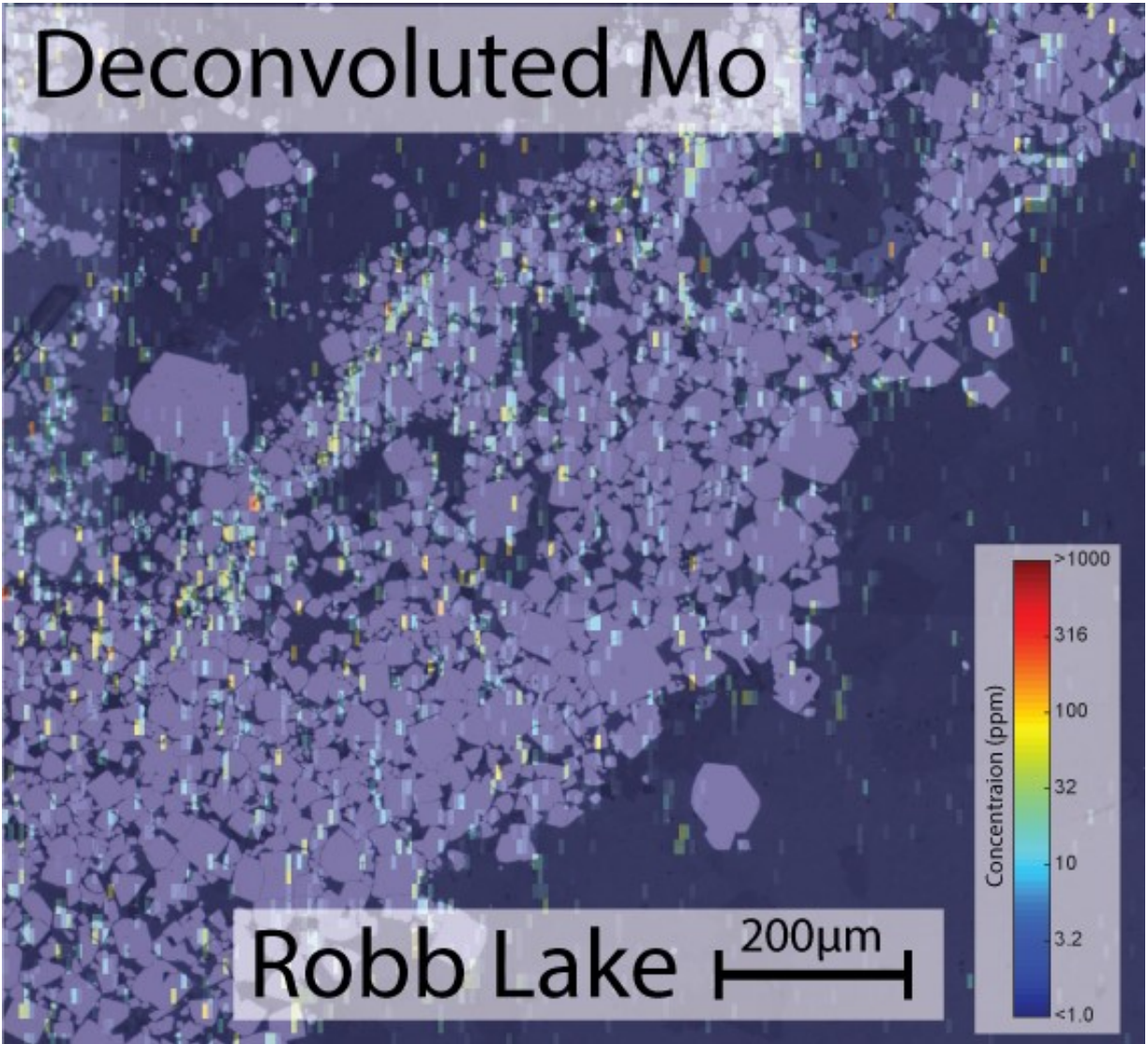


Figure 5.32: Compositional map for sample DDH 726 from Robb Lake. LA-ICPMS Mo map that was deconvoluted from the original image in Fig. 4.17. Hotter colours represent higher concentrations.

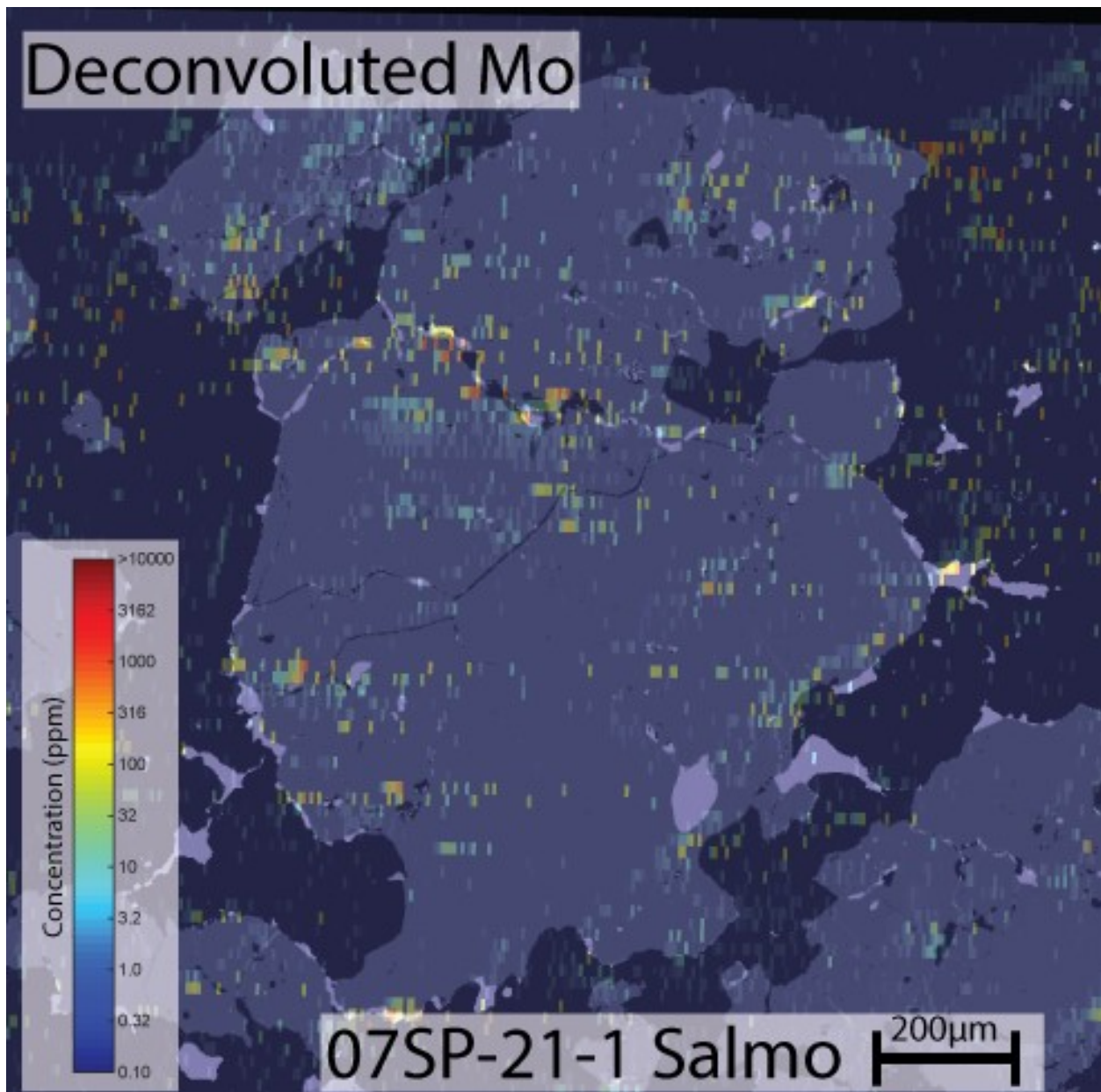


Figure 5.33: Compositional map for sample DDH 726 from Robb Lake. LA-ICPMS Mo map that was deconvoluted from the original image in Fig. 4.17. Hotter colours represent higher concentrations.

6.0: Rhenium-Osmium Isotopic systematics of surface, shallow and deep groundwater from the Western Canada Sedimentary Basin (WCSB)

6.1: Introduction

Using the Re-Os isotopic system to study Earth systems processes is becoming increasingly commonplace, with mantle geochemistry, cosmochemistry, and crustal geochronology being common applications. With current analytical capabilities it is now feasible to develop the Os isotopic system for geochemical and environmental tracing. For isotopic tracing to be viable it is critical to define different reservoirs (e.g. mantle, crust, and ocean) and to determine how an element is transported between, and within, these reservoirs (e.g. rivers, hydrothermal fluids, and groundwater; Fig. 6.1). Arguably the most poorly constrained of these for the Re-Os isotopic system is its behaviour during groundwater transport in sedimentary basins, as no datasets currently exist for fluids contained within deep confined aquifers in continental sedimentary basins.

For this study we have chosen to analyze waters surface waters from the Athabasca River in Alberta, Canada to optimized the analytical protocol for measuring Re-Os in natural waters. Following the development of proper analytical protocols the project focused on obtaining samples from most of the major aquifers of the Williston Basin in Saskatchewan, Canada. The dataset produced from these analyses provide the first constraints on the Os isotopic variability within the deep pore waters of a continental sedimentary basin. Several secondary objectives of this study included (1) Testing the oil-water partitioning of Re and Os in natural situations by sampling co-produced water and oil. (2) Establishing constraints on the sources of Os found in basinal sediment-hosted ore deposits. (3) Testing the applicability of using Os isotopes for geochemical or environmental tracing.

6.2: Re-Os Reservoirs and Transportation

Osmium is a platinum group element that has its isotopic composition influenced by the radioactive decay of ^{187}Re to ^{187}Os (half life of 42 billion years, Smoliar et al., 1996). Both Re and Os are siderophile in nature and therefore are primarily sequestered in the mantle and core

(Brenan and McDonough, 2005, 2009). Current estimates put the $^{187}\text{Os}/^{188}\text{Os}$ composition of the primitive upper mantle at approximately 0.1296 with a $^{187}\text{Re}/^{188}\text{Os}$ value of less than 1 (Meisel et al., 2001). During partial melting, Re behaves more incompatibly than Os (Shirley and Walker, 1998) allowing $^{187}\text{Os}/^{188}\text{Os}$ to evolve to a much higher value in the crust than the mantle. Whereas the average $^{187}\text{Os}/^{188}\text{Os}$ of the average continental crust is quite poorly constrained, a $^{187}\text{Os}/^{188}\text{Os}$ of 1.40 ± 0.30 based on Os isotopic measurements of loess is commonly cited (Peucker-Ehrenbrink and Jahn, 2001). Weathering of crustal material results in the mobilization of Re and Os into rivers, which, are in turn important inputs into both the groundwater and oceanic system. River systems show a large range of Os isotopic compositions ($^{187}\text{Os}/^{188}\text{Os} = 0.17 - 2.94$) and concentrations (3 - 41.8 parts per quadrillion (ppq)) reflecting the variety of potential sources of Os present along the river's flow path (Levasseur et al., 1999, 2000; Sharma et al., 1999; Sharma et al., 2007a). Shallow groundwater systems (< 74 m) appear to contain comparable Os isotopic signatures, but at higher concentrations, to that of local river systems (Paul et al., 2010). Direct measurements of active hydrothermal vents from the Juan de Fuca Ridge ($^{187}\text{Os}/^{188}\text{Os} = 0.135 - 0.387$; Sharma et al., 2000; Sharma et al., 2007b) are consistent with mixing of a mantle $^{187}\text{Os}/^{188}\text{Os}$ end member with ambient seawater values ($^{187}\text{Os}/^{188}\text{Os} = 1.05$, [Os] = 10.4 ppq; Sharma et al., 2007b). Seawater in general is a very homogenous reservoir with $^{187}\text{Os}/^{188}\text{Os}$ values of 1.02 - 1.07 at concentrations of 6.8 to 10.4 ppq reported in the literature (Woodhouse et al., 1999; Sharma et al., 2007b; Gannoun and Burton, 2014).

The organophilic nature of Re and Os can result in localized enrichments of these elements in either sediments or living organisms (e.g. Ravizza et al., 1991; Racionero-Gomez et al., 2017). Upon thermal maturation of the organic matter and production of petroleum, Re and Os become preferentially sequestered inside the asphaltene portion of the petroleum products (Selby et al., 2007; Georgiev et al., 2016; DiMarzio et al., 2018). As both Re and Os are also chalcophile they can also be enriched upon the precipitation of sulphides from fluids or magma (Crocket et al., 1992). Hence, the accumulation of sulphides that comprise metallic ore deposits will be an important local sink for Re and Os.

6.3: Speciation in Aqueous Solutions

Both Re and Os can exist in a number of different valence states depending on the redox conditions present within a solution. The behavior of Re, and to a lesser extent Os, have been

tested under both oxic and anoxic conditions with recent summaries provided in Yamashita et al. (2007) and Vorlicek (2012).

In oxic conditions, Re is a conservative solute existing as $\text{Re}^{\text{VII}}\text{O}_4^-$ (Anbar et al., 1992; Hodge et al., 1996), although experiments on synthetic oxygenated groundwater containing $\text{Re}^{\text{VII}}\text{O}_4^-$ show that Re can be mildly adsorbed into bentonite clays (Vinsova et al., 2004). Under reducing conditions, Re is thought to convert to $\text{Re}^{\text{IV}}(\text{OH})_4$ or $\text{Re}^{\text{VII}}\text{O}_{4-x}\text{S}_x^-$ if reduced sulphur is available (Xiong, 2003; Tossel, 2005; Chappaz et al., 2008; Helz and Dolor, 2012). Seawater-sediment interface experiments have shown that Re is gradually removed from the aqueous phase during reduction by organic compounds or sulphides found in sediment (e.g. Yamashita et al., 2007; Chappaz et al., 2008). This behavior accounts for accumulation of Re in organic rich sediments (e.g. Ravizza et al., 1991; Chappaz et al., 2008).

In oxygenated environments (e.g. open ocean), Os may exist in its fully oxidized state (e.g. $\text{H}_3\text{Os}^{\text{VIII}}\text{O}_6^{2-}$) although more reduced species (e.g. $\text{Os}^{\text{VI}}\text{O}_4^{2-}$) cannot be discounted (Woodhouse et al., 1999). Interaction with reduced metals (e.g. Fe^{2+} , Mn^{2+}) are expected to reduce Os^{8+} to the Os^{4+} state resulting in chloride or hydroxyl complexes. The hydroxyl complexes are thought to aid in the accumulation of Os in ferromanganese oxides and may allow Os to adsorb onto clays (e.g. Palmer et al., 1988, McDaniel et al., 2004; Yamashita et al., 2007). When organic matter is the reducing agent, as may be the case in anoxic environments, Os may be reduced into insoluble Os^{3+} , resulting in its incorporation within organic compounds in sediment (Yamashita et al., 2007).

6.4: Sampling Locations

The first sample set consists of archived surface water and shallow groundwater from the Athabasca river system near Fort McMurray, Alberta (see Shotyk et al., 2017 for details), which provide a baseline value for near-surface waters, as well as being used to test and refine the methodology developed for this study. The majority of basinal water samples were collected from oil wells and water source wells from the Williston Basin located in the southern half of Saskatchewan during the summers of 2016 and 2017 (Fig. 6.2). The entire sampling program was designed to collect water from all major aquifers of the Williston Basin, however due to the logistics of the sampling program, the lateral extent of sampling occurred over thousands of square kilometres (Figs. 6.2-6.3; Table 6.1). Tertiary (Ravenscrag Formation) and Cretaceous

(Belly River, Viking, and Mannville formations) clastic-dominated aquifers represent formations that lie above the major oil reservoirs in Saskatchewan. The water collected from the Belly River Formation represent pore waters that are far travelled, having migrated east from Alberta (Singh et al., 2014) over 300 km away. The Viking Formation at the sampling location is part of a flow regime that transports water north from Montana, and east of the Viking oil fields in Saskatchewan (Jensen et al., 2015). The Cretaceous formations are all known to be oil reservoirs to the west in Alberta (Belly River, Mannville) and Saskatchewan (Viking), but do not hold appreciable reserves in the sampling area (Dawson et al., 1994; Hayes et al., 1994). Below the Mannville are several oil reservoirs that were sampled. The Jurassic carbonate-dominated Shaunavon Formation represents the shallowest oil well sample collected in this study. Both oil wells (Ratcliffe Formation) and water source wells were sampled from the carbonate-dominated Mississippian Madison Group. The clastic-dominated Upper Devonian Bakken Formation underlies the Madison Group and was sampled using oil wells. Other carbonate-dominated Upper Devonian formations that were sampled include the Birdbear Formation (oil well) and the Duperow Formation, which represents the deepest water source well collected during field work, and the Middle Devonian Winnipegosis Formation. Jurassic and older aquifers are part of a regional flow system in which water is currently migrating north from Montana (Jensen et al., 2015). The Ordovician-Cambrian formations that directly overlie the Precambrian basement could not be accessed during field work, therefore archived samples of these formations were obtained from the University of Alberta.

6.5: Sampling Protocol

All materials required for sample collection and storage were thoroughly cleaned using a similar process to that recommended by Sharma et al. (2012) and Gannoun and Burton (2014). At each well site the samples were collected in pre-cleaned 8L plastic jugs prior to being transferred to pre-cleaned 125mL Teflon bottles for permanent storage. These plastic jugs were cleaned by filling them with soapy water and letting them sit for ~24 hrs. Each jug was then rinsed 3 times with MQ water and then filled with MQ water for an additional 24 hours. The jugs were then emptied and rinsed three more times with MQ water. The Teflon bottles used for permanent storage were cleaned using the following steps: (1) Rinsed with acetone, (2) soaked in soapy water for ~24 hrs, (3) rinsed 3 times with MQ water, (4) cleaned with Seastar 9N HBr by

adding ~10mL of acid to the bottle and letting it sit for ~ 7 days at ~80°C, (5) rinsed 3 times with MQ water, (6) cleaned by adding ~10 mL of MQ water to the bottle and letting it sit for ~ 7 days at ~80°C, and (7) rinsed 3 times with MQ water.

The collection process begins with purging the first several litres of water produced at the well site to remove any debris and stagnant water within the piping system. Approximately 4L of water was then collected from each well site and stored for a short time (< 8 hrs) in the pre-cleaned 8L plastic jugs. During this time the samples were allowed to degas any H₂S dissolved within the water.

Water co-produced with oil requires extensive filtering to extract oil free water. For these samples, the water-oil mixture were poured through a plastic funnel containing glass wool, this processes was repeated several times until the oil was removed. Once the oil is removed, all samples were then filtered into the pre-cleaned 125mL Teflon bottles by hand using a 0.45µm cellulose acetate filter attached to a plastic syringe. All samples were then acidified with the equivalent of 5 mL of 6N HCl. Any oil that was co-produced with the water was collected and stored in 50mL glass tubes.

Archived Athabasca River system samples were collected in rinsed Teflon bottles. Archived Williston Basin samples used for this study had been stored in HDPE bottles or glass vials for timeframes of many years. Unfortunately, experiments by Sharma et al. (2012) show that HDPE bottles can in some cases cause sorption of Os onto the bottle walls while releasing Os contained within the plastic into solution. In their experiments the concentration and isotopic ratios of seawater could be affected by close to 10% for water stored for one year. Therefore all data collected from archived samples cannot be guaranteed to represent pristine isotopic compositions and concentrations.

6.6: Analytical Procedures

Re-Os analyses on water and oil samples were carried out at the Crustal Re-Os Geochronology Laboratory at the University of Alberta. For oil samples, 10-100 mg of asphaltene was extracted from crude oil using a procedure very similar to that described by Selby et al. (2007). The asphaltene was then chemically processed using the methods outlined in Hnatyshin et al. (2016). Water samples (25-35mL) were prepared for digestion in a specific manner to minimize the risk of the oxidizing agent (CrO₃) reacting with the sample or spike Re-

Os prior to sealing and incubation (Fig. 6.4). For this study the sample-spike solution was oxidized and equilibrated using a $\text{CrO}_3\text{-H}_2\text{SO}_4$ solution (0.008 - 0.24g CrO_3 in 0.1-3mL of 4N H_2SO_4) and reacted at 240°C for 72 hrs. These conditions were chosen as lower temperatures and shorter durations run the risk of incomplete oxidation (Gannoun and Burton, 2014). The Os is extracted and chemically processed as outlined in Hnatyshin et al. (2016). After Os is removed from the digested sample the Re is purified using a modified version of the acetone-NaOH extraction method outlined in Du et al. (2004). In our modified version we added ~10 mL of pre-cleaned ~17N NaOH directly to 20 mL of the digested solution. Once these solutions are thoroughly mixed acetone is then added to extract the Re from the NaOH-sample solution. The acetone is then transferred to a 22mL glass vial and dried down at 55°C. The sample is further purified using anion exchange chromatography and resin bead clean up as outlined in Hnatyshin et al. (2016). We note that it has been recommended by some studies that anion exchange chromatography and bead clean up are not necessary and can adversely affect the intensity of Re during isotopic analysis (Wang et al., 2013; Georgiev et al., 2018). However, the high salinity of many of these water sample necessitates the use of additional purification. Isotopic measurements on chemically purified Re and Os were carried out using negative-TIMS as outlined by Hnatyshin et al. (2016).

Elemental analysis of each water sample collected for this study was analyzed using a Perkin Elmer Elan 6000 Quadrupole Inductively Coupled Plasma Mass Spectrometer (ICPMS) at the University of Alberta.

6.7: Analysis

The samples collected in this study are analytically challenging with count rates for the isotopes of ^{187}Os and ^{188}Os generally being below 1000 cps on a secondary electron multiplier (SEM). Similarly, the Re measurements for many samples required the use of a SEM, not Faraday cup detectors that are commonly used to measure Re during TIMS analysis. In addition to analytical uncertainties, the isotopic data produced is strongly affected by blank contribution. For the samples collected in 2016 (16-XXX) the blank correction was 0.089 ± 0.058 pg for Os at a $^{187}\text{Os}\text{-}^{188}\text{Os}$ ratio of 0.21 ± 0.063 and 3.6 ± 2.7 pg for Re. For archived samples and samples collected in 2017 (17-XXX, 01-XXX) the Os blank correction is 0.068 ± 0.046 pg at a $^{187}\text{Os}\text{-}^{188}\text{Os}$ ratio of 0.39 ± 0.18 , with the Re correction being 5.9 ± 4.0 pg. For many samples, applying

these blank corrections produce overcorrected values resulting in negative concentrations and/or isotopic ratios. The sources of the blank Os is likely heavily influenced by the platinum wire used in TIMS analysis as varying the amount of reagents used during chemistry does not appear to influence the Os blank. The Re blank values are primarily from the use of NaOH during the Re extraction procedure. As a result of the blank corrections and low count rates the uncertainty on $^{187}\text{Os}/^{188}\text{Os}$ can be extremely large. Only water samples that contain ≥ 10 ppq have $^{187}\text{Os}/^{188}\text{Os}$ values we consider reliable.

6.8: Results

The Re-Os data produced is compiled in Table 6.2 and are presented in Fig. 6.3, with cation concentrations for water samples presented in the Appendix (Table 6.3). The Athabasca River system contain $^{187}\text{Os}/^{188}\text{Os}$ of 2.1 ± 0.2 , 22 ± 15 ppq Os, and 3.1 ± 3.0 ppq Re, with higher Os concentrations typically associated with the tributaries and groundwater. For the Williston Basin project, the samples 17-013 Ravenscrag, 17-012 Birdbear Oil, 17-014 Winnipegosis, and 17-016 Winnipegosis are considered contaminated and are not used for the summary below, however they will be discussed in the next section. Concentrations of Os from water source wells vary from 95 ppq to below detection limits (~ 1 ppq), however only the shallowest aquifers (Ravenscrag and Belly River) have concentrations exceeding 5 ppq. With the exception of one Ravenscrag sample (17-015) which shows 56737 ppq Re, all other samples have Re below 1220 ppq, with the majority below the detection limit (~ 300 ppq). Oil well waters also contain low concentrations of Re and Os, comparable to what is observed in deeper water source wells. Only the Bakken sample 17-019 contains appreciable Os (10 ppq), with all other samples containing ≤ 5 ppq Os. Rhenium values are below detection limit for the Ratcliffe Formation, Shaunovan Formation, and two Birdbear Formation samples (17-009 and 17-010). Higher Re concentration can be found in the other Birdbear Formation samples and the Bakken Formation, with maximum concentrations of 3253 and 1508 ppq, respectively. For the majority of samples the large blank correction applied resulted in very imprecise and in some cases meaningless $^{187}\text{Os}/^{188}\text{Os}$ values. The shallowest samples, Athabasca River, Ravenscrag Formation (17-015, 17-015rpt), and Belly River Formation (16-101, 16-101rpt, 16-102, 16-102rpt), contain meaningful $^{187}\text{Os}/^{188}\text{Os}$, with average values of 1.75, 1.38 ± 0.06 , and 1.64 ± 0.14 , respectively. One deeper sample from the Winnipeg Formation (13-89) contained more radiogenic osmium

with a value of $^{187}\text{Os}/^{188}\text{Os}$ 10.13 ± 0.19 . All other samples contained significant errors approaching or exceeding 50%.

The asphaltene samples collected from oils are in general highly enriched in Re and Os compared to waters but show extreme variability in concentrations that are unrelated to stratigraphic level (Fig. 6.3). Normalized to the volume of oil used to extract the asphaltene (1-4 mL) Os concentrations in oil vary from 70 ppq (17-019 Bakken Oil) to 10701 ppq (16-012 Shaunavon Oil). Rhenium shows a similar variation of 891 ppq (17-019 Bakken Oil) to 1101379 ppq (16-012 Shaunavon Oil). The average $^{187}\text{Os}/^{188}\text{Os}$ isotopic compositions were determined to be 3.28, 2.58, 1.20, 2.67, and 5.60, for the Shaunavon, Ratcliffe, Bakken, Birdbear (excluding 17-012), and Winnipegosis, respectively.

6.9: Sample Contamination

Due to the nature of oil field operations there is always the potential that samples can be contaminated by well casing, piping, or through the mixing of different fluids during extraction. In our dataset we have identified four suspect samples that may have been contaminated. Sample 17-013 Ravenscrag was collected from a water source well that was not active for the day assigned for sample collection. As a result the well had to be brought up to operation and therefore the sample collected cannot be guaranteed to represent a fresh sample of Ravenscrag Formation water. Furthermore, the nearby (< 2km) 17-015 Ravenscrag sample has a drastically different composition, containing ~ 57000 ppq Re and ~ 95 ppq Os compared to the 17-013 sample that had ~700 ppq Re and ~ 5 ppq Os. Such a drastic change in composition is very unlikely at such short distance scales.

The oil collected from 17-012 Birdbear Oil has a Re-Os ratio of < 1, such an extreme depletion of Re cannot be explained as Re-Os ratios are strictly > 1 for all but mantle rocks, meteorites, and specific mineral accumulations (e.g. ferromanganese oxides). Both the Re-Os ratio and the $^{187}\text{Os}/^{188}\text{Os}$ of 0.18 is anomalous for the interior of a sedimentary basin and are quite different than other samples collected in this study. The preferred explanation for this observation is that metal particles from oil well piping may have become dislodged during pumping and became suspended within the oil during collection, although this is speculative.

The water source wells that collect water from the Ravenscrag Formation (e.g. 17-013, 17-015) are used for the extraction of oil from Winnipegosis wells (e.g. 17-014, 17-016). To test

for possible mixing between Winnipegosis Formation water and injected Ravenscrag Formation archived Winnipegosis Formation waters from these wells were analyzed to test for contamination. Isotopic (i.e. $\delta^{18}\text{O}$, δD) and cation concentrations suggest that 23-25% of the water collected from the Winnipegosis well (17-014, 17-016) was sourced from the Ravenscrag Formation (B. Rostron, pers comm. 2018). The Re-Os data are consistent with this observation, as both the $^{187}\text{Re}/^{188}\text{Os}$ and $^{187}\text{Os}/^{188}\text{Os}$ for water collected from the Winnipegosis Formation oil wells is comparable to that of the Ravenscrag Formation (17-015). If it is assumed that Winnipegosis Formation water has negligible Os, as is the case for most other co-produced waters, then the Re-Os data implies that the Winnipegosis Formations samples contain ~20% water from the Ravenscrag Formation.

6.10: Discussion

6.10.1: Re-Os distribution in surface and groundwater

Compared to seawater, the Os concentrations for the Athabasca River system samples are higher (22 ± 15 ppq) and more radiogenic ($^{187}\text{Os}/^{188}\text{Os} = 2.1 \pm 0.2$), but are comparable to what has been reported in previous studies on river systems (Levasseur, 1999; Sharma et al., 1999; Levasseur et al., 2000; Sharma et al., 2007). The Athabasca river system provides a useful baseline measurement of possible Re-Os isotopic composition of water prior to infiltration into deeper basal aquifers. Although these samples were collected far away from the groundwater samples (> 500 km) we presume that Re-Os concentrations and isotopic composition will be broadly similar for the surface waters that flow east of the Rocky Mountains into Saskatchewan. It is expected that water infiltrating into subsurface aquifers will contain measurable levels of Re and Os with $^{187}\text{Os}/^{188}\text{Os}$ values more radiogenic than seawater. Any anomalies that significantly modify groundwater from the broad values reported for river systems may be due to subsurface processes.

The water analyses reported in this study represent the first dataset of Re-Os isotopic data from pore water collected directly from deep confined aquifers. The only previous large scale dedicated Os groundwater study is from Paul et al. (2010). In the Paul et al. (2010) study shallow aquifers (< 74 m) were found to be enriched in Os compared to local surface water and contained Os with concentrations up to 192 ppq. For the shallowest aquifer sampled in our study, the Ravenscrag Formation, Os (95 ppq) is also enriched compared to values of reported for rivers (< 50 ppq; This study; Levasseur, 1999; Sharma et al., 1999; Levasseur et al., 2000; Sharma et al.,

2007). The Belly River Formation also shows slight enrichment (15-34 ppq) in the northern most samples (16-101, 16-102) but drops to below 5 ppq in the southern samples (16-107, 16-108, 16-109). The depleted concentration of Os and Re with respect to potential source waters (e.g. meteoric, seawater) seen in formations below the Belly River Formation is indicative of Re and Os being removed from pore waters as they migrate through the basin.

When in contact with oil, experiments have shown that Re and Os is efficiently transferred from water into oil on the time scales of days (Mahdaoui et al., 2015). Therefore, the observation that the majority of the oil well water samples are devoid of Re and Os is unsurprising. A few notable exceptions can be seen in the Bakken and Winnipegosis formations and will be discussed in the next section. The surprising finding that deep water source wells also are also extremely depleted in Re-Os is difficult to reconcile using the oil-water interaction mechanism. Many of these formations (e.g. Belly River, Mannville formations) do host oil far (> 100 km) from our collection sites (Dawson et al., 1994; Hayes et al., 1994; Jensen et al., 2015), it is highly unlikely that the water has reacted with petroleum. Moreover, these waters would then not have appreciably regained Re and Os via water-rock interactions through hundreds of kilometers of migration and recharge from bounding aquifers.

In situations where the interaction with a large amount of petroleum is unlikely, other mechanisms must be considered for Re and Os depletion in deep pore fluids. The redox sensitivity of Re and Os may play an important role in this regard. Previous research into the speciation of Re and Os in both oxic and reducing environments provide possible mechanisms for removal of Re and Os from the aqueous phase. Both Re and Os may be incorporated within organic material during reduction (e.g. Chappaz et al., 2008) and experiments by Yamashita et al. (2007) show that greater than 50% of Re and Os can be removed in a matter of days during interaction with organic substrates. These studies focused on anoxic regimes with high organic contents, but we speculate it may be possible that the smaller organic contents of typical sediments, such as organics found on the surfaces and within the interlayers of phyllosilicates (Kennedy et al., 2014), may be able to effectively scavenge Re and Os as water migrates through and between the aquifers over thousands of years. In more oxic regimes it appears that Re and Os are more mobile, however experiments have also shown that both Re and Os can possibly be adsorbed onto mineral surfaces (e.g. clays and ferromanganese oxides) under these conditions providing another pathway for the gradual loss of these elements (Vinson et al., 2004;

Yamashita et al., 2007). The behavior of other redox sensitive elements (e.g. V, Cr, Mo) and conservative solutes (e.g. Na) do not clearly mimic that of Re or Os, suggesting dissimilar behaviors in groundwater systems.

The archived samples represent analyses of pore water that are much closer to the basement and generally show an enrichment (> 5 ppq) in Os concentrations compared to overlying aquifers. It should be noted that these samples were not collected with the analysis of Re and Os in mind, hence do not follow the protocols suggested by Sharma et al. (2012) or Gannoun and Burton (2014). One sample that produced particularly interesting results is the Winnipeg Formation sample 13-92 which was sampled from a CO₂ injection well. The Winnipeg Formation is very close to basement rocks and the single sample analyzed contains extremely high Os concentrations (1906 ppq) with a very radiogenic character ($^{187}\text{Os}/^{188}\text{Os} = 10.13 \pm 0.19$). To explain this sample either requires that the sample was contaminated or that Os can be significantly leached from the Proterozoic-Archean basement rocks, possibly consistent with the highly radiogenic Os composition. Unfortunately, no repeat analyses were able to be made on this sample, and no similar samples were available to be analyzed. As such we suggest approaching this value with a great deal of caution until similar examples are published.

6.10.2: Water-Oil Interactions

Experimental work by Mahdaoui et al. (2015) on water-oil interactions demonstrate that even at low temperatures (25°C - 45°C) Re and Os appear to transfer efficiently ($> 50\%$) from aqueous solutions into oil. The effectiveness of transfer also appeared to be positively correlated with temperature, asphaltene content, and the sulphur content of the oil. Mahdaoui et al. (2015) went on to caution that based on their laboratory experiments, oil samples could acquire Re and Os from basinal fluids therefore negatively influencing the potential for using the Re-Os geochronometer to date oil generation, or be used for oil-source rock correlation.

One key observation from our dataset is that pore waters are in general severely depleted in Re and Os in the deep subsurface, especially compared to that expected based on previous groundwater analyses (e.g. Paul et al., 2010). If depleted values of Re and Os of < 500 ppq and < 5 ppq, respectively, are the norm in subsurface aquifers then the amount of Re - Os that can be transferred to oils may be minor, even if the transfer between the phases is efficient. At least from the data collected from Williston basin aquifers, oil may not gain appreciable Re and Os

from basinal water. However, there is still the open question as to what process groundwater appears to lose its Re and Os, and if the other sinks for Re and Os may indirectly affect the oil during its generation or migration.

The Bakken Formation sample 17-019 challenges the findings in Mahdaoui et al. (2015) that Re and Os is always effectively transferred between oil and water. In this sample, the water contains 843 ppq Re and 10 ppq Os with a $^{187}\text{Os}/^{188}\text{Os}$ of 5.18 ± 2.48 , whereas the oil contains 891 ppq Re and 70 ppq Os with a $^{187}\text{Os}/^{188}\text{Os}$ of 0.78 ± 0.15 , with the assumption all the Re and Os is within the asphaltene. These concentrations are quite similar, especially compared to what is observed in other formations (i.e. Shaunovan, Birdbear, and Ratcliffe formations), but more importantly have very different $^{187}\text{Os}/^{188}\text{Os}$, showing that the water and oil are not in Os isotopic equilibrium (Fig. 6.5). A similar trend can be seen within the Winnipegosis sample 17-016 where the sample has not reached isotopic equilibrium even during the presumed injection of Ravenscrag Formation water prior to sampling and the vigorous mixing that occurs during extraction of the sample from the oil well. The reason for these samples not reaching isotopic equilibrium may be a result to the oil composition. For the Bakken Formation sample, the asphaltene content is only $\sim 0.3\%$, compared to the approximately 1-5% for the other oils collected, the 5% and 20% tested by Mahdaoui et al. (2015). In the experiments performed by Mahdaoui et al. (2015) the lower asphaltene oils were $\sim 65\%$ as efficient at removing Re than the oil containing 20% asphaltene. The extremely low asphaltene contents of the Bakken Formation oil may result in poor transfer of Re and Os from water to oil. Unfortunately, for all other oil well samples the uncertainties on the water $^{187}\text{Os}/^{188}\text{Os}$ are too high to test if these waters are in isotopic equilibrium with the co-produced oil.

6.10.3: Implications for Re-Os geochronology of sediment-hosted ore deposits.

Pyrite Re-Os geochronology is commonly used to date sediment-hosted ore deposits (e.g. Hnatyshin et al., 2015; Hnatyshin et al., 2016), which are proposed to form by focusing deeply-sourced fluids (e.g. hydrothermal or basinal fluids) into regimes where they mix with secondary fluids and/or carbonate rocks (e.g. Leach et al., 2010; Wilkinson, 2010; Turner, 2011). Metal-bearing fluids are thought to gain their metals through scavenging from either the aquifer skeletons or underlying basement rocks. Rhenium and Os appear to only be mobilized by oxic fluids (Yamashita et al., 2007) and are clearly lost during fluid migration in midlevel aquifers,

based on results presented here. The Re and Os incorporated into the sulphides that form sediment-host ore deposits may, therefore, come from two sources based on our dataset. If the mineralizing fluids are at least partially derived from a near surface source, the Re and Os characteristics may reflect the infiltration and recharge of either meteoric or seawater, under the assumption that the redox conditions are suitable for mobilization. Fluids that interact with basement rocks may also scavenge Os (and Re?) and could be the source of the Os (and Re?) found in the sulphides of these ore deposits.

Isotopically distinguishing between these two potential sources is difficult due the lack of constraints for the Os isotopic ratios found for basement aquifers. For stratigraphically higher units in the Williston Basin for example, $^{187}\text{Os}/^{188}\text{Os}$ values are mildly radiogenic with values of 1.34-1.78, which are similar to North American river and average continental crustal isotopic compositions (Levasseur et al., 1999; Peucker-Ehrenbrink and Jahn, 2001; This study), and hence may be typical for shallow water aquifers in continental settings. In marine settings, a similar pattern is likely to emerge with $^{187}\text{Os}/^{188}\text{Os}$ following that of contemporaneous seawater. If the initial $^{187}\text{Os}/^{188}\text{Os}$ calculated using the isochron method exceeds that of river ($^{187}\text{Os}/^{188}\text{Os} > \sim 3$; Sharma et al., 1999) or seawater sources ($> \sim 1.1$) then a case may be made for Os may being sourced from the basement.

6.10.4: Os Tracing

The use of Os isotopes to trace environmental changes has been attempted in the past for surface environments by comparing natural $^{187}\text{Os}/^{188}\text{Os}$ values with values from anthropogenic sources of Os (e.g. Rodushkin, et al., 2007; Almecija et al., 2015). Due to the extremely low concentrations of Re and Os found in the majority of the aquifers studied, contamination from anthropogenic sources should be easily recognized. In sedimentary settings such as the Williston basin, natural $^{187}\text{Os}/^{188}\text{Os}$ values are expected to be more radiogenic than seawater (> 1) therefore extremely anomalous values such as was found in the Birdbear Formation oil sample 17-012 ($^{187}\text{Os}/^{188}\text{Os} = 0.18$, $^{187}\text{Re}/^{188}\text{Os} = 1.5$) are difficult to explain without anthropogenic contamination. Another example from our dataset showing a possibility to fingerprint unnatural anomalies is with the Winnipegosis oil well. This well contains water with appreciable Re and Os, which is uncharacteristic of water being co-produced with oil. This observation is clearly flagged as an anomaly and is likely caused by mixing for Ravenscrag and Winnipegosis waters.

Based on these examples, Re-Os may be a good tracer of water contamination in certain circumstances when used in conjunction with other geochemical or physical observations.

6.11: Conclusions

This study provides the first information for how Re and Os behave in the deep subsurface of a continental sedimentary basin. Shallow aquifers may be relatively enriched in Re and Os (> 1000 ppq Re, > 10 ppq Os) with $^{187}\text{Os}/^{188}\text{Os}$ very similar to riverine Os, suggesting that infiltration and recharge may play an important role in keeping waters enriched in Re and Os. Mid-level aquifers do not contain appreciable Re (< 300 ppq) and Os (< 5 ppq) and do not clearly follow other redox sensitive elements (e.g. Mo, V, Cr) or conservative solutes such as Na. These depleted values imply that Re and Os is removed from pore waters in the mid- to deep subsurface. The geochemical behavior of Re and Os may be responsible for their removal from pore waters as the commonly reduced nature of groundwater may promote sorption onto clays and/or organic material. If sulphur is available, precipitation of sulphides may also remove Re and Os from groundwater. The slow migration rate of fluids in these aquifers may allow for the gradual removal of these elements, while slow recharge rates may be unable to replenish any lost Re or Os. Archived samples that were collected close to the basement of the Williston basin are consistent with additional leaching of Os, although follow up studies will be needed to confirm this observation, as the sampling protocol for these waters was not optimal. The samples studied provide a great deal of insight into the Re-Os system in subsurface fluids, a number of outstanding questions still exist and could be the focus of future studies. These include:

- (1) What are the kinetics of groundwater Re-Os loss?
- (2) Can these results be applied to basins without significant petroleum reserves?
- (3) Does interaction with the basement, or igneous/metamorphic rocks, influence the concentration and/or isotopic ratios of Re and Os in coexisting waters?
- (4) Are pore waters in isotopic equilibrium with all oils?

6.12: References

Almécija, C., Sharma, M., Cobelo-García, A., Santos-Echeandía, J., & Caetano, M. (2015). Osmium and platinum decoupling in the environment: evidences in intertidal sediments (Tagus Estuary, SW Europe). *Environmental Science & Technology*, 49(11), 6545-6553.

Anbar, A. D., Creaser, R. A., Papanastassiou, D. A., & Wasserburg, G. J. (1992). Rhenium in seawater: Confirmation of generally conservative behavior. *Geochimica et Cosmochimica Acta*, 56(11), 4099-4103.

Brenan, J. M., McDonough, W. F., & Ash, R. (2005). An experimental study of the solubility and partitioning of iridium, osmium and gold between olivine and silicate melt. *Earth and Planetary Science Letters*, 237(3-4), 855-872.

Brenan, J. M., & McDonough, W. F. (2009). Core formation and metal–silicate fractionation of osmium and iridium from gold. *Nature Geoscience*, 2(11), 798.

Chappaz, A., Gobeil, C., & Tessier, A. (2008). Sequestration mechanisms and anthropogenic inputs of rhenium in sediments from Eastern Canada lakes. *Geochimica et Cosmochimica Acta*, 72(24), 6027-6036.

Crocket, J. H., Fleet, M. E., & Stone, W. E. (1992). Experimental partitioning of osmium, iridium and gold between basalt melt and sulphide liquid at 1300 C. *Australian Journal of Earth Sciences*, 39(3), 427-432.

Dawson, F.W., Evans, C.G., Marsh, R., Richardson, R. (1994): Uppermost Cretaceous and Tertiary Strata of the Western Canada Sedimentary Basin; in Geological Atlas of the Western Canada Sedimentary Basin, G.D. Mossop and I. Shetsen (comp.), Canadian Society of Petroleum Geologists and Alberta Research Council, URL: <http://ags.aer.ca/publications/chapter-24-uppermost-cretaceous-and-tertiary-strata>.

DiMarzio, J. M., Georgiev, S. V., Stein, H. J., & Hannah, J. L. (2018). Residency of rhenium and osmium in a heavy crude oil. *Geochimica et Cosmochimica Acta*, 220, 180-200.

Du, A., Wu, S., Sun, D., Wang, S., Qu, W., Markey, R., ... & Malinovskiy, D. (2004). Preparation and certification of Re - Os dating reference materials: Molybdenites HLP and JDC. *Geostandards and Geoanalytical Research*, 28(1), 41-52.

Gannoun, A., & Burton, K. W. (2014). High precision osmium elemental and isotope measurements of North Atlantic seawater. *Journal of Analytical Atomic Spectrometry*, 29(12), 2330-2342.

Georgiev, S. V., Stein, H. J., Hannah, J. L., Galimberti, R., Nali, M., Yang, G., & Zimmerman, A. (2016). Re–Os dating of maltenes and asphaltenes within single samples of crude oil. *Geochimica et Cosmochimica Acta*, 179, 53-75.

Georgiev, S. V., Zimmerman, A., Yang, G., Goswami, V., Hurtig, N. C., Hannah, J. L., & Stein, H. J. (2018). Comparison of chemical procedures for Re-isotopic measurements by N-TIMS. *Chemical Geology*.

Hayes, B.J.R., Christopher, J.E., Rosenthal, L., Los, G., MecKercher, B. (1994):Cretaceous Mannville Group of the Western Canada Sedimentary Basin; in Geological Atlas of the Western Canada Sedimentary Basin, G.D. Mossop and I. Shetsen (comp.), Canadian Society of Petroleum Geologists and Alberta Research Council, URL: <http://ags.aer.ca/publications/chapter-19-cretaceous-mannville-group>.

Helz, G. R., & Dolor, M. K. (2012). What regulates rhenium deposition in euxinic basins?. *Chemical Geology*, 304, 131-141.

Hnatyshin, D., Creaser, R. A., Wilkinson, J. J., & Gleeson, S. A. (2015). Re-Os dating of pyrite confirms an early diagenetic onset and extended duration of mineralization in the Irish Zn-Pb ore field. *Geology*, 43(2), 143-146.

Hnatyshin, D., Kontak, D. J., Turner, E. C., Creaser, R. A., Morden, R., & Stern, R. A. (2016). Geochronologic (ReOs) and fluid-chemical constraints on the formation of the Mesoproterozoic-hosted Nanisivik ZnPb deposit, Nunavut, Canada: Evidence for early diagenetic, low-temperature conditions of formation. *Ore Geology Reviews*, 79, 189-217.

- Hodge, V. F., Johannesson, K. H., & Stetzenbach, K. J. (1996). Rhenium, molybdenum, and uranium in groundwater from the southern Great Basin, USA: evidence for conservative behavior. *Geochimica et Cosmochimica Acta*, 60(17), 3197-3214.
- Jensen, G. K. S., Rostron B. J., Palombi, D., Meinik, A. (2015). Open File 2015-1 Saskatchewan Phanerozoic fluids and petroleum systems project: Hydrogeology of the Phanerozoic-aged Strata of Saskatchewan. Saskatchewan Geological Survey, Saskatchewan Ministry of the Economy.
- Kennedy, M. J., Löhr, S. C., Fraser, S. A., & Baruch, E. T. (2014). Direct evidence for organic carbon preservation as clay-organic nanocomposites in a Devonian black shale; from deposition to diagenesis. *Earth and Planetary Science Letters*, 388, 59-70.
- Leach, D. L., Bradley, D. C., Huston, D., Pisarevsky, S. A., Taylor, R. D., & Gardoll, S. J. (2010). Sediment-hosted lead-zinc deposits in Earth history. *Economic*
- Levasseur, S., Birck, J. L., & Allegre, C. J. (1999). The osmium riverine flux and the oceanic mass balance of osmium. *Earth and Planetary Science Letters*, 174(1-2), 7-23.
- Levasseur, S., Rachold, V., Birck, J. L., & Allegre, C. J. (2000). Osmium behavior in estuaries: the Lena River example. *Earth and Planetary Science Letters*, 177(3-4), 227-235.
- McDaniel, D. K., Walker, R. J., Hemming, S. R., Horan, M. F., Becker, H., & Grauch, R. I. (2004). Sources of osmium to the modern oceans: new evidence from the 190Pt-186Os system. *Geochimica et Cosmochimica Acta*, 68(6), 1243-1252.
- Mahdaoui, F., Michels, R., Reisberg, L., Pujol, M., & Poirier, Y. (2015). Behavior of Re and Os during contact between an aqueous solution and oil: consequences for the application of the Re–Os geochronometer to petroleum. *Geochimica et Cosmochimica Acta*, 158, 1-21.

Meisel, T., Walker, R. J., Irving, A. J., & Lorand, J. P. (2001). Osmium isotopic compositions of mantle xenoliths: a global perspective. *Geochimica et Cosmochimica Acta*, 65(8), 1311-1323.

Palmer, M. R., Falkner, K. K., Turekian, K. K., & Calvert, S. E. (1988). Sources of osmium isotopes in manganese nodules. *Geochimica et Cosmochimica Acta*, 52(5), 1197-1202.

Paul, M., Reisberg, L., Vigier, N., Zheng, Y., Ahmed, K. M., Charlet, L., & Huq, M. R. (2010). Dissolved osmium in Bengal plain groundwater: Implications for the marine Os budget. *Geochimica et Cosmochimica Acta*, 74(12), 3432-3448.

Peucker - Ehrenbrink, B., & Jahn, B. M. (2001). Rhenium - osmium isotope systematics and platinum group element concentrations: Loess and the upper continental crust. *Geochemistry, Geophysics, Geosystems*, 2(10).

Ravizza, G., Turekian, K. K., & Hay, B. J. (1991). The geochemistry of rhenium and osmium in recent sediments from the Black Sea. *Geochimica et Cosmochimica Acta*, 55(12), 3741-3752.

Racionero-Gómez, B., Sproson, A. D., Selby, D., Gannoun, A., Gröcke, D. R., Greenwell, H. C., & Burton, K. W. (2017). Osmium uptake, distribution, and $^{187}\text{Os}/^{188}\text{Os}$ and $^{187}\text{Re}/^{188}\text{Os}$ compositions in Phaeophyceae macroalgae, *Fucus vesiculosus*: Implications for determining the $^{187}\text{Os}/^{188}\text{Os}$ composition of seawater. *Geochimica et Cosmochimica Acta*, 199, 48-57.

Rodushkin, I., Engström, E., Sörlin, D., Pontér, C., & Baxter, D. C. (2007). Osmium in environmental samples from Northeast Sweden. Part II. Identification of anthropogenic sources. *Science of the total environment*, 386(1-3), 159-168.

Selby, D., Creaser, R. A., & Fowler, M. G. (2007). Re–Os elemental and isotopic systematics in crude oils. *Geochimica et Cosmochimica Acta*, 71(2), 378-386.

Sharma, M., Papanastassiou, D. A., & Wasserburg, G. J. (1997). The concentration and isotopic composition of osmium in the oceans. *Geochimica et Cosmochimica Acta*, 61(16), 3287-3299.

Sharma, M., Wasserburg, G. J., Hofmann, A. W., & Chakrapani, G. J. (1999). Himalayan uplift and osmium isotopes in oceans and rivers. *Geochimica et Cosmochimica Acta*, 63(23-24), 4005-4012.

Sharma, M., Wasserburg, G. J., Hofmann, A. W., & Butterfield, D. A. (2000). Osmium isotopes in hydrothermal fluids from the Juan de Fuca Ridge. *Earth and Planetary Science Letters*, 179(1), 139-152.

Sharma, M., Balakrishna, K., Hofmann, A. W., & Shankar, R. (2007a). The transport of osmium and strontium isotopes through a tropical estuary. *Geochimica et Cosmochimica Acta*, 71(20), 4856-4867.

Sharma, M., Rosenberg, E. J., & Butterfield, D. A. (2007b). Search for the proverbial mantle osmium sources to the oceans: Hydrothermal alteration of mid-ocean ridge basalt. *Geochimica et Cosmochimica Acta*, 71(19), 4655-4667.

Sharma, M., Chen, C., & Blazina, T. (2012). Osmium contamination of seawater samples stored in polyethylene bottles. *Limnology and Oceanography: Methods*, 10(9), 618-630.

Shotyk, W., Bicalho, B., Cuss, C. W., Donner, M. W., Grant-Weaver, I., Haas-Neill, S., ... & Zaccone, C. (2017). Trace metals in the dissolved fraction (< 0.45 µm) of the lower Athabasca River: Analytical challenges and environmental implications. *Science of the Total Environment*, 580, 660-669.

Shirey, S. B., & Walker, R. J. (1998). The Re-Os isotope system in cosmochemistry and high-temperature geochemistry. *Annual Review of Earth and Planetary Sciences*, 26(1), 423-500.

Singh, A., Palombi, D., Huff, R. (2014), Application of response surface based calibration methods for regional hydrogeological modelling in the Western Canada Sedimentary Basin. Abstract H53B-0853 presented at 2014 Fall Meeting, AGU, San Francisco, Calif., 15-19 Dec

Smoliar, M. I., Walker, R. J., Morgan, J.W. (1996). Re-Os ages of group IIA, IIIA, IVA, and IVB iron meteorites. *Science*, 271, 1099.

Sun, W., Arculus, R. J., Bennett, V. C., Eggins, S. M., & Binns, R. A. (2003). Evidence for rhenium enrichment in the mantle wedge from submarine arc-like volcanic glasses (Papua New Guinea). *Geology*, 31(10), 845-848.

Tossell, J. A. (2005). Calculation of the UV-visible spectra and the stability of Mo and Re oxysulfides in aqueous solution. *Geochimica et cosmochimica Acta*, 69(10), 2497-2503.

Turner, E. C. (2011). Structural and stratigraphic controls on carbonate-hosted base metal mineralization in the Mesoproterozoic Borden Basin (Nanisivik District), Nunavut. *Economic Geology*, 106(7), 1197-1223.

Vinsova, H., Konirova, R., Koudelkova, M., & Jedinakova-Krizova, V. (2004). Sorption of technetium and rhenium on natural sorbents under aerobic conditions. *Journal of Radioanalytical and nuclear chemistry*, 261(2), 407-413.

Vorlicek, T. P. (2012). Speciation and Removal Mechanisms of Rhenium in Anoxic Waters: Roles of Zero-Valent Sulfur, Mineral Oxide Catalysis, and Pyrite Surfaces. *All Private Grants. Paper 1*.

Wang, L. B., Qu, W. J., Li, C., Zhou, L. M., Du, A. D., & Zu, B. (2013). Method Study on the Separation and Enrichment of Rhenium Measured by Negative Thermal Ionization Mass Spectrometry. *Rock and Mineral Analysis*, 3, 008.

Wilkinson, J. J. (2010). A review of fluid inclusion constraints on mineralization in the Irish ore field and implications for the genesis of sediment-hosted Zn-Pb deposits. *Economic Geology*, *105*(2), 417-442.

Woodhouse, O. B., Ravizza, G., Falkner, K. K., Statham, P. J., & Peucker-Ehrenbrink, B. (1999). Osmium in seawater: vertical profiles of concentration and isotopic composition in the eastern Pacific Ocean. *Earth and Planetary Science Letters*, *173*(3), 223-233.

Xiong, Y. (2003). Solubility and speciation of rhenium in anoxic environments at ambient temperature and applications to the Black Sea. *Deep Sea Research Part I: Oceanographic Research Papers*, *50*(5), 681-690.

Yamashita, Y., Takahashi, Y., Haba, H., Enomoto, S., & Shimizu, H. (2007). Comparison of reductive accumulation of Re and Os in seawater–sediment systems. *Geochimica et Cosmochimica Acta*, *71*(14), 3458-3475.

Table 6.1: Location data

| Sample Name | Sample Type | Unique Well Identifier | Latitude | Longitude | Depth (m) |
|-------------------------------------|---------------|------------------------------|-----------|------------|---------------|
| A5w-SW - Athabasca System | Surface water | - | 57.57222 | 111.5136 | 0 |
| A5w-GW - Athabasca System | Groundwater | - | 57.57222 | 111.5136 | N/A |
| A17w-SW - Athabasca System | Surface water | - | 56.99527 | 111.4547 | 0 |
| A17w-GW - Athabasca System | Groundwater | - | 56.99527 | 111.4547 | N/A |
| A19e-Athabasca - Athabasca System | Surface water | - | 56.8975 | 111.4163 | 0 |
| A19e-McleanCreek - Athabasca System | Surface water | - | 56.8975 | 111.4163 | 0 |
| A20e-Adoe - Athabasca System | Surface water | - | 56.84028 | 111.4113 | 0 |
| A20e-Creek - Athabasca System | Surface water | - | 56.84028 | 111.4113 | 0 |
| 17-013 Ravenscrag | WSW | 141/08-22-002-09W2/00 (1231) | 49.13611 | 103.11986 | 94-101 |
| 17-015 Ravenscrag | WSW | 122/09-22-002-09W2/00 (1231) | 49.13915 | 103.12311 | 118-124 |
| 16-101 BellyRiver | WSW | 13/14-09--031-21W2 | 51.76694 | 180.92111 | N/A |
| 16-102 Belly River | WSW | 103/12-08/031/21W3 | 51.64303 | 108.95444 | N/A |
| 16-107 Belly River | WSW | 122/13-11-007-20W3 | 49.55089 | 108.62222 | N/A |
| 16-108 Belly River | WSW | 141/16-33-009-18W3 | 49.78392 | 108.37917 | N/A |
| 16-109 Belly River | WSW | 103/09-05-010-18W3 | 49.7932 | 108.37917 | N/A |
| 17-001 Viking | WSW | 101/07-36-004-19W2/00 (2273) | 49.33897 | 104.43631 | N/A |
| 17-002 Viking | WSW | 101/09-25-004-19W2/00 (2273) | 49.32849 | 104.43006 | N/A |
| 17-003 Viking | WSW | 111/06-31-004-18W2/02 (0000) | 49.33776 | 104.41764 | N/A |
| 17-004 Viking | WSW | 101/09-01-004-17W2/00 (2273) | 49.26992 | 104.16123 | N/A |
| 16-104 Mannville | WSW | 141/07-21-018-17W3 | 50.53385 | 108.28194 | N/A |
| 16-105 Mannville | WSW | 121/08-21-18-17W3 | 50.53385 | 108.27611 | N/A |
| 17-017 Mannville | WSW | 141/01-26-006-09W2/00 (2300) | 49.4968 | 103.10729 | N/A |
| 17-018 Mannville | WSW | 111/09-10-008-09W2/00 (2300) | 49.63302 | 103.13582 | N/A |
| 17-020 Mannville | WSW | 121/01-14-009-08W2/00 (2300) | 49.72715 | 102.98093 | N/A |
| 17-022 Mannville | WSW | 121/03-32-008-07W2/00 (2300) | 49.68398 | 102.92417 | N/A |
| 17-023 Mannville | WSW | 31/08-17-006-13W2/00 (2300) | 49.46855 | 103.7087 | 1026.6-1056.7 |
| 17-024 Mannville | WSW | 102/16-28-5-13W2 | 49.41919 | 103.69122 | 1042-1081.5 |
| 16-111 Shaunavon | OW | 191/16-30-011-18W3 | 49.94431 | 108.44194 | N/A |
| 17-007 Ratcliffe | OW | 191/7-26-2-19W2 | 49.15217 | 104.43887 | 1861-1863 |
| 17-008 Ratcliffe | OW | 121/10-26-2-19W2 | 49.15358 | 104.4407 | 1871-1878 |
| 17-009 Ratcliffe | OW | 131/10-26-2-19W2 | 49.15577 | 104.44095 | 1871-1878 |
| 16-112 Madison | WSW | 131/02-8-12-18W3 | 49.97676 | 108.42528 | N/A |
| 17-019 Bakken | OW | 5D9-10/1C12-10-8-9W2 | 49.63358 | 103.155325 | N/A |
| 17-021 Bakken | OW | 131/12-24-9-8W2 | 49.750089 | 102.974708 | N/A |
| 17-006 Birdbear | OW | 131/6-26-2-19W2 | 49.15158 | 104.4463 | 2301-2316 |
| 17-010 Birdbear | OW | 101/10-26-2-19W2 | 49.15422 | 104.44044 | 2306-2309 |
| 17-011 Birdbear | OW | 131/13-3-1-16W2 | 49.01323 | 104.07324 | 2410-2430 |
| 17-012 Birdbear | OW | 111/11-15-1-16W2 | 49.03712 | 104.06629 | 2412-2429 |
| 16-103 Duperow | WSW | 101/03-27-032-23W3 | 51.76694 | 109.185 | N/A |
| 17-014 Winnipegosis* | OW | 111/8-22-2-9W2 | 49.1356 | 103.1 | 2575-2584 |
| 17-016 Winnipegosis* | OW | 121/9-22-2-9W2 | 49.13887 | 103.12314 | 2571-2575 |
| 13-89 Winnipeg | A-CO2 | N/A | 49.093438 | 103.078067 | 3197 |
| 13-92 Deadwood | A-CO2 | N/A | 49.093438 | 103.078067 | 3310.3 |
| 01-162 Winnipeg | A-OW | 91/08-06-010-15W2 | 49.790737 | 104.019348 | 2507-2527 |
| 01-164 Winnipeg | A-OW | 32-07-02-010-9W2 | 49.791344 | 103.121857 | 2406-2427 |
| 01-176 Deadwood | A-WSW | 2/12-21-031-21W3 | 51.672020 | 108.929581 | 2027-2049 |
| 01-202 Deadwood | A-OW | SW/NE-S3-T163N-R87W | 48.976666 | 101.939347 | 2786-2803 |
| 01-221 Winnipeg | A-OW | 91-08-06-010-15W2 | 49.790768 | 104.019905 | 2507-2527 |
| 01-540 Winnipeg | A-OW | 31/11-14-007-10W2 | 49.561481 | 103.264587 | 2642-2649 |

Samples are names as follows; the prefix for non-Athabasca samples refers to the year collect in addition to a sample identifier (e.g. 17-001 means the sample 001 was collected in 2017). For samples collected in 2013, 2016, 2017 the formations follow the sample identifier. For the samples collected in 2001 only the age of the formation is given. For the "Sample Type Column" the following acronyms are used WSW = water source well, OW = Oil well, CO₂ = CO₂ injection well, A = Archived groundwater sample. *Data from Shoty et al. (2017).

Table 6.2: Analytical data

| Sample Name | Sample Type | [Na] ppm | [Re] ppq ± 2s | [Os] ppq ± 2s | 187Re / 188Os ± 2s | 187Os / 188Os ± 2s | | | | |
|-------------------------------------|---------------|----------|---------------|---------------|--------------------|--------------------|------|------|-------|------|
| A5w-SW - Athabasca System | Surface water | 15** | 5.0 | 0.04 | 13.4 | 0.8 | 2266 | 343 | 2.04 | 0.31 |
| A5w-GW - Athabasca System | Groundwater | N/A | 0.8 | 0.05 | 14.2 | 2.7 | 352 | 190 | 2.49 | 1.35 |
| A17w-SW - Athabasca System | Surface water | 10.1** | 2.3 | 0.03 | 13.0 | 0.8 | 1068 | 166 | 1.99 | 0.31 |
| A17w-GW - Athabasca System | Groundwater | N/A | 2.6 | 0.03 | 53.1 | 1.0 | 285 | 11 | 1.81 | 0.07 |
| A19e-Athabasca - Athabasca System | Surface water | 9.8* | 1.9 | 0.03 | 11.8 | 0.8 | 977 | 168 | 2.08 | 0.36 |
| A19e-McLeanCreek - Athabasca System | Surface water | 55.6** | 9.7 | 0.04 | 24.8 | 0.8 | 2351 | 192 | 2.04 | 0.17 |
| A20e-Adoe - Athabasca System | Surface water | 14.9** | 1.4 | 0.03 | 10.4 | 0.8 | 806 | 158 | 2.10 | 0.41 |
| A20e-Creek - Athabasca System | Surface water | N/A | 1.2 | 0.03 | 34.6 | 0.9 | 207 | 14 | 2.11 | 0.12 |
| 17-013 Ravenscrag* | WSW | 1009 | 742 | 269 | 5 | 1 | 925 | 781 | 2.90 | 2.24 |
| 17-013 Ravenscrag rpt* | WSW | 1009 | 216 | 269 | 5 | 1 | 301 | 454 | 2.82 | 2.43 |
| 17-015 Ravenscrag | WSW | 473 | 14490 | 273 | 17 | 1 | 4670 | 925 | 1.42 | 0.29 |
| 17-015 Ravenscrag rpt | WSW | 473 | 56737 | 316 | 95 | 2 | 3319 | 121 | 1.34 | 0.05 |
| 16-101 BellyRiver | WSW | 416 | 214 | 180 | 18 | 2 | 67 | 59 | 1.46 | 0.37 |
| 16-101 BellyRiver rpt | WSW | 416 | 183 | 180 | 15 | 2 | 69 | 71 | 1.61 | 0.49 |
| 16-102 Belly River | WSW | 389 | 1072 | 125 | 32 | 1 | 193 | 25 | 1.72 | 0.11 |
| 16-102 Belly River rpt | WSW | 389 | 1220 | 180 | 34 | 2 | 211 | 42 | 1.78 | 0.25 |
| 16-107 Belly River | WSW | 1120 | <DL | <DL | <DL | <DL | N/A | N/A | N/A | N/A |
| 16-108 Belly River | WSW | 603 | <DL | <DL | <DL | <DL | N/A | N/A | N/A | N/A |
| 16-109 Belly River | WSW | 597 | <DL | <DL | 5 | 2 | N/A | N/A | N/A | N/A |
| 17-001 Viking | WSW | 3039 | 92 | 269 | <DL | <DL | N/A | N/A | N/A | N/A |
| 17-002 Viking | WSW | 3049 | <DL | <DL | <DL | <DL | N/A | N/A | N/A | N/A |
| 17-003 Viking | WSW | 3010 | <DL | <DL | <DL | <DL | N/A | N/A | N/A | N/A |
| 17-004 Viking | WSW | 3427 | <DL | <DL | <DL | <DL | N/A | N/A | N/A | N/A |
| 16-104 Mannville | WSW | 2960 | 26 | 180 | <DL | <DL | N/A | N/A | N/A | N/A |
| 16-105 Mannville | WSW | 2900 | <DL | <DL | <DL | <DL | N/A | N/A | N/A | N/A |
| 17-017 Mannville | WSW | 6629 | <DL | <DL | 4 | 1 | N/A | N/A | N/A | N/A |
| 17-018 Mannville | WSW | 12364 | 80 | 269 | 3 | 1 | N/A | N/A | N/A | N/A |
| 17-020 Mannville | WSW | 17170 | <DL | <DL | <DL | <DL | N/A | N/A | N/A | N/A |
| 17-022 Mannville | WSW | 32672 | <DL | <DL | <DL | <DL | N/A | N/A | N/A | N/A |
| 17-023 Mannville | WSW | 5880 | <DL | <DL | 4.3 | 1 | N/A | N/A | N/A | N/A |
| 17-024 Mannville | WSW | 6801 | <DL | <DL | 4.2 | 1 | N/A | N/A | N/A | N/A |
| 16-111 Shaunavon | OW-Water | 3350 | 119 | 180 | 0 | 1 | N/A | N/A | N/A | N/A |
| 16-111 Shaunavon Oil | OW-Oil | - | 1101379 | 3387 | 10701 | 60 | 700 | 3 | 3.28 | 0.02 |
| 17-007 Ratcliffe | OW-Water | 63708 | <DL | <DL | <DL | <DL | N/A | N/A | N/A | N/A |
| 17-007 Ratcliffe Oil | OW-Oil | - | 202615 | 828 | 963 | 10 | 1340 | 23 | 2.59 | 0.04 |
| 17-008 Ratcliffe | OW-Water | 69949 | <DL | <DL | <DL | <DL | N/A | N/A | N/A | N/A |
| 17-008 Ratcliffe Oil | OW-Oil | - | 134892 | 702 | 1035 | 10 | 829 | 13 | 2.57 | 0.04 |
| 17-009 Ratcliffe | OW-Water | 61289 | <DL | <DL | <DL | <DL | N/A | N/A | N/A | N/A |
| 16-112 Madison | WSW | 1210 | 234 | 180 | <DL | <DL | N/A | N/A | N/A | N/A |
| 17-019 Bakken | OW-Water | 79230 | 843 | 269 | 10 | 1 | 658 | 378 | 5.18 | 2.48 |
| 17-019 Bakken Oil | OW-Oil | - | 891 | 583 | 70 | 5 | 66 | 45 | 0.78 | 0.15 |
| 17-021 Bakken | OW-Water | 78867 | 1370 | 269 | 5 | 1 | 1968 | 1773 | 4.16 | 3.69 |
| 17-021 Bakken rpt | OW-Water | 78867 | 1508 | 269 | <DL | <DL | N/A | N/A | N/A | N/A |
| 17-021 Bakken Oil | OW-Oil | - | 12814 | 294 | 170 | 3 | 434 | 21 | 1.62 | 0.07 |
| 17-006 Birdbear | OW-Water | 61236 | 1200 | 269 | 3 | 1 | 1877 | 1845 | 0.63 | 0.75 |
| 17-006 Birdbear Oil | OW-Oil | - | 313953 | 1079 | 1754 | 13 | 1086 | 10 | 2.11 | 0.02 |
| 17-010 Birdbear | OW-Water | 96623 | <DL | <DL | <DL | <DL | N/A | N/A | N/A | N/A |
| 17-010 Birdbear Oil | OW-Oil | - | 41048 | 595 | 629 | 10 | 443 | 14 | 3.26 | 0.10 |
| 17-011 Birdbear | OW-Water | 109164 | 3253 | 270 | - | - | 280 | 29 | 1.44 | 0.12 |
| 17-012 Birdbear | OW-Water | 102538 | 734 | 269 | 3 | 1 | 1200 | 1278 | 0.95 | 1.06 |
| 17-012 Birdbear Oil* | OW-Oil | - | 14965 | 584 | 49471 | 59 | 1 | 0 | 0.18 | 0.00 |
| 16-103 Duperow | WSW | 61200 | <DL | <DL | <DL | <DL | N/A | N/A | N/A | N/A |
| 17-014 Winnipegosis* | OW-Water | 93456 | 14014 | 272 | 21 | 1 | 3727 | 611 | 1.23 | 0.21 |
| 17-014 Winnipegosis* | OW-Water | 93456 | 13790 | 272 | 18 | 1 | 4402 | 864 | 1.38 | 0.28 |
| 17-016 Winnipegosis* | OW-Water | 93550 | 14490 | 273 | 17 | 1 | 4670 | 925 | 1.42 | 0.29 |
| 17-016 Winnipegosis Oil | OW-Oil | - | 49176 | 601 | 483 | 11 | 841 | 38 | 5.60 | 0.27 |
| 13-89 Winnipeg | A-CO2 | 94400 | - | - | 1905.9 | 30 | - | - | 10.13 | 0.19 |
| 13-92 Deadwood | A-CO2 | 88200 | - | - | 14.5 | 2 | - | - | 0.76 | 0.30 |
| 01-162 Winnipeg | A-OW | 94342 | 394 | 269 | 6.1 | 1 | 315 | 265 | 0.16 | 0.24 |
| 01-164 Winnipeg | A-OW | 100237 | 997 | 269 | <DL | <DL | N/A | N/A | N/A | N/A |
| 01-176 Deadwood | A-WSW | 123053 | 1042 | 269 | <DL | <DL | N/A | N/A | N/A | N/A |
| 01-202 Deadwood | A-OW | 90667 | 1724 | 269 | 4.6 | 1 | 2032 | 1499 | 1.05 | 0.83 |
| 02-221 Winnipeg | A-OW | 92190 | 781 | 269 | 8.6 | 1 | 540 | 295 | 1.94 | 0.85 |
| 01-540 Winnipeg | A-OW | 102652 | 789 | 269 | 5.7 | 1 | 769 | 529 | 1.30 | 0.82 |

Samples are names as follows; the prefix for non-Athabasca samples refers to the year collect in addition to a sample identifier (e.g. 17-001 means the sample 001 was collected in 2017). For samples collected in 2013, 2016, 2017 the formations follow the sample identifier. For the samples collected in 2001 only the age of the formation is given. For the "Sample Type Column" the following acronyms are used WSW = water source well, OW = Oil well, CO₂ = CO₂ injection well, A = Archived groundwater sample. *Samples that are considered contaminated, see text for discussion. **Data from Shotyk et al. (2017). <DL are samples that contain less than 300 ppq Re and 3 ppq Os and do not produce reliable ¹⁸⁷Re-¹⁸⁸Os and ¹⁸⁷Os-¹⁸⁸Os isotopic ratios.

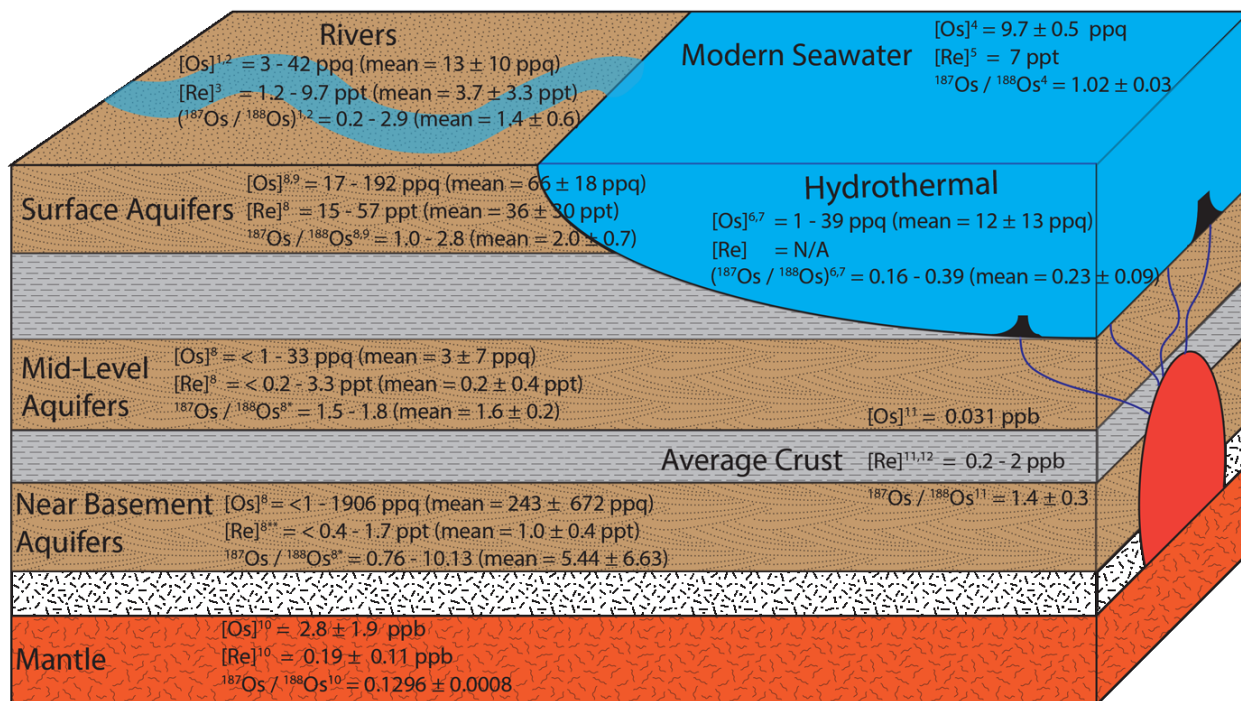


Figure 6.1: Overview of the range of Re-Os values seen in various reservoirs, see the text and references for additional details. "Surface Aquifers" are defined shallow unconfined aquifers (e.g. Ravenscrag Formation). Mid-Level Aquifers represent water analyses between the top most aquifer (i.e. Ravenscrag Formation) and the Winnipegosis Formation. "Near Basement Aquifers" represent the pore waters of the Winnipeg and Deadwood formations from this study. ¹Levasseur et al. (1999); ²Sharma and Wasserburg (1997); ³Unpublished; ⁴Gannoun and Burton; ⁵Anbar et al. (1992); ⁶Sharma et al. (2000); ⁷Sharma et al. (2007); ⁸This Study, ^{8*}Only data with > 10 ppq Os; ⁹Paul et al. (2010); ¹⁰Meisel et al. (2001); ¹¹Peucker-Ehrenbrink and Jahn (2001); ¹²Sun et al. (2003). ppb - parts per billion, ppt - parts per trillion, ppq - parts per quadrillion.

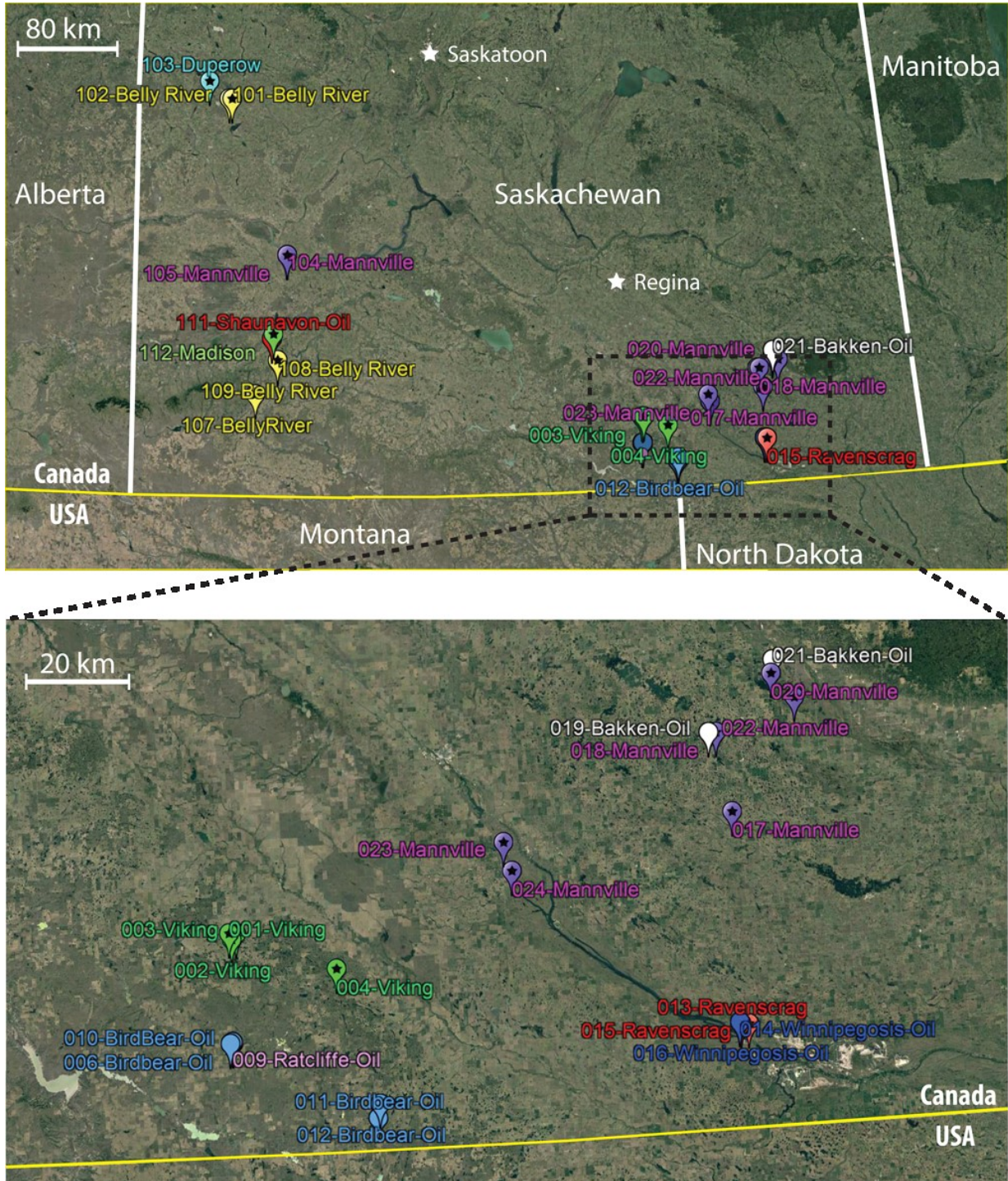


Figure 6.2: Sampling locations used in this study. Sample names include both the sample number and the formation. The notation also denotes whether they were collected from water source wells (e.g. 101-Belly River) or oil wells (e.g. 111-Shaunavon-Oil). Maps from Google Earth (2018).

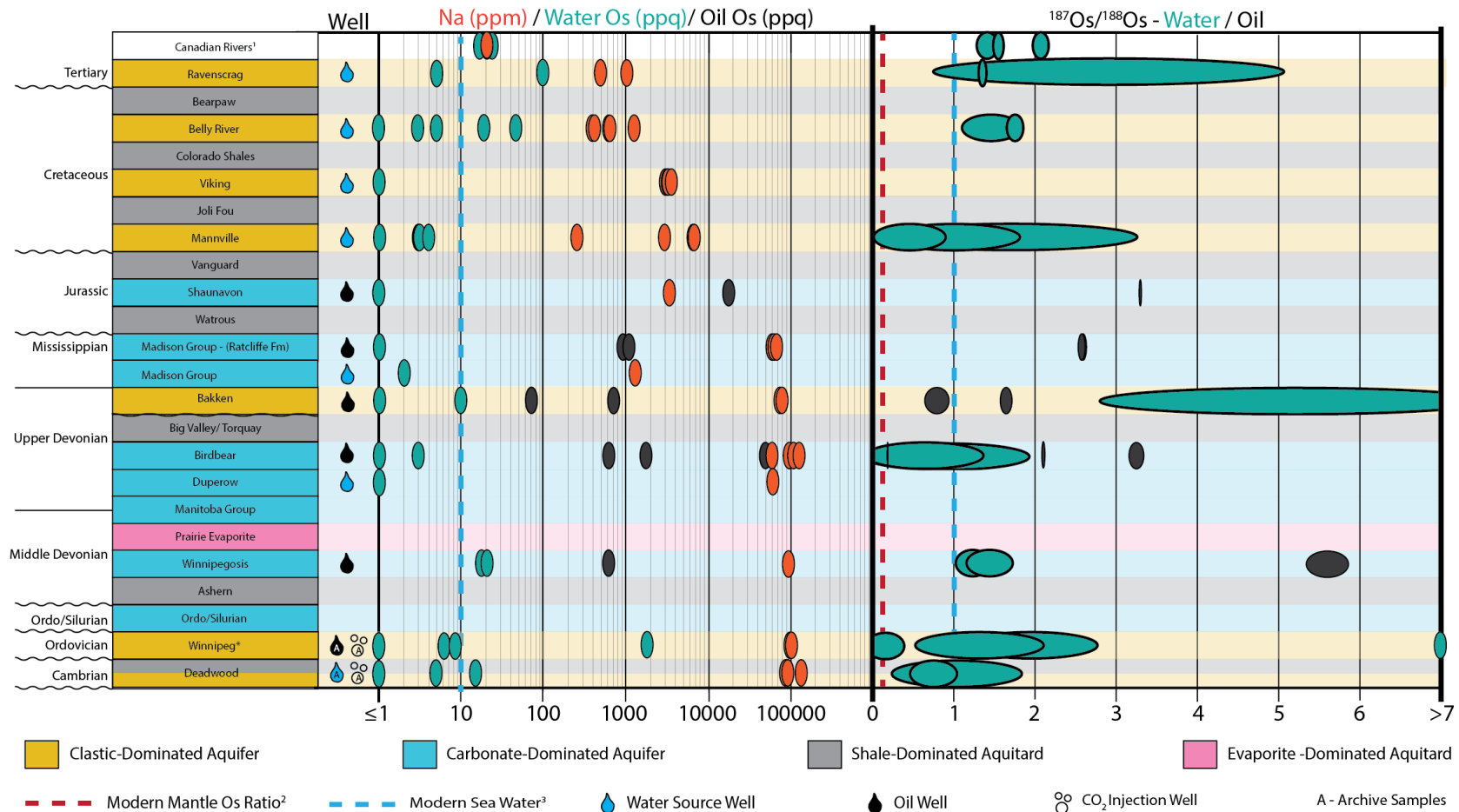


Figure 6.3: Analytical results plotted on the generalized stratigraphy of Saskatchewan. Stratigraphic chart was constructed based on the stratigraphic correlation chart provided by Saskatchewan Ministry of the Economy (2014). Numerical values for data points are tabulated in Table 6.2. For samples with repeated analyses only the sample with the lowest uncertainty is plotted. Concentrations are plotted without uncertainty, while the data ellipses for the $^{187}\text{Os}/^{188}\text{Os}$ ratio represent 2σ , however only data with 2σ values less than 2.5 are plotted for clarity. ¹Levasseur et al. (1999) and the Athabasca system from this study; ²Peucker-Ehrenbrink and Jahn (2002); ³Gannoun and Burton (2014). *Samples collected in 2001 are plotted in this section.

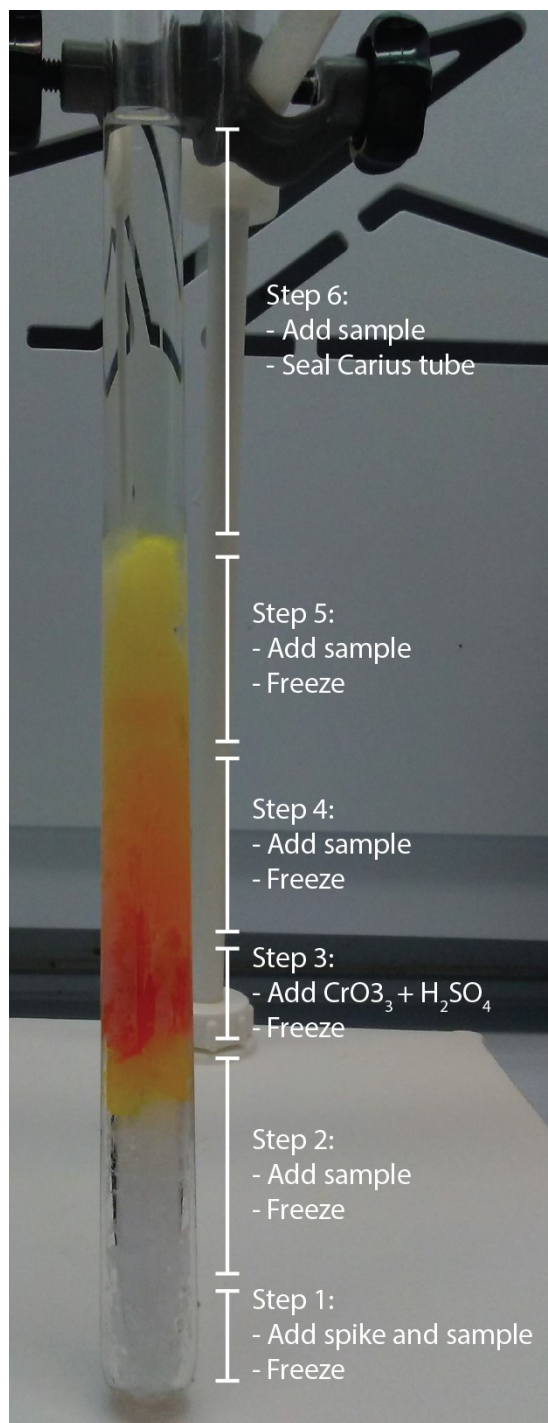


Figure 6.4: A diagram of the incremental steps used to ensure that the oxidant (i.e. CrO_3) is isolated (Steps 2, 4 and 5) from the spike and a large proportion of the sample prior to sealing of the Carius tube and incubation of the sample.

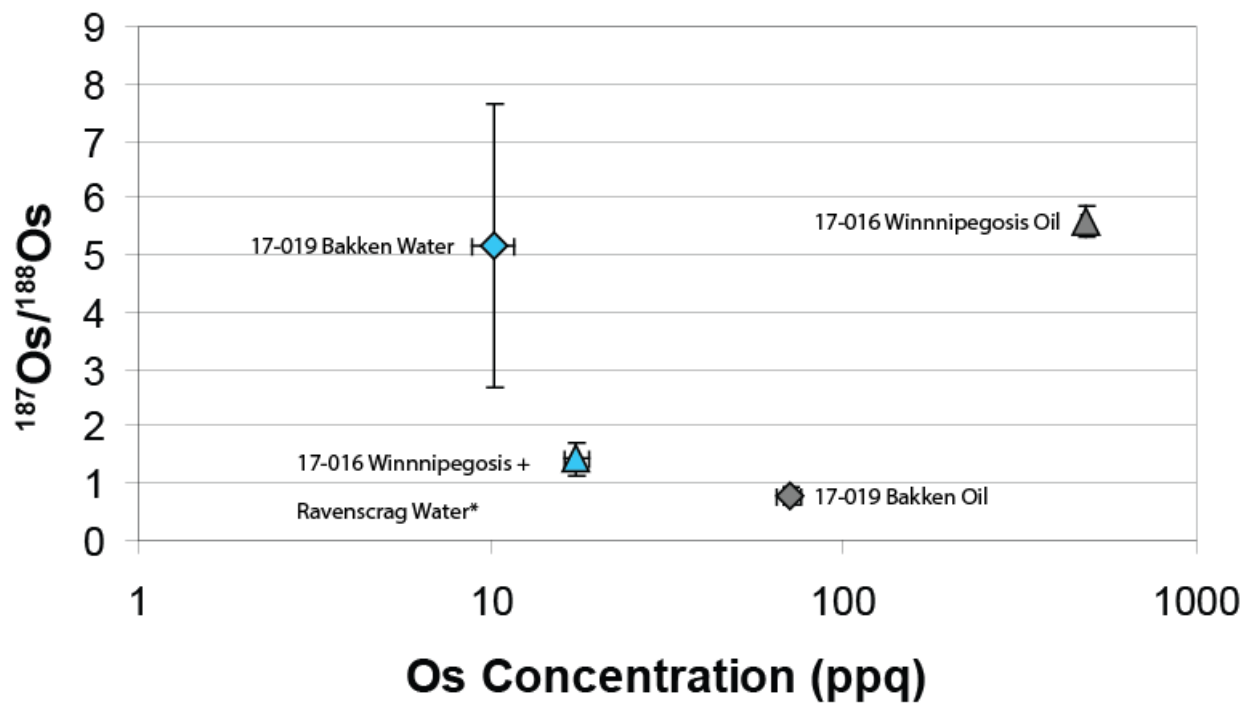


Figure 6.5: Os disequilibrium plot showing that samples 17-016 and 17-019 have differences outside analytical errors. *The water from 17-016 likely is dominated by Ravenscrag Formation water (see text for discussion)

6.13: Appendix

| Sample | 16-101 | 16-102 | 16-104 | 16-105 | 16-107 | 16-108 | 16-109 | 16-109 duplica | 16-111 | |
|---------|-----------------------|----------|------------|------------|------------|------------|-------------|----------------|-------------|------------|
| Analyte | Detection Limits (DL) | | Units | | | | | | | |
| Li | 0.00005 ppm | 0.071352 | 0.05351214 | 0.39306481 | 0.33302254 | 0.12245167 | 0.078718591 | 0.078512169 | 0.079482582 | 0.31410705 |
| Be | 0.0001 ppm | <DL | <DL | <DL | <DL | <DL | <DL | <DL | <DL | <DL |
| B | 0.002 ppm | 1.619312 | 1.47096025 | 5.10708772 | 4.78254445 | 3.30773416 | 3.702702055 | 3.631403344 | 3.70677601 | 10.0723762 |
| Na | 0.0005 ppm | 439.9338 | 397.338632 | N/A | N/A | N/A | 538.5079434 | 525.5479959 | 534.1781195 | #VALUE! |
| Mg | 0.002 ppm | 0.601275 | 0.47768344 | 9.81892389 | 9.45619086 | 2.0979576 | 0.735498672 | 0.676231948 | 0.679199319 | 35.2050926 |
| Al | 0.0002 ppm | <DL | 0.01516173 | <DL | <DL | <DL | <DL | <DL | <DL | 0.00016147 |
| P | 0.005 ppm | 0.316534 | 0.29939226 | <DL | <DL | 0.04137514 | 0.017829891 | 0.009544423 | 0.018419975 | 0.08435305 |
| K | 0.006 ppm | 2.390672 | 2.13666196 | 12.043728 | 10.330068 | 4.04813239 | 2.841329923 | 2.867770671 | 2.917969488 | 20.1251976 |
| Ca | 0.031 ppm | 2.865452 | 2.23324144 | 23.4875189 | 18.9382187 | 10.2453247 | 3.61100538 | 3.846595854 | 3.829621054 | 91.8280986 |
| Ti | 0.00009 ppm | 0.224375 | 0.46547471 | 0.00130295 | 0.00109912 | 0.00091982 | <DL | 0.000358886 | 0.000632558 | 0.00393303 |
| V | 0.00005 ppm | 0.002291 | 0.00478043 | 0.02649311 | 0.03021524 | 0.01335726 | 0.005067887 | 0.00425142 | 0.003935587 | 0.03464644 |
| Cr | 0.00005 ppm | 0.011143 | 0.00945342 | 0.01222417 | 0.01349579 | 0.00237291 | 0.017697251 | 0.016420117 | 0.014211239 | 0.01524315 |
| Fe | 0.0037 ppm | 0.147357 | 0.36357418 | <DL | <DL | 0.01955415 | 0.017523967 | <DL | <DL | 0.01841326 |
| Mn | 0.00003 ppm | 0.010046 | 0.0126379 | 0.04348849 | 0.04272804 | 0.00947102 | 0.008336911 | 0.007940031 | 0.006800288 | 0.02357803 |
| Co | 0.00003 ppm | 0.000469 | 0.00051253 | <DL | <DL | <DL | <DL | <DL | <DL | 0.00016253 |
| Ni | 0.00006 ppm | <DL | 0.00264962 | 0.00058528 | 0.00178417 | <DL | <DL | <DL | <DL | 0.0002821 |
| Cu | 0.00003 ppm | 0.008394 | 0.00993422 | 0.11030813 | 0.08138353 | 0.02074015 | 0.00911287 | 0.007927396 | 0.007844774 | 0.06854912 |
| Zn | 0.00008 ppm | <DL | <DL | <DL | <DL | <DL | <DL | <DL | <DL | <DL |
| Ga | 0.00001 ppm | 0.000163 | 0.00020758 | <DL | 0.00010477 | <DL | <DL | <DL | <DL | 0.00015103 |
| Ge | 0.00002 ppm | 0.000142 | 0.000176 | 0.00625425 | 0.00511627 | <DL | <DL | <DL | <DL | 0.00981439 |
| As | 0.00006 ppm | 0.004241 | 0.00451018 | 0.01677265 | 0.01736408 | 0.00837786 | 0.00483928 | 0.004108262 | 0.003848198 | 0.02291667 |
| Se | 0.0002 ppm | 0.004243 | 0.00313276 | 0.04376232 | 0.0462751 | 0.01948616 | 0.009642061 | 0.006309566 | 0.007646049 | 0.05872865 |
| Rb | 0.00004 ppm | 0.003486 | 0.00313043 | 0.01275761 | 0.01059325 | 0.0052005 | 0.004266564 | 0.004409111 | 0.004460069 | 0.01512622 |
| Sr | 0.00003 ppm | 0.066029 | 0.06142005 | 2.45983629 | 2.3561294 | 0.45110353 | 0.126115469 | 0.122169039 | 0.12292198 | 6.32120246 |
| Y | 0.00002 ppm | 0.001126 | 0.00165292 | <DL | <DL | <DL | <DL | <DL | <DL | 0.00028427 |
| Zr | 0.00009 ppm | 0.002933 | 0.00967737 | <DL | <DL | <DL | <DL | <DL | <DL | <DL |
| Nb | 0.00004 ppm | 0.000735 | 0.00145873 | <DL | <DL | <DL | <DL | <DL | <DL | 0.00030883 |
| Mo | 0.00002 ppm | 0.001142 | 0.0013262 | 0.00235853 | <DL | 0.00013652 | 0.001216432 | 0.001625101 | 0.001596375 | 0.00081365 |
| Ru | 0.00001 ppm | 0.000148 | <DL | 0.00022175 | 0.00022513 | <DL | <DL | <DL | <DL | 0.00085459 |
| Pd | 0.00001 ppm | 0.001251 | 0.00078049 | 0.00122984 | 0.00116238 | 0.00052053 | <DL | <DL | <DL | 0.01774337 |
| Ag | 0.00001 ppm | 0.000591 | 0.00032001 | 0.00044528 | 0.00044931 | 0.00024317 | 0.000200886 | 0.000150441 | 0.000157264 | 0.02485412 |
| Cd | 0.00006 ppm | <DL | <DL | <DL | <DL | <DL | <DL | <DL | <DL | <DL |
| Sn | 0.00006 ppm | <DL | <DL | <DL | <DL | <DL | <DL | <DL | <DL | <DL |
| Sb | 0.00001 ppm | 0.000984 | 0.00057352 | 0.00035953 | 0.00045381 | 0.00048174 | 0.000481736 | 0.000477532 | 0.000395958 | 0.00254453 |
| Te | 0.00002 ppm | <DL | <DL | <DL | <DL | <DL | <DL | <DL | <DL | <DL |
| Cs | 0.00002 ppm | 0.000222 | 0.00012444 | 0.00131961 | 0.00099972 | 0.00018718 | 9.84511E-05 | 9.35429E-05 | 8.75762E-05 | 0.00090671 |
| Ba | 0.00003 ppm | 0.044925 | 0.08175824 | 2.38653145 | 1.78023413 | 0.48395463 | 0.123140347 | 0.11484875 | 0.113488812 | 13.0146548 |
| La | 0.00003 ppm | 0.001253 | 0.00224902 | <DL | <DL | <DL | <DL | <DL | <DL | 0.00034319 |
| Ce | 0.00003 ppm | 0.002443 | 0.00435078 | <DL | <DL | <DL | <DL | <DL | <DL | 0.00013916 |
| Pr | 0.00004 ppm | 0.000423 | 0.0005654 | <DL | <DL | <DL | <DL | <DL | <DL | 0.00012619 |
| Nd | 0.00003 ppm | 0.001293 | 0.00210358 | <DL | <DL | <DL | <DL | <DL | <DL | 7.3165E-05 |
| Sm | 0.00004 ppm | 0.000355 | 0.00047573 | <DL | <DL | <DL | <DL | <DL | <DL | 0.00019187 |
| Eu | 0.00003 ppm | 0.000179 | 0.00013932 | <DL | <DL | <DL | <DL | <DL | <DL | 0.0006572 |
| Gd | 0.00003 ppm | 0.000353 | 0.00046746 | <DL | <DL | <DL | <DL | <DL | <DL | 0.00011809 |
| Tb | 0.00003 ppm | 0.00017 | 0.00010092 | <DL | <DL | <DL | <DL | <DL | <DL | 0.000129 |
| Dy | 0.00004 ppm | 0.00034 | 0.00036995 | <DL | <DL | <DL | <DL | <DL | <DL | 0.00011961 |
| Ho | 0.00002 ppm | 0.000163 | 0.00011195 | <DL | <DL | <DL | <DL | <DL | <DL | 0.0001195 |
| Er | 0.00004 ppm | 0.000225 | 0.00020243 | <DL | <DL | <DL | <DL | <DL | <DL | 0.00011461 |
| Tm | 0.00006 ppm | 0.000119 | 4.7861E-05 | <DL | <DL | <DL | <DL | <DL | <DL | 0.00010025 |
| Yb | 0.00005 ppm | 0.000212 | 0.00018885 | <DL | <DL | <DL | <DL | <DL | <DL | 0.00012784 |
| Lu | 0.00004 ppm | 0.000141 | 6.5896E-05 | <DL | <DL | <DL | <DL | <DL | <DL | 0.00012625 |
| Hf | 0.00005 ppm | <DL | <DL | <DL | <DL | <DL | <DL | <DL | <DL | <DL |
| W | 0.00008 ppm | 0.000891 | 0.00104552 | <DL | <DL | 0.0002763 | 0.000876032 | 0.000804276 | 0.000885303 | 0.0007876 |
| Re | 0.00003 ppm | <DL | <DL | <DL | <DL | <DL | <DL | <DL | <DL | <DL |
| Ir | 0.00004 ppm | <DL | <DL | <DL | <DL | <DL | <DL | <DL | <DL | <DL |
| Pt | 0.00001 ppm | <DL | <DL | <DL | <DL | <DL | <DL | <DL | <DL | <DL |
| Tl | 0.00005 ppm | <DL | <DL | <DL | <DL | <DL | <DL | <DL | <DL | <DL |
| Pb | 0.00003 ppm | 0.000736 | 0.00153302 | <DL | <DL | <DL | 0.000121575 | 0.000105028 | 7.90684E-05 | 0.00012266 |
| Th | 0.00001 ppm | 0.000926 | 0.00181672 | <DL | <DL | <DL | <DL | <DL | <DL | 0.00015236 |
| U | 0.00003 ppm | 0.000192 | 0.000493 | <DL | <DL | <DL | <DL | <DL | <DL | <DL |

Table 6.3: ICPMS analyses for samples collected in 2016. Detection limits do not represent uncertainty in the measurement.

| Analyte | Unit | 17-001 | 17-002 | 17-003 | 17-004 | 17-006 | 17-007 | 17-008 | 17-009 | 17-010 | O10 dupli | 17-011 | 17-012 | 17-013 | 17-014 | 17-015 | 17-016 | 17-017 | 17-018 | 17-019 | 17-020 | O20 dupli | 17-022 | 17-023 | 17-024 | |
|---------|------|---------|---------|---------|---------|---------|---------|---------|---------|---------|-----------|---------|---------|---------|---------|---------|---------|---------|---------|---------|---------|-----------|---------|---------|---------|---------|
| Li | ppm | 0.317 | 0.301 | 0.333 | 0.380 | 18.5 | 18.3 | 17.0 | 14.1 | 12.6 | 10.3 | 6.61 | 5.28 | 0.0677 | 10.1 | 0.0692 | 12.6 | 0.456 | 1.27 | 11.7 | 1.87 | 2.19 | 4.05 | 0.485 | 0.602 | |
| Be | ppm | <DL | <DL | <DL | <DL | 0.0014 | 0.0013 | 0.0023 | 0.0015 | 0.0042 | 0.0029 | 0.0046 | 0.0033 | 0.0011 | 0.0025 | <DL | 0.0038 | 0.0011 | <DL | 0.0036 | <DL | <DL | <DL | <DL | <DL | |
| B | ppm | 7.50 | 6.78 | 7.33 | 8.98 | 140 | 159 | 183 | 175 | 219 | 190 | 126 | 134 | 1.46 | 16.2 | 0.782 | 13.9 | 2.44 | 2.65 | 24.7 | 2.53 | 2.68 | 11.7 | 4.38 | 4.99 | |
| Na | ppm | 3039 | 3049 | 3010 | 3427 | 61236 | 63708 | 69949 | 61289 | 96623 | 99410 | 109164 | 102538 | 1009 | 93456 | 473 | 93550 | 6629 | 12364 | 79230 | 17170 | 17398 | 32672 | 5879.63 | 6800.54 | |
| Mg | ppm | 10.1 | 9.12 | 9.40 | 6.87 | 573 | 609 | 895 | 504 | 2383 | 2487 | 3393 | 4679 | 1.34 | 1987 | 90.9 | 2195 | 8.80 | 125 | 797 | 270 | 295 | 244 | 28.1 | 27.0 | |
| Al | ppm | 0.0114 | 0.0128 | 0.0113 | 0.0140 | 0.357 | 0.178 | 0.0394 | 0.0345 | 0.0988 | 0.0939 | 0.138 | 0.274 | 0.0275 | 0.0166 | 0.0258 | 0.0016 | 0.0286 | 0.0511 | 0.0305 | 0.0326 | 0.202 | 0.0067 | 0.0057 | | |
| Si | ppm | 13.1 | 12.4 | 12.7 | 14.1 | 13.8 | 13.2 | 12.7 | 7.91 | 15.8 | 17.0 | 21.7 | 23.6 | 3.64 | 16.6 | 4.11 | 14.1 | 9.45 | 9.78 | 10.5 | 8.01 | 8.64 | 6.46 | 8.30 | 9.22 | |
| P | ppm | 0.041 | 0.032 | <DL | 0.239 | <DL | <DL | <DL | 0.397 | <DL | <DL | 818 | 35.9 | <DL | <DL | <DL | <DL | <DL | <DL | 2.09 | 0.306 | 0.369 | 0.429 | <DL | <DL | |
| K | ppm | 10.3 | 9.31 | 9.91 | 9.09 | 1595 | 1573 | 2549 | 1133 | 6929 | 6985 | 11862 | 13592 | 2.07 | 4601 | 10.1 | 4564 | 14.9 | 34.9 | 1742 | 74.6 | 77.2 | 354 | 16.2 | 17.9 | |
| Ca | ppm | 24.3 | 22.0 | 22.9 | 15.7 | 1334 | 1304 | 2137 | 1036 | 6507 | 6777 | 11240 | 14020 | 6 | 10046 | 277 | 10436 | 33 | 272 | 2272 | 719 | 728 | 1283 | 42 | 37 | |
| Ti | ppm | 0.00163 | 0.00154 | 0.00153 | 0.00213 | 0.0548 | 0.0609 | 0.0587 | 0.0817 | 0.0329 | 0.0298 | 0.0466 | 0.0384 | 0.00211 | 0.0323 | 0.0195 | 0.0367 | 0.0182 | 0.0434 | 0.0469 | 0.0488 | 0.0487 | 0.0468 | 0.0178 | 0.0245 | |
| V | ppm | 0.0208 | 0.0229 | 0.0255 | 0.0265 | 0.258 | 0.266 | 0.303 | 0.296 | 0.437 | 0.426 | 0.438 | 0.488 | 0.0340 | 0.476 | 0.0272 | 0.550 | 0.0661 | 0.101 | 0.443 | 0.147 | 0.146 | 0.250 | 0.0636 | 0.0704 | |
| Cr | ppm | 0.0167 | 0.0119 | 0.0163 | 0.0368 | 0.0337 | 0.0111 | 0.00571 | 0.0400 | 0.00983 | 0.00835 | 0.0597 | 0.0217 | 0.0297 | 0.0170 | 0.00447 | 0.0102 | 0.0233 | 0.00847 | 0.0134 | 0.00715 | 0.00707 | 0.00914 | 0.0209 | 0.0174 | |
| Fe | ppm | <DL | <DL | <DL | 0.0107 | 0.0624 | <DL | <DL | 0.883 | 0.790 | 0.815 | 185 | 19.4 | 0.181 | 4.41 | 0.212 | 1.83 | 0.121 | 1.52 | 9.36 | 0.346 | 0.347 | 0.701 | 0.113 | 0.133 | |
| Mn | ppm | 0.0249 | 0.0306 | 0.0299 | 0.0165 | 0.0480 | 0.0087 | 0.0367 | 0.149 | 0.150 | 0.154 | 2.11 | 0.470 | 0.0343 | 0.370 | 0.632 | 0.404 | 0.0325 | 0.712 | 0.434 | 1.39 | 1.39 | 1.27 | 0.134 | 0.114 | |
| Co | ppm | 0.00023 | 0.00021 | 0.00026 | 0.00048 | 0.00374 | 0.00345 | 0.00424 | 0.00427 | 0.00599 | 0.00573 | 0.0183 | 0.00989 | 0.00026 | 0.00900 | 0.00786 | 0.0112 | 0.00073 | 0.00135 | 0.00645 | 0.00214 | 0.00196 | 0.00372 | 0.00079 | 0.00051 | |
| Ni | ppm | 0.00006 | 0.00122 | 0.00054 | 0.00594 | 0.0517 | 0.0493 | 0.0706 | 0.0769 | 0.181 | 0.178 | 0.373 | 0.352 | 0.00372 | 0.286 | 0.0573 | 0.344 | 0.00602 | 0.0188 | 0.109 | 0.0377 | 0.0390 | 0.0681 | 0.0468 | 0.00331 | |
| Cu | ppm | 0.133 | 0.118 | 0.124 | 0.132 | 5.14 | 3.64 | 3.25 | 3.04 | 5.40 | 6.94 | 21.9 | 15.1 | 0.110 | 8.22 | 0.0541 | 7.64 | 0.403 | 0.637 | 5.50 | 1.13 | 1.00 | 2.39 | 0.345 | 0.354 | |
| Zn | ppm | 0.00069 | 0.00566 | 0.00097 | 0.0429 | 0.0488 | 0.0242 | 0.00798 | 0.0230 | 0.129 | 0.137 | 0.236 | 0.203 | 0.00389 | 0.349 | 0.00161 | 0.293 | <DL | 0.00677 | 0.0234 | 0.0116 | 0.0124 | 0.123 | <DL | <DL | |
| Ga | ppm | 0.00010 | <DL | <DL | 0.00011 | 0.00059 | 0.00064 | 0.00053 | 0.00084 | 0.00103 | 0.00115 | 0.00500 | 0.00100 | 0.00013 | 0.00089 | <DL | 0.00117 | 0.00024 | 0.00053 | 0.00048 | 0.00048 | 0.00067 | 0.00017 | 0.00020 | 0.00017 | 0.00020 |
| Ge | ppm | 0.0592 | 0.0476 | 0.0287 | 0.0121 | 0.0279 | 0.0319 | 0.0254 | 0.00808 | <DL | <DL | <DL | <DL | <DL | <DL | <DL | <DL | <DL | <DL | 0.00310 | <DL | <DL | <DL | 0.00627 | 0.00385 | |
| As | ppm | 0.0236 | 0.0228 | 0.0243 | 0.0247 | 0.399 | 0.323 | 0.388 | 0.284 | 0.865 | 0.852 | 1.52 | 1.52 | 0.0316 | 1.46 | 0.0128 | 1.55 | 0.0425 | 0.0969 | 0.513 | 0.136 | 0.132 | 0.266 | 0.0385 | 0.0404 | |
| Se | ppm | 0.0666 | 0.0633 | 0.0669 | 0.0678 | 1.09 | 0.889 | 1.09 | 0.803 | 2.50 | 2.49 | 3.84 | 4.23 | 0.0416 | 4.17 | 0.0352 | 4.48 | 0.122 | 0.269 | 1.42 | 0.372 | 0.365 | 0.725 | 0.105 | 0.113 | |
| Rb | ppm | 0.0130 | 0.0113 | 0.0123 | 0.0118 | 3.86 | 3.64 | 4.45 | 3.40 | 8.52 | 8.86 | 12.1 | 12.9 | 0.00409 | 15.2 | 0.00884 | 15.8 | 0.0194 | 0.0460 | 5.32 | 0.0746 | 0.0733 | 0.933 | 0.0197 | 0.0218 | |
| Sr | ppm | 2.29 | 2.12 | 2.18 | 1.78 | 62.7 | 53.4 | 84.8 | 42.3 | 366 | 383 | 836 | 974 | 0.2601 | 564 | 2.74 | 591 | 5.8 | 3.4 | 122 | 59.0 | 59.1 | 93.2 | 7.37 | 7.34 | |
| Y | ppm | <DL | <DL | <DL | <DL | 0.00090 | 0.00081 | 0.00073 | 0.00096 | 0.00124 | 0.00124 | 0.00266 | 0.00292 | <DL | 0.00449 | 0.00016 | 0.00201 | <DL | 0.00018 | 0.00082 | 0.00031 | 0.00033 | 0.00064 | <DL | <DL | |
| Zr | ppm | <DL | <DL | <DL | <DL | 0.00312 | 0.0788 | 0.00439 | 0.00234 | 0.00663 | 0.00596 | 0.0158 | 0.0119 | 0.00114 | 0.0111 | <DL | 0.00959 | <DL | 0.00055 | 0.00237 | 0.00067 | 0.00054 | 0.00465 | <DL | <DL | |
| Nb | ppm | <DL | <DL | <DL | <DL | 0.00016 | 0.00014 | 0.00020 | 0.00018 | 0.00031 | 0.00027 | 0.00085 | 0.00075 | <DL | 0.00048 | <DL | 0.00052 | <DL | <DL | 0.00013 | <DL | <DL | <DL | <DL | <DL | |
| Mo | ppm | 0.00185 | 0.00115 | 0.00089 | 0.00088 | 0.00867 | 0.00761 | 0.00864 | 0.0102 | 0.0163 | 0.0145 | 0.0453 | 0.0486 | <DL | 0.00066 | 0.0369 | 0.00013 | 0.00035 | 0.00948 | 0.00212 | 0.00219 | 0.00830 | <DL | <DL | <DL | |
| Ru | ppm | 0.00040 | 0.00032 | 0.00037 | 0.00025 | 0.00637 | 0.00539 | 0.00775 | 0.00476 | 0.0252 | 0.0236 | 0.0480 | 0.0554 | 0.00012 | 0.0425 | 0.00069 | 0.0470 | 0.00106 | 0.00518 | 0.0120 | 0.00988 | 0.00065 | 0.0136 | 0.00121 | 0.00128 | |
| Rh | ppm | 0.00043 | 0.00606 | 0.00213 | 0.00118 | 0.00354 | 0.00757 | 0.00294 | 0.00656 | 0.00343 | 0.00268 | 0.0793 | 0.00985 | 0.00022 | 0.00536 | <DL | 0.00632 | 0.00065 | 0.00114 | 0.00344 | 0.00187 | 0.00153 | 0.00353 | 0.00277 | 0.00322 | |
| Ag | ppm | <DL | <DL | <DL | <DL | 0.00091 | 0.00063 | 0.00046 | 0.00086 | 0.00049 | 0.00051 | 0.00358 | 0.00074 | <DL | 0.00045 | <DL | 0.00049 | <DL | <DL | 0.00064 | <DL | <DL | 0.00026 | <DL | <DL | |
| Cd | ppm | <DL | <DL | <DL | <DL | 0.00020 | 0.00021 | 0.00013 | 0.00039 | 0.00078 | 0.00077 | 0.00276 | 0.00181 | <DL | 0.00154 | <DL | 0.00152 | <DL | <DL | 0.00024 | <DL | <DL | <DL | <DL | <DL | |
| Sb | ppm | <DL | <DL | <DL | <DL | 0.00081 | 0.00096 | 0.00031 | 0.00042 | 0.00049 | 0.00035 | 0.00070 | 0.00145 | 0.00052 | 0.00109 | <DL | 0.00032 | <DL | <DL | 0.00017 | <DL | <DL | 0.00064 | <DL | <DL | |
| Sn | ppm | 0.00079 | 0.00081 | 0.00137 | 0.00133 | 0.00276 | 0.00082 | 0.00118 | 0.00075 | 0.00343 | 0.00335 | 0.0114 | 0.00846 | 0.00069 | 0.00623 | 0.00068 | 0.00066 | 0.00046 | 0.00135 | 0.00059 | 0.00052 | 0.00053 | 0.00032 | 0.00066 | 0.00066 | |
| Te | ppm | <DL | <DL | <DL | <DL | <DL | <DL | <DL | <DL | <DL | <DL | <DL | <DL | <DL | <DL | <DL | |
| Cs | ppm | 0.00098 | 0.00090 | 0.00092 | 0.00102 | 0.464 | 0.424 | 0.552 | 0.357 | 1.18 | 1.16 | 1.25 | 1.32 | 0.00038 | 0.832 | 0.00020 | 0.870 | 0.00188 | 0.00403 | 0.540 | 0.00544 | 0.00543 | 0.0276 | 0.00130 | 0.00151 | |
| Ba | ppm | 1.58 | 1.36 | 1.32 | 1.04 | 142 | 142 | 0.00897 | 0.00556 | 3.55 | 3.66 | 8.78 | 11.7 | 0.316 | 16.5 | 0.0737 | 17.0 | 0.0956 | 0.0903 | 0.265 | 0.0949 | 0.0965 | 0.339 | 0.0726 | 0.0628 | |
| La | ppm | 0.00066 | <DL | <DL | <DL | 0.00162 | 0.00132 | 0.00147 | 0.00280 | 0.00427 | 0.00401 | 0.00502 | 0.00494 | <DL | 0.00385 | <DL | 0.00422 | <DL | <DL | 0.00211 | <DL | <DL | <DL | <DL | <DL | |
| Ce | ppm | <DL | <DL | <DL | <DL | 0.00366 | 0.00452 | 0.00004 | 0.00024 | 0.00010 | 0.00008 | 0.00022 | 0.00011 | 0.00180 | 0.00051 | <DL | 0.00014 | <DL | <DL | <DL | <DL | <DL | 0.00357 | <DL | <DL | |
| Pr | ppm | <DL | <DL | <DL | <DL | 0.00070 | 0.00060 | 0.00076 | 0.00060 | 0.00215 | 0.00173 | 0.00239 | 0.00245 | <DL | 0.00189 | <DL | 0.00221 | <DL | <DL | 0.00134 | <DL | <DL | <DL | <DL | <DL | |
| Nd | ppm | <DL | <DL | <DL | <DL | 0.00009 | 0.00016 | 0.00010 | 0.00006 | 0.00047 | 0.00050 | 0.00106 | 0.00124 | <DL | 0.00091 | <DL | 0.00098 | < | | | | | | | | |

7.0: Conclusions

7.1: Mineralization in the Irish Orefield

Re-Os geochronology for the Silvermines deposit in Ireland produced a similar age (334.0 ± 6.1 Ma) as the previously dated Lisheen deposit (346.6 ± 3.0 Ma). Both of these ages require that mineralization occurred in the shallow subsurface prior to extensive burial. The slight differences in the ages of Lisheen and Silvermines also suggest that the Irish orefield had a protracted, likely episodic, mineralization history. The robustness of these dates also indicate that previous paleomagnetic ages represent remagnetization ages associated with heating during the Variscan orogeny rather than primary magnetization associated with the formation of the ore deposits. The precise initial $^{187}\text{Os}/^{188}\text{Os}$ obtained for Lisheen (0.253 ± 0.045) and Silvermines (0.453 ± 0.006) reflect the Os isotopic composition of the hydrothermal fluids that formed the deposits. The low initial $^{187}\text{Os}/^{188}\text{Os}$ calculated for these deposits is consistent either with the sourcing of metals from the Paleozoic basement or mixing between a mantle and a crustal source.

7.2: Re-Os systematics and the recommended approach to Re-Os geochronology

The primary goal of this thesis was to determine which techniques and methods could be applied to pyrite Re-Os geochronology to increase the probability that precise and accurate age data is produced. Through the various datasets referenced and produced in this thesis important recommendations can be made when developing a Re-Os geochronology project.

When selecting rocks for Re-Os geochronology, an emphasis should be put on collecting paragenetically simple samples in order to minimize potential mineral contaminants which have been shown through LA-ICPMS and TIMS analysis to have a significant negative impact on the quality of isochron regression (e.g. LK 451 and LK 359 from Chapter 4). The proportion of samples that produced highly precise isochrons in this study was small, it is suggested that many different samples are collected to enhance the likelihood that a high quality sample was collected.

Each sample should be examined petrographically to indicate its location in the paragenetic sequence and to document any areas of concern (e.g. impurities, alteration). Follow

up investigations using compositional mapping (e.g. EMPA, LA-ICPMS) may reveal complexity that is not evident during petrographic investigation (e.g. Hawker Creek samples from Chapter 4). Whereas Re compositional mapping is the most direct method for understanding the Re-Os systematics of a particular sample, useful information can be gleaned from Mo mapping, as it mimics the behaviour of Re in sulphides. Other elements such as Si, Al, and K as well as sulphur isotopes may be useful in identifying regions impacted by alteration.

Samples should be crushed to a size that allows for the efficient use of heavy liquid and magnetic separation. Both of these methods should be applied for all samples as they can remove impurities and alteration products from crushed samples. If carbonate material is present within the crushed samples it is recommended that dilute HCl (e.g. 0.2N) is used to remove any remaining carbonate that remains after heavy liquid separation. Follow up investigation of all prepared mineral separates should be used to document the mineralogy and paragenetic location of the minerals remaining after these processing steps have been finished.

Interpreting the isotopic data obtained from these mineral separates should be done carefully. For regressions that produce unreasonable initial Os ratios or require unreasonable variation in the initial Os ratio only cautious statements should be made about the age obtained. It is in these cases that supplemental data (e.g. petrographic images, composition analysis) may be required to correctly interpret the dataset, as shown in Chapters 4 and 5.

This thesis focused on Zn-Pb metallic ore deposits found in sedimentary basins, however these recommendations can be generalized to the application of Re-Os geochronology to other ore deposit types

7.3: Mineralization in the Canadian Cordillera

The methods chosen for the analysis and preparation of the Cordilleran samples were based on the lessons learned from the Irish and Baffin Island deposits (Chapters 3 and 4). Although highly precise isochrons were not produced for the Cordilleran deposits, the additional context provided by the compositional mapping program helped in interpreting the Re-Os dataset, providing some additional confidence that the data produced represents reliable geochronological information. All three deposit locations (Prairie Creek, Robb Lake, and the Salmo district mines) produced Re-Os ages > 300 Ma and are consistent with the deposits being related to the active tectonic margin that existed along the western margin of North America

during the Paleozoic. Younger paleomagnetic ages associated with the Laramide orogeny appear to represent remagnetization ages, as opposed to primary mineralization ages.

7.4: Sources and Sinks of Re-Os within Sedimentary Basins

Water samples from the Williston basin of Saskatchewan were used to produce the first dataset of Re-Os isotopic values for groundwater in deep subsurface. Osmium in the deep aquifers appear to be depleted compared to the ≥ 10 ppq concentrations expected from source waters (e.g. seawater, meteoric), and typically had levels < 10 ppq and in many cases < 1 ppq. The geochemical behaviour of Re and Os is quite different than most other solutes as they remain depleted even in highly saline brines suggesting that removal processes dominate any leaching from the minerals found in the aquifer skeleton. The removal mechanism is not known with confidence, but in regions where petroleum accumulates Re and Os typically are extremely depleted in the co-produced water samples. In aquifers without accumulations of petroleum it is speculated that Re and Os absorb on to or into clays or organic matter as water migrates through the aquifer. The observation that Re and Os are depleted in basinal brines puts into question the original source of Re and Os found in sulphides from sediment-hosted ore deposits. If Re and Os are from these basinal brines, as is expected for the majority of metals, then the brines that form ore deposits must have a peculiar chemistry (e.g. oxic) or are leaching from rock types not confidently sampled in our study (e.g. basement). Alternatively, Re-Os may be sourced from a separate reservoir than other metals, such as near surface water, as these reservoirs typically contain higher concentrations of Re and Os.

7.5: Future Considerations and Unanswered Questions

The original premise of this thesis was to increase the knowledge base of the still-developing Re-Os system, with a primary application to the geochronology of pyrite in sediment-hosted ores. In this regard the thesis was successful, however there are still many unanswered questions about the Re-Os system that will require more dedicated studies in the future.

From a mineral separation perspective, further experiments could be undertaken on the leaching procedure experimented with in this thesis. The most enigmatic result from the leaching procedures is the low Re-Os ratios produced from leachate material. The Re-Os ratios, and more importantly the $^{187}\text{Os}/^{188}\text{Os}$ values, of the leachates do not clearly mimic known mineral hosts in

many samples. A dedicated study that carefully measures the influence of grain size, mineral composition, and acid concentration may need to be undertaken to understand this behaviour. Until this issue is resolved, applying these leaching procedures for Re-Os studies should be done cautiously. Magnetic separation is an empirically useful technique, successfully purifying samples and even separating different generations of pyrite in one case (i.e. Hawker Creek). At a fundamental level it is unclear what controls the magnetic susceptibility of pyrite and why there is an apparent correlation with Re concentration in many samples. Full understanding on what controls magnetic susceptibility in pyrite (and other minerals) may require micron scale in-situ magnetic susceptibility measurements (e.g. scanning SQUID microscopy).

A major conclusion of this thesis is that paleomagnetic dates associated with sediment-hosted Zn-Pb deposits do not typically agree with Re-Os dating, however sphalerite Rb-Sr ages consistently overlap with dates produced herein from pyrite Re-Os geochronology. Sphalerite Rb-Sr geochronology is infrequently used due to lingering questions about its robustness and susceptibility to becoming contaminated, but the consistent agreement with Re-Os ages suggests it may be a system with value. In particular it may be useful for future studies, using the methodology recommendations suggested in this thesis, to use both pyrite Re-Os and sphalerite Rb-Sr dating in tandem to determine the age of an ore deposit.

Perhaps the greatest potential for further work is in understanding how Re-Os behave in groundwater systems, as a result of the limited dataset available. In the Williston Basin samples it is unclear at what rate groundwater loses Re and Os in the deep subsurface. A study that follows groundwater from recharge to discharge areas may be able to answer this question. A second unanswered question is if the observations of the Williston basin are applicable to basins without significant petroleum reserves, the latter being implicated as a sink for aqueous Re and Os through oil-water interaction. Such a study should define the importance of non-petroleum sinks such as clays, or other Organic matter. The groundwater samples used in this study were stratigraphically extensive but many important rock types were not sufficiently sampled. In particular, water interacting with basement rock was not properly analyzed and the influence of other rock types (e.g. igneous and metamorphic rocks) on the Re-Os character of fluids were not studied. Finally, some of the co-produced oil-water samples imply water and oil not being in isotopic equilibrium. However, the low concentration of Re and Os within these water samples prevent definitive statements to be made. Therefore, future research should focus on creating

cleaner analytical protocols, or work with larger samples than used in this thesis. Once these difficulties and questions have been overcome, applying Re-Os isotopes in tracing studies of deep groundwaters will become more tractable.

Bibliography

Abbott, J. G. (1986). Setting of sediment-hosted stratiform lead-zinc deposits in Yukon and northeastern British Columbia. *Mineral Deposits of the Northern Cordillera. Canadian Inst. Mining Metal.*, 37, 1-18.

Acken, D., Su, W., Gao, J., & Creaser, R. A. (2014). Preservation of Re - Os isotope signatures in pyrite throughout low - T, high - P eclogite facies metamorphism. *Terra Nova*, 26(5), 402-407.

Almécija, C., Sharma, M., Cobelo-García, A., Santos-Echeandía, J., & Caetano, M. (2015). Osmium and platinum decoupling in the environment: evidences in intertidal sediments (Tagus Estuary, SW Europe). *Environmental Science & Technology*, 49(11), 6545-6553.

Amthor, J. E., Mountjoy, E. W., & Machel, H. G. (1993). Subsurface dolomites in Upper Devonian Leduc Formation buildups, central part of Rimbey-Meadowbrook reef trend, Alberta, Canada. *Bulletin of Canadian Petroleum Geology*, 41(2), 164-185.

Anbar, A. D., Creaser, R. A., Papanastassiou, D. A., & Wasserburg, G. J. (1992). Rhenium in seawater: Confirmation of generally conservative behavior. *Geochimica et Cosmochimica Acta*, 56(11), 4099-4103.

Anderson, I.K., Ashton, J.H., Boyce, A.J., Fallick, A.E., and Russell, M.J., 1998, Ore depositional processes in the Navan Zn-Pb deposit, Ireland: *Economic Geology*, v. 93, p. 535–563

Arne, D. C., Bierlin, F. P., Morgan, J. W., & Stein, H. J. (2001). Re-Os dating of sulfides associated with gold mineralization in central Victoria, Australia. *Economic Geology*, 96(6), 1455-1459.

Barra, F., Ruiz, J., Mathur, R., & Titley, S. (2003). A Re–Os study of sulfide minerals from the Bagdad porphyry Cu–Mo deposit, northern Arizona, USA. *Mineralium Deposita*, 38(5), 585-596.

Belasky, P., Stevens, C. H., & Hanger, R. A. (2002). Early Permian location of western North American terranes based on brachiopod, fusulinid, and coral biogeography. *Palaeogeography, Palaeoclimatology, Palaeoecology*, 179(3-4), 245-266.

Birck, J. L., Barman, M. R., & Capmas, F. (1997). Re - Os isotopic measurements at the femtomole level in natural samples. *Geostandards newsletter*, 21(1), 19-27.

Boyce, A.J., Coleman, M.L., and Russell, M.J., 1983, Formation of fossil hydrothermal chimneys and mounds from Silvermines, Ireland: *Nature*, v. 306, p. 545–550.

Boyce, A.J., Litle, C.T.S., Russel, M.J., 2003, A new fossil vent biota in the Balleynoe barite deposit, Silvermines, Ireland: Evidence for intracratonic sea-floor hydrothermal activity about 352 Ma: *Economic Geology*, v.92, p. 649-656.

Bradley, D. C., & Leach, D. L. (2003). Tectonic controls of Mississippi Valley-type lead–zinc mineralization in orogenic forelands. *Mineralium Deposita*, 38(6), 652-667.

Bradley, D. C., Leach, D. L., Symons, D., Emsbo, P., Premo, W., Breit, G., & Sangster, D. F. (2004). Reply to Discussion on “Tectonic controls of Mississippi Valley-type lead–zinc mineralization in orogenic forelands” by SE Kesler, JT Christensen, RD Hagni, W. Heijlen, JR Kyle, KC Misra, P. Muchez, and R. van der Voo, *Mineralium Deposita*. *Mineralium Deposita*, 39(4), 515-519.

Brenan, J. M., Cherniak, D. J., & Rose, L. A. (2000). Diffusion of osmium in pyrrhotite and pyrite: implications for closure of the Re–Os isotopic system. *Earth and Planetary Science Letters*, 180(3-4), 399-413.

Brenan, J. M., McDonough, W. F., & Ash, R. (2005). An experimental study of the solubility and partitioning of iridium, osmium and gold between olivine and silicate melt. *Earth and Planetary Science Letters*, 237(3-4), 855-872.

Brenan, J. M., & McDonough, W. F. (2009). Core formation and metal–silicate fractionation of osmium and iridium from gold. *Nature Geoscience*, 2(11), 798.

Burgardt, P., & Seehra, M. S. (1977). Magnetic susceptibility of iron pyrite (FeS₂) between 4.2 and 620 K. *Solid State Communications*, 22(2), 153-156.

Canadian Zinc Corporation 2010. *Main Report for Developer's Assessment Report*, Canadian Zinc Corporation submission to Mackenzie Valley Review Board in support of Environmental Assessment of Prairie Creek Mine EA 0809-002.

Canadian Zinc Corporation 2017. *Prairie Creek Property Feasibility Study NI 43-101 Technical Report*.

Cathles, L. M., & Smith, A. T. (1983). Thermal constraints on the formation of Mississippi Valley-type lead-zinc deposits and their implications for episodic basin dewatering and deposit genesis. *Economic Geology*, 78(5), 983-1002.

Cathles, L. M., Erendi, A. H. J., & Barrie, T. (1997). How long can a hydrothermal system be sustained by a single intrusive event?. *Economic Geology*, 92(7-8), 766-771.

Carboni, V., Walsh, J. J., Stewart, D. R. A., Güven, J. F., & Eliopoulos, D. G. (2003). Timing and geometry of normal faults and associated structures at the Lisheen Zn/Pb deposit, Ireland—investigating their role in the transport and the trapping of metals. In *Mineral Exploration and Sustainable Development: Proceedings of the 7th Biennial SGA Meeting* (pp. 665-668).

Chadwick, R. A., Evans, D. J., & Holliday, D. W. (1993). The Maryport fault: the post-Caledonian tectonic history of southern Britain in microcosm. *Journal of the Geological Society*, 150(2), 247-250.

Chappaz, A., Gobeil, C., & Tessier, A. (2008). Sequestration mechanisms and anthropogenic inputs of rhenium in sediments from Eastern Canada lakes. *Geochimica et Cosmochimica Acta*, 72(24), 6027-6036.

Chew, D.M., and Stillman, C.J., 2009, Late Caledonian orogeny and magmatism, *in*, Holland, C.H., and Sanders, I.S., eds., *The Geology of Ireland*, 2nd edition: Edinburgh, Dunedin Academic Press, p. 143–173.

Christensen, J. N., Halliday, A. N., Kesler, S. E., & Sangster, D. F. (1993). Further evaluation of the Rb-Sr dating of sphalerite: the Nanisivik Precambrian MVT deposit, Baffin Island, Canada. In *Abstracts with Programs-Geological Society of America* (Vol. 25, p. 471).

Clayton, G., Haughey, N., Sevastopulo, G. D., & Burnett, R. (1989). *Thermal maturation levels in the Devonian and Carboniferous rocks of Ireland*. Geological Survey of Ireland.

Claypool, G. H., Holster, W. T., Kaplan, I. R., Saki, H., & Zak, I. (1980). The age curves for sulphur and oxygen isotopes in marine sulphur and their interpretation. *Chemical Geology*, 54, 149-155.

Creaser, R. A., Wilkinson, J. J., & Hnatyshin, D. (2009). Re-Os dating of sulfide mineralization (pyrite) from the Lisheen Pb-Zn deposit, Ireland. In *2009 Portland GSA Annual Meeting*.

Crocket, J. H., Fleet, M. E., & Stone, W. E. (1992). Experimental partitioning of osmium, iridium and gold between basalt melt and sulphide liquid at 1300 C. *Australian Journal of Earth Sciences*, 39(3), 427-432.

Colpron, M., & Nelson, J. L. (Eds.). (2006). Paleozoic evolution and metallogeny of pericratonic terranes at the ancient Pacific margin of North America, Canadian and Alaskan Cordillera. Geological Association of Canada.

Coney, P. J., Jones, D. L., & Monger, J. W. (1980). Cordilleran suspect terranes. *Nature*, 288(5789), 329.

Cousens, B. L. (2007). Radiogenic isotope studies of Pb-Zn mineralization in the Howards Pass area, Selwyn Basin. *Mineral and Energy Resource Potential of the Proposed Expansion to the Nahanni National Park Reserve, North Cordillera, Northwest Territories: Geological Survey of Canada, Open File, 5344*, 14.

Cook, D.G. (1977). Two stages of faulting, Virginia Falls map-area, District of Mackenzie; Report of Activities, Part A, Geological Survey of Canada, Paper 77-1A, 113-115.

Dalai, T. K., & Ravizza, G. (2006). Evaluation of osmium isotopes and iridium as paleoflux tracers in pelagic carbonates. *Geochimica et Cosmochimica Acta*, 70(15), 3928-3942.

Danyushevsky, L. V., Robinson, P., Gilbert., S.E. (2011). Routine quantitative multi-element analysis of sulphide minerals by laser ablation ICP-MS: Standard development and consideration of matrix effects. *Geochemistry Exploration Environment Analysis*, 11(1), 51-60.

Davidheiser-Kroll, B., Stuart, E.M., and Boyce, A.J., 2014, Mantle heat drives hydrothermal fluids responsible for carbonate-hosted base metal deposits: Evidence from $^3\text{He}/^4\text{He}$ ore fluids in the Irish Pb-Zn ore district: *Mineralium Deposita*, v. 49, p. 547–553.

Dawson, F.W., Evans, C.G., Marsh, R., Richardson, R. (1994): Uppermost Cretaceous and Tertiary Strata of the Western Canada Sedimentary Basin; in Geological Atlas of the Western Canada Sedimentary Basin, G.D. Mossop and I. Shetsen (comp.), Canadian Society of Petroleum Geologists and Alberta Research Council, URL: <http://ags.aer.ca/publications/chapter-24-uppermost-cretaceous-and-tertiary-strata>.

Dekkers, M. J. (1988). Magnetic properties of natural pyrrhotite Part I: Behaviour of initial susceptibility and saturation-magnetization-related rock-magnetic parameters in a grain-size dependent framework. *Physics of the Earth and Planetary Interiors*, 52(3-4), 376-393.

de Wit, R., Gronberg, E.C., Richards, W.B., & Richmond, W.O. (1973). Tathlina area, District of MacKenzie; in *The Future Petroleum Provinces of Canada – Their Geology and Potential*, (ed.) R.G. McCrossan; Canadian Society of Petroleum Geologists, Memoir 1, 187-212.

DiMarzio, J. M., Georgiev, S. V., Stein, H. J., & Hannah, J. L. (2018). Residency of rhenium and osmium in a heavy crude oil. *Geochimica et Cosmochimica Acta*, 220, 180-200.

Ding, C., Nie, F., Bagas, L., Dai, P., Jiang, S., Ding, C., ... & Shao, G. (2016). Pyrite Re–Os and zircon U–Pb dating of the Tugurige gold deposit in the western part of the Xing'an–Mongolia Orogenic Belt, China and its geological significance. *Ore Geology Reviews*, 72, 669-681.

Dixon, P.R., LeHuray, A.P., and Rye, D.M., 1990, Basement geology and tectonic evolution of Ireland as deduced from Pb isotopes: *Journal of the Geological Society* [London], v. 147, p. 121–132.

Drivet, E., & Mountjoy, E. W. (1997). Dolomitization of the Leduc Formation (Upper Devonian), southern Rimbey-Meadowbrook reef trend, Alberta. *Journal of Sedimentary Research*, 67(3).

Du, A., Wu, S., Sun, D., Wang, S., Qu, W., Markey, R., ... & Malinovskiy, D. (2004). Preparation and certification of Re - Os dating reference materials: Molybdenites HLP and JDC. *Geostandards and Geoanalytical Research*, 28(1), 41-52.

Earls, G. (1995). A Review of the Prairie Creek Deposit, NWT, Canada; Internal Report, San Andreas Resources Corporation, 36 p.

Enkin, R. J., Osadetz, K. G., Baker, J., & Kisilevsky, D. (2000). Orogenic remagnetizations in the Front Ranges and Inner Foothills of the southern Canadian Cordillera: Chemical harbinger and thermal handmaiden of Cordilleran deformation. *Geological Society of America Bulletin*, 112(6), 929-942.

Findlay, A. (2000). Geology and Exploration Potential of the Stratabound Massive Sulphides, Prairie Creek Mine, NWT;. Internal Report, Canadian Zinc Corporation, 17 p.

Fraser, S. C., (1996). Geology and Geochemistry of the Prairie Creek Zn, Pb, Ag Deposits, Southern Mackenzie Mountains, NWT; M.Sc. thesis, University of Alberta, Edmonton, Alberta, 146 p.

Fusciardi, L. P., Guven, J. F., Stewart, D. R. A., Carboni, V., & Walshe, J. J. (2003). The geology and genesis of the Lisheen Zn-Pb deposit, Co. Tipperary, Ireland. *Europe's major base metal deposits: Dublin, Irish Association for Economic Geology*, 455-481.

Fyles, J. T., & Hewlett, C. G. (1959). *Stratigraphy and structure of the Salmo lead-zinc area*. Department of Mines.

Garven, G. (1985). The role of regional fluid flow in the genesis of the Pine Point deposit, western Canada sedimentary basin. *Economic Geology*, 80(2), 307-324.

Garven, G., Ge, S., Person, M. A., & Sverjensky, D. A. (1993). Genesis of stratabound ore deposits in the Midcontinent basins of North America; 1, The role of regional groundwater flow. *American Journal of Science*, 293(6), 497-568.

Gannoun, A., & Burton, K. W. (2014). High precision osmium elemental and isotope measurements of North Atlantic seawater. *Journal of Analytical Atomic Spectrometry*, 29(12), 2330-2342.

Georgiev, S. V., Stein, H. J., Hannah, J. L., Galimberti, R., Nali, M., Yang, G., & Zimmerman, A. (2016). Re–Os dating of maltenes and asphaltenes within single samples of crude oil. *Geochimica et Cosmochimica Acta*, 179, 53-75.

Gillen, K. P., Van der Voo, R., & Thiessen, J. H. (1999). Late Cretaceous-early Tertiary remagnetization of the Devonian Swan Hills Formation recorded in carbonate cores from the Caroline gas field, Alberta, Canada. *AAPG bulletin*, 83(8), 1223-1235.

Ghazban, F., Schwarcz, H. P., & Ford, D. C. (1990). Carbon and sulfur isotope evidence for in situ reduction of sulfate, Nanisivik lead-zinc deposits, Northwest Territories, Baffin Island, Canada. *Economic Geology*, 85(2), 360-375.

Godwin, C. I., Gabites, J. E., & Andrew, A. (1988). *LEADTABLE: A galena lead isotope data base for the Canadian Cordillera, with a guide to its use by explorationists*. Province of British Columbia, Ministry of Energy, Mines and Petroleum Resources.

Goodfellow, W.D., Lydon, J.W., and Turner, R.J.W., 1993, Geology and genesis of stratiform sediment-hosted (SEDEX) zinc-lead-silver sulphide deposits, *in*, Kirkham, R.V., Sinclair, W.D., Thorpe, R.I., and Duke, J.M., eds., *Mineral Deposit Modeling: Geological Association of Canada Special Paper 40*, p. 201–251.

Graham, J.R., 2001, Variscan structures, *in* Holland, C.H., ed., *The geology of Ireland: Edinburgh, Dunedin Academic Press*, p. 312–330.

Gustafson, L.B., and Williams, N., 1981, Sediment-hosted stratiform deposits of copper, lead, and zinc, *in* Skinner, B.J., ed., *Economic Geology 75th Anniversary Volume: Lancaster, Penn., Lancaster Press*, p. 139–178.

Hayes, B.J.R., Christopher, J.E., Rosenthal, L., Los, G., MecKercher, B. (1994):Cretaceous Mannville Group of the Western Canada Sedimentary Basin; in *Geological Atlas of the Western Canada Sedimentary Basin*, G.D. Mossop and I. Shetsen (comp.), Canadian Society of Petroleum

Geologists and Alberta Research Council, URL: <http://ags.aer.ca/publications/chapter-19-cretaceous-mannville-group>.

Helz, G. R., Erickson, B. E., & Vorlicek, T. P. (2014). Stabilities of thiomolybdate complexes of iron; implications for retention of essential trace elements (Fe, Cu, Mo) in sulfidic waters. *Metallomics*, 6(6), 1131-1140.

Hitzman, M.W., 1999, Extensional faults that localize Irish syndiagenetic Zn-Pb deposits and their reactivation during Variscan compression, *in*, McCaffrey, K.J.W., Lonergan, L., and Wilkinson, J.J., eds, Fractures, Fluid Flow and Mineralization: Geological Society, London Special Publication 155, p. 233–245.

Hitzman, M.W., and Beaty, D.W., 1996, The Irish Zn-Pb-(Ba) orefield, *in* Sangster, D.F., ed., Carbonate-Hosted Lead-Zinc Deposits: Littleton, Colo., Society of Economic Geologists, Inc., Special Publication 6, p. 112–143.

Hitzman, M.W., Redmond, P.B., and Beaty, D.W., 2002, The carbonate hosted Lisheen Zn-Pb-Ag deposit, County Tipperary, Ireland: *Economic Geology*, v. 97, p. 1627–1655.

Hnatyshin, D. (2012). Geochronology and Trace Element Characteristics of Pyrite from Selected Carbonate Hosted Pb-Zn Ore Deposits. M.Sc. thesis, University of Alberta, Edmonton, Alberta, 138 p.

Hnatyshin, D., Creaser, R. A., Wilkinson, J. J., & Gleeson, S. A. (2015). Re-Os dating of pyrite confirms an early diagenetic onset and extended duration of mineralization in the Irish Zn-Pb ore field. *Geology*, 43(2), 143-146.

Hnatyshin, D., Kontak, D. J., Turner, E. C., Creaser, R. A., Morden, R., & Stern, R. A. (2016). Geochronologic (ReOs) and fluid-chemical constraints on the formation of the Mesoproterozoic-hosted Nanisivik ZnPb deposit, Nunavut, Canada: Evidence for early diagenetic, low-temperature conditions of formation. *Ore Geology Reviews*, 79, 189-217.

- Hodge, V. F., Johannesson, K. H., & Stetzenbach, K. J. (1996). Rhenium, molybdenum, and uranium in groundwater from the southern Great Basin, USA: evidence for conservative behavior. *Geochimica et Cosmochimica Acta*, 60(17), 3197-3214.
- Huang, X. W., Qi, L., Gao, J. F., & Zhou, M. F. (2013). First Reliable Re–Os Ages of Pyrite and Stable Isotope Compositions of Fe (- Cu) Deposits in the Hami Region, Eastern Tianshan Orogenic Belt, NW China. *Resource Geology*, 63(2), 166-187.
- Jiang, S. H., Bagas, L., & Liang, Q. L. (2017). Pyrite Re-Os isotope systematics at the Zijinshan deposit of SW Fujian, China: Constraints on the timing and source of Cu-Au mineralization. *Ore Geology Reviews*, 80, 612-622.
- Jackson, G. D., & Iannelli, T. R. (1981). Rift-related cyclic sedimentation in the Neohelikian Borden Basin, northern Baffin Island. *Geological Survey of Canada, Paper*, 81-10.
- Jensen, G. K. S., Rostron B. J., Palombi, D., Meinik, A. (2015). Open File 2015-1 Saskatchewan Phanerozoic fluids and petroleum systems project: Hydrogeology of the Phanerozoic-aged Strata of Saskatchewan. Saskatchewan Geological Survey, Saskatchewan Ministry of the Economy.
- Jones, G. L. (1992). Irish Carboniferous conodonts record maturation levels and the influence of tectonism, igneous activity and mineralization. *Terra nova*, 4(2), 238-244.
- Kampschulte, A., & Strauss, H. (2004). The sulfur isotopic evolution of Phanerozoic seawater based on the analysis of structurally substituted sulfate in carbonates. *Chemical Geology*, 204(3-4), 255-286.
- Keevil, H. K. (2011). Mineralogical and Geochemical Characterization of Supergene Carbonate-hosted Nonsulphide Zn-Pb Mineralization in Southern and Central British Columbia.

Kelley, K. D., Selby, D., Falck, H., & Slack, J. F. (2017). Re-Os systematics and age of pyrite associated with stratiform Zn-Pb mineralization in the Howards Pass district, Yukon and Northwest Territories, Canada. *Mineralium Deposita*, 52(3), 317-335.

Kendall, B. S., Creaser, R. A., Ross, G. M., & Selby, D. (2004). Constraints on the timing of Marinoan “Snowball Earth” glaciation by ^{187}Re – ^{187}Os dating of a Neoproterozoic, post-glacial black shale in Western Canada. *Earth and Planetary Science Letters*, 222(3-4), 729-740.

Kennedy, M. J., Löhr, S. C., Fraser, S. A., & Baruch, E. T. (2014). Direct evidence for organic carbon preservation as clay-organic nanocomposites in a Devonian black shale; from deposition to diagenesis. *Earth and Planetary Science Letters*, 388, 59-70.

Kesler, S. E., Chesley, J. T., Christensen, J. N., Hagni, R. D., Heijlen, W., Kyle, J. R., ... & Van der Voo, R. (2004). Discussion of “Tectonic controls of Mississippi Valley-type lead-zinc mineralization in orogenic forelands” by DC Bradley and DL Leach. *Mineralium Deposita*, 39(4), 512-514.

Klepacki, D. W., & Wheeler, J. O. (1985). Stratigraphic and structural relations of the Milford, Kaslo and Slocan groups, Goat Range, Lardeau and Nelson map areas, British Columbia. *Current research, part A. Geological Survey of Canada, Paper*, 277-286.

Koehler, G., Kyser, T. K., Enkin, R., & Irving, E. (1997). Paleomagnetic and isotopic evidence for the diagenesis and alteration of evaporites in the Paleozoic Elk Point Basin, Saskatchewan, Canada. *Canadian Journal of Earth Sciences*, 34(12), 1619-1629.

Kozdon, R., Kita, N. T., Huberty, J. M., Fournelle, J. H., Johnson, C. A., & Valley, J. W. (2010). In situ sulfur isotope analysis of sulfide minerals by SIMS: Precision and accuracy, with application to thermometry of ~ 3.5 Ga Pilbara cherts. *Chemical Geology*, 275(3), 243-253.

Large, R. R., Danyushevsky, L., Hollit, C., Maslennikov, V., Meffre, S., Gilbert, S., & Singh, B. (2009). Gold and trace element zonation in pyrite using a laser imaging technique: Implications

for the timing of gold in orogenic and Carlin-style sediment-hosted deposits. *Economic Geology*, 104(5), 635-668.

Lawley, C. J. M., & Selby, D. (2012). Re-Os geochronology of quartz-enclosed ultrafine molybdenite: Implications for ore geochronology. *Economic Geology*, 107(7), 1499-1505.

Lawley, C., Selby, D., & Imber, J. (2013). Re-Os molybdenite, pyrite, and chalcopyrite geochronology, lupa goldfield, southwestern Tanzania: tracing metallogenic time scales at midcrustal shear zones hosting orogenic Au deposits. *Economic Geology*, 108(7), 1591-1613.

Leach, D. L., Bradley, D., Lewchuk, M. T., Symons, D. T., de Marsily, G., & Brannon, J. (2001). Mississippi Valley-type lead-zinc deposits through geological time: implications from recent age-dating research. *Mineralium Deposita*, 36(8), 711-740.

Leach, D. L., Bradley, D., Lewchuk, M., Symons, D. T., Premo, W., Brannon, J., & de Marsily, G. (2002). Reply to Discussion on " Mississippi Valley-type lead-zinc deposits through geological time: implications from recent age-dating research" by SE Kesler and CW Carrigan (2001) *Mineralium Deposita* 36: 711–740. *Mineralium Deposita*, 37(8), 803-805.

Leach, D.L., Sangster, D.F., Kelley, K.D., Large, R.R., Garven, G., Allen, C.R., Gutzmer, J., and Walters, S., 2005, Sediment-hosted lead-zinc deposits: A global perspective, in Hedenquist, J.W., Thompson, J.F.H., Goldfarb, R.J., and Richards, J.P., eds., *Economic Geology One Hundredth Anniversary Volume, 1905–2005*: Littleton, Colo., Society of Economic Geologists, Inc., p. 561–607.

Leach, D. L., Bradley, D. C., Huston, D., Pisarevsky, S. A., Taylor, R. D., & Gardoll, S. J. (2010). Sediment-hosted lead-zinc deposits in Earth history. *Economic Geology*, 105(3), 593-625.

Lee, M.J., and Wilkinson, J.J., 2002, Cementation, hydrothermal alteration, and Zn-Pb mineralization of carbonate breccias in the Irish Midlands: *Economic Geology*, v. 97, p. 653-662.

- Levasseur, S., Birck, J. L., & Allegre, C. J. (1999). The osmium riverine flux and the oceanic mass balance of osmium. *Earth and Planetary Science Letters*, 174(1-2), 7-23.
- Levasseur, S., Rachold, V., Birck, J. L., & Allegre, C. J. (2000). Osmium behavior in estuaries: the Lena River example. *Earth and Planetary Science Letters*, 177(3-4), 227-235.
- Lewchuk, M. T., & Symons, D. T. A. (1995). Age and duration of Mississippi Valley-type ore-mineralizing events. *Geology*, 23(3), 233-236.
- Lewchuk, M. T., Symons, D. T., & Sangster, D. F. (1997). Paleomagnetism of the Monarch-Kicking Horse Pass Mississippi Valley-type (MVT) Ore Deposits in Southeastern British Columbia and Laramide Fluid Flow in the Western Canada Sedimentary Basin (WCSB).
- Li, Y., Selby, D., Condon, D., & Tapster, S. (2017). Cyclic Magmatic-Hydrothermal Evolution in Porphyry Systems: High-Precision U-Pb and Re-Os Geochronology Constraints on the Tibetan Qulong Porphyry Cu-Mo Deposit. *Economic Geology*, 112(6), 1419-1440.
- Liu, J., Wu, G., Li, Y., Zhu, M., & Zhong, W. (2012). Re-Os sulfide (chalcopyrite, pyrite and molybdenite) systematics and fluid inclusion study of the Duobaoshan porphyry Cu (Mo) deposit, Heilongjiang Province, China. *Journal of Asian Earth Sciences*, 49, 300-312.
- Luck, J. M., & Allègre, C. J. (1982). The study of molybdenites through the ^{187}Re - ^{187}Os chronometer. *Earth and Planetary Science Letters*, 61(2), 291-296.
- Ludvigsen, R. (1975). Ordovician formations and faunas, southern Mackenzie Mountains. *Canadian Journal of Earth Sciences*, 12(4), 663-697.
- Ludwig, K. R. (2003). Isoplot 3.00: A geochronological toolkit for Microsoft Excel, 71 pp. *Berkeley Geochronol. Center Spec. Publ.*, 4.

Macdonald, A. S. (1973). The Salmo lead-zinc deposits: A study of their deformation and metamorphic features. Ph.D. thesis, University of British Columbia, Vancouver, British Columbia, p. 258.

Machel, H. G., & Mountjoy, E. W. (1987). General constraints on extensive pervasive dolomitization--and their application to the Devonian carbonates of western Canada. *Bulletin of Canadian Petroleum Geology*, 35(2), 143-158.

Macqueen, R. W., & Thompson, R. I. (1978). Carbonate-hosted lead-zinc occurrences in northeastern British Columbia with emphasis on the Robb Lake deposit. *Canadian Journal of Earth Sciences*, 15(11), 1737-1762.

McDaniel, D. K., Walker, R. J., Hemming, S. R., Horan, M. F., Becker, H., & Grauch, R. I. (2004). Sources of osmium to the modern oceans: new evidence from the 190Pt-186Os system. *Geochimica et Cosmochimica Acta*, 68(6), 1243-1252.

Mahdaoui, F., Michels, R., Reisberg, L., Pujol, M., & Poirier, Y. (2015). Behavior of Re and Os during contact between an aqueous solution and oil: consequences for the application of the Re-Os geochronometer to petroleum. *Geochimica et Cosmochimica Acta*, 158, 1-21.

Manns, F.T. (1981). Stratigraphic aspects of the Silurian-Devonian sequence hosting zinc and lead mineralization near Robb Lake, northeastern British Columbia. Ph.D. thesis, University of Toronto, Toronto, Ontario, p. 252.

Mathur, R., Ruiz, J., & Tornos, F. (1999). Age and sources of the ore at Tharsis and Rio Tinto, Iberian Pyrite Belt, from Re-Os isotopes. *Mineralium Deposita*, 34(8), 790-793.

McCandless, T. E., Ruiz, J., & Campbell, A. R. (1993). Rhenium behavior in molybdenite in hypogene and near-surface environments: Implications for Re-Os geochronometry. *Geochimica et Cosmochimica Acta*, 57(4), 889-905.

McClay, K. R., Insley, M. W., & Anderton, R. (1989). Inversion of the Kechika Trough, Northeastern British Columbia, Canada. *Geological Society, London, Special Publications*, 44(1), 235-257.

McCusker, J., and Reed, C., 2013, The role of intrusions in the formation of Irish-type mineralization: *Mineralium Deposita*, v. 48, p. 687–695.

Meisel, T., Walker, R. J., Irving, A. J., & Lorand, J. P. (2001). Osmium isotopic compositions of mantle xenoliths: a global perspective. *Geochimica et Cosmochimica Acta*, 65(8), 1311-1323.

Monger, J. W., Nokleberg, W. J., Coyner, A. R., & Fahey, P. L. (1996). Evolution of the northern North American Cordillera: generation, fragmentation, displacement and accretion of successive North American plate-margin arcs. *Geology and Ore Deposits of the American Cordillera. Geological Society of Nevada*, 1133-1152.

Morelli, R. M., Creaser, R. A., Selby, D., Kelley, K. D., Leach, D. L., & King, A. R. (2004). Re-Os sulfide geochronology of the red dog sediment-hosted Zn-Pb-Ag deposit, Brooks Range, Alaska. *Economic Geology*, 99(7), 1569-1576.

Morelli, R., Creaser, R. A., Seltmann, R., Stuart, F. M., Selby, D., & Graupner, T. (2007). Age and source constraints for the giant Muruntau gold deposit, Uzbekistan, from coupled Re-Os-He isotopes in arsenopyrite. *Geology*, 35(9), 795-798.

Morelli, R. M., Bell, C. C., Creaser, R. A., & Simonetti, A. (2010). Constraints on the genesis of gold mineralization at the Homestake Gold Deposit, Black Hills, South Dakota from rhenium–osmium sulfide geochronology. *Mineralium Deposita*, 45(5), 461-480.

Morrow, D. W. (1984). Sedimentation in Root Basin and Prairie Creek Embayment--Siluro-Devonian, Northwest Territories. *Bulletin of Canadian Petroleum Geology*, 32(2), 162-189.

Morrow, D. W., & Cumming, G. L. (1982). Interpretation of lead isotope data from zinc-lead mineralization in the northern part of the western Canadian Cordillera. *Canadian Journal of Earth Sciences*, 19(5), 1070-1078.

Morrow, D. W., & Cook, D. G. (1987). The Prairie Creek embayment and Lower Paleozoic strata of the southern Mackenzie mountains. *Memoir/Canada. Geological survey*.

Morrow, D. W., Cumming, G. L., & Aulstead, K. L. (1990). *The Gas-bearing Devonian Manetoe Facies, Yukon, and Northwest Territories* (No. 400). Geological Survey of Canada.

Morrow, D. W., Potter, J., Richards, B., & Goodarzi, F. (1993). Paleozoic burial and organic maturation in the Liard Basin region, northern Canada. *Bulletin of Canadian Petroleum Geology*, 41(1), 17-31.

Mountjoy, E. W., Machel, H. G., Green, D., Duggan, J., & Williams-Jones, A. E. (1999). Devonian matrix dolomites and deep burial carbonate cements: a comparison between the Rimbey-Meadowbrook reef trend and the deep basin of west-central Alberta. *Bulletin of Canadian Petroleum Geology*, 47(4), 487-509.

Munhá, J., Relvas, J. M. R. S., Barriga, F. J. A. S., Conceição, P., Jorge, R. C. G. S., Mathur, R., ... & Tassinari, C. C. G. (2005). Osmium isotope systematics in the Iberian Pyrite Belt. In *Mineral deposit research: Meeting the global challenge* (pp. 663-666). Springer, Berlin, Heidelberg.

Nakai, S. I., Halliday, A. N., Kesler, S. E., Jones, H. D., Kyle, J. R., & Lane, T. E. (1993). Rb-Sr dating of sphalerites from Mississippi Valley-type (MVT) ore deposits. *Geochimica et Cosmochimica Acta*, 57(2), 417-427.

Nelson, J. L., Paradis, S., & Zantvoort, W. (1998). The Robb Lake carbonate-hosted lead-zinc deposit, northeastern British Columbia: a Cordilleran MVT deposit. *Geological Fieldwork*, 1999-1.

Nelson, J., Paradis, S., Christensen, J., & Gabites, J. (2002). Canadian Cordilleran Mississippi Valley-type deposits: A case for Devonian-Mississippian back-arc hydrothermal origin. *Economic Geology*, 97(5), 1013-1036.

Nelson, J. L., Colpron, M., Piercey, S. J., Dusel-Bacon, C., Murphy, D. C., & Roots, C. F. (2006). Paleozoic tectonic and metallogenetic evolution of pericratonic terranes in Yukon, northern British Columbia and eastern Alaska. *Paleozoic evolution and metallogeny of pericratonic terranes at the ancient Pacific margin of North America, Canadian and Alaskan Cordillera: Geological Association of Canada Special Paper*, 45, 323-360.

Nelson, J., & Colpron, M. (2007). Tectonics and metallogeny of the British Columbia, Yukon and Alaskan Cordillera, 1.8 Ga to the present. *Mineral Deposits of Canada: A Synthesis of Major Deposit-Types, District Metallogeny, the Evolution of Geological Provinces, and Exploration Methods*. Edited by WD Goodfellow. Geological Association of Canada, Mineral Deposits Division, Special Publication, 5, 755-791.

Nesbitt, B. E., & Muehlenbachs, K. (1994). Paleohydrogeology of the Canadian Rockies and origins of brines, Pb-Zn deposits and dolomitization in the Western Canada Sedimentary Basin. *Geology*, 22(3), 243-246.

Norris, A.W., & Uyeno, T. T. (1981). *Lower Devonian (Lochkovian) Brachiopods and Conodonts from the 'Delorme' Formation, Cathedral Mountain, Southwestern District of Mackenzie*. Geological survey of Canada.

Olson, R. A. (1984). Genesis of paleokarst and strata-bound zinc-lead sulfide deposits in a Proterozoic dolostone, northern Baffin Island, Canada. *Economic Geology*, 79(5), 1056-1103.

Ootes, L., Morelli, R. M., Creaser, R. A., Lentz, D. R., Falck, H., & Davis, W. J. (2011). The timing of Yellowknife gold mineralization: A temporal relationship with crustal anatexis?. *Economic Geology*, 106(4), 713-720.

Pan, H., & Symons, D. T. A. (1993). Paleomagnetism of the Mississippi Valley - type Newfoundland zinc deposit: Evidence for Devonian mineralization and host rock remagnetization in the northern Appalachians. *Journal of Geophysical Research: Solid Earth*, 98(B12), 22415-22427.

Palmer, M. R., Falkner, K. K., Turekian, K. K., & Calvert, S. E. (1988). Sources of osmium isotopes in manganese nodules. *Geochimica et Cosmochimica Acta*, 52(5), 1197-1202.

Pannalal, S.J., Symons, D.T.A., and Sangster, D.F., 2008a, Paleomagnetic evidence for an Early Permian age of the Lisheen Zn-Pb deposit, Ireland: *Economic Geology*, v. 103, p. 1641–1655.

Pannalal, S.J., Symons, D.T.A., and Sangster, D.F., 2008b, Paleomagnetic evidence of a Variscan age for the epigenetic Galmoy zinc-lead deposit, Ireland: *Terra Nova*, v. 20, p. 385–393.

Paradis, S. J. (2007). *Carbonate-hosted Zn-Pb Deposits in Southern British Columbia: Potential for Irish-type Deposits*. Geological Survey of Canada.

Paradis, S., & Simandl, G. J. (2010) Carbonate-hosted sulphide and nonsulphide Pb-Zn Mineralization, British Columbia, Canada; focus on new exploration criteria.

Paradis, S., Keevil, H., Simandl, G. J., & Raudsepp, M. (2015). Carbonate-hosted nonsulphide Zn–Pb mineralization of southern British Columbia, Canada. *Mineralium Deposita*, 50(8), 923-951.

Paradis, S., & Simandl, G. J. (2016). Is there a genetic link between the SEDEX and MVT deposits of the Canadian Cordillera?. *Targeted Geoscience Initiative*, 107-113.

Paul, M., Reisberg, L., Vigier, N., Zheng, Y., Ahmed, K. M., Charlet, L., & Huq, M. R. (2010). Dissolved osmium in Bengal plain groundwater: Implications for the marine Os budget. *Geochimica et Cosmochimica Acta*, 74(12), 3432-3448.

- Paton, C., Hellstrom, J., Paul, B., Woodhead, J., & Hergt, J. (2011). Iolite: Freeware for the visualisation and processing of mass spectrometric data. *Journal of Analytical Atomic Spectrometry*, 26(12), 2508-2518.
- Patterson, K. M., Powis, K., Sutherland, R. A., & Turner, E. C. (2003). Stratigraphy and structural geology of the Nanisivik area, northern Baffin Island: Geological Survey of Canada Open File 1552.
- Paul, M., Reisberg, L., Vigier, N., Zheng, Y., Ahmed, K. M., Charlet, L., & Huq, M. R. (2010). Dissolved osmium in Bengal plain groundwater: Implications for the marine Os budget. *Geochimica et Cosmochimica Acta*, 74(12), 3432-3448.
- Petke, T., & Diamond, L. W. (1996). Rb–Sr dating of sphalerite based on fluid inclusion-host mineral isochrons: a clarification of why it works. *Economic Geology*, 91(951), e956.
- Peucker - Ehrenbrink, B., & Jahn, B. M. (2001). Rhenium - osmium isotope systematics and platinum group element concentrations: Loess and the upper continental crust. *Geochemistry, Geophysics, Geosystems*, 2(10).
- Pierson-Wickmann, A. C., Reisberg, L., & France-Lanord, C. (2002). Impure marbles of the Lesser Himalaya: another source of continental radiogenic osmium. *Earth and Planetary Science Letters*, 204(1-2), 203-214.
- Quinn, D., Meere, P. A., & Wartho, J. A. (2005). A chronology of foreland deformation: Ultra-violet laser $^{40}\text{Ar}/^{39}\text{Ar}$ dating of syn/late-orogenic intrusions from the Variscides of southwest Ireland. *Journal of Structural Geology*, 27(8), 1413-1425.
- Quinn, D., Meere, P.A., and Wartho, J., 2005, A chronology of foreland deformation: Ultra-violet laser $^{40}\text{Ar}/^{39}\text{Ar}$ dating of syn/late-orogenic intrusions from the Variscides of southwest Ireland: *Journal of Structural Geology*, v. 27, p. 1413–1425.

Ravizza, G., Turekian, K. K., & Hay, B. J. (1991). The geochemistry of rhenium and osmium in recent sediments from the Black Sea. *Geochimica et Cosmochimica Acta*, 55(12), 3741-3752.

Racionero-Gómez, B., Sproson, A. D., Selby, D., Gannoun, A., Gröcke, D. R., Greenwell, H. C., & Burton, K. W. (2017). Osmium uptake, distribution, and 187Os/188Os and 187Re/188Os compositions in Phaeophyceae macroalgae, *Fucus vesiculosus*: Implications for determining the 187Os/188Os composition of seawater. *Geochimica et Cosmochimica Acta*, 199, 48-57.

Reed C.P., and Wallace M.W., 2004, Zn-Pb mineralisation in the Silvermines district, Ireland: A product of burial diagenesis: *Mineralium Deposita*, v. 39, p. 87–102.

Rodushkin, I., Engström, E., Sörlin, D., Pontér, C., & Baxter, D. C. (2007). Osmium in environmental samples from Northeast Sweden. Part II. Identification of anthropogenic sources. *Science of the total environment*, 386(1-3), 159-168.

Root, K. G. (2001). Devonian Antler fold and thrust belt and foreland basin development in the southern Canadian Cordillera: implications for the Western Canada Sedimentary Basin. *Bulletin of Canadian Petroleum Geology*, 49(1), 7-36.

Rowan, E. L., & Goldhaber, M. B. (1995). Duration of mineralization and fluid-flow history of the Upper Mississippi Valley zinc-lead district. *Geology*, 23(7), 609-612.

Rubin, C. M., Miller, M. M., & Smith, G. M. (1990). Tectonic development of Cordilleran mid-Paleozoic volcano-plutonic complexes; Evidence for convergent margin tectonism.

Russell, M.J., 1978, Downward-excavating hydrothermal cells and Irish-type ore deposits: Importance of an underlying thick Caledonian prism: *Transactions of the Institution of Mining and Metallurgy*, v. 87, sec. B (Applied Earth Science), p. 168–171.

Russell, M.J., Solomon, M., and Walshe, J.L., 1981, The genesis of sediment-hosted exhalative zinc + lead deposits: *Mineralium Deposita*, v. 16, p. 113–127.

Sangster, D.F. (1973): Geology of Canadian lead and zinc deposits; *Geological Survey of Canada*, Paper 73-1, Part A, 129-130.

Sangster, D. F. (1990). Mississippi Valley-type and sedex lead-zinc deposits: a comparative examination. *Trans. Inst. Mining and Metall.*, 99, 21-42.

Schneider, J., Quadt, A. V., Wilkinson, J. J., Boyce, A. J., & Andrew, C. J. (2007, August). Age of the Silvermines Irish-type Zn-Pb deposit from direct Rb-Sr dating of sphalerite. In *Digging Deeper: Proceedings of the 9th Biennial Meeting of the Society for Geology Applied to Mineral Deposits, Dublin, Ireland* (pp. 20-23).

Selby, D., & Creaser, R. A. (2003). Re-Os geochronology of organic rich sediments: an evaluation of organic matter analysis methods. *Chemical Geology*, 200(3), 225-240.

Selby, D., & Creaser, R. A. (2004). Macroscale NTIMS and microscale LA-MC-ICP-MS Re-Os isotopic analysis of molybdenite: Testing spatial restrictions for reliable Re-Os age determinations, and implications for the decoupling of Re and Os within molybdenite. *Geochimica et Cosmochimica Acta*, 68(19), 3897-3908.

Selby, D., Kelley, K. D., Hitzman, M. W., & Zieg, J. (2009). Re-Os sulfide (bornite, chalcopyrite, and pyrite) systematics of the carbonate-hosted copper deposits at Ruby Creek, southern Brooks Range, Alaska. *Economic Geology*, 104(3), 437-444.1.

Sharma, M., Papanastassiou, D. A., & Wasserburg, G. J. (1997). The concentration and isotopic composition of osmium in the oceans. *Geochimica et Cosmochimica Acta*, 61(16), 3287-3299.

Sharma, M., Wasserburg, G. J., Hofmann, A. W., & Chakrapani, G. J. (1999). Himalayan uplift and osmium isotopes in oceans and rivers. *Geochimica et Cosmochimica Acta*, 63(23-24), 4005-4012.

Sharma, M., Wasserburg, G. J., Hofmann, A. W., & Butterfield, D. A. (2000). Osmium isotopes in hydrothermal fluids from the Juan de Fuca Ridge. *Earth and Planetary Science Letters*, 179(1), 139-152.

Sharma, M., Balakrishna, K., Hofmann, A. W., & Shankar, R. (2007a). The transport of osmium and strontium isotopes through a tropical estuary. *Geochimica et Cosmochimica Acta*, 71(20), 4856-4867.

Sharma, M., Rosenberg, E. J., & Butterfield, D. A. (2007b). Search for the proverbial mantle osmium sources to the oceans: Hydrothermal alteration of mid-ocean ridge basalt. *Geochimica et Cosmochimica Acta*, 71(19), 4655-4667.

Sharma, M., Chen, C., & Blazina, T. (2012). Osmium contamination of seawater samples stored in polyethylene bottles. *Limnology and Oceanography: Methods*, 10(9), 618-630.

Shirey, S. B., & Walker, R. J. (1995). Carius tube digestion for low-blank rhenium-osmium analysis. *Analytical Chemistry*, 67(13), 2136-2141.

Sherlock, R. L., Lee, J. K., & Cousens, B. L. (2004). Geologic and geochronologic constraints on the timing of mineralization at the Nanisivik zinc-lead Mississippi Valley-type deposit, northern Baffin Island, Nunavut, Canada. *Economic Geology*, 99(2), 279-293.

Shotyk, W., Bicalho, B., Cuss, C. W., Donner, M. W., Grant-Weaver, I., Haas-Neill, S., ... & Zaccone, C. (2017). Trace metals in the dissolved fraction (< 0.45 µm) of the lower Athabasca River: Analytical challenges and environmental implications. *Science of the Total Environment*, 580, 660-669.

Silberling, N.J., Jones, D.L., Monger, J.W.H., Coney, P.J., Berg, H.C. and Plafker, G. (1994). Lithotectonic terrane map of Alaska and adjacent parts of Canada, in Plafker, G. and Berg, H.C., eds., *The Geology of Alaska: Geological Society of America, The Geology of North America*, v. G-1, Plate 3, scale 1:2,500,000.

Singh, A., Palombi, D., Huff, R. (2014), Application of response surface based calibration methods for regional hydrogeological modelling in the Western Canada Sedimentary Basin. Abstract H53B-0853 presented at 2014 Fall Meeting, AGU, San Francisco, Calif., 15-19 Dec

Simandl, G. J., & Paradis, S. (2008). Carbonate-hosted, nonsulphide, zinc-lead deposits in the southern Kootenay arc, British Columbia (NTS 082F/03). *Geological Fieldwork*, 2009-1.

Singer, D.A., 1995, World class base and precious metal deposits – A quantitative analysis: *Economic Geology*, v. 90, p. 88–104.

Smethurst, M. T., Sangster, D. F., Symons, D. T. A., & Lewchuk, M. T. (1999). Paleomagnetic age for Zn-Pb mineralization at Robb Lake, northeastern British Columbia. *Bulletin of Canadian Petroleum Geology*, 47(4), 548-555.

Sommerville, I.D., Strogen, P., Jones, G.L., 1992, Biostratigraphy of Dinantian limestones and associated volcanic rocks in the Limerick Syncline, Ireland: *Geological Journal*, v. 27, p. 201-220.

Smoliar, M. I., Walker, R. J., & Morgan, J. W. (1996). Re-Os ages of group IIA, IIIA, IVA, and IVB iron meteorites. *Science*, 271(5252), 1099-1102.

Stein, H. J., Markey, R. J., Morgan, J. W., Du, A., & Sun, Y. (1997). Highly precise and accurate Re-Os ages for molybdenite from the East Qinling molybdenum belt, Shaanxi Province, China. *Economic Geology*, 92(7-8), 827-835.

Stein, H. J., Sundblad, K., Markey, R. J., Morgan, J. W., & Motuza, G. (1998). Re-Os ages for Archean molybdenite and pyrite, Kuittila-Kivisuo, Finland and Proterozoic molybdenite, Kabeliai, Lithuania: testing the chronometer in a metamorphic and metasomatic setting. *Mineralium Deposita*, 33(4), 329-345.

Stein, H. J., Morgan, J. W., & Scherstén, A. (2000). Re-Os dating of low-level highly radiogenic (LLHR) sulfides: The Harnas gold deposit, southwest Sweden, records continental-scale tectonic events. *Economic Geology*, 95(8), 1657-1671.

Stein, H., Scherstén, A., Hannah, J., & Markey, R. (2003). Subgrain-scale decoupling of Re and ¹⁸⁷Os and assessment of laser ablation ICP-MS spot dating in molybdenite. *Geochimica et Cosmochimica Acta*, 67(19), 3673-3686.

Stravinga, D.B. (2014). Trace element geochemistry and metal mobility of oxide mineralization at the Prairie Creek Zinc-Lead-Silver Deposit, NWT. M.Sc. thesis, Queen's University, Kingston, Ontario, 294 p.

Strogen, P., 1995, Lower Carboniferous volcanic rocks of the Limerick Syncline, in Anderson, I.K., Ashton, J., Earls, G., Hitzman, M., and Tear, S., eds. Irish Carbonate-Hosted Zn-Pb Deposits: Littleton, Colo., Society of Economic Geologists, Inc., Guidebook Series, v. 21, p.75–79.

Sutherland, R. A., & Dumka, D. (1995). Geology of Nanisivik mine, NWT, Canada. *Carbonate-hosted Lead-Zinc-Fluorite-Barite Deposits of North America. Edited by KC Misra. Society of Economic Geologists, Guide Book Series, 22, 4-12.*

Sun, W., Arculus, R. J., Bennett, V. C., Eggins, S. M., & Binns, R. A. (2003). Evidence for rhenium enrichment in the mantle wedge from submarine arc-like volcanic glasses (Papua New Guinea). *Geology*, 31(10), 845-848.

Suzuki, K., Kagi, H., Nara, M., Takano, B., & Nozaki, Y. (2000). Experimental alteration of molybdenite: evaluation of the Re–Os system, infrared spectroscopic profile and polytype. *Geochimica et Cosmochimica Acta*, 64(2), 223-232.

Suzuki, K., Feely, M., & O'Reilly, C. (2001). Disturbance of the Re-Os chronometer of molybdenites from the late-Caledonian Galway Granite, Ireland, by hydrothermal fluid circulation. *Geochemical Journal*, 35(1), 29-35.

Suzuki, K. (2004). Reply to "Accurate and precise Re-Os molybdenite dates from the Galway Granite, Ireland" by D. Selby et al.: Critical comment on "Disturbance of the Re-Os chronometer of molybdenites from the late-Caledonian Galway Granite, Ireland, by hydrothermal fluid circulation". *Geochemical Journal*, 38(3), 295-298.

Symons, D. T. A., & Sangster, D. F. (1991). Paleomagnetic age of the central Missouri barite deposits and its genetic implications. *Economic Geology*, 86(1), 1-12.

Symons, D. T. A., Pan, H., Sangster, D. F., & Jowett, E. C. (1993). Paleomagnetism of the Pine Point Zn-Pb deposits. *Canadian Journal of Earth Sciences*, 30(5), 1028-1036.

Symons, D. T. A., MacDonald, M., Lewchuk, M. R., & Sangster, D. F. (1996). Late Cretaceous age for the Monarch-Kicking Horse Mississippi Valley-type deposit in the southern Rocky Mountains of Canada from paleomagnetism. *EOS*, 77, 160.

Symons, D. T. A., Lewchuk, M. T., & Sangster, D. F. (1998). Laramide orogenic fluid flow into the Western Canada sedimentary basin; evidence from paleomagnetic dating of the Kicking Horse Mississippi valley-type ore deposit. *Economic Geology*, 93(1), 68-83.

Symons, D. T. A., Symons, T. B., & Sangster, D. F. (2000). Paleomagnetism of the Society Cliffs dolostone and the age of the Nanisivik zinc deposits, Baffin Island, Canada. *Mineralium Deposita*, 35(7), 672-682.

Symons, D. T. A., Smethurst, M. T., & Ashton, J. H. (2002). Paleomagnetism of the Navan Zn-Pb deposit, Ireland. *Economic Geology*, 97(5), 997-1012.

Symons, D. T. A., Pannalal, S. J., Kawasaki, K., Sangster, D. F., Stanley, G. A., & Andrew, C. J. (2007). Paleomagnetic age of the Magcobar Ba deposit, Silvermines, Ireland. *Mineral exploration and research: Digging deeper: Dublin, Irish Association for Economic Geology*, 377-380.

Taylor, S., 1984, Structural and paleotopographic controls of lead-zinc mineralization in the Silvermines orebodies, Republic of Ireland: *Economic Geology*, v. 79, p. 529–548.

Thompson, R. I. (1989). Stratigraphy, tectonic evolution and structural analysis of the Halfway River map area (94B), northern Rocky Mountains, British Columbia. *Geological Survey of Canada*, 425, 1-119.

Torrealdy, H. I., Hitzman, M. W., Stein, H. J., Markley, R. J., Armstrong, R., & Broughton, D. (2000). Re-Os and U-Pb dating of the vein-hosted mineralization at the Kansanshi copper deposit, northern Zambia. *Economic Geology*, 95(5), 1165-1170.

Tossell, J. A. (2005). Calculation of the UV-visible spectra and the stability of Mo and Re oxysulfides in aqueous solution. *Geochimica et cosmochimica Acta*, 69(10), 2497-2503.

Turner, E. C. (2009). Mesoproterozoic carbonate systems in the Borden Basin, Nunavut. *Canadian Journal of Earth Sciences*, 46(12), 915-938.

Turner, E. C. (2011). Structural and stratigraphic controls on carbonate-hosted base metal mineralization in the Mesoproterozoic Borden Basin (Nanisivik District), Nunavut. *Economic Geology*, 106(7), 1197-1223.

Turner, E. C., Long, D. G., Rainbird, R. H., Petrus, J. A., & Rayner, N. M. (2016). Late Mesoproterozoic rifting in Arctic Canada during Rodinia assembly: impactogens, trans - continental far - field stress and zinc mineralisation. *Terra Nova*, 28(3), 188-194.1.

Van Acken, D., Su, W., Gao, J., & Creaser, R. A. (2014). Preservation of Re - Os isotope signatures in pyrite throughout low - T, high - P eclogite facies metamorphism. *Terra Nova*, 26(5), 402-407.

Vernon, R., Holdsworth, R. E., Selby, D., Dempsey, E., Finlay, A. J., & Fallick, A. E. (2014). Structural characteristics and Re–Os dating of quartz-pyrite veins in the Lewisian Gneiss Complex, NW Scotland: Evidence of an Early Paleoproterozoic hydrothermal regime during terrane amalgamation. *Precambrian Research*, 246, 256-267.

Vinsova, H., Konirova, R., Koudelkova, M., & Jedinakova-Krizova, V. (2004). Sorption of technetium and rhenium on natural sorbents under aerobic conditions. *Journal of Radioanalytical and nuclear chemistry*, 261(2), 407-413.

Völkening, J., Walczyk, T., & Heumann, K. G. (1991). Osmium isotope ratio determinations by negative thermal ionization mass spectrometry. *International Journal of Mass Spectrometry and Ion Processes*, 105(2), 147-159.

Vorlicek, T. P., Kahn, M. D., Kasuya, Y., & Helz, G. R. (2004). Capture of molybdenum in pyrite-forming sediments: role of ligand-induced reduction by polysulfides 1. *Geochimica et Cosmochimica Acta*, 68(3), 547-556.

Von Quadt, A., Erni, M., Martinek, K., Moll, M., Peytcheva, I., & Heinrich, C. A. (2011). Zircon crystallization and the lifetimes of ore-forming magmatic-hydrothermal systems. *Geology*, 39(8), 731-734.

Waters, C.N., Somerville, I.D., Jones, N.S., Cleal, C.K., Collinson, J.D., Waters, R.A., Besly, B.M., Dean, M.T., Stephenson, M.H., Davies, J.R., Freshney, E.C., Jackson, D.I., Mitchell, W.I., Powell, J.H., Barclay, W.J., Browne, M.A.E, Leveridge, B.E., Long, S.L., and Maclean, D., 2011, A Revised Correlation of Carboniferous Rocks in the British Isles: The Geological Society of London Special Report 26, 188 p.

Wheeler, J.O. & McFeely, P. 1991. Tectonic assemblage map of the Canadian Cordillera and adjacent parts of the United States of America: Geological Survey of Canada, Map 1712A, scale 1:2,000,000.

Wilkinson, J. J. (2010). A review of fluid inclusion constraints on mineralization in the Irish ore field and implications for the genesis of sediment-hosted Zn-Pb deposits. *Economic Geology*, 105(2), 417-442.

Wilkinson, J.J., 2014, Sediment-hosted zinc-lead mineralization: Processes and perspectives, in Scott, S.D., ed., *Geochemistry of Mineral Deposits: Treatise on Geochemistry*, 2nd Edition, v. 13, p. 219–249.

Wilkinson, J.J.. and Hitzman, M.W, 2014, The Irish Zn-Pb Orefield: The View from 2014. In S.M. Archibald and S.J. Piercey, eds., *Current Perspectives in Zinc Deposits*. Irish Association of Economic Geology, 59-73.

Wilkinson, J. J., Eyre, S. L., & Boyce, A. J. (2005). Ore-forming processes in Irish-type carbonate-hosted Zn-Pb deposits: Evidence from mineralogy, chemistry, and isotopic composition of sulfides at the Lisheen mine. *Economic Geology*, 100(1), 63-86.

Woodcock, N., and Strachan, R., 2000, *Geological history of Britain and Ireland: Oxford, Blackwell Science*, 423 p.

Woodhouse, O. B., Ravizza, G., Falkner, K. K., Statham, P. J., & Peucker-Ehrenbrink, B. (1999). Osmium in seawater: vertical profiles of concentration and isotopic composition in the eastern Pacific Ocean. *Earth and Planetary Science Letters*, 173(3), 223-233.

Wu, N., Farquhar, J., & Strauss, H. (2014). $\delta^{34}\text{S}$ and $\Delta^{33}\text{S}$ records of Paleozoic seawater sulfate based on the analysis of carbonate associated sulfate. *Earth and Planetary Science Letters*, 399, 44-51.

- Xiong, Y. (2003). Solubility and speciation of rhenium in anoxic environments at ambient temperature and applications to the Black Sea. *Deep Sea Research Part I: Oceanographic Research Papers*, 50(5), 681-690.
- Yamashita, Y., Takahashi, Y., Haba, H., Enomoto, S., & Shimizu, H. (2007). Comparison of reductive accumulation of Re and Os in seawater–sediment systems. *Geochimica et Cosmochimica Acta*, 71(14), 3458-3475.
- York, D. (1968). Least squares fitting of a straight line with correlated errors. *Earth and planetary science letters*, 5, 320-324.
- Yin, L., Li, J., Liu, J., Li, C., Sun, S., Liang, H., & Xu, J. (2017). Precise and accurate Re–Os isotope dating of organic-rich sedimentary rocks by thermal ionization mass spectrometry with an improved H₂O₂-HNO₃ digestion procedure. *International Journal of Mass Spectrometry*, 421, 263-270.
- Zhang, L., Xiao, W., Qin, K., Qu, W., & Du, A. (2005). Re–Os isotopic dating of molybdenite and pyrite in the Baishan Mo–Re deposit, eastern Tianshan, NW China, and its geological significance. *Mineralium Deposita*, 39(8), 960-969.
- Zhang, P., Huang, X. W., Cui, B., Wang, B. C., Yin, Y. F., & Wang, J. R. (2016). Re-Os isotopic and trace element compositions of pyrite and origin of the Cretaceous Jinchang porphyry Cu-Au deposit, Heilongjiang Province, NE China. *Journal of Asian Earth Sciences*, 129, 67-80.
- Zimmerman, A., Stein, H.J., Morgan, J.W., Markey, R.J., and Watanabe, Y., 2014, Re-Os geochronology of the El Salvador porphyry Cu-Mo deposit, Chile: Tracking analytical improvements in accuracy and precision over the past decade: *Geochimica et Cosmochimica Acta*, v. 131, p. 13–32.